Copernicus Marine Service Ocean State Report, Issue 4

Karina von Schuckmann ((Editor)), Pierre-Yves Le Traon ((Editor)), Neville Smith (Chair) ((Review Editor)), Ananda Pascual ((Review Editor)), Samuel Djavidnia ((Review Editor)), Jean-Pierre Gattuso ((Review Editor)), Marilaure Grégoire ((Review Editor)), Glenn Nolan ((Review Editor)), Signe Aaboe , Enrique Álvarez Fanjul , Lotfi Aouf , Roland Aznar , T. H. Badewien , Arno Behrens , Maristella Berta , Laurent Bertino , Jeremy Blackford , Giorgio Bolzon , Federica Borile , Marine Bretagnon , Robert J.W. Brewin , Donata Canu , Paola Cessi , Stefano Ciavatta , Bertrand Chapron , Thi Tuyet Trang Chau , Frédéric Chevallier , Boriana Chtirkova , Stefania Ciliberti , James R. Clark , Emanuela Clementi , Clément Combot , Eric Comerma , Anna Conchon , Giovanni Coppini , Lorenzo Corgnati , Gianpiero Cossarini , Sophie Cravatte , Marta de Alfonso , Clément de Boyer Montégut , Christian De Lera Fernández , Francisco Javier de los Santos , Anna Denvil-Sommer , Álvaro de Pascual Collar , Paulo Alonso Lourenco Dias Nunes , Valeria Di Biagio , Massimiliano Drudi , Owen Embury , Pierpaolo Falco , Odile Fanton d'Andon , Luis Ferrer , David Ford , H. Freund , Manuel García León , Marcos García Sotillo , José María García-Valdecasas , Philippe Garnesson , Gilles Garric , Florent Gasparin , Marion Gehlen , Ana Genua-Olmedo , Gerhard Geyer , Andrea Ghermandi , Simon A. Good , Jérôme Gourrion , Eric Greiner , Annalisa Griffa , Manuel González , Annalisa Griffa , Ismael Hernández-Carrasco , Stéphane Isoard , John J. Kennedy , Susan Kay , Anton Korosov , Kaari Laanemäe , Peter E. Land , Thomas Lavergne , Paolo Lazzari , Jean-François Legeais , Benedicte Lemieux , Bruno Levier , William Llovel , Vladyslav Lyubartsev , Pierre-Yves Le Traon , Vidar S. Lien , Leonardo Lima , Pablo Lorente , Julien Mader , Marcello G. Magaldi , Ilja Maljutenko , Antoine Mangin , Carlo Mantovani , Veselka Marinova , Simona Masina , Elena Mauri , J. Meyerjürgens , Alexandre Mignot , Robert McEwan , Carlos Mejia , Angélique Melet , Milena Menna , Benoît Meyssignac , Alexis Mouche , Baptiste Mourre , Malte Müller , Giulio Notarstefano , Alejandro Orfila , Silvia Pardo , Elisaveta Peneva , Begoña Pérez-Gómez , Coralie Perruche , Monika Peterlin , Pierre-Marie Poulain , Nadia Pinardi , Yves Quilfen , Urmas Raudsepp , Richard Renshaw , Adèle Révelard , Emma Reyes-Reyes , M. Ricker , Pablo Rodríguez-Rubio , Paz Rotllán , Eva Royo Gelabert , Anna Rubio , Inmaculada Ruiz-Parrado , Shubha Sathyendranath , Jun She , Karina von Schuckmann , Cosimo Solidoro , Emil V. Stanev , Joanna Staneva , Andrea Storto , Jian Su , Tayebeh Tajalli Bakhsh , Gavin H. Tilstone , Joaquín Tintoré , Cristina Toledano , Jean Tournadre , Benoit Tranchant , Rivo Uiboupin , Arnaud Valcarcel , Nadezhda Valcheva , Nathalie Verbrugge , Mathieu Vrac , J.-O. Wolff , Enrico Zambianchi , O. Zielinski , Ann-Sofie Zinck & Serena Zunino

OCEAN STATE REPORT

European Commission

Copernicus
Europe's eyes on Earth

Copernicus
Marine Service

Implemented by
MERCATOR OCEAN
INTERNATIONAL

Taylor & Francis
Taylor & Francis Group

INSTITUTE OF
MARINE
Engineering, Science & Technology

Journal of Operational Oceanography

Aims and scope

The *Journal of Operational Oceanography* will publish papers which examine the role of oceanography in contributing to the fields of:

• Numerical Weather Prediction
• Development of Climatologies
• Implications of Ocean Change
• Ocean and Climate Forecasting
• Ocean Observing Technologies
• Eutrophication
• Climate Assessment
• Shoreline Change
• Marine and Sea State Prediction
• Model Development and Validation
• Coastal Flooding
• Reducing Public Health Risks
• Short-Range Ocean Forecasting
• Forces on Structures
• Ocean Policy
• Protecting and Restoring Ecosystem health
• Controlling and Mitigating Natural Hazards
• Safe and Efficient Marine Operations

The *Journal of Operational Oceanography* will also publish papers which address the requirements of the:

• Global Ocean Observing System (GOOS)
• Global Climate Observing System (GCOS)
• Global Monitoring for Environment and Security (GMES)
• Global Earth Observing System of Systems (GEOSS)

The *Journal of Operational Oceanography* will also publish papers which address the needs of one or more of a wide range of end user communities including:

• Shipping
• Marine Energy
• Weather Services
• Fishing
• Port Management
• Wastewater Management
• Search and Rescue
• National Security
• Charting and Navigational Services
• Public Health
• Conservation
• Insurance and Re-insurance
• Recreation and tourism
• Marine Mineral Extraction
• Environmental Regulation
• Education
• Aquaculture
• Coastal Management

All submitted manuscripts are subject to initial appraisal by the Editor, and, if found suitable for further consideration, enter peer review by independent, anonymous expert referees. All peer review is single blind.

Authors are requested to submit manuscripts via the journal's online submission system following the Instructions for Authors.

Submitting to *Journal of Operational Oceanography*

For more information about the journal and guidance on how to submit, please see www.tandfonline.com/tjoo

COPERNICUS MARINE SERVICE OCEAN STATE REPORT, ISSUE 4

Editors

Karina von Schuckmann   Pierre-Yves Le Traon

Review Editors

Neville Smith (Chair)   Ananda Pascual   Samuel Djavidnia

Jean-Pierre Gattuso   Marilaure Grégoire   Glenn Nolan

Cover photo: Eric Cros – www.seastemic.com

AUTHOR AFFILIATIONS (ALPHABETICAL BY NAME)

Signe Aaboe, MET Norway, Norway
Enrique Álvarez Fanjul, Puertos del Estado, Spain
Lotfi Aouf, Météo-France, France
Roland Aznar, Nologin - Puertos del Estado, Spain
T. H. Badewien, Institute for Chemistry and Biology of the Marine Environment, University of Oldenburg, Germany
Arno Behrens, Helmholtz Zentrum Geesthacht, Germany
Maristella Berta, National Research Council of Italy, Institute of Marine Sciences, Italy
Laurent Bertino, Nansen Center (NERSC), Norway
Jeremy Blackford, Plymouth Marine Laboratory, UK
Giorgio Bolzon, National Institute of Oceanography and Applied Geophysics, Italy
Federica Borile, University of Bologna, Euro-Mediterranean Center on Climate Change, Italy
Marine Bretagnon, ACRI-ST, France
Robert J.W. Brewin, University of Exeter, Plymouth Marine Laboratory, UK
Donata Canu, National Institute of Oceanography and Applied Geophysics, Itlay
Paola Cessi, Scripps Institution of Oceanography, USA
Stefano Ciavatta, Plymouth Marine Laboratory, UK
Bertrand Chapron, LOPS/Ifremer, France
Thi Tuyet Trang Chau, Laboratoire des sciences du climat et de l'environnement, France
Frédéric Chevallier, Laboratoire des sciences du climat et de l'environnement, France
Boriana Chtirkova, Sofia University "St. Kliment Ohridski", Bulgaria
Stefania Ciliberti, Fondazione Centro Euro-Mediterraneo sui Cambiamenti Climatici, Italy
James R. Clark, Plymouth Marine Laboratory, UK
Emanuela Clementi, Euro-Mediterranean Center on Climate Change, Italy
Clément Combot, LOPS/Ifremer, France
Eric Comerma, RPS Ocean Science, USA
Anna Conchon, CLS, France
Giovanni Coppini, Euro-Mediterranean Center on Climate Change, Italy
Lorenzo Corgnati, National Research Council of Italy, Institute of Marine Sciences, Lerici, Italy
Gianpiero Cossarini, National Institute of Oceanography and Applied Geophysics, Italy
Sophie Cravatte, LEGOS, Université de Toulouse, IRD, CNES, CNRS, UPS, Toulouse, France
Marta de Alfonso, Puertos del Estado, Spain
Clément de Boyer Montégut, LOPS/Ifremer, France
Christian De Lera Fernández, Centro de Seguridad Marítima Integral Jovellanos, Salvamento Marítimo, Gijón, Spain
Francisco Javier de los Santos, Algeciras Bay Port Authority, Spain
Anna Denvil-Sommer, Laboratoire des sciences du climat et de l'environnement, France
Álvaro de Pascual Collar, Nologin - Puertos del Estado, Spain
Paulo Alonso Lourenco Dias Nunes, Food and Agriculture Organization of the United Nations, Climate, Biodiversity, Land and Water Department, Itlay
Valeria Di Biagio, National Institute of Oceanography and Applied Geophysics, Italy
Massimiliano Drudi, Euro-Mediterranean Center on Climate Change, Italy
Owen Embury, University of Reading, UK
Pierpaolo Falco, Università degli Studi di Napoli Parthenope, Consorzio Nazionale Interuniversitario per le Scienze del Mare, Italy
Odile Fanton d'Andon, ACRI-ST, France
Luis Ferrer, AZTI-Marine Research, Pasaia, Spain
David Ford, Met Office, UK
H. Freund, Institute for Chemistry and Biology of the Marine Environment, University of Oldenburg, Germany
Manuel García León, Universitat Politecnica de Catalunya - Puertos del Estado, Spain
Marcos García Sotillo, Puertos del Estado, Spain
José María García-Valdecasas, Puertos del Estado, Spain
Philippe Garnesson, ACRI-ST, France
Gilles Garric, Mercator Ocean international, France
Florent Gasparin, Mercator Ocean international, France
Marion Gehlen, Laboratoire des sciences du climat et de l'environnement, France
Ana Genua-Olmedo, Department of Biology & CESAM, University of Aveiro, Portugal
Gerhard Geyer, Helmholtz Zentrum Geesthacht, Germany
Andrea Ghermandi, Department of Natural Resources and Environmental Management, University of Haifa, Israel
Simon A. Good, Met Office, UK
Jérôme Gourrion, OceanScope, France
Eric Greiner, CLS, France
Annalisa Griffa, National Research Council of Italy, Institute of Marine Sciences, Lerici, Italy

(Continued from previous page)

Manuel González, AZTI Marine Research, Pasaia, Spain
Annalisa Griffa, National Research Council of Italy, Institute of Marine Sciences, Italy
Ismael Hernández-Carrasco, Mediterranean Institute for Advanced Studies (CSIC-UIB), Esporles, Spain
Stéphane Isoard, European Environment Agency, Denmark
John J. Kennedy, Met Office, UK
Susan Kay, Plymouth Marine Laboratory, Met Office, UK
Anton Korosov, Nansen Center (NERSC), Norway
Kaari Laanemäe, Tallinn University of Technology, Estonia
Peter E. Land, Plymouth Marine Laboratory, UK
Thomas Lavergne, MET Norway, Norway
Paolo Lazzari, National Institute of Oceanography and Applied Geophysics, Italy
Jean-François Legeais, CLS, France
Benedicte Lemieux, Fondazione Centro Euro-Mediterraneo sui Cambiamenti Climatici, Italy
Bruno Levier, Mercator Ocean international, France
William Llovel, LLOVEL, LOPS/CNRS, France
Vladyslav Lyubartsev, Euro-Mediterranean Center on Climate Change, Italy
Pierre-Yves Le Traon, Mercator Ocean international, France
Vidar S. Lien, Institute of Marine Research, Norway
Leonardo Lima, Fondazione Centro Euro-Mediterraneo sui Cambiamenti Climatici, Italy
Pablo Lorente, NOLOGIN / Puertos del Estado, Spain
Julien Mader, AZTI Marine Research, Pasaia, Spain
Marcello G. Magaldi, National Research Council of Italy, Institute of Marine Sciences, Italy
Ilja Maljutenko, Tallinn University of Technology, Estonia
Antoine Mangin, ACRI-ST, France
Carlo Mantovani, National Research Council of Italy, Institute of Marine Sciences, Italy
Veselka Marinova, Institute of Oceanology - Bulgarian Academy of Sciences, Bulgaria
Simona Masina, Euro-Mediterranean Center on Climate Change, Italy
Elena Mauri, National Institute of Oceanography and Applied Geophysics, Italy
J. Meyerjürgens, Institute for Chemistry and Biology of the Marine Environment, University of Oldenburg, Germany
Alexandre Mignot, Mercator Ocean international, France
Robert McEwan, Met Office, UK
Carlos Mejia, Laboratoire d'océanographie et du climat, France
Angélique Melet, Mercator Ocean international, France
Milena Menna, National Institute of Oceanography and Applied Geophysics, Italy
Benoît Meyssignac, LEGOS, France
Alexis Mouche, LOPS/Ifremer, France
Baptiste Mourre, SOCIB - Balearic Islands Coastal Ocean Observing and Forecasting System-, Palma. Spain
Malte Müller, MET Norway, Norway
Giulio Notarstefano, National Institute of Oceanography and Applied Geophysics, Italy
Alejandro Orfila, Mediterranean Institute for Advanced Studies (CSIC-UIB), Esporles, Spain
Silvia Pardo, Plymouth Marine Laboratory, UK
Elisaveta Peneva, Sofia University "St. Kliment Ohridski", Bulgaria
Begoña Pérez-Gómez, Puertos del Estado, Spain
Coralie Perruche, Mercator Ocean international, France
Monika Peterlin, European Environment Agency, Denmark
Pierre-Marie Poulain, National Institute of Oceanography and Applied Geophysics, Italy
Nadia Pinardi, University of Bologna, Department of Physics and Astronomy, Italy
Yves Quilfen, LOPS/Ifremer, France
Urmas Raudsepp, Tallinn University of Technology, Estonia
Richard Renshaw, Met Office, UK
Adèle Révelard, SOCIB - Balearic Islands Coastal Ocean Observing and Forecasting System-, Palma. Spain
Emma Reyes-Reyes, SOCIB - Balearic Islands Coastal Ocean Observing and Forecasting System-, Palma. Spain
M. Ricker, Institute for Chemistry and Biology of the Marine Environment, University of Oldenburg, Oldenburg, Germany
Pablo Rodríguez-Rubio, Huelva Port Authority, Spain
Paz Rotllán, SOCIB - Balearic Islands Coastal Ocean Observing and Forecasting System-, Palma. Spain
Eva Royo Gelabert, European Environment Agency, Denmark
Anna Rubio, AZTI Marine Research, Pasaia, Spain
Inmaculada Ruiz-Parrado, SOCIB - Balearic Islands Coastal Ocean Observing and Forecasting System-, Palma. Spain
Shubha Sathyendranath, Plymouth Marine Laboratory, UK
Jun She, Danish Meteorological Institute, Denmarek
Karina von Schuckmann, Mercator Ocean international, France
Cosimo Solidoro, National Institute of Oceanography and Applied Geophysics, Italy

(Continued from previous page)

Emil V. Stanev, Institute of Coastal Research, Helmholtz-Zentrum Geesthacht, Institute for Chemistry and Biology of the Marine Environment, University of Oldenburg, Germany

Joanna Staneva, Helmholtz Zentrum Geesthacht, Germany

Andrea Storto, Fondazione Centro Euro-Mediterraneo sui Cambiamenti Climatici, Centre for Maritime Research and Experimentation, Itlay

Jian Su, Danish Meteorological Institute, Denmark

Tayebeh Tajalli Bakhsh, RPS Ocean Science, USA

Gavin H. Tilstone, Plymouth Marine Laboratory, UK

Joaquín Tintoré, SOCIB - Balearic Islands Coastal Ocean Observing and Forecasting System-, Palma, Mediterranean Institute for Advanced Studies, Spain

Cristina Toledano, Nologin - Puertos del Estado, Spain

Jean Tournadre, LOPS/Ifremer, France

Benoit Tranchant, CLS, France

Rivo Uiboupin, Tallinn University of Technology, Estonia

Arnaud Valcarcel, University of Otago, Ocean Physics, New Zealand

Nadezhda Valcheva, Institute of Oceanology - Bulgarian Academy of Sciences, Bulgaria

Nathalie Verbrugge, CLS, France

Mathieu Vrac, Laboratoire des sciences du climat et de l'environnement, France

J.-O. Wolff, Institute for Chemistry and Biology of the Marine Environment, University of Oldenburg, Germany

Enrico Zambianchi, Università degli Studi di Napoli Parthenope, Consorzio Nazionale Interuniversitario per le Scienze del Mare, Itlay

O. Zielinski, Institute for Chemistry and Biology of the Marine Environment, University of Oldenburg, German Research Center for Artificial Intelligence (DFKI), RG Marine Perception, Germany

Ann-Sofie Zinck, Physics of Ice, Climate and Earth, Niels Bohr Institute, University of Copenhagen, Denmark

Serena Zunino, National Institute of Oceanography and Applied Geophysics, Italy

Journal of Operational Oceanography

Special Issue: Copernicus Marine Service Ocean State Report, Issue 4

CONTENTS

Taylor & Francis
Taylor & Francis Group

Chapter 1: Introduction and the European Environment policy framework

Section 1.1. Introduction and main outcomes

Authors: Karina von Schuckmann, Pierre-Yves Le Traon

The ocean is a central element of the Earth system and dominates the global water, energy and carbon cycles (Abram et al. 2019; von Schuckmann et al. 2019). Human communities depend heavily upon the goods and services provided by the ocean. These include provisioning services that directly provide human sustenance (e.g. fisheries, raw materials, renewable energy); regulating services (e.g. carbon and heat uptake); cultural services for cultural experiences, tourism, and identity to humans; and supporting services (e.g. primary production and the provision of marine habitats) (e.g. Bindoff et al. 2019).

However, changes to the ocean have impacted these ocean services and stretched them to unsustainable limits. As stated in the Intergovernmental Panel on Climate Change (IPCC) Special Report on Ocean and Cryosphere (IPCC SROCC), major ocean stressors from climate change include ocean warming, ocean acidification, sea level rise, loss of oxygen and sea ice retreat (IPCC 2019). The IPCC SROCC further assessed that the projected responses of the ocean to past and current human-induced greenhouse gas emissions and ongoing global warming include climate feedbacks, changes over decades to millennia that cannot be avoided, thresholds of abrupt change, and irreversibility. Human communities in close connection with the ocean environment – including also those a bit further from the coast (as of 2010, 28% of the global population (1.9 billion people) were living in areas less than 100 km from the coastline and less than 100 m above sea level, including 17 major cities which are each home to more than 5 million people (IPCC 2019) – are particularly exposed to changes in the ocean, such as for example through extreme weather events and sea level rise. More than ever a long term, comprehensive and systematic monitoring, assessment and reporting of the ocean is required to ensure a sustainable science-based management of the ocean for societal benefit.

The development of the annual Copernicus Marine Service (CMEMS) Ocean State Report is one of the priority tasks given by the EU Delegation Agreement for the CMEMS implementation (CMEMS 2014). The Ocean State Report activity was launched with the publication of the first OSR (von Schuckmann et al. 2016), together with a summary for policy makers (see https://marine.copernicus.eu/science-learning/ocean-state-report/). Currently, the Ocean State Report activity is in its fourth cycle of reporting of the state, variability and change in the marine environment.

The report is organised within four principal chapters (Figure 1.1.1):

- Chapter 1 provides the introduction and a synthesised overview, together with an informative box on the European Environment policy framework established in collaboration with European Environment Agency (EEA).
- Chapter 2 includes various new scientific analysis methods covering aspects in the marine environment and addressing various time scales, including long-term trends, year-to-year variations, seasonal variations, and shorter time scales.
- Chapter 3 aims to report on specific characteristics and processes taking place in the marine environment, while also discussing the societal and economic benefit.
- Chapter 4 highlights specific events during the year 2018.

The major outcomes of the fourth issue of the Copernicus Marine Service Ocean State Report are synthesised in Figure 1.1.2.

The reporting and indicators are focused on the seven Copernicus Marine Service regions, i.e. the global ocean, the Arctic, the North-West-Shelf, the Iberia-Biscay-Ireland, the Baltic Sea, the Mediterranean Sea and the Black Sea. The fourth issue of the OSR provides a view on changes in the marine environment concentrating on the period 1993 to 2018, and a specific focus on the year 2018. The uncertainty assessment based on a 'multi-product-approach' is also used here (see von Schuckmann et al. 2018 for more details). The OSR is predominantly based on CMEMS products. An overview on all products can be found on the web
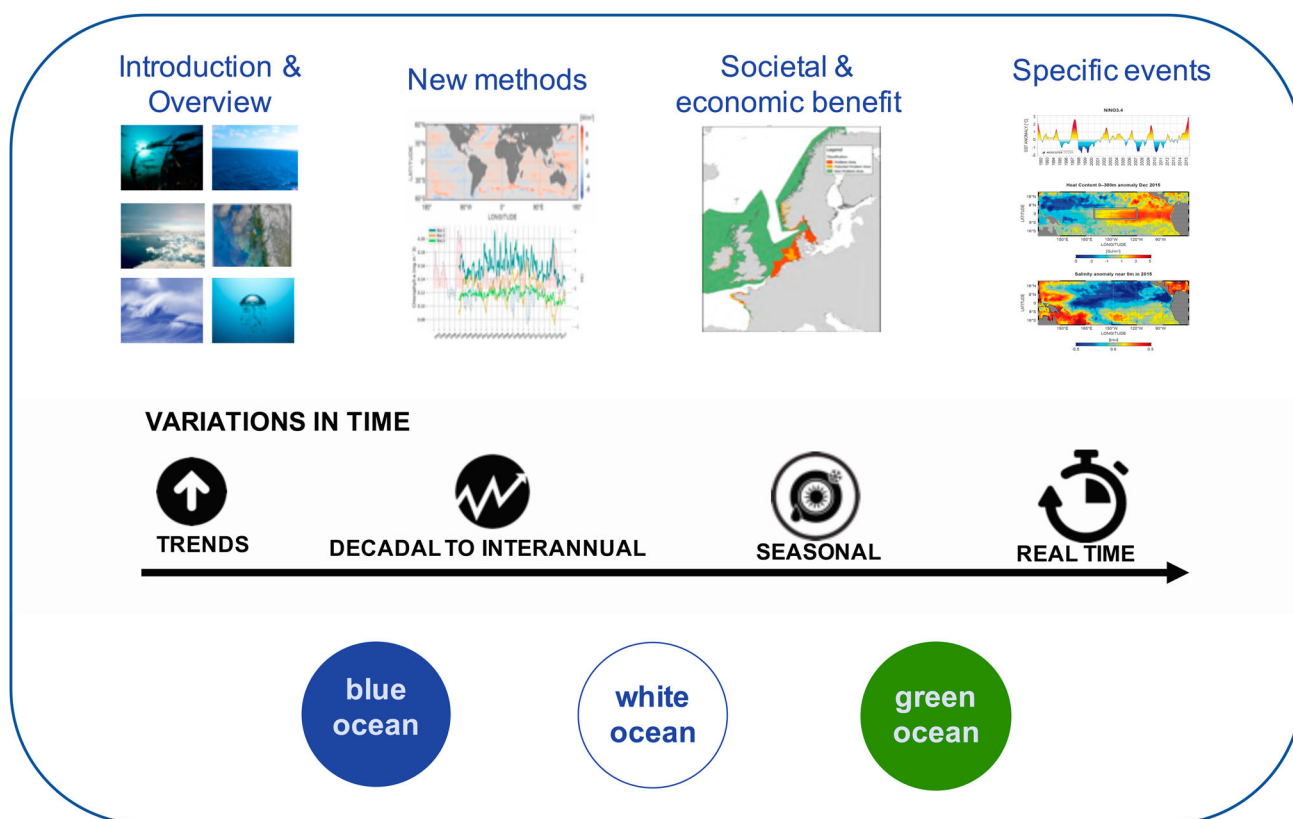
Figure 1.1.1. Schematic presentation of the organisation of the Copernicus Marine Service Ocean State Report, which contains three principal chapters, introduced by an overview chapter. Topics cover aspects of the blue (e.g. thermo & hydrodynamics), the green (e.g. biogeochemical processes), and the white ocean (e.g. sea ice), and tackle various variations in time, covering past changes to close to real time.

portal (https://marine.copernicus.eu/wp-content/uploads/catalogue-cmems.pdf). CMEMS includes both satellite and in-situ high level products prepared by the Thematic Assembly Centres (TACs) – including reprocessed products – and modelling and data assimilation products prepared by Monitoring and Forecasting Centres (MFCs). Products are described in Product User Manuals (PUMs) and their quality in the Quality Evaluation Documents (QUID; include a reference). Within this report, all CMEMS products used are linked to their product name, and download links to corresponding QUID and PUM documents are provided. A few additional products have been used, in particular from the Copernicus Climate Change Service. All data sources are given in the corresponding sections.

1.1.1. Summary of outcomes of chapter 2

In chapter 2, marine diatoms obtained from remote sensing data have been analysed in the North Atlantic Ocean (Section 2.1). Marine diatoms generate most of the organic matter that serves as food for life in the ocean; their changes can influence global climate, atmospheric carbon dioxide concentration and marine ecosystem function; and a large part of oxygen consumption through photosynthesis is carried out by diatoms. The results show that diatom chlorophyll concentration during the spring bloom was on record low since 1997, and the period of diatom dominance has decreased by one week over 1993–2018. Primary production (Section 2.2) is at the base of oceanic food-webs, and results show that major hot spots of most productive areas are located in coastal areas, as well as in the Arctic Ocean. Over the past 20 years, a small significant decrease of primary production is reported. In the Mediterranean Sea, primary production has slightly increased over the same period.

Also, in chapter 2, a study on barrier layer thickness has been performed in the tropical Pacific (Section 2.3). Barrier layers act to isolate the mixed layer from the cooler waters below, and changes in thickness have thus the potential to influence the ocean heat budget, the Madden Julian Oscillation, tropical cyclones, and the development of El Nino events. Knowledge on barrier layer thickness is thus an important indicator for sub-seasonal and seasonal forecasting. Results show that the barrier layer is generally thickening over 1993–2018 in the western Pacific and thinning in the central Pacific.
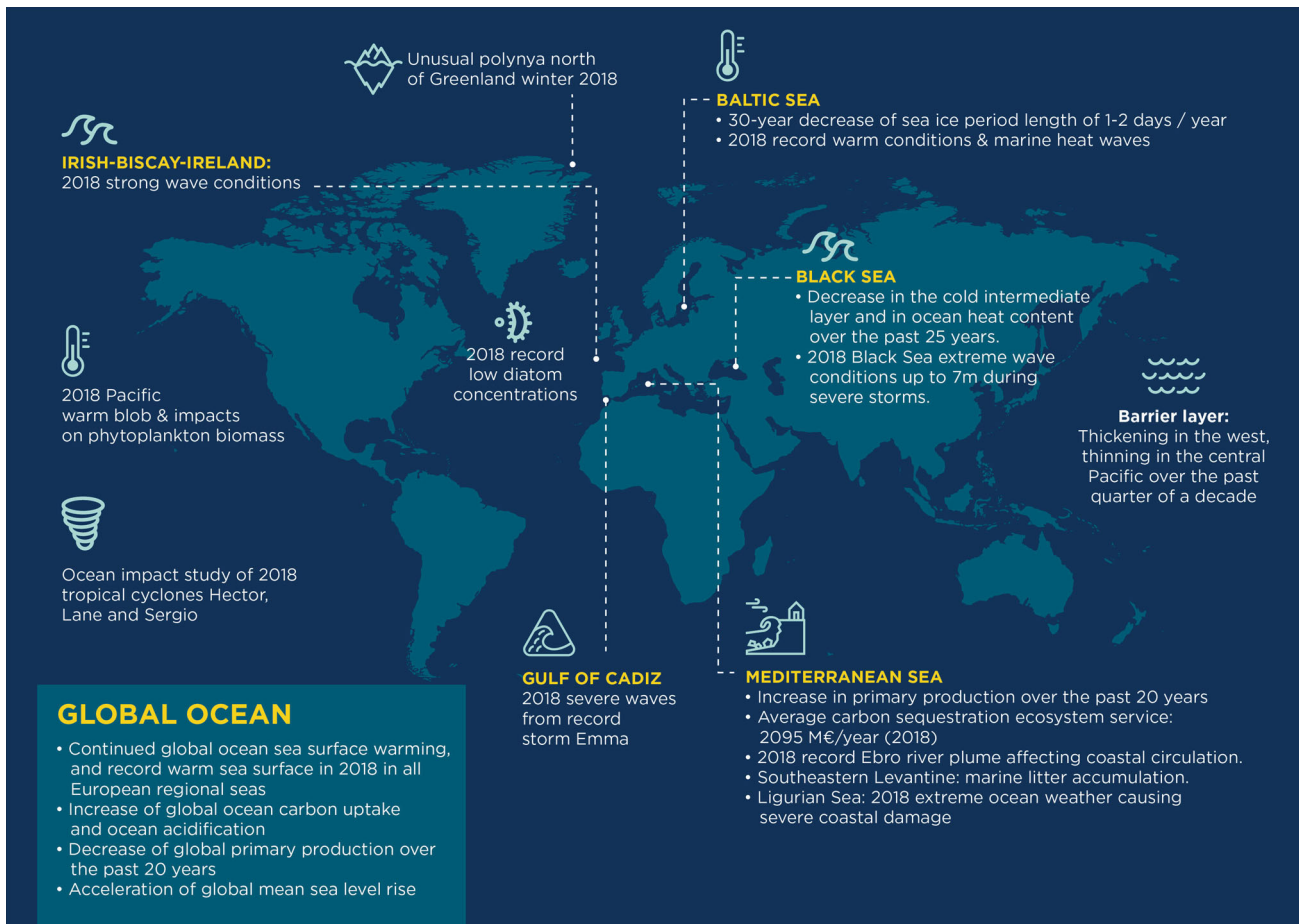
Figure 1.1.2. Overview on the major outcomes of the fourth issue of the Copernicus Marine Service Ocean State Report.

Section 2.4 describes an indicator for the Mediterranean Sea Meridional Overturning Circulation – the major circulation system in this regional sea. Outcomes of this study highlight the basin-wide impacts of the so called 'Eastern Mediterranean Transient'. Studies in the Black Sea show a decrease of the Cold Intermediate Layer thickness (Section 2.5) and in upper ocean heat content (Section 2.6) over the past 25 years, which represent a major threat for the Black Sea thermohaline balance and ecosystem function.

Extreme waves can entail severe impacts over the coastal environment and infrastructures. A specific study in the Iberia-Biscay-Ireland region (Section 2.7) reports 3–5% higher-than-average incidence of strong wave conditions in the open ocean at latitudes south of 50°N, but do not show significant trends of the strong wave conditions over the period 1992–2017. Depicting the Lagrangian behaviour of surface currents in terms of residence times in coastal zones is key to identify high-risk scenarios for pollution of the coastal areas and to quantify transport and retention of larvae or other planktonic organisms, with impact for fishery and Marine Protected Areas management. Such a

study has been performed in two pilot coastal study areas of the Mediterranean Sea (Section 2.8).

A study of sea surface temperatures (Section 2.9) reveals that between 1993 and 2018, the global average linear trend amounts to 0.014 ± 0.001°C/year (95% confidence interval) with warming trends occurring over most of the globe. The average temperature in 2018 was cooler than the previous three years. This reflects changes from El Niño to La Niña conditions during that time, although El Niño thresholds were again reached by the end of 2018. The European sea surface temperatures were high, linked to severe heat waves in large areas of Europe. Since the onset of the industrial era the ocean took up about 28% of the excess CO_2 emitted to the atmosphere by human activities, which results in ocean acidification. Results in Section 2.10 show that the ocean carbon sink increased over the period of reconstruction at a rate of 0.08 ± 0.1 PgC yr^{-1}, mirrored by a negative trend in global mean pH of 0.0017 ± 0.0002 pH units over the past two decades. These studies have the potential to provide new methods for the CMEMS Ocean Monitoring Indicator framework.

1.1.2. Summary of outcomes of chapter 3

Chapter 3 provides studies that have immediate socio-economic relevance. Global mean sea level rise is a key indicator of the on-going global warming. In Section 3.1, global mean sea level rise amounts to 3.1 ± 0.4 mm/yr (90% confidence level) over the altimetry era (1993-present), with an acceleration of 0.12 ± 0.073 mm/yr^2. Section 3.2 tackles a subset of the Oslo-Paris (OSPAR) indicators for eutrophication, and results show that eutrophication was low in the year 2018 in most known problem areas, including coastal areas within the Southern North Sea.

In Section 3.3, the average carbon sequestration ecosystem service value for the Mediterranean Sea basin and at the Exclusive Economic Zone (EEZ) level has been derived. The average value for the Mediterranean Sea is 1733 M€/year for the period 2004–2014 and 2095 M€/year for 2018. Yearly updates of this information on the basis of both ecological and economic trends is of great added value for natural capital accounting.

Section 3.4 assesses a down-stream service for Search and Rescue operators and marine emergency responders (IBISAR). The results highlight the importance of a state-of-the-art skill assessment of all models available in a specific period of interest, since it can have a significant impact in minimising the response time, optimising search area planning, thus finally improving search and rescue and pollution control operations. Section 3.5 analyses ocean circulation patterns in the Mediterranean Sea and reinforces the work of the scientific-societal communities in defining the southeastern Levantine basin as the most critical area of marine litter accumulation.

1.1.3. Summary of outcomes of chapter 4

An unusual opening in the sea-ice pack (also called polynya) occurred north of Greenland mid-winter 2018 (Section 4.1). Never before has a polynya of such dimensions been observed during winter in this region of the Arctic Ocean, which is known for its very compact and thick sea ice. Section 4.2 discusses sea ice conditions (sea ice extent, ice probability, ice mobility and start, end and length of the ice period) in the Baltic Sea for the period 1982–2019. The Bothnian Bay, the Bothnian Sea, the Gulf of Finland and the Gulf of Riga are covered by sea ice during winter. Results show that the Baltic sea ice conditions are heavily impacted by climate modes such as the North Atlantic Oscillation. Moreover, in the Bothnian Bay, the northeastern Gulf of Finland, coastal and archipelago areas, the ice processes are dominated by ice thermodynamics, while in the Bothnian Sea, the southern and central Gulf of Finland and the Gulf of

Riga, by the ice dynamics and are characterised by high ice mobility (i.e. drift ice conditions). Finally, it is reported that the ice period length has a statistically significant trend between −1 and −2 days/year in the almost entire Bothnian Bay.

The northeast Pacific experienced unusual warm and fresh near-surface water conditions in 2018, the so called 'warm blob' as reported in Section 4.3. The results also discuss how these warm anomalies impacted phytoplankton biomass. In Section 4.4, record warm conditions in the Baltic sea over the past 37 years are reported, and the area had experienced strong marine heat waves over the entire summer period (May–September), particularly in the southern Baltic Sea. Tropical Cyclones are among the most devastating and destructive natural hazards. Section 4.5 demonstrates the benefit of combined use remote sensing data and subsurface ocean measurements during the year 2018 (storms 'Hector', 'Lane' and 'Sergio') for improved prediction of the intensity and evolution of tropical cyclones.

The Gulf of Cadiz region suffered the most severe wave storm over the past 20 years produced by the storm Emma in March 2018. The combined effect of high waves and sea level surge aggravated the storm risk potential. Section 4.6 shows how the CMEMS products, the local wave and sea level forecasting systems (PORTUS system) and their associated alerts and downstream services worked properly. Warnings were sent in advance to the users. Several actions were carried out to mitigate the impact of the event. For example, harbours stopped operations to prevent accidents and assure safety. The material damages were considerable but, probably due to the preventive actions, no personal damages were suffered.

Over the past decade, European seas have been affected by severe storms, which caused serious damages in offshore and coastal zones, and particularly the Black Sea had been hit by severe storms at the beginning of 2018. Section 4.7 analyses the wave conditions during these events, and the maximum value of the significant wave height reached more than 7 m. Moreover, the predictability of the expected largest wave heights during the winter marine storms in 2018 is demonstrated.

The understanding of the 'ocean weather' and related processes that can modify horizontal and vertical transport is necessary to comprehend bio-physical interactions that may have a significant impact on the coastal marine ecosystems (e.g. fisheries, primary production, carbon budget, etc.). Section 4.8 investigates ocean weather conditions in 2018 which caused extensive damage along the coast of the Ligurian Sea in the western Mediterranean Sea. Section 4.9 describes a study of circulation reversal in the North Sea through a

combined use of GPS-drifter observations and CMEMS model results. The results demonstrate that the CMEMS surface current products agree well with drifter observations, even under extreme wind conditions, which adds to their credibility. The year 2018 was characterised by a record Ebro river plume affecting Mediterranean Sea surface circulation (Section 3.10). This was the most extreme event recorded over the past 15 years in the western Mediterranean Sea.

1.1.4. CMEMS and the COVID-19 crisis

Mercator Ocean International has taken all measures needed to ensure a nominal level of service for EU Copernicus Marine Service. Despite exceptional working conditions, the service provision has remained state-of-the-art and operational during the first semester of 2020.

MOi has regularly monitored the CMEMS operational production during this crisis. At the time of writing, no operational issues were noted, i.e. neither serious slow-down in input data flows (observations), nor alarming slow-down in output data flows (user downloads). Focusing on the in-situ data stream, all the automatic stations (HF Radars, Tide gauges, Moorings, Argo, Gliders, drifting buoys) have been operating normally; a medium-term concern could come from the lack of maintenance of such stations, stopped during the present situation, that may affect the data delivery later in autumn and winter. A decrease has been detected in the Ferrybox and Research Vessel data flow, since the majority of vessels had to return to port. The stop of the research vessels could notably affect some of the biogeochemical and carbon time series, however this might become noticeable only in the coming months when updated products will be released. Depending on the different countries, the European research vessels are expected to resume their activities between early June and early September. This together with the temporary closure of some instrument manufacturers may also impact the deployment of Argo floats and drifters, leading to a potential decrease in the number of observations in the coming months since re-seeding cannot be done.

Section 1.2. The EU environment policies and the European Green Deal

Authors: Monika Peterlin, Stéphane Isoard, Eva Royo Gelabert

1.2.1. Introduction

This section provides an overview of the EU's main policies and related legislations that are currently in place to guide the sustainable use of Europe's and global seas and oceans. EU legislation usually sets the guidelines and requirements on how the environment should be monitored (e.g. data, information, indicators) and progress reported. In the last decades, monitoring was developed for many environmental topics and has led to a substantial increase in data availability, especially with regards to climate change, air pollution and related human activities. In this context, the monitoring of seas and oceans needs to be strengthened to provide a solid data set and informed knowledge platform that further supports progress towards the sustainable use of Europe's and global seas and oceans.

A comprehensive European policy framework is being implemented to guide the sustainable use of our seas and oceans. This framework is adressing individual human activities, sectors, pressures, species and habitats, and entire ecosystems through individual pieces of policy and legislation, which are all framed by four overarching policy initiatives providing a clear vision of ecological sustainability to be reached by 2050 (Figure 1.2.1). These 'framing' policies are the European Green Deal, the 7th and 8th Environmental Action Plans (EAP), the EU Biodiversity Strategies to 2020 and to 2030 (EC 2011; EU 2020), and the EU Action Plan for the circular economy (EC 2020b; EEA 2020). These policies pursue the following objectives: (i) to protect, conserve and enhance the EU's natural capital; (ii) to turn the EU into a resource-efficient, green and competitive low-carbon economy and (iii) to safeguard the EU's citizens from environment-related pressures and risks to their health and well-being. The 8th EAP, starting from 2021, is expected to be adopted by the European Commission before the end of 2020 for subsequent adoption by the European Parliament and the Council.

1.2.1. The European Green Deal and links to international initiatives

The *European Green Deal (*EU 2019a*)* outlines the primary political objectives of the current (2020–2024) European Commission. Its main goal is making the EU's economy sustainable, which is understood, *inter alia*, as being climate neutral. It envisages turning climate and environmental challenges into opportunities across all policy areas and making the transition just and inclusive for all. As such, it is supposed to guide and influence the work at EU, regional, national, and local levels for the years to come. The Green Deal, which was put forward by the new Commission in 2019, brings new targets and calls for improved cooperation among EU institutions at all levels. It focuses, amongst other topics, on climate change,
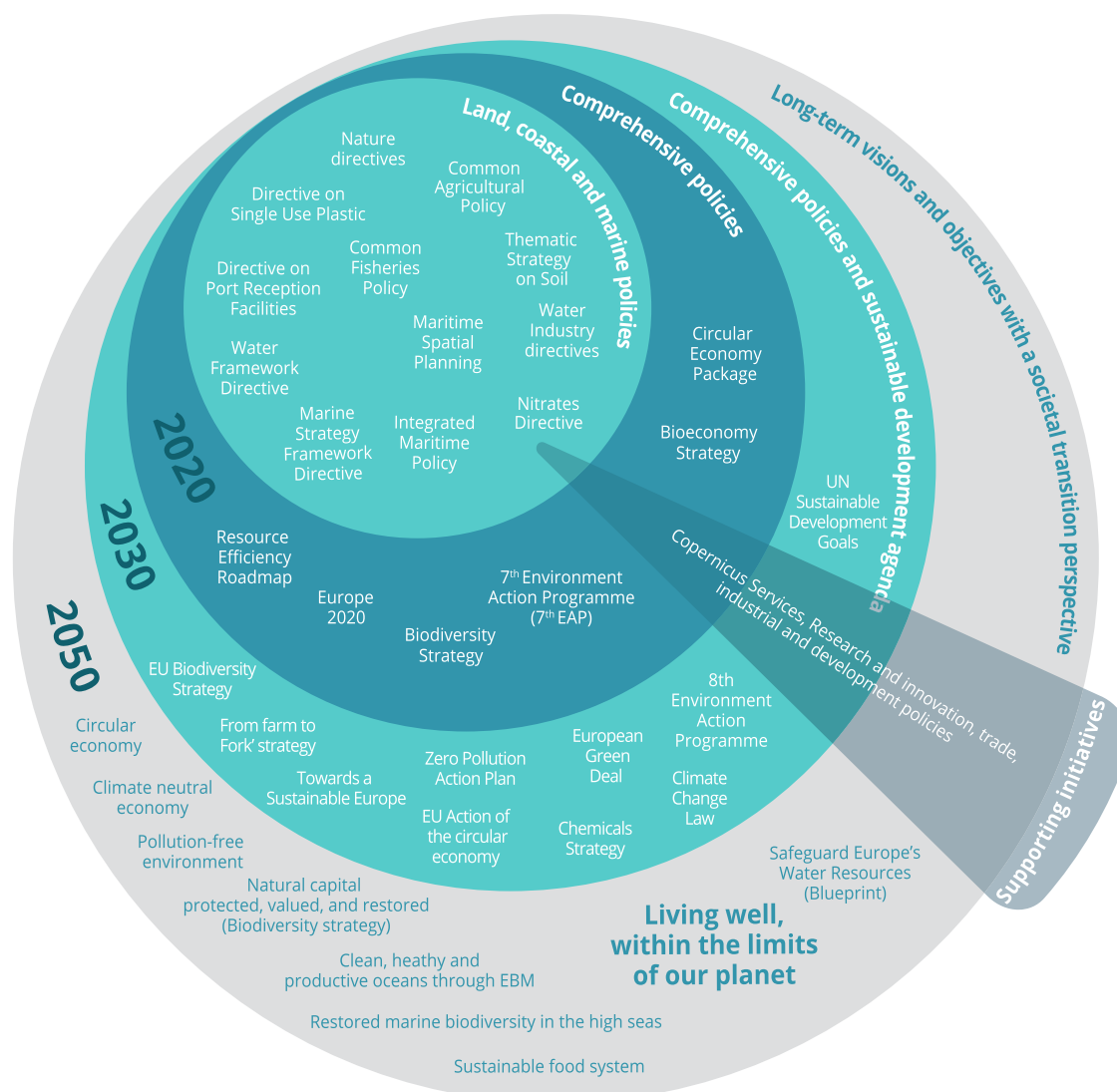
Figure 1.2.1. An illustration of EU legislation and policies relevant for the maintenance of Europe's seas ecosystem capital, including human activities using marine natural capital and those capable of impacting marine ecosystems through land-based and atmospheric emissions and freshwater discharges. Source: EEA (2016).

biodiversity conservation and restoration, farming, fishing and aquaculture, zero pollution, chemicals and a circular economy. The scope is very broad, and strong emphasis is given to implementing existing legislation and policy; improving policy reporting, monitoring and review; and achieving a comprehensive, informed management of human activities. The Green Deal also envisages the introduction of new policy and legislative initiatives. Several of these are relevant for seas and oceans including a new *8th EAP*, which is expected to bring, among others, a new monitoring and outlook mechanism to ensure that the EU remains on track to meet its environmental objectives.

The renewed EU *Biodiversity Strategy* to 2030, proposed in May 2020, aims at continuing the fight against biodiversity loss (IPBES 2018; EC 2020a; EEA 2020). The 2030 Biodiversity Strategy addresses the key gaps that

were identified in the implementation of its predecessor (EC 2011), including insufficient data, monitoring and reporting tools, which hamper evaluating the success of protective measures, in particular for marine areas (Herold et al. 2019; EEA 2020). The 2030 Biodiversity Strategy includes a series of ambitious targets addressing protected areas (i.e. widening the network to 30% of land and marine space, with 10% under strict protection) and restoration through 14 key commitments, including: legally binding nature restoration targets; the full implementation of the Marine Strategy Directive (MSFD; EU 2008b), Common Fisheries Policy (CFP; EU 2008a; EC 2013) and Birds and Habitats Directives (EEC 1992; EC 2009) and an ecosystem-based approach to the marine environment; a reduction of 50% in nutrients loss, of 20% in fertilisers use and of 50% in pesticides use.

The *EU Climate Action policy* aims at supporting implementation of the Paris Agreement (UNFCCC 2015), which sets the ambitious goal to stop the increase in the global average temperature to below 2°C above pre-industrial levels and to pursue efforts to limit the temperature increase to 1.5°C above pre-industrial levels. The *European Green Deal* also brings new targets for fighting climate change, including an EU climate-neutrality commitment for 2050. A key instrument to achieve that is the European Climate Law (EC 2020c), which was proposed by the European Commission in March 2020.

A *'From farm to Fork' strategy*[1] is also included in the European Green Deal. Its objective is to ensure that food remains safe, nutritious and of high quality across the EU. In addition, food must be produced with minimum impact on nature. This strategy is, thus, closely related to the EU Biodiversity Strategy to 2030, the Zero-pollution Action Plan and to the implementation of European Climate Law.

The Green Deal also includes a strategy to eliminate pollution, the *Zero-pollution Action Plan*, which will address pollution in air, soil, waters and oceans.[2] Its ultimate objective is to reach a 'pollution-free environment' by 2050. The Zero-pollution Action Plan is expected to be published in 2021. It will aim to achieve clean waters, preserve terrestrial and aquatic biodiversity, reduce pollution from excess nutrients and other substances (link to the 'Farm to Fork' Strategy, see above), reduce pollution from plastics and from pharmaceuticals, and prevent air and noise pollution. A strong focus will also be placed on developing tools for regular monitoring and outlook provision, with a global perspective.

Sustainable development is addressed in the Commission's publication 'Towards a Sustainable Europe in 2030 (EC 2020b), which presents the sustainable development challenges facing the EU and the advantages from having the Union as a whole tackling them, as well as outlines scenarios for the future development of EU policy to achieve that. Globally, the concepts of 'planetary boundaries' and 'safe operating space' are at the core of the UN Agenda 2030 (UN 2015a), and the 17 Sustainable Development Goals (SDG) aiming at achieving a sustainable future for humankind by 2030. SDG 14 ('Life below water') aims at protecting ocean health, focussing on conservation, reduction of pressures and their impacts, and the sustainable and fair use of seas and oceans (UN 2015b). It is closely related to, amongst others, SDG 6 and SDG 13. The EU has adopted and embraced these goals, which are to be delivered through a series of policies and legislation (EEA 2020).

The UN Decade of Ocean Science for Sustainable Development (2021–2030) implementation plan will be discussed and agreed in 2020. As currently drafted, the mission of the Decade is to 'generate and use knowledge for the transformational action needed to achieve a healthy, safe, and resilient ocean for sustainable development by 2030 and beyond'. Activities under the auspices of the Decade aim 'to support efforts to reverse the cycle of decline in ocean health and create improved conditions for sustainable development of the Ocean' (UNESCO 2020). The Vision of the Science decade is to develop ocean Science that is fit for purpose and will encourage the science community, the policy-makers, the private sector and the civil society to think beyond business as usual and aspire for real change (UN 2019; UNESCO 2020); main objectives defined are to achieve:

- A clean ocean where sources of pollution are identified and removed;
- A sustainably harvested and productive ocean ensuring the provision of food supply;
- A healthy and resilient ocean where marine ecosystems are mapped and protected;
- A safe ocean where people are protected from ocean hazards;
- A predictable ocean where society has the capacity to understand current and future ocean conditions;
- A transparent ocean with open access to data, information and technologies.

The European Green Deal embraces objectives of international initiatives and agreements, such as the UN 2030 Agenda on Sustainable Development (UN 2015a), the UN Convention on Biological Diversity, the UN Framework Convention on Climate Change, and the UN Decade of Ocean Science (UNESCO 2020). The EU will strive to reach a major global agreement on marine biodiversity in the high seas (e.g. UNCLOS BBNJ) and improve management of oceans in general in view of climate change.[3] A common thread across the European Green Deal strategies is a requirement for a strengthened process for policy implementation, reporting, monitoring and review.

1.2.2. Main European environmental acquis addressing oceans

1.2.2.1. The integrated maritime policy

The EU Integrated maritime policy (IMP) seeks to provide a coherent approach to maritime activities and issues. This includes increased coordination between various policy areas (e.g. fisheries, environmental protection, maritime sectors and blue growth) in order to promote a 'sustainable blue economy' (EC 2007; EU 2016).

As such, it guides 'blue growth', where the EU's maritime economy – referred to as the 'Blue economy' – is a driver of socio-economic growth and of ocean-based industries. Coastal and maritime activities include traditional/established sectors, such as fishing, shipping, tourism, aquaculture and the extraction of non-living resources, as well as emerging sectors, such as offshore renewable energies, desalination, blue biotechnology and the extraction of mineral resources specifically in the deep-sea (EC 2019a, 2019d). All these sectors use the natural capital held in Europe's seas one way or another.

Maritime transport remains a key element of global trade and the economy. In the EU alone, it handles 75% of the its external trade and 35% of all intra EU trade. The maritime transport sector is also working towards its sustainability. The European Commission's Directives on Port Reception Facilities (EC 2019a) and Single Use Plastic (EC 2019b), seek to reduce the discharges of waste from ships, and further improve the efficiency of maritime operations in ports, by seeking to ensure that more waste is delivered on shore, in particular garbage, including waste from the fishing sector such as derelict fishing gear. They also aim to contribute to the Circular Economy, by improving the adequacy of waste reception facilities, in particular as regards their environmental operation.

The IMP is supported by the EU Common Fisheries Policy (CFP; EU 2008a; EC 2013) and other sectoral legislation (e.g. on short sea shipping), and it should be implemented in a coherent way through the Maritime Spatial Planning Directive (MSPD, EU 2014; ETC/ICM 2019; EEA 2020). MSPD sets the basis for management of European waters more coherently given the competition for space. The IMP aims at ensuring human activities take place in an efficient, safe and sustainable way. Its ambition is to reduce conflicts, encourage investments, increase cross-border cooperation and protect the environment through implementation of MSFD, which is its environmental pillar.

Fisheries play a key role when considering the sustainable use of marine resources. The CFP went through many revisions since 1970s to make fisheries environmentally, economically and socially sustainable. The rationale behind this was that fair exploitation means healthier fish stocks, larger catches, more money and and more jobs at sea and on land. The geographical scope for the application of the CFP and its effectiveness differs significantly among Europe's seas. Decreased fishing pressure in recent years has translated into significant progress in reaching maximum sustainable yields for commercially exploited fish and shellfish stocks in the North-East Atlantic Ocean and Baltic Sea, meeting EU policy targets for fishing mortality or reproductive

capacity or both in 2017 (EEA 2019). Most of the assessed commercially exploited fish and shellfish stocks in the Mediterranean Sea and Black Sea were still overfished in 2017 (EEA 2019). This means that the CFP's 2020 objective requiring that all stocks across all EU marine regions are exploited at such a rate, which is also reflected in the MSFD, is unlikely to be met (EEA 2019).

1.2.2.2. The marine strategy framework directive

The Marine Strategy Framework Directive (MSFD; EU 2008b) is the first EU legislation specifically devoted to the marine environment. It is designed as the environmental pillar of the IMP because it defines the sustainable use of Europe's seas through the concept of 'good environmental status' (GES). The MSFD is, therefore, the main driver to achieve clean, healthy and productive seas and oceans across the EU.

The MSFD aims at protecting and restoring the marine environment and phasing out pollution, so that there are no significant impacts on or risks to marine biodiversity, human health and the legitimate use of marine resources. It enshrines an ecosystem-based management approach in EU marine policy to ensure the sustainable use of the marine environment for current and future generations. It actually requires the achievement of 'good environmental status' (GES) in all EU marine waters by 2020 (EEA 2020). This objective is defined in detail by the Commission Decision 2017/848 (EU 2017a, 2017b) through a series of elements grouped into 11 GES descriptors; namely: D1 biodiversity, D2 non-indigenous species, D3 commerical fish and shellfish, D4 foodwebs, D5 eutrophication, D6 seafloor integrity, D7 hydrographic conditions, D8 contaminants (in the environment), D9 contaminants in food for human consumption, D10 marine litter, D11 underwater noise. The directive follows a 6-yearly cycle by which Member States need to define GES and GES targets for their marine waters, and which should be done in coordination with others within the same marine region. Then they need to draw marine strategies to achieve those targets, which should include assessments of the current situation and management measures to maintain or improve the situation to reach GES.

Climate change was not explicitly addressed in the MSFD, but physical and chemical elements that are relevant for the assessment of pressures caused by climate change are included in the Descriptor 7 – hydrographic conditions (EU 2017a, 2017b). This means that, unless these elements are monitored and assessed, managemet measures to reduce climate change impacts on hydrographic conditions won't be effective in delivering GES for D7. However, climate change impacts can go beyond

that. So a challenge for MSFD implementation is to include geographical and climatic conditions in the assessment of the state of Europes' seas and in the management of human activities upon them. Thus, these conditions all affect the state of marine predominant habitats and the distribution and abundance of marine species, and whether these can keep or reach GES. The understanding of how climate change can affect GES is required for ecosystem-based management of land-based and sea-based human activities, will need to be supported by relevant data flows and assessment schemes. The same challenge is faced for the implementation of the European Climate Law.

1.2.3. The need for coherent data and knowledge on the oceans to support EU policy implementation

Human society has always been dependent on the seas. Failure to reach good environmental status for our seas and oceans is not an option. Marine ecosystem services sustain people by providing us with vital direct inputs, such as seafood to eat and oxygen to breathe. They also provide about 30% of global climate regulation contributing to the habitability of our ambient environment, which is under increasing pressure. All recent EU and global assessments of the state of seas and ocean give a coherent general message: we are not doing well (EEA 2020). In the EU, this is mainly through insufficient implementation of the current environmental acquis. Europe is not reaching objectives defined in agreed legislations, monitoring is not sufficient and data availability does not support informed integrated management (ETC/ICM 2019).

All EU policies stated above need coherent and timely data on the state of our seas to support an effective and timely policy implementation. The Copernicus Programme has shown that its products can be instrumental in supporting EU policies. For example, products from the Copernicus Monitoring Atmosphere Service are directly supporting implementation of legislation on air pollution and climate change; and CORINE Land Cover products, from the Copernicus Land Monitoring Service, are used in the implementation of several policies, like the Water Framework Directive (EU 2000). The Copernicus Marine Environment Monitoring Service (CMEMS) provides various services for marine applications and a host of Ocean Monitoring Indicators, especially at global level. There is a high potential for the work undertaken by CMEMS to contribute significantly to the implementation of EU policies that need to be supported by timely and high quality data and information. This is instrumental in order to support decision-making

and implement an ecosystem-based management approach for Europe's seas. CMEMS is increasingly considered one of the few key tools able to deliver reliable, coherent and timely data to further support the implementation of EU environmental and climate policy. There is a need to better use the scientific work that has been developed sucessfully since Copernicus is operational, and develop reliable, high-resolution marine products that match directly the needs of EU marine and maritime policies. This would support Member States' efforts to achieve their objectives, close the implementation gap and feed into the European Green Deal's monitoring mechanism to ensure that the EU is on track to meet its environmental and climate objectives.

Establishing cooperation both at EU level and across European regions is instrumental to support a coherent approach to the implementation of environmental policy, the effective management of human activities in Member States, and support the European Commision's effort to measure progress towards a good condition of marine, terrestrial, and freshwater ecosystems and biodiversity. In this context, the EU Copernicus Marine Environment Monitoring Service, in cooperation with the European Environment Agency and its Eionet network, could provide additional support to this process in future. At present CMEMS and EEA cooperate particularly with regard to the use of CMEMS products in EEA activities and the Ocean State Reports. The new EU policy developments, which carry ambitious targets, require state-of-the-art implementation of environmental measures based on actionable data and knowldge, which in turn stem from closer strategic cooperation.

Notes

1. https://www.foodnavigator.com/Article/2020/03/17/EU-farm-to-fork-strategy-aims-to-feed-sustainable-food-system.
2. https://ec.europa.eu/commission/presscorner/detail/en/fs_19_6729.
3. https://ec.europa.eu/commission/commissioners/2019-2024/sinkevicius/announcements/commissioner-virginijus-sinkevicius-keynote-speech-conference-sustainable-oceans-future-call-green_en.

References

Section 1.1

Abram N, Gattuso J-P, Prakash A, Cheng L, Chidichimo MP, Crate S, Enomoto H, Garschagen M, Gruber N, Harper S, et al. 2019. Framing and context of the report. In: Pörtner HO, Roberts DC, Masson-Delmotte V, Zhai P, Tignor M, Poloczanska E, Mintenbeck K, Alegría A, Nicolai M, Okem A, Petzold J, Rama B, Weyer NM, editors. IPCC

special report on the ocean and cryosphere in a changing climate, in press; p. 73–129. https://www.ipcc.ch/srocc/.

Bindoff NL, Cheung WWL, Kairo JG. 2019. Changing oean, marine ecosystems, and dependent communities. In: Pörtner HO, Roberts DC, Masson-Delmotte V, Zhai P, Tignor M, Poloczanska E, Mintenbeck K, Alegría A, Nicolai M, Okem A, Petzold J, Rama B, Weyer NM, editors. Special report: the ocean and cryosphere in a changing climate summary for policymakers, in press; p. 447–587. https://www.ipcc.ch/report/srocc/.

CMEMS. 2014. Technical annex to the delegation agreement with Mercator Ocean for the implementation of the Copernicus Marine Environment Monitoring Service (CMEMS). https://www.copernicus.eu/sites/default/files/library/CMEM_TechnicalAnnex_PUBLIC.docx.pdf.

IPCC. 2019. Summary for policymakers. In: Pörtner HO, Roberts DC, Masson-Delmotte V, Zhai P, Tignor M, Poloczanska E, Mintenbeck K, Alegría A, Nicolai M, Okem A, Petzold J, Rama B, Weyer NM, editors. Special report: the ocean and cryosphere in a changing climate summary for policymakers, in press. https://www.ipcc.ch/srocc/.

von Schuckmann K, Traon P-YL, Alvarez-Fanjul E, Axell L, Balmaseda M, Breivik L-A, Brewin RJW, Bricaud C, Drevillon M, Drillet Y, et al. 2016. The Copernicus marine environment monitoring service ocean state report. J Oper Oceanogr. 9(Suppl. 2):s235–s320. DOI:10.1080/1755876X.2016.1273446.

von Schuckmann K, Le Traon P-Y, Smith N, Pascual A, Brasseur P, Fennel K, Djavidnia S, Aaboe S, Fanjul EA, Autret E, et al. 2018. Copernicus marine service ocean state report. J Oper Oceanogr. 11(supp. 1):S1–S142. doi:10.1080/1755876X.2018.1489208.

von Schuckmann K, Le Traon P-Y, Smith N, Pascual A, Djavidnia S, Gattuso J-P, Grégoire M, Nolan G, Aaboe S, Aguiar E, et al. 2019. Copernicus marine service ocean state report, issue 3. J Oper Oceanogr. 12:S1–S123. doi:10.1080/1755876X.2019.1633075.

Section 1.2

EC. 2007. Communication from the Commission to the Council, the European Parliament, the European Economic and Social Committee and the Committee of the Regions — an integrated maritime policy for the European Union (COM(2007) 575 final).

EC. 2009. Directive 2009/147/EC of the European Parliament and of the Council of 30 November 2009 on the conservation of wild birds, OJ L 20, 26.1.2010, p. 7–25, ELI: https://data.europa.eu/eli/dir/2009/147/oj.

EC. 2011. Communication from the Commission to the European Parliament, the Council, the European Economic and Social Committee and the Committee of the Regions., Our life insurance, our natural capital: an EU biodiversity strategy to 2020 /* COM/2011/0244 final */.

EC. 2013. General union environment action programme to 2020 — living well, within the limits of our planet. Luxembourg: Publications Office of the European Union. [accessed 2019 Oct 7]. https://publications.europa.eu/en/publication-detail/-/publication/1d861dfb-ae0c-4638-83ab-69b234bde376.

EC. 2019a. Directive (EU) 2019/883 of the European Parliament and of the Council of 17 April 2019 on port reception facilities for the delivery of waste from ships, amending Directive 2010/65/EU and repealing Directive 2000/59/EC. ELI: http://data.europa.eu/eli/dir/2019/883/oj.

EC. 2019b. Directive (EU) 2019/904 of the European Parliament and of the Council of 5 June 2019 on the reduction of the impact of certain plastic products on the environment. ELI: http://data.europa.eu/eli/dir/2019/904/oj.

EC. 2019c. Reflection Paper, Towards a Sustainable Europe by 2030, COM(2019) 22 final. https://eur-lex.europa.eu/legal-content/EN/ALL/?uri=COM%3A2019%3A22%3AFIN

EC. 2019d. The EU blue economy report. Luxembourg: European Commission, Publications Office of the European Union.

EC. 2020a. Communication from the Commission to the European Parliament, the Council, the European Economic and Social Committee and the Committee of the Regions. EU Biodiversity Strategy for 2030 Bringing nature back into our lives. COM/2020/380 final. https://eur-lex.europa.eu/legal-content/EN/TXT/?qid=1590574123338&uri=CELEX:52020DC0380

EC. 2020b. Communication from the Commission to the European Parliament, the Council, the European Economic and Social Committee and the Committee of the Regions. A new Circular Economy Action Plan. COM(2020) 98 final. https://ec.europa.eu/environment/circular-economy/pdf/new_circular_economy_action_plan_annex.pdf

EC. 2020c. REGULATION OF THE EUROPEAN PARLIAMENT AND OF THE COUNCIL establishing the framework for achieving climate neutrality and amending Regulation (EU) 2018/1999 (European Climate Law). https://ec.europa.eu/info/sites/info/files/commission-proposal regulation-european-climate-law-march-2020_en.pdf.

EEA. 2016. Seafood in Europe, EEA Report No 25/2016, European Environment Agency.

EEA. 2019. The European environment — state and outlook 2020: knowledge for transition to a sustainable Europe. European Environment Agency. [accessed 2019 Dec 9]. https://www.eea.europa.eu/soer-2020.

EEA. 2020. Marine messages II, EEA Report No 17/2019, European Environment Agency. https://www.eea.europa.eu/publications/marine-messages-2.

EEC. 1992. Council Directive 92/43/EEC of 21 May 1992 on the conservation of natural habitats and of wild fauna and flora. OJ L. 206:7–50. ELI: https://data.europa.eu/eli/dir/1992/43/oj.

ETC/ICM. 2019. Multiple pressures and their combined effects in Europe's seas. European Topic Centre for Inland, Coastal and Marine Waters. ETC ICM Technical Report.

EU. 2000. Directive 2000/60/EC of the European Parliament and of the Council of 23 October 2000 establishing a framework for Community action in the field of water policy OJ L 327, 22.12.2000, p. 1–73, ELI: https://data.europa.eu/eli/dir/2000/60/oj.

EU. 2008a. Council Regulation (EC) No 1005/2008 of 29 September 2008 establishing a Community system to prevent, deter and eliminate illegal, unreported and unregulated fishing, amending Regulations (EEC) No 2847/93, (EC) No 1936/2001 and (EC) No 601/2004 and repealing

Regulations (EC) No 1093/94 and (EC) No 1447/1999 (OJ L 286/1, 29.10.2008. p. 1–32).

EU. 2008b. Directive 2008/56/EC of the European Parliament and of the Council of 17 June 2008 establishing a framework for community action in the field of marine environmental policy (Marine Strategy Framework Directive) (OJ L 164, 25.6.2008, pp. 19–40).

EU. 2014. Directive 2014/89/EU of the European Parliament and of the Council of 23 July 2014 establishing a framework for maritime spatial planning (OJ L 257, 28.8.2014, pp. 135–145).

EU. 2016. Opinion of the European Economic and Social Committee on 'Prospects for long-term smart, sustainable development of European offshore industry and its relations with the EU's maritime sectors' (2016/C 013/12) (OJ C 13/73, 15.1.2016).

EU. 2017a. Commission Decision (EU) 2017/848 of 17 May 2017 laying down criteria and methodological standards on good environmental status of marine waters and specifications and standardised methods for monitoring and assessment, and repealing Decision 2010/477/EU (OJ L 125, 18.5.2017, p. 43-74).

EU. 2017b. Commission Directive (EU) 2017/845 of 17 May 2017 amending Directive 2008/56/EC of the European Parliament and of the Council as regards the indicative lists of elements to be taken into account for the preparation of marine strategies (OJ L 125, 18.5.2017, pp. 27–33).

EU. 2019a. Communication No. 640/2019/EC from the Commission to the European Parliament, the European economic and social Committee and the Committee of the Regions 'The European Green Deal', https://ec.europa.eu/info/publications/communication-european-green-deal_en.

Herold A, Cook V, Baron Y, Cames M, Gores S, Graichen J, Kasten P, Mehlhart G, Siemons A, Urrutia C, Wolff F. 2019. EU environment and climate change policies – state of play, current and future challenges, study for the committee on the environment, public health and food safety. Luxembourg: Policy Department for Economic, Scientific and Quality of Life Policies, European Parliament.

IPBES. 2018. Intergovernmental science-policy platform on biodiversity and ecosystem services, regional assessment report on biodiversity and ecosystem services for Europe and Central Asia. https://www.ipbes.net/assessment-reports/eca.

UN. 2015a. Transforming our world: the 2030 Agenda for sustainable development, A/RES/70/1, United Nations. https://sustainabledevelopment.un.org/content/documents/21252030%20Agenda%20for%20Sustainable%20Development%20web.pdf.

UN. 2015b. Sustainable development goals. United Nations. [accessed 26 Dec 2019]. https://www.un.org/sustainabledevelopment/sustainable-development-goals/.

UN. 2019. The Science We Need for the Ocean We Want, United Nations The United Nations Decade of Ocean Science for Sustainable Development (2021–2030). https://www.unesco.org/new/fileadmin/MULTIMEDIA/HQ/SC/pdf/IOC_Gatefold_Decade_SinglePanels_PRINT.pdf.

UNESCO. 2020. United Nations Decade of Ocean Science for Sustainable Development (2021–2030). https://en.unesco.org/ocean-decade/about.

UNFCCC. 2015. Paris Agreement under the United Nations Framework Convention on Climate Change, United Nations, Framework Convention on Climate Change, FCCC/CP/2015/L.9/Rev.1, https://unfccc.int/resource/docs/2015/cop21/eng/l09r01.pdf.

CMEMS OSR4, Chapter 2: State, variability and change in the ocean

Section 2.1: Diatom dynamics in the North Atlantic

Authors: Silvia Pardo, Robert J. W. Brewin, Shubha Sathyendranath

Statement of main outcome: Phytoplankton size classes are closely related to many phytoplankton functions (Nair et al. 2008; IOCCG 2014; Brewin et al. 2017) related to processes such as carbon cycling and are therefore important for data assimilation in biogeochemical models. Each size class has a well-defined role in the carbon cycle, with diatoms being an important functional type contributing to the biological carbon pump. The diatom chlorophyll product (Brewin et al. 2017) developed within the Copernicus Marine Environment Monitoring Service through the TOSCA (Towards Operational Size-class Chlorophyll Assimilation) Project is a remote sensing product, in which the macro-phytoplankton size class is partitioned into diatoms and dinoflagellates. It is based on climate records provided by the Ocean Colour Climate Change Initiative (OC-CCI), and were used to monitor interannual variability and anomalies in diatom chlorophyll concentration. The diatom concentration for the year 2018 was, on average over the region, slightly lower (5%) than the climatological value. Some regions presented distinct anomalies, with diatom concentrations reaching double (North Atlantic oligotrophic gyre) or half (northwest of Ireland and Scotland) the climatological values. In 2018, the peak value of diatom chlorophyll concentration during the spring bloom, averaged over the entire study area, was the lowest for the entire 1997–2018 period. Diatoms continue to be the dominating functional group in the coastal regions of the English Channel and the North Sea in 2018, but the period of diatom dominance was, on average, one week shorter than the 1997–2017 climatological value.

Products used:

Ref. No.	Product name and type	Documentation
2.1.1	ATL OC-CCI REP dataset OCEANCOLOUR_ATL_ CHL_L3_REP_OBSERVATIONS_ 009_067	PUM: http://marine.copernicus .eu/documents/PUM/CMEM S-OC-PUM-009-ALL.pdf QUID: http://marine. copernicus.eu/documents/ QUID/CMEMS-OC-QUID-009- 066-067-068-069-088-091. pdf

2.1.1. Introduction

Phytoplankton community structure is a key factor for many processes in marine biogeochemistry and ecology, such as photosynthesis, growth, light absorption, nutrient uptake, carbon export, and the transfer of energy through the marine food chain (Brewin et al. 2017). Due to its ecological importance, it is critical to monitor changes in community structure and assess the links between these changes and climate variability. The phytoplankton community structure can be described in several ways as, for example, taxonomic composition, size structure, or functional types. Phytoplankton size classes are particularly relevant in the context of climate studies, due to the distinct role that cell size plays in the carbon cycle: large cells tend to have higher sinking rates, and hence a higher chance of reaching the sea floor and confining their associated carbon before they decompose, whereas small cells remain suspended for longer and are available to processes that release carbon dioxide into the upper ocean (IOCCG 2014). Of the different size classes, microphytoplankton is typically made up of diatoms and dinoflagellates, which have quite different functionalities. Remote-sensing techniques for detecting size and functional types have been developed that exploit differences in their optical characteristics – scattering and absorption – that can be extracted from ocean-colour data (Sathyendranath et al. 2004; Loisel et al. 2006). Several indirect methods have also been proposed for determining size structure from total chlorophyll concentration (Nair et al. 2008; IOCCG 2014). More recently, Brewin et al. (2017) partitioned the microphytoplankton size class into two components: diatoms and dinoflagellates, which have been successfully assimilated into biogeochemical models (e.g. Ciavatta et al. 2018).

The mechanisms that govern the spatial and temporal distribution of the different size classes have been subject of multiple studies (e.g. Chavez 1989; Chisholm 1992; Marañon et al. 2001; Arin et al. 2002; Pannard et al. 2007). Current efforts target the response of phytoplankton community structure to climate change using in situ observations and biogeochemical models (Cermeño et al. 2008; Finkel et al. 2009; Marinov et al. 2010). Diatoms, being the functional type responsible for around 40% of the biological pump of CO_2 (Tréguer et al. 2018), have been given a prominent place in these studies (e.g.

Bopp et al. 2005; Leterm et al. 2005; Hinder et al. 2012). Diatoms are typically large in size (>10 μm), and combined with the presence of silica frustules that protect the cell, they are negatively buoyant. Therefore they can sink rapidly out of the surface layer of the ocean, contributing to the export of compounds such as carbon and silica to deeper waters (IOCCG 2014). In the North Atlantic their chlorophyll concentration can range from <0.01 mg m^{-3} in the subtropical gyre to greater than 3 mg m^{-3} in productive coastal regions during the spring bloom (Brewin et al. 2017). The purpose of this paper is to exploit the 21-year climate-quality CMEMS diatom dataset to study the interannual variability of diatom concentration and dominance, hence providing a remote-sensing counterpart to these model calculations.

2.1.2. Method

The Copernicus Marine Environment Monitoring Service (CMEMS) project 'Toward Operational Size-class Chlorophyll Assimilation (TOSCA)' has developed satellite-based chlorophyll products that are partitioned into size classes and some important phytoplankton types (diatoms and dinoflagellates), accompanied by per-pixel estimates of uncertainty (Brewin et al. 2017) that are compatible with those provided by the European Regional Seas Ecosystem model (ERSEM; Butenschn et al. 2016). These ocean-colour products provide daily chlorophyll concentrations of three size-classes of chlorophyll, with the microphytoplankton size class partitioned into two, yielding four phytoplankton groups – nano, pico and microphytoplankton (separated into dinoflagellates and diatoms) – over the North Atlantic area, at 1 km resolution, and covering the period from 4th September 1997 to 31st December 2018. This dataset is distributed within CMEMS as part of the North Atlantic chlorophyll reprocessed observation product (product ref. 2.1.1).

From this daily dataset, we computed regional weekly, monthly and annual mean composites of diatom chlorophyll concentration and its fractional contribution to total chlorophyll-*a* concentration (Brewin et al. 2017). The regional annual anomaly in diatom concentration for 2018 was computed by subtracting a reference annual climatology (1997–2017) from the 2018 annual mean concentration. A time series of the monthly area-averaged diatom concentration was derived; and seasonal cycles and trends over the 1997–2018 time period were calculated for both the absolute and fractional concentrations.

For the diatom domination analysis, and starting again from the daily dataset (product ref. 2.1.1), we created a time series of 8-day rolling composite of concentration (in chlorophyll units) of the diatom size classes. We then performed an analysis of the weekly composites on a pixel-by-pixel basis, by flagging the pixels where diatoms dominated. We assigned diatoms as the dominant size class if their contribution to the total chlorophyll concentration was > 50%. Using this weekly composite time series as input, we also computed annual maps of a diatom index. The diatom index represents the relative duration of diatom domination over a year, i.e. it is the ratio of the number of rolling 8-day weeks when diatoms were the dominating size class to the total number of available rolling 8-day week composites for that year. The regional anomaly for diatom index for 2018 was computed by subtracting a reference climatology (1997–2017) from the 2018 annual mean diatom index.

2.1.3. Results

The annual average diatom concentration in the North Atlantic for 2018 (Figure 2.1.1(a)) was 0.11 mg m^{-3}, with values reaching 1 mg m^{-3} in the coastal areas of the English Channel, the North Sea and the upwelling waters off Cape Blanc in Africa. The diatom distribution in the annual average map is consistent with the 1997–2017 climatology, with very low diatom concentration in the North Atlantic gyre and increased concentration at high latitudes and nutrient-rich coastal and upwelling waters. The patterns in the annual average map also match existing knowledge on size-class and diatom distributions obtained from in situ observations (San Martin et al. 2006), models (Rousseaux and Gregg 2015) and satellite data (Sathyendranath et al. 2004; Brewin et al. 2010).

Differences between the log-transformed annual and climatological averages on a pixel by pixel basis are shown in Figure 2.1.1(c). The average annual diatom regional anomaly in log10 (Chl) for 2018 was −0.02, showing that the 2018 values were about 5% lower than the climatological value. The maximum anomaly was 1.4 and the minimum −3.9, but most of the values were confined to ±0.3 in the log scale (2018 values half/twice the climatological values in linear scale). The most significant negative anomalies were detected around the Rockall Plateau to the northwest of Ireland and Scotland, and in the area surrounding the Azores archipelago. Areas showing strong positive signals include the core of oligotrophic North Atlantic Gyre and the Iberian Abyssal Plain west of Portugal and Spain.

The seasonal dependencies of North Atlantic diatom concentration are well known, with studies indicating that seasonal information is the second most important factor contributing to variations in predicting diatom concentration in the area (Raitsos et al. 2011). The annual cycle obtained using the CMEMS TOSCA product (product ref. 2.1.1) match these observations: the time series of total concentration (Figure 2.1.2(a)) exhibits a spring
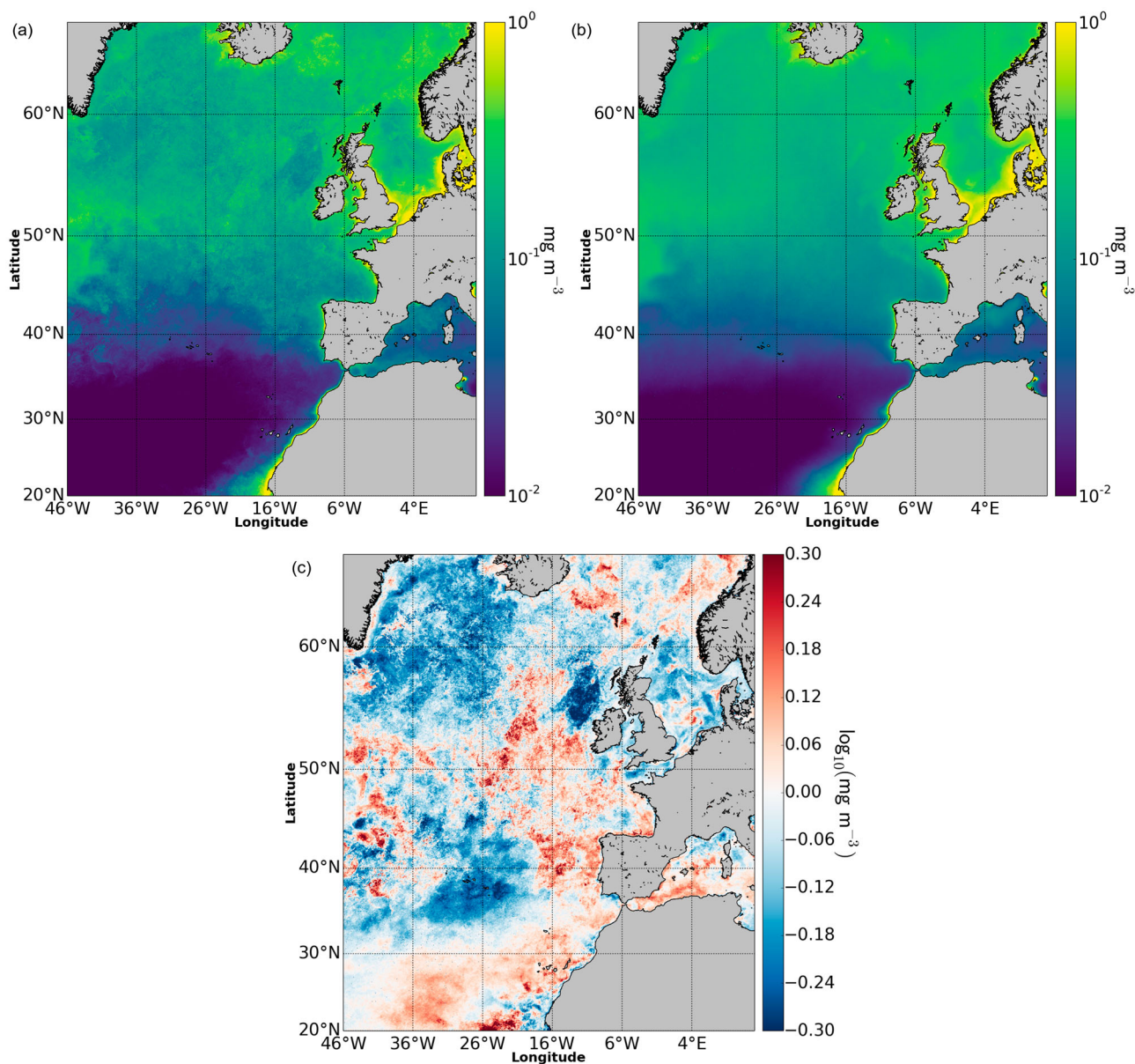
Figure 2.1.1. (a) Regional annual mean diatom concentration for 2018; (b) climatology (1997–2017) of diatom concentration; and (c) anomaly in annual mean diatom concentration for 2018 with respect to the climatology shown in (b); all based on the CMEMS diatom chlorophyll concentration product (product ref. 2.2.1).

bloom that peaks consistently in the first / second week of May, with the exception of years 2002 and 2009, when the peak was delayed until the first week of June. The correlation between the phenology of the spring bloom, sea surface temperature and the North Atlantic Oscillation Index (Zhai et al. 2013) might explain these anomalies.

No appreciable changes in the timing of the spring bloom was observed in 2018, though its peak area-averaged magnitude (0.176 mg m^{-3}) was slightly lower than the time series average for the 1997–2017 period (0.20 mg m^{-3}), and the lowest in the time series since 1999 (0.172 mg m^{-3}). The linear trend for the 1997–2018 period is slightly positive for the total concentration

(0.11% per year). However, there are several half-decadal cycles in the non-linear trend (Figure 2.1.2), and it appears that 2018 is in the declining phase of one of these cycles, which started in 2016. In particular, the annual average for the region in 2018 is 0.118 mg m^{-3}, the lowest in the 22-year time series.

The time series of fractional concentration of chlorophyll associated with diatoms (Figure 2.1.2(b)) also presents a distinct seasonality and semi-decadal cycles in the non-linear trend, similar to those observed for the diatom concentration itself (Figure 2.1.2(a)). The fractional information is better understood in juxtaposition with the total chlorophyll time series for the area, as published
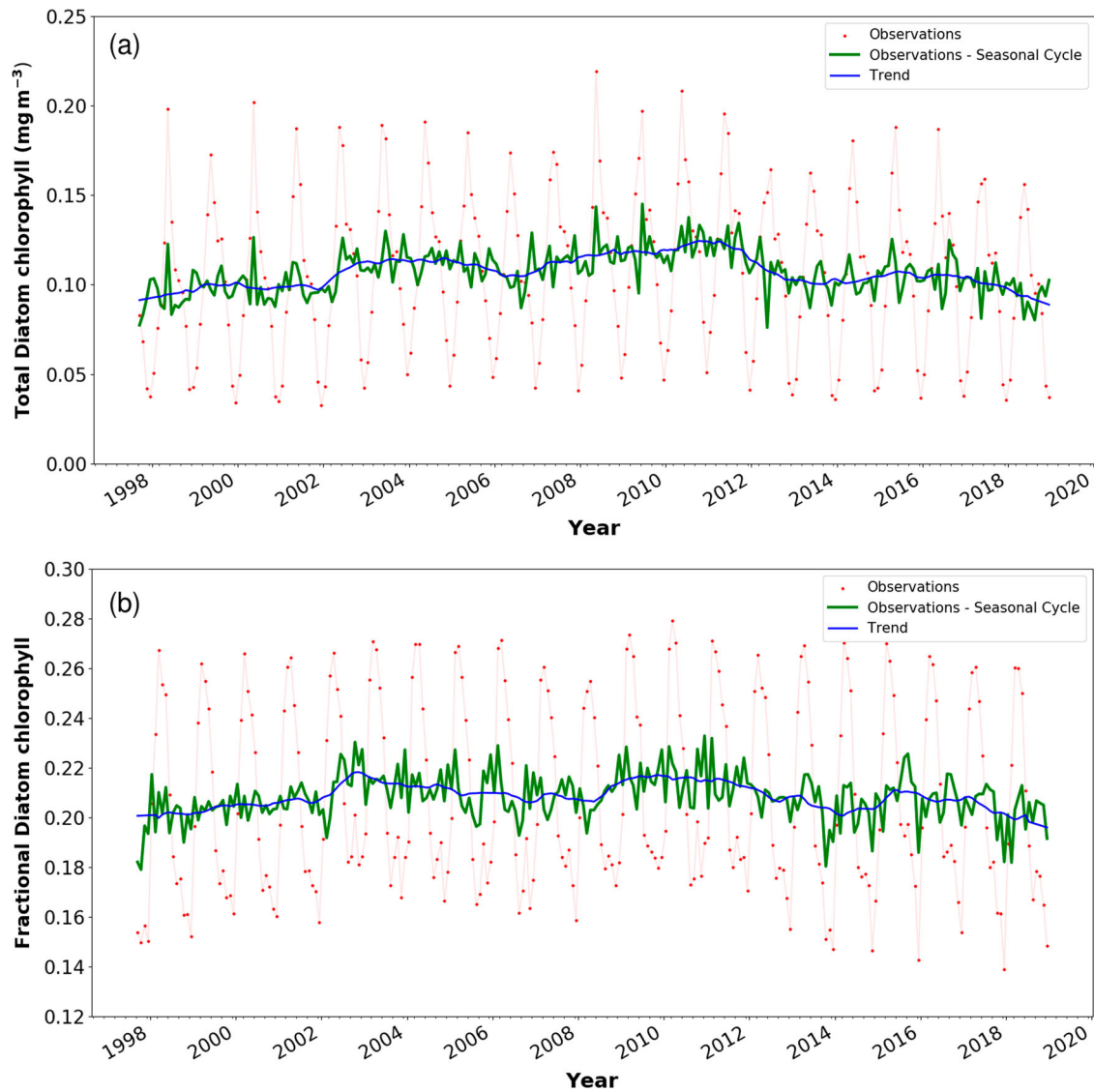
Figure 2.1.2. (a) Regional North Atlantic time series of the monthly average chlorophyll concentration associated with diatoms, deseasonalised time series and trend. (b) Regional North Atlantic time series of the monthly average fraction of total chlorophyll concentration associated with diatoms, deseasonalised time series and trend. Both plots are based on the CMEMS diatom fractional chlorophyll concentration product (product ref. 2.2.1). The whole 1997–2018 period was considered to calculate the seasonal cycle and trend components of the signal.

in the previous CMEMS Ocean State Report (Sathyendranath et al. 2018). In particular, a decline in diatom fraction without any corresponding changes in total chlorophyll concentration can be observed between 2003 and 2010. This result is consistent with those obtained by Agirbas et al. (2015) using Atlantic Meridional Transect data for the same period.

The analyses presented in previous paragraphs provide valuable information regarding the interannual and regional variability of diatom chlorophyll concentration, but very little insight on the relative dominance of diatoms over the other size classes. In fact, diatoms were the dominating size class during 5.5% of the time for 2018, on average over the North Atlantic box

(indexdiat = 0.055, where the index is defined as the number of days in a year when diatoms contributed more than 50% to the total chlorophyll, divided by the total number of days in the year when observations were available), with values reaching 78% for the year (indexdiat = 0.78) in the coastal areas of the English Channel, the North Sea and off Africa at around 20–25 degrees north (Figure 2.1.3(a)). Note that a considerable portion of the region does not present sustained diatom domination – neither for the 2018 index map nor for the index climatology. The average 2018 diatom index anomaly for the area was −0.017, that is to say that the period of diatom dominance over the North Atlantic was one week shorter than the 1997–2017 climatological
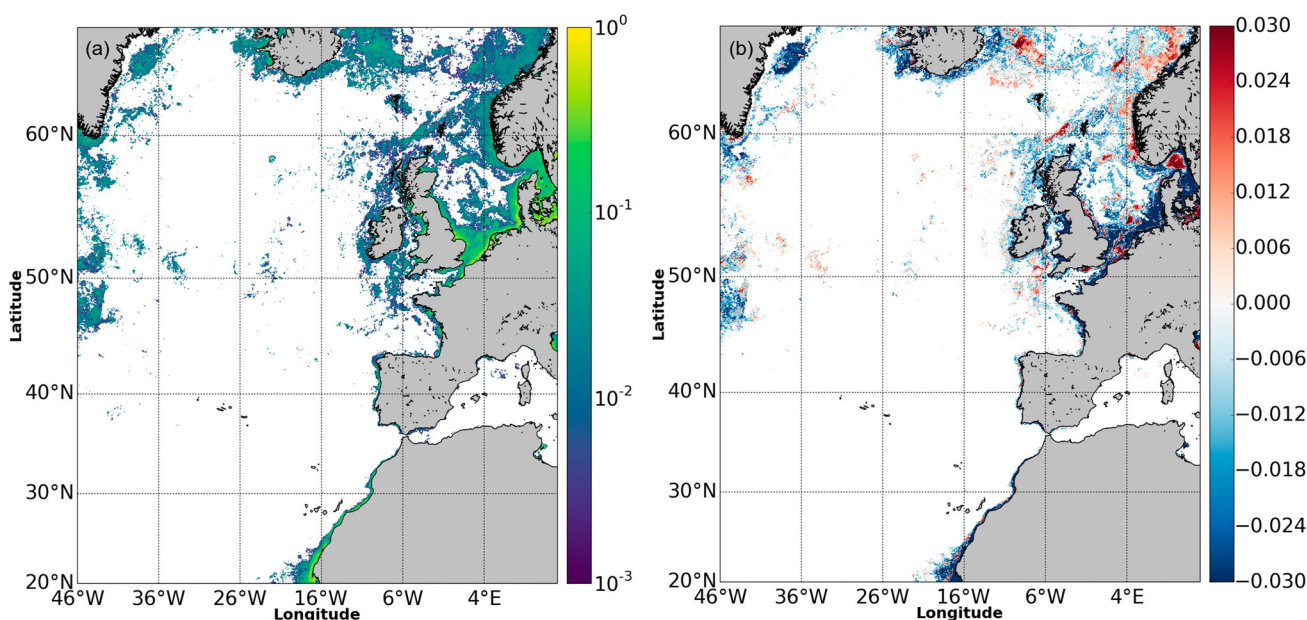
Figure 2.1.3. Regional 2018 mean diatom index (a) and regional 2018 diatom index anomaly (b) with respect to the 1997–2017 climatology of the diatom index, based on the CMEMS diatom fractional chlorophyll concentration product (product ref. 2.2.1).

value. The most important negative anomalies were detected in the coastal regions of the North Sea. A full time series analysis of the diatom index and corresponding indices for the other functional types and size classes is required to put this annual anomaly in the context of the decrease in diatom dominance predicted in the literature, as one of the consequences of climate change.

It has been predicted on the basis of models and observations that climate change can impact phytoplankton community structure, and that the distribution of diatoms in particular could be affected (Bopp et al. 2005; Cermeño et al. 2008; Marinov et al. 2010). The diatom products presented here offer a satellite-based tool to study spatial and temporal variations in diatom dynamics at high resolution in space and over long time scales. The time series of the climate-quality ocean-colour products is now 20 years long and growing, and the value of these products can only increase as the length of the time series grows. Ciavatta et al. (2018) have demonstrated that information on community structure of phytoplankton, when assimilated into ecosystem models, can help improve model performance.

Section 2.2: Primary production

Authors: Gianpiero Cossarini, Marine Bretagnon, Valeria Di Biagio, Odile Fanton d'Andon, Philippe Garnesson, Antoine Mangin, Cosimo Solidoro
Statement of main outcome: Primary production is at the base of the marine food web and an important factor in the Earth's carbon cycle. In this study, we used a

remote sensing algorithm to estimate the reference state and trend of the global ocean primary production. Given the availability of the CMEMS reanalysis for the Mediterranean Sea, we focus on this marginal sea providing a merged estimate and its uncertainty. Spatial variability is high in the global ocean with the most productive areas located in the Arctic and coastal regions. Temporally, the seasonal cycle is an important component of the productivity of marine ecosystems. The most productive period is observed during summer time (austral or boreal) for each Hemisphere globally and also for the Mediterranean Sea regionally. A small but significant decrease in primary production has been observed over the past 20 years for the global ocean, whereas a small but significant increase has been observed in the Mediterranean Sea. High interannual variability is also reported and possibly triggered by year-to-year changes in physical forcing, such as the strength of the vertical mixing.

Product used:

Ref. No.	Product name and type	Documentation
2.2.1	MEDSEA_REANALYSIS_ BIO_006_008	PUM: http://marine. copernicus.eu/documents/ PUM/CMEMS-MED-PUM-00 6-008.pdf QUID: http://marine. copernicus.eu/documents/ QUID/CMEMS-MED-QUID- 006-008.pdf
2.2.2	SST_GLO_SST_L4_REP_ OBSERVATIONS_010_011 SST_GLO_SST_L4_NRT_ OBSERVATIONS_010_001	PUM: http://marine.copernicu s.eu/documents/PUM/CME MS-OSI-PUM-010-011.pdf QUID: http://marine.copernic

(Continued)

Continued.

Ref. No.	Product name and type	Documentation
		us.eu/documents/QUID/CMEMS-OSI-QUID-010-011.pdf
2.2.3	OCEANCOLOUR_GLO_ OPTICS_L4_REP_ OBSERVATIONS_ 009_081	PUM: http://marine.copernicus.eu/documents/PUM/CMEMS-OC-PUM-009-ALL.pdf QUID: http://marine.copernicus.eu/documents/QUID/CMEMS-OC-QUID-009-030-032-033-037-081-082-083-085-086-098.pdf
2.2.4	Climatology of the Mixed Layer depth (http://www.ifremer.fr/cerweb/deboyer/mld/Surface_Mixed_Layer_Depth.php)	http://www.ifremer.fr/cerweb/deboyer/mld/Data_Description.php
2.2.5	OCEANCOLOUR_GLO_CHL_ L4_REP_OBSERVATIONS_ 009_082 OCEANCOLOUR_GLO_CHL_ L4_NRT_OBSERVATIONS_ 009_033	PUM: http://resources.marine.copernicus.eu/documents/PUM/CMEMS-OC-PUM-009-ALL.pdf QUID: http://resources.marine.copernicus.eu/documents/QUID/CMEMS-OC-QUID-009-030-032-033-037-081-082-083-085-086-098.pdf
2.2.6	MEDSEA_REANALYSIS_PHY_ 006_004	PUM: http://marine.copernicus.eu/documents/PUM/CMEMS-MED-PUM-006-004.pdf QUID: http://marine.copernicus.eu/documents/QUID/CMEMS-MED-QUID-006-004.pdf

2.2.1. Introduction

Marine primary production is a fundamental component of marine ecosystem functioning and related ecosystem services (Hattam et al. 2015; Watson et al. 2015). It is at the base of oceanic food-webs and contributes to atmospheric CO_2 sequestration through CO_2 fixation and subsequent organic carbon sink (Siegel et al. 2016; Morrow et al. 2018). During daylight phytoplankton fixes carbon and nutrients through biological conversion of solar radiation (i.e. photosynthesis) and produces oxygen and organic matter (Falkowski 2003). Primary production drives the biological carbon pump and affects the amount of atmospheric carbon potentially sequestrated by the ocean, which highlights one of the roles of the ocean in the global carbon cycle (Falkowski et al. 1998; Henson et al. 2012; Le Quéré et al. 2018). In addition, primary production is a proxy of the potentially available food for higher trophic levels, thus serving as a potential indicator for the fishery management strategies, such as the Common Fisheries Policy EU directive (Chassot et al. 2010). Furthermore, primary production can be an important indicator for descriptors of the EC Marine Strategy Framework Directive such as D4 'Food Web' (Lynam et al. 2016) and D5 'Eutrophication' (OPEC project, D2.8, opec-marine.eu). Marine primary production varies generally between 440 $mgC.m^{-2}.d^{-1}$ in the open ocean and oligotrophic areas, and 1400 $mgC.m^{-2}.d^{-1}$ in the most productive waters, such as

upwelling systems (Chavez et al. 2011). The spatial distribution of primary production is generally linked to nutrients supply and its temporal dynamics usually follow a seasonal cycle, constrained by the seasonality of solar radiation, nutrient supply and stability of the water column (Longhust 1995). At interannual or longer timescales, oceanic primary production is essentially a function of the physical parameter variability (Chavez et al. 2011). Consistently with the Ocean State Report guidelines, the aim of this study is to provide the reference state (1999–2014 period), the trend analysis (1999–2018) and the 2018 anomalies of primary production in the global ocean, with a focus on some European seas (i.e. North Atlantic Sea, Baltic Sea and Mediterranean Sea), using a satellite archive. Satellite estimates of primary production are merged with modelling results available for the Mediterranean domain, which is often considered as a 'miniature ocean' (e.g. Béthoux and Gentili 1999; Lejeusne et al. 2010), with a western basin about 50% more productive than the eastern basin (Moutin and Raimbault 2002). The Mediterranean Sea represents a sensible region to study environmental forcing and climate change impacts on primary production. Here we provide some insights on the influence of winter vertical mixing, nutrient supply and solar radiation on the ecosystem productivity. Finally, this study provides insights in similarities and discrepancies between the two approaches (i.e. modelling and satellite), addressing the uncertainty associated to the estimation of this important ecosystem functioning indicator.

2.2.2. Method

Photosynthesis occurs in the euphotic layer, generally characterised by a homogeneous production profile in case of mixing conditions and by a subsurface maximum in case of stratification. Estimates of the marine ecosystem primary production are usually integrated vertically over the productive layer. In the present study the vertically integrated primary production at global and regional scales is assessed through combining satellite-derived datasets of chlorophyll-*a* and model reanalysis over the past 20 years (1999–2018). Satellite results are integrated over the productive layer (i.e. 1.5 times the euphotic depth), while the Mediterranean Sea model output is integrated over 0–200 m depth, which safely covers the whole productive layer.

At the global scale, primary production is estimated with the Antoine and Morel satellite algorithm (Antoine and Morel 1996) using the Copernicus Marine Environment Monitoring Service (CMEMS) monthly merged ocean colour product (chlorophyll-*a* and photosynthetic

active radiation) from CMEMS (cf. 2.2.3 in the product table) with a spatial resolution of 4 km. Monthly averaged sea surface temperature comes from the OSTIA product from CMEMS, at 1/12° spatial resolution (Donlon et al. 2012, cf. 2.2.2 in the product table), and it is linearly interpolated to 4km.

In the Mediterranean Sea, vertically integrated primary production is estimated by averaging the aforementioned product (cf. 2.2.3) with the results of the CMEMS Mediterranean reanalysis (cf. 2.2.1). To estimate the uncertainties associated to the merged product, we computed the signal-to-noise ratio, as the ratio between mean and standard deviation of the monthly maps of primary production from satellite data and modelling output. The difference between satellite and model values is estimated as the reciprocal of this ratio and it is equal to 20% on average.

The CMEMS reanalysis is provided by the coupled physical-biogeochemical reanalysis model NEMO3.4 (Simoncelli et al. 2014) and OGSTM-BFM (Lazzari et al. 2012, 2016; Canu et al. 2015; Cossarini et al. 2015, Teruzzi et al. 2016) with data assimilation of temperature and salinity vertical profiles and satellite sea level anomaly (Dobricic and Pinardi 2008), and surface chlorophyll concentration (Teruzzi et al. 2014, 2018). The horizontal grid resolution of the model is 1/16° (ca. 6–7 km) and the unevenly spaced vertical levels are 72. The modelled net primary production is computed as the difference between the gross primary production and the phytoplankton respiration (Lazzari et al. 2012; Vichi et al. 2015). Following Geider et al. (1997), the Biogeochemical Flux Model (BFM) parameterisation describes the gross primary production in terms of photosynthetic available radiation (PAR), temperature, carbon quota in phytoplankton cells, chlorophyll content per unit of carbon biomass (i.e. chlorophyll dynamics is decoupled from uptake and growth dynamics and includes synthesis, degradation and photo adaptation), and nutrient (nitrogen, phosphorus, silicon) availability. Respiration includes both active (i.e. coupled to the production) and rest (i.e. correlated to the phytoplankton biomass) terms.

2.2.3. Reference state and seasonal cycle of primary production

At the global scale, primary production is on average of 57.6 GtC.yr^{-1}, in line with previous satellite estimations (31.2–72.8 GtC.yr^{-1}; Carr et al. 2006; Westberry et al. 2008). The highest values (>800 mgC.m^{-2}.d^{-1}) are observed in coastal regions and in upwelling areas (Figure 2.2.1(a)), where nutrients are injected in the surface layer. In contrast, the lowest values (<200 mgC.m^{-2}.d^{-1}) are observed in the open ocean, in the

oligotrophic gyres, where nutrient concentration is low (Perruche et al. 2018). Note that due to lack of light, the high latitudes (> 60°) are not covered by satellite observations. However, the North Atlantic is more productive than the surrounding area, with values up to 700 mgC.m^{-2}.d^{-1}. The high productivity in the subpolar north Atlantic is mainly due to the deep winter mixing, which brings an important amount of nutrients into the surface layer. In the Gulf Stream area, the high productivity is explained by the meso- and submesoscale activity (Lévy et al. 2001, 2012).

In the Mediterranean Sea, primary production (Figure 2.2.1(b)) shows a west-to-east decreasing gradient with the highest values in the Alboran Sea. Local higher maxima are found in coastal areas influenced by river input, such as in Aegean and Adriatic Seas (Salon et al. 2019). These results are consistent with previous basin wide studies (Bosc et al. 2004; Lazzari et al. 2012) and with the general view of increasing west–east oligotrophication gradient (Siokou-Frangou et al. 2010). The overall mean value of primary production equals to 385 mgC.m^{-2}.d^{-1}, but large differences are observed between the western and eastern basins. The mean values in the western and the eastern (excluding the marginal seas) areas are 488 and 306 mgC.m^{-2}.d^{-1}, respectively, which fall between previous estimations (i.e. 216–526 mgC.m^{-2}.d^{-1} for the western basin and 189–427 mgC.m^{-2}.d^{-1} for the eastern basin; Bosc et al. 2004; Uitz et al. 2012). Satellite and model estimates are quite consistent, with an average difference of 20%. We observe differences greater than 33% (i.e. with a signal-to-noise ratio lower than 3) for 6 or more months only in few limited areas (e.g. mainly coastal and central Levantine areas, Figure 2.2.1(b)).

Primary production is driven by the seasonal cycle of stability of the water column, illumination and nutrient supply (Longhust 1995). Distinctive seasonal regimes can be recognisable for biogeographical regions of the global oceans (Longhust 1995; Ducklow 2003). For sake of brevity and without claim of exhaustiveness, we provided an essential overview of the seasonal cycle of primary production in global ocean and selected European seas (Figure 2.2.2). In the global ocean (Figure 2.2.2(a)) the seasonal cycle is characterised by two peaks and two minima and a quite smooth temporal variability, since it takes into account the north and south hemispheres and the presence of wide oligotrophic areas with weak seasonality. The most productive season occurs in boreal summer, with a peak in June of about 430 mgC m^{-2} d^{-1}. The second maximal production occurs in austral summer, between December and January, and reach a rate of about 380 mgC m^{-2} d^{-1}. In the Baltic Sea, the increasing of primary production as the
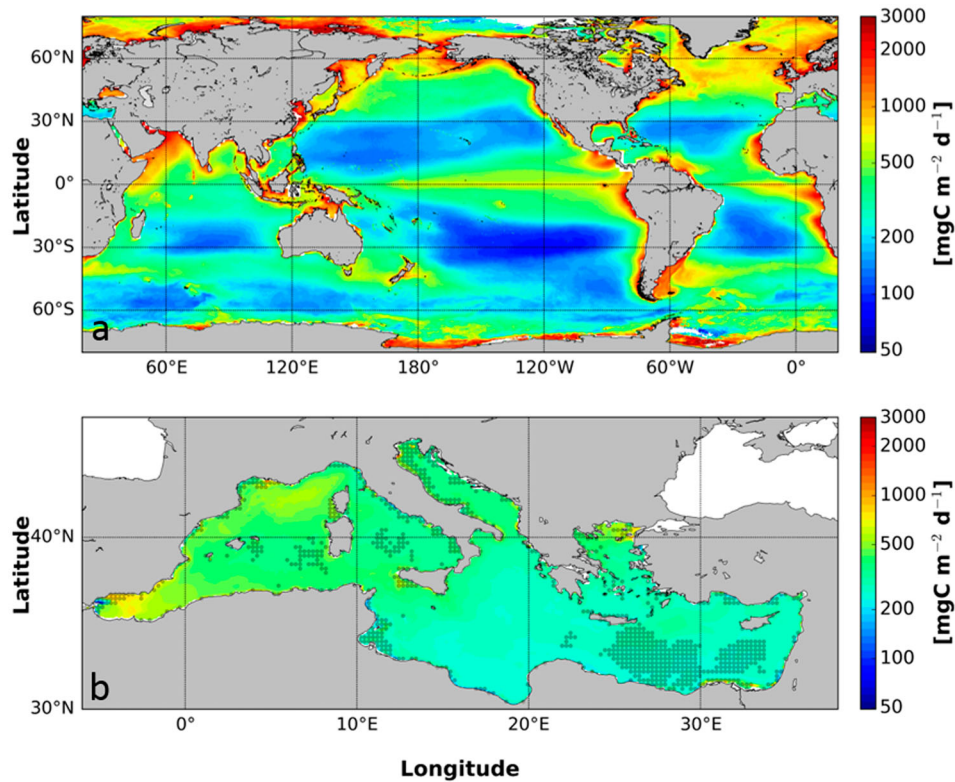
Figure 2.2.1. Map of 1999–2014 climatology of vertically integrated primary production (1999–2014 average) at global scale (a) and in the Mediterranean Sea (b). The global map is provided by satellite archive, whereas the Mediterranean map is the merged product (average of the satellite and model maps) reported to the 1/16° resolution. The areas with signal-to-noise ratio lower than 3 for 6 or more months are marked by the black dots. (Products 2.2.5 and cf.2.2.1).

consequence of the summer bloom is the strongest compared to the other marginal seas here considered (Figure 2.2.2(a,b)). Indeed, primary production in summer (up to 3100 mgC m^{-2} d^{-1} in August) is almost three times higher than winter values (down to 1300 mgC m^{-2} d^{-1} in February) . Also, due to the winter night, primary production can not be monitored from remote sensing between November and January. In this region, primary production appears to be limited by the light availability and the sea ice cover. The North Atlantic seasonal cycle (Figure 2.2.2(a)) is characterised by summer maxima, when the highest primary production values (up to 1300 mgC m^{-2} d^{-1} in June) are coincident with the maximum of the light availability.

In the Mediterranean Sea, the seasonal cycle of primary production presents two significant increases at a basin scale (Figure 2.2.2(b)). First, a rapid increase in primary production occurs in March (about 400 mgC m^{-2} d^{-1}) due to late winter-early spring phytoplankton blooms sustained by winter vertical mixing that supplies nutrients into the surface layer (Lazzari et al. 2012). Second, a year maximum occurs during summer, concurrent with the seasonal variation of light availability for the photosynthesis (Antoine et al. 1995; Bosc et al.

2004). Note that the intensity of the seasonal cycle is higher than for the oceans above mentioned. Indeed, while production in summer is twice as high as production in winter for the Mediterranean Sea, production increases only about 40% between winter and summer for the global ocean. The Mediterranean Sea can be subdivided in two parts linked to the well-known oligotrophic west-to-eastern gradients (Moutin and Raimbault 2002; Siokou-Frangou et al. 2010). Our results confirm that the western part (i.e. from 5°W to the Sicily channel at 12°E in Figure 2.2.1) is about 44% more productive than the eastern part and has a less smooth seasonal pattern (Figure 2.2.2(b)). Hovmöller diagrams of Figure 2.2.2(c,d) report the monthly means along the water column and shed some light on the two different mechanisms driving the different regimes in the Mediterranean basins. In the western basin the increase due to the late winter-early spring primary production is restricted to the upper layer (Figure 2.2.2(c)) and is due to intense blooms at surface, where nutrients are supplied into the shallow euphotic layer by the winter mixing (Lòpez-Jurado et al. 2005; Schroeder et al. 2008; Volpe et al. 2012; Mayot et al. 2017). The surface winter-early spring bloom accounts for up to 40% of the
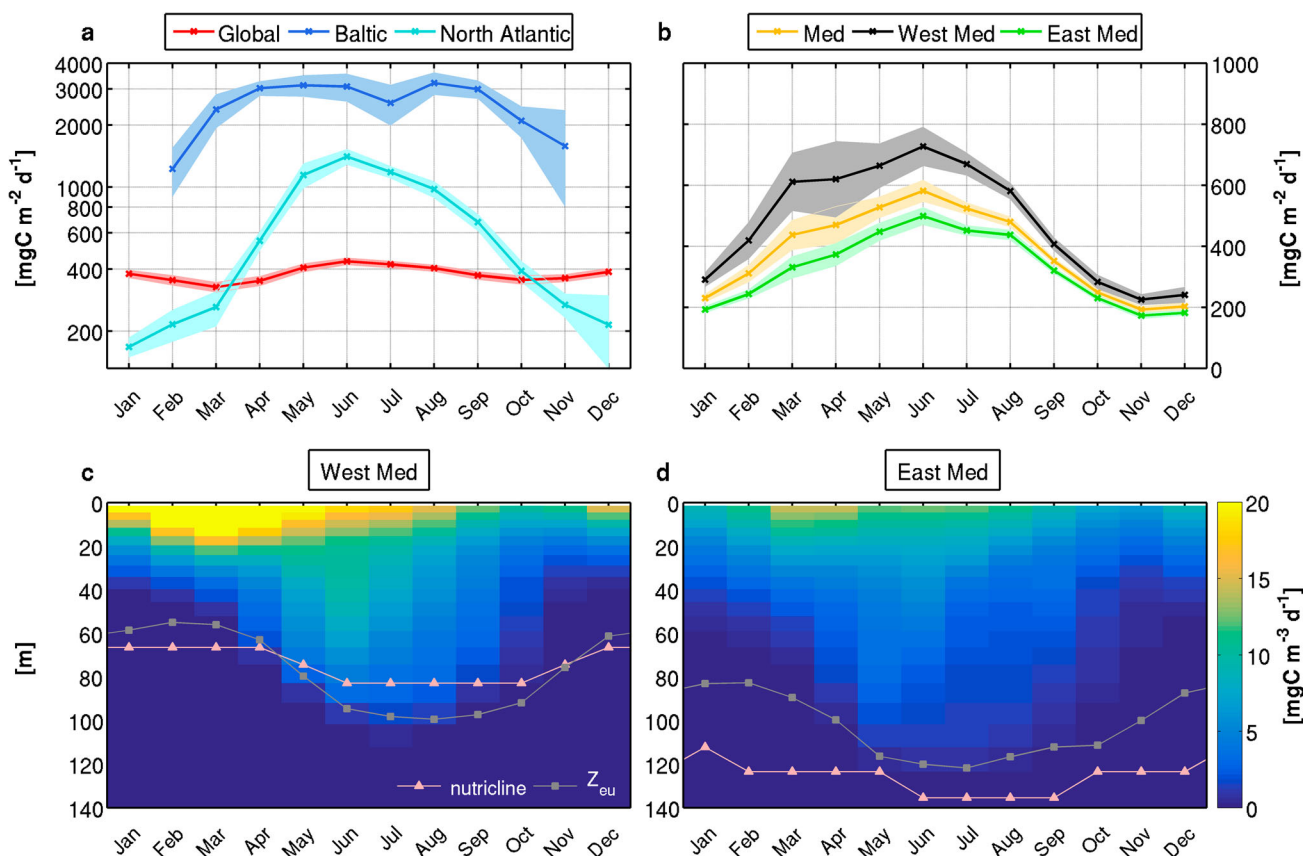
Figure 2.2.2. (a) Average seasonal cycle of primary production calculated in global ocean (red line), Baltic Sea (blue line) and North Atlantic Sea (cyan line) from the satellite archive in the reference period (1999–2014). (b) Average seasonal cycle of primary production calculated in Mediterranean Sea (yellow line) and in the western basin (black line) and eastern basin (green line) from the merged product in the reference period (1999–2014); envelopes in (a) and (b) represent the standard deviation as inter-annual variability. Hov-möller diagrams of mean monthly volumetric primary production [mgC m^{-3} d^{-1}] for the western (c) and eastern (d, excluding marginal seas) Mediterranean basins, computed from the reanalysis archive in the reference period (1999–2014); pink triangles represent the mean monthly nutricline, computed as the depth which separates levels of values of nitrate concentration higher and lower than 1 mmol m^{-3}, on the 1999–2014 reanalysis archive; grey squares represent the monthly mean euphotic depth (Zeu), as the depth at which the modelled PAR is 1% of its surface value, according to BFM formulation (Lazzari et al. 2012). (Products 2.2.5 and 2.2.1).

mean annual primary production. Beside the late winter-early spring surface increase, the second highest contribution to the annual primary production values are observed in the subsurface layer in late spring and summer (Figure 2.2.2(c,d)). The eastern basin has generally lower values of volumetric primary production, associated to a deeper nutricline (120 m depth in winter, Figure 2.2.2(d)) with respect to the western basin (70 m, Figure 2.2.2(c)), which makes less effective the upward nutrient supply by winter mixing. Nevertheless, the depth of the euphotic layer in the eastern basin is greater than that of the western basin (120 and 100 m of maximum depth in summer, respectively) and substantial productivity, up to 15 mgC.m^{-3}.d^{-1}, can be found down to 120–130 meters depth in July and August (Figure 2.2.2(d)). The thickness of the productive layer follows the onset of the deep chlorophyll maximum, which is common in the subsurface layer of the oligotrophic stratified waters of the Mediterranean Sea (Barbieux et al.

2019) and is found at greater depth in the eastern Mediterranean basin than in the western basin (Lavigne et al. 2015; Cossarini et al. 2019).

2.2.4. Trend and interannual variability

Following the Vantrepotte and Mélin census I methods (Vantrepotte and Mélin 2009), the time series of the spatially averaged monthly primary production is decomposed into the seasonal component (shown in Figure 2.2.2) and an anomaly, from which the linear trend is estimated (Figure 2.2.3). Over the archive 1999–2018, the time series of primary production highlight the interannual variability with respect to the mean seasonal component for the global ocean and the European regional seas (Figure 2.2.3(a–f)). Indeed, the first years of the time series (Figure 2.2.3(a)) exhibit higher values, which might be explained by a La Niña event, as it impacts upwelling and therefore nutrient
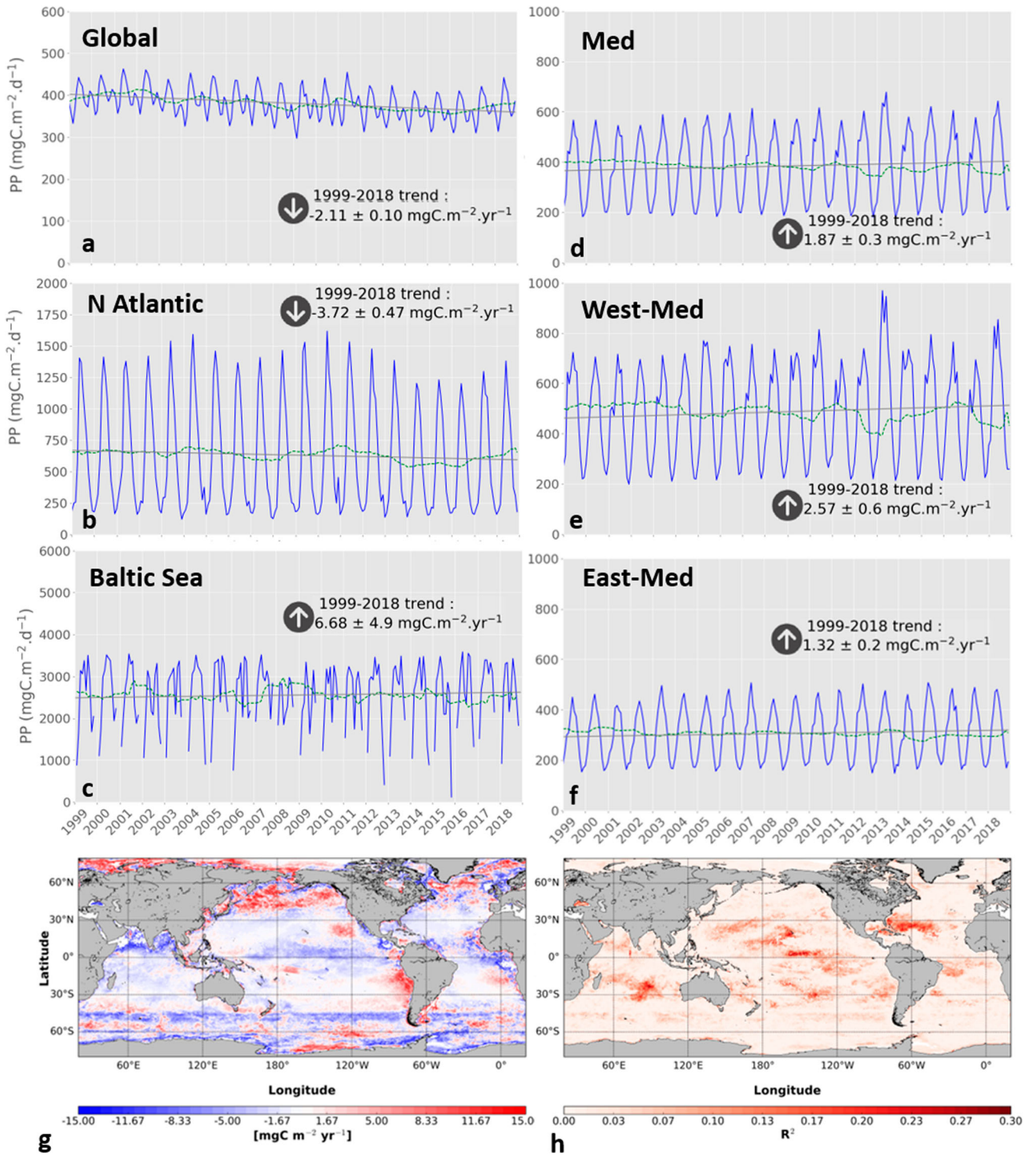
Figure 2.2.3. Primary production time series over the 1999–2018 period, for the satellite archive in global ocean (a), North Atlantic Sea (b) Baltic Sea (c), and for the merged product in Mediterranean Sea (d), Western Mediterranean Sea (e), Eastern Mediterranean Sea (f). Each plot reports the monthly time series (blue line), the time series obtained by subtracting the seasonal and residual components (green line) and the trend (grey line), which is estimated following the Vantrepotte and Mélin census I method (Vantrepotte and Mélin 2009). For each basin, the arrow indicates the sign of the trend, which is reported in terms of annual variation and standard error. Panel (g) presents the map of the trend of primary production at the global scale, computed at each pixel except in Mediterranean Sea from the satellite archive and panel (h) the coefficient of determination for the trend estimated at each pixel. (Product 2.2.5 for the global ocean, and 2.2.5 and 2.2.1 for the Mediterranean Sea).

availability (Behrenfeld et al. 2006). In addition to El Niño Southern Oscillation variations, other climate indexes (e.g. Pacific Decadal Oscillation, North Atlantic Oscillation) may contribute to explain the interannual variability (Rousseaux and Gregg 2014). Indeed, the evolution of primary production anomalies (after seasonal cycle removal) in the North Atlantic Sea appears to be negatively correlated with NAO phases (not shown). Generally, periods of positive anomalies of at least 5 months long are associated with negative NAO and vice versa. This is particularly evident during some events: in summer 2013 (i.e. negative primary production anomaly and positive NAO) and in summer 2008 and 2010 (i.e. positive primary production anomalies and negative NAO).

Primary production decreases of 2.11 ± 0.10 mgC.m^{-2}.yr^{-1} ($R^2 = 0.64$) at the global scale over the temporal archive (Figure 2.2.3(a)). The decline of primary production at the global scale can be explained by the warming of water column, which induces stratification (Von Schuckmann et al. 2019) and nutrient surface depletion. However, the decrease in primary production is not homogeneous and we observe a high spatial variability (Figure 2.2.3(g)), which is related to local environment conditions. For example, a positive trend of primary production is observed in the south Greenland area and it is related to the nutrient supply after sea ice melting (Bhatia et al. 2013; Hawkings et al. 2015; Lawson et al. 2014). Thinning and shortening of sea ice cover in the Baltic Sea (Tedesco et al. 2017) explains the positive, even if not significant, trend in the Baltic Sea (6.68 ± 4.9 mgC.m^{-2}.yr^{-1}, Figure 2.2.3 (c)). Conversely, primary production over the entire North Atlantic decreases of 3.72 ± 0.47 mgC.m^{-2}.yr^{-1} ($R^2 = 0.25$). This decline in primary production appears to be related to the increasing stratification and the decreasing of upwelling favourable wind (Kwiatkowski et al. 2019). The increasing primary production off Greenland and the global decrease in the North Atlantic highlight the spatial and temporal variability in this region. In general, our trend map is in good agreement with chlorophyll trend estimated by Gregg et al. (2017), with both maps reporting, for instance, positive trends in the south east Pacific area, even if the coefficient of determination is relatively low for the considered archive.

A small positive and significant trend is estimated for the whole Mediterranean Sea over the period 1999–2018 (1.87 ± 0.3 mgC m^{-2} yr^{-1}, $p < .01$, Figure 2.2.3(d)), while the western basin displays a significant positive trend of about 2.57 ± 0.6 mgC m^{-2} yr^{-1} (Figure 2.2.3(e)). Our result in the western Mediterranean Sea is in agreement with the positive trend of chlorophyll detected in the same area by Salgado-Hernanz et al. (2019) who report

an increase of the amplitude and duration of the phytoplankton growing period, on the 1999–2014 subset of Product 2.2.5. Different long term signals have been reported for other Mediterranean regions (e.g. negative or neutral) supporting the conclusion that environmental and climate forcings have local and complex impacts in the Mediterranean Sea (Salgado-Hernanz et al. 2019).

The Mediterranean time series (Figure 2.2.3(d)) displays also substantial interannual variability, which is larger than the trend signal (not shown). The fluctuations are higher in the western Mediterranean Sea than in the eastern basin (Figure 2.2.3(e,f)). This spatial heterogeneity is related to the different oceanographic characteristics of the two basins: generally stratified and oligotrophic the eastern basin and influenced by intense winter mixing and the presence of some frontal systems the western basin (Siokou-Frangou et al. 2010). Insights into the impact of interannual variability of the winter mixing on primary production anomalies are provided in Figure 2.2.4. The highest values of winter mixed layer depth are generally followed by positive anomalies of primary production (i.e. productivity higher than the average in 2006, 2010, 2013, 2014 and 2018; Figure 2.2.4). Indeed, the interannual variability of the winter-early spring primary productivity is pretty well explained by the late autumn–winter interannual variability of the winter deep mixing: the correlation between time series of November-February averages of mixed layer depth (data from cf. 2.2.6 in the product table) and January-May averages of primary production is 0.77, $p < .005$.

Strong interannual variability and a stepwise increase of the dense water formation in the north-western Mediterranean is reported starting from winter 1999 after a period of low convective activity during the 1990s (Somot et al. 2018). Increased number of winters with enhanced mixing in the most recent years can have impacted the nutrient supply in the euphotic layer determining the positive trend of primary production in the western basin (Kessouri et al. 2018).

2.2.5. The 2018 anomaly

At global scale, the anomalies for 2018 relative to the reference period 1999–2014 indicate a lower-than-average primary production in 2018, indeed the average of the 2018 anomaly map is about −17% (Figure 2.2.5(a). In the Gulf Stream area and along the North American coast, primary production anomalies are below the average. Lower-than-average primary production values in the Californian upwelling are potentially linked to the intensification of the wind drop-off, known to affect
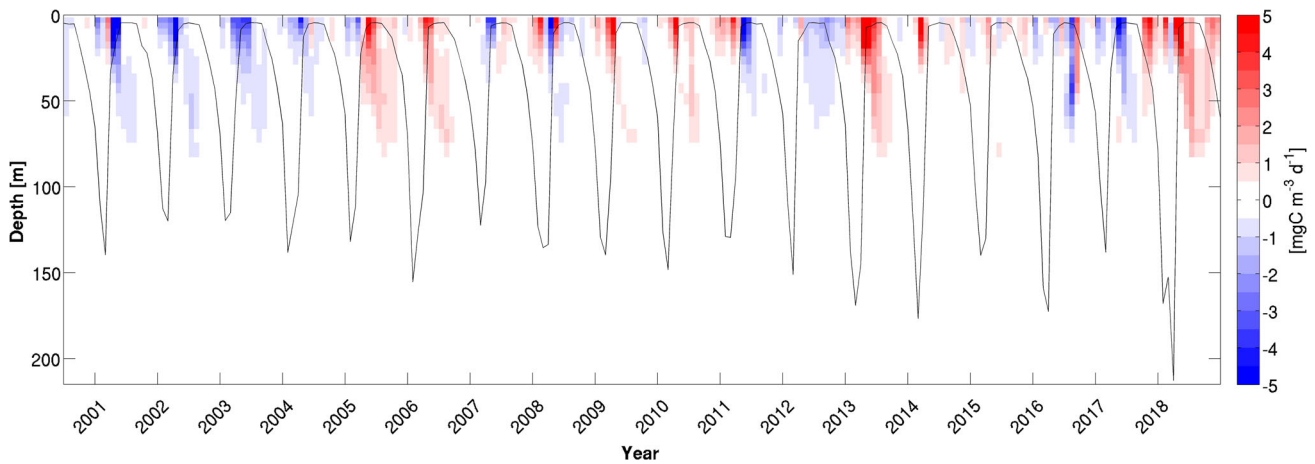
Figure 2.2.4. Time series of the monthly anomalies of the modelled primary production (product. 2.2.1) along the water column with respect to the 1999–2014 monthly means of Figure 2.2.2(c), and time series of mixed layer depth (black line) in the western part of the Mediterranean Sea (Product 2.2.6).

primary production in this region (Renault et al. 2016). Higher-than-average values (increasing productivity) are observed in the south subtropical Pacific. However, since the subtropical ocean is oligotrophic, a small increase in productivity can represent a relatively large positive anomaly.

In the Mediterranean Sea the anomalies for 2018 (Figure 2.2.5(b)) are generally positive in the western basin, consistently with the positive spring increase shown in the time series of anomalies (Figure 2.2.4). Intense vertical mixing in the autumn 2017-winter 2108 period (Figure 2.2.4) triggered a larger nutrient supply to the euphotic layer (as inferred from Figure 2.2.2(c)) and, thus, caused the positive anomaly in 2018. The eastern Mediterranean Sea is characterised by an almost balanced overall anomaly with no
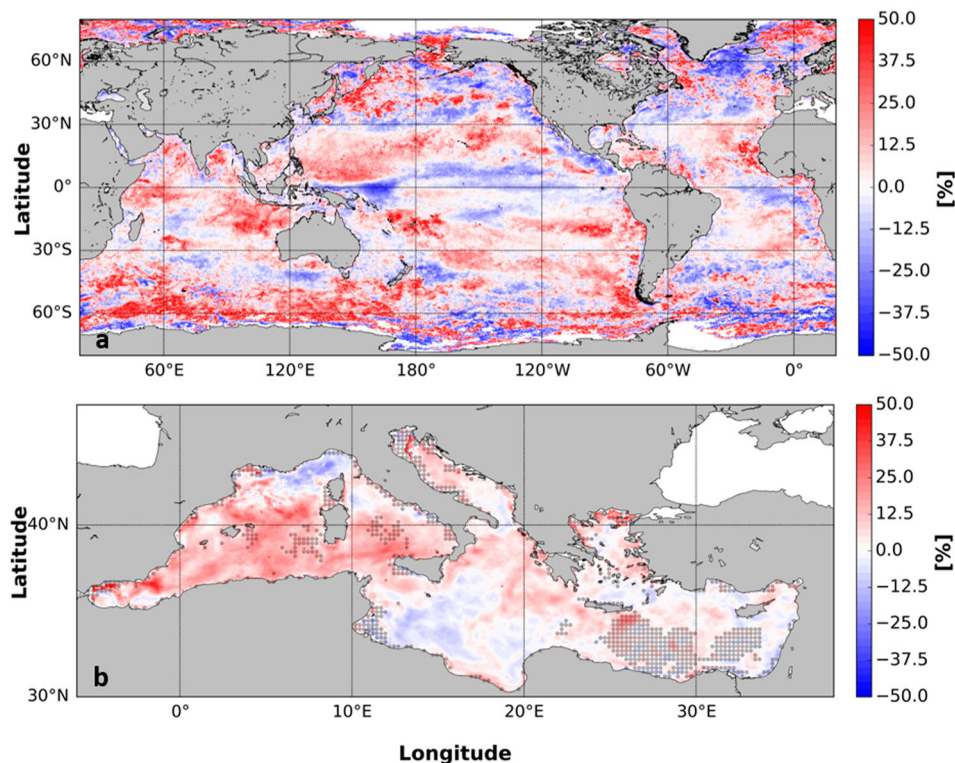
Figure 2.2.5. Map of the relative anomalies of 2018 with respect to the 1999–2014 reference state for the global ocean except Mediterranean Sea (a), estimated from satellite observation, and for the Mediterranean Sea (b), estimated from the merged product. (Products 2.2.5 and 2.2.1). The black dots area indicates the signal-to-noise ratio of the reference state map

particular spatial patterns. High positive anomalies in the northern Adriatic Sea and Northern Aegean Sea should be considered with caution since affected by low signal-to-noise ratios.

Section 2.3: Barrier layer thickness in the Pacific Ocean

Authors: Greiner Eric, Nathalie Verbrugge, Sophie Cravatte, Benoit Tranchant, Arnaud Valcarcel

Statement of main outcome: Barrier layers are ubiquitous in the tropical Pacific, with significant interannual, and decadal variations. Barrier layers act to trap the heat and motion in a thinner mixed layer. It is therefore an important indicator for subseasonal and seasonal forecasting (Madden-Julian Oscillations, El Nino, etc.). The 2018 anomaly is not very different from climatology. The barrier layer is generally thickening over 1993–2018 in the western Pacific and thinning in the central Pacific. Barrier layers may also be an indicator of water cycle changes. The barrier layer indicator could help to monitor these long-term changes and their impacts in near-surface stratification.

Products used:

Ref. No.	Product name & type	Documentation
2.3.1	Global Ocean Observation-based Products MULTIOBS_GLO_ PHY_REP_015_002	PUM: http://marine.copernicus.eu /documents/PUM/CMEMS-MOB -PUM-015-002.pdf QUID: http://marine.copernicus.e u/documents/QUID/CMEMS-M OB-QUID-015-002.pdf
2.3.2	Pacific Decadal Oscillation Index (NOAA)	http://research.jisao.washington. edu/pdo/
2.3.3	Southern Oscillation Index (JISAO)	https://www.cpc.ncep.noaa.gov/ data/indices/soi
2.3.4	Global Ocean- CORA – In-situ Observations Yearly Delivery in Delayed Mode INSITU_GLO_TS_REP_ OBSERVATIONS_013_001_b	http://marine.copernicus.eu/docu ments/PUM/CMEMS-INS-PUM-0 13-001-b.pdf http://marine.copernicus.eu/docu ments/QUID/CMEMS-INS-QUID -013-001b.pdf

2.3.1. Introduction

The mixed layer depth is controlled by temperature stratification in most areas of the world ocean. This is not the case in the tropics, where salinity stratification near the surface plays a dominant role, creating barrier layers (de Boyer Montégut et al. 2007; Mignot et al. 2007). A barrier layer is a quasi uniform isothermal layer located above the top of the thermocline, separated from the surface mixed layer by salinity stratification. It isolates the mixed layer from the cooler waters below. Barrier layers in the tropical Pacific are quasi-permanent, formed by a mix of complex physical processes including rainfall freshening, advection, and stretching (e.g. Cronin et al. 2002). They act to trap momentum and heat in a layer shallower than it would be with temperature stratification alone, and inhibit cooling by turbulent mixing with underlying waters, inducing higher sea surface temperature (Bosc et al. 2009) and stronger eastward zonal jets potentially contributing to the eastward displacement of the Warm Pool. They have thus the potential to influence the ocean heat budget, the Madden Julian Oscillation, the tropical cyclones, and the development of El Nino events (Maes et al. 2002). Better tracking them, and their thickness is thus key for subseasonal to seasonal predictions (Zhao et al. 2014; Zhu et al. 2014).

Barrier layers thickness is computed as the difference between the isothermal layer depth and the mixed layer depth. It varies at different timescales. A weak seasonal cycle of barrier layers in the western tropical Pacific has been found related to the eastern extension of the Warm Pool, and to seasonal variations in precipitation (Mignot et al. 2007). Most of the variability in tropical Pacific barrier layer thickness is on interannual time scale (Ando and McPhaden 1997; Bosc et al. 2009). Liu et al. (2009) indicated that barrier layers are thinning (thickening) during El Niño (La Niña) west of 160°E due to the change in precipitation. The changes in barrier layers' position and thickness however depend on the flavor of El Nino (Wang and Liu 2016) and the SST anomalies location (i.e. emergence in the central or eastern Pacific).

At decadal and longer timescales, variations in barrier layer thickness are harder to detect due to a lack of sufficient high-vertical resolution data. The sea surface salinity and barrier layer thickness variations appear to be closely linked to the Pacific Decadal Oscillation (Delcroix et al. 2007; Wang and Xu 2018), and to shifts in precipitation areas. During positive phases of the Pacific Decadal Oscillation, surface salinity anomalies exhibit a pattern similar to that of El Nino Southern Oscillation, with a larger meridional extent: surface salinity is lower in the western-central equatorial Pacific and higher in the south and north-western Pacific. Patterns of barrier layer thickness anomalies are more complex: barrier layers are thicker in the central-eastern equatorial Pacific, and thinner (by around 15 m) in the far western Pacific and in the southwest (Wang and Xu 2018).

Terray et al. (2012) and Durack (2015) found that the Western Pacific is freshening, following the global water cycle intensification attributed to anthropogenic change. Deser et al. (2012) have shown that, in the atmosphere, the response to anthropogenic forcing is more detectable in surface temperature than in

precipitation or wind. Monitoring of observed climate change may be better served by focusing on integrated quantities such as ocean heat storage rather than on surface quantities (Cheng et al. 2017). Increasing trends in equatorial barrier layer thickness along 137°E and 165°E are associated with the freshening and warming of the western Pacific Warm Pool over the period 1955–2003 (Cravatte et al. 2009). Thus, large-scale, persistent barrier layer monitoring may offer a more robust signature for the intensification of the water cycle than the change in surface salinity. Yet, competing mechanisms at work (such as erosion of the barrier layer by strong wind events, changes in sheared currents), might render the interpretation not straightforward.

Due to the insufficient concurrent temperature and salinity profiles observations, a comprehensive description of the decadal variability and trend of the barrier layers in the last three decades is still lacking. In this study, we utilise the CMEMS ARMOR3D (Guinehut et al. 2012, product ref: 2.3.1) monthly dataset over the 1993–2018 period to compute inter-annual fluctuations and trends of barrier layers in the tropical Pacific. This multi-observation product takes advantage of the resolution of the satellites (altimetry and sea surface temperature) to complement the in situ observations (TAO moorings, XBT lines and ARGO profiles). In the following, we validate the product with in situ data over the 2013–2015 period; we analyse the long term signal over 1993–2018, and we present the 2018 anomaly.

2.3.2. Method

ARMOR3D is a weekly global product with a 1/4° spatial resolution and 33 vertical levels (0, 10, 20, 30, 50, 75, 100 m …). It provides temperature, salinity, geostrophic currents and mixed layer gridded fields from 1993 to present. In a first step, 3D temperature and salinity fields are synthesised through a statistical projection of satellite altimetry and sea surface temperature. In a second step, these synthetic 3D fields are combined with all available in situ data by optimal interpolation. In situ data include vertical profiles from moorings, scientific campaigns, autonomous profilers, gliders, ships of opportunity, sea mammals, as well as surface data from various buoys and ferry boxes. The method used to calculate the barrier layer thickness (BLT) is similar to Montégut et al. (2007) and Wang and Xu (2018). We introduce the reference depth z* (10 m) to avoid the diurnal variability of ocean surface water. T* and S* are the potential temperature and salinity at this depth (level 2 in ARMOR3D). The mixed layer depth (MLD)

is the depth where the change in density from z* is equivalent to a 0.2°C decrease:

$$\rho(\mathrm{MLD}) = \rho(z*; T* - 0.2°\mathrm{C}, S*)$$

$\rho(z) = \rho[z; T(z), S(z)]$ is the potential density at depth z

The isothermal depth layer (ILD) is the depth where the change in temperature from z* is equivalent to a 0.2°C decrease:

$$T(\mathrm{ILD}) = T* - 0.2°\mathrm{C}$$

The barrier layer thickness is the difference between the ILD and the MLD:

$$\mathrm{BLT} = \mathrm{ILD} - \mathrm{MLD}$$

2.3.3. Time average

The mean BLT from ARMOR3D is shown in Figure 2.3.1, and is consistent with the De Boyer Montégut climatology (Mignot et al. 2007). Thick BLTs (more than 20 m) mainly occur under convergence regions: in the Pacific warm pool where surface temperature and precipitation are maximum and surface salinity is minimum, and under the Inter Tropical Convergence Zone and the South Pacific Convergence Zone. Thick BLTs are also seasonally found in winter on the equatorial flank of the subtropical salinity maximum regions in each hemisphere between 10° and 20°, and are visible here (see Mignot et al. 2007 for more discussion on the mechanisms at play). Peak values of BLT appear in the tropical Pacific near the dateline, which can be up to 35 m, whereas domain average for isothermal depth layer and mixed layer depth are 42 and 36 m respectively.

2.3.4. Validation

The contributions of the different steps of ARMOR3D processing have been investigated (not shown). In the first step of ARMOR3D processing, 3D temperature and salinity fields are synthesised through a statistical downward projection of satellite altimetry and sea surface temperature. The barrier layer thickness anomalies obtained with these synthetic profiles reveal that altimetry data alone already carries an important portion of the barrier layer variability signal. For instance, the El Niño onset in 2015 is associated with positive BLT anomalies shifting towards the centre of the basin. The satellite sea surface temperature brings additional refinement, in particular near the central american coast. Using in situ data in the second step brings improvement through large-scale corrections.
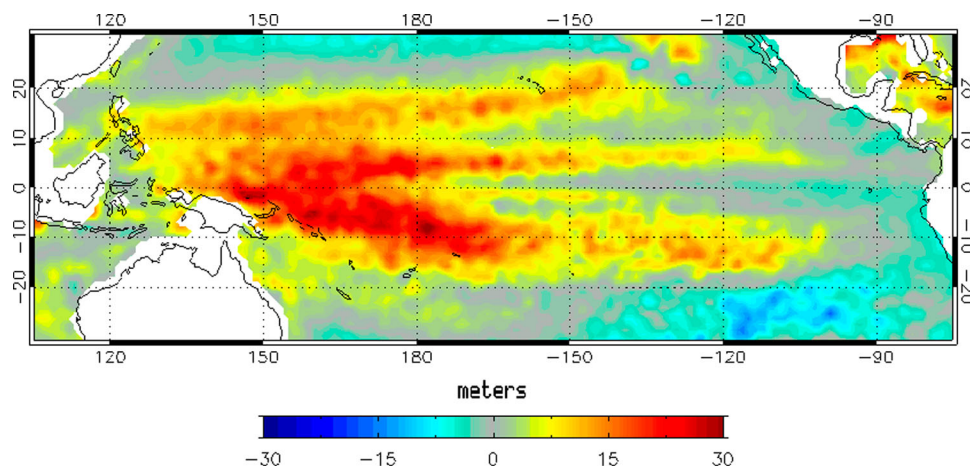
Figure 2.3.1. ARMOR3D (product 2.3.1): Mean barrier layer thickness over 1993–2014, seasonal signal included; units are in metres.

ARMOR3D BLT are validated against collocated in situ Argo profiles measurements (product 2.3.4), which have a good vertical resolution.

The comparison between the BLT deduced from ARMOR3D and Argo profiles is shown in Figure 2.3.2 for the 2013–2015 period. On average over the Tropical Pacific, the mean difference between the BLT deduced from ARMOR3D and the Argo profiles is 1.3 m. Rms error is 10 m. This error is partly explained by the fact that we compare weekly mean values from ARMOR3D and instantaneous values from in situ profiles. As a reference, typical values in the warm pool from both in situ data and ARMOR3D are about 30–40 m, up to 60 m. The maximum BLT over 1993–2018 in the warm pool is about 100 m. Near 10°N, the amplitude of the seasonal signal is about 40 m. The BLT as represented in the ARMOR3D product are thus close to the observations. The ARMOR3D vertical resolution is a limiting factor for an adequate barrier layer thickness resolution. It will be increased in a future version of the product. The variance of the ARMOR3D BLT is underestimated but there is a positive linear relationship since the slope of the linear regression is 0.66.

2.3.5. Interannual variability

We use decompositions in Empirical Orthogonal Functions to explore the Pacific variability. The seasonal cycle was removed before the decompositions. The empirical function 1 of isothermal depth layer (not shown), mixed layer depth (not shown), and BLT (Figure 2.3.3(a)) over 1993–2018 are similar to those found over 1979–2015 with a different dataset (Wang and Xu 2018, Fig. 2) and over 1951–2010 in the western Pacific (Wang and Liu 2016), both in terms of spatial pattern and timing. The patterns reflect the El Nino Southern Oscillation pattern in sea surface salinity (Singh et al. 2011), and barrier layer (Wang and Liu 2016), also similar to the Pacific Decadal Oscillation K-shape pattern in sea surface salinity and barrier layer (Cravatte et al. 2009, Wang and Xu, 2018), although the amplitude of the signal is weaker. Over the 1993–2018 period (Figure 2.3.3 (b)), a correlation of 63% is found between the PC1 time series and the Pacific Decadal Oscillation index (product 2.3.2). Correlation reaches 78% with the Southern Oscillation Index (product 2.3.3). The 1997–1998 and 2015–2016 El Niño events, as well as the

Figure 2.3.2. BLT comparisons between ARMOR3D weekly (product 2.3.1) and in situ: scatterplot diagram between Argo profiles in situ BLT in the Tropical Pacific (15°N-15°S,130°E-80°W) (abcissa), and the corresponding collocated BLT from ARMOR3D (ordinate); units are metres. The black line along the diagonal corresponds to the perfect fit; the flatter blue line corresponds to the linear regression between ARMOR3D and in situ data.

Figure 2.3.3. ARMOR3D (product 2.3.1) 1993–2018 first empirical mode of Barrier Layer Thickness (8% of variance): spatial pattern (a), times series (b) of the first empirical mode (black line), negative Pacific Decadal Oscillation index (product 2.3.2) (orange) and Southern Oscillation index (product 2.3.3) (blue); a 3-month smoothing was applied.

2010 La Nina event are strong events that help to reach such high correlations with the BLT. The BLT gets thicker in the western equatorial Pacific and thinner in the central and eastern Pacific during La Nina events and negative Pacific Decadal Oscillation. This pattern is due to an eastward shift of the Pacific Warm Pool and to changes in precipitation and advection.

The second empirical mode in BLT (not shown) is essentially limited to the area between Papua-New Guinea and the dateline, and between 5°N and 10°S. It perfectly mirrors the Pacific Decadal Oscillation influence on the freshwater flux budget (Wang & Xu, 2018, Fig. 3c).

2.3.6. Trend

Sea surface temperature and salinity vary on a multidecadal timescale, in correlation with the Pacific Decadal Oscillation (Cravatte et al. 2009). The associated BLT changes are not straightforward. Here, we find that during the 1993–2018 period, both the ILD and MLD undergo increasing trends (cumulative trends over 1993–2018 are shown in Figure 2.3.4(a,b)) in most of the tropical Pacific associated with the change in trade winds and the westward shift of precipitations (England et al. 2014). On average over the domain, the mean total

change since 1993 is 3.4 m in ILD, and 3.6 m in MLD: both quantities thicken at the same place, and the resulting change is smaller in BLT with opposite effects in ILD and MLD. The convergence of heat and mass in the western and central Pacific largely (about 5 m per decade) deepens the isotherms (Figure 2.3.4(a)). The fresher surface and saltier subsurface layers between 0° and 8° N tend to shoal the MLD (about 5 m per decade) west of the dateline (Figure 2.3.4(b)). Subsequently, the BLT (Figure 2.3.4(c)) is generally thickening in the far western equatorial Pacific and thinning off equator and in the equatorial central Pacific. The BLT trend is negligible in the East.

Over the last decades, the western Pacific has become fresher and the subtropical Atlantic saltier (Terray et al. 2012). The observed Pacific and interbasin-averaged salinity changes exceed the range of internal variability provided from control climate simulations, whereas changes in the tropical and midlatitudes Atlantic salinity levels are not significant compared to internal variability. Moreover, the recent freshening of the North Atlantic subpolar gyre (Tesdal et al. 2018) could make the detection even more difficult in the Atlantic. Hence, the salinity changes are more significant in the Pacific.
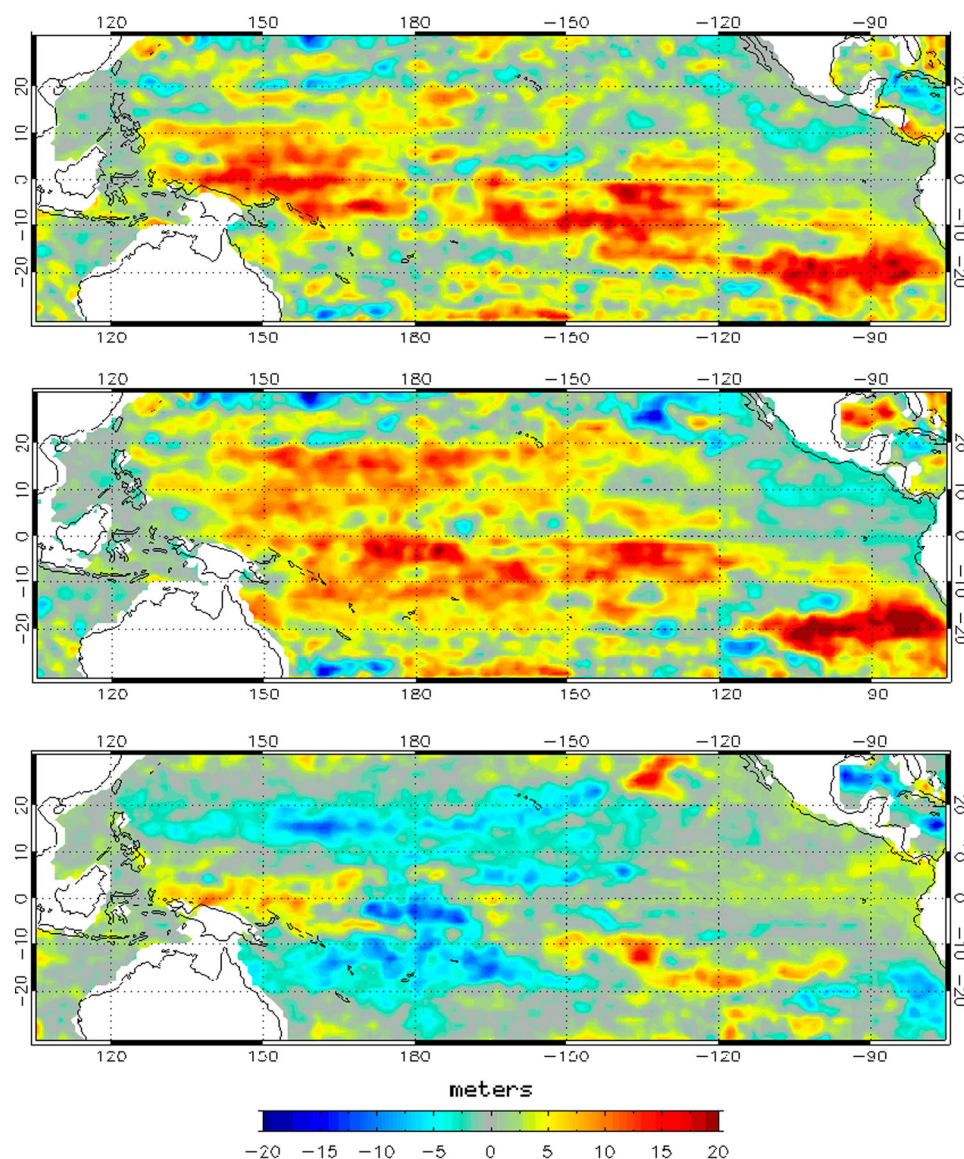
Figure 2.3.4. ARMOR3D (product 2.3.1) 1993–2018 cumulative trend of Isothermal Layer Thickness [a], Mixed Layer Depth [b] and Barrier layer Thickness [c]; units are metres. The cumulative trend is the linear trend multiplied by the number of sample minus 1. The linear trend was computed over the monthly fields.

Aretxabaleta et al. (2017) suggest that the acceleration of the water cycle is at work, but the data span is still too short and can suffer from a sampling effect. Llovel et al. (2018) findings about the sea level trends suggest that the time of emergence (the time when the signal will emerge from the climate variability) is reduced west of the Date-line (their Fig. 4), with less than 10 years needed to exceed the noise level (and at least 30 years in the Atlantic gyres). So, the BLT in the Pacific warm pool is a good candidate, if well observed, for an early detection of the water cycle change.

Yet, the BLT trend does not exhibit a pattern obviously linked with the change in water cycle. Changes in surface salinity do not follow expected patterns of amplified salinity contrasts. It points out the importance of ocean advection and natural climate variability in shaping patterns of decadal change in surface salinity (Vinogradova and Ponte 2017). Our study confirms that the cumulative trend of BLT over 1993–2018 is still dominated by internal variations. This period is still too short, and the data sampling effects must be minimised to detect an anthropogenic fingerprint in the tropical salinity changes (increased precipitation and freshening).

2.3.7. Anomaly in 2018

The fluctuations of the yearly BLT are illustrated by the anomalies for 2008 and 2015 (Figure 2.3.5(a,b)), corresponding respectively to strongly positive and negative Southern Oscillation indexes. In general, anomalies are

stronger in the Western Pacific where the mean BLT is thicker (Figure 2.3.2). The 2008 and 2015 anomalies fit well the first empirical mode pattern (Figure 2.3.3). In 2015, the BLT is thicker in the centre of the basin, in response to the strong eastern Pacific El Nino. On the contrary, the 2018 anomaly does not show any clear signal. More would be needed to explain the pattern seen, but it is likely internal variability, with little correspondence with the first empirical modes of ILD, MLD and BLT, or with the trend in BLT. 2018 looks like a transitional year, with weak La Nina regime in 2017–2018. Only noticeable is the reduced BLT on the southern flank of the subtropical maximum salinity, near 10°N. This could be the imprints of the extra-equatorial sea surface salinity fresh anomalies associated with 2015 El Nino (Hasson et al. 2018).

2.3.8. Conclusions

The barrier layer plays an important role for ocean-atmosphere interactions by trapping heat and motion in a thinner mixed layer, with a noticeable impact on seasonal forecasting. Even if the isothermal and mixed layer depths undergo increasing trends in most of the tropical Pacific associated with changes in trade winds and westward shift of precipitation, the trend in BLT is mainly limited to an equatorial thickening west of the Dateline. Fluctuations of the past few years, including 2018 yearly anomaly, are still dominated by internal Pacific variability. Correlations with the Pacific Decadal Oscillation and the Southern Oscillation are significant, even if the dynamics controlling interannual and decadal BLT anomalies are not well understood yet. The BLT in the
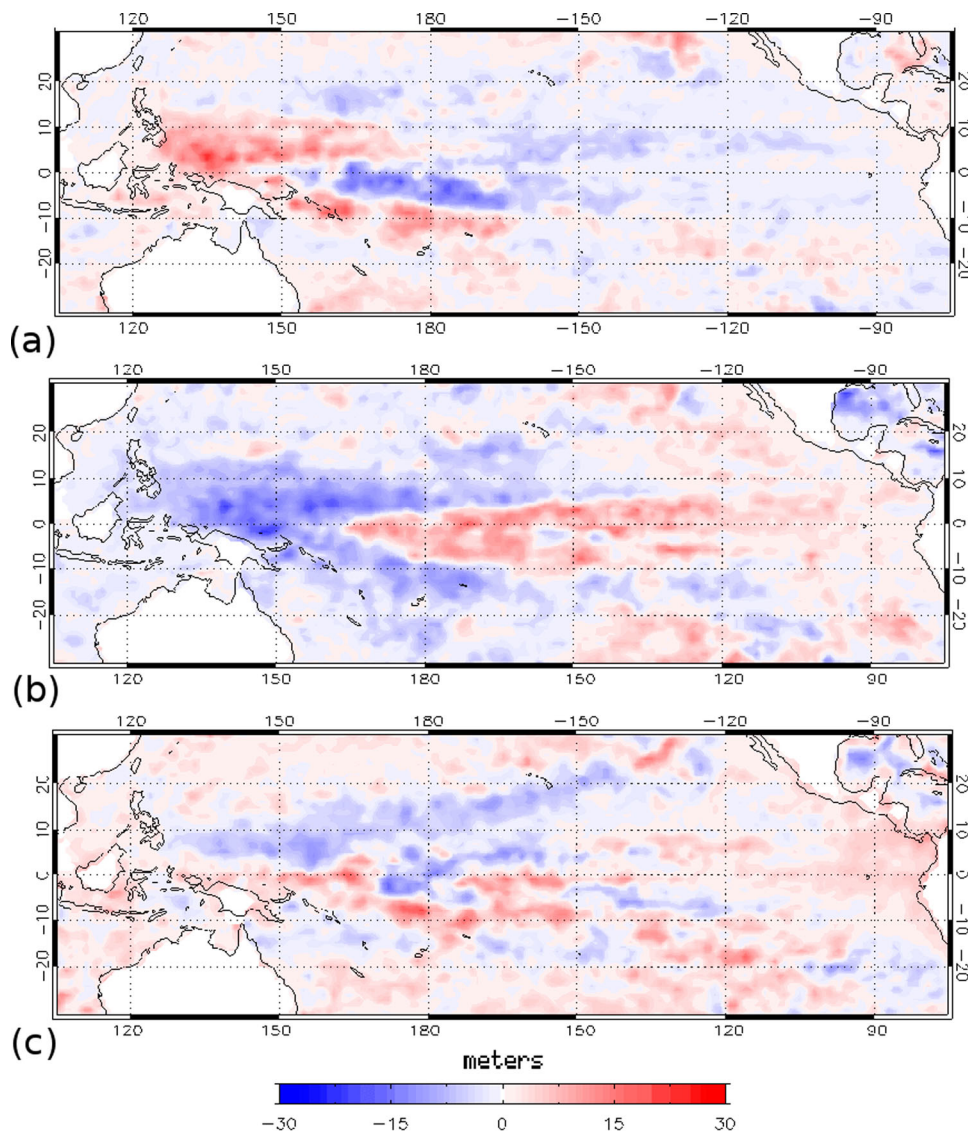
Figure 2.3.5. ARMOR3D (product 2.3.1): yearly anomaly of Barrier layer Thickness (relative to 1993–2014) in 2008 (a), 2015 (b), and 2018 (c.); units are metres.

Pacific warm pool is an important monitoring variable, both for seasonal forecasting, and as a potential candidate, for an early detection of water cycle change.

Section 2.4: Interannual variability in the eastern and western Mediterranean Overturning Index

Authors: V. Lyubartsev, F. Borile, E. Clementi, S. Masina, M. Drudi, G. Coppini, P. Cessi, N. Pinardi

Statement of Main Outcomes: The western and eastern Mediterranean clockwise meridional overturning circulation is connected to deep-water formation processes, which are responsible for the ventilation of deep pelagic and benthic ecosystems. In this study, we used an eddy resolving CMEMS reanalysis of a 32-year-period (1987–2018) to discuss for the first time the interannual variability of the Meridional overturning index. This index is defined here as the maxima of the clockwise cells in the eastern and western Mediterranean Sea. The meridional overturning circulation is more vigorous in the eastern than in the western basin, and reached its maximum value in 1992, during the Eastern Mediterranean Transient (Roether et al. 1996). In the western Mediterranean Sea, the overturning circulation became greater after the western Mediterranean Transition occurred in 2005–2006.

Products used:

Ref. No.	Product name and type	Documentation
2.4.1	MEDSEA_REANALYSIS_ PHYS_006_004	PUM: http://marine.copernicus.eu/ documents/PUM/CMEMS-MED-PUM-006-004.pdf QUID: http://marine.copernicus.eu/ documents/QUID/CMEMS-MED-QUID-006-004.pdf DOI: https://doi.org/10.25423/medsea_ reanalysis_phys_006_004http://marine. copernicus.eu/documents/QUID/CMEMS-MED-QUID-006-004.pdf

2.4.1. Introduction

The Mediterranean Sea reanalysis (Simoncelli et al. 2014) over the latest 32 years (1987–2018) was used to assess the Mediterranean Sea Eulerian overturning circulation (in both the Eulerian and residual frameworks) which is composed of multiple zonal and meridional cells (Pinardi et al. 2019). The clockwise overturning cells are associated with deep and intermediate water mass formation processes that occur in specific areas of the basin: Gulf of Lion, Southern Adriatic Sea, Cretan Sea and Rhodes Gyre (Pinardi et al. 2015). These processes are responsible for the transfer of biogeochemical tracers

to the deep-water, such as oxygen and inorganic and organic matter, which then ventilate and feed the deep pelagic and benthic ecosystems (Houpert et al. 2016). Clockwise cells occupy the upper water column, with maxima in the upper 1500 m of the water column, while the Mediterranean abyssal regions are characterised by anti-clockwise cells.

The overturning circulation of the eastern Mediterranean Sea is affected by the dense Aegean waters outflowing through the Cretan Straits during the Eastern Mediterranean Transient (Gertman et al. 2006), a climatic event that occurred between 1988 and 1995. In the western Mediterranean it has been recognised that a climate shift occurred after 2005 (the Western Mediterranean Transient, Schroeder et al. 2016).

A compact representation of the overturning circulation of the basin has been conventionally given by the mean meridional Eulerian streamfunctions, and more recently the residual transport in density coordinates has also been considered. In this section, we focus on the Eulerian framework, because this has been traditionally explored in the context of the Atlantic Meridional Overturning Circulation, allowing in the future the intercomparison of the two systems.

Here we here propose the Mediterranean overturning index as a measure of the strength of the Mediterranean Eulerian clockwise meridional overturning circulation, computed separately for the eastern and western subbasins. This measure is representative of the transport of water volume, while the residual overturning is more representative of the tracers' transport. The latter will be the focus of future work.

The goal of this work is to describe the observational evidence of the interannual variability of the Mediterranean Sea overturning system using an eddy-resolving model with data assimilation and a Meridional overturning index. This approach enables the systematic monitoring of the ventilation of the deep ocean layers in the Mediterranean Sea.

2.4.2. Methods

Time mean meridional Eulerian streamfunctions were computed using the velocity field estimate provided by the CMEMS Mediterranean Sea reanalysis over the last 32 years (1987–2018). The Eulerian meridional streamfunction was evaluated by integrating meridional velocity daily data first in a vertical direction, then in a meridional direction, and finally averaging over the reanalysis period:where – H refers to the bathymetry, x_{B1} and x_{B2} define the zonal boundaries, and $T = t_1 - t_0$ represents the time interval of interest (Pinardi et al. 2019).

The Mediterranean overturning indices were derived for the eastern (Equation 2.4.2) and western (Equation 2.4.3) Mediterranean Sea by computing the annual streamfunction in the two areas separated by the Strait of Sicily around 36.5°N, and then considering the associated maxima.

$$\text{WMOI} = \max\ \{\psi\ (y \geq 40°\text{N},\ z < -300\ \text{m})\} \quad (2.4.2)$$

$$\text{EMOI} = \max\ \{\psi\ (y < 36.5°\text{N},\ z)\} \quad (2.4.3)$$

In each case a geographical constraint focused the computation on the main region of interest. For the western index, we were interested in deep-water formation regions, thus we excluded both the effect of shallow physical processes and the Gibraltar net inflow. For the eastern index, we investigated the Levantine and Cretan areas corresponding to the strongest meridional overturning cell locations, thus we only defined a zonal constraint.

2.4.3. Results and discussion

The mean meridional Eulerian streamfunctions for the Mediterranean Sea were evaluated for the entire Mediterranean Sea reanalysis period (1987–2018) for both the western (Figure 2.4.1(a)) and eastern (Figure 2.4.1(b)) sub-basins separated by the Strait of Sicily around 36.5°N. In both sub-basins, clockwise cells (red arrows in Figure 2.4.1) occupy the upper water column, with maxima in the upper 1500 m of the water column. The
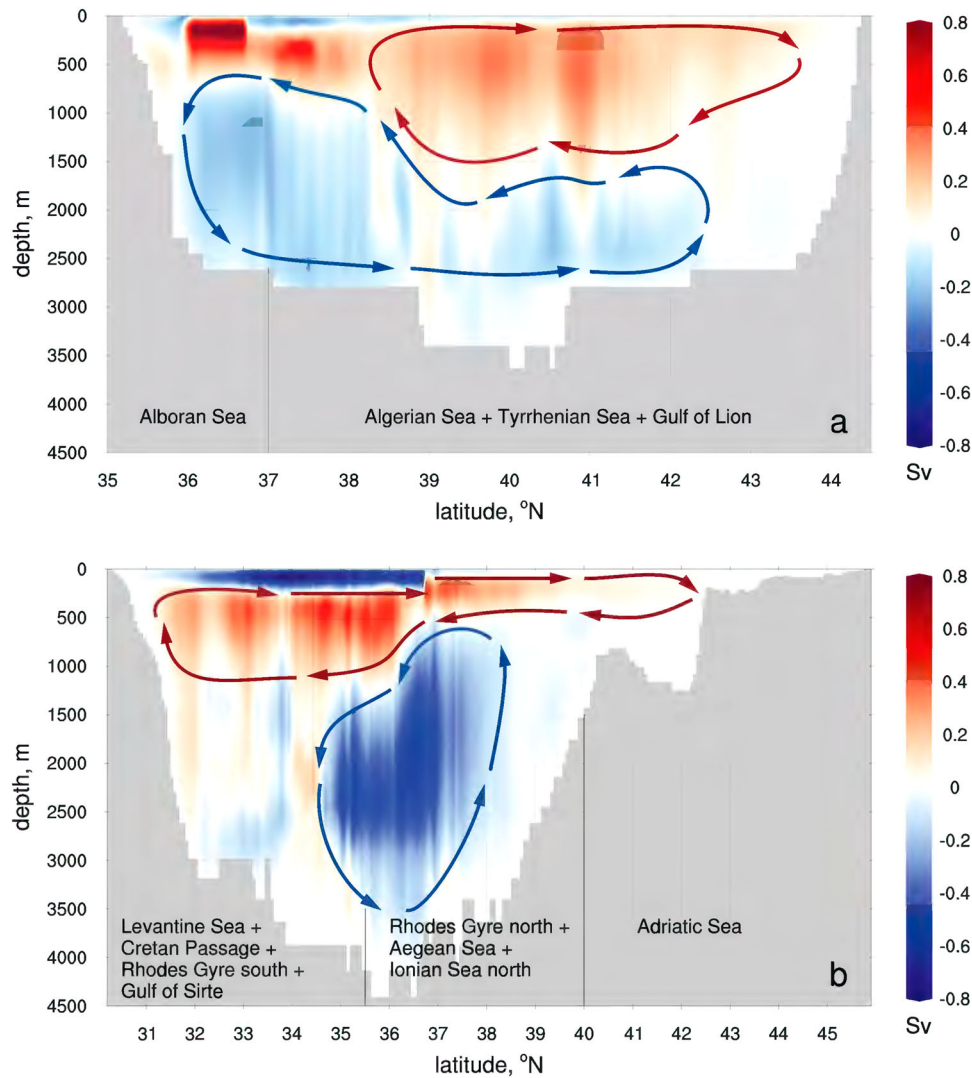
Figure 2.4.1. Mean (1987–2018) Eulerian meridional overturning streamfunctions evaluated using Equation (1) for the western (a) and eastern (b) Mediterranean Sea basins. Red clockwise arrows indicate patterns associated with deep and intermediate water mass formation; blue anticlockwise arrows indicate the pattern of abyssal cells. The Mediterranean Sea regions considered in the latitudinal averaging are described in the bottom panels. Data used: Mediterranean Sea Reanalysis MEDSEA_REANALYSIS_PHYS_006_004 (product 2.4.1).

counter-clockwise cells (blue arrows in Figure 2.4.1) characterise the Mediterranean abyssal regions. The large positive values in the upper 500 m between 36°N and 36.5°N, seen in Figure 2.4.1(a), correspond to the Gibraltar Strait inflow (Pinardi et al. 2019).

The western sub-basin clockwise overturning circulation is associated with the deep-water formation area of the Gulf of Lion, while the eastern clockwise meridional overturning circulation is composed of multiple cells associated with different intermediate and deep-water sources in the Levantine, Aegean, and Adriatic Seas. Traditionally the eastern clockwise overturning circulation has been associated with the Adriatic and Aegean Sea deep-water formation processes. However, Pinardi et al. (2019) reported that strong clockwise meridional overturning cells are also forced by intermediate and deep-water formation processes in the Rhodes Gyre and Cretan Sea areas, south of 36°N.

The yearly western (Equation 2.4.2) and eastern (Equation 2.4.3) Mediterranean overturning indices derived using the meridional Eulerian streamfunctions were computed for 1987–2018 and are shown in Figure 2.4.2.

The eastern overturning indices had higher values than the western index during the period 1987–2000. This indicates a more vigorous meridional overturning circulation in eastern Mediterranean. The difference is mostly related to the occurrence of the Eastern Mediterranean Transient climatic event, where the Aegean Sea discharged unusually dense water masses into the eastern Mediterranean abyssal layer (Roether et al. 2014). The Aegean outflow forced the clockwise overturning circulation from 1992 to 1995, and in line with this, the related peak of the eastern Mediterranean overturning index is located in 1992.

In 2000 the difference between the eastern and western Mediterranean overturning indices started to become smaller because the water masses formed during the Eastern Mediterranean Transient reached the Strait of Sicily and propagated into the western Mediterranean (Schroeder et al. 2016). The effect of this water propagation inside the western basin is known as the Western Mediterranean Transition and strongly affects the western Mediterranean overturning index thereafter. In particular, a large peak in the western Mediterranean overturning index is found in 2006: it could be connected to the anomalous deep-water formation event in the western Mediterranean discussed by Smith et al. (2008) and Schroeder et al. (2016).

Finally, the other peak in the western basin in 2013 may reflect the significant climate shift in the dense water formation in the western Mediterranean reported by Houpert et al. (2016). Our analysis shows the largest western Mediterranean index peak in 2018, but no observations documenting an extreme in deep water formation processes still exist. In summary, the proposed western Mediterranean overturning index can potentially be used as the basis of long-term climate monitoring of overturning changes in the Mediterranean Sea.

2.4.4. Conclusions

The high resolution, multidecadal Mediterranean Sea reanalysis has enabled us, for the first time, to assess the Mediterranean overturning circulation and develop indices that can play a key role in monitoring climate variability in the basin.

The western and eastern Mediterranean overturning indices are synthetic indices of changes in the
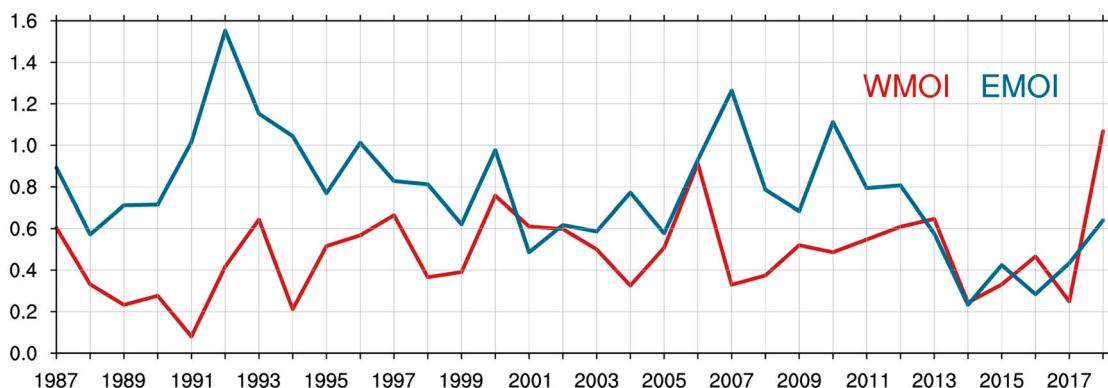
Figure 2.4.2. Mediterranean overturning indices [Sverdrup] calculated from the annual means of meridional streamfunction from 1987 to 2018. Blue: Eastern Mediterranean Overturning Index – EMOI (lat<36.5°N); Red: Western Mediterranean Overturning Index (lat≥40°N, z>300m) – WMOI, defined in equation 2.4.2 and 2.4.3. Data used: Mediterranean Sea Reanalysis MEDSEA_REANALYSIS_PHYS_006_004 (product 2.4.1).

thermohaline properties of the Mediterranean basin related to changes in the main drivings of the basin scale circulation. In particular, the eastern Mediterranean overturning index was found to have higher amplitude than the western one, with the largest peak occurring in 1992 during the Eastern Mediterranean Transient, while the western Mediterranean index maximum occurs in 2006 during the Western Mediterranean Transition.

As in the global ocean, the overturning circulation of the western and eastern Mediterranean are paramount to determine the stratification of the basins (Cessi 2019). In turn, the stratification and deep water formation mediate the exchange of oxygen and other tracers between the surface and the deep ocean (e.g. Johnson et al 2009; Yoon et al. 2018). In this sense, the overturning indices are potential gauges of the ecosystem health of the Mediterranean Sea, in particular they could instruct early warning indices for the Mediterranen Sea to fulfil the Sustainable Development Goal (SDG) 13 Target 13.3.

Section 2.5: Spatio-temporal variability of the Black Sea Cold Intermediate Layer properties derived from in situ data

Authors: Valcheva, Nadezhda, Veselka Marinova, Elisaveta Peneva**,** Leonardo Lima, Stefania Ciliberti, Simona Masina

Statement of Main Outcome: Representing the interface between surface and deep waters, the Cold Intermediate Layer is a distinctive feature of the Black Sea thermo-haline dynamics. The presence of cold intermediate waters is extremely important for the Black Sea ecosystem because they are rich in oxygen and mark the upper boundary of the anoxic zone. Therefore, more than 5000 temperature profiles originating from both in-situ shipboard and Argo profiling floats observations were used to explore and analyse spatial and temporal variability of various cold intermediate layer properties such as thickness and core temperature at subregional and seasonal to interannual scales. The findings show that the process of regional warming penetrating downward to intermediate depths results in a decrease of the thickness and reduced replenishment of the layer. Concurrently, the core temperature has risen with about 2.0°C over the past 25 years resulting even in cold intermediate layer disappearance in several instances. In spite of the subsequent recovery, occurred in the span of a year, the drop of temperature difference between boundary and core waters as well as shoaling of the layer's lower limit represent a major threat for the Black Sea thermo-haline balance and ecosystem function.

Product used:

Ref. No.	Product name & type	Documentation
2.5.1	INSITU_BS_NRT_OBSERVATIONS_013_034	PUM: http://marine.copernicus.eu/documents/PUM/CMEMS-INS-PUM-013.pdf QUID: http://marine.copernicus.eu/documents/QUID/CMEMS-INS-QUID-013-030-036.pdf
2.5.2	INSITU_BS_TS_REP_OBSERVATIONS_013_042	PUM: http://marine.copernicus.eu/documents/PUM/CMEMS-INS-PUM-013.pdf QUID: http://marine.copernicus.eu/documents/QUID/CMEMS-INS-QUID-013-042.pdf

2.5.1. Introduction

The Black Sea is a marginal semi-closed basin. Both the large freshwater river flux at the surface and inflow of saltier Mediterranean waters, spreading in the deep sea through the strait of Bosphorus, create the conditions for a unique two-layer termo-haline water stratification. Hence, a sharp halo-pycno-cline located at the depths of 50–100 m is formed, which separates the upper and the deep basin layers (Özsoy and Ünlüata 1997; Ivanov and Belokopytov 2013). One of the features of a fundamental importance is the Cold Intermediate Layer, which represent the interface between surface and deep Black Sea waters. Its lower boundary corresponds to the permanent pycnocline, while in the second half year (from June to December) the layer's upper boundary is limited by the seasonal thermocline. Traditionally confined by the 8°C isotherm, the cold intermediate layer contains water with the lowest temperatures along the entire column, including those of the upper pycnocline (Oguz and Besiktepe 1999; Ivanov et al. 2001).

It has been established that the cold intermediate layer is formed both in the centres of cyclonic gyres and by extreme cooling of waters in the north-western shelf and continental slope (Ivanov et al. 1997; Staneva and Stanev 1997; Stanev et al. 2003), which are afterwards advected throughout the Black Sea between depths of approximately 50–100 m through the cyclonic circulation dominated by the Rim Current. Baroclinic eddies formed on both sides of the Rim Current play an important role in the horizontal exchange of heat and salt (Staneva et al. 2001; Shapiro et al. 2010; Kubryakov et al. 2018). Vertical movements in the eddies displace the isopycnal surfaces resulting in a dome-like vertical distribution of thermohaline and chemical layers being shallower at the cyclonic centre of the basin and deeper at the anticyclonic surroundings (Ginzburg et al. 2008; Ivanov and Belokopytov 2013). In particular, in summer, when the Rim Current weakens, large anticyclonic eddies

are formed over the continental slope as a result of current instability (Kubryakov and Stanichny 2015), which can penetrate down to depths of 500–1000 m, therefore affecting the turbulence generation and deep basin ventilation (Korotaev et al. 2006). Therefore, the depth of temperature minimum – cold intermediate layer core – can sink down to more than 110 m in anticyclonic edge and rise up to 30 m in cyclonic centre (Zatsepin et al. 2003; Akpinar et al. 2017) with respect to average values of 60–90 m for the continental slope. In addition, cold intermediate waters are extremely important for the Black Sea ecosystem because they are rich in oxygen and represent upper boundary of the anoxic zone. With this respect, analysis of historical oxygen profiles and recent Argo floats showed a long-term deoxygenation trend of the open Black Sea as the most alarming manifestation is the shoaling of the oxycline depth from 140 (1955) to 90 m (2010–2015) (Capet et al. 2016).

During the past decade, the cold intermediate layer thickness has been found to decrease considerably or even to disappear, which affects its cooling capacity (Capet et al. 2018; Miladinova et al. 2018; Stanev et al. 2019). The process of global warming penetrating downward to intermediate depths is influenced by the climate change, which could be a response to anthropogenic pressure (Barnet et al. 2001), and might have regional implications (Piotukh et al. 2011). Hence, it is of utmost importance to monitor the spatio-temporal variability of the cold intermediate layer properties.

2.5.2. Data and methods

The present study covers the entire Black Sea basin where cold intermediate layer can be fully observed (both upper and lower limit present), typically at depths of more than 200 m. In order to distinguish between areas of specific mesoscale dynamics, the basin is divided into 5 subregions, of which four were delimited within the anticyclonic periphery – western, northern, eastern and southern; and one comprising the cyclonic interior, confined approximately by the 1400-m isobath (denoted hereafter as 1, 2, 3, 4 and 5, see Figure 2.5.1(A)). The proposed spatial division conforms to a certain extent with the relative contribution of different Black Sea regions to cold intermediate waters formation as stated in Stanev et al. (2003) but considered in balance with the existing disparity in data spatial coverage.

The studied time period encompasses 26 years (1993–2018). Assessment is performed for two timespans (seasons) within each calendar year, during which the cold intermediate layer is observable as a vertical profile feature. These are successive months of June-July-August-September and October-November-December roughly corresponding to summer and autumn, respectively.

Data in use consist of temperature profiles originating from both in-situ shipboard and Argo profiling floats observations. The following CMEMS products have been employed: Black Sea In Situ Near Real Time Observations (product ref. 2.8.1) and Black Sea In Situ Observations yearly delivery in delayed mode (product 2.8.2). More than 5000 profiles have been processed, 48% of which represent shipboard observations and 52% are data derived from Argo floats (starting from 2005). A seasonal bias in sampling is observed as profiles sampled in autumn represent only 38% of total coverage (Figure 2.5.1 (B–E)). The number of profiles is largest during 1993–2000 (∼ 40%) and 2011–2018 (41.7%), whereas in 2001–2010 the quantity is less than half – 18.7% (Figure 2.5.1(D,E)). Almost 45% of the data were measured in the deep basin. The largest amount of data for basin periphery is available for subregions 4 (16.8%) and 2 (14.5%) and subregion 1 was the most undersampled (10.3%). The seasonal bias is most distinct for subregions 4 and 2 as the contribution of autumn observations is 35 and 38%, respectively (Figure 2.5.1(D,E)).

Several cold intermediate layer features were monitored such as thickness, core temperature and depth, isotherm defining layer's boundaries, and temperature difference between boundary and core waters as an indicator of the cold intermediate layer cooling capacity. Several authors suggested that currently cold intermediate layer should comprise waters having temperature lower than 8.35°C (Stanev et al. 2013; Capet et al. 2014; Miladinova et al. 2018) and even 8.7°C (Stanev et al. 2019). Therefore, in order to determine the isotherm surface marking out the layer's limits, herewith, a dynamic criterion was adopted rather than fixed values.

Dynamic criteria in use concerns determination of the lower cold intermediate layer margin and is based on detection of thermal conditions in the profiles' mid-pycnocline area as suggested by Ivanov et al. (2001). They reported that the core occurs at potential density anomaly $\sigma_t = 14.2–14.8$, while the lower boundary corresponds to $\sigma_t = 15.3–15.9$ given that the temperature is 8°C. Stanev et al. (2003) have further specified that under the dominating density stratification (controlled by salinity) the isopycnic level beyond which the water penetrates into the core is $\sigma_t = 14.5$, whereas the lower boundary is at $\sigma_t = 15.5$.

More specifically, the method involves: (1) calculation of potential density anomaly by the international equation of state of seawater EOS-80 (UNESCO 1983) using the derived variable potential temperature and the measured pressure and salinity; (2) careful joint examination of temperature and density profiles, in
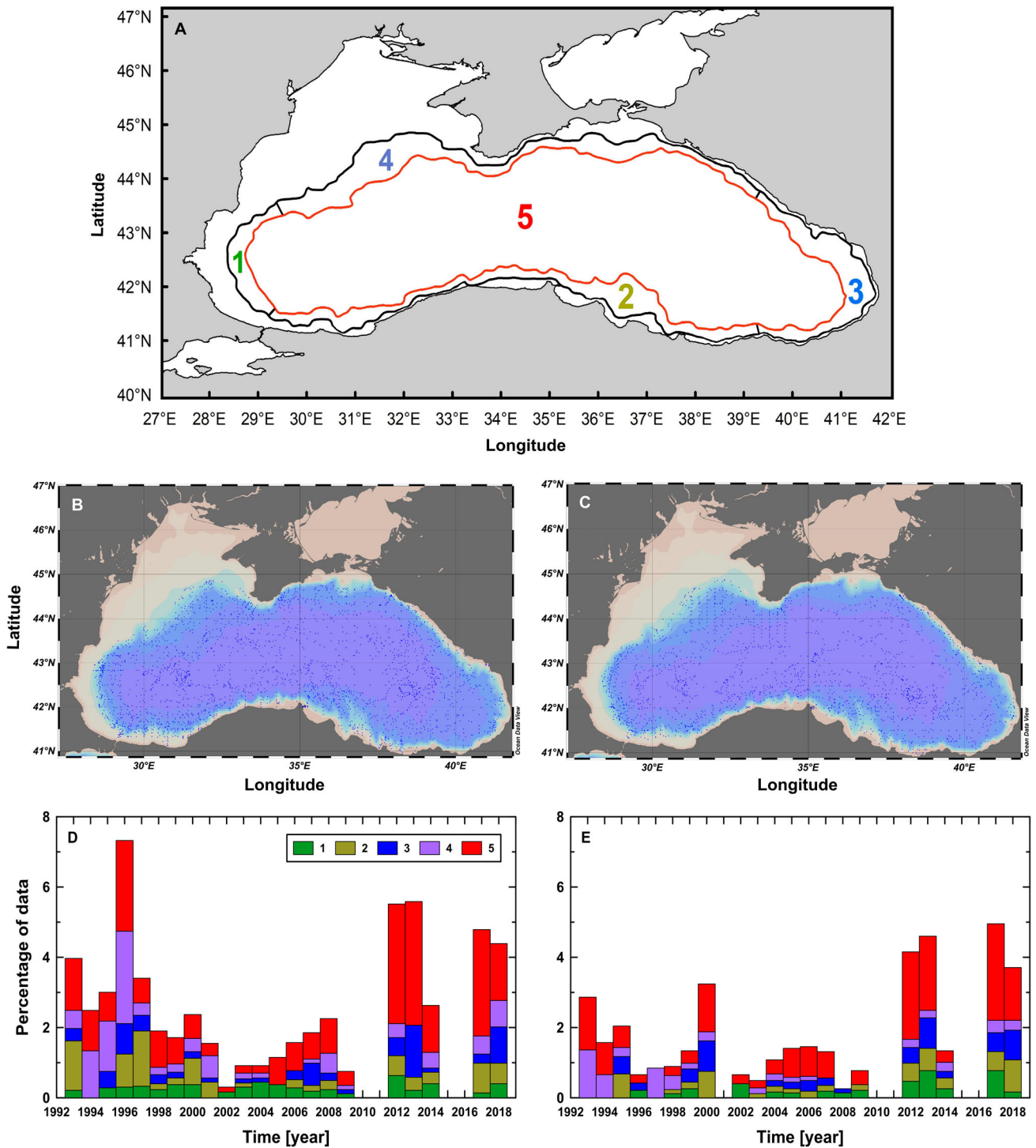
Figure 2.5.1. Scheme of the study area (A): 1400-m isobath (thick red line) delimitates interior basin while 200-m isobath (thick black line) marks out the peripheral boundary; 1 denotes western, 2 – southern, 3 – eastern, 4 – northern anticyclonic and 5 – central cyclonic subregions. Spatial data coverage of both in-situ shipboard and Argo profiling floats observations is presented for: (B) summer and (C) autumn, as well as a detailed inventory of data availability per year and subregion for: (D) summer and (E) autumn.

particular within the main pycnocline extent, together with inspection of related temperature gradients; (3) determination of the mid-pycnocline depth, which is considered as cold intermediate layer lower limit depth, and the corresponding isotherm; (4)

determination of the layer's upper boundary depth (no criteria was applied assuming that one and the same isotherm defines the boundaries); (5) calculation of cold intermediate layer thickness; (6) detection of temperature minimum within the layer extent and the

corresponding depth; and (7) calculation of temperature difference between boundary and core waters.

The further analysis involves an assessment of spatial and temporal variability of the monitored cold intermediate layer features at subregional and seasonal to interannual scales. Seasonal time series of averaged monitored parameters were obtained for each subregion and each year. However, due to relatively small areal extent of peripheral subregions a certain disparity of data coverage is apparent. In order to evaluate how this variance in data spatial distribution influences the seasonal means of studied properties, the standard error of the mean (SE_{mean}), referred hereafter as standard error, is calculated using the following formulation:

$$SE_{mean} = \frac{\text{Standard deviation of sample}}{\sqrt{\text{Sample size}}} \quad (2.5.1)$$

Besides, space–time averages of standard error of each property mean were calculated and regarded as a threshold value, against which the uncertainty of the obtained estimates was assessed.

2.5.3. Results and discussion

The cold intermediate layer thickness interannual variability reveals a steady decreasing trend of this property. The cold intermediate layer was found to grow thinner as its thickness dropped by more than half in the course of the study period, from hundred in the beginning to several tens of meters by the end depending on the subregion. More specifically, in summer, the thickness changed from 95–125 m in 1993–45–55 m in 2018 in the anticyclonic periphery, and between 73 and 38 m, respectively, in the basin interior (Figure 2.5.2(A)). The cold intermediate layer was thickest in subregions 3 and 4 (123 and 125 m) opposed to 86 m (subregion 1) and 95 m (subregion 2) and it thinned out to 54, 45, 63 and 60 m each. This means that the sharpest decrease in thickness was observed for 3 and 4 (2.3–2.8 times), whilst for 1 and 2 the decrease was not so distinct (less than 1.6 times). The interannual variability also indicates that the contrast between peripheral areas reduces in the course of the study period.

In autumn, the cold intermediate layer grows even thinner: thickness decreased from 72–95 m in 1993 to 42–56 m in 2018 within the margins, and from 70 to 27 m, respectively, in the inner basin (Figure 2.5.2(C)). Besides, in the basin periphery, the layer thickness has well expressed seasonal variability since by autumn it decreases with approximately 11 m (from 62.7–51.3 m averaged over the whole peripheral area). This is not the case within cyclonic gyres where the thickness remains almost unchanged during the second half of the year – about 39 m. Altogether, the cold layer is less thick in subregions 1 and 2 with respect to 3 and 4 but, in autumn, this difference narrows.

In general, the standard error temporal variability displays the opposite to data availability tendency – the largest is the error for the middle time-span of the study period, when there was a deficit of measurements, while it is the smallest in the past decade (Figure 2.5.2(B,D)). The space–time averages of standard errors of the cold intermediate layer thickness means are 2.8 m in summer and 2.6 m in autumn. In 28% (summer) and 19% (autumn) of cases these values are exceeded, most notably in subregions 1 – 3.0 m, 3 – 3.25 m and 4 – 3.14 m (in summer), and 1 – 2.97 m and 4 – 3.11 m (in autumn). In both seasons, the standard error is the smallest for subregion 5 – 1.62 and 1.93 m, respectively.

It was previously reported that the last 50 year have been characterised by the alternation of intensity of the upper layer ventilation (Belokopytov 2011). The analysis of current datasets reveals that cold intermediate layer thickness fluctuations are (quasi) synphase in all subregions as periods of rise and fall alter every 4–5 years (Figure 2.5.2(A)). In autumn, perhaps due to the larger data gaps, an 8-year variation cycle can be detected (Figure 2.5.2(C)). This is corroborated by the correlation between data series, which is higher than 0.87 for both seasons and across all subregions. In general, the correlation between basin periphery and interior is slightly weaker in comparison with the correlation between the peripheral subregions themselves, as the lowest one is observed between 4 and 5 (0.89). This outcome indicates that the variability in the cyclonic gyres is not similar to the one in area 4, which partially confirms the importance of slope convection, occurring on the northwestern shelf, for evolution of the cold intermediate waters (Stanev et al. 2003). Logically, the weakest is the correlation between the pairs 1–3 and 2–4 as there is no exchange mechanism between these areas. In summer, the strongest is correlation between subregions 3 and 4 (0.96) closely followed by 2 and 3 (0.94). In autumn, the correlation between the thickness in the pairs 2–3 and 3–4 is still high but correlation between cyclonic and anticyclonic subregions also increases, in particular regarding the pairs 3–5 and 2–5.

The suggested cycle of cold intermediate layer thickness interannual variability is in agreement with previous studies (e.g. Oguz et al. 2006; Capet et al. 2012), which imply the existence of teleconnection between Black Sea regional atmospheric condition and large scale atmospheric pattern driven by the North Atlantic Oscillation. More specifically, this refers to a sequence of cold and mild winter cycles with approximately 5-year
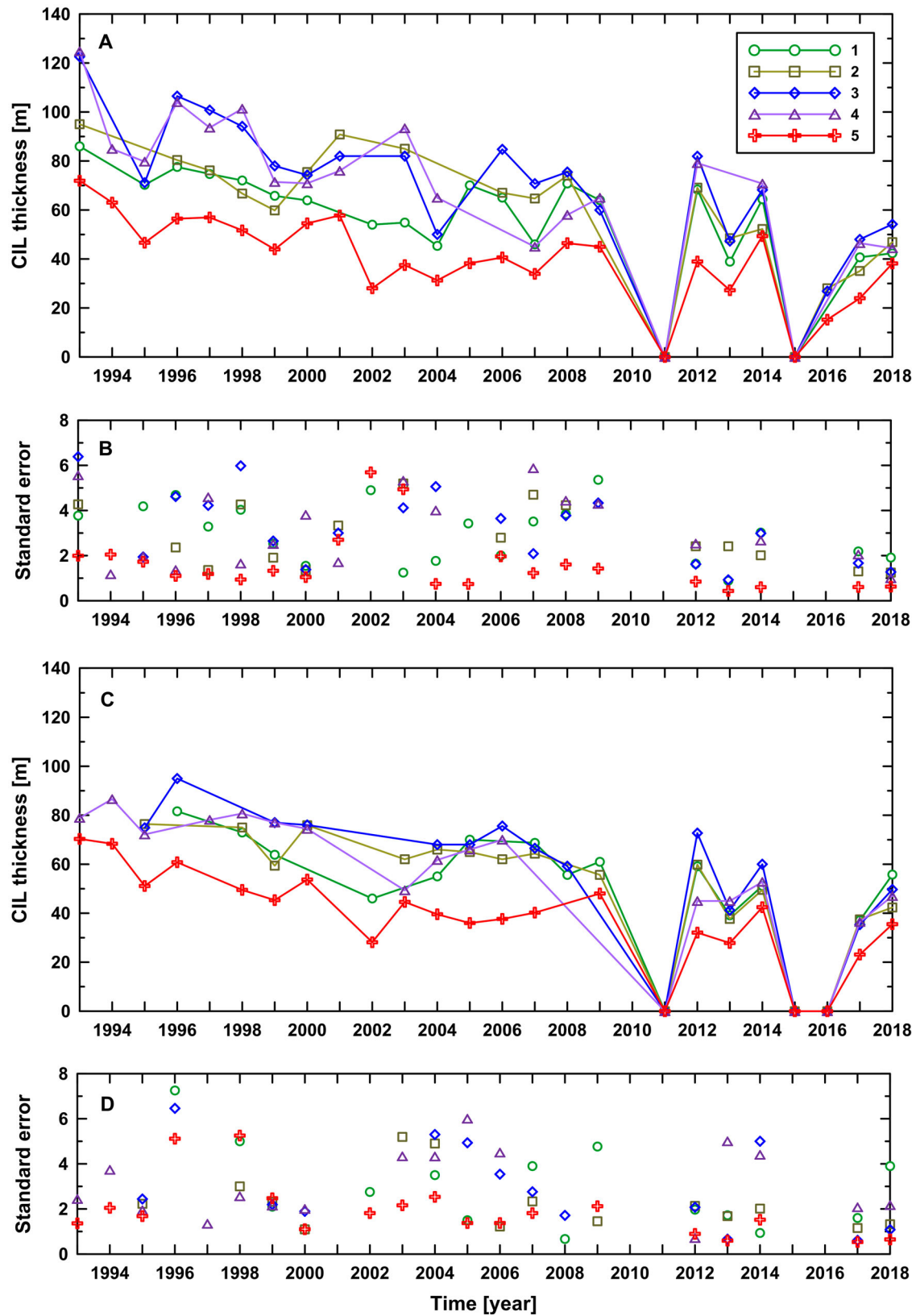
Figure 2.5.2. Interannual variability of cold intermediate layer thickness (product ref. 2.5.1 and 2.5.2) averaged over: (A) summer (June, July, August and September) and (C) autumn (October, November and December), and for each subregion. Symbols show years for which data are available; thick lines depict the interannual course; 1 denotes western, 2 – southern, 3 – eastern, 4 – northern anticyclonic and 5 – central cyclonic subregions. Associated standard errors of the mean are shown as well for: (B) summer and (D) autumn.

duration that roughly follows the North Atlantic Oscillation positive and negative cycles. Moreover, it was found that positive and negative phases of cold content correspond to similar phases of the intensity of the Rim Current suggesting that an intensified circulation facilitates the cold intermediate water formation (Capet et al. 2012). A more intense Rim Current would promote a sharper dome-like shape of the main picnoclyne, thus enabling cold layer formation in the open sea due to stronger upwelling and its deepening along the periphery resulting in reduced summer warming related erosion.

Ever since 1995, the intensity of cold intermediate layer replenishment has been reducing and according to Belokopytov (2011) it was weaker than the climatic mean. Several exceptions were noted in 2003, 2004, and 2006, which corresponds to the mean climatic conditions and more intense winter cooling (Piotukh et al. 2011). The result in Figure 2.8.1 supports this finding. Later on, following a sequence of not particularly cold winters, bringing forth a weak ventilation of active layer, the cold intermediate layer disappeared twice – in 2011 and 2015–2016. There is no sound evidence for its presence in 2010 either since the available Argo data are of questionable quality. Moreover, they are of coarse vertical resolution in the upper mixed layer and seasonal thermocline and present limited spatial coverage, both hampering the correct thickness valuation. In addition, 2010 shipboard data sampled in both western periphery and gyre also did not show clear existence of the layer. Therefore, no data are presented for 2010.

Nevertheless, it appears that the thickness decrease (so as the layer shrinking) is not an irreversible process since as a result of the 2012 winter cooling, in only a year timespan, the cold intermediate layer grew thicker being renewed to reach the levels of the mid-2000s. Evidently, the occurrence of severe winter cooling with consequent intensification of vertical and horizontal mixing leads to pycnocline deepening so as to a more effective cold layer replenishment. Most recently, a slight recovery has also been observed since the thickness drop in 2016. It seems that such cases are not isolated as a process of weak upper layer ventilation was also detected back in the 1960s, leading to its collapse in 1962 and 1966 (Miladinova et al. 2016).

Together with the decrease of cold intermediate layer thickness, the temperature in its core has been constantly growing higher from 6.3°C in 1993 to the absolute maxima of 8.2°C observed in 2014–2016 – the period in which the layer was disrupted (Figure 2.5.3(A)). Overall, the core temperature exhibits no considerable variability between the subregions. Nevertheless, temperature in the peripheral parts of the sea is slightly lower. By autumn,

due to anticyclonic eddies activity, it increases with 0.15°C on average (maximum increase of 0.26°C is noted for subregion 1) while in the inner basin no temperature changes were registered (Figure 2.5.3(C)). The cold intermediate layer recovery in 2003, 2006 and 2012 was accompanied by lowering of the core temperature down to about 7°C, which was the level in the late 1990s. The maximum cooling with 1.13°C was observed in 2012.

The space–time averages of standard errors of the core temperature means is 0.03°C in summer and 0.02°C in autumn. In 19% (summer) and 23% (autumn) of cases these values are slightly exceeded, in subregions 1 and 4 (in both seasons) in particular, whilst the standard error is the smallest for the areas 2 and 3 (Figure 2.5.3(B,D)).

Several authors (e.g. Oguz et al. 2003; Stanev et al. 2014) suggested that the cold intermediate layer shrinking is mainly associated with the atmospheric warming of the sea surface layer. With this respect, winter sea surface temperature and surface air temperature can be used as indicators of the cooling intensity (Piotukh et al. 2011). For example, Miladinova et al. (2016) reported that winter sea surface temperature was higher than 9°C in 2001 and 2011. Our analysis shows that no winter temperature less than 8.3°C was registered in the water column prior to the layer disruption in 2011 and 2015. Moreover, during the whole 2015, the cold layer was confined below the thermocline in the area of eastern gyre, i.e. it was not properly ventilated. Eventually, it resulted in presence of subsurface water mass with temperature of about 8.5°C in autumn. In both cases, the cold intermediate layer was replenished during the following year.

The process of increased warming of the Black Sea surface waters for the past 10 years has led to alteration of isotherm surfaces marking out the cold intermediate layer limits. Historically defined by the isotherm 8°C, since 2007 it has been gradually shifting towards higher values to reach 8.4°C during the period preceding the 2012 cooling. After the recovery, this temperature was increasing again and in recent years it has been set in the range of 8.4–8.5°C. The interannual variation of this characteristic is presented in Figure 2.8.3 together with the averaged over entire basin variation of the temperature difference between the layer's core and boundary. The latter was found to diminish in the course of the study period from more than 1.6°C in summer and 1.2°C in autumn to less than 0.4°C and 0.3°C, respectively, which indicates considerable lowering of the cold content. In the years with weak ventilation of intermediate waters, in particular after 2007, even if the layer was observable as a profile feature
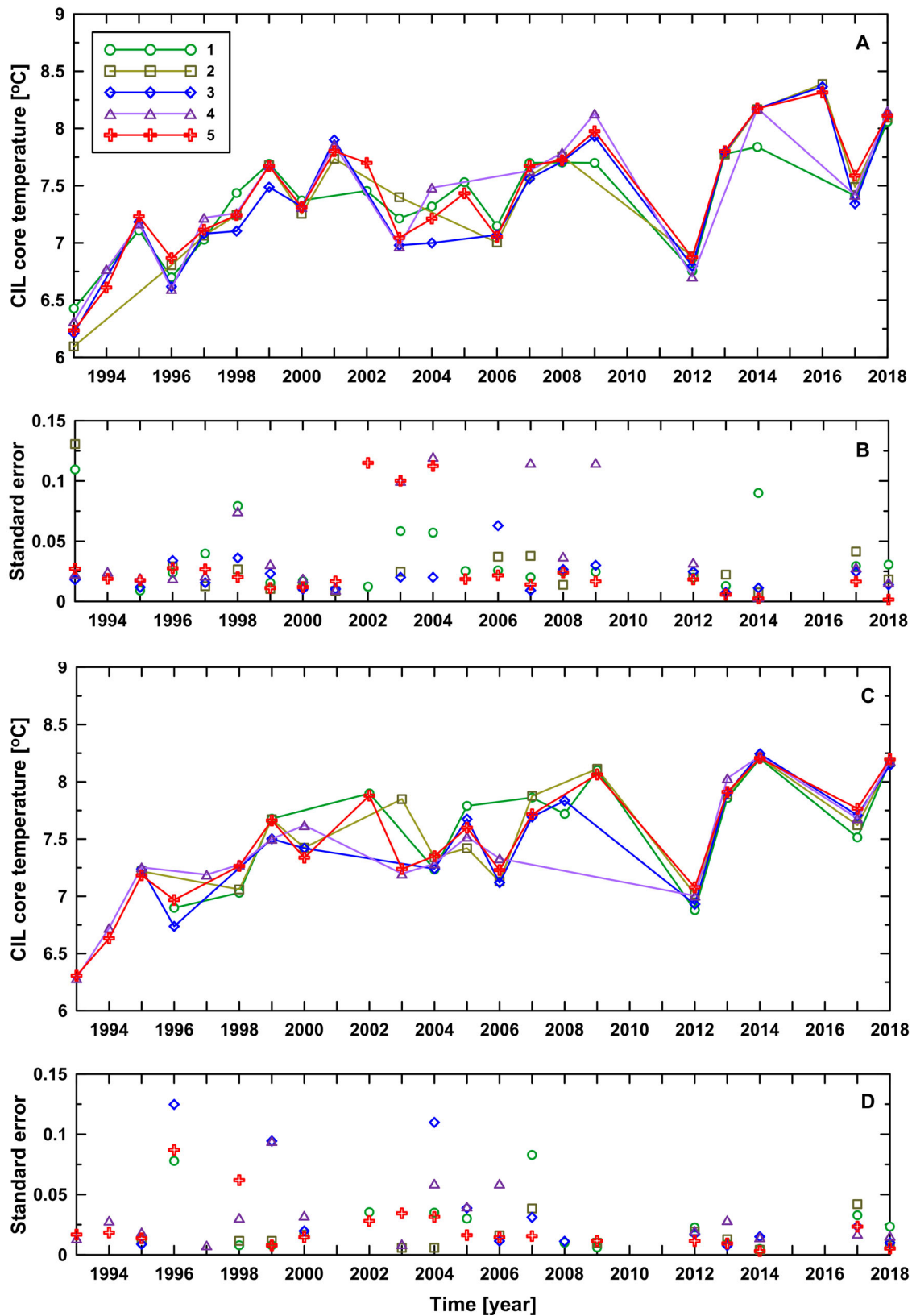
Figure 2.5.3. Same as Figure 2.5.2 but for cold intermediate layer core temperature (product ref. 2.5.1 and 2.5.2) averaged over: (A) summer (June, July, August and September) and (C) autumn (October, November and December), and for each subregion. Associated standard errors of the mean are shown as well for: (B) summer and (D) autumn.

and its thickness appeared substantial the temperature differences were so small that its function was undoubtedly disturbed.

In addition, while examining the isopycnal surface marking the cold intermediate waters base, it was found out that in the beginning of the study period the layer's lower boundary was associated with $\sigma_t = 15.3$–15.9, while during the past several years (2013–2018) it corresponds to $\sigma_t = 14.9$–15.2.

The space–time average of standard errors of the temperature difference means is 0.03°C for both seasons (Figure 2.5.4). In 19% (summer) and 15% (autumn) of cases these values are slightly exceeded, especially in the area 4. As for the boundary isotherm, the standard errors of this property means tend practically to zero.

Moreover, in order to answer the question what level of uncertainty the aforementioned standard errors are associated with, the proportion of each property magnitude, that the standard error represents, was calculated.

Following results are obtained: for thickness, it is in the range of 4.0–5.3% (more specifically for 1–5.3%, 2–4.8%, 3–4.8%, 4–4.6%, 5–4.0%); for core temperature, it varies between 0.3 and 0.6% (1–0.5%, 2–0.4%, 3–0.3%, 4–0.6%, 5–0.4%); and for temperature difference it falls in the range 2.8–5.2% (1–5.2%, 2–3.4%, 3–2.8%, 4–4.3%, 5–4.1%). The above indicates that the level of uncertainty is not significant.

Finally, the cold intermediate layer core depth was found to exhibit no significant seasonal and interannual fluctuations. It is located at an average depth of 68 m in the periphery and 53 m in the central part. The analysis of interannual variability of its boundaries' depths reveals that the observed thickness decrease is related to deepening of the upper and shoaling of the lower limits as the latter process is more pronounced. This is considered as a consequence of not sufficient cooling, which weakens the ventilation of intermediate waters and results in only a partial renewal of the layer.
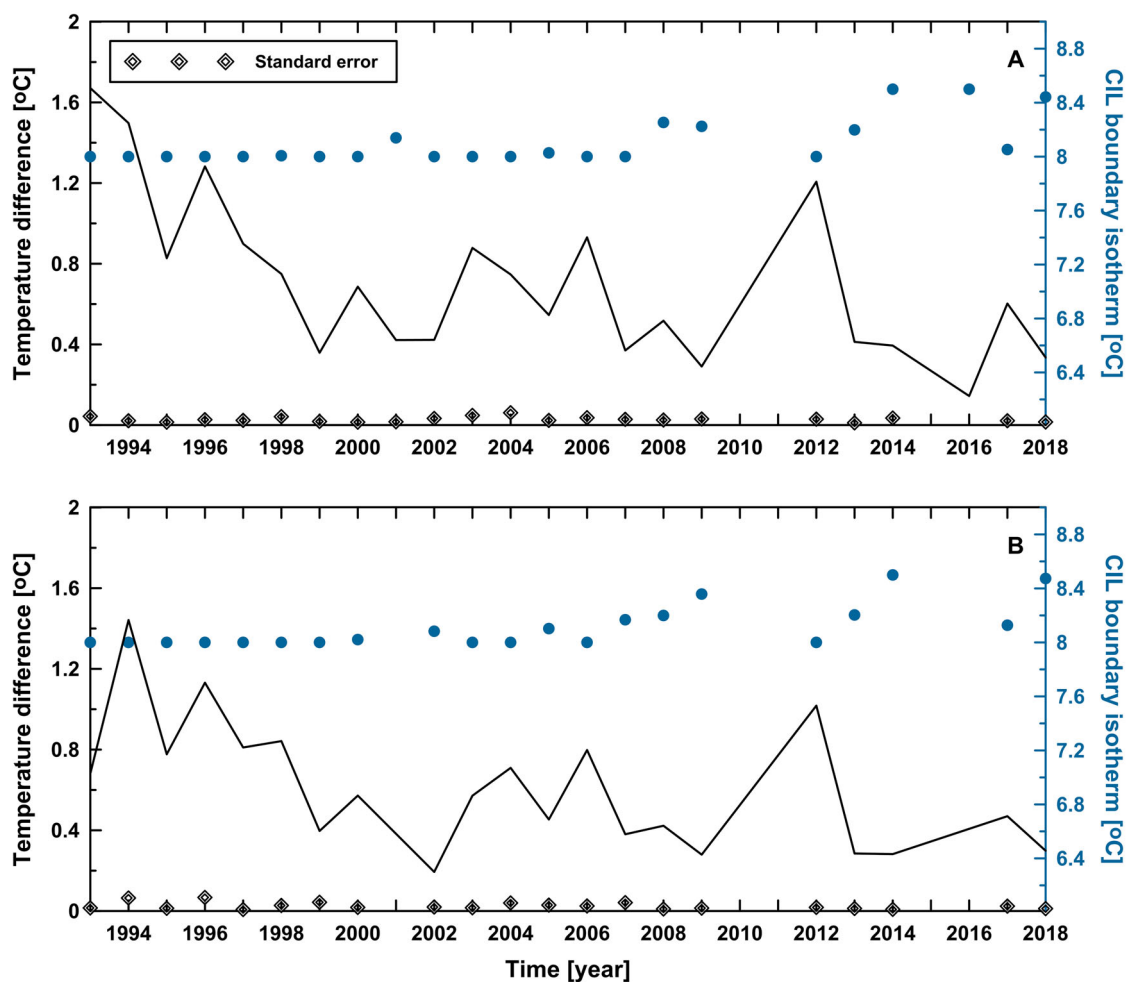
Figure 2.5.4. Interannual variability of isotherm defining cold intermediate layer boundaries (dots) and temperature difference between core and boundary (thick line) (product ref. 2.5.1 and 2.5.2) averaged over: (A) summer (June, July, August and September) and (B) autumn (October, November and December). Standard error of the temperature difference mean is depicted with black rhomb.

2.5.4. Conclusions

The study dealt with assessment of spatial and temporal variability of several key cold intermediate layer properties at sub-regional and seasonal to interannual scales. The main finding is that the cold intermediate layer thickness shows a steady decreasing trend as it dropped by more than half in the course of the study period –35–60 m depending on season and subregion. The analysis shows this is primarily related to shoaling of the layer's lower limit. This is considered as a consequence of inefficient cooling, which weakens ventilation of intermediate waters and results in only a partial replenishment with cold waters. Ever since 1995, the intensity of this process has been reducing with several exceptions observed in 2003, 2004, and 2006, which corresponds to the mean climatic conditions and more intense winter cooling. The layer even disappeared in 2011 and 2015–2016. However, this shrinking is not an irreversible process since as a result of the 2012 winter cooling the layer was recovered. Results indicate that the variability in the cyclonic gyres is not similar to the one in the periphery, in particular the northern subregion which underpins the difference in contribution of various areas to cold intermediate layer formation and evolution. The variability also displays a reduction of contrast between peripheral areas in both seasonal and interannual aspect.

Together with the decrease of cold intermediate layer thickness, the core temperature has risen with about 2.0°C over the study period. This growth is related to the increased surface warming during the past 10 years. This process has led to alteration of isotherm surfaces marking out the layer limits. Initially defined by the isotherm 8°C, it was gradually shifting towards higher values and in recent years it has been tending to 8.4–8.5°C. This has led to a shift of the isopycnal surface marking the cold intermediate waters base, which during the past several years (2013–2018) corresponds to potential density anomaly 14.9–15.2.

Judging by the standard error of the means, which hardly exceed 5% of the thickness and temperature difference and 0.6% of the core temperature magnitudes, while for the boundary isotherm tends to zero, it can be assumed that the level of uncertainty does not compromise the validity of estimates and trends obtained in this study.

Finally, it can be inferred that the upper layer thermal properties are modified as a result of temperature rise. After the disruption in 2015–2016, the cold layer seemed to recover but its cooling potential is substantially reduced. This represents a major threat since it can negatively affect the Black Sea thermo-haline balance and ecosystem function.

Section 2.6: Ocean heat content in the Black Sea

Authors: Leonardo Lima, Elisaveta Peneva, Stefania Ciliberti, Simona Masina, Benedicte Lemieux, Andrea Storto, Boriana Chtirkova

Statement of Main Outcomes: Several studies over the past decade have discussed the surface warming trends in the Black Sea and the potential impact on its ecological state. However, these estimates were limited to sea surface temperature analysis only. In this study, we use the CMEMS global and Black Sea objective analysis and reanalysis products to reveal the seasonal and inter-annual variability and trends in subsurface water temperature and heat content in the upper 1000 m of depth and over the period 2005–2018. The results show a notable seasonal cycle down to 100 m depth with amplitudes of temperature exceeding 15°C in the uppermost levels. A minimum of ocean heat content anomaly is registered close to –0.50 J m^{-2} in 2012, whereas positive values below 0.50 J m^{-2} are found in 2014 and 2015. Trends estimated from monthly anomalies of ocean heat content indicate a non-homogeneous warming at depths (0–1000 m) during the period 2005–2015, which is intensified as thicker layers starting from the surface are considered. However, longer time series are needed for a better understanding of how climate change impacts on the Black Sea.

Product used:

Ref. No.	Product name and type	Documentation
2.6.1	BLKSEA_REANALYSIS_ PHYS_007_004	PUM: http://marine.copernicus.eu/ documents/PUM/CMEMS-BS-PUM-007-004.pdf QUID: http://marine.copernicus.eu/ documents/QUID/CMEMS-BS-QUID-007-004.pdf
2.6.2	GLOBAL_REANALYSIS_ PHY_001_025	PUM: http://marine.copernicus.eu/ documents/PUM/CMEMS-GLO-PUM-001-025.pdf QUID: http://marine.copernicus.eu/ documents/QUID/CMEMS-GLO-QUID-001-025.pdf
2.6.3	GLOBAL_REANALYSIS_ PHY_001_030	PUM: http://marine.copernicus.eu/ documents/PUM/CMEMS-GLO-PUM-001-030.pdf QUID:http://marine.copernicus.eu/ documents/QUID/CMEMS-GLO-QUID-001-030.pdf
2.6.4	Simple Ocean Data Assimilation version 3.4.2	Download link: https://www.atmos.umd. edu/~ocean/index_files/soda3.4.2_mn_ download.htm Information link:https://www.atmos.umd. edu/~ocean/index_files/soda3_readme. htm
2.6.5	INSITU_GLO_TS_OA_ REP_OBSERVATIONS_ 013_002_b	PUM: http://marine.copernicus.eu/ documents/PUM/CMEMS-INS-PUM-013-002-ab.pdf QUID: http://marine.copernicus.eu/

Continued.

Ref. No.	Product name and type	Documentation
		documents/QUID/CMEMS-INS-QUID-013-002b.pdf
2.6.6	EN4 version 4.2.1 objective analysis	Download and information link: https://www.metoffice.gov.uk/hadobs/en4/download-en4-2-1.html

2.6.1. Introduction

The Black Sea is a semi-enclosed basin with very peculiar characteristics like a positive net freshwater balance, which is mainly related to the inflow from some of the largest European rivers (e.g. Danube, Dnieper, Dniester). This balance is also modulated by the atmospheric forcing such as evaporation and precipitation rates (Stanev et al. 2003; Romanou et al. 2010). Major inflow of sea water originates from the Mediterranean Sea, which crosses the Marmara Sea and impacts the Black Sea circulation through the Bosporus Strait (Peneva et al. 2001; Stanev et al. 2001). Several studies have already addressed the seasonal and interannual variability of ocean properties in the Black Sea, such as temperature and/or salinity (e.g. Ginzburg et al. 2004; Knysh et al. 2011; Shapiro et al. 2011), sea level and eddies (e.g. Korotaev et al. 2003; Kara et al. 2008; Kubryakov and Stanichny 2015), mixed layer depth (e.g. Kara et al. 2005; Kara et al. 2009; Capet et al. 2014), chlorophyll concentration (e.g. Finenko et al. 2014; Vostokov et al. 2019).

Many studies have investigated the thermohaline structure in the Black Sea (e.g. Blatov et al. 1984; Simonov and Altman 1991; Oguz et al. 1994; Tuzhilkin 2007). An extensive review about its oceanography is provided by Ivanov and Belokopytov (2013), who described with some details important aspects regarding the heat balance, thermohaline structure, circulation and so on. Knysh et al. (2011) conducted a pioneer study of the hydrophysical fields using a long-term reanalysis and found that the fall-winter water cooling leads to the formation of the upper mixing layer and freshened cold intermediate layer, and the spring–summer warming leads to the formation of a seasonal thermocline and a new cold intermediate layer. Kara et al. (2005) considered the penetrative solar radiation as the major component of the heat balance in the Black Sea in an investigation of the seasonal mixed layer depth variability. Their model simulations revealed that the dynamics of the mixed layer are quite sensitive to solar radiation attenuation. Miladinova et al. (2017) investigated long-term trends and variations of thermohaline properties and showed that temperature is seasonally variable at the surface, decreasing with depth down to the coldest intermediate layer.

There have been several works that have estimated the recent temperature trends in the Black Sea using databases and model results. Ginzburg et al. (2004) used satellite measurements to reveal a positive trend of 0.09°C year^{-1} in sea surface temperature over the years 1982–2000, whereas Degtyarev (2000) noted a positive temperature trend of 0.016°C year^{-1} in the 50–100 m layer from 1985 to 1997. Shapiro et al. (2010) noted a warming trend starting in the 1990s. Miladinova et al. (2017) found that the surface layers do not display a trend in temperature while results of temperature at 200 m indicated a positive trend of 0.005°C year^{-1} over the years 1960–2015. Previous reports indicated a surface warming of the Black Sea in recent years (Mulet et al. 2018). The temperature variations for the period 1950–1990 are discussed in detail in Simonov and Altman (1991), as well as the relation with the thermal, heat and water fluxes. They found a negative temperature trend in the shallow north-western part (depth 0–50 m) and a slightly positive trend for the deeper open sea (75–200 m). Such a long-term investigation can be considered an exception since most studies have generally estimated the trend over relatively short periods in such a way that may not reflect long-term climate trends. In addition, the majority of studies has given estimations of temperature trends for the upper layers in the Black Sea, which is mainly due to the scarcity of subsurface observations before the ARGO period.

However, few studies have concentrated efforts to assess the ocean heat content variability in the Black Sea. Schrum et al. (2001) used ECMWF atmospheric reanalysis for the period 1979–1993 and revealed a mean thermal exchange between the atmosphere and the ocean that exhibited a cooling in the northern Black Sea and warming along the southern coast of almost equal magnitude. Matsoukas et al. (2007) investigated the seasonal ocean heat budget in the Black Sea, and a maximum evaporation period was found during August to October. They have explained this pattern by the occurrence of relatively large net shortwave radiation, specific environmental conditions and thermal energy release. Climatological mean averages of heat content in the cold intermediate layer showed the lowest values during February to March, especially in the western part of the Rim Current (Miladinova et al. 2018). Kubryakov et al. (2018) applied an eddy identification method based on altimetry together with historical hydrological measurements and they have found the largest values of heat content in the area of quasi-stationary eddies such as the Batumi eddy located in the easternmost basin of the Black Sea.

Nevertheless, the information on the seasonal and interannual variability and trends of ocean properties in the Black Sea is still limited, particularly regarding

the ocean heat content. This study aims to evaluate the Black Sea ocean heat content variability and its uncertainty estimated from six ocean products including global and regional reanalyses and observation-based objective analyses (product ref. 2.6.1–2.6.6).

2.6.2. Data and method

In order to investigate the ocean heat content variability in the Black Sea and to provide an estimate of its uncertainty, we used a range of oceanic products: four reanalyses (product ref. 2.6.1–2.6.4) and two objective analyses CORA5.2 (Tanguy et al. 2019; product ref. 2.6.5) and EN4.2.1 (Good et al. 2013; product ref. 2.6.6). No studies have been conducted to assess the ocean heat content in the Black Sea using a set of ocean products, especially for the recent period. Since there are few in situ measurements of vertical temperature and salinity available for data assimilation and validation in the Black Sea like during 1998–2004, we started our investigation using the monthly averaged values of temperature for the period from 2005 to 2018. The ocean heat content anomalies were computed according to the Equation 2.6.1 and the anomalies were defined as the deviation from the reference period of 2005–2014.

$$OHC = \int_{z_1}^{z_2} \rho_0 \, c_p (T_m - T_{clim}) dz \qquad (2.6.1)$$

with ρ_0 equal to 1020 kg m^{-3} and c_p equal to 4181.3 J kg^{-1}°C^{-1} are, respectively, the density and specific heat capacity; and dz indicates the thickness of a certain ocean layer of the ocean; T_m corresponds to the monthly average temperature and T_{clim} is the climatological temperature of the corresponding month that varies

according to each individual product. Time series considered the basin-averaged values calculated from results limited by the depths z_1 and z_2.

The mixed layer depth was determined based on the criteria in which the density changes by 0.125 kg m^{-3} relative to the density at 2.5 m, the shallowest model depth (Kara et al. 2009). We also estimated the ensemble mean and spread of temperature, mixed layer depth and ocean heat content anomaly using the ocean reanalyses (product ref. 2.6.1–2.6.4). The ensemble spread is defined as the standard deviation of the ensemble member realisations, so it provides a quantitative estimate of the uncertainty (Table 2.6.1).

2.6.3. Results and discussion

Figure 2.6.1 reveals the climatological seasonal cycle for both the mixed layer depth and temperature. An increase in stratification occurs after March with the mixed layer depth reaching values shallower than 10 m from May to August. Our results agree with those from the literature, e.g. Titov (2004), Kara et al. (2009), Capet et al. (2014). According to Kara et al. (2009), mixed layer depth is very shallow (< 20 m) in the Black Sea during spring and summer, and rarely exceeds 50 m during winter. Capet et al. (2014) calculated the mixed layer depth from interpolated in situ data over the period 1955–2011 and found a very clear seasonal cycle, revealing the stronger mixing in February, the sharp onset of the thermocline from March to May, and the slower deepening of the mixed layer from August to February. Their results exhibited a mixed layer depth that reached 40 m during the winter and became as shallow as 5 m during the summer. Our results show that the

Table 2.6.1. List of ocean reanalyses including the regional reanalysis (product ref. 2.6.1) and the global reanalyses GLORYS2v4 (product ref. 2.6.2) and GLORYS12v1 (product ref. 2.6.3) from the CMEMS and the Simple Ocean Data Assimilation version 3.4.2 (SODA3.4.2) (Carton et al. 2018; product ref. 2.6.4).

	Name	Model resolution	Atmospheric forcing	Data assimilation scheme	Assimilated observations
1	BS-PHY RAN	NEMO3.4 0.037° x 0.028° 31 z-levels	ERA-interim (Dee et al. 2011)	3DVAR (Dobricic and Pinardi 2008; Storto et al. 2014)	in situ T/S profiles from EN4.2.1, along-track SLA, CMEMS 0.0417° x 0.0417° SST-L4
2	GLORYS2v4	NEMO3.1-LIM2 ¼° x ¼° 75 z-levels	ERA-interim	Reduced-Kalman SEEK filter (Pham et al. 1998)	Reynolds ¼ AVHRR-only SST, AVISO SLA, in situ T/S profiles from Coriolis CORA4.1 database, CERSAT sea ice concentration
3	GLORYS12v1	NEMO3.1 0.083° x 0.083° 50 z-levels	ERA-interim	Reduced-Kalman SEEK filter (Pham et al. 1998)	Reynolds ¼° AVHRR-only SST, AVISO SLA, in situ T/S profiles from Coriolis CORA4.1 (until 2003), CORA5.0 (2004 – 2015), CORA5.1 (2016) database, CERSAT sea ice concentration
4	SODA3.4.2	GFDL-MOM5 ¼° x ¼° 50 z-levels	ERA-interim	Optimal interpolation (Carton et al. 2018)	WOD13 and COADS2.1
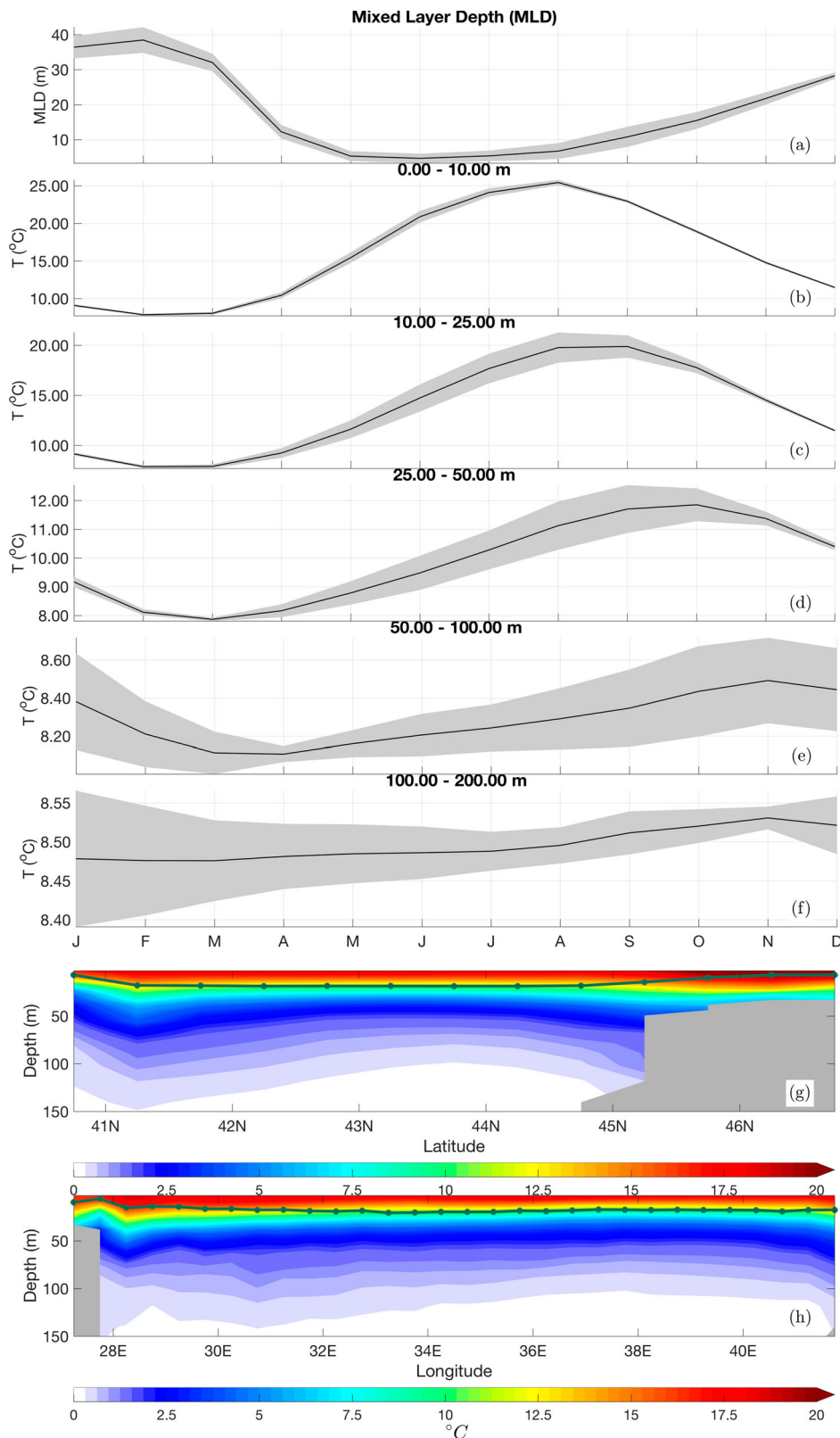
Figure 2.6.1. The ensemble mean and spread calculated from the climatological seasonal cycle of the basin-averaged (a) mixed layer depth (in metres) and temperature (in °C) for the period of 2005–2014 in different depth ranges: (b) 0–10 m, (c) 10–25 m, (d) 25–50 m, (e) 50–100 m e (f) 100–200 m. The bottom colourful panels indicate the ensemble means of the amplitude of the seasonal cycle (in °C) based on the monthly average temperature results. For each individual reanalysis, this amplitude is assessed as the difference between the temperature values (in °C) of the warmest and coldest months in each year from 2005 to 2014, such that the (g) zonal and (h) meridional ensemble means also consider the average in time. The green contours indicate ensemble means of the mixed layer depth for the corresponding horizontal direction. All ensemble statistics derive from the results of four reanalyses (product ref. 2.6.1–2.6.4).

uncertainty of mixed layer depth ensemble ranges from 1.52–3.17 m in January and July respectively.

In the near-surface layer (0–10 m), the temperature seasonal variations are within the range 8°C in winter and 25°C in summer with the minimum and maximum values respectively in February and August. The seasonal amplitude rapidly decreases with depth: down to 12°C in 10–25 m and 4°C in 25–50 m with the minimum (maximum) values respectively in February (September) and March (October). This pattern was also identified by Ivanov and Belokopytov (2013). Below 100 m in fact the seasonal cycle of temperature is not very clear. The timing of the minimal and maximal temperatures agrees with the study of Ginzburg et al. (2004) based on the Advanced Very High Resolution Radiometer and hydrographic measurements of the sea surface temperature in the Black Sea during the period 1981–2000. Above 50 m of depth, the ensemble uncertainties of temperature are higher in summer compared to other seasons. The uncertainties increase in depth and a seasonal pattern is viewed down to the 50–100 m layer. This seasonal pattern of temperature uncertainties does not reflect on the uncertainty pattern of the mixed layer depth. This leads us to infer that salinity uncertainties counter-balance the temperature uncertainties in such a way that the ensemble of density-based mixed layer depth presents a nearly uniform uncertainty over the months.

The two bottom panels in Figure 2.6.1 show largest amplitudes of temperature in surface waters, exceeding 20°C north of 45°N. The values above the time-averaged mixed layer depth exceed 12°C. Comparatively, Ginzburg et al. (2004) reported the maximum amplitude of the seasonal sea surface temperature of 19.8, 20.4, and 20.3°C, respectively in the years 1987, 1992, and 1998. The signature of the seasonal cycle rapidly decreases at depth, practically no seasonal changes are seen below 100–150 m. This corroborates with the results from model simulations performed by Miladinova et al. (2017), who show the seasonal variation of temperature predominantly near the surface.

Time series of ocean heat content anomalies show significant interannual variability, alternating between cool and warm events (Figure 2.6.2). However the ensemble spread of the global reanalysis products exhibits a larger signal as compared to the amplitudes of the year-to-year fluctuations, particularly at the beginning of the time series. The products exhibit a good agreement after the year 2006 when the in situ data coverage increased. The ensemble spread decreases over time due to the increase of the assimilated Argo profiles which makes the ocean heat content estimates of the global reanalyses converging over time. As thicker layers are considered,

an important characteristic becomes evident over the years 2012–2015, as we highlight with blue, green and red shades in Figure 2.6.2: a minimum of ocean heat content anomaly is registered close to -0.50 J m^{-2} in 2012, followed by values close to zero in 2013 and positive values below 0.50 J m^{-2} in 2014 and 2015.

The trends estimated from the monthly anomalies of ocean heat content indicate positive values that are even more evident if we consider deeper layers: the trend is 0.063 W m^{-2} in layer 0–10 m and reaches 1.082 W m^{-2} in the layer 0–1000 m (Figure 2.6.2). In general, the studies indicate a warming trend of sea surface temperature in the recent years. There is a scarcity of studies that have investigated the trends of ocean variables at deeper layers. Miladinova et al. (2017) estimated temperature trends of 0.009°C year^{-1} and 0.005°C year^{-1} respectively at 50 m (approximately located at the core of the cold intermediate layer) and 200 m, by considering the years 1960–2015. The warming of the cold Intermediate layer is due to the fact that winter cooling is not so efficient in recent years, e.g. the tendency for milder winters in the region, which prevents the feeding of the cold intermediate layer with cold water (Stanev et al. 2019). The negative anomaly in the ocean heat content happens in the years with low winter air temperature (2006, 2012, 2017).

Figure 2.6.3 exhibits the maps of ocean heat content anomalies in the upper 200 m of the Black Sea. According to Figure 2.6.2, we focus on the years 2012–2015 to investigate the transition between a cold year (i.e. anomalies lower-than-average amplitude), a neutral year (i.e. anomalies fluctuate around climatological mean), and two warm years (i.e. anomalies higher-than-average amplitudes). In 2012, there is a predominance of negative values in such a way the most negative values are concentrated at the margin of the basin. Nevertheless, it is possible to find low values of positive anomalies in small areas in the central part of the basin and throughout the northwest region. The anomaly map is specific in 2013 when there is an almost equal division with a predominance of positive (negative) values in the east (west) region. An important characteristic is that this year shows the highest positive anomalies in the southeast region on the Batumi eddy, one of the most intense and persistent anticyclonic eddy in the Black Sea (Korotaev et al. 2003). The years 2014 and 2015 register positive anomalies over almost the entire domain. Again, the extreme values are exhibited along the margin areas like in the Batumi eddy region. The positive anomaly pattern in the Batumi eddy corroborates with the results reported by Kubryakov et al. (2018), who found positive temperature anomalies in the upper
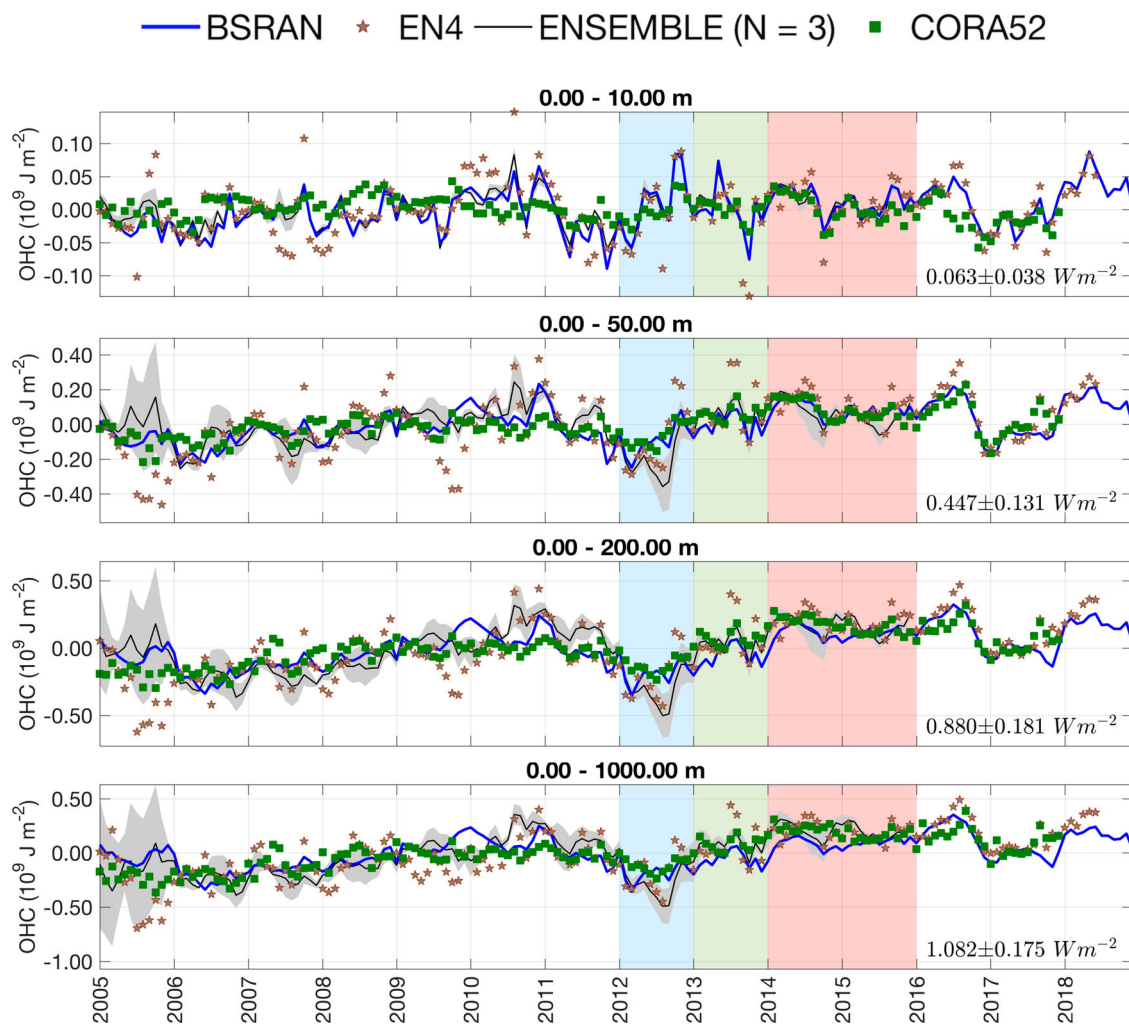
Figure 2.6.2. Monthly basin-averaged of the ocean heat content anomalies (in 10^9 J m^{-2}) estimated from the depth-averaged temperature over different ocean layers from the regional reanalysis (product ref. 2.6.1; blue), the ensemble of global reanalyses (product ref. 2.6.2–2.6.4; black), the objective analyses CORA5.2 (product ref. 2.6.5; green squares) and EN4.2.1 (product ref. 2.6.6; brown stars). The monthly ocean heat content anomalies are defined as the deviation from the climatological ocean heat content mean (2005–2014) of each corresponding month. The blue, green and red shading indicates the years in which the ocean heat content anomalies are presented in Figure 2.6.3.

layers of anticyclonic eddies, and negative in the deeper layers, because of the vertical displacement of the waters of the cold intermediate layer.

Both the maps of ocean heat content trend from the regional reanalysis (product ref. 2.6.1) and the ensemble of global reanalyses (product ref. 2.6.2–2.6.4) exhibit only positives values (Figure 2.6.3). We highlight the region of the Batumi eddy, where both maps show higher positive trends as compared to the remaining domain. This common characteristic suggests that reanalysis products well represent an intensification of the Batumi eddy in recent years as was reported by Kubryakov et al. (2017). With the exception of this region, the trend maps are quite different, highlighting the fact that interannual fluctuations are very strong and mask the long-term warming signal. This is

particularly a problem because the period of study, i.e. short time series to investigate the ocean heat content evolution and capture the warming signal properly, which limits the attribution studies for climate change imprints. The regional reanalysis generally generates lower values of ocean heat content trends in the west basin so that there is an increasing toward the east in such a way that the values increase from about 0.39 W m^{-2} at 28.97°E, 0.99 W m^{-2} at 34.31°E at 1.10 W m^{-2} 39.81°E along the latitude of 43 °N. We can compare our results with Ginzburg et al. (2004), who presented the western deep-sea region getting warmer more slowly (about 0.08°C year^{-1}) as compared with the eastern one (about 0.11°C year^{-1}). The trends from the global reanalysis ensemble do not present this behaviour and the map generally shows higher values (Figure 2.6.3(f)),
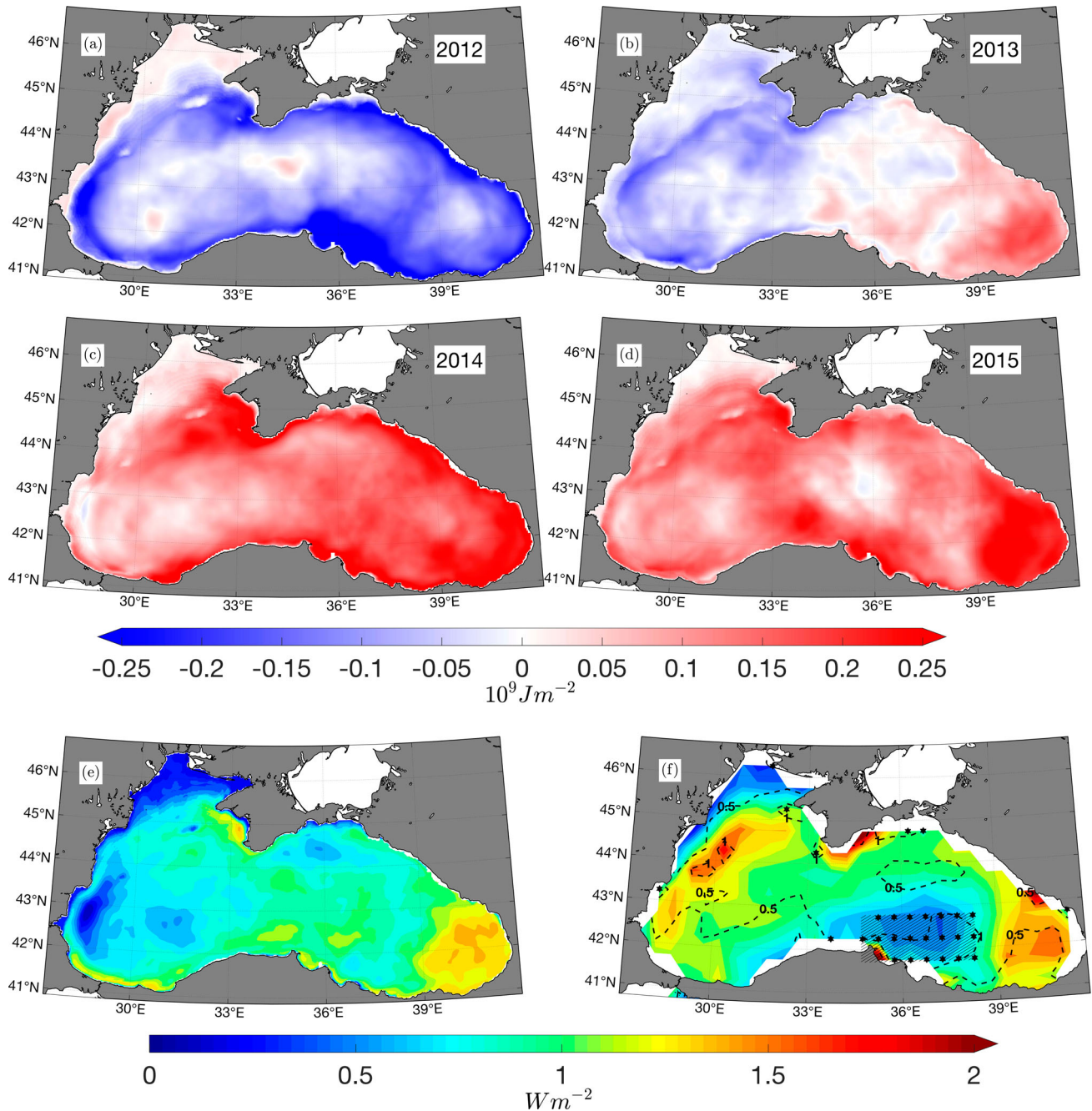
Figure 2.6.3. The upper panels represent yearly anomalies of the depth-integrated (0–200 m) ocean heat content (in 10^9 J m^{-2}) in (a) 2012, (b) 2013, (c) 2014 e (d) 2015 estimated from the regional reanalysis (product ref. 2.6.1) and defined as the deviation from the reference period of 2005–2014. The bottom panels represent the ocean heat content trends (in W m^{-2}) for the (e) regional reanalysis (product ref. 2.6.1) and (f) ensemble of global reanalyses (product ref. 2.6.2–2.6.4) in the upper 200 m, so that the dashed black contours indicate the ensemble spread and black dots indicate areas where the noise exceeds the signal, i.e. the products show low agreement. The hatched region highlights one of these areas. The ocean heat content trends consider the period of 2005–2015.

except in a region south of 43°N and between 34°E and 39°E. However, black dots overlapping this region indicate that the discrepancy of the reanalysis ensemble is greater than its mean signal, which highlights the fact that using global reanalyses may be inadequate for the Black Sea.

2.6.4. Conclusions

The seasonal cycle in the Black Sea impacts subsurface temperature layers down to 150 m depth, with a maximum during July–September, and minimum during February–March. The trend analysis reveals a weak warming

signal in the Black Sea of the upper and intermediate layers (0–1000 m), which is masked by interannual variability with basin-wide and high amplitudes: transition between cold, neutral (west–east pattern) and warm years, which can persist between 1–3 years. An important finding is that the warming trend is more pronounced over intermediate layers than for surface one, a characteristic of the Black Sea. This reflects the fact that the Cold Intermediate Layer is warming during the recent decade (see Section 2.5), following the mild winter tendency. This leads us to consider that the usage of sea surface temperature itself is not sufficient to comprehensively address the warming trend in the Black Sea. In order to detect and attribute climate change impacts on the Black Sea temperature change, longer time series are needed. This mainly requires a sustained ocean observing system (Palazov et al. 2019), so that the accuracy and skill of reanalysis products can also improve.

Section 2.7: Monitoring of wave sea state in the Iberia-Biscay-Ireland regional seas

Authors: Álvaro de Pascual Collar, Bruno Levier, Roland Aznar, Cristina Toledano, José María García-Valdecasas, Manuel García León, Marcos García Sotillo, Lotfi Aouf, Enrique Álvarez

Statement of Main Outcomes: Ocean waves have a high relevance over the coastal ecosystems and human activities. Extreme wave events can entail severe impacts over human infrastructures and coastal dynamics. However, the incidence of severe (90th percentile) wave events also has valuable relevance affecting the development of human activities and coastal environments. The Strong Wave Incidence index based on the CMEMS regional analysis and reanalysis product provides information on the frequency of severe wave events. The objective of the work is to propose and evaluate an Ocean Monitoring Indicator that detects: (1) regions where the strong wave incidence is higher/lower than the climatic average and (2) historic events/trends of incidence of severe wave conditions. The proposed index is correlated with NAO index and is able to detect past wave events described in literature. The analysis of the index in the last decades do not show significant trends of the strong wave conditions over the period 1992–2017. The year 2018 in the Iberia-Biscay-Ireland region can be considered as a higher-than-average period influenced by strong wave conditions over the study period. In 2018, higher-than-average incidence of strong wave conditions are reported in the open ocean at latitudes south of 50°N, which corresponds to an increase of 3–5% of the frequency of strong wave conditions. In

the Gulf of Biscay and west of the British Islands, lower-than-average incidence of strong wave conditions occurred in 2018.

Products used:

Ref. No.	Product name & type	Documentation
1/1	IBI_REANALYSIS_ WAV_005_006 Reanalysis model	PUM: http://marine.copernicus.eu/ documents/PUM/CMEMS-IBI-PUM-005-006.pdf QUID: http://marine.copernicus.eu/ documents/QUID/CMEMS-IBI-QUID-005-006.pdf
2.7.2	IBI_ANALYSIS_FORECAST_ WAV_005_005 Analysis model	PUM: http://marine.copernicus.eu/ documents/PUM/CMEMS-IBI-PUM-005-005.pdf QUID: http://marine.copernicus.eu/ documents/QUID/CMEMS-IBI-QUID-005-005.pdf
2.7.3	North Atlantic Oscillation index	NOAA National Weather Service. 2005. North Atlantic Oscillation (NAO), available at: https://www.cpc.ncep. noaa.gov/products/precip/CWlink/ pna/nao.shtml, Last access: 30 May 2019.

2.7.1. Introduction

Waves constitute one of the most relevant ocean processes affecting the human activities and nearshore environment. Sea state and its long-term ocean climatology affect all marine anthropogenic activities (Savina et al. 2003; Gonzalez-Marco et al. 2008), inhabitants of coastal areas (Gonzalez-Marco et al. 2008), coastal ecosystems (Hewit et al. 2003) and coastal dynamics (Mei and Liu 1993; Hewitt et al. 2003). Extreme wave events can also severely damage coastal infrastructures and loss of human lives.

The Iberia-Biscay-Ireland (IBI) is one of the CMEMS Monitoring and Forecasting Centres (MFCs). The IBI-MFC covers the Europe's Atlantic coast in a region bounded by the 26°N and 56°N parallels, and the 19°W and 5°E meridians. The western European coast is located at the end of the long fetch of the subpolar North Atlantic (Mørk et al. 2010), one of the world's greatest wave generating regions (Folley 2017). Several studies have analysed changes of the ocean wave variability in the North Atlantic Ocean (Bacon and Carter 1991; Kursnir et al. 1997; WASA Group 1998; Bauer 2001; Wang and Swail 2004; Dupuis et al. 2006; Wolf and Woolf 2006; Dodet et al. 2010; Young et al. 2011; Young and Ribal 2019). The observed variability is composed of fluctuations ranging from the weather scale to the seasonal scale, together with long-term fluctuations on interannual to decadal scales associated with large-scale climate oscillations. Since the ocean surface state is mainly driven by wind stresses, part of this variability in Iberia-Biscay-Ireland region is connected to the North Atlantic Oscillation

(NAO) index (Bacon and Carter 1991; Hurrell 1995; Bouws et al. 1996, Bauer 2001; Woolf et al. 2002; Tsimplis et al. 2005; Gleeson et al. 2017). However, later studies have quantified the relationships between the wave climate and other atmospheric climate modes such as the East Atlantic (EA) pattern, the Arctic Oscillation (AO) pattern, the East Atlantic Western Russian (EA/WR) pattern and the Scandinavian (SCAN) pattern (Izaguirre et al. 2011; Matínez-Asensio et al. 2016).

The development of Ocean Monitoring Indicators pursues the summarising of oceanographic information to ease recognition of anomalous processes occurring in the ocean. The use simplified monitoring indicators enables the automatic and routine diagnosis of the climate system. Such early diagnossis provides tools for near-real-time climate monitoring and decision making in several areas such as coastal management. Additionally, these indicators can be used in several scientific fields such as the study of the linkages between processes and variables in the ocean and atmosphere.

In the present work, a statistic methodology is proposed to evaluate the anomaly of the occurrence of strong wave events. The work is aimed to: (1) Propose a monitoring indicator providing a clear description of the indicator as well as its interpretation, (2) discuss the results comparing them with other scientific works, (3) provide an analysis of the atmospheric patterns that enhance the development of strong wave events in the Iberia-Biscay-Ireland region, and (5) the detection of the strong wave events in the last decades as well as the description of the state of the ocean in the last years.

The objective is to provide a methodology for the systematic monitoring of the severe wave variability and trends in the Iberia-Biscay-Ireland regional seas. The procedure follows the commonly used definition of wave storm by defining the strong wave conditions as the exceeding threshold above the 90th percentile of Significant Wave Height (Eastoe et al. 2013; Bernardara et al. 2014).

2.7.2. Method

The operational wave forecast and reanalysis delivered by Iberia-Biscay-Ireland Monitoring and Forecasting Center, hereinafter named as CMEMS reference products 2.7.2 and 2.7.1, respectively, provide two different datasets with hourly instantaneous fields of Significant Wave Height. These fields have a 0.1° horizontal resolution. The CMEMS product 2.7.2 delivers the best estimates of the system spanning the time period from 2015 up to the present, whereas the CMEMS product 2.7.1 is a product that currently ranges 1992–2016. More information on the system description and validation can be found in its corresponding Product User Manuals available in the CMEMS web page, see the products table.

The Strong Wave Incidence index is proposed to quantify the variability of strong wave conditions in the Iberia-Biscay-Ireland regional seas. The anomaly of exceeding a threshold of Significant Wave Height is used to characterise the wave behaviour. It is widely recognised that the final estimation could significantly depend on the chosen threshold (Onoz and Bayazit 2001; Lin-Ye et al. 2016). Hence, a sensitivity test has been performed evaluating the differences using several thresholds (percentiles 75, 80, 85, 90, and 95). From this analysis, it has been selected the 90th percentile as the most representative, coinciding with the state-of-the-art (Eastoe et al. 2013; Bernardara et al 2014).

The Strong Wave Incidence index (SWI) is defined as the difference between the climatic frequency of exceedance (F_{clim}) and the observational frequency of exceedance (F_{obs}) of a given threshold (Th) of Significant Wave Height (SWH):

$$SWI = F_{obs}(SWH > Th) - F_{clim}(SWH > Th)$$

In this study, we use the climatic 90th percentile of Significant Wave Height as the threshold to consider strong wave conditions. This threshold is computed on a monthly basis from product 2.7.1 using the reference period 1993–2014. Since the percentile is computed as a frequency, it can be used as the climatic frequency to compute the index. On the other hand, the observational frequency for the index is obtained from the frequency of threshold exceedance on a monthly basis. Since the Strong Wave Incidence index is defined as a difference of a climatic mean and an observed value, it can be considered as an anomaly. Such index represents the percentage that the stormy conditions have occurred above/below the climatic average. Thus, positive/negative values indicate the percentage of hourly data that exceed the threshold above/below the climatic average, respectively. Additionally, the definition of the index as the difference of two percentages entails a mathematical limit of the values that the index can take. On the one hand, the climatic frequency is a constant (10% in this study). On the other hand, the observational frequency is a percentage that ranges from 0% up to 100%. Therefore, the index may vary from −10% up to 90%.

The objective of this study is to provide a set of indexes to monitor the variability and behaviour of severe events of Significant Wave Height. Therefore, the results of the index are displayed using two different approaches: The spatial distribution of Significant Wave Height is monitored by representing the map of the
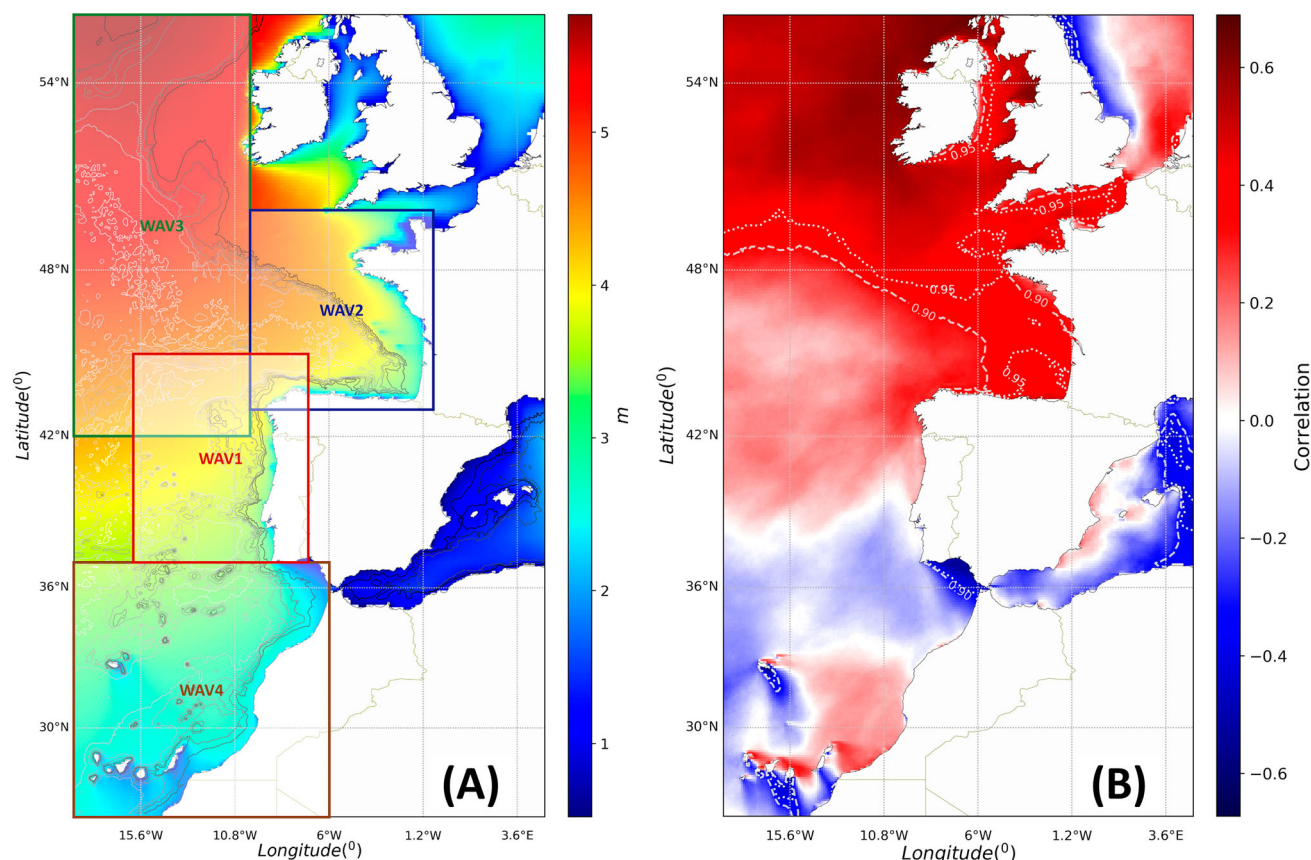
Figure 2.7.1. (A) Mean monthly 90th percentile (%) of Sea Wave Height computed from CMEMS reference product 2.7.1 at an hourly basis (climatic reference period 1993–2014). Red, blue, green and brown squared regions denote the four monitoring areas defined in the text (WAV1, WAW2, WAV3, and WAV4, respectively). (B) Shaded colours represent the temporal correlation coefficient between annual Strong Wave Incidence index (computed from CMEMS reference product 2.7.1) and North Atlantic Oscillation index (product ref. 2.7.3). Dashed and dotted contour lines represent the minimum statistical significance of the correlation values (levels 90% and 95%, respectively).

index on a yearly basis for the time period covered by CMEMS reference product 2.7.2. The temporal variability and trends of Significant Wave Height is monitored analysing the time series of the index spatially averaged in four monitoring domains (WAV1, WAV2, WAV3, and WAV4, see Figure 2.7.1).

2.7.3. Results

Several scientific studies have analysed the high correlation between the North Atlantic Oscillation index and the Significant Wave Height (specially for winter months). An increase in Significant Wave Height can be induced by stronger mean westerly winds in the mid-latitudes as a consequence of larger North Atlantic Oscillation indices (Bacon and Carter 1993; Kushnir et al. 1997; WASA Group 1998; Bauer 2001; Woolf et al. 2002; Tsimplis et al. 2005; Martinez-Asensio et al. 2016). The correlation between Strong Wave Incidence index and North Atlantic Oscillation shown in Figure 2.7.1(B) is coherent with results found by Bauer (2001).

The Strong Wave Incidence index shows significant positive correlations in latitudes above 48° and in the Gulf of Biscay, while the correlation is lower and not significant in latitudes below 45°. Although, some significant inverse correlations are found southeast of the Canary and Azores islands and in the northeast region of the Gulf of Cadiz. The high NAO values forces storm tracks northward then causing these negative or non-significant correlations in the southern regions of the IBI domain.

The spatial distribution of strong events in the years 2015–2018 shows high temporal variability (Figure 2.7.2). The spatial pattern of each year is defined by the main direction and intensity of strong wind events during the year. The anomaly of sea state in 2018 shows a higher-than-average incidence of strong events in latitudes below 50° (approximately 3–5% higher incidence than the climatic average). However, the negative values of Strong Wave Incidence index in the shelf of the Gulf of Biscay and west of the British Islands denote a lower-than-average incidence of strong wave conditions.
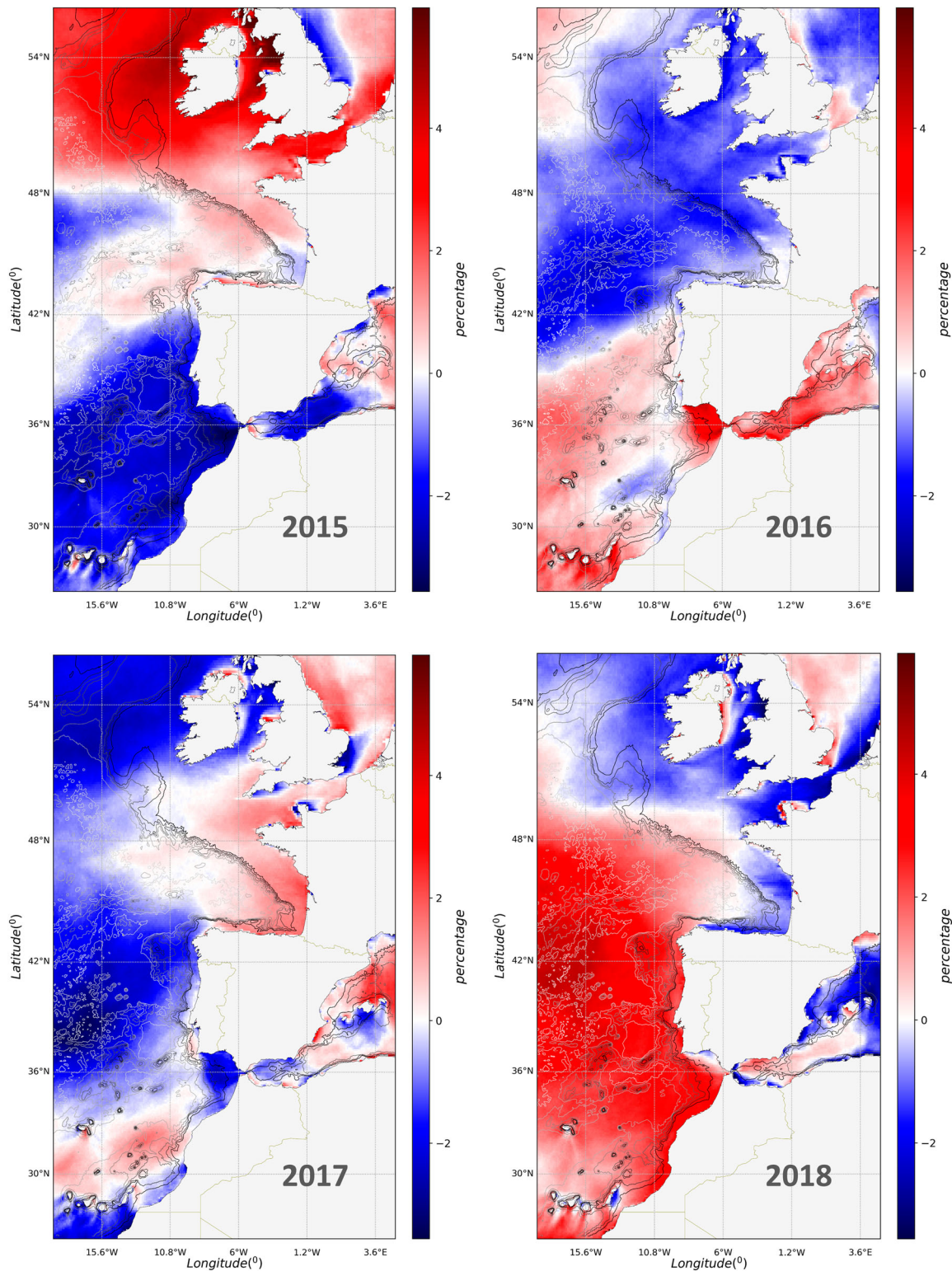
Figure 2.7.2. Maps of Strong Wave Incidence index (%) over the years 2015–2018, computed from reference product 2.7.2 product. Maps show the frequency (percentage of hourly data) where the threshold was exceeded above/below the climatic average. Red/blue areas denote higher-than-average/lower-than-average incidence of strong wave conditions, respectively.

The east–west coastline orientation of the Northern Iberian Peninsula has enhanced shadow areas where the coastal fringe has been sheltered against the dominant wave conditions during 2018.

Figure 2.7.3 shows the spatially averaged time series of the Strong Wave Incidence index in the monitoring region defined in Figure 2.7.1. The strongest wave incidence events are found in the monitoring regions
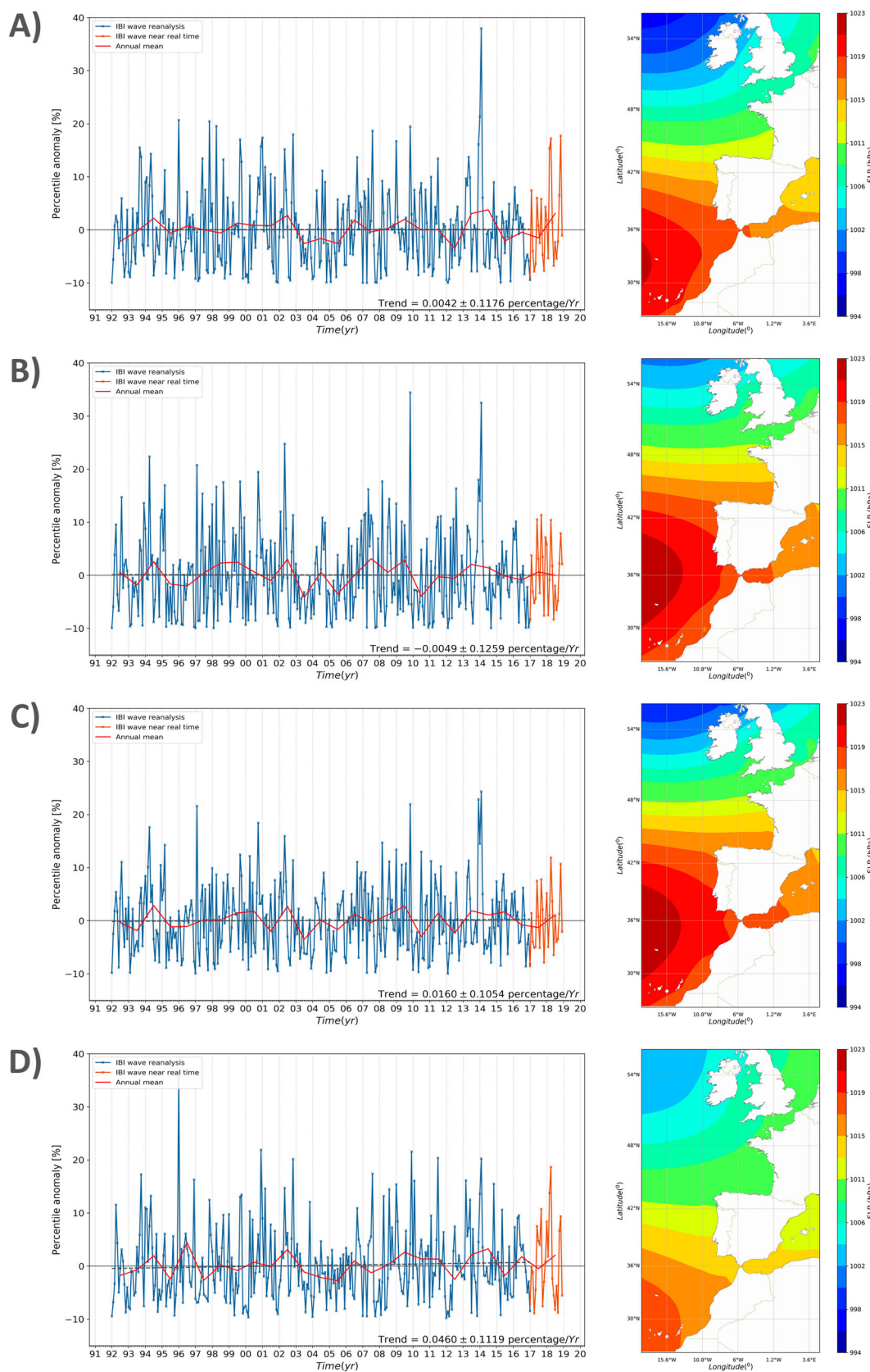
Figure 2.7.3. Left column: Time series of Strong Wave Incidence index (%) spatially averaged at monitoring regions. Blue/orange lines correspond to the index computed on a monthly basis from CMEMS reference products 2.13.1 and 2.13.2, respectively. Red line corresponds to the yearly averaged values of the index from CMEMS products 2.13.1 and 2.13.2. Black dashed line represents the trend line of product 2.13.2. Trend and 99% confidence interval of the trend are included in the right bottom corner of each panel. Right column: Composite of SLP in Iberia-Biscay-Ireland region obtained from the 10% of highest values of Strong Wave Incidence index in the period computed with the product 2.13.2. Rows compile information for monitoring regions: (A) WAV1, (B) WAV2, (C) WAV3, and (D) WAV4.

WAV1, WAV2, and WAV4. In these regions, some periods show index values above 30%. Which means a 30% higher-than-average incidence of strong conditions. The event of high index values in early 2014 at regions WAV1 and WAV2, correspond to a sequence of extreme storms that, in January and February 2014, affected the Northern coast of Spain and UK. This event was characterised by huge wind waves and severe coastal impacts described by BBC (2014) and Pérez-Gomez et al. (2016). Despite that the 2014 event can be found in the region WAV3, the value of the index in WAV3 (approximately 20%) is considerably lower than in WAV1 and WAV2 regions. The trend analysis shows that none of the monitoring regions presents a statistically significant trend of the incidence of strong wave conditions over the period 1992–2017 (Figure 2.7.3). This finding is consistent with those obtained by Young et al. (2011) and Young and Ribal (2019).

Right panels of Figure 2.7.3 show the composites of Sea Level Pressure (product referenced 2.7.4 in the product table) computed from the 10% of the highest values of Strong Wave Incidence index computed with the product 2.7.1. Since the regions WAV2 and WAV3 share the same latitudes, in both regions the most intense wave events are generated under the influence of a similar pattern. This pattern shows a strong pressure gradient (from 43°N to 54°N) that influences the Gulf of Biscay and the Celtic Sea. On the other hand, the pressure gradient that affects the most intense wave events in the WAV1 region shows slight differences with the previous one. In this case the pressure gradient moves southward and the orientation of isobars rotates to east-southeast. Under these conditions the coast of Iberian Peninsula is more influenced by the sharp pressure gradient than the northern regions of Gulf of Biscay and Celtic Sea. The SLP field associated to the intensity of wave events in region WAV4 shows a weaker pressure gradient that also affects the whole Iberia-Biscay-Ireland domain. However, this pattern is not a key driver of strong wave events in northern regions such as WAV1, WAV2, and WAV3 due to its realtively weak pressure gradient.

As previously stated in the analysis of the spatial patterns, 2018 is characterised by a high incidence of strong wave conditions in latitudes below 50°. Such high values of the index can be detected in the annual averages of WAV1 and WAV4 monitoring domains. The higher values of Strong Wave Incidence index in 2018 are mainly found in autumn and winter months of the year where several values ranging from 10% to 20% can be seen. Comparing the higher values in 2018 with the time series of monitoring domains WAV1 and WAV4, the events show a similar magnitude than previously recorded events. Therefore, 2018 can be considered as an average year with high incidence of severe wave conditions.

2.7.4. Summary and conclusions

The delivery of information about the climatic variability as well as the monitoring of anomalous events is one of the main tasks of operational monitoring services such as CMEMS. The huge amount of information routinely produced by operational services must be synthesised to provide simplified monitoring indicators. These indicators allow to evaluate the climatic deviation of events in order to make possible a fast and easy diagnosis of the climate system.

The present study proposes a statistic methodology to detect anomalous events of Significant Wave Height. The methodology computes the anomaly of exceedance of a threshold defined by the 90th percentile of Significant Wave Height. The proposed index is applied to make an analysis of the wave incidence in the Iberia-Biscay-Ireland region from 1992 up to 2019. The data provided by the CMEMS wave forecast and reanalysis systems in Iberia-Biscay-Ireland region has been used for this study (products referenced as 2.7.1 and 2.7.2). Since the validation of those systems is published in the QUID documents (both referenced in the Products Table), we consider the Significant Wave Height provided by this dataset reliable.

The robustness of the proposed indicator has been tested by (1) comparing its results with the North Atlantic Oscillation index, (2) comparing the anomalous events detected in the last decades with events described in literature, and (3) examining the atmospheric patterns associated to the occurrence of intense wave events.

Part of the study has analysed the relationships between the Strong Wave Incidence index and the large-scale atmospheric patterns. On one hand, the correlation of the Strong Wave Incidence index with the North Atlantic Oscillation has shown coherent results with other studies describing the relationships between the North Atlantic Oscillation and the Significant Wave Height in the North Atlantic. On the other hand, this study has described the atmospheric patterns that forces the occurrence of intense wave events in four different subregions. The physical consistence of results leads to conclude that the Strong Wave Incidence index is not only representative of the Significant Wave Height but also of the physical processes conditioning the wave behaviour in the region.

Additionally, the study has described the stronger wave events occurred in the last decades in the region. Results have shown that the Strong Wave Incidence index is able to detect past wave events described in

literature, as it is the case of the one occurred in early 2014 that affected the European Coast from Ireland up to Cape St. Vincent. However, the analysis has shown two more anomalous events in the past decades: the first one affected the WAV2 region in October 2009 and the second one affected region WAV4 in January 1996. The year 2018 in the Iberia-Biscay-Ireland region can be considered as a higher-than-average period influenced by strong wave conditions. In 2018, higher-than-average incidence of strong wave conditions were reported in the open ocean at latitudes south of 50°N, which corresponds to an increase of 3–5% of the frequency of strong wave conditions. On the contrary, in the Gulf of Biscay and west of the British Islands, lower-than-average incidence of strong wave conditions were detected in 2018.

The present study has evaluated the skill of the proposed methodology to detect anomalous events of Significant Wave Height. However, it worth to mention that this methodology standardises time series considering the internal distribution of the data, therefore, it can be potentially applied to several datasets and variables. Thus, this work lefts open the evaluation of this methodology to compute multi-product indices combining data obtained from different sources (e.g. different modelling systems and observations) or the use of this methodology to evaluate anomalous events of other variables such as temperature, salinity or biogeochemical variables.

Section 2.8: A Lagrangian approach to monitor local particle retention conditions in coastal areas

Authors: Anna Rubio, Ismael Hernández-Carrasco, Alejandro Orfila, Manuel González, Emma Reyes, Lorenzo Corgnati, Maristella Berta, Annalisa Griffa and Julien Mader

Statement of Main Outcomes: A Lagrangian model applied on surface ocean current observations and simulations in two different coastal areas is showcased as a promising approach for the monitoring of local particle retention conditions. Surface currents from a numerical model and HF radars are the principal baseline for this study. The local retention conditions in the two target coastal areas are characterised for more than 20 years by means of the escape rate, an approach that permits to obtain an estimation of residence times at a low computational cost. In addition, a classical estimation of the residence times is also used to illustrate the spatial variability of the local retention conditions. Findings show a significant spatial and temporal variability on the residence times values, characterised by a strong

seasonality and unveiling areas of higher capacity for water retention, directly linked to the mean circulation variability and very likely influenced by other mechanisms (e.g. wind and wave-induced currents, mesoscale processes and fronts). Depicting the Lagrangian behaviour of surface currents in terms of residence times in coastal zones is key to identify high-risk scenarios for pollution of the coastal areas or to quantify transport and retention of larvae or other planktonic organisms, with impact for fishery and Marine Protected Areas management.

Products used:

Ref. No.	Product name and type	Documentation
2.8.1	Atlantic -Iberian Biscay Irish-Ocean Physics Reanalysis Product IBI_REANALYSIS_ PHYS_005_002 Model	QUID: http://marine.copernicus.eu/ documents/QUID/CMEMS-IBI-QUID-005-002.pdf PUM: http://cmems-resources.cls.fr/ documents/PUM/CMEMS-IBI-PUM-005-002.pdf
2.8.2	In-Situ: High frequency radar derived surface currents Product INSITU_GLO_UV_L2_REP_ OBSERVATIONS_013_044 In Situ	PUM: http://marine.copernicus.eu/ documents/PUM/CMEMS-INS-PUM-013-044.pdf QUID: http://marine.copernicus.eu/ documents/QUID/CMEMS-INS-QUID-013-044.pdf REVIEW PAPER: https://doi.org/10.3389/fmars.2017. 00008 EUROPEAN HF STANDARD FOR HF RADAR DATA AND METADATA: http://www.marineinsitu.eu/wp-content/uploads/2018/02/ EGU2018-13317_presentation.pdf Bay of Biscay (Solabarrieta et al. 2016). Ibiza Channel (Lana et al. 2016)

2.8.1. Introduction

Coastal waters are enriched in nutrients from river outflows, sediment resuspension and coastal upwelling, they can also contain increased quantities of pollutants (e.g. floating marine litter). The physical mechanisms that contribute to the offshore transport of these mesotrophic coastal waters to the oligotrophic offshore areas are critically important for boosting oceanic primary production and sustaining the trophic chain. The mechanisms that can influence the escape times of these waters in a target area, need to be monitored in order to identify high-risk scenarios for pollution of the coastal areas and to quantify transport and retention of larvae, with impact for fishery and Marine Protected Area management.

The transport properties of the surface flow can be monitored using continuous High Frequency (HF) radar observations and model simulations of coastal surface currents, by means of different diagnostics based on

the Lagrangian approach. HF radars are capable to measure ocean surface currents over wide areas (reaching distances from the coast over 100 km) with high spatial (300 m-5 km) and temporal (≤ 1 h) resolution. Recent studies have demonstrated the potential of this land-based remote sensing technology for different applications in the field of coastal oceanography (e.g. Rubio et al. 2017; Roarty et al. 2019). Using as input gap-filled HF radar velocity fields and those simulated by a realistic model, a Lagrangian Particle-Tracking Model (Lagrangian model hereinafter), is implemented here to simulate particle trajectories. Then, from the Lagrangian model outputs, we study the characteristic time-scales for transport processes in the HF radar footprint area by means of the escape rate of active particles (Lai and Tel 2011; Hernández-Carrasco et al. 2013). The main objective of this analysis is to monitor conditions and identify the different scenarios that favour the local retention and dispersal of shelf waters in two study areas under the influence of ocean boundary currents. A similar approach was used in Rubio et al. (2018) and in Declerk et al. (2019) to study eddy-induced cross-shelf transport and particle retention in the South-East Bay of Biscay during 2014–2015. An additional example of this type of Lagrangian analysis aimed at quantifying retention and its impact on the recruitment of small pelagics has been recently performed using HF radar data in the Adriatic Sea (Sciascia et al. 2018). Here we propose a general methodology that allows to extend and better quantify these properties. Based on this methodology a future Ocean Monitoring Indicator could

consist in a time series of escape times/rates by study area to be used as an indicator of high/low retention conditions in target coastal areas or along the whole coastal strip.

2.8.2. Methods

To study surface ocean coastal transport, a Lagrangian model is applied on surface ocean currents observations and simulations over the Southeast Bay of Biscay and over the Ibiza Channel. On one hand we use historical data of HF radar observations. The HF radar system located in the South-East Bay of Biscay (www.euskoos. eus) emits at a central frequency of 4.463 MHz and a 30-kHz bandwidth and provides hourly current maps with a spatial resolution of 5 km in an area up to 150 km from the coast (Figure 2.8.1, left panel). The HF radar in Ibiza Channel (www.socib.es) transmits at 13.5 MHz and a 90 kHz bandwidth, providing hourly surface current maps of the eastern side of the Ibiza Channel with a spatial resolution of 3 km, covering an area to 60 km offshore (Figure 2.8.1, right panel).

For both systems, surface currents are re-processed to obtain gap-filled currents using the Open-boundary Modal Analysis (Kaplan and Lekien 2007). The historical HF radar data used here cover the period 2009–2018 for the Bay of Biscay system and 2012–2019 for the Ibiza Channel (product ref. 2.8.2). On the other hand, modelled surface currents in the period 1992–2016 are obtained from the CMEMS Atlantic-Iberian Biscay Irish reanalysis model (product ref. 2.8.1, e.g. Sotillo
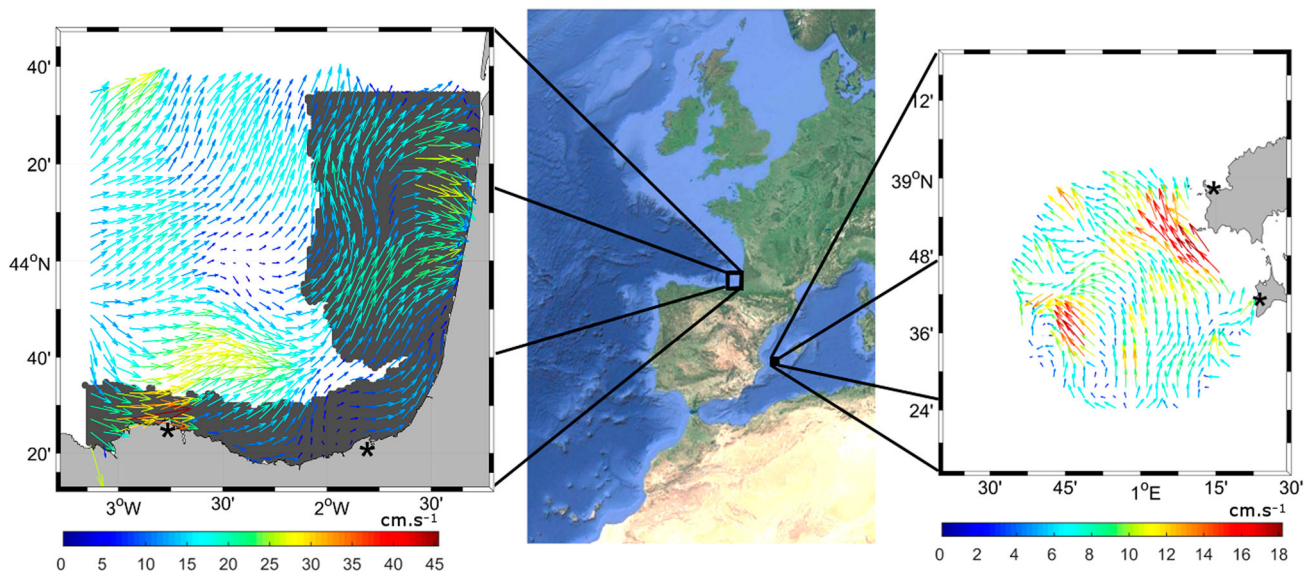
Figure 2.8.1. Study areas inside the CMEMS-IBI-MFC domain (central plot) and location of the antennas (asterisks) from the two HF radar systems used in this study (South-East Bay of Biscay – left-, Ibiza Channel – right-). A snapshot of HF radar currents (product ref. 2.8.2) is shown for each region. The grey-shaded area in the Southeast Bay of Biscay corresponds to the continental shelf (delimited by the 200m isobath) and particles' release region used for the escape time computation.

et al. 2015; hereafter CMEMS-IBI-MFC), for both areas. CMEMS-IBI-MFC provides hourly mean surface currents with a spatial resolution of 1/12 degree, and assimilates altimeter data, in situ temperature and salinity vertical profiles and satellite sea surface temperature.

The properties of the flow are studied by means of the Lagrangian model used in Rubio et al. (2018). A comparison of virtual trajectories obtained from this model using HF radar currents and real trajectories from drifters deployed in the study area (Lana et al. 2016; Solabarrieta et al. 2016; Hernández-Carrasco et al. 2018), demonstrates the skills of the Lagrangian model applied to different HF radar products (including Open-boundary Modal Analysis HF radar gap-filled velocities).

Using the trajectories obtained from the Lagrangian model, we study the characteristic time-scales for transport processes in the HF radar footprint area by means of the residence times and the escape rate/times (Lai and Tel 2011; Hernández-Carrasco et al. 2013). The main objective of this analysis is to investigate how the variability of ocean conditions impact the local retention of particles in the study areas.

First, to obtain the residence times we integrate $N_0 \sim 5000$ particle trajectories advected during one month in the region covered by the HF radars in both study areas. Then we compute the time needed for a particle to escape from this initial domain and we mapped the residence times using each particle initial position.

To study the temporal evolution of the retention conditions we complement the previous approach by means of the escape rate (Lai and Tel 2011; Hernández-Carrasco et al. 2013). The escape rates are obtained by analysing how the particles initially located in a given subregion inside the study areas (see Figure 2.8.1) escape from the release region with time. Assuming that the number of particles remaining inside the footprint area (N_t) decays exponentially with time (t) we can estimate the escape rate (κ) from

$$N_t \approx N_0 e^{-kt} \qquad (2.8.1)$$

where N_0 is the initial number of particles. Then, the escape time (τ) is estimated as the inverse of the escape rate ($1/\kappa$). This quantity provides information on how quickly the particles leave the HF radar area. The estimation of the escape times and offshore export of shelf particles is performed daily, using 1-month integration periods, and an initial number of particles $N_0 \sim 5000$. The particles for each simulation are launched every 24 h following a regular grid of locations, over the continental shelf area delimited by the 200m isobath (in the South-East Bay of Biscay, see the grey-shaded area in Figure 2.8.1) and covering the entire domain (in the

Ibiza Channel). Note that an exponential decay of particles escaping the domain over time is a requirement to properly apply Equation 2.8.1. This happens when the dynamics of the flow are determined by the hyperbolic effects (for instance, in the case of presence of sub or mesoscale flow features like eddies, fronts or filaments and when boundary conditions have no effect, which usually occurs for short integration times). Figure 2.8.2 shows that the averaged decay of particles (N_t) in the Ibiza Chanel domain over 5000 initialisations is exponential, within an interval of integration of 1–5 days. A similar behaviour is observed in the South-East Bay of Biscay (not shown). This supports the hypothesis that the hyperbolic processes dominate in both study areas at short integration scales and validates the use of an exponential fit to infer the escape times from the escape rates given in Equation (2.8.1).

When these conditions are not fulfilled the decay is not exponential, but as a power law, and the computation of the escape rates following this approach would not be accurate enough. To consider only the
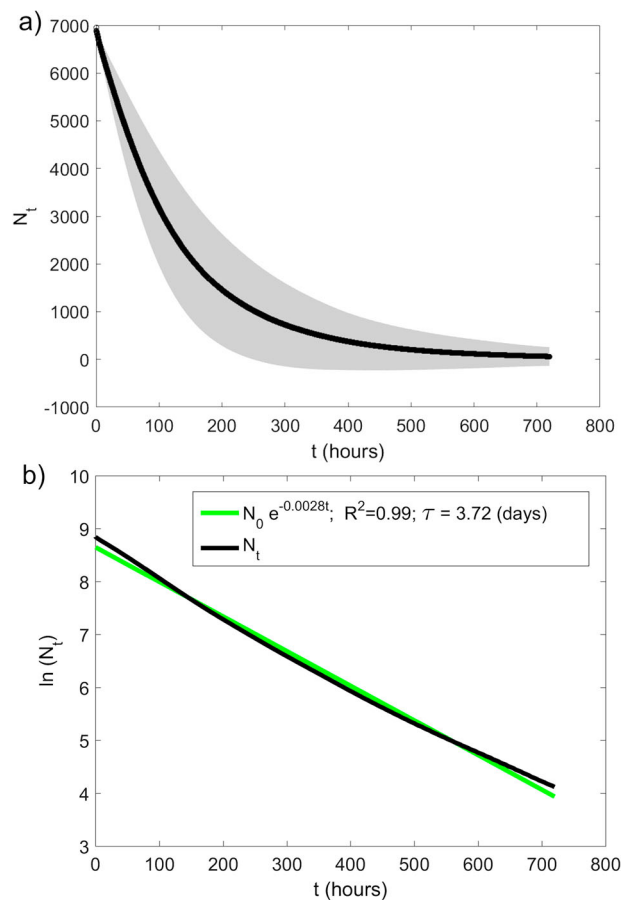
Figure 2.8.2. (a) Time evolution of the number of particles inside the area (HF radar coverage for the Ibiza Chanel domain) as a function of time, averaged over 5000 initializations. (b) Result of the exponential fit (green curve) to the averaged curve (in black) shown in (a). In (b) ln (N_t) is displayed on the *y*-axis.

periods when the decay is exponential, we use, for each initialisation, the Pearson's correlation (R) to evaluate the goodness of the fit between the decay of the particles curve and the fitted exponential curve, which is used to compute τ. We exclude then the periods where $R < 0.8$, which represent < 5% of the computed periods for both study areas and datasets.

2.8.3. Results and discussion

Figure 2.8.3 shows several examples of residence times (given in hours) maps computed for different dates and seasons for the two study areas and illustrates the high geographical and temporal variability of the retention conditions of the particles (representing e.g. pollutants or coastal enriched waters) launched during the Lagrangian simulations. It has to be noted that the maps shown here are only snapshots, thus they cannot be used to characterise the temporal variability of the retention patterns. Indeed, even in simulations performed a few days apart (and with overlapping days) we can observe clear fluctuations in terms of both maximum values and spatial patterns of the residence times. The high variability of the residence time spatial patterns highlights the impact of the small-scale surface coastal dynamics in the retention of particles within the coastal area.

As showcased by the chosen examples for winter (Figure 2.8.3(a,b,e,f)) and summer (Figure 2.8.3(c,d,g, h)) periods, and as we will demonstrate quantitatively

later on, difference in the values of the residence times in both study areas for different months suggests a seasonal behaviour, with much higher residence times in spring/summer than in autumn/winter. In the example given in Figure 2.8.3, the spatial distribution of residence times for 6–8 January 2014 (a,b) shows a meridional gradient, with higher values over the south of the domain, while a zonal gradient is observed for 8–9 July 2014 (c, d) with larger retention times (over one week) at the eastern half of the domain. The residence times in 5–8 January 2013 (e,f) for the Ibiza Channel region are very low and under 2–3 days for almost all the area with higher values distributed along filaments, while in the example for August 21 (h), larger times (> 12 days) can be observed almost for the whole domain. For all the examples, the meandering and on some occasions sharp shape of the areas of high retention puts in evidence the role of mesoscale structures and frontal dynamics in organising the coastal flow and associated transport.

The time series of escape times in Figure 2.8.4 allows us to further explore the temporal variability of the retention conditions in both study areas. In the case of the South-East Bay of Biscay the time series are representative of the retention in the shelf area, since particles are released exclusively over the continental shelf and this is also the control area used for the computations of the escape rates. For both study areas the conditions favourable to retention (given by periods of larger
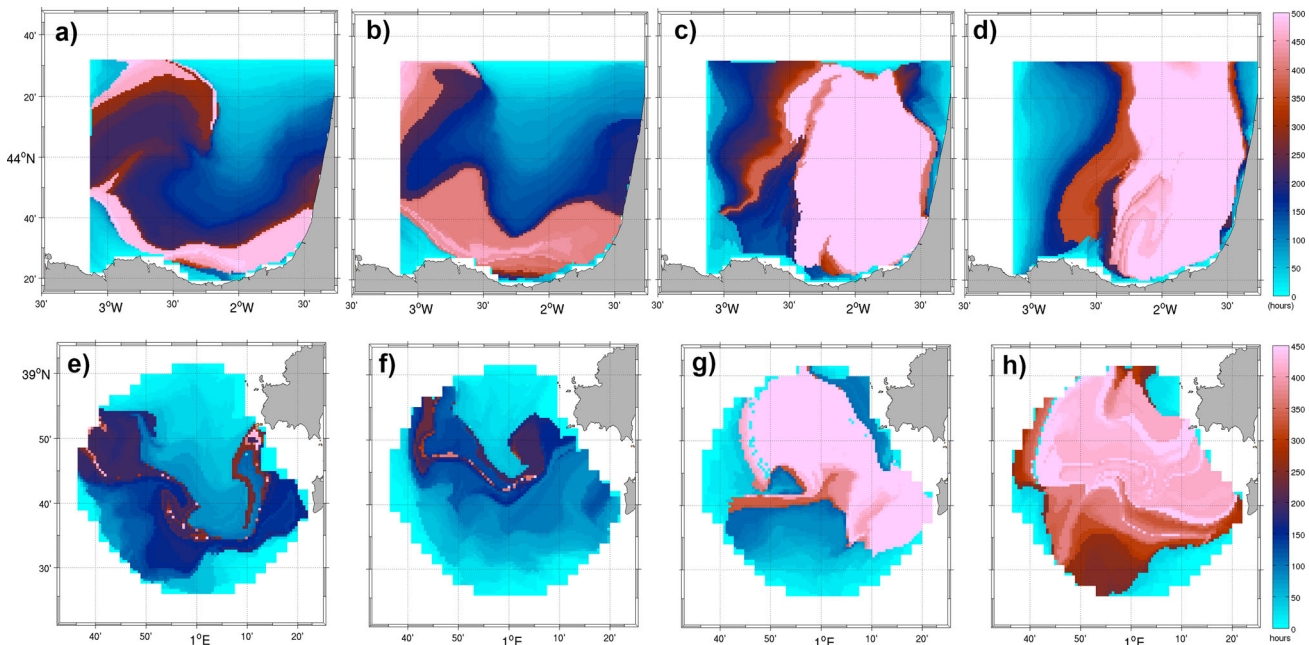
Figure 2.8.3. Maps of particle residence times (hours) computed for different dates and seasons, from HF radar observations (product reference 2.8.2) in the two study areas. The upper panels show the residence times for the South-East Bay of Biscay in (a, b) winter and (c, d) summer, the lower for the Ibiza Channel in (e, f) winter and (g, h) summer periods. Dates of the experiments: a – 06/01/2014; b – 08/01/2014; c – 02/07/2014; d – 08/07/2014; e – 05/01/2013; f – 08/01/2013; g – 18/08/2013; h – 21/08/2013.

scape times) will be those prone to high-risk scenarios for pollution of the coastal areas from land-based sources (e.g. river discharges). For the escape times, both simulated and observed surface currents are used and the results show similar general trends in the South-East Bay of Biscay, with some differences in terms of absolute values and in specific periods, while higher differences are observed in the Ibiza Channel. Shorter escape times (20–30%) are observed when using the observed currents in both areas. The escape times are much higher in the shelf of the South-East Bay of Biscay (of 18.5/14.4 days from model/observations) than in the Ibiza Channel (3.82/ 2.68 days from model/observations), which was expected because of the different extension and configuration of the study areas. In both areas, we can observe a seasonal modulation of the escape times. In the South-East Bay of Biscay shelf, the lower escape times are observed in autumn and are around 14.7 (12.3) days for the CMEMS-IBI-MFC (HF radar) datasets, while escape times are between 30 and 40% higher at the end of winter (for CMEMS-IBI-MFC dataset) or spring (for the HF radar dataset). In this area in autumn both the wind and slope current regime favour the rapid evacuation of the particles through the northern frontier of the computation domain. High-retention conditions are observed for certain periods like winter/spring of 1994, 1996, 2005, 2007, 2009, 2014, 2015 and 2016, or summer 2000.

For the Ibiza Channel, the escape times from the CMEMS-IBI-MFC dataset suggests higher retention in autumn and winter (>4 days; 40% higher than in summer), while the periods of higher retention from the HF radar data are spring and summer (3–3.3 days; 38% higher than in autumn). In this area again wind induced currents and the northward branch of the Atlantic inflow circulating along the eastern side of the channel are

expected to be the main mechanisms of particle evacuation through (mainly) the northern boundary of the computation domain (Font et al. 1988; Garcia-Lafuente et al. 1995; André et al. 2005; Heslop et al. 2012; Sayol et al. 2013). The very different spatial resolution of the datasets in this area can explain the discrepancies in terms of escape rates observed at shorter and seasonal timescales, partially because part of the observed mesoscale and sub mesoscale processes are not properly resolved by the CMEMS-IBI-MFC, of much coarser resolution. Besides, the HF radar could better capture wind-induced currents. High-retention conditions are observed for certain periods like autumn/winter of 1992, 1993, 1995, 1997, 2004, 2007 and spring of 2001, 2003, 2012.

2.8.4. Conclusion

The information on escape rates and residence times provides a spatial estimation of the permanence of the water bodies (and in turn of the substances or particles found in those waters, like pollutants or biological quantities) in the different areas of a study domain wider than an instantaneous or averaged current map. Thus, depicting these Lagrangian quantities in the coastal zones arises as an effective approach to monitor/study the vulnerability of the coastal zone to different sources of pollutants, regardless of their source (e.g. riverine or open waters sources). Residence times are directly correlated to water quality since they account for the water renewal capacity of the marine flow, allowing a detailed visualisation of the interchange of fluid particles between the coastal waters and the open sea. Its assessment has proved to be useful to identify pollution pathways or conditions for red tides (Braunschweig et al. 2003; Olascoaga 2010). In addition, residence times from HF radars have been used to plan the sanitation management and space
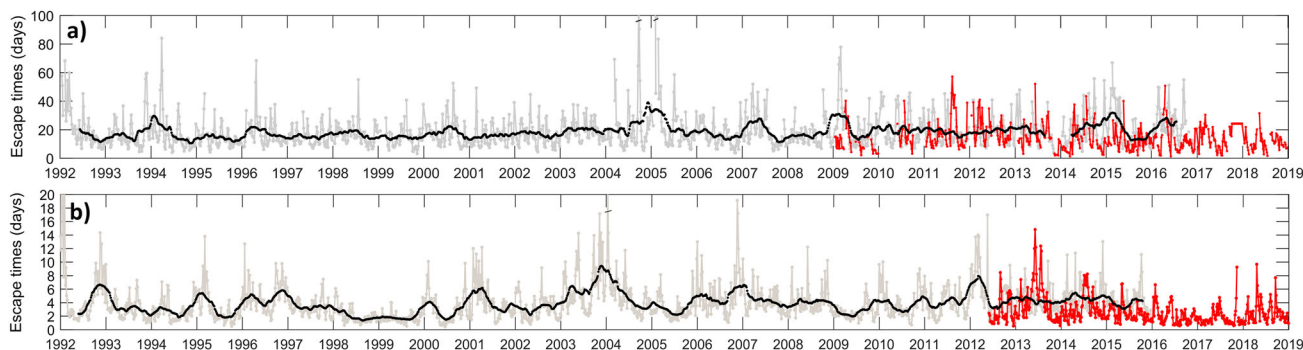
Figure 2.8.4. Time-series of escape times (in days) for (a) the South-East Bay of Biscay and (b) the Ibiza Channel (product ref. 2.8.2), using (grey) CMEMS-IBI-MFC (product ref. 2.8.1) surface current simulations and (red) HF radar surface current observations (product reference 2.8.2). The black line shows the 30-day running average computed from the timeseries of escape times from surface current simulations. The values of the escape times are shown only for Lagrangian simulations where the decay of the number of particles remaining inside the footprint (Nt) is exponential with time.

requirements for aquaculture farms in South Korea (Roarty et al. 2019) as well as for obtaining optimal release times of agricultural runoff in Monterrey Bay (Couliette et al. 2007). Findings show a significant variability on the escape rates and residence times in different areas and seasons, directly linked to the mean circulation variability and influenced by other mechanisms (e.g. wind-induced currents, mesoscale processes and fronts). In both pilot areas the temporal evolution of the retention conditions is seasonally modulated although it is shown that there is also variability at shorter (i.e. days) and longer (i.e. interannual) scales. Spatially the residence times show complex patterns highlighting the strong role that coastal mesoscale structures and frontal dynamics play in organising the coastal flow and associated transports. The combined use of Lagrangian indicators like the residence times and escape times is proven to be an interesting approach, allowing to monitor retention conditions in coastal areas at low computational cost. However, this technique is limited to ocean regimes where the dynamics are determined by the hyperbolic effects (i.e. the decay of the particles is exponential with time). When the condition of an exponential decay of the particles is not fulfilled the retention conditions could be evaluated by the classical approach of the residence times. In addition to the evaluation of the coastal retention conditions with time, the characterisation of the retention in function of different forcing (like winds, wave conditions, slope current regime, or the presence of fronts related to river discharges or mesoscale structures) could be also a very valuable information for the integrated management of target coastal areas. The increasing number of HF radar systems continuously monitoring coastal surface currents and the available long-term high resolution hindcasts and forecasts of simulated currents enable the expansion of this approach to other coastal regions and its use to predict retention conditions in key coastal areas.

Section 2.9: Global sea surface temperature anomalies in 2018 and historical changes since 1993

Authors: Simon A. Good, John J. Kennedy, Owen Embury

Statement of main outcome: Sea surface temperatures since 1993 have been assessed using a new climate data record from the European Space Agency Climate Change Initiative on sea surface temperature and an interim climate data record from the Copernicus Climate Change Service, with a focus on sea surface temperature anomalies relative to the 1993–2014 average during 2018. Between 1993 and 2018, the global average linear trend amounts to 0.014 ± 0.001°C / year (95% confidence interval) with warming trends occurring over most of the globe. However, the global average temperature in 2018 was cooler than the previous three years. This reflects changes from El Niño to La Niña conditions during that time, although El Niño thresholds were again reached by the end of 2018. Other features of the SST anomalies in 2018 included above average temperatures around Europe, which corresponded to a severe heat wave which affected large areas of Europe, North Africa and the Middle East between May and September.

Products used:

Ref. No.	Product name and type	Documentation
2.9.1	ESA SST CCI and C3S sea surface temperature analyses: SST-GLO-SST-L4-REP-OBSERVATIONS-010-024 Satellite sea surface temperature observational product	QUID: http://marine.copernicus.eu/documents/QUID/CMEMS-SST-QUID-010-024.pdf PUM: http://marine.copernicus.eu/documents/PUM/CMEMS-SST-PUM-010-024.pdf

2.9.1. Introduction

Sea surface temperature is an important ocean variable to monitor because of its many applications including determining how the temperature of the oceans has varied over time and tracking changes in modes of variability in the ocean and atmosphere. Recently a new climate data record from the European Space Agency Climate Change Initiative (ESA CCI) on sea surface temperature (Merchant et al. 2019) has been produced, covering the period late-1981 through to 2016. This is being extended as an interim climate data record by the Copernicus Climate Change Service (C3S). These products have a high level of stability throughout the record (Berry et al. 2018) and hence they are ideal for evaluating changes in sea surface temperature over time. These datasets have been used here to examine changes since 1993, with a focus on temperatures in 2018.

2.9.2. Method

The daily, global, spatially complete sea surface temperature maps on a regular grid ('L4' data) from the ESA CCI and C3S datasets were aggregated to create monthly and annual means. These were further averaged over the period 1993–2014 to generate a climatology. From these, anomalies (the difference between the monthly and annual averages and the climatology) were calculated.

The monthly anomalies were aggregated over the full globe and in regions using grid cell area weighted averaging to generate time series. These were further analysed to calculate a linear trend estimate using the

procedure described in Mulet et al. (2016). In summary, the time series were each decomposed into a residual seasonal component, a trend component and errors using the X-11 seasonal adjustment method (e.g. Pezzulli et al. 2005). The slope of the trend component was assessed using Sen's method (Sen 1968), which provides a robust estimate of the linear trend and its 95% confidence range. This linear trend calculation was also performed for the time series for each spatial grid point.

The Niño3.4 index was calculated following the method defined by Trenberth (2019). It is the average monthly anomaly within the range −5° to 5° in latitude and −170° to −120° in longitude, which is smoothed using a 5 day running mean and then normalised by dividing by the standard deviation of the running means during the 1993–2014 climatology period.

2.9.3. Results

2.9.3.1. Changes in sea surface temperature over the period 1993–2018

Figure 2.9.1(a) shows the time series of global average monthly sea surface temperature anomalies (thin black line) and the trend component generated using the X-11 seasonal adjustment method (thick black line). The estimate of the linear trend in global average sea surface temperature is 0.014 ± 0.001°C / year (95% confidence range). Therefore, there has been a statistically significant warming trend in sea surface temperature over the period 1993–2018 according to these data and this statistical model. Huang et al. (2019) reported similar trends calculated from three different datasets, although for a shorter period of 2000–2018. The trend in one dataset was 0.013°C / year and 0.016°C / year in the other two with an uncertainty of between ±0.006 and ±0.009°C / year. They also provided trends for the period 1950–2018 from two datasets. These were 0.008 and 0.010°C / year. Hausfather et al. (2017) examined four datasets and found trends of 0.007–0.012°C / year for 1997 through to 2015, although they found that 'instrumentally homogeneous' in situ data and an earlier, experimental version of the ESA CCI data were most consistent with the dataset with the largest trend.

The residual differences between the trend component and the linear trend line are shown in Figure 2.9.1(b) (black line). The residuals contain structure, indicating that a linear trend is an incomplete statistical
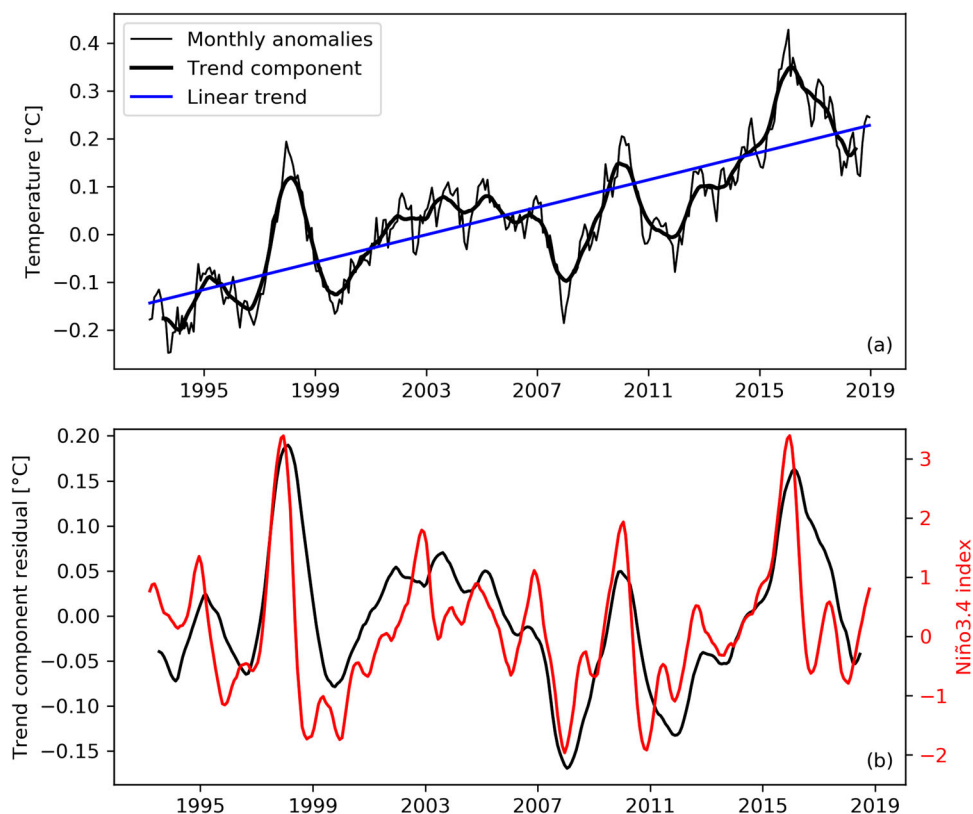
Figure 2.9.1. (a) Thin black line: monthly global average SST anomalies relative to the 1993–2014 average calculated from the ESA CCI and C3S datasets (product 2.9.1); thick black line: trend component derived from the monthly anomalies using the X-11 seasonal adjustment method; blue line: the estimated linear trend. (b) Black line: residual differences between the trend component and the linear trend shown in (a); red line: the Niño3.4 index.

model of the features within the global average sea surface temperature over this time period. The El Niño – Southern Oscillation is a mode of variability that is well known to impact on sea surface temperatures. Shifts between El Niño conditions, characterised in sea surface temperatures by warm anomalies in the eastern tropical Pacific, and La Niña conditions, which are associated with a cool eastern tropical Pacific, occur on timescales of the order 3–7 years (Trenberth 2019) and might explain the structure within the residuals. An index of El Niño – Southern Oscillation variability – the Niño3.4 index – is shown in Figure 2.9.1(b) (red line). The correlation coefficient between the residuals and the Niño3.4 index is 0.67, indicating that the El Niño – Southern Oscillation mode of variability does explain much of the residual structure including the two prominent peaks in 1997/8 and 2015/6 which correspond to strong El Niño events.

The strong El Niño – Southern Oscillation variability within the time series might impact on the linear trend estimate, despite the use of a robust method to calculate this. For example, a strong La Niña at the start of the time series accompanied by an El Niño at the end could increase the estimated linear trend, and the reverse situation could decrease it. To check this, estimates of linear trend were calculated for the tropical Pacific (defined as between $-15°$ to $15°$ in latitude and $160°$ to $-80°$ in longitude) and for the globe excluding that region. These were found to be $0.007 \pm 0.006°C$ / year and $0.015 \pm 0.001°C$ / year respectively. Therefore, the tropical Pacific is found to have a lower linear trend estimate over the period 1993–2018 than the rest of the world and this region does not significantly affect the linear trend estimate for the globe. This is further confirmed by Figure 2.9.2(a), which shows the linear trend estimated for each grid point across the globe and indicates that the strongest areas of warming and cooling occurred away from the tropical Pacific.

According to Figure 2.9.2(a), the Arctic Ocean contains some of the largest warming trends over the 1993–2018 period. Warming in this region, including amplification of the effect due to, for example, changes in surface albedo as ice melts, is discussed in the Intergovernmental Panel on Climate Change report (IPCC 2013). In contrast the North Atlantic has a prominent region to the south of Greenland where there is a cooling trend. This area has cooled on centennial time scales (IPCC 2013) possibly reflecting a slowdown of the
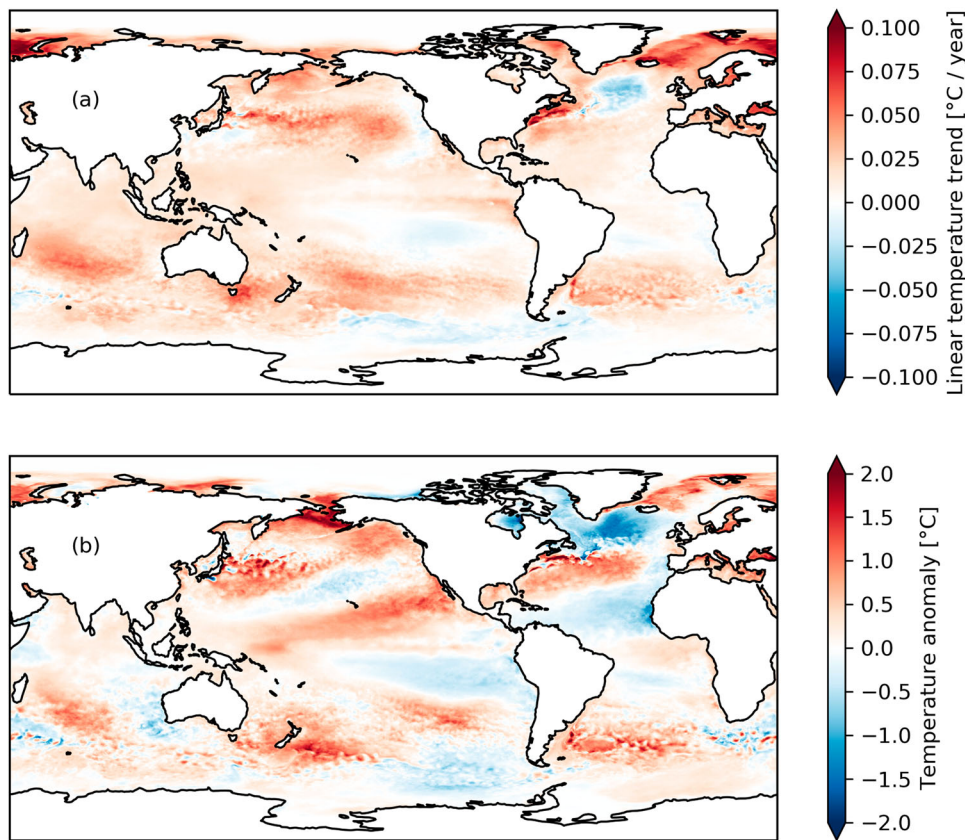
Figure 2.9.2. (a) Linear sea surface temperature trends over the period 1993–2018 calculated from the ESA CCI and C3S datasets (product 2.9.1). (b) Annual average sea surface temperature anomalies for the year 2018 relative to the 1993–2014 average, calculated from the ESA CCI and C3S datasets (product 2.9.1).

Atlantic meridional overturning circulation (Sevellec et al. 2017; Caesar et al. 2018). Another feature in Figure 2.9.2(a) is a pattern of warming trends in the mid-northern Pacific and cooling trends in the north-east and mid-southern Pacific, which is reminiscent of the Pacific Decadal Oscillation. This climate mode has a similar pattern of variability to the El Niño – Southern Oscillation but with more prominence in the Northern Pacific and a longer timescale (Deser et al. 2016). An index of Pacific Decadal Oscillation variability is shown in Kim (2018). According to this, it transitioned from positive values (associated with cool mid-northern Pacific temperatures) in the 1990s to negative values (warm mid-northern Pacific temperatures) in the late-2000s to early-2010s, but in recent years the index has been positive.

2.9.3.2. Sea surface temperatures in 2018

Figure 2.9.1(a) shows that global sea surface temperatures in 2018 were lower than in the previous three years and 2018 is nominally the fourth warmest year in the period 1993–2018 according to these data. This reflects the shift from El Niño conditions, which held sway at the end of 2015 and start of 2016 (nominally the second warmest and warmest years respectively), to weak La Niña conditions in early 2018. Later in 2018, sea surface temperature anomalies in the tropical Pacific increased to El Niño thresholds, though atmospheric indicators of El Niño were largely absent, and there are indications in the time series of a corresponding increase in global average temperatures.

The map of annual average anomalies for 2018 is shown in Figure 2.9.2(b). The transition from La Niña to El Niño conditions is clear in the tropical Pacific in monthly anomalies (Figure 2.9.3), but the cool anomalies at the start of the year largely cancel the end of year warm anomalies in the annual average. The North Pacific has a pattern of anomalies that mirror the trends shown in Figure 2.9.2(a), with cool anomalies surrounded by warm water, which could reflect the changes in the Pacific Decadal Oscillation discussed previously.

Other features in Figure 2.9.2(b) include a distinctive tripole pattern in the sea surface temperature anomalies in the North Atlantic with below-average sea surface temperatures to the south of Greenland and Iceland, and in an area extending from the coast of west Africa to the southern Caribbean, while above average temperatures were observed in an area extending from the east coast of the US towards western Europe. This spatial pattern is associated with the positive phase of the North Atlantic Oscillation (Visbeck et al. 2001).

Figure 2.9.2(b) shows that the waters around Europe were overall warmer than average during 2018 to the south and east, but cooler to the north and west. However, time series of sea surface temperature in the European North West Shelf seas, the Mediterranean Sea, the Black Sea and the Baltic Sea (Mulet et al. 2016) show that these regions exhibit significant intra-annual variability and this was also the case in 2018. A prolonged and severe heatwave affected large areas of Europe, North Africa and the Middle East between May and September, and strong warm sea surface temperature anomalies occurred during that time in the European region (Figure 2.9.3).

In the Southern Hemisphere spring (September - November), sea surface temperatures in the Indian Ocean were characteristic of the positive phase of the Indian Ocean Dipole (Saji et al. 1999) with above-average sea surface temperatures in the west and below-average temperatures in the east. The Indian Ocean Dipole impacts on precipitation in the surrounding land. For example, in its positive phase, the Indian Ocean Dipole is associated with drier conditions in Australia (Ummenhofer et al. 2009).

Australia was sandwiched between cooler-than-average waters to the west and warmer than average waters to the east. Late 2017 and early 2018 saw a marine heat wave affect the Tasman Sea (Perkins-Kirkpatrick et al. 2019). Daily sea-surface temperatures exceeded 4°C above average in places. A marine heatwave also affected the Tasman Sea in the Southern Hemisphere summer of 2015/16 which at the time was considered 'unprecedented' (Oliver et al. 2017).

2.9.4. Conclusions

Changes in global sea surface temperature between 1993 and 2018 have been examined using new data records from the ESA CCI and C3S projects. The time series of global average temperature contains a linear trend of 0.014 ± 0.001°C / year (95% confidence range). Residual differences between the linear trend and the time series exhibit variability that correlates well (correlation coefficient = 0.67) with an index of El Niño – Southern Oscillation variability. Although there is an overall warming trend, the spatial distribution of the linear trends in sea surface temperature shows that some regions of the oceans have cooled, for example the North Atlantic south of Greenland, while others have warmed more than others, such as the Arctic Ocean.

Temperature anomalies in 2018 relative to the 1993–2014 average were examined in detail. This was nominally the fourth warmest in the dataset, ranking behind the previous three years. This relative cooling is associated with a transition between El Niño and weak La Niña conditions. Sea surface temperature anomalies in the North Atlantic showed a tripole pattern consistent with the positive
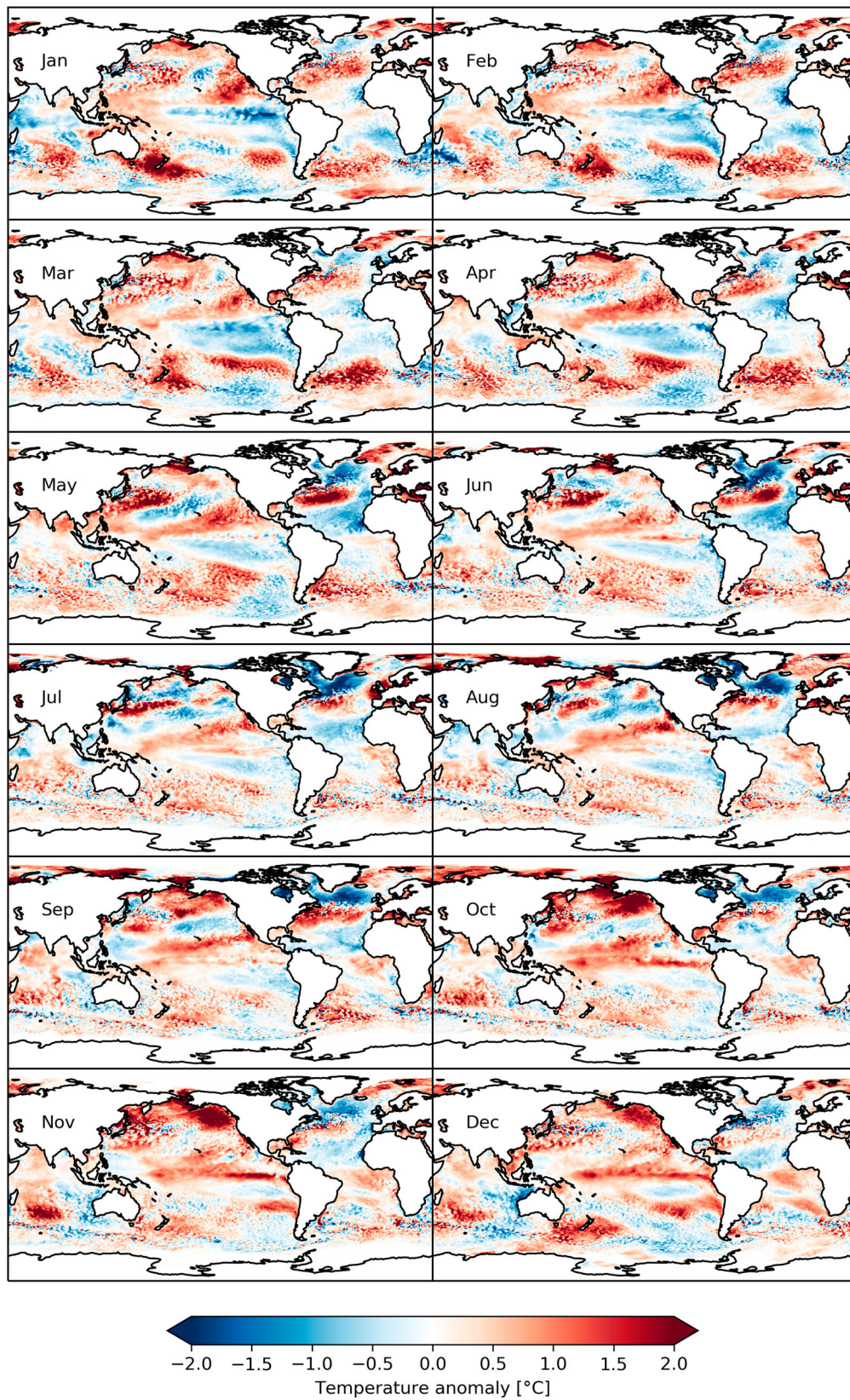
Figure 2.9.3. Average sea surface temperature anomalies for each month of 2018 relative to the 1993–2014 average, calculated from the ESA CCI and C3S datasets (product 2.9.1).

phase of the North Atlantic Oscillation. The waters around Europe exhibited strong warm anomalies around the middle of the year, corresponding to a heatwave that affected the region. Anomalies in the Indian Ocean corresponded to the positive phase of the Indian Ocean Dipole during the Southern Hemisphere spring, while the Tasman Sea experienced a marine heatwave, which started in late 2017 and lasted into early 2018.

Section 2.10: Ocean acidification

Authors: Marion Gehlen, Thi Tuyet Trang Chau, Anna Conchon, Anna Denvil-Sommer, Frédéric Chevallier, Mathieu Vrac, Carlos Mejia

Statement of main outcome: Since the onset of the industrial era the ocean took up about 28% of the excess CO_2 emitted to the atmosphere by human activities. While the ecosystem service 'carbon sequestration' provided by the world oceans mitigates global warming, it also results in profound changes of seawater chemistry referred to as ocean acidification. Carbon dioxide is a weak acid that reacts with water in a suite of reactions that lead to a decrease in pH. Ocean acidification is thus a direct consequence of CO_2 uptake by the ocean. Hence, this section presents and discusses the temporal evolution of the global carbon sink, the driver of ocean acidification, and of surface ocean pH from 2001 to 2016. Both time series correspond to novel Ocean Monitoring Indicators released in 2019 by CMEMS. The ocean carbon sink increased over the period of reconstruction at a rate of 0.08 ± 0.1 PgC yr^{-1}, mirrored by a negative trend in global mean pH of 0.0017 ± 0.0002 pH units.

Data use:

Ref. No.	Product name and type	Documentation
2.10.1	CMEMS Global Ocean Surface Carbon (MULTIOBS_GLO_BIO_REP_015_005)	PUM: http://marine.copernicus.eu/documents/PUM/CMEMS-MOB-PUM-015-005.pdf QUID: http://marine.copernicus.eu/documents/QUID/CMEMS-MOB-QUID-015-005.pdf
2.10.2	a. Global Ocean Carbon sink, (GLOBAL_OMI_HEALTH_carbon_co2_flux_integrated) b. Global Ocean pH, (GLOBAL_OMI_HEALTH_carbon_pH_area_averaged)	PUM: http://marine.copernicus.eu/documents/PUM/CMEMS-OMI-PUM-GLO-HEALTH-carbon.pdf QUID: http://marine.copernicus.eu/documents/QUID/CMEMS-OMI-QUID-GLO-HEALTH-carbon-ph-area-averaged.pdf

2.10.1. Introduction

Between the onset of the Industrial Era (1750) and 2011, mankind has emitted 555 ± 85 Pg of Carbon (PgC) to the atmosphere by burning fossil fuels, producing cement and changing land use (Ciais et al. 2013). Over the same period, only 240 ± 10 PgC accumulated in the atmosphere. The remainder has been taken up by the ocean (155 ± 30 PgC) and terrestrial ecosystems (180 ± 80 PgC) (Ciais et al. 2013). The uptake of CO_2 by the ocean, the ocean carbon (C) sink, is evaluated on a yearly basis since 2007 by the Global Carbon Project (GCP, https://www.globalcarbonproject.org/). Ocean C sink estimates derived from atmospheric inversions, forced biogeochemical ocean general circulation models and statistical interpolation converge on the amplitude of the global integrated ocean C sink at yearly and decadal time scales. However, uncertainties subsist on the magnitude of the sink and its variability at the scale of oceanic regions (e.g. North Atlantic, Southern Ocean) (Le Quéré et al. 2018).

The ocean mitigates thus global warming by taking up excess CO_2 (or anthropogenic C) emitted to the atmosphere, a 'service' that comes at the cost of profoundly modifying seawater chemistry. Carbon dioxide is a weak acid that reacts with water in a suite of reactions consuming carbonate ions (CO_3^{2-}) and releasing hydrogen ions (H^+). The increase in H^+ corresponds to an increase in acidity (ocean acidification), generally measured as a decrease in pH (pH = - log [H^+]). The average pH of surface ocean seawater has already deceased by 0.1 pH unit (26% increase the concentration of H^+) since 1870–1899 (Gattuso et al. 2015). Many biological processes depend on a tight regulation of pH at the cellular level and mechanisms of pH regulation are present across many taxa (Seibel and Walsh 2001). Ocean acidification occurs together with warming, loss of oxygen and changes in nutrient availability for marine primary production (Bopp et al. 2013), and it constitutes a threat to marine organisms, including species of commercial value (e.g. shell fish), ecosystems and dependent services (Hilmi et al. 2013; Gattuso et al. 2015).

Surface ocean pH is monitored internationally through a coordinated effort (www.goa-on.org). The monitoring of average ocean pH at agreed sampling sites also contributes to the Sustainable Development Goal (SDG) 14 ('Conserve and sustainably use the oceans, seas and marine resources for sustainable development') by providing indicator 14.3.1. CMEMS complements these efforts by the development of gridded monthly maps of surface ocean pH (Product 2.10.2a) from reconstructed surface ocean pCO$_2$ (Product 2.10.2a) and alkalinity estimates. From these monthly maps a novel Ocean Monitoring Indicator 'surface ocean pH' is derived as the global yearly mean pH (Product 2.10.2b). The OMI is initially computed from global ocean gridded monthly maps of surface ocean pH for the period 2001–2016 and it will be extended annually in phase with the yearly update of Product 2.10.2a.

2.10.2. Method

A novel neural-network based approach (Denvil-Sommer et al. 2019) is applied to reconstruct monthly surface ocean pCO_2 fields (Product 2.10.1) at 1°x1° spatial resolution over the period 2001–2016 with the help of CMEMS observed ocean physics products (sea surface salinity, sea surface temperature, sea surface height) and global analyses of the chlorophyll-*a*, the atmospheric CO_2 mole fraction (Surface Ocean CO_2 Atlas, https://www.socat.info/, Bakker et al. 2016) and the mixed layer depth. CMEMS will deliver annual extensions of the reconstruction time series. Together with knowledge of wind speed and atmospheric pCO_2, these fields allow estimating air-to-sea CO_2 fluxes at the same spatial and temporal resolution. The air-to-sea CO_2 fluxes, in turn, provide the basis for the Ocean Monitoring Indicator (OMI) 'Global Surface Ocean CO_2 flux' (Product 2.10.2a), corresponding to the yearly integrated uptake of CO_2 by the ocean, the ocean C sink.

Monthly surface ocean pH fields (Product 2.10.1) are calculated from reconstructed surface ocean pCO_2 and alkalinity using the speciation software CO2sys (Lewis and Wallace 1998; Van Heuven et al. 2011). Time and space varying surface ocean alkalinity fields are obtained from the multivariate linear regression model LIAR (Carter et al. 2016, 2018) as a function of sea surface temperature and salinity, as well as nitrate and dissolved silica from World Ocean Atlas v2 2013 (https://www.nodc.noaa.gov/OC5/woa13/). Global monthly maps of surface ocean pH at 1°x1° spatial resolution are averaged to compute the OMI 'pH area averaged' (Product 2.10.2b)

2.10.3. Results and discussion

2.10.3.1. Air-to-sea fluxes of CO_2

The maps of reconstructed yearly mean air-to-sea fluxes of CO_2 (Figure 2.10.1) highlight the regional variability of fluxes. Outgassing of CO_2 is associated with the upwelling of CO_2-rich subsurface waters (e.g. Equatorial Pacific). The northern and southern mid to high latitudes are sink regions. The North Atlantic stands out as a major area of CO_2 uptake explained by a marked strong cooling in winter and a vigorous phytoplankton bloom in spring and early summer. A region of enhanced uptake is also associated with the subtropical convergence zone in the southern hemisphere (Takahashi et al. 2009). At inter-annual time scales, natural modes of climate variability modulate the intensity of CO_2 fluxes over large source and sink areas. This is illustrated for the last strong El Niño event that took place in 2015–2016 (Chatterjee et al. 2017). During El Niño events, a warm anomaly propagates across the Equatorial Pacific which suppresses the strength of the Eastern Equatorial Upwelling and hence the outgassing of CO_2 associated with upwelled waters rich in dissolved inorganic carbon (DIC). The El Niño Southern Oscillation (ENSO) is an important mode of tropical climate variability with a well-documented imprint on atmospheric CO_2 (Feely et al. 1999). Figure 2.10.1 presents yearly average air-to-sea fluxes of CO_2 for 2014 (neutral conditions prior to El Niño) and 2015 (El Niño) (Santoso et al. 2017). The suppressed outgassing East of the date line is clearly seen.

Figure 2.10.2 represents the net CO_2 uptake by the ocean from which the uptake of anthropogenic CO_2 is derived after adjusting for the outgassing of 0.45 PgC yr^{-1} of river C input to the ocean (Jacobson et al. 2007). After adjustment, the global ocean sink was 2.50 PgC (range: 2.31–2.74 PgC yr^{-1}) in 2016, in close agreement of the estimate by Le Quéré et al. (2018) of 2.6 ± 0.5 PgC yr^{-1}. The global integrated yearly ocean uptake of CO_2 increased from 0.85 (range: 0.50–0.99) PgC yr^{-1} in 2001, to 2.05 (range: 1.86–2.29) PgC yr^{-1} in 2016, in response to increasing atmospheric CO_2 concentrations (Denvil-Sommer et al. 2019). Here, we took advantage of the cross-validation and the reconstruction step to compute the spread defined as the empirical 95%
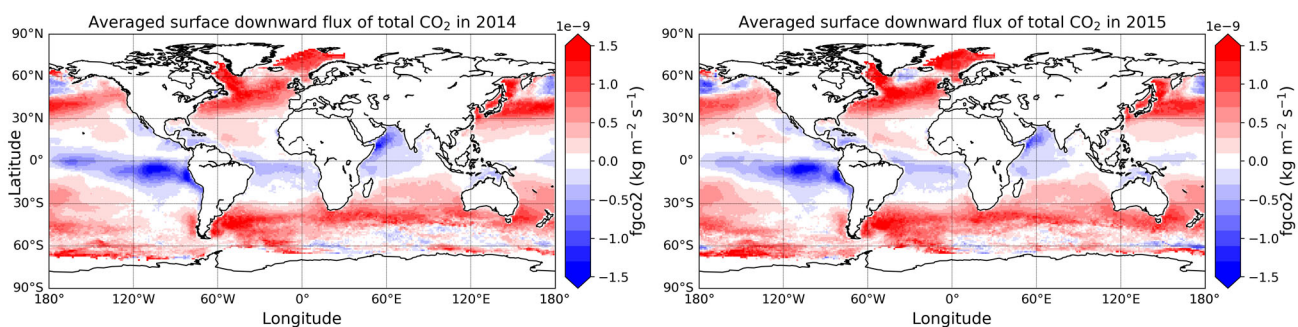
Figure 2.10.1. Yearly mean air-to-sea reconstructed fluxes of CO_2 derived from the CMEMS Global Ocean Surface Carbon (Product 2.10.1). Left panel: pre El Niño conditions; right panel: El Niño conditions.
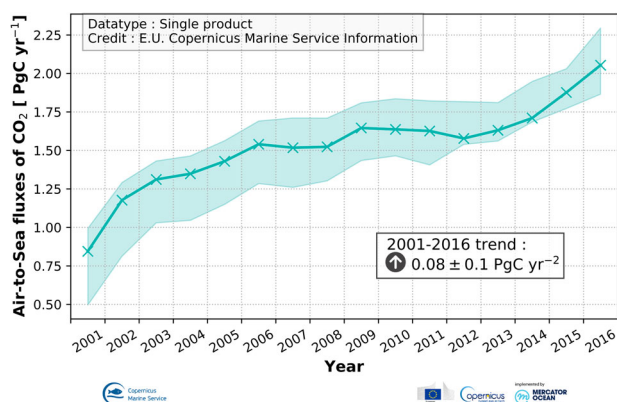
Figure 2.10.2. Global integrated yearly ocean uptake of CO_2 derived from the Ocean Monitoring Indicator (OMI) 'Global Surface Ocean CO_2 flux' (Product 2.10.2a). Plain line, best model after Denvil-Sommer et al. (2019); range, empirical 95% confidence interval computed from 25 samples.

confidence interval of 25 network realisations. It corresponds to a conservative estimate of the uncertainty of the best model solution (Figure 2.10.1, plain line).

2.10.3.2. Surface ocean pH

As a consequence of the ongoing uptake of excess CO_2 from the atmosphere, the pH of surface ocean waters declines with a trend of 0.0017 ± 0.0002 pH units yr^{-1} (Figure 2.10.3). The global average trend of pH is similar to estimates derived from time series stations located in the Atlantic (Bermuda Atlantic Time Series, BATS, -0.0017 ± 0.0003 pH units yr^{-1}, Bates et al. 2014) and in the tropical Pacific (Hawaii Ocean Time-series, HOT, -0.0016 ± 0.0001 pH units yr^{-1}, Bates et al. 2014). The atmospheric CO_2 concentration is the main driver for the surface ocean pH, which explains the relative homogeneity of these trends.
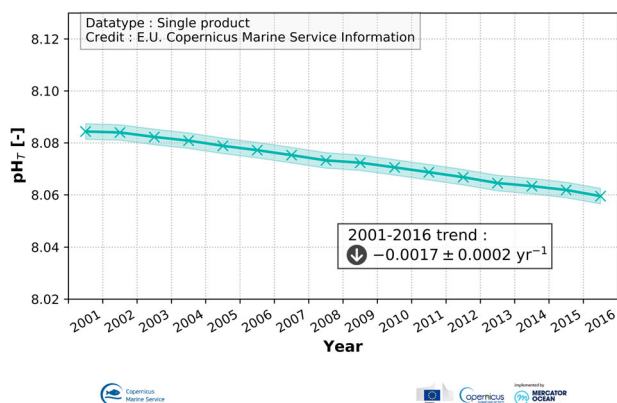
Figure 2.10.3. Annual global mean surface seawater pH derived from the Ocean Monitoring Indicator 'surface ocean pH' (Product 2.10.2b).

The total uncertainty of yearly mean surface seawater pH is 0.003 pH unit. It corresponds to the combined contributions of (1) speciation uncertainty, (2) mapping uncertainty, (3) uncertainty due to spatial averaging:

(1) *Speciation uncertainty* is evaluated through uncertainty propagation following Orr et al. (2018) within the speciation software CO2sys (Lewis and Wallace 1998; Van Heuven et al. 2011). Inputs to the uncertainty propagation routine were default values for dissociation constants, and uncertainty estimates for alkalinity fields from LIAR (Carter et al., 2016; 2018), respectively biome-scale estimates for pCO_2 from Denvil-Sommer et al. (2019). The RMSE computed from monthly error maps is taken as an estimate of (1): 0.0143 pH unit.

(2) *Mapping uncertainty* is set equal to the RMSE computed from the comparison between reconstructed pH values and the Glodapv2 bottle data set: 0.0285 pH unit.

(3) Uncertainty due to pH space and time variability is taken as the standard deviation of monthly reconstructed pH fields: 0.0340 pH unit.

Contributions of individual uncertainty terms are squared, divided by the effective degrees of freedom (N_{eff}) and summed to yield (total uncertainty)^2. The effective degree of freedom takes pH decorrelation length scales into account. Those were not assessed for this release. Here we use a constant decorrelation length scale of 20° and 3 months which for a latitude band extending from 65°S to 65°N and excluding land points yields $N_{eff} = 327$.

References

Section 2.1. Diatom dynamics in the North Atlantic

Agirbas E, Martinez-Vicente V, Brewin R, Racault M, Airs R, Llewellyn CA. 2015. Temporal changes in total and size-fractioned chlorophyll-A in surface waters of three provinces in the Atlantic Ocean (September to November) between 2003 and 2010. J Mar Sys. 150:56–65. DOI:10.1016/j.jmarsys.2015.05.008.

Arin L, Morán XA, Estrada M. 2002. Phytoplankton size distribution and growth rates in the Alboran Sea (SW Mediterranean): short term variability related to mesoscale hydrodynamics. J Plankton Res. 24(10):1019–1033. DOI:10.1093/plankt/24.10.1019.

Bopp L, Aumont O, Cadule P, Alvain S, Gehlen M. 2005. Response of diatoms distribution to global warming and potential implications: a global model study. Geophys Res Lett. 32:1–4.

Brewin R, Sathyendranath S, Hirata T, Lavender SJ, Barciela RM, Hardman-Mountford NJ. 2010. A three-component

model of phytoplankton size class for the Atlantic Ocean. Ecol Modell. 221(11):1472–1483. DOI:10.1016/j.ecolmodel.2010.02.014.

Brewin RJW, Ciavatta S, Sathyendranath S, Jackson T, Tilstone G, Curran K, Airs RL, Cummings D, Brotas V, Organelli E, et al. 2017. Uncertainty in ocean-color estimates of chlorophyll for phytoplankton groups. Front Marine Sci. 4:104. DOI:10.3389/fmars.2017.00104.

Butenschön M, Clark J, Aldridge JN, Allen JI, Artioli Y, Blackford J, et al. 2016. ERSEM 15.06: a generic model for marine biogeochemistry and the ecosystem dynamics of the lower trophic levels. Geosci Model Dev. 9:1293–1339. DOI:10.5194/gmd-9-1293-2016.

Cermeño P, Dutkiewicz S, Harris RP, Follows M, Schofield O, Falkowski PG. 2008. The role of nutricline depth in regulating the ocean carbon cycle. PNAS. 105:20344. DOI:10.1073/pnas.0811302106.

Chavez FP. 1989. Size distribution of phytoplankton in the central and eastern tropical Pacific. Global Biogeochem Cycles. 3(1):27–35. DOI:10.1029/GB003i001p00027.

Chisholm SW. 1992. Phytoplankton size. In: Falkowski PG, Woodhead AD, editors. Primary productivity and biogeochemical cycles in the sea. New York (NY): Springer; p. 213–237.

Ciavatta S, Brewin RJW, Skakala J, Polimene L, de Mora L, Artioli Y, Allen JI. 2018. Assimilation of oceancolor plankton functional types to improve marine ecosystem simulations. J Geophys Res Oceans. 123. DOI:10.1002/2017JC013490.

Finkel ZV, Beardall J, Flynn KJ, Quigg A, Rees TAV, Raven JA. 2009. Phytoplankton in a changing world: cell size and elemental stoichiometry. J Plankton Res. 32:119–137. DOI:10.1093/plankt/fbp098.

Hinder SL, Hays G, Edwards M, Roberts EC, Walne AW, Gravenor M. 2012. Changes in marine dinoflagellate and diatom abundance under climate change. Nat Clim Change. 2:271–275. DOI:10.1038/nclimate1388.

IOCCG. 2014. Phytoplankton functional types from space. In: Sathyendranath S, editor. Reports of the international ocean-colour coordinating group, No. 15. Dartmouth: IOCCG.

Leterme SC, Edwards M, Seuront L, Attrill MJ, Reid PC, John AWG. 2005. Decadal basin-scale changes in diatoms, dinoflagellates, and phytoplankton colour across the North Atlantic. Limnol Oceanogr. 50:1244–1253.

Loisel H, Nicolas J-M, Sciandra A, Stramski D, Poteau A. 2006. Spectral dependency of optical backscattering by marine particles from satellite remote sensing of the global ocean. J Geophys Res. 111:C09024. DOI:10.1029/2005JC003367.

Marañon E, Holligan PM, Barciela R, González-Benítez N, Mourino B, Pazo MJ, Varela M. 2001. Patterns of phytoplankton size structure and productivity in contrasting open-ocean environments. Mar Ecol Progr Ser. 216:43–56. DOI:10.3354/meps216043.

Marinov I, Doney S, Lima ID. 2010. Response of ocean phytoplankton community structure to climate change over the 21st century: partitioning the effects of nutrients, temperature and light. Biogeosci Discuss. 7. DOI:10.5194/bg-7-3941-2010.

Nair A, Sathyendranath S, Platt T, Morales J, Stuart V, Forget M-H, Devred E, Bouman H. 2008. Remote sensing of phytoplankton functional types. Remote Sens Environ. 112:3366–3375.

Pannard A, Bormans M, Lefebvre S, Claquin P, Lagadeuc Y. 2007. Phytoplankton size distribution and community structure: influence of nutrient input and sedimentary loss. J Plankton Res. 29(7):583–598. DOI:10.1093/plankt/fbm040.

Raitsos D, Lavender SS, Maravelias C, Haralabous J, McQuatters-Gollop A, Edwards M, Reid P. 2011. Macroscale factors affecting diatom abundance: a synergistic use of continuous plankton recorder and satellite remote sensing data. Int J Remote Sens. 32. DOI:10.1080/01431161003645832.

Rousseaux CS, Gregg WW. 2015. Recent decadal trends in global phytoplankton composition. Global Biogeochem Cycles. 29:1674–1688. DOI:10.1002/2015GB005139.

San Martin E, Harris RP, Irigoien X. 2006. Latitudinal variation in plankton size spectra in the Atlantic Ocean. Deep Sea Res Part II. 53(14–16):1560–1572. DOI:10.1016/j.dsr2.2006.05.006.

Sathyendranath S, Pardo S, Benincasa M, Brando VE, Brewin RJW, Mélin F, Santoleri R. 2018. 2.5. Essential variables: ocean colour in copernicus marine service ocean state report – issue 2. J Operat Oceanogr. 11(sup1):1–142. DOI:10.1080/1755876X.2018.1489208.

Sathyendranath S, Watts L, Devred E, Platt T, Caverhill C, Maass H. 2004. Discrimination of diatoms from other phytoplankton using ocean-colour data. Marine Ecol Prog Series. 272:59–68.

Tréguer P, Bowler C, Moriceau B, Dutkiewicz S, Gehlen M, Aumont O, Bittner L, Dugdale R, Finkel Z, Iudicone D, Jahn O. 2018. Influence of diatom diversity on the ocean biological carbon pump. Nat Geosci. 11:27–37. DOI:10.1038/s41561-017-0028-x.

Zhai L, Platt T, Tang C, Sathyendranath S, Walne A. 2013. The response of phytoplankton to climate variability associated with the North Atlantic oscillation. Deep Sea Res Part II. 93:159–168. DOI:10.1016/j.dsr2.2013.04.009.

Section 2.2. Primary production

Antoine D, Morel A. 1996. Oceanic primary production: 1. Adaptation of a spectral light-photosynthesis model in view of application to satellite chlorophyll observations. Global Biogeochem Cycles. 10(1):43–55.

Antoine D, Morel A, André JM. 1995. Algal pigment distribution and primary production in the eastern Mediterranean as derived from coastal zone color scanner observations. J Geophys Res Oceans. 100(C8):16193–16209.

Barbieux M, Uitz J, Gentili B, de Fommervault OP, Mignot A, Poteau A, Schmechtig C, Taillandier V, Leymarie E, Penkerc'h C, d'Ortenzio F. 2019. Bio-optical characterization of subsurface chlorophyll maxima in the Mediterranean Sea from a biogeochemical-Argo float database. Biogeosciences. 16(6):1321–1342.

Behrenfeld MJ, O'Malley RT, Siegel DA, McClain CR, Sarmiento JL, Feldman GC, Milligan AJ, Falkowski PG, Letelier RM, Boss ES. 2006. Climate-driven trends in contemporary ocean productivity. Nature. 444(7120):752.

Béthoux J-P, Gentili B. 1999. Functioning of the Mediterranean Sea: past and present changes related to freshwater input and climate changes. J Mar Syst. 20:33–47.

Bhatia MP, Kujawinski EB, Das SB, Breier CF, Henderson PB, Charette MA. 2013. Greenland meltwater as a significant

and potentially bioavailable source of iron to the ocean. Nature Geosci. 6(4):274–278.

Bosc E, Bricaud A, Antoine D. 2004. Seasonal and interannual variability in algal biomass and primary production in the Mediterranean Sea, as derived from 4 years of SeaWiFS observations. Global Biogeochem Cycles. 18:GB1005. DOI:10.1029/2003GB002034.

Canu DM, Ghermandi A, Nunes PA, Lazzari P, Cossarini G, Solidoro C. 2015. Estimating the value of carbon sequestration ecosystem services in the Mediterranean Sea: an ecological economics approach. Glob Environ Change. 32:87–95.

Carr ME, Friedrichs MA, Schmeltz M, Aita MN, Antoine D, Arrigo KR, Bidigare R. 2006. A comparison of global estimates of marine primary production from ocean color. Deep Sea Res Part II. 53(5–7):741–770.

Chassot E, Bonhommeau S, Dulvy NK, Mélin F, Watson R, Gascuel D, Le Pape O. 2010. Global marine primary production constrains fisheries catches. Ecol Lett. 13(4):495–505.

Chavez FP, Messié M, Pennington JT. 2011. Marine primary production in relation to climate variability and change. Ann Rev Mar Sci. 3:227–260.

Cossarini G, Lazzari P, Solidoro C. 2015. Spatiotemporal variability of alkalinity in the Mediterranean Sea. Biogeosciences. 12(6):1647.

Cossarini G, Mariotti L, Feudale L, Mignot A, Salon S, Taillandier V, Teruzzi A, D'Ortenzio F. 2019. Towards operational 3D-Var assimilation of chlorophyll biogeochemical-Argo float data into a biogeochemical model of the Mediterranean Sea. Ocean Model. 133:112–128.

Dobricic S, Pinardi N. 2008. An oceanographic three-dimensional variational data assimilation scheme. Ocean Model. 22(3–4):89–105.

Donlon CJ, Martin M, Stark J, Roberts-Jones J, Fiedler E, Wimmer W. 2012. The operational sea surface temperature and sea ice analysis (OSTIA) system. Remote Sens Environ. 116:140–158.

Ducklow HW. 2003. Biogeochemical provinces: towards a JGOFS synthesis. In: Fasham MJR, editors. Ocean biogeochemistry. Global change — the IGBP series (closed). Berlin: Springer.

Falkowski PG. 2003. Biogeochemistry of primary production in the sea. In: Heinrich DH, Karl KT, ediotrs. Treatise on geochemistry. Oxford: Pergamon; p. 185–213.

Falkowski PG, Barber RT, Smetacek V. 1998. Biogeochemical controls and feedbacks on ocean primary production. Science. 281(5374):200–206.

Geider RJ, MacIntyre HL, Kana TM. 1997. Dynamic model of phytoplankton growth and acclimation: responses of the balanced growth rate and the chlorophyll a: carbon ratio to light, nutrient-limitation and temperature. Mar Ecol Prog Ser. 148:187–200.

Gregg WW, Rousseaux CS, Franz BA. 2017. Global trends in ocean phytoplankton: a new assessment using revised ocean colour data. Remote Sens Lett. 8(12):1102–1111.

Hattam C, Atkins JP, Beaumont N, Börger T, Böhnke-Henrichs A, Burdon D, De Groot R, Hoefnagel E, Nunes PA, Piwowarczyk J. 2015. Marine ecosystem services: linking indicators to their classification. Ecol Indic. 49:61–75.

Hawkings JR, Wadham JL, Tranter M, Lawson E, Sole A, Cowton T, Tedstone AJ, Bartholomew I, Nienow P,

Chandler D, Telling J. 2015. The effect of warming climate on nutrient and solute export from the Greenland Ice Sheet. Geochem Perspect Lett. 1:94–104.

Henson SA, Sanders R, Madsen E. 2012. Global patterns in efficiency of particulate organic carbon export and transfer to the deep ocean. Global Biogeochem Cycles. 26:GB1028. DOI:10.1029/2011GB004099.

Kessouri F, Ulses C, Estournel C, Marsaleix P, D'Ortenzio F, Severin T. 2018. Vertical mixing effects on phytoplankton dynamics and organic carbon export in the western Mediterranean Sea. J Geophys Res Oceans. 123(3):1647–1669.

Kwiatkowski L, Naar J, Bopp L, Aumont O, Defrance D, Couespel D. 2019. Decline in Atlantic primary production accelerated by Greenland ice sheet melt. Geophys Res Lett. 46(20):11347–11357.

Lavigne H, D'ortenzio F, d'Alcalà MR, Claustre H, Sauzède R, Gacic M. 2015. On the vertical distribution of the chlorophyll a concentration in the Mediterranean Sea: a basin-scale and seasonal approach. Biogeosciences. 12(16):5021–5039.

Lawson EC, Wadham JL, Tranter M, Stibal M, Lis GP, Butler CE, Laybourn-Parry J, Nienow P, Chandler D, Dewsbury P. 2014. Greenland Ice Sheet exports labile organic carbon to the Arctic oceans. Biogeosciences. 11(14).

Lazzari P, Solidoro C, Ibello V, Salon S, Teruzzi A, Béranger K, Colella S, Crise A. 2012. Seasonal and inter-annual variability of plankton chlorophyll and primary production in the Mediterranean Sea: a modelling approach. Biogeosciences. 9:217–233. DOI:10.5194/bg-9-217-2012.

Lazzari P, Solidoro C, Salon S, Bolzon G. 2016. Spatial variability of phosphate and nitrate in the Mediterranean Sea: a modeling approach. Deep Sea Res Part I. 108:39–52.

Le Quéré C, Andrew RM, Friedlingstein P, Sitch S, Hauck J, Pongratz J, et al. 2018. Global carbon budget 2018. Earth System Science Data. 10:4.

Lejeusne C, Chevaldonné P, Pergent-Martini C, Boudouresque CF, Pérez T. 2010. Climate change effects on a miniature ocean: the highly diverse, highly impacted Mediterranean Sea. Trends Ecol Evol. 25(4):250–260.

Lévy M, Iovino D, Resplandy L, Klein P, Madec G, Tréguier AM, Masson S, Takahashi K. 2012. Large-scale impacts of submesoscale dynamics on phytoplankton: local and remote effects. Ocean Modell. 43:77–93.

Lévy M, Klein P, Treguier AM. 2001. Impact of sub-mesoscale physics on production and subduction of phytoplankton in an oligotrophic regime. J Marine Res. 59(4):535–565.

Longhurst A. 1995. Seasonal cycles of pelagic production and consumption. Prog Oceanogr. 36(2):77–167.

López-Jurado JL, González-Pola C, Vélez-Belchí P. 2005. Observation of an abrupt disruption of the long-term warming trend at the Balearic Sea, western Mediterranean Sea, in summer 2005. Geophys Res Lett. 32:L24606. DOI:10.1029/2005GL024430.

Lynam CP, Uusitalo L, Patrício J, Piroddi C, Queirós AM, Teixeira H, Rossberg AG, Sagarminaga Y, Hyder K, Niquil N, Möllmann C. 2016. Uses of innovative modeling tools within the implementation of the marine Strategy framework directive. Front Marine Sci. 3:182.

Mayot N, D'Ortenzio F, Taillandier V, Prieur L, De Fommervault OP, Claustre H, Conan P. 2017. Physical and biogeochemical controls of the phytoplankton blooms in

North western Mediterranean Sea: a multiplatform approach over a complete annual cycle (2012–2013 DEWEX experiment). J Geophys Res Oceans. 122(12):9999–10019.

Morrow RM, Ohman MD, Goericke R, Kelly TB, Stephens BM, Stukel MR. 2018. CCE v: primary production, mesozooplankton grazing, and the biological pump in the California current ecosystem: variability and response to El Niño. Deep Sea Res Part I. 140:52–62.

Moutin T, Raimbault P. 2002. Primary production, carbon export and nutrients availability in western and eastern Mediterranean Sea in early summer 1996 (MINOS cruise). J Mar Sys. 33:273–288.

Perruche C, Solidoro C, Salon S. 2018. Chapter 1.6: nitrates; in von Schuckmann, K., Le Traon, P.-Y., Smith, N., Pascual,A., Brasseur, P., Fennel, K. J. The Copernicus marine service ocean state report. J Operat Oceanogr. 11(Sup 1):S1–S142. DOI:10.1080/1755876X.2018.1489208.

Renault L, Deutsch C, McWilliams JC, Frenzel H, Liang JH, Colas F. 2016. Partial decoupling of primary productivity from upwelling in the California current system. Nat Geosci. 9(7):505.

Rousseaux C, Gregg W. 2014. Interannual variation in phytoplankton primary production at a global scale. Remote Sens. 6(1):1–19.

Salgado-Hernanz PM, Racault MF, Font-Muñoz JS, Basterretxea G. 2019. Trends in phytoplankton phenology in the Mediterranean Sea based on ocean-colour remote sensing. Remote Sens Environ. 221:50–64.

Salon S, Cossarini G, Bolzon G, Feudale L, Lazzari P, Teruzzi A, Solidoro C, Crise A. 2019. Marine ecosystem forecasts: skill performance of the CMEMS Mediterranean Sea model system. Ocean Sci Discuss. DOI:10.5194/os-2018-145.

Schroeder K, Borghini M, Cerrati G, Difesca V, Delfanti R, Santinelli C, Gasparini GP. 2008. Multiparametric mixing analysis of the deep waters in the western Mediterranean Sea. Chem Ecol. 24(S1):47–56.

Siegel DA, Buesseler KO, Behrenfeld MJ, Benitez-Nelson CR, Boss E, Brzezinski MA, Perry MJ. 2016. Prediction of the export and fate of global ocean net primary production: the EXPORTS science plan. Front Marine Sci. 3:22.

Simoncelli S, Fratianni C, Pinardi N, Grandi A, Drudi M, Oddo P. 2014. Mediterranean Sea physical reanalysis (MEDREA 1987-2017). DOI:10.25423/MEDSEA_REANALYSIS_PHYS_006_004.

Siokou-Frangou I, Christaki U, Mazzocchi MG, Montresor M, Ribera d'Alcalá M, Vaqué D, Zingone A. 2010. Plankton in the open Mediterranean Sea: a review. Biogeosciences. 7 (5):1543–1586.

Somot S, Houpert L, Sevault F, Testor P, Bosse A, Taupier-Letage I, Bouin M-N, Waldman R, Cassou C, Sanchez-Gomez E, et al. 2018. Characterizing, modelling and understanding the climate variability of the deep water formation in the North-western Mediterranean Sea. Clim Dyn. 51 (3):1179–1210.

Tedesco L, Miettunen E, An BW, Haapala J, Kaartokallio H. 2017. Long-term mesoscale variability of modelled sea-ice primary production in the northern Baltic Sea. Elem Sci Anth. 5.

Teruzzi A, Bolzon G, Salon S, Lazzari P, Solidoro C, Cossarini G. 2018. Assimilation of coastal and open sea biogeochemical data to improve phytoplankton simulation in the Mediterranean Sea. Ocean Model. 132:46–60.

Teruzzi A, Cossarini G, Lazzari P, Salon S, Bolzon G, Crise A, Solidoro C. 2016. Mediterranean Sea biogeochemical reanalysis (CMEMS MED REA-biogeochemistry 1999–2015). Copernicus Monit Environ Mar Serv. DOI:10.25423/MEDSEA_REANALYSIS_BIO_006_008.

Teruzzi A, Dobricic S, Solidoro C, Cossarini G. 2014. A 3-D variational assimilation scheme in coupled transport-biogeochemical models: forecast of Mediterranean biogeochemical properties. J Geophy Res Oceans. 119(1):200–217.

Uitz J, Stramski D, Gentili B, D'Ortenzio F, Claustre H. 2012. Estimates of phytoplankton class-specific and total primary production in the Mediterranean Sea from satellite ocean color observations. Global Biogeochem Cycles. 26:GB2024. DOI:10.1029/2011GB004055.

Vantrepotte V, Mélin F. 2009. Temporal variability of 10-year global SeaWiFS time-series of phytoplankton chlorophyll a concentration. ICES J Mar Sci. 66(7):1547–1556.

Vichi M, Lovato T, Lazzari P, Cossarini G, Gutierrez Mlot E, Mattia G. 2015. The biogeochemical flux model (BFM): equation description and user manual. BFM Version. 5:755.

Volpe G, Nardelli BB, Cipollini P, Santoleri R, Robinson IS. 2012. Seasonal to interannual phytoplankton response to physical processes in the Mediterranean Sea from satellite observations. Remote Sens Environ. 117:223–235.

Von Schuckmann K, Le Traon PY, Smith N, Pascual A, Djavidnia S, Gattuso JP, et al., (2019). Copernicus Marine Service Ocean State Report, Issue 3. J Oper Oceanogr. 12 (Supp1):S1–S123.

Watson RA, Nowara GB, Hartmann K, Green BS, Tracey SR, Carter CG. 2015. Marine foods sourced from farther as their use of global ocean primary production increases. Nat Commun. 6:7365.

Westberry T, Behrenfeld MJ, Siegel DA, Boss E. 2008. Carbon-based primary productivity modeling with vertically resolved photoacclimation. Global Biogeochem Cycles. 22: GB2024. DOI:10.1029/2007GB003078.

Section 2.3: Barrier layer thickness in the Pacific Ocean

Ando K, McPhaden MJ. 1997. Variability of surface layer hydrography in the tropical Pacific. J Geophys Res. 102 (C10):23,063–23,078. DOI:10.1029/97JC01443.

Aretxabaleta A, Smith K, Kalra T. 2017. Regime changes in global sea surface salinity trend. J Marine Sci Eng. 5:57. DOI:10.3390/jmse5040057.

Bosc C, Delcroix T, Maes C. 2009. Barrier layer variability in the western Pacific warm pool from 2000 to 2007. J Geophys Res. 114:C06023. DOI:10.1029/2008JC005187.

Cheng L, Trenberth KE, Fasullo J, Abraham J, Boyer TP, von Schuckmann K, Zhu J. 2017. Taking the pulse of the planet. Eos. 98. DOI:10.1029/2017EO081839. [accessed 2017 September 13]. https://eos.org/opinions/taking-the-pulse-of-the-planet.

Cravatte S, Delcroix T, Zhang D, McPhaden M, Leloup J. 2009. Observed freshening and warming of the western Pacific warm pool. Clim Dyn. 33(4):565–589. DOI:10.1007/s00382-009-0526-7.

Cronin MF, McPhaden MJ. 2002. Barrier layer formation during westerly wind bursts. J Geophys Res. 107 (C12):8020. SRF 21-1– SRF 21-12.

de Boyer Montégut C, Mignot J, Lazar A, Cravatte S. 2007. Control of salinity on the mixed layer depth in the world ocean: 1. General description. J Geophys Res. 112:C06011. doi:10.1029/2006JC003953.

Delcroix T, Cravatte S, McPhaden MJ. 2007. Decadal variations and trends in tropical Pacific sea surface salinity since 1970. J Geophys Res. 112:C03012. DOI:10.1029/2006JC003801.

Deser C, Phillips A, Bourdette V, Teng H. 2012. Uncertainty in climate change projections: the role of internal variability. Clim Dyn. 38:527. DOI:10.1007/s00382-010-0977-x.

Durack PJ. 2015. Ocean salinity and the global water cycle. Oceanography. 28(1):20–31. DOI:10.5670/oceanog.2015.03.

England MH, McGregor S, Spence P, Meehl GA, Timmermann A, Cai W, Gupta AS, McPhaden MJ, Purich A, Santoso A. 2014. Recent intensification of wind-driven circulation in the Pacific and the ongoing warming hiatus. Nat Clim Chang. 4(3):222–227.

Guinehut S, Dhomps A, Larnicol G, Le Traon P-Y. 2012. High resolution 3-D temperature and salinity fields derived from in situ and satellite observations. Ocean Sci. 8(5):845–857.

Hasson A, Puy M, Boutin J, Guilyardi E, Morrow R. 2018. Northward pathway across the tropical North Pacific Ocean revealed by surface salinity: How do El Nino anomalies reach Hawaii? J Geophys Res Oceans. 123:2697–2715. DOI:10.1002/2017JC013423.

Liu H, Grodsky SA, Carton JA. 2009. Observed subseasonal variability of oceanic barrier and compensated layers. J Clim. 22(22):6104–6119.

Llovel W, Penduff T, Meyssignac B, Molines J-M, Terray L, Bessieres L, Barnier B. 2018. Contributions of atmospheric forcing and chaotic ocean variability to regional sea level trends over 1993–2015. Geophys Res Lett. 45. DOI:10.1029/2018GL080838.

Maes C, Picaut J, Belamari S. 2002. Salinity barrier layer and onset of El Niño in a Pacific coupled model. Geophys Res Lett. 29(24):2206–2259. DOI:10.1029/2002GL016029.

Mignot J, de Boyer Montégut C, Lazar A, Cravatte S. 2007. Control of salinity on the mixed layer depth in the world ocean: 2. tropical areas. J Geophys Res Oceans. 112(10):1–12. DOI:10.1029/2006JC003954.

Singh A, Delcroix T, Cravatte S. 2011. Contrasting the flavors of El Niño-southern oscillation using sea surface salinity observations. J Geophys Res. 116:C06016. DOI:10.1029/2010JC006862.

Terray L, Corre L, Cravatte S, Delcroix T, Reverdin G, Ribes A. 2012. Near-surface salinity as nature's rain gauge to detect human influence on the tropical water cycle. J Climate. 25:958–977. DOI:DOI:10.1175/JCLI-D-10-05025.1.

Tesdal J, Abernathey RP, Goes JI, Gordon AL, Haine TW. 2018. Salinity trends within the upper layers of the subpolar North Atlantic. J Climate. 31:2675–2698. DOI:10.1175/JCLI-D-17-0532.1.

Vinogradova NT, Ponte RM. 2017. In search of fingerprints of the recent intensification of the ocean water cycle. J Climate. 30(14):5513–5528. DOI:10.1175/JCLI-D-16-0626.1.

Wang L, Fanghua U. 2018. Decadal variability and trends of oceanic barrier layers in tropical Pacific. Ocean Dyn. 68. DOI:10.1007/s10236-018-1191-3.

Wang X, Liu H. 2016. Seasonal-to-interannual variability of the barrier layer in the western Pacific warm pool associated with ENSO. Clim Dyn. 47:375. DOI:10.1007/s00382-015-2842-4.

Zhao M, Hendon HH, Alves O, Yin Y. 2014. Impact of improved assimilation of temperature and salinity for coupled model seasonal forecasts. Clim Dyn. 42. DOI:10.1007/s00382-014-2081-0.

Zhu J, Huang B, Zhang R-H, Hu Z-Z, Kumar A, Balmaseda MA, Marx L, Kinter JL. 2014. Salinity anomaly as a trigger for ENSO events. Sci. Rep. 4:6821.

Section 2.4: Interannual variability in the eastern and western Mediterranean overturning index

Cessi P. 2019. The global overturning circulation. Ann Rev Mar Sci. 11:249–270. DOI:10.1146/annurev-marine-010318-095241.

Gertman I, Pinardi N, Popov Y, Hecht A. 2006. Aegean Sea water masses during the early stages of the eastern Mediterranean climatic Transient (1988–1990). J Phys Oceanogr. 36(9):1841–1859. DOI:10.1175/JPO2940.1.

Houpert L, Durrieu de Madron X, Testor P, Bosse A, D'Ortenzio F, Bouin MN, Dausse D, Le Goff H, Kunesch S, Labaste M, et al. 2016. Observations of open-ocean deep convection in the northwestern Mediterranean Sea: seasonal and interannual variability of mixing and deep water masses for the 2007–2013 period. J Geophys Res Oceans. 121:8139–8171. DOI:10.1002/2016JC011857.

Johnson KS, Berelson WM, Boss ES, Chase Z, Claustre H, Emerson SR, Gruber N, Körtzinger A, Perry MJ, Riser SC. 2009. Observing biogeochemical cycles at global scales with profiling floats and gliders: prospects for a global array. Oceanography. 22:216–225. DOI:10.5670/oceanog.2009.81.

Pinardi N, Cessi P, Borile F, Wolfe CLP. 2019. The Mediterranean Sea overturning circulation. J Phys Oceanogr. 49:1699–1721. DOI:10.1175/JPO-D-18-0254.1.

Pinardi N, Zavatarelli M, Adani M, Coppini G, Fratianni C, Oddo P, Tonani M, Lyubartsev V, Dobricic S, Bonaduce A. 2015. Mediterranean Sea large-scale, low-frequency ocean variability and water mass formation rates from 1987 to 2007: a retrospective analysis. Prog Oceanogr. 132:318–332. DOI:10.1016/j.pocean.2013.11.003.

Roether W, Klein B, Hainbucher D. 2014. Chap 6. The eastern Mediterranean transient. In: GL Eusebi Borzelli, M Gacic, P Lionello, P Malanotte-Rizzoli, editors. The Mediterranean Sea. American Geophysical Union (AGU); p. 75–83. DOI:10.1002/9781118847572.ch6.

Roether W, Manca BB, Klein B, Bregant D, Georgopoulos D, Beitzel V, Kovačević V, Luchetta A. 1996. Recent changes in the eastern Mediterranean deep waters. Science. 271:333–335. DOI:10.1126/science.271.5247.333.

Schroeder K, Chiggiato J, Bryden H, Borghini M, Ismail SB. 2016. Abrupt climate shift in the western Mediterranean Sea. Sci Rep. 6:23009. DOI:10.1038/srep23009.

Simoncelli S, Fratianni C, Pinardi N, Grandi A, Drudi M, Oddo P, Dobricic S. 2014. Mediterranean Sea physical reanalysis (MEDREA 1987-2015) (version 1) [dataset]. Copernicus Monit Environ Marine Serv. DOI:10.25423/medsea_reanalysis_phys_006_004.

Smith RO, Bryden HL, Stansfield K. 2008. Observations of new western Mediterranean deep water formation using Argo floats 2004-2006. Ocean Sci. 4(2):133–149.

Yoon S, Chang K, Nam S, Rho TK, Kang DJ, Lee T, Park KA, Lobanov V, Kaplunenko D, Tishchenko P, Kim KR. 2018. Re-initiation of bottom water formation in the East Sea (Japan Sea) in a warming world. Sci Rep. 8:1576. DOI:10.1038/s41598-018-19952-4.

Section 2.5: Spatio-temporal variability of the Black Sea Cold Intermediate Layer properties derived from in situ data

Akpinar A, Fach BA, Oguz T. 2017. Observing the subsurface thermal signature of the Black Sea cold intermediate layer with Argo profiling floats. Deep Sea Res Part I. 124:140–152.

Barnett TP, Pierce DW, Schnur R. 2001. Detection of anthropogenic climate change in the world's oceans. Science. 292:270–274. DOI:10.1126/science.1058304.

Belokopytov V. 2011. Interannual variations of the renewal of waters of the cold intermediate layer in the Black Sea for the last decades. Phys Oceanogr. 20(5):347–355.

Capet A, Barth A, Beckers J-M, Grégoire M. 2012. Interannual variability of Black Sea's hydrodynamics and connection to atmospheric patterns. Deep Sea Res Part II. 77–80:128–142.

Capet A, Stanev EV, Beckers J-M, Murray JW, Grégoire M. 2016. Decline of the Black Sea oxygen inventory. Biogeosciences. 13:1287–1297.

Capet A, Troupin C, Carstensen J, Grégoire M, Beckers J-M. 2014. Untangling spatial and temporal trends in the variability of the Black Sea cold intermediate layer and mixed layer depth using the DIVA detrending procedure. Ocean Dyn. 64(3):315–324.

Capet A, Vandenbulcke L, Grégoire M, Marinova V. 2018. Decline of the Black Sea oxygen inventory. In: copernicus marine Service ocean state report, Issue 2. J Operat Oceanogra. 11(Sup1):103–106.

Ginzburg AI, Zatsepin AG, Kremenetskii VV, Piotukh VB. 2008. Mesoscale dynamics of the Black Sea waters. Oceanology at the start of the 21st century, Nauka, Moscow, p. 11–42.

Ivanov LI, Backhaus JO, Özsoy E, Wehde H. 2001. Convection in the Black Sea during cold winters. J Mar Syst. 31:65–76.

Ivanov LI, Besiktepe ST, Özsoy E. 1997. The Black Sea cold intermediate layer. In: Sensitivity to change: Black Sea, Baltic Sea and North Sea. Kluwer Academic Publisher; p. 253–264.

Ivanov VA, Belokopytov VN. 2013. Oceanography of the Black Sea. In L Tuchkovenko Yu S, Loieva ID, editors. National Academy of Sciences of Ukraine, Marine Hydrophysical Institute, ECOSY-Gidrofizika, Sevastopol; p. 210.

Korotaev G, Oguz T, Riser S. 2006. Intermediate and deep currents of the Black Sea obtained from autonomous profiling floats. Deep Sea Res Part II. 53(17):1901–1910.

Kubryakov A, Plotnikov E, Stanichny S. 2018. Reconstructing large-and mesoscale dynamics in the Black Sea region from satellite imagery and altimetry data – a comparison of two methods. Remote Sens. 10(2):239.

Kubryakov AA, Stanichny SV. 2015. Seasonal and interannual variability of the Black Sea eddies and its dependence on

characteristics of the large-scale circulation. Deep Sea Res Part I. 97:80–91.

Miladinova S, Stips A, Garcia-Gorriz E, Macias Moy D. 2018. Formation and changes of the Black Sea cold intermediate layer. Prog Oceanogr. 167:11–23.

Miladinova-Marinova S, Stips A, Garcia-Gorriz E, Macias Moy D. 2016. Black Sea ecosystem model: setup and validation. JRC Science Hub, 42.

Oguz T, Besiktepe S. 1999. Observations on the rim current structure, CIW formation and transport in the western Black Sea. Deep Sea Res Part I. 46(10):1733–1753.

Oguz T, Cokacar T, Malanotte-Rizzoli P, Ducklow HW. 2003. Climatic warming and accompanying changes in the ecological regime of the Black Sea during the 1990s. Global Biogeochem Cycles. 17:1088.

Oguz T, Dippner JW, Kaymaz Z. 2006. Climatic regulation of the Black Sea hydro-meteorological and ecological properties at interannual to decadal time scales. J Mar Syst. 60:235–254.

Özsoy E, Ünlüata Ü. 1997. Oceanography of the Black Sea: a review of some recent results. Earth Sci Rev. 42(4):231–272.

Piotukh VB, Zatsepin AG, Kazmin AS, Yakubenko VG. 2011. Impact of the winter cooling on the variability of the thermohaline characteristics of the active layer in the Black Sea. Oceanology. 51:221–230.

Shapiro GI, Aleynik DL, Mee LD. 2010. Long term trends in the sea surface temperature of the Black Sea. Ocean Sci. 6:491–501.

Stanev EV, Bowman MJ, Peneva EL, Staneva JV. 2003a. Control of Black Sea intermediate water mass formation by dynamics and topography: comparison of numerical simulations, surveys and satellite data. J Mar Res. 61(1):59–99.

Stanev EV, He Y, Grayek S, Boetius A. 2013. Oxygen dynamics in the Black Sea as seen by Argo profiling floats. Geophys Res Lett. 40(12):3085–3090.

Stanev EV, He Y, Staneva J, Yakushev E. 2014. Mixing in the Black Sea detected from the temporal and spatial variability of oxygen and sulfide – Argo float observations and numerical modelling. Biogeosciences. 11(20):5707–5732.

Stanev EV, Peneva E, Chtirkova B. 2019a. Climate change and regional ocean water mass disappearance: case of the Black Sea. J Geophys Res C Oceans. 124(7):4803–4819.

Staneva JV, Dietrich DE, Stanev EV, Bowman MJ. 2001. Rim current and coastal eddy mechanisms in an eddy-resolving Black Sea general circulation model. J Marine Syst. 31(1–3):137–157.

Staneva JV, Stanev EV. 1997. Cold intermediate water formation in the Black Sea. Analysis on numerical model simulations. In: Ozsoy E, Mikaelyan A, editor. Sensitivity to change: Black Sea, Baltic Sea and North Sea. NATO ASI series (ASEN2, Vol. 27). Kluwer Academic Publishers; p. 375–393.

UNESCO (Fofonoff, P, Millard, RC). 1983. Algorithms for computation of fundamental properties of seawater. UNESCO Tech. Pap. in Mar. Sci., No. 44, 53 pp. (https://unesdoc.unesco.org/ark:/48223/pf0000059832).

Zatsepin AG, Ginzburg AI, Kostianoy AG. 2003. Observation of Black Sea mesoscale eddies and associated horizontal mixing. J Geophys Res. 108(C83246):1–27.

Section 2.6: Ocean heat content in the Black Sea

Blatov AS, Bulgakov NP, Ivanov VA. 1984. Variability of hydrophysical fields in the Black Sea. Leningrad: Gidrometeoizdat. Russian.

Capet A, Troupin C, Carstensen J, Grégoire M, Beckers J-M. 2014. Untangling spatial and temporal trends in the variability of the Black Sea cold intermediate layer and mixed layer depth using the DIVA detrending procedure. Ocean Dynam. 64:315–324. DOI:10.1007/s10236-013-0683-4.

Carton JA, Chepurin GA, Chen L. 2018. SODA3: a new ocean climate reanalysis. J Climate. 31:6967–6983. DOI:10.1175/JCLI-D-18-0149.1.

Dee DP, Uppala SM, Simmons AJ, Berrisford P, Poli P, Kobayashi S, Andrae U, Balmaseda MA, Balsamo G, Bauer P. 2011. The ERA-interim reanalysis: configuration and performance of the data assimilation system. Q J Roy Meteor Soc. 137(656):553–597. DOI:10.1002/qj.828.

Degtyarev AK. 2000. Estimation of temperature increase of the Black Sea active layer during the period 1985–1997. Meteorilogiya i Gidrologiya. 6:72–76. Russian.

Dobricic S, Pinardi N. 2008. An oceanographic three-dimensional variational data assimilation scheme. Ocean Model. 22(3–4):89–105. DOI:10.1016/j.ocemod.2008.01.004.

Finenko ZZ, Suslin VV, Kovaleva IV. 2014. Seasonal and long-term dynamics of the chlorophyll concentration in the Black Sea according to satellite observations. Oceanology. 54(5):596–605. DOI:10.1134/S0001437014050063.

Ginzburg AI, Kostianoy AG, Sheremet NA. 2004. Seasonal and interannual variability of the Black Sea surface temperature as revealed from satellite data (1982–2000). J Marine Syst. 52(1–4):33–50. DOI:10.1016/j.jmarsys.2004.05.002.

Good SA, Martin MJ, Rayner NA. 2013. EN4: quality controlled ocean temperature and salinity profiles and monthly objective analyses with uncertainty estimates. J Geophys Res-Oceans. 118(12):6704–6716. DOI:10.1002/2013JC009067.

Ivanov VA, Belokopytov VN. 2013. Oceanography of the Black Sea. Sevastopol: Marine Hydrophysical Institute of National Academy of Science of Ukraine.

Kara AB, Barron CN, Wallcraft AJ, Oguz T. 2008. Interannual variability of Sea surface height over the Black Sea: relation to climatic patterns. Earth Interact. 23:1–12. DOI:10.1175/2008EI259.1.

Kara AB, Helber RW, Boyer TP, Elsner JB. 2009. Mixed layer depth in the Aegean, Marmara, Black and Azov seas: part I: general features. J Marine Syst. 78:S169–S180. DOI:10.1016/j.jmarsys.2009.01.022.

Kara AB, Wallcraft AJ, Hurlburt HE. 2005. How does solar attenuation depth affect the ocean mixed layer? water Turbidity and atmospheric forcing impacts on the simulation of Seasonal mixed layer variability in the Turbid Black Sea. J Climate. 18:389–409. DOI:10.1175/JCLI-3159.1.

Knysh VV, Korotaev GK, Moiseenko VA, Kubryakov AI, Belokopytov VN, Inyushina NV. 2011. Seasonal and inter-annual variability of Black Sea hydrophysical fields reconstructed from 1971–1993 reanalysis data. IZV Atmos Ocean Phy. 47:399–411. DOI:10.1134/S000143381103008X.

Korotaev G, Oguz T, Nikiforov A, Koblinsky C. 2003. Seasonal, interannual, and mesoscale variability of the Black Sea upper layer circulation derived from altimeter data. J Geophys Res Oceans. 108(C4,3122):19-1–19-15. DOI:10.1029/2002JC001508.

Kubryakov AA, Bagaev AV, Stanichny SV, Belokopytov VN. 2018. Thermohaline structure, transport and evolution of the Black Sea eddies from hydrological and satellite data. Prog Oceanogr. 167:44–63. DOI:10.1016/j.pocean.2018.07.007.

Kubryakov AA, Stanichny SV, Volkov DL. 2017. Quantifying the impact of basin dynamics on the regional sea level rise in the Black Sea. Ocean Sci. 13(3):443–452. DOI:10.5194/os-13-443-2017.

Matsoukas C, Banks AC, Pavlakis KG, Hatzianastassiou N, Stackhouse PW, Vardavas I. 2007. Seasonal heat budgets of the Red and Black Seas. J Geophys Res Oceans. 112(C10). DOI:10.1029/2006JC003849.

Miladinova S, Stips A, Garcia-Gorriz E, Macias Moy D. 2017. Black Sea thermohaline properties: long-term trends and variations. J Geophys Res Oceans. 122(7):5624–5644. DOI:10.1002/2016JC012644.

Miladinova S, Stips A, Garcia-Gorriz E, Macias Moy D. 2018. Formation and changes of the Black Sea cold intermediate layer. Progress Oceanogr. 167:11–23. DOI:10.1016/j.pocean.2018.07.002.

Mulet S, Nardelli BB, Good S, Pisano A, Greiner E, Monier M, Autret E, Axell L, Boberg F, Ciliberti S. 2018. Ocean temperature and salinity. In: Copernicus marine service ocean state report, issue 2. J Operat Oceanogr. 11(Sup1):s11–ss4. DOI:10.1080/1755876X.2018.1489208.

Oguz T, Aubrey DG, Latun VS, Demirov E, Koveshnikov L, Sur HI, Diaconu V, Besiktepe S, Duman M, Limeburner R, Eremeev V. 1994. Mesoscale circulation and thermohaline structure of the Black Sea observed during HydroBlack'91. Deep Sea Res Pt I. 41(4):603–628. DOI:10.1016/0967-0637(94)90045-0.

Palazov A, Ciliberti S, Peneva E, Gregoire M, Staneva J, Lemieux-Dudon B, Masina S, Pinardi N, Vandenbulcke L, Behrens A. 2019. Black Sea observing system. Front Mar Sci. 6:315. DOI:10.3389/fmars.2019.00315.

Peneva E, Stanev E, Belokopytov V, Le Traon P-Y. 2001. Water transport in the Bosphorus straits estimated from hydro-meteorological and altimeter data: seasonal to decadal variability. J Marine Syst. 31(1–3):21–33. DOI:10.1016/S0924-7963(01)00044-6.

Pham DT, Verron J, Roubaud MC. 1998. A singular evolutive extended Kalman filter for data assimilation in oceanography. J Marine Syst. 16(3–4):323–340. DOI:10.1016/S0924-7963(97)00109-7.

Romanou A, Tselioudis G, Zerefos CS, Clayson C-A, Curry JA, Andersson A. 2010. Evaporation–precipitation variability over the Mediterranean and the Black Seas from satellite and reanalysis estimates. J Climate. 23:5268–5287. DOI:10.1175/2010JCLI3525.1.

Schrum C, Staneva J, Stanev E, Özsoy E. 2001. Air–sea exchange in the Black Sea estimated from atmospheric analysis for the period 1979–1993. J Marine Syst. 31(1–3):3–19. DOI:10.1016/S0924-7963(01)00043-4.

Shapiro GI, Aleynik DL, Mee LD. 2010. Long term trends in the sea surface temperature of the Black Sea. Ocean Sci. 6(2):491–501. DOI:10.5194/os-6-491-2010.

Shapiro GI, Wobus F, Aleynik DL. 2011. Seasonal and inter-annual temperature variability in the bottom waters over

the western Black Sea shelf. Ocean Sci. 7(5):585–596. DOI:10.5194/os-7-585-2011.

Simonov AI, Altman EN, editors. 1991. Hydrometeorology and hydrochemistry of the USSR seas. Project "Seas of the USSR".vol. IV. The Black Sea, 1, hydrometeorological conditions. Gidrometeoizdat, St.-Petersburg. 429 pp. Russian.

Stanev EV, Bowman MJ, Peneva EL, Staneva JV. 2003. Control of Black Sea intermediate water mass formation by dynamics and topography: comparison of numerical simulations, surveys and satellite data. J Mar Res. 61:59–99. DOI:10.1357/002224003321586417.

Stanev EV, Peneva E, Chtirkova B. 2019. Climate change and regional ocean water mass disappearance: case of the Black Sea. J Geophys Res Oceans. 124(7):4803–4819. DOI:10.1029/2019JC015076.

Stanev EV, Simeonov JA, Peneva EL. 2001. Ventilation of Black Sea pycnocline by the Mediterranean plume. J Marine Syst. 31(1–3):77–97. DOI:10.1016/S0924-7963(01)00048-3.

Storto A, Masina S, Dobricic S. 2014. Estimation and impact of non-uniform horizontal correlation length-scales for global ocean physical analyses. J Atmos Ocean Tech. 31:2330–2349. DOI:10.1175/JTECH-D-14-00042.1.

Tanguy S, Jerome G, Sylvie P, Gilles R, Frederic M. 2019. CORA, Coriolis ocean dataset for reanalysis. SEANOE. DOI:10.17882/46219.

Titov VB. 2004. Formation of the upper convective layer and the cold intermediate layer in the Black Sea in relation to the winter severity. Oceanology. 44:327–330.

Tuzhilkin VS. 2007. Thermohaline structure of the Sea. In: Kostianoy AG, Kosarev AN, editors. The Black Sea environment. The handbook of environmental chemistry, Vol. 5Q. Berlin: Springer; p. 217–253.

Vostokov SV, Lobkovskiy LI, Vostokova AS, Solov'ev DM. 2019. Seasonal and interannual variability of phytoplankton in the Black Sea on the basis of remote sensing data and In situ measurements of chlorophyll-A. Dokl Earth Sci. 485:293–297. DOI:10.1134/S1028334X19030097.

Section 2.7: Monitoring of wave sea state in the Iberia-Biscay-Ireland regional seas

Bacon S, Carter DJT. 1991. Wave climate changes in the north Atlantic and North Sea. Int J Climatol. 11:545–558.

Bacon S, Carter DJT. 1993. A connection between mean wave height and atmospheric pressure gradient in the North Atlantic. Int J Climatol. 13:423–436.

Bauer E. 2001. Interannual changes of the ocean wave variability in the North Atlantic and in the North Sea. Clim Res. 18:63–69.

BBC. 2014. UK storms: extreme weather caused 'years of erosion'. BBC News Magazine. [accessed 2019 November]. http://www.bbc.com/news/uk-26277373.

Bernardara P, Mazas F, Kergadallan X, Hamm L. 2014. A two-step framework for over-threshold modelling of environmental extremes. Nat Hazards Earth Syst Sci. 14:635–647.

Bouws E, Jannink D, Komen GJ. 1996. The increasing wave height in the North Atlantic Ocean. Bull Am Met Soc. 77:2275–2277.

Dodet G, Bertin X, Taborda R. 2010. Wave climate variability in the North-East Atlantic Ocean over the last six decades. Ocean Modell. 31:120–131.

Dupuis H, Michel D, Sottolichio A. 2006. Wave climate evolution in the Bay of Biscay over two decades. J Mar Sys. 63:105–114.

Eastoe E, Koukoulas S, Jonathan P. 2013. Statistical measures of extremal dependence illustrated using measured sea surface elevations from a neighbourhood of coastal locations. Ocean Eng. 62:68–77.

Folley M. 2017. The wave energy resource. In: Pecher A, Kofoed JP, editors. Handbook of ocean wave energy, ocean engineering & oceanography 7. DOI:10.1007/978-3-319-39889-1_3.

Gleeson E, Gallagher S, Clancy C, Dias F. 2017. NAO and extreme ocean states in the northeast Atlantic Ocean. Adv Sci Res. 14:23–33. DOI:10.5194/asr-14-23-2017.

González-Marco D, Sierra JP, Ybarra OF, Sánchez-Arcilla A. 2008. Implications of long waves in harbor management: the Gijón port case study. Ocean Coast Manag. 51:180–201. DOI:10.1016/j.ocecoaman.2007.04.001.

Hewit JE, Cummings VJ, Elis JI, Funnell G, Norkko A, Talley TS, Thrush SF. 2003. The role of waves in the colonisation of terrestrial sediments deposited in the marine environment. J Exp Mar Biol Ecol. 290:19–47. DOI:10.1016/S0022-0981(03)00051-0.

Hurrell JW. 1995. Decadal trends in the North Atlantic oscillation: regional temperatures and precipitation. Science. 269:676–679.

Izaguirre C, Méndez FJ, Menéndez M, Losada IJ. 2011. Global extreme wave height variability based on satellite data Cristina. Geoph Res Lett. 38:L10607. DOI:10.1029/2011GL047302.

Kushnir Y, Cardone VJ, Greenwood JG, Cane MA. 1997. The recent increase in North Atlantic wave heights. J Clim. 10:2107–2113.

Lin-Ye J, Garcia-Leon M, Gracia V, Sanchez-Arcilla A. 2016. A multivariate statistical model of extreme events: an application to the Catalan coast. Coastal Eng. 117:138–156.

Martínez-Asensio A, Tsimplis MN, Marcos M, Feng F, Gomis D, Jordàa G, Josey SA. 2016. Response of the North Atlantic wave climate to atmospheric modes of variability. Int J Climatol. 36:1210–1225. DOI:10.1002/joc.4415.

Mei CC, Liu PL-F. 1993. Surface waves and coastal dynamics. Annu Rev Fluid Mech. 25:215–240.

Mørk G, Barstow S, Kabush A, Pontes MT. 2010. Assessing the global wave energy potential. Proceedings of OMAE2010 29th International Conference on Ocean, Offshore Mechanics and Arctic Engineering June 6–11, 2010, Shanghai.

Onoz B, Bayazit M. 2001. Effect of the occurrence process of the peaks over threshold on the flood estimates. J Hydrol. 244:86–96.

Pérez-Gómez B, Manzano F, Álvaroez-Fanjul E, González C, Cantavella JV, Schindelé F. 2016. Lessons derived from two high-frequency sea level events in the Atlantic: implications for coastal risk analysis and tsunami detection. Front Marine Sci. 3:206. DOI:10.3389/fmars.2016.00206.

Savina H, Lefevre J-M, Josse P, Dandin P. 2003. Definition of warning criteria. Proceedings of MAXWAVE Final Meeting, October 8–11, Geneva.

Tsimplis MN, Woolf DK, Osborn TJ, Wakelin S, Wolf J, Flather R, Shaw AGP, Woodworth P, Challenor P, Blackman D, et al. 2005. Towards a vulnerability assessment of the UK and northern European coasts: the role of regional climate variability. Phil Trans R Soc A. 363:1329–1358. DOI:10.1098/rsta.2005.1571.

Wang X, Swail V. 2004. Historical and possible future changes of wave heights in northern hemisphere oceans. In: Perrie W, editor. Atmosphere ocean interactions, Vol. 2, No. 2. Ashurst: Wessex Institute of Technology Press; p. 240.

WASA-Group. 1998. Changing waves and storms in the northeast Atlantic? Bull Am Meteorol Soc. 79:741–760.

Wolf J, Woolf DK. 2006. Waves and climate change in the north-east Atlantic. Geophys Res Lett. 33:L06604. DOI:10.1029/2005GL025113.

Woolf DK, Challenor PG, Cotton PD. 2002. Variability and predictability of the North Atlantic wave climate. J Geophys Res. 107(C10):3145. DOI:10.1029/2001JC001124.

Young IR, Ribal A. 2019. Multiplatform evaluation of global trends in wind speed and wave height. Science. 364:548–552. DOI:10.1126/science.aav9527.

Young IR, Zieger S, Babanin AV. 2011. Global trends in wind speed and wave height. Science. 332(6028):451–455. DOI:10.1126/science.1197219.

Section 2.8: A Lagrangian approach to monitor local particle retention conditions in coastal areas

André G, Garreau P, Vernier V, Fraunié P. 2005. Modelled variability of the sea surface circulation in the North-western Mediterranean Sea and in the Gulf of Lions. Ocean Dyn. 55:294–308. DOI:10.1007/s10236-005-0013-6.

Braunschweig F, Martins F, Chambel P, Neves R. 2003. A methodology to estimate renewal time scales in estuaries: the Tagus Estuary case. Ocean Dyn. 53:137–145. DOI:10.1007/s10236-003-0040-0.

Coulliette C, Lekien F, Paduan JD, Haller G, Marsden JE. 2007. Optimal pollution Mitigation in Monterey Bay based on coastal radar data and Nonlinear dynamics. Environ Sci Technol. 41(18):6562–6572. DOI:10.1021/es0630691.

Declerck A, Delpey M, Rubio A, Ferrer L, Basurko OC, Mader J, Louzao M. 2019. Transport of floating marine litter in the coastal area of the south-eastern Bay of Biscay: a Lagrangian approach using modelling and observations. J Oper Oceanogr. DOI:10.1080/1755876X.2019.1611708.

Font J, Salat J, Tintoré J. 1988. Permanent features of the circulation in the Catalan Sea. Oceanol Acta. 9:51–57.

Garcı´a-Lafuente J, López-Jurado J, Cano-Lucaya N, Vargas-Yanez M, Aguiar-Garcı´a J. 1995. Circulation of water masses through the Ibiza Channel. Oceanol Acta. 18 (2):245–254.

Hernández-Carrasco I, López C, Orfila A, Hernández-García E. 2013. Lagrangian transport in a microtidal coastal area: the Bay of Palma, island of Mallorca, Spain. Nonlin Processes Geophys. 20:921–933. DOI:10.5194/npg-20-921-2013.

Hernández-Carrasco I, Solabarrieta L, Rubio A, Esnaola G, Reyes E, Orfila A. 2018. Impact of HF radar current gap-filling methodologies on the Lagrangian assessment of coastal dynamics. Ocean Sci. 14:827–847. DOI:10.5194/os-14-827-2018.

Heslop E, Ruiz S, Allen J, López-Jurado JL, Renault L, Tintoré J. 2012. Autonomous underwater gliders monitoring variability at choke points in our ocean system: a case study in the western Mediterranean Sea. Geophys Res Lett. 39: L20604. DOI:10.1029/2012GL053717.

Kaplan DM, Lekien F. 2007. Spatial interpolation and filtering of surface current data based on open-boundary modal analysis. J Geophys Res Oceans. 112:C12007. DOI:10.1029/2006JC003984.

Lai Y, Tel T. 2011. Transient chaos complex dynamics on finite-time scales. Applied mathematical sciences. Vol. 173. Cham: Springer; p. 1–858.

Lana A, Marmain J, Fernández V, Tintoré J, Orfila A. 2016. Wind influence on surface current variability in the Ibiza Channel from HF radar. Ocean Dyn. 66(4):483–497. DOI:10.1007/s10236-016-0929-z.

Olascoaga MJ. 2010. Isolation on the West Florida shelf with implications for red tides and pollutant dispersal in the Gulf of Mexico. Nonlinear Process Geophys. 17:685–696.

Roarty H, Cook T, Hazard L, George D, Harlan J, Cosoli S, Wyatt L, Alvarez Fanjul E, Terrill E, Otero M, et al. 2019. The global high frequency radar network. Front Mar Sci. 6:164. DOI:10.3389/fmars.2019.00164.

Rubio A, Caballero A, Orfila A, Hernandez-Carrasco I, Ferrer L, Gonzalez M, Solabarrieta L, Mader J. 2018. Eddy-induced cross-shelf export of high Chl-a coastal waters in the SE Bay of Biscay. Remote Sens Environ. 205. DOI:10.1016/j.rse.2017.10.037.

Rubio A, Mader J, Corgnati L, Mantovani C, Griffa A, Novellino A, Quentin C, Wyatt L, Schulz-Stellenfleth J, Horstmann J, et al. 2017. HF radar activity in European coastal seas: Next steps toward a Pan-European HF radar network. Front Mar Sci. 4(8). DOI:10.3389/fmars.2017.00008.

Sayol JM, Orfila A, Simarro G, López C, Renault L, Galán A, Conti D. 2013. Sea surface transport in the western Mediterranean Sea: a Lagrangian perspective. J Geophys Res Ocean. 118:6371–6384. DOI:10.1002/2013JC009243.

Sciascia R, Berta M, Carlson DF, Griffa A, Panfili M, La Mesa M, Corgnati L, Mantovani C, Domenella E, Fredj E, et al. 2018. Linking sardine recruitment in coastal areas to ocean currents using surface drifters and HF radar: a case study in the Gulf of Manfredonia. Adriatic Sea Ocean Sci. 14:1461–1482. DOI:10.5194/os-14-1461-2018.

Solabarrieta L, Frolov S, Cook M, Paduan J, Rubio A, Gonzalez M, Mader J, Charria G. 2016. Skill assessment of HF radar derived products for Lagrangian simulations in the Bay of Biscay. J Atmos Ocean Technol. 33:2585–2597. DOI:10.1175/JTECH-D-16-0045.1.

Sotillo MG, Cailleau S, Lorente P, Levier B, Aznar R, Reffray G, Amo-Baladrón A, Chanut J, Benkiran M, Alvarez-Fanjul E. 2015. The MyOcean IBI ocean forecast and reanalysis systems: operational products and roadmap to the future Copernicus service. J Operat Oceanogr. DOI:10.1080/1755876X.2015.1014663.

Section 2.9: Global sea surface temperature anomalies in 2018 and historical changes since 1993

Berry DI, Corlett GK, Embury O, Merchant CJ. 2018. Stability assessment of the (A)ATSR Sea surface temperature climate

dataset from the European Space Agency Climate Change Initiative. Remote Sens. 10:126. DOI:10.3390/rs10010126.

Caesar L, Rahmstorf S, Robinson A, Feulner G, Saba V. 2018. Observed fingerprint of a weakening Atlantic Ocean overturning circulation. Nature. 556:191. DOI: 10.1038/s41586-018-0006-5.

Deser C, Trenberth K, National Center for Atmospheric Research Staff, editors. 2016. The climate data guide: Pacific Decadal Oscillation (PDO): definition and indices. https://climatedataguide.ucar.edu/climate-data/pacific-decadal-oscillation-pdo-definition-and-indices.

Hausfather Z, Cowtan K, Clarke DC, Jacobs P, Richardson M, Rohde R. 2017. Assessing recent warming using instrumentally homogeneous sea surface temperature records. Sci Adv. 3(1):e1601207. DOI:10.1126/sciadv.1601207.

Huang B, Kennedy J, Xue Y, Zhang H-M. 2019. Sea surface temperatures [in "State of the Climate in 2018"]. Bull Amer Meteor Soc. 100(9):S70–S72. DOI:10.1175/2019BAMSStateoftheClimate.1.

IPCC. 2013. Climate change 2013: The Physical Science Basis. Contribution of working group I to the Fifth Assessment Report of the Intergovernmental Panel on Climate Change. [Stocker, T.F., D. Qin, G.-K. Plattner, M. Tignor, S.K. Allen, J. Boschung, A. Nauels, Y. Xia, V. Bex and P.M. Midgley (eds.)]. Cambridge University Press, Cambridge, United Kingdom and New York, NY, USA, 1535 pp.

Kim H. 2018. River discharge and run off [in "State of the Climate in 2017"]. Bull Amer Meteor Soc. 99(8):S33–S34. DOI:10.1175/2018BAMSStateoftheClimate.1.

Merchant CJ, Embury O, Bulgin CE, Block T, Corlett GK, Fiedler E, Good SA, Mittaz J, Rayner NA, Berry D, Eastwood S, Michael Taylor, Yoko Tsushima, Alison Waterfall, Ruth Wilson & Craig Donlon. 2019. Satellite-based time-series of sea-surface temperature since 1981 for climate applications. Sci Data. 6:223. DOI:10.1038/s41597-019-0236-x.

Mulet S, Buongiorno Nardelli B, Good S, Pisano A, Greiner E, Monier M. 2016. Ocean temperature and salinity. In: von Schuckmann et al. 2018, the Copernicus Marine Service Ocean State Report. J Operat Ocean. 11(Sup1):S1–S142. DOI:10.1080/1755876X.2018.1489208.

Oliver EC, Benthuysen JA, Bindoff NL, Hobday AJ, Holbrook NJ, Mundy CN, Perkins-Kirkpatrick SE. 2017. The unprecedented 2015/16 Tasman Sea marine heatwave. Nat Commun. 8:16101. DOI:10.1038/ncomms16101.

Perkins-Kirkpatrick SE, King AD, Cougnon EA, Holbrook NJ, Grose MR, Oliver ECJ, Lewis SC, Pourasghar F. 2019. The role of natural variability and anthropogenic climate change in the 2017/18 Tasman Sea marine heatwave. Bull Am Meteorol Soc. 100(1):S105–S110. DOI:10.1175/BAMS-D-18-0116.1.

Pezzulli S, Stephenson DB, Hannachi A. 2005. The variability of seasonality. J Clim. 18:71–88. DOI:10.1175/JCLI-3256.1.

Saji NH, Goswami BN, Vinayachandran PN, Yamagata T. 1999. A dipole mode in the tropical Indian Ocean. Nature. 401:360. DOI:10.1038/43854.

Sen PK. 1968. Estimates of the regression coefficient based on Kendall's tau. J Am Statist Assoc. 63:1379–1389. DOI:10.1080/01621459.1968.10480934.

Sévellec F, Fedorov AV, Liu W. 2017. Arctic sea-ice decline weakens the Atlantic meridional overturning circulation. Nat Clim Change. 7:604. DOI:10.1038/nclimate3353.

Trenberth K, National Center for Atmospheric Research Staff, editors. 2019. The climate data guide: Nino SST indices (Nino 1 + 2, 3, 3.4, 4; ONI and TNI). https://climatedataguide.ucar.edu/climate-data/nino-sst-indices-nino-12-3-34-4-oni-and-tni.

Ummenhofer CC, England MH, McIntosh PC, Meyers GA, Pook MJ, Risbey JS, Gupta AS, Taschetto AS. 2009. What causes southeast Australia's worst droughts? Geophys Res Lett. 36:L04706. DOI:10.1029/2008GL036801.

Visbeck MH, Hurrell JW, Polvani L, Cullen HM. 2001. The North Atlantic Oscillation: past, present, and future. Proc Natl Acad Sci USA. 98(23):12876–12877. DOI:10.1073/pnas.231391598.

Section 2.10: Ocean acidification

Bakker DCE, Pfeil B, Landa CS, Metzl N, O'Brien KM, Olsen A, Smith K, Cosca C, Harasawa S, Jones SD, et al. 2016. A multi-decade record of high-quality CO_2 data in version 3 of the surface ocean CO_2 Atlas (SOCAT). Earth Syst Sci Data. 8:383–413. DOI:10.5194/essd-8-383-2016.

Bates NR, Astor Y, Church M, Currie K, Dore J, González-Dávila M, Lorenzoni L, Muller-Karger F, Olafsson J, Santana-Casiano JM. 2014. A time-series view of changing ocean chemistry due to ocean uptake of anthropogenic CO_2 and ocean acidification. Oceanography. 27(1):126–141. DOI:10.5670/oceanog.2014.16.

Bopp L, Resplandy L, Orr JC, Doney SC, Dunne JP, Gehlen M, Halloran P, Heinze C, Ilyina T, Séférian R, et al. 2013. Multiple stressors of ocean ecosystems in the 21st century: projections with CMIP5 models. Biogeosciences. 10:6225–6245. DOI:10.5194/bg-10-6225-2013.

Carter BR, Williams NL, Gray AR, Feely, RA. 2016. Locally interpolated alkalinity regression for global alkalinity estimation. Limnol Oceanogr Methods. 14:268–277. DOI:10.1002/lom3.10087.

Carter, BR, Feely RA, Williams NL, Dickson AG, Fong MB, Takeshita Y. 2018. Updated methods for global locally interpolated estimation of alkalinity, pH, and nitrate. Limnol Oceanogr Methods. 16(2):119–131.

Chatterjee A, Gierach MM, Sutton AJ, Feely RA, Crisp D, Eldering A, Gunson MR, O'Dell CW, Stephens BB, Schimel DS. 2017. Influence of El Niño on atmospheric CO_2 over the tropical Pacific Ocean: findings from NASA's OCO-2 mission. Science. 358:eaam5776. DOI:10.1126/science.aam5776.

Ciais P, Sabine C, Bala G, Bopp L, Brovkin V, Canadell J, Chhabra A, DeFries R, Galloway J, Heimann M, et al. 2013. Carbon and other biogeochemical cycles. In: TF Stocker, D Qin, G-K Plattner, M Tignor, SK Allen, J Boschung, A Nauels, Y Xia, V Bex, PM Midgley, editors. Climate change 2013: the physical science basis. Contribution of working group I to the fifth assessment report of the Intergovernmental panel on climate change. Cambridge: Cambridge University Press.

Denvil-Sommer A, Gehlen M, Vrac M, Mejia C. 2019. LSCE-FFNN-v1: a two-step neural network model for the reconstruction of surface ocean pCO2 over the global ocean. Geosci Model Develop. 12(5):2091–2105.

Feely RA, Wanninkhof R, Takahashi T, Tans P. 1999. Influence of El Nina on the equatorial Pacific contribution to atmospheric CO_2 accumulation. Nature. 398:597–601.

Gattuso J-P, Magnan A, Billé R, Cheung WWL, Howes EL, Joos F, Allemand D, Bopp L, Cooley SR, Eakin CM, et al. 2015. Contrasting futures for ocean and society from different anthropogenic CO_2 emissions scenarios. Science. 349: aac4722. DOI:10.1126/science.aac4722.

Hilmi N, Allemand D, Dupont S, Safa A, Haraldsson G, Nunes PALD, Moore C, Hattam C, Reynaud S, Hall-Spencer JM, et al. 2013. Towards improved socio-economic assessments of ocean acidification's impacts. Mar Biol. 160:1773–1787. DOI:10.1007/s00227-012-2031-5.

Jacobson AR, Fletcher SEM, Gruber N, Sarmiento JL, Gloor M. 2007. A joint atmosphere-ocean inversion for surface fluxes of carbon dioxide: 1. Methods and global-scale fluxes. Glob Biogeochem Cycles. 21. DOI:10.1029/2005GB002556.

Le Quéré C, Andrew RM, Friedlingstein P, Sitch S, Pongratz J, Manning AC, Korsbakken JI, Peters GP, Canadell JG, Jackson RB, et al. 2018. Global carbon budget 2017. Earth Syst Sci Data. 10:405–448. DOI:10.5194/essd-10-405-2018.

Lewis E, Wallace DWR. 1998. Program developed for CO_2 system calculations, ORNL/CDIAC-105. Oak Ridge, TN: Carbon Dioxide Information Analysis Center, Oak Ridge National Laboratory. 38 pp. https://salish-sea.pnnl.gov/media/ORNL-CDIAC-105.pdf.

Orr JC, Epitalon J-M, Dickson AG, Gattuso J-P. 2018. Routine uncertainty propagation for the marine carbon dioxide system. Mar Chem. DOI:10.1016/j.marchem.2018.10.006.

Santoso A, Mcphaden MJ, Cai W. 2017. The defining characteristics of ENSO extremes and the strong 2015/2016 El Niño. Rev Geophys. 55:1079–1129. DOI:10.1002/2017RG000560.

Seibel BA, Walsh PJ. 2001. Potential impacts of CO_2 injection on deep-sea biota. Science. 294(5541):319–320.

Takahashi T, Sutherland SC, Wanninkhof R, Sweeney C, Feely RA, Chipman DW, Hales B, Friederich G, Chavez F, Sabine C, et al. 2009. Climatological mean and decadal change in surface ocean pCO_2, and net sea–air CO_2 flux over the global oceans. Deep Sea Res Part II. 56:554–577. DOI:10.1016/j.dsr2.2008.12.009.

van Heuven S, Pierrot D, Rae JWB, Lewis E, Wallace DWR. 2011. MATLAB program developed for CO_2 system calculations. ORNL/CDIAC-105b. Oak Ridge, TN: Carbon Dioxide Information Analysis Center, Oak Ridge National Laboratory, U.S. Department of Energy. DOI:10.3334/CDIAC/otg.CO2SYS_MATLAB_v1.1.

CMEMS OSR4, Chapter 3: Case studies

Section 3.1: Evidence of the TOPEX-A altimeter instrumental anomaly and acceleration of the global mean sea level

Authors: J.-F. Legeais, W. Llovel, A. Melet, B. Meyssignac

Statement of main outcome: Global mean sea level rise is a key indicator of the on-going global warming (WMO 2018). Contemporary global mean sea level rise has predominantly been caused by ocean thermal expansion and by land ice mass loss from mountain glaciers and the Antarctic and Greenland ice sheets (WCRP 2018). Knowledge of sea level change is fundamental for policy-makers as it allows to better characterise the social and economic consequences of the sea level rise affecting coastal populations and low-lying areas (e.g. Neumann et al. 2015; Vousdoukas et al. 2018). Global mean sea level has been routinely measured by high-precision satellite altimetry since 1993. The first 6 years of the record (1993–1998) have been affected by an instrumental anomaly on the TOPEX-A altimeter, leading to a drift of the altimeter global mean sea level record which has been estimated with several approaches. The correction of this drift leads to a reduced rate of global mean sea level rise from 3.4 to 3.1 ± 0.4 mm/yr (in a 90% confidence level) over the total altimetry era (1993–present). Correcting for the drift also modifies the global mean sea level time-series over the past 25 years from linear to quadratic, with an acceleration of the associated rise estimated to 0.12 ± 0.073 mm/yr^2 (90% confidence interval). This change of behaviour is of major importance given the socio-economic impact of the sea level rise on coastal populations.

Products used:

Ref. No.	Product name and type	Documentation
3.1.1	SEALEVEL_GLO_PHY_ CLIMATE_L4_REP_ OBSERVATIONS_008_057:: http://marine.copernicus.eu/ services-portfolio/access-to-products/?option=com_ csw&view=details&product_ id=SEALEVEL_GLO_PHY_ CLIMATE_L4_REP_ OBSERVATIONS_008_057, redistributed from the Copernicus Climate Change	CMEMS PUM: http://marine. copernicus.eu/documents/PUM/ CMEMS-SL-PUM-008-056-058.pdf CMEMS QUID: http://marine. copernicus.eu/documents/QUID/ CMEMS-SL-QUID-008-056-058. pdf C3S Product User Guide: http://datastore.copernicus-climate.eu/documents/satellite-sea-level/D3.SL.1-v1.2_PUGS_of_ v1DT2018_SeaLevel_products_

(Continued)

Continued.

Ref. No.	Product name and type	Documentation
	Service (C3S) Climate Data Store: https://cds.climate.copernicus. eu/cdsapp#!/dataset/ satellite-sea-level-global? tab=overview Remote sensing	v2.4.pdf C3S Product Quality Assessment Report: http://datastore.copernicus-climate.eu/c3s/published-forms/ c3sprod/satellite-sea-level-global/D2.SL.2-v1.1_PQAR_of_ v1DT2018_SeaLevel_products_ v2.2.pdf
3.1.2	Time series of global mean sea level based on TOPEX/ Poseidon, Jason-1, Jason-2 and Jason-3 missions, from CNES/AVISO Remote sensing	https://www.aviso.altimetry.fr/en/ data/products/ocean-indicators-products/mean-sea-level.html
3.1.3	Time series of global mean sea level based on TOPEX/ Poseidon, Jason-1, Jason-2 and Jason-3 missions, from ESA SL_cci Remote sensing	https://www.esa-sealevel-cci.org/ products
3.1.4	Time series of global mean sea level based on TOPEX/ Poseidon, Jason-1, Jason-2 and Jason-3 missions, from University of Colorado Remote sensing	http://sealevel.colorado.edu/
3.1.5	Time series of global mean sea level based on TOPEX/ Poseidon, Jason-1, Jason-2 and Jason-3 missions, from CSIRO Remote sensing	http://www.cmar.csiro.au/sealevel/ sl_data_cmar.html
3.1.6	Time series of global mean sea level based on TOPEX/ Poseidon, Jason-1, Jason-2 and Jason-3 missions, from NASA/GSFC Remote sensing	https://sealevel.nasa.gov/
3.1.7	Time series of global mean sea level based on TOPEX/ Poseidon, Jason-1, Jason-2 and Jason-3 missions, from NOAA Remote sensing	https://www.climate.gov/maps-data/dataset/global-mean-sea-level-graph
3.1.8	Glaciers contribution to sea level Model	Marzeion et al. 2012
3.1.9	Greenland ice sheet contribution to sea level Model	IMBIE, Shepherd et al. (2012)
3.1.10	Antarctic ice sheet contribution to sea level Space gravimetry from GRACE	IMBIE, Shepherd et al. (2012)
3.1.11	Terrestrial Water storage contribution to sea level Model	ISBA-CTRIP model (Decharme et al. 2019)
3.1.12	EN4-Gouretski 0–700 m thermosteric sea level In situ	Gouretski and Reseghetti 2010
3.1.13	EN4-Levitus 0–700 m thermosteric sea level In situ	Levitus et al. 2012

(Continued)

Continued.

Ref. No.	Product name and type	Documentation
3.1.14	IAP 0–700 m thermosteric sea level In situ	Cheng et al. 2017
3.1.15	NOAA 700–2000 m thermosteric sea level In situ	NOAA, Levitus et al. 2012
3.1.16	Deep (below 2000 m) thermosteric sea level In situ	Purkey and Johnson 2010

Around 10% of the world's population live in low-elevation coastal zone (defined as the contiguous and hydrologically connected zone of land along the coast and below 10m of elevation, McGranahan et al. 2007) and about 40% of the world's population lives within 100 km of the coast (United Nations 2017). The growth in coastal zone population and urbanisation is projected to continue over the coming years (United Nations Projections 2015). This evolution is accompanied by the development of tourism and industries, the latter being often located close to megacities' harbours (among them Bombay, Shanghai, Miami, Alexandrie or New-York city) (Jouzel 2015).

Increasing human settlement in coastal regions affects local environmental ecosystems and leads to more serious exposure to natural and anthropogenic hazards for people living nearby the sea (Birkmann et al. 2014). Among them, sea level rise is one of the major threats in highly populated coastal regions and in all low-lying coastal areas of the world (Wong et al. 2014). Global mean sea level rise is one of the most direct consequences of the on-going global warming since the rise is caused by both the ocean thermal expansion (93% of the excess of heat of the Earth's system in response to climate change is stored in the oceans) (von Schuckmann et al. 2016) and the mass loss of land ice through melting and ice discharge (Church et al. 2013). Among all the consequences of sea level rise in coastal areas, the following ones directly affect local population: shoreline erosion, submersion, floods and impeded drainage, salinisation of coastal aquifers and surface waters, degradation of ecosystems (Cazenave and Le Cozannet 2014; Hinkel et al. 2014; Oppenheimer et al. 2019). Global mean sea level rise is expected to increase and could cost the world $14 trillion a year by 2100 under global warming scenarios of 1.5 or 2°C (Jevrejeva et al. 2018). Sea level change and the management of the associated risks have been largely studied by the scientific community (Dasgupta et al. 2009; Kebede and Nicholls 2012; Wong et al. 2014) and have now entered the public debate. Long-term and accurate sea level measurements are essential to better understand the response of the

Earth's system to climate change and to adapt urbanisation in coastal regions and protect local population.

Long-term sea level records derived from in-situ tide gauge reconstructions provide estimates of the global mean sea level rate of rise varying from 1.1 ± 0.3 mm/yr to 1.9 ± 0.3 mm/yr during the twentieth century (Church and White 2011; Ray and Douglas 2011; Jevrejeva et al. 2014; Hay et al. 2015; Dangendorf et al. 2017). Such instruments can provide measurements with a high temporal resolution but the drawback is that only local coastal areas are sampled and they are not homogeneously distributed over the coasts (hemispheric bias). In addition, most tide gauges are not equipped with a Global Navigation Satellite System (GNSS) station, which prevents the associated records to be corrected for vertical land motion (Wöppelmann and Marcos 2016).

Since 1993, satellite altimetry missions have delivered accurate sea level measurements, allowing the monitoring of sea level variations on different spatial and temporal scales (Escudier et al. 2017; Cazenave et al. 2018; Taburet et al. 2019). The precision of the sea surface height estimates has continuously increased, now close to 1 cm, following a regular evolution of the radar technology and efforts made to reduce the different sources of errors of sea level measurements (e.g. orbit solutions: Couhert et al. 2014; wet troposphere correction: Legeais et al. 2014; all required altimeter corrections: Quartly et al. 2017 and Escudier et al. 2017). At global scale, after correcting for the glacial isostatic adjustment (subtracting a −0.3 mm/yr value, Peltier 2004), the altimeter mean sea level rate of rise during the 25 year-long period (Jan. 1993–Sep. 2018) is estimated to 3.3 mm/yr (Nerem et al. 2017; Ablain, Legeais, et al. 2017; Legeais, Ablain, et al. 2018; Legeais, von Schuckmann, et al. 2018; Copernicus ESOTC 2019). The associated uncertainty is 0.4 mm/yr within a 90% confidence interval (Ablain et al. 2019). Compared with the trends cited above during the twentieth century, the increased value observed during the last 25 years highlight the on-going acceleration of the global mean sea level rise. According to climate model projections, unless anthropogenic greenhouse gases emissions are strictly controlled to constrain global warming of the Earth surface close to 2°C, the rate of sea level rise will continue to accelerate during the twenty-first century reaching up to 15+/−5 mm/yr in 2100 (Oppenheimer et al. 2019).

An anomaly in the calibration correction on board the TOPEX-A altimetry mission has been identified in 1998, affecting estimates of significant wave heights (Hayne and Hancock 1998; Ablain and Philipps 2005). The redundant TOPEX-B instrument was used after February 1999 (included) and the global mean sea level time

series has been assumed to be unaffected by this instrumental drift. However, during the past few years, several studies based on different methodologies have demonstrated that it has a substantial effect on the global mean sea level change. One approach to quantify this drift is the comparison of the global mean sea level inferred by satellite altimetry with the independent sea level budget closure inferred from the different contributions to global mean sea level rise (ocean mass and steric sea level components), as done for example by Llovel et al. (2010, 2014), Dieng et al. (2017) and Chen et al. (2017). Here we apply the same approach over the 1993–2010 period because of the availability of data to constrain both ocean warming and ocean mass changes and because it covers the focused period of this study (1993–1998). We use individual mass contributions estimated from glaciers mass loss (Marzeion et al. 2012) (prod. ref. 3.1.8), ice sheet mass loss from Greenland (IMBIE, Shepherd et al. 2012) (prod. ref. 3.1.9) and Antarctica (IMBIE, Shepherd et al. 2012) (prod. ref. 3.1.10) and terrestrial water storage in equivalent sea level from the ISBA-CTRIP model outputs (prod. ref. 3.1.11). The full-depth thermosteric sea level contribution is estimated as the sum of different products according to the ocean layers considered: three gridded products are used for the 0–700 m ocean layer: EN4-Gouretski (Gouretski and Reseghetti 2010) (prod. ref. 3.1.12), EN4-Levitus (Levitus et al. 2012) (prod. ref. 3.1.13) and IAP (Cheng et al. 2017) (prod. ref. 3.1.14). For the intermediate layer (i.e. 700m-2000m), we consider the product from NOAA and its associated uncertainty (Levitus et al. 2012) (prod. ref. 3.1.15). Finally, we add a linear trend of 0.11 mm/yr to consider the deep ocean contribution (below 2000m depth) to the thermosteric sea level change (Purkey and Johnson 2010) (prod. ref. 3.1.16).

Figure 3.1.1 depicts the global sea level time-series with the observed sea level rise from satellite altimetry (blue curve from product reference 3.1.1 – the gridded merged multi-satellite product distributed by C3S/CMEMS) and the global sea level budget from the sum of all components (green curve). The agreement between the two curves is good after 1998 but there is a significant mismatch from 1993 to 1998, in agreement with the drift
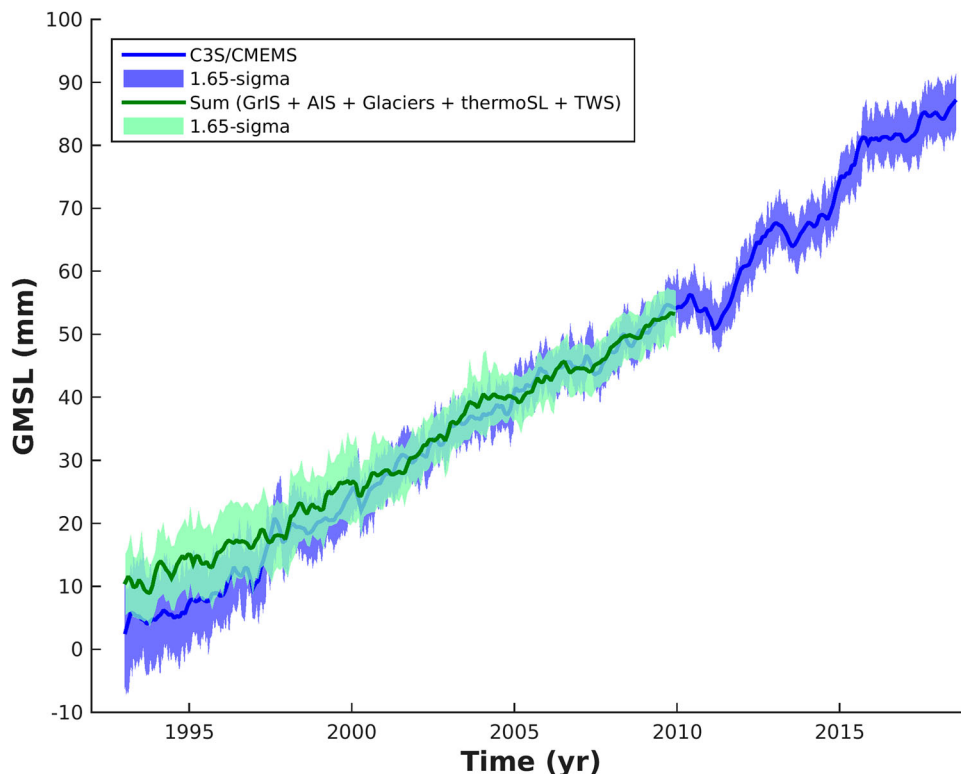
Figure 3.1.1. Global mean sea level time-series: the blue curve represents the observed global mean sea level change (with a reference period of 1993–2012) during 1993–2018 based on satellite altimetry data from product reference 3.1.1 (C3S/CMEMS). The green curve represents the sum of all the components of the global sea level budget during 1993–2010: glaciers (prod. ref. 3.1.8) and ice sheet mass loss from Greenland (prod. ref. 3.1.9) and Antarctica (prod. ref. 3.1.10), terrestrial water storage ('TWS') (prod. ref. 3.1.11) and full-depth thermosteric sea level ('thermo') (prod. ref. 3.1.12–3.1.16) (see text for more details). The blue envelope denotes the 90% confidence level interval of the altimeter global mean sea level time series (prod. ref. 3.1.1) based on Ablain et al. (2019). The green envelope denotes the 90% confidence level interval of the sum of the individual sea level components.

of 1.5 ± 0.5 mm/yr identified by Dieng et al. (2017). The 90% confidence envelope of the altimeter global mean sea level has been derived from the square root of the diagonal error covariance matrix estimated by Ablain et al. (2018) and the 90% confidence envelope of the sum of the sea level contributions has been estimated from the uncertainties of the individual components on a monthly basis. Given the different origins of these individual sea level components and the inhomogeneity of their temporal and spatial sampling, the reliability of this latter envelope remains questionable but this is a best estimate.

Two other approaches have been used to quantify the TOPEX-A instrumental drift on the global mean sea level rate of rise. As this drift comes from a malfunction of the internal calibration mode of TOPEX-A, a possible solution is to recompute the whole TOPEX-A raw data and removing the internal calibration mode range correction included in the TOPEX 'net instrument' correction (Beckley et al. 2017; Nerem et al. 2018). At last, the third approach consists in comparing the altimeter global mean sea level evolution with in-situ tide gauge measurements: Watson et al. (2015) have shown that this instrumental drift leads to overestimating the global mean sea level rate by 1.5 ± 0.5 mm/yr during the 1993–1998 period. By also comparing with tide gauges,

Ablain, Jugier, et al. (2017) provide a drift of 1.3 mm/yr during the 1993–1998 period but they suggest that it may be better described by a V-shape function which trends amount to −1.0 ± 1.0 mm/yr between 01/1993 and 07/1995 and to +3.0 ± 1.0 mm/yr between 08/1995 and 02/1999 (uncertainty at the 90% confidence level).

Note that all proposed approaches lead to similar sea level curves (see Fig. 2 in WCRP 2018, reproduced here in Figure 3.1.2). In terms of global mean sea level trend, this figure indicates that correcting the altimeter sea level record for the TOPEX-A drift leads to a reduced rate of rise from 3.4 mm/yr to about 3.1 mm/yr during January 1993–March 2018.

Beyond the reduction of the global mean sea level trend over the altimetric period, the corrected global mean sea level time series appears to be significantly modified. An adjustment of the curve with a 2nd-order polynomial reveals an acceleration of the global mean sea level during the 25-year altimetry era (January 1993 to March 2018), as illustrated in Figure 3.1.3 (see also Fig. 1 of Cazenave et al. 2018). The different estimates of this acceleration during this period are in good agreement, between 0.1 mm/yr^2 (WCRP 2018) and 0.12 ± 0.073 mm/yr^2 (90% confidence interval; Ablain et al. 2019). As an illustration, with such an acceleration, the decadal trend of the global mean sea level increases
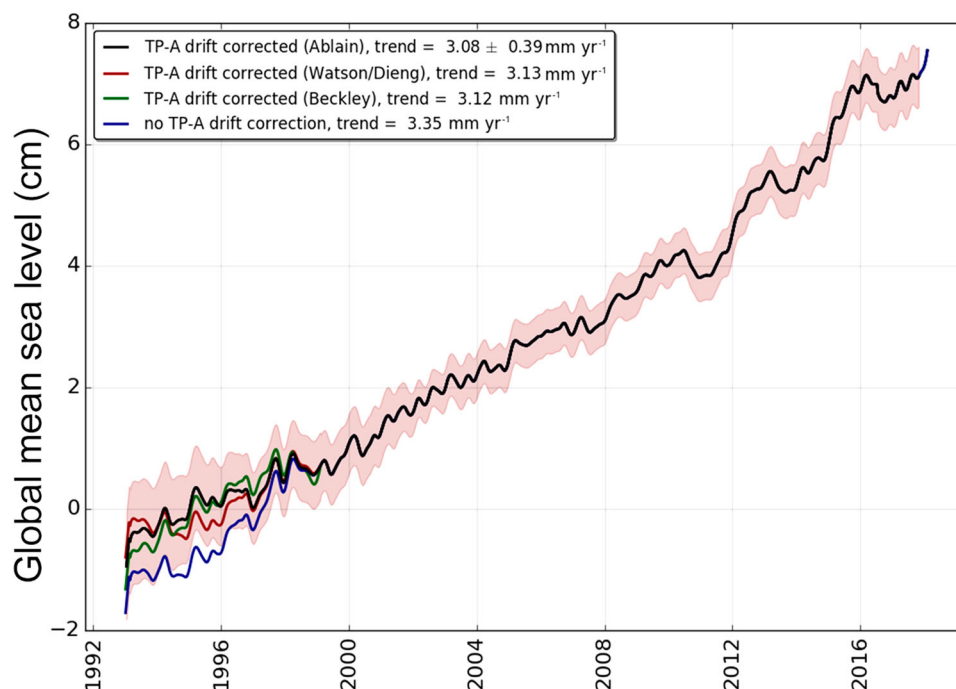
Figure 3.1.2. Evolution of ensemble mean global mean sea level time series (average of the six global mean sea level products from product references 3.1.2–3.1.7). On the black, red and green curves, the TOPEX-A drift correction is applied respectively based on Ablain, Jugier, et al. (2017), Watson et al. (2015), Dieng et al. (2017), and Beckley et al. (2017). Annual signal has been removed and a 6-month smoothing has been applied; Glacial Isostatic Adjustment correction has also been applied. Uncertainties (90% confidence interval) of correlated errors over a 1-year period are superimposed for each individual measurement (shaded area). Credit: WCRP (2018).
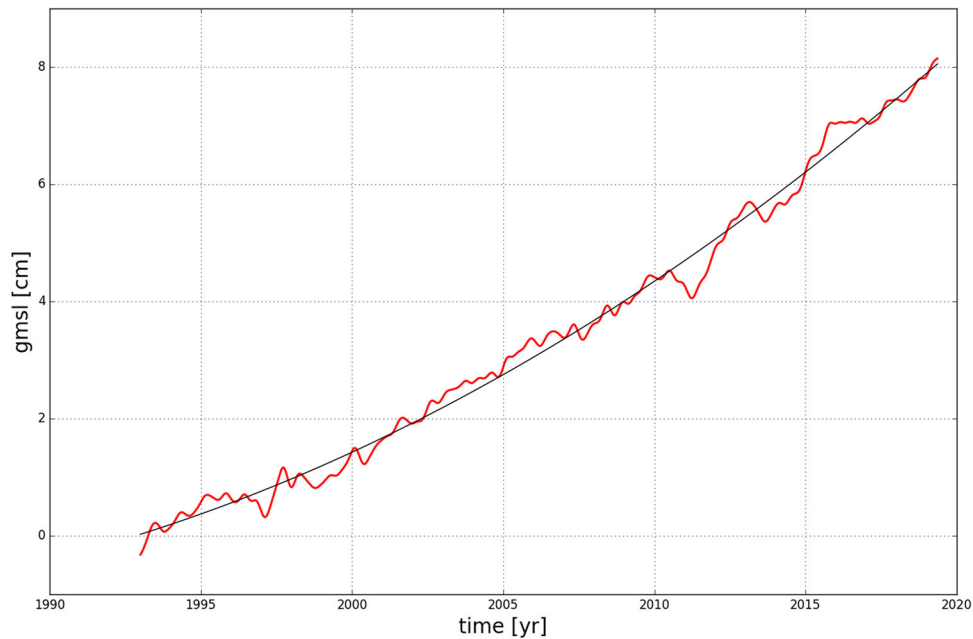
Figure 3.1.3. Global mean sea level time series (in red) between January 1993 and September 2018 based on satellite altimetry data from product reference 3.1.1, corrected for the TOPEX-A drift during 1993–1998 following Ablain, Jugier, et al. (2017). The black curve is the quadratic function fitted to the data. Annual and semi-annual signals have been filtered and a Glacial Isostatic Adjustment correction has been applied.

from about 2.5 mm/yr during the first altimetry decade (1993–2002) to 4.2 mm/yr during the recent decade (2008–2017) (WCRP 2018). This change of behaviour of the global mean sea level rise from linear to quadratic is of major importance given the socio-economic impacts of this rise on coastal and low-lying areas, as discussed earlier (Wong et al. 2014). Indeed, adaptation strategies are impacted by a change in the rate of sea level rise since it has consequences on the remaining time required to implement decisions in order to cope with a given sea level rise. However, a clear overlap is observed before 1998 in Figure 3.1.1 between the confidence envelopes of the altimeter global mean sea level and the one of the sea level budget approach, suggesting that this acceleration is not virtually certain. This comes in agreement with Kleinherenbrink et al. (2019) who conclude, based on crossover differences between TOPEX and ERS-1&2, that the observed acceleration of the global mean sea level is only likely possible. On top of this, note that the altimeter sea level record started in 1993 in highly anomalous environmental conditions, two years after the volcanic eruption of Mt Pinatubo in 1991. This eruption has been followed by a reduction in ocean heat content, leading to a sea level drop of 5–7 mm (Fasullo et al. 2016). This means that this eruption has likely masked the acceleration that would have otherwise occurred (Church et al. 2005; Gleckler et al. 2006; Gregory et al. 2006). The observed trend of the global mean sea level has likely been anomalously higher than

what would have been experienced without the eruption by as much as 0.5 mm/yr on average in the decade following the eruption (Fasullo et al. 2016) and the associated observed acceleration has been smaller (see Fig. 1 of Nerem et al. 2018).

Due to the significant impact of the TOPEX-A drift on the evolution of the global mean sea level, the 'satellite altimetry' community agrees that it is necessary to correct the TOPEX-A record to improve the accuracy and the uncertainty of the total sea level time series. However, a consensus has not yet been reached regarding the best approach to estimate the drift correction. This explains why the altimeter sea level products currently distributed to the users (e.g. Copernicus datasets) are not yet corrected for this drift.

A reprocessing of the TOPEX-A dataset is currently in progress by JPL/CNES space agencies and the recommendation of the Ocean Surface Topography Science Team is that the altimeter sea level products distributed to the users should not be corrected for the TOPEX-A drift before the release of this reprocessed dataset (expected in 2020). However, in case the drift issue will not be solved thanks to this reprocessing effort, the community will have to find an agreement regarding the correction to be used. As presented above, three different approaches are available, based on an update of the altimeter range correction, comparison with in situ data or with independent contributions to the sea level.

The anomaly of the onboard calibration correction is not expected to have any spatial signature on the regional sea level trends since it affects all measurements equally. However, whatever the selected solution for the global mean sea level, the impact on a regional scale should be also assessed so that altimeter gridded maps can also benefit for the drift correction.

At the extreme, it could be recommended to exclude the TOPEX-A period and start from 1999 onwards (with the use of TOPEX-B) when computing the altimeter global mean sea level record. In this case, the global mean sea level rate of rise during the shortened period spanning Jan. 1999 to Sep. 2018 amounts to 3.3 mm/yr, which is similar to the 3.4 mm/yr value found during the 25 year-long altimetry record (not corrected for the TOPEX-A drift). Ablain et al. (2019) have demonstrated that the uncertainty of the record during the reduced period would even be slightly smaller (0.35 mm/yr) than the uncertainty associated with the total period (0.4 mm/yr), precisely because the TOPEX-A period is not considered any more. Even with a shortened period, the altimeter sea level would thus remain a relevant indicator of climate change.

Section 3.2: Using CMEMS satellite and model data to help assess eutrophication status in Northwest European Shelf Seas

Authors: James R. Clark, Gavin H. Tilstone, Jerry Blackford, Stefano Ciavatta, David Ford, Susan Kay, Peter E. Land, Robert McEwan, Richard Renshaw

Statement of main outcome: We explore the use of CMEMS satellite and model data for eutrophication status assessments in Northwest European Shelf Seas. The study covers the period 1998–2018, with a focus on the year 2018. A subset of the Oslo-Paris (OSPAR) indicators for eutrophication, including: (i) the concentration of chlorophyll-*a* (Chl-a) in sea water; and (ii) the bottom concentration of dissolved oxygen are analysed. Relative to the reference period 2009–2014, there was a general decrease in satellite derived chlorophyll-*a* 90 percentile (Chl-a P90) concentrations in 2018 in known problem areas, including coastal areas within the Southern North Sea. Throughout the model domain, simulated minimum daily mean bottom oxygen concentrations for 2018 are above OSPAR threshold concentrations used to identify problem areas – this is reflected in anomalies relative to the reference period 1998–2014, that are generally positive, with the exception of some areas within the Southern North Sea. The location of low oxygen zones is generally consistent with those identified in past observational and modelling studies; however, simulated values should be used with care and

may need bias correction. When used appropriately in combination with indicators derived from in situ data, we conclude that the two products have the potential to enhance existing eutrophication assessment procedures.

Data use:

Ref. No.	Product name and type	Documentation
3.2.1	OCEANCOLOUR_ATL_ CHL_L4_REP_ OBSERVATIONS_009_091 Remote sensing data	PUM: http://marine.copernicus.eu/ documents/PUM/CMEMS-OC-PUM-009-ALL.pdf QUID: http://marine.copernicus.eu/ documents/QUID/CMEMS-OC-QUID-009-066-067-068-069-088-091.pdf
3.2.2	NORTHWESTSHELF_ REANALYSIS_BIO_004_011 Marine biogeochemical model data	PUM: http://marine.copernicus.eu/ documents/PUM/CMEMS-NWS-PUM-004-011.pdf QUID: http://marine.copernicus.eu/ documents/QUID/CMEMS-NWS-QUID-004-011.pdf

European coastal areas are commercially important for fishing and tourism, yet are subject to the increasingly adverse effects of eutrophication (Grizzetti et al. 2012; Romero et al. 2013), harmful algal blooms (Báez et al. 2014; Glibert et al. 2014) and climate change (McQuatters-Gollop et al. 2007). Eutrophication is the anthropogenic enrichment of water by nutrients that causes an accelerated growth of algae and higher forms of plant life, which produce undesirable disturbances to the balance of organisms in the water, and the quality of the water itself. Eutrophication in the European coastal zone was recognised as a problem in the 1960s and reached damaging proportions by the 1980s in several European coastal regions (Ferreira et al. 2011; and references therein).

Management action to reduce riverine nutrient sources to the North Sea started in the 1980s. The OSPAR convention was signed by bordering Northeast Atlantic States in 1992. OSPAR introduced the objective to reduce anthropogenic inputs of nitrogen and phosphorus by 50% relative to input levels in 1985 (OSPAR 2008). Central to the OSPAR Eutrophication Strategy is a set of harmonised methods for the assessment of eutrophication by Contracting Parties. In the latest OSPAR Eutrophication Assessment Report (OSPAR 2017), the Common Procedure for the classification of the Eutrophication Status of the OSPAR Maritime Area included 10 assessment criteria or indicators, spanning four categories. The primary indicators for eutrophication are nitrate and phosphate concentrations. Secondary indicators include a range of biological and chemical variables which respond, either directly or indirectly, to increases in nutrients, including (among others): the concentration of chlorophyll-*a* (Chl-a) in sea water and the concentration of dissolved oxygen ($c(O_2)$).

Chl-a is a photo-synthetically active pigment of phytoplankton which can increase in concentration under

eutrophic conditions. The 90th percentile (P90) of Chl-a has been adopted as a measure of eutrophication in coastal waters (OSPAR 2008), because it is a robust ecological indicator of trophic status (Novoa et al. 2012). Chl-a P90 is defined as the concentration of Chl-a such that 90 per cent of the observations over a given time window are equal to or lower than this value. A target Chl-a P90 threshold is defined and compared to the actual observed P90 value to determine eutrophication risk and non-risk areas. Assessment levels used by Contracting Parties vary by area. In the North Sea, assessment levels range from < 4 mg m^{-3} to > 20 mg m^{-3}, reflecting gradients from inshore to offshore waters (OSPAR 2017). Following reductions in nitrate and phosphate concentrations, the concentration of Chl-a has reduced in some regions (Gohin et al. 2019).

Oxygen (O_2) is essential for complex marine life, including commercially important species of fish and shellfish. Oxygen concentration, $c(O_2)$, is influenced by multiple interdependent factors. Natural phenomena, such as respiration by aerobic organisms or limited exchange with the atmosphere, can drive down $c(O_2)$, especially in bottom waters during seasonal stratification events (Topcu and Brockmann 2015; Große et al. 2016). O_2 depletion is also a known indirect consequence of eutrophication, in which high nutrient inputs fuel elevated levels of biological production, which leads to an increase in O_2 demand as sinking organic material is decomposed at depth, with potentially severe consequences for aerobic, bottom dwelling species including demersal fish species (Best et al. 2007). For this reason, $c(O_2)$ was adopted as an indirect identifier of Eutrophication problem areas under the OSPAR Common Procedure. Contracting Parties applying the OSPAR Common Procedure use assessment levels ranging from 2 to 6 mg L^{-1} to help identify Eutrophication problem areas. Within OSPAR, near seafloor oxygen concentrations > 6 mg L^{-1} are considered to be of minimal concern (OSPAR 2017). Concentrations < 2 mg L^{-1} – a threshold often used to define hypoxic conditions – are known to cause severe problems (Levin et al. 2009) and are considered to be of high concern. However, species' tolerances to low oxygen conditions are known to vary, and many organisms are known to experience sub-lethal or lethal effects at concentrations above 2 mg L^{-1} (Vaquer-Sunyer and Duarte 2008).

Using the OSPAR indicators, the detection of eutrophication is targeted at coastal and shelf waters where the influence of excessive nutrients from river run-off is most likely to be found. By the time run-off from NW European rivers reaches the NE Atlantic any residual eutrophication signature will be undetectable. Methods are typically based on the collection and analysis of in situ data at designated monitoring sites, which allows for long-term time series to be built up and trends identified. In the latest OSPAR Eutrophication Assessment Report covering the period 2006–2014 (OSPAR 2017), it was shown that, despite significant reductions in nutrient inputs since 1990, eutrophication still exists within the OSPAR Maritime Area, particularly in coastal areas sensitive to nutrient discharges, such as estuaries. The Greater North Sea – in particular, areas bordering the Belgian, German and Dutch coasts – and localised areas of the Celtic Seas, were highlighted as the main areas of concern. These findings are repeated in the Wadden Sea Quarterly Status Report (van Beusekom et al. 2017), which evidences lower values for many eutrophication indicators, but also levels above target thresholds for non-problem areas.

The potential value of both satellite and model data for eutrophication assessments has been highlighted within OSPAR (OSPAR 2017). After the launch of SeaWiFS in 1997, Chl-a estimates from satellite ocean colour were recognised as a cost effective means of monitoring eutrophication at high temporal and spatial scales in coastal waters and shelf seas (Schaeffer et al. 2012), that could not be achieved through conventional water sampling techniques. Satellite data in tandem with in situ data are becoming an accepted means by which water quality can be monitored over broader spatial and temporal areas. Meanwhile, models can help to fill data gaps for assessment variables where there is only limited data available. They can also be used to help guide in situ monitoring efforts by identifying potential problem areas; to unpick the role different natural and anthropogenic processes play in driving observed patterns; and to test the likely effectiveness of different management interventions. Satellite ocean colour and models are also integrated in CMEMS by means of data assimilative systems information (e.g. Skákala et al. 2018), which complements their paired use. In the following, we explore the combined use of CMEMS satellite and model data for the assessment of Eutrophication Status in Northwest European Shelf Seas. In so doing, we address the question of what type of information can the data products usefully provide, and what caveats should be attached to their use.

3.2.1. Method

We use 8-day satellite sea surface Chl-a (mg m^{-3}) composites at 1 km resolution (OCEANCOLOUR_ATL_CHL_L4_REP_OBSERVATIONS_009_091). The data are derived from ESA Ocean Colour CCI Remote Sensing Reflectance data using the regional OC5CI chlorophyll algorithm (Sathyendranath et al. 2016). The data covers the time period from January 1998 to

December 2018, and a spatial area that extends over the Northwest European Shelf Seas. OC5CI is a switching algorithm that applies the OC5 model in case 2 coastal regions and the colour index (CI) in case 1 open ocean areas. Chl-a P90 values are computed on a per-pixel basis over the months March to October inclusive, covering the phytoplankton growing season. In autumn and winter months, the spatial coverage of ocean colour data is limited in the study region, due to the high average solar zenith angle. An assessment of the product's skill in the area can be found in the accompanying QUality Information Document (QUID; see Data Use table).

For model data, we use output from the coupled marine hydrodynamic-biogeochemical model NEMO-FABM-ERSEM, which has been run on the 7 km Atlantic Margin Model (AMM7) domain from January 1998 through to December 2018 (NORTHWESTSHELF_REANALYSIS_BIO_004_011). The NEMO AMM7 configuration is described in O'Dea et al. (2017). A full description of ERSEM can be found in Butenschön et al. (2016), while the coupled NEMO-FABM-ERSEM configuration is described in the Product User Manual (PUM) and accompanying QUID (see Data Use table). Physical variables are not assimilated during the reanalysis run; however, sea surface chlorophyll data from satellite is, ensuring consistency with the sea surface chlorophyll data presented here. From the model, we use daily mean sea surface Chl-a (mg m^{-3}) and depth resolved c(O$_2$) (mg L^{-1}).

In the satellite and model data, anomalies in Chl-a P90 for the year 2018 were computed by calculating the difference in Chl-a P90 for 2018 relative to the 6 year reference period 2009–2014. Year-to-year variations in Chl-a P90 within different regions of the Greater North Sea are also analysed. Minimum daily mean bottom c(O$_2$) is computed on a per-pixel basis by finding the minimum daily mean c(O$_2$) within the grid cell that sits immediately above the sea floor. The minimum value is computed over the full year.

3.2.2. Results and discussion

Satellite-derived Chl-a P90 concentrations are already used to complement in situ measurements within OSPAR assessment reports (OSPAR 2017). As shown in the product QUID, summary skill metrics show a close fit to in situ data. In Figure 3.2.1(A), we map satellite-derived Chl-a P90 concentrations for the reference period 2009–2014. Data for 2018 are shown in Figure 3.2.1(C), while 2018 anomalies relative to the reference period are shown in Figure 3.2.1(E). The corresponding model data is shown in Figure 3.2.1(B,D,F), respectively. In the reference period, the highest P90 values are found

around the continental coast in the Southern North Sea. Assessment threshold concentrations – in particular, the 15 mg L^{-1} threshold for coastal waters used by the UK, France, and Belgium – are generally not exceeded, with the exception of localised areas near to the mouths of major estuaries in the Southern North Sea. With the exception of the area around Dogger Bank, satellite-derived Chl-a P90 anomalies for 2018 relative to the reference period are generally negative in off shore waters throughout the Greater North Sea and English Channel, indicating lower Chl-a P90 concentrations. The picture is more mixed near to the continental coast in the Southern North Sea, with positive anomalies evident near to the Rhine-Meuse-Scheldt delta and in the Wadden Sea, and negative anomalies evident along other areas of the French, Belgian and Dutch coasts. The picture is also more mixed within the Celtic Seas, where significant upward trends were observed in offshore waters over the period 2006–2014 (OSPAR 2017). Since there is no direct river-run off into the central Celtic Sea, the positive Chl-a P90 anomaly in 2018 is unlikely to be driven by anthropogenic nutrient inputs, but rather climatic or biological effects, such as a change in grazing pressure.

In past OSPAR assessments, Eutrophication problem areas have been identified within sub-regions of the Greater North Sea. Following Tinker et al. (2019), we divided the AMM7 model domain into 8 sub-regions (Figure 3.2.2(A)), and examine spatial and temporal variations in Chl-a P90 concentrations in the Northern North Sea, the Norwegian Trench and the Southern North Sea sub-regions (Figure 3.2.2(B–D)). Each sub-region covers a range of environments, where spatial and temporal variability in Chl-a P90 is influenced by both natural and anthropogenic factors. This is particularly evident in the Southern North Sea (Figure 3.2.2(D)), where the spread in Chl-a P90 concentrations is largest, and the highest concentrations, representing areas adjacent to the continental coast where eutrophication is most likely to occur, are found. No statistically significant long-term temporal trends in the data were found in the selected sub-regions.

The duration and extent of conditions in which modelled bottom c(O$_2$) fell below 6 mg L^{-1} for the years 1998–2018 are shown in Figure 3.2.3(A). In the model, concentrations generally stayed above 4 mg L^{-1}, while at no point were hypoxic conditions (c(O$_2$) < 2 mg L^{-1}) simulated. The sub-regions most frequently impacted by c(O$_2$) < 6 mg L^{-1} are the Northwest and Southwest Approaches, then the Norwegian Trench and Southern North Sea. While the former have also been identified as potential problem areas in a past modelling study (Ciavatta et al. 2016), there is limited in situ data to reinforce this prediction. The simulation of low
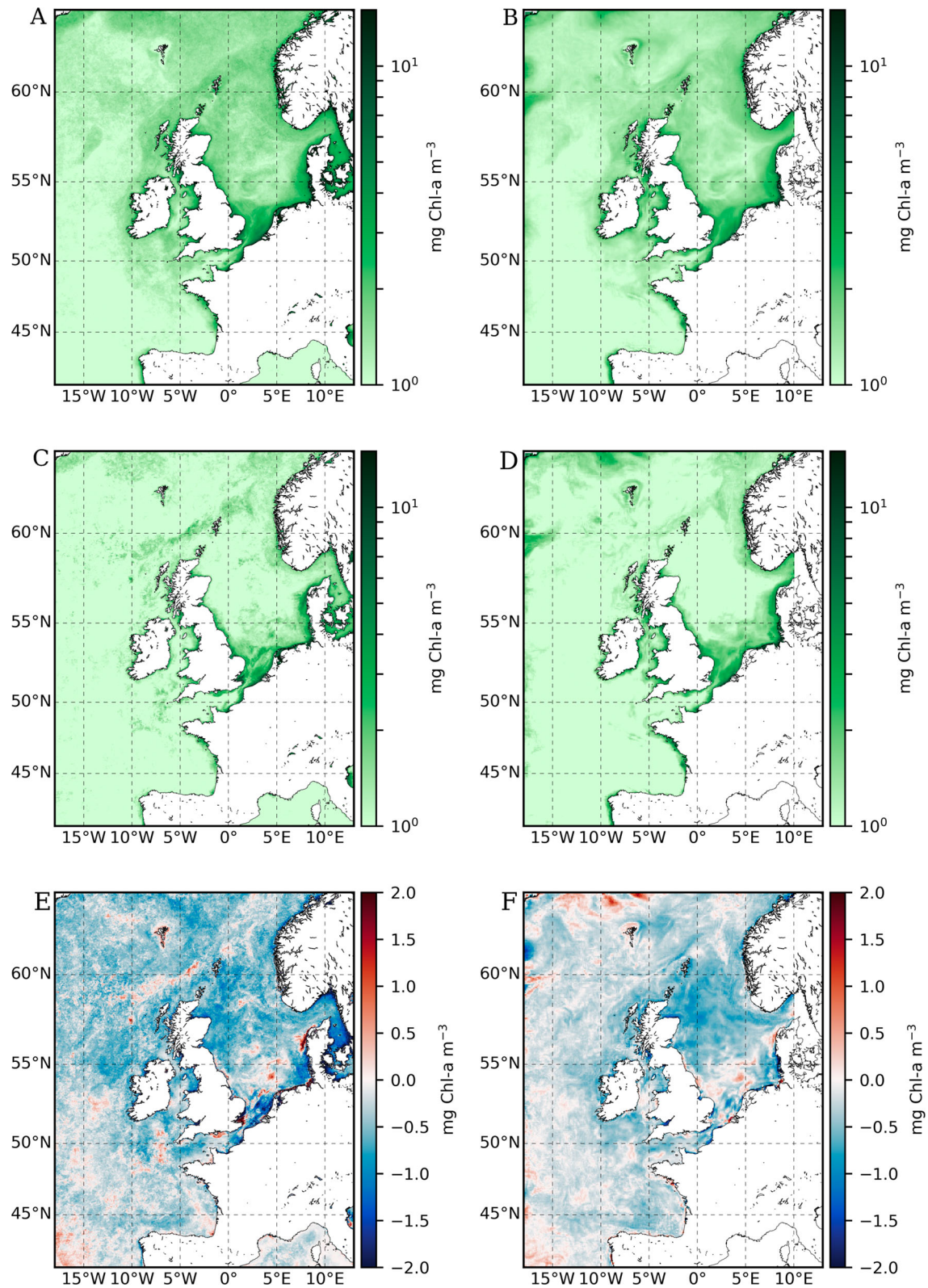
Figure 3.2.1. Chl-a P90 over the Northwest European Shelf based on satellite (product OCEANCOLOUR_ATL_CHL_L4_REP_OBSERVA-TIONS_009_091) and model (product NORTHWESTSHELF_REANALYSIS_BIO_004_011) surface Chl-a concentrations. (A) Satellite-derived Chl-a P90 at 1 km resolution for the reference period 2009–2014, computed over the growing season (March to October inclus-ive). (B) As in (A), but based on modelled surface ocean Chl-a concentrations at 7 km resolution. (C) Satellite-derived Chl-a P90 at 1 km resolution for 2018, computed over the growing season (March to October inclusive). (D) As in (C), but based on modelled surface ocean Chl-a concentrations at 7 km resolution. (E) Satellite-derived Chl-a P90 anomalies for 2018 relative to the reference period 2009–2014. (F) As in (E), but based on model Chl-a P90 data.
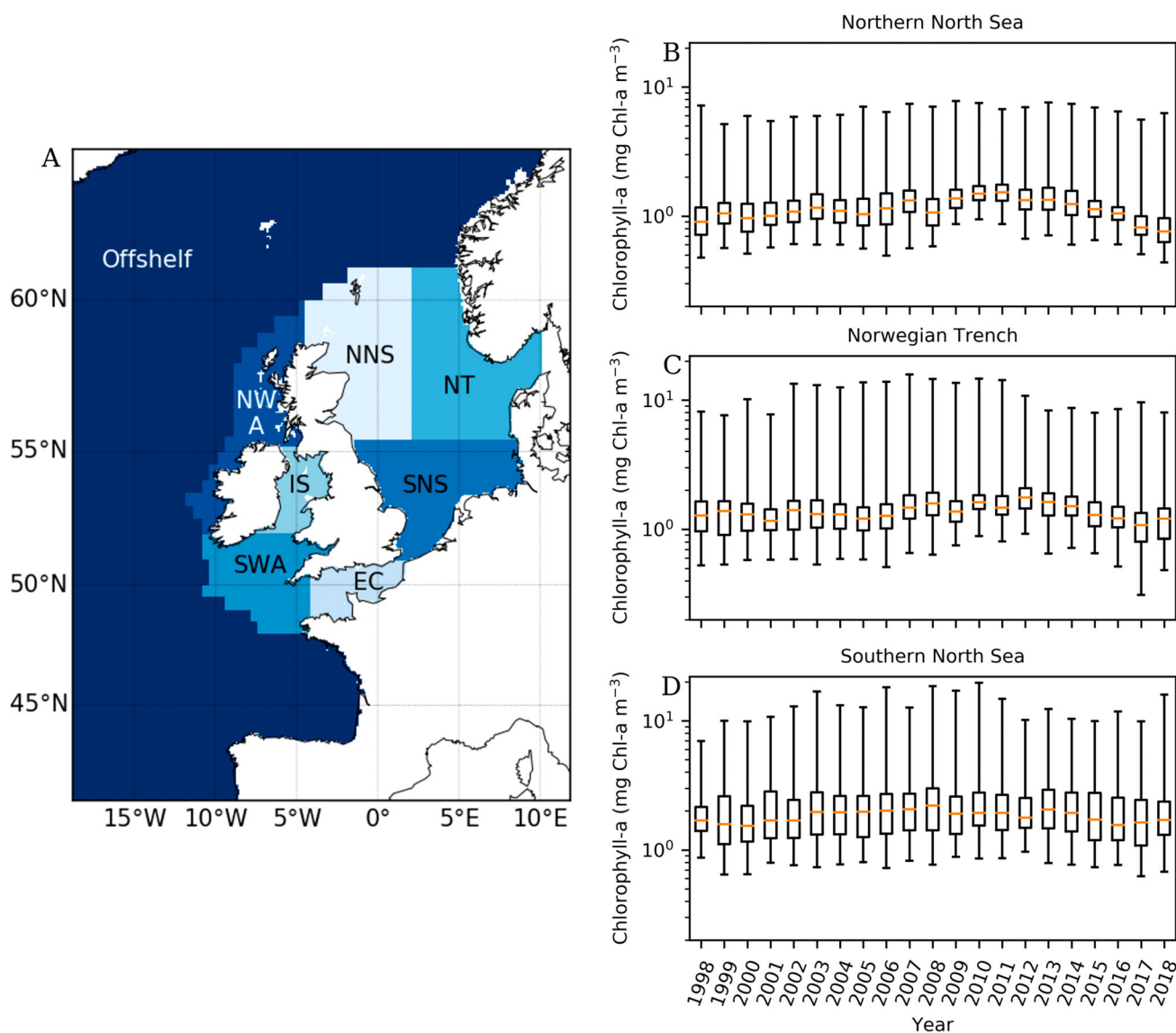
Figure 3.2.2. Annual variations in model Chl-a P90 within the Greater North Sea, based on model surface ocean Chl-a concentrations (product NORTHWESTSHELF_REANALYSIS_BIO_004_011). (A) Map of the greater North Sea and its sub-regions, following Tinker et al. (2019). The sub-regions include the South Western Approaches (SWA); the English Channel (EC), the Southern North Sea (SNS), the Norwegian Trench (NT), the Northern North Sea (NNS), the North Western Approaches (NWA), the Irish Sea (IS) and off-shelf areas (Offshelf). (B) – (D) Chl-a P90 calculated on a per-pixel basis for three sub-regions within the Greater North Sea. Chl-a P90 concentrations are calculated over the growing season March – October inclusive for each year from 1998 through to 2018. The box plots show the median Chl-a P90 concentration for each region (yellow line), the interquartile range (box edges) and min/max values (whiskers) for each year.

oxygen conditions within the Southern North Sea, and in particular the German Bight, is in keeping with OSPAR assessments (OSPAR 2017). Minimum daily mean bottom $c(O_2)$ data for 2018 are shown in Figure 3.2.3(B), while anomalies relative to the 1998–2014 reference period are shown in Figure 3.2.3(C). In the 2018 model data, the 6 mg L^{-1} threshold concentration was seldom breached, with an exception being near to the eastern coast of the Bay of Biscay; and anomalies were generally positive over the entire continental shelf. Sub-regions with the lowest oxygen concentrations include the

Southern North Sea, the Northwest and Southwest Approaches, and areas off the Northwest coast of France (in agreement with, e.g. Ciavatta et al. 2016).

The advantages of using satellite derived Chl-a P90 concentrations in eutrophication status assessments are well appreciated (Novoa et al. 2012; Gohin et al. 2019), and satellite derived ocean colour data is already being combined with in situ measures by several Contracting Parties within OSPAR. In terms of resolution, a minimum of 1km is generally required for such studies; given the tendency for river nutrient fertilisation effects
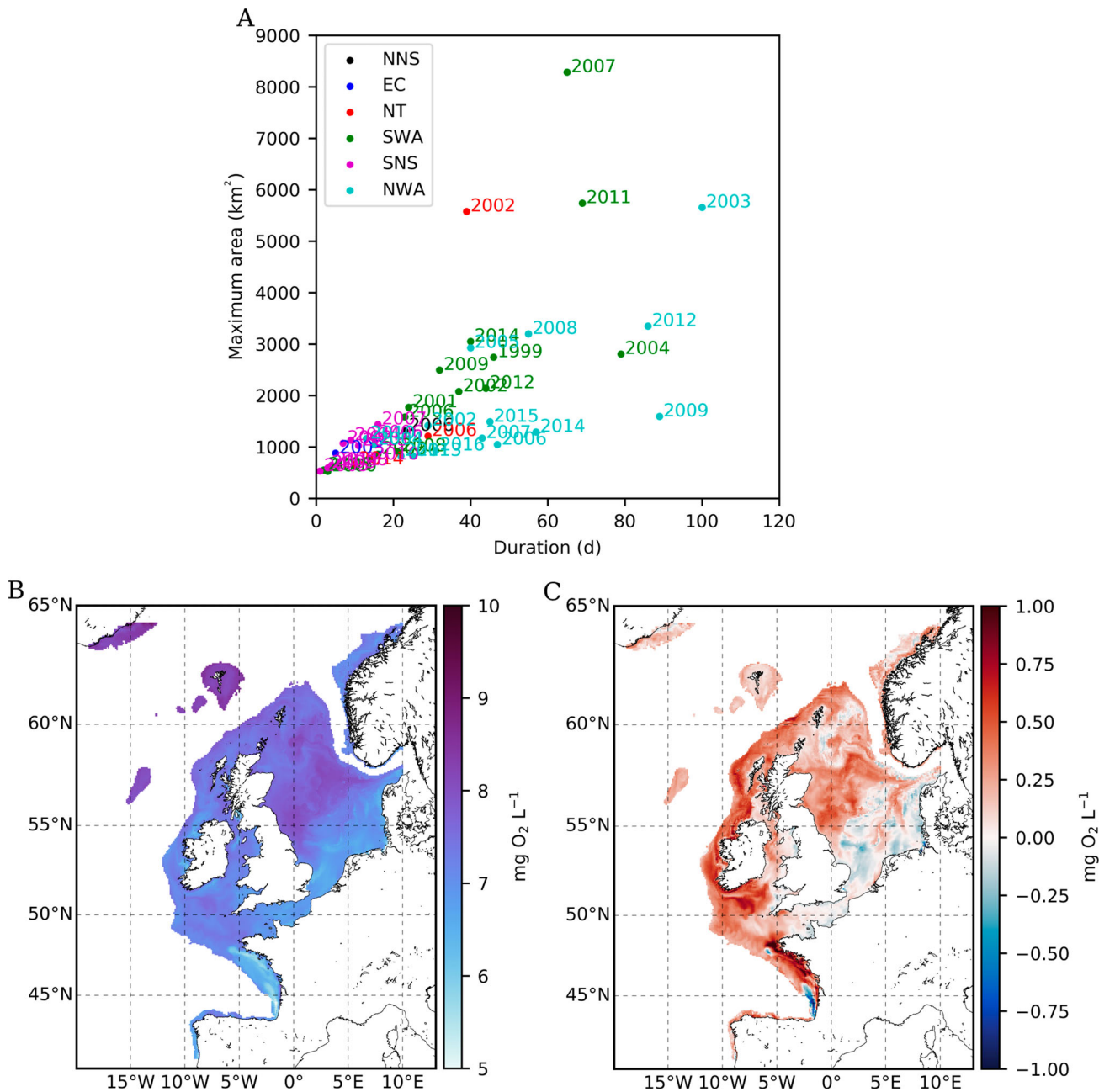
Figure 3.2.3. Duration and extent of low bottom oxygen conditions based on modelled bottom oxygen concentration (product NORTHWESTSHELF_REANALYSIS_BIO_004_011). (A) Areal extent and duration of low bottom oxygen conditions over the period 1998–2018 for the sub-regions defined in Figure 3.2.2(A), based on a threshold concentration of 6 mg L^{-1}. (B) Minimum daily mean bottom oxygen concentration in 2018, calculated over the full year. (C) Anomalies in the minimum daily mean bottom oxygen concentration in 2018 relative to the reference period 1998–2014.

to become diluted further away from the shore, it is desirable to resolve near shore areas in as much detail as possible. The trade-off in moving to even higher resolution products, as they become available, comes in temporal coverage, which generally worsens at higher resolutions. For this particular region, CMEMs model derived Chl-a data are currently only available at 7 km resolution, meaning fine-scale, near coast signals are not resolved.

The model provides many other variable fields from which different eutrophication status indicators can be derived, and their interdependencies explored. These include nutrient concentrations and bottom oxygen concentrations. The ability of the model to successfully identify areas that are known to experience low oxygen concentrations is encouraging. Furthermore, the agreement with Ciavatta et al. (2016), where results were derived from a 100 member ensemble generated by

perturbing model states and forcings, indicate the result is reproducible within an estimated range of model uncertainty. Building on this, we propose the outputs could be explored further, and used to identify potential problem areas that are not closely monitored at the present time. A further potential application of models is to identify the relevant importance of different natural and anthropogenic drivers on eutrophication indicators. This was explored for bottom oxygen concentrations by Große et al. (2016), who investigated the relative influence of spatial and temporal variations in seasonal stratification and primary production on $c(O_2)$. However, some care must be taken in this context. The use of chlorophyll data assimilation in the reanalysis makes the interpretation of governing relationships and their interdependencies in the model more complex. Furthermore, it is evident from comparisons with in situ data that the model dataset contains some significant biases compared to observed values (see QUID). Specifically, there is an overall negative median bias in oxygen concentrations of ~0.5 mg L^{-1} when compared with on shelf in situ observations from the ICES databases, which likely result from a warm bias in temperature; while nitrate concentrations are generally positively biased, especially in the Southern North Sea, which has direct relevance to studies of eutrophication, given the history of this area. If used to support eutrophication assessments, it is important that these errors are taken into consideration.

Section 3.3: The value of carbon sink ecosystem services in the Mediterranean Sea

Authors: Canu, D., A. Ghermandi, P. Lazzari, G. Bolzon, P.A.L.D. Nunes, S. Zunino, C. Solidoro

Statement of main outcome: Marine ecosystems services worldwide are often ignored or underestimated, due to their limited or indirect visibility and it is critically important to assess them to improve marine management and policy. Using the air–sea carbon fluxes CMEMS products and new estimates of the social cost of carbon (SCC), i.e. the net present value of the cumulative, worldwide impact of one additional ton of carbon emitted to the atmosphere at a specific point in time over its residence time in the atmosphere (Watkiss et al. 2005), we computed the carbon sink ecosystem service (CSES) value for the period 2002–2014 and for the year 2018, for the Mediterranean Sea basin and at the Exclusive Economic Zone (EEZ) level (Flanders Marine Institute 2018). Considering the total surface of $(2.48 \cdot 10^6 \text{ km}^2)$, the average CSES value for the Mediterranean Sea is 1733 M€/year for the period 2004–2014 and 2095 M€/year for 2018, with spatial

differences according to the variability of air–sea carbon fluxes, which are associated to the combined action of marine circulation, heat fluxes and the biological pump. Accounting for the value of sea carbon sink is tis of particular importance since such benefits are still poorly understood. In fact, key information about the natural capital of oceans and the ecosystem services flows that it generates is missing or invisible in the System of National Accounts (SNA), including the Gross Domestic Product (GDP). Moreover, yearly updating this information on the basis of both ecological and economic trends is of great added value for natural capital accounting.

Product used:

Ref no.	Data name	Documentation	Type of product
3.3.1.	MEDSEA_REANALYSIS_ BIO_006_008	PUM: http:/marine. copernicus.eu/ documents/PUM/ CMEMS-MED-PUM- 006-008.pdf QUID: http:/marine. copernicus.eu/ documents/QUID/ CMEMS-MED-QUID- 006-008.pdf	Model data
3.3.2	EU-ETS (European Emission Trading System) Average auction price 2012–2018	https://www.eex.com/ en/market-data/ environmental- markets/auction- market/european- emission-allowances- auction/european- emission-allowances- auction-download.	Auction data
3.3.3	SCC (social cost of carbon) estimates	Tol RJS (2018) The economic impact of climate change. Review of Environmental Economics and Policy 12(1): 4–25.	Literature review
3.3.4	SCC (social cost of carbon) estimates	van den Bergh JCJM, Botzen WJW (2014) A lower bound to the social cost of CO_2 emissions. Nature Climate Change 4: 253–258.	Literature review
3.3.5	SCC (social cost of carbon) estimates	Nordhaus WD (2017) Revisiting the social cost of carbon. PNAS 114(7): 1518–1523	Literature review

3.3.1. Valuation: results and discussion

The aim of this contribution is to provide a new aggregated indicator that could be used to capture the information on the state and trends of Carbon Sink Ecosystem Service (CSES) of the Mediterranean Sea.

Marine ecosystems provide a variety of benefits to human well being, supporting a wide range of services that include all the main categories of provisioning,

regulating, and cultural services (MEA 2005; TEEB 2010; CICES 2018). Marine systems provide a substantial contribution to climate regulation, through the maintenance of the CO_2/O_2 (carbon dioxide/oxygen) balance, the maintenance of the ozone (O_3) layer and sulphur oxides (SOx) and through thermal regulation (Beaumont et al. 2007; Pörtner et al. 2014). The ecosystem services framework is relevant for re-connecting people to nature highlighting the link between good environmental status and benefits for human society. The new concepts of the Maritime Spatial Planning Directive (Directive 2014/89/EU) and the EU Blue Growth agenda (2012) point out the necessity to develop a future sustainable use of the marine resources. In this contest, the ecosystem services framework can be a powerful tool to highlight the trade-offs and the conflicts arising from multiple uses and impacts and to consider as beneficiaries in the decision-making process not only the single economic sectors but the entire humanity (Liquete et al. 2016).

Globally, the ocean system absorbs an important fraction of anthropogenic CO_2 from the atmosphere. The global estimate for 2016 was 2.65 PgC/year (Perruche et al. 2018) which accounts for 25% of the anthropogenic emissions for the same period, estimated by Le Quéré et al. (2018) in 10.8 GtC/year. Considering only the total fossil fuel and cement-manufacturing emissions in the period from 1800 to 1994 ocean carbon sink was responsible for the sequestration about 48% of such emissions (Sabine et al. 2004). These values underline the relevance of the ocean carbon sequestration service (Beaumont et al. 2007) which is sustained by the interaction of three main categories of functions: the physics that governs ocean water advection and mixing, the biogeochemistry, which is defined by the trophic interactions among primary and secondary producers, and the carbonate chemistry, which directly responds to CO_2 air concentration (Gattuso et al. 2015). Due to the dynamic nature of seas and oceans, the carbon sequestration service is variable over time and space, responding not only to the atmospheric CO_2 concentration, but also to changes in ocean dynamics and properties, such as the dynamics of dense water formation and upwelling, the variability of temperature and salinity, and the variability of primary producers (e.g. phytoplankton and macrophytes). The contribution of these processes to carbon sequestration, is still poorly known, and, due to the public nature of such service, poorly captured by the markets.

Melaku Canu et al. (2015) provided the first estimate of the economic value of carbon sequestration in the Mediterranean Sea by combining the CO_2 fluxes, computed with a state-of-the-art biogeochemical model, with estimates of the social cost of carbon (SCC). Here we use the term 'sink' rather than sequestration for

consistency with the definition adopted by IPCC 2019, which requires a centennial time range to assess 'sequestration'. Such previous valuation was conducted both in terms of the total net CO_2 flux – which aggregates the value of the physical, solubility and biological pumps – and for the biological pump only, which was intended to assess the contribution of biological processes to the marine "blue carbon" absorption. As in Melaku Canu et al. (2015), in CMEMS global reanalysis (Data Ref #: 3.3.1) the carbon biological pump of the pelagic ecosystem is resolved at the lower trophic level (plankton), as detailed in Le Quéré et al. (2018). Using conservative estimates of the cost of carbon emissions, the computed value for the whole Mediterranean Sea ranged between 127 and 1722 million €/year. The results have also been aggregated at the level of each Mediterranean country, by computing the CO_2 fluxes (and their relative economic value) for their relative Exclusive Economic Zone (EEZ) areas. The SCC is a central concept for understanding and implementing climate change policies: it represents the economic cost caused by an additional ton of carbon dioxide emissions or its equivalent (Nordhaus 2016). Since the publication of the previous valuation paper in 2015, however, the number of papers and estimates of the SCC has grown rapidly (Tol 2018). On parallel, new CO_2 air–sea fluxes datasets have been made available from model re-analysis relative to the period 1999–2018 thus allowing to extend the valuation over a multi-year period and to make comparisons between target years and the climatology (2004–2014). The availability of new, updated information, therefore calls for the reassessment of the previous estimates in light of the new knowledge that is carried out in the present work. Along with SCC estimates, our analysis also considers market price information from the EU ETS for its policy relevance.

Consistently with previous research (Perruche et al. 2018), our results show that the Mediterranean Sea acts as a weak sink of atmospheric carbon. Carbon is absorbed in particular in the northern part of the basin, also linked to dense water forming systems. Air–sea carbon fluxes in the Mediterranean Sea respond to the global increase in atmospheric pCO_2, showing a positive trend over the period 2004–2018 as illustrated in Figure 3.3.1(panel a) with an average sink value of 6.9 TgC/year for the decade 2004–2014. This value corresponds to an average in-flux of 2.9 tonC/km^2 with an increase of 0.16 tonC/km^2/year. This trend of CO_2 air-to-sea flux is the same magnitude of the global carbon budget estimates (Le Quéré et al. 2018). In the same figure (Figure 3.3.1(panel b)) the red line represents the evolution of the carbon sink at the basin scale, while the grey lines indicate the ± standard deviation of the

a)

b)

c)
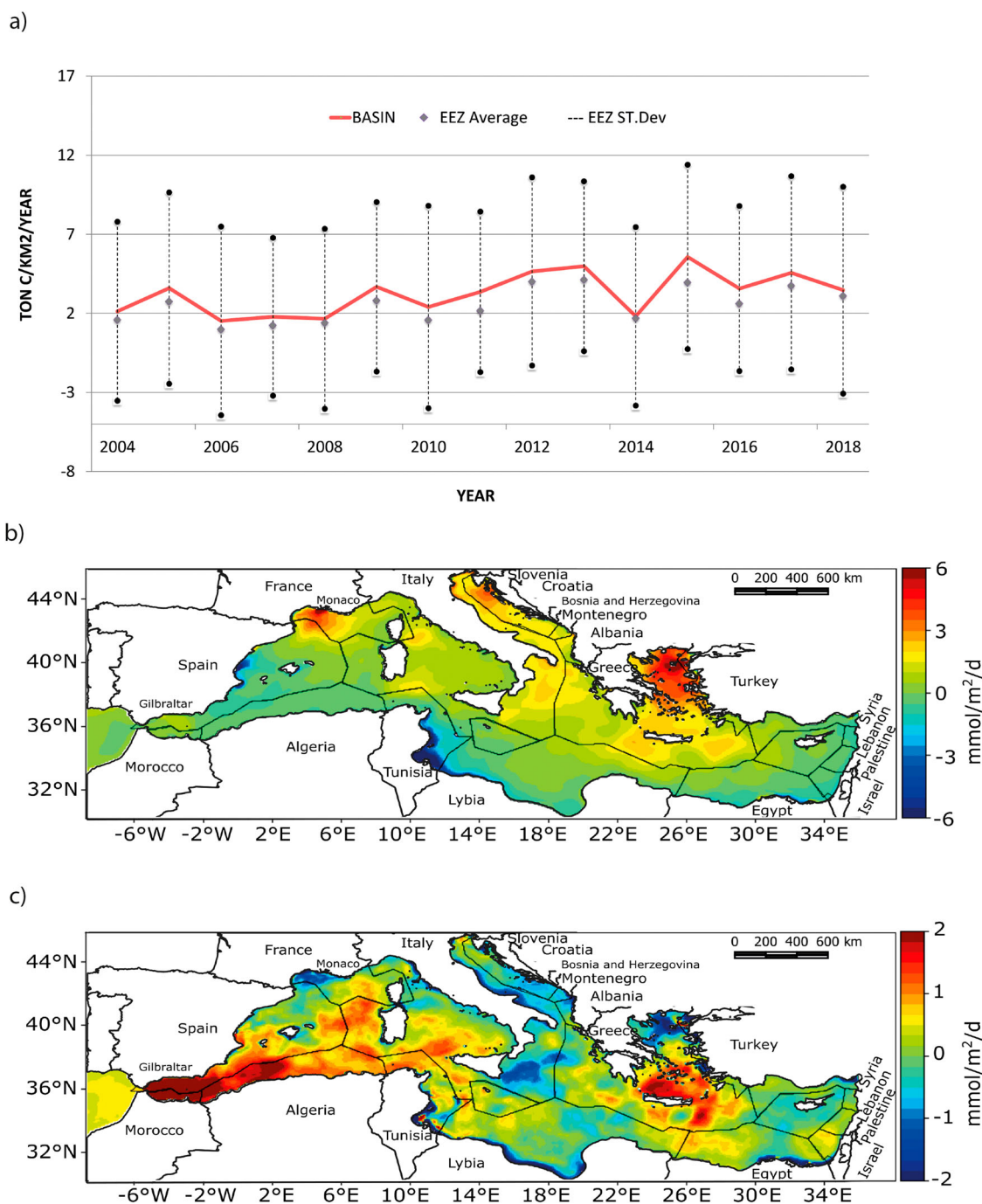
Figure 3.3.1. Carbon sink, computed as net annual CO_2 fluxes at the sea surface using the CMEM global reanalysis using data presented in Table 3.3.1 (Data Ref #: 3.3.1). (a) Range of carbon sink (tonC/km²/year) for the different Mediterranean EEZ expressed as Standard deviation (Grey bars) and average value (grey dot). Basin average (red line) for the period 2004–2018. (b) Climatological mean of net air-to-sea flux for CO_2 (mmol C/m²/day) over the period 2004–2014 (c) The corresponding anomaly of net air-to-sea flux for CO_2 (mmol C/m²/day) for year 2018 over the climatological mean.

carbon sink values computed for each EEZ, which present a noticeable variability. According to the map of Figure 3.3.1(panel b) in the period 2004–2014, the carbon sink is particularly strong in the area of Aegean Sea, Gulf of Lion and northern Adriatic Sea, while outgassing occurs mainly along the coasts in the Southern part of the basin. The spatial variability is a result of

the superposition of several processes (spatially variable) including: (1) latitudinal gradient in CO_2 solubility, associated to the temperature gradient; (2) the east/west gradient due to the signature of the Atlantic water incoming though Gibraltar; (3) the biological activity; (4) the riverine alkalinity inputs. The anomaly map shown in Figure 3.3.1(panel c), highlights an increase

in carbon sink in some areas (at the dense water formation sites, at Gibraltar, in the southwestern part of the Basin and in the Aegean Sea, close to the Dardanelles strait) and a decrease in several other spots, i.e. along the southern coast, Adriatic Sea, and French coast.

Large uncertainties in the evaluation of the social costs of climate change have resulted in a wide range of estimates of the SCC (Tol 2018). To partially account for such variability and consistently with Melaku et al. (2015), we consider in this work a range of estimates to characterise the economic value of carbon sink flows in the Mediterranean based on the carbon fluxes calculated for the period under investigation (see Table 3.3.1). In particular, we consider the following sources: a recent review of SCC estimates in the literature (Tol 2018), the SCC from the baseline scenario in Nordhaus (2017), and the lower bound value calculated by van den Bergh and Botzen (2014). The yearly average exchange price in the EU Emission Trading Scheme (ETS) for the period 2012–2018 (EUA 2019) was also considered in the analysis as a market-based information on carbon prices. Prices in the EU ETS have substantially increased in 2018–2019, with the average auction price in March 2019 being 3.8 times higher than the average price during 2018.

All SCC estimates are converted to 2017 EUR using the 5-year average nominal exchange rate and GDP (Gross Domestic Product) deflators from the World Bank.[1] Given that the studies do not provide the necessary information for retroactively calculate SCC back to 2002, such values were applied over the entire period. Several recent studies have focused on producing estimates of individual countries' contribution to the SCC. In this paper, however, we retain a focus on a global SCC, which is the correct value to use from a global perspective (Ricke et al. 2018). Other approaches exist to account for the variability in SCC. Pendleton et al. (2012), for instance, suggested to use a stochastic approach. A comprehensive discussion on SCC estimates can be found in van den Bergh and Botzen (2014).

The temporal evolution of Carbon Sink Ecosystem Service in the Mediterranean Sea is shown in Figure 3.3.1(panel a) This value is the product of the service and the economic value associated with the service, depending on human preferences and on the human perception of the costs associated to the emission of an additional ton of carbon in the atmosphere. In details, the flow of the economic value of the CSES derived from the specific sea surface S, the in the time frame (t0, t1) is calculated in Equation (1) as:

$$V_0 = {}^{x\,y}\int_{t0}^{t1} C_{Flux}(x,\ y,\ t) \times SCC\,(t)dtdxdy \qquad (1)$$

where C_{FLUX} is the carbon dioxide flux, at each point of longitude (x) and latitude (y) of the sea surface at the time t, measured in ton/km^2/day (Data Ref #: 3.3.1) and is the cost associated to the emission of one additional ton of carbon at the time t (Full details of the method are provided in Melaku Canu et al. (2015)).

The valuation was done using the values of Table 3.3.1, that are almost constant during the whole period, except for the last few years, for which a nominal value was available (Figure 3.3.2).

When valuing the carbon sink service at the EEZ level, spatial differences appear among the different EEZ as a consequence of the differences in the surface of the different EEZ and due to the spatial variability of the carbon sink ecosystem service, as shown in the maps of Figure 3.3.1. CSES for the Mediterranean EEZ have been calculated for the year 2018, using the data presented in Products used table, as shown in Figure 3.3.3. When computing the ES value at the EEZ level, some countries will be associated with benefits for such service, while others may be located in the areas of negligible

Table 3.3.1. SCC estimates and market price of carbon emissions used in this analysis, with corresponding sources. (Data Ref # 3.3.2, 3.3.3, 3.3.4, 3.3.5 Products used table).

Data Source		Value (€/tonC)
EU-ETS	Average auction price 2018	55
Tol (2018)	SCC estimate, 33 percentile	114
Tol (2018)	SCC estimate, 67 percentile	412
van den Bergh and Botzen (2014)	SCC estimate	579
Nordhaus (2017)	SCC estimate Baseline	119

Figure 3.3.2. Temporal trend of CSES for the Mediterranean Sea for the period 2002–2018 calculated using the different carbon price estimates presented in Products used table (Data Ref. #: 3.3.1,.3.3.2,.3.3.3,.3.3.4, 3.3.5) and Table 3.3.1.
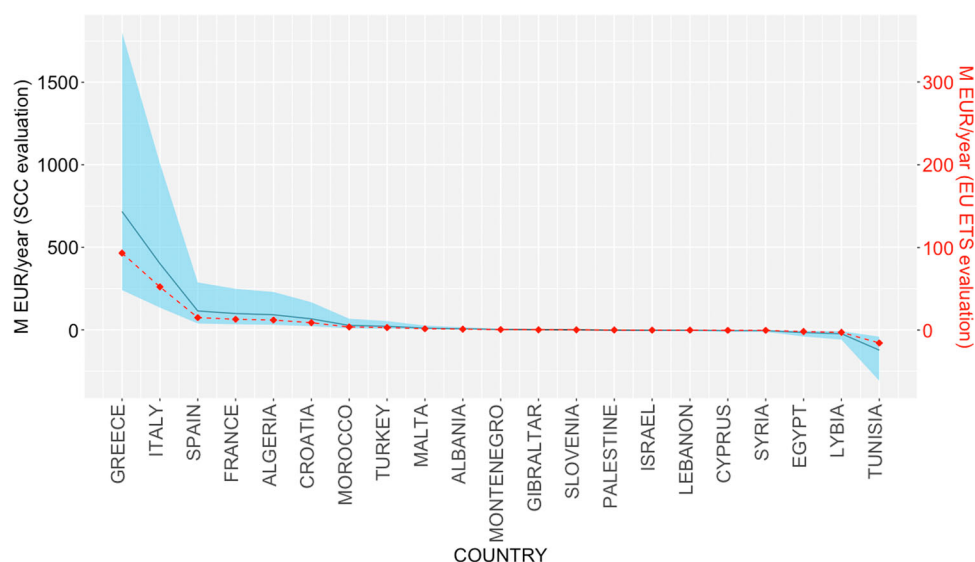
Figure 3.3.3. Ocean carbon sink ecosystem services values calculated for the exclusive economic zones EEZ of the Mediterranean countries using the net carbon fluxes at the EEZ elaborated from data presented in Products used table and the valuation of SCC and EU auction prices presented in Products used table (Data Ref # 3.3.1) and in Table 3.3.1 (van den Bergh and Botzen 2014; Nordhaus 2017; Tol 2018). Light blue area (primary axis): range of estimates using the range of SCC values. Red dots, (second axis): Values calculated using the 2018 yearly averaged EU-ETS auction are presented for comparison.

fluxes, or assigned a negative value if located along areas, which are mainly outgassing. Although we present here the value flows aggregated at the EEZ level because this is consistent with the country-level National Greenhouse Gas Inventory approach of the UNFCCC (https://unfccc.int/), already in use, the dynamic nature of sea and oceans instead calls for a basin scale governance, collective actions and coordinate responses in order to guarantee the commitment to sustainability goals.

Section 3.4: IBISAR service for real-time data ranking in the IBI area for emergency responders and SAR operators

Authors: Emma Reyes, Ismael Hernández-Carrasco, Adèle Révelard, Baptiste Mourre, Paz Rotllán, Eric Comerma, Tayebeh Tajalli Bakhsh, Anna Rubio, Julien Mader, Luis Ferrer, Christian De Lera Fernández, Enrique Álvarez-Fanjul, Joaquín Tintoré

Statement of Main Outcome: Reliable information of wind and currents is critical for responding effectively to maritime emergencies at an early stage of a disaster. IBISAR – www.ibisar.es – is a downstream service aiming to facilitate decision-making for Search and Rescue operators and marine emergency responders, by guiding them to select the most accurate ocean current prediction for a specific period and area of interest within the Iberian-Biscay-Irish regional seas. It combines multiple Copernicus Marine Service and allied complementary

data products, evaluates the skill of each model available and synthesises the information in a user-friendly way. This section focuses on the application and test of the assessment methodology envisioned by the service in two pilot areas: the Balearic Sea and the southeastern Bay of Biscay. Findings show that the modelling performance is strongly region-dependent and scenario-specific. This highlights the importance of the IBISAR service to keep up-to-date the skill assessment of all models available in the area and period of interest, since it can have a significant impact in minimising the response time, optimising search area planning, thus finally improving search and rescue and pollution control operations.

Products used:

Ref. No.	Product name and type	Documentation
3.4.1	GLOBAL_ANALYSIS_FORECAST_PHY_001_024 (Global Ocean 1/12 Physics analysis and forecast updated daily) Model	PUM:http://marine.copernicus.eu/documents/PUM/CMEMS-GLO-PUM-001-024.pdf QUID:http://resources.marine.copernicus.eu/documents/QUID/CMEMS-GLO-QUID-001-024.pdf
3.4.2	IBI_ANALYSIS_FORECAST_PHYS_005_001 (Atlantic Iberian-Biscay-Irish Ocean Physics Analysis and Forecast) Model	PUM:http://marine.copernicus.eu/documents/PUM/CMEMS-IBI-PUM-005-001.pdf QUID:http://resources.marine.copernicus.eu/documents/QUID/CMEMS-IBI-QUID-005-001.pdf

(Continued)

Continued.

Ref. No.	Product name and type	Documentation
3.4.3	MEDSEA_ANALYSIS_ FORECAST_PHY_006_013 (Mediterranean Sea Physics Analysis and Forecast) Model	PUM:http://resources.marine. copernicus.eu/documents/ PUM/CMEMS-MED-PUM-006- 013.pdf QUID:http://marine.copernicus. eu/documents/QUID/CMEMS- MED-QUID-006-013.pdf
3.4.4	NORTHWESTSHELF_ ANALYSIS_FORECAST_ PHYS_004_001_b (Atlantic – European North West Shelf – Ocean Physics Analysis and Forecast) Model	PUM:http://marine.copernicus. eu/documents/PUM/CMEMS- NWS-PUM-004-001.pdf QUID:http://resources.marine. copernicus.eu/documents/ QUID/CMEMS-NWS-QUID- 004-001-b.pdf
3.4.5	INSITU_GLO_UV_NRT_ OBSERVATIONS_013_048 (Global ocean in-situ near real time observations of ocean surface currents) In Situ	PUM: http://resources.marine. copernicus.eu/do cuments/PUM/CMEM S-INS-PUM-013-048.pdf QUID http://resources.marine. copernicus.eu/documents/ QUID/CMEMS-INS-QUID-013- 048.pdf Data source: Ibiza Channel: http://socib.es/? seccion=observingFacilitie s&facility=radar http://thredds.socib.es/ thredds/catalog/hf_radar/hf_ radar_ibiza-scb_ codarssproc001/catalog.html Bay of Biscay: http://www. euskoo s.eus/en/radar-higer-en/ Scientific references: Ibiza Channel (Lana et al. 2015) Bay of Biscay (Solabarrieta et al. 2014)
3.4.6	INSITU_MED_NRT_ OBSERVATIONS_013_035 (Mediterranean Sea in-situ near real time observations) In Situ	PUM: http://marine.copernicus. eu/documents/PUM/CMEMS- INS-PUM-013.pdf QUID: http://marine.copernicus. eu/documents/QUID/CMEMS- INS-QUID-013-030-036.pdf
3.4.7	SOCIB-WMOP (Balearic Islands Coastal Observing and forecasting System – Western Mediterranean OPerational forecasting system) Model	System description: http:// www.socib.eu/?seccion= modelling&facility=forecast_ system_description Data source: http://thredds. socib.es/thredds/catalog/ operational_models/ocea nographical/hydrodyna mics/wmop/catalog.html Scientific references: Juza et al. (2016) and Mourre et al. (2018).
3.4.8	PUERTOS-SAMOA (System of Meteorological and Oceanographic Support for Port Authorities) CST_BIL (Bilbao coastal domain – SE Bay of Biscay) Model	System description: http://www. puertos.es/es-es/proyectos/ Paginas/SAMOA.aspx https://upcommons.upc.edu/ bitstream/handle/2117/ 116102/21977687.pdf; jsessionid=7B06B93423F8 927B783F87804504FD1E? sequence=3 Data source http://opendap. puertos.es/thredds/catalog/ circulation_coastal_bil/catalog. html Scientific references: Álvarez-Fanjul (2018)

(Continued)

Continued.

Ref. No.	Product name and type	Documentation
3.4.9	SASEMAR- Drifters In-Situ	Data source: internal data base from the Spanish Maritime Safety Agency Drifter1: ZUNIBAL- ZSP001000033 (deployed in summer from 2018) Drifter2: ZUNIBAL- BTK003000873 (deployed in winter from 2019) Scientific references: paper in prep.

Operational oceanography aims to provide timely and accurate observations and predictions of the marine environment and offer dedicated services to marine stakeholders and the general public. In order to support their decisions, government agencies and private companies in charge of maritime safety and marine pollution control use Search and Rescue and environmental risk modelling applications. These tools, mostly based on Lagrangian models for trajectory prediction of e.g. drifting targets or oil spills, ultimately rely on accurate wind and current forecasts to properly determine the optimal search region.

The multiple ocean forecasts available, with different parameterisations and levels of complexity, ensure the data availability in near real-time for a specific region. As a drawback, when each model provides a different outcome, the key concern of many targeted users is: which ocean current prediction should I select to run my applications? Skill assessment methods are required to estimate the level of confidence in the different predictions, and this information should be displayed in a user-friendly way, using easily interpretable metrics.

Addressing user needs, the IBISAR service (www. ibisar.es) provides real-time data of the ocean current forecasts available in the Iberian-Biscay-Irish regional seas and evaluates their performance. Built on an existing operational service developed by RPS Ocean Science (www.rpsgroup.com/) it consists of an automated process that helps the user to identify the most accurate ocean current prediction. The service includes three elements (as schematised in Figure 3.4.1): (1) the regularly updated database of current forecasts and observations; (2) the graphical user interface, acting as a single access point for serving and visualising all available data; (3) the skill assessment functionality, which evaluates the reliability of the different current forecasts. In this section, we apply and test the quantitative method used by the science-based service for assessing the skill of each data source and discuss the results obtained in two pilot areas with varying dynamical conditions.
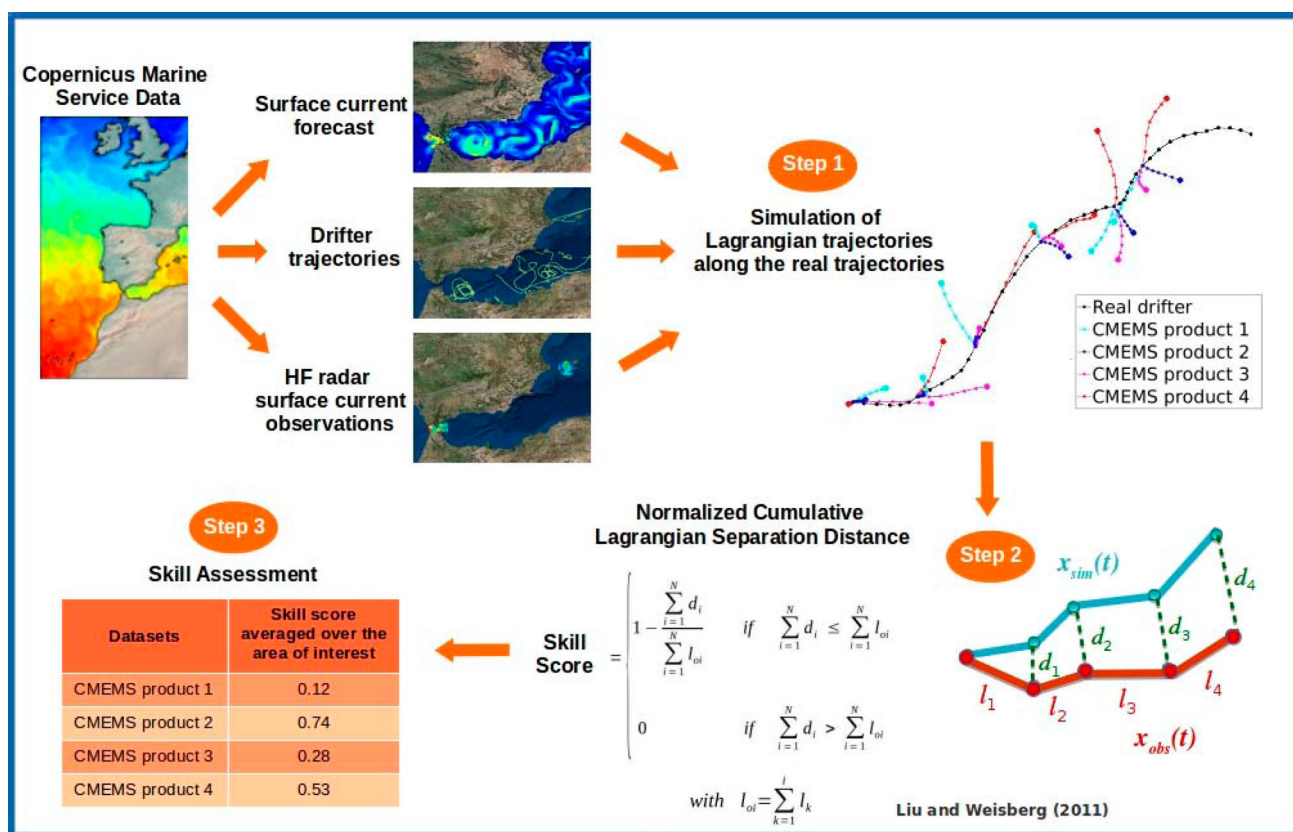
Figure 3.4.1. Schema showing how Copernicus marine service data products are used to assess the performance of different forecasts in the IBISAR downstream data service. Starting from the top-left corner, the figure shows the Copernicus Marine Service models (product ref 3.4.1–3.4.4) and in-situ observations (product ref. 3.4.5–3.4.6) datasets integrated in the IBISAR catalogue. The visualisation of all datasets is displayed by means of an integrated OGC OpenGIS® Web Map Service (WMS) interface standard. The methodology envisioned by the IBISAR Skill Assessment is summarised in three steps: (1) it simulates trajectories using all available current forecast models within the period and region of interest; (2) it compares simulated against observed drifter trajectories according to the Normalized Cumulative Lagrangian Separation (NCLS) distance developed by Liu and Weisberg (2011) and finally (3) it computes the averaged skill score obtained for each dataset. The model reliability information is finally synthesised and displayed in a table.

In the operational ocean model assessment framework, IBISAR supports ongoing efforts to develop adequate evaluation tools, which are essentially built on statistical metrics obtained by comparing against in-situ data (Hernández et al. 2015; Mourre et al. 2018). Moreover, it is also aligned with the validation and verification of ocean numerical simulations activities to implement the long-term strategy developed by CMEMS (Hernández and Melet 2016; Le Traon et al. 2017). IBISAR is accessible online since December 2019, under subscription.

The IBISAR service includes all Copernicus Marine Service forecast models (product ref 3.4.1–3.4.4) available in the Iberian-Biscay-Irish regional seas as well as several downscaling of the formers over regional and coastal areas. Within the latter, SOCIB-WMOP for the Western Mediterranean (Tintoré et al. 2013; Juza et al. 2016; Mourre et al. 2018, product ref 3.4.7) and PUERTOS-SAMOA for the Bilbao harbour (Álvarez-Fanjul 2018, product ref 3.4.8) are used in this section.

In order to assess the performance of the forecast, satellite-tracked surface drifter trajectories are used as reference (ground-truth) source. In the Balearic Sea, four shallow drogued ODi sphere surface drifters (product ref. 3.4.6), with minimal wind drag effects, were tracked from the 28th July to September 2016. In the Bay of Biscay, two Zunibal drifters (product ref 3.4.9), which respond to surface currents and partially to the direct wind drag effect, were deployed and tracked by the Spanish Maritime Safety Agency during its routine exercises on the 17–19th September 2018 and 12–14th February 2019. An additional novelty of IBISAR is the integration of HF radar surface currents (product ref. 3.4.5), one of the observing platforms from the CMEMS new service release of the 16th April 2019. From all Spanish HF radar systems available in the service, those from the Ibiza Channel (Lana et al. 2015) and the Bay of Biscay (Solabarrieta et al. 2014) are considered here. With the purpose of obtaining radar-derived Lagrangian trajectories, the generation of HF radar gap-filled products

are required (Solabarrieta et al. 2016; Hernández-Carrasco, Orfila, et al. 2018, Hernández-Carrasco, Solabarrieta, et al. 2018). To do this we apply the Open-boundary Modal Analysis methodology, implemented by Lekien et al. (2004) and further optimised by Kaplan and Lekien (2007), using the modules of the HFR Progs Matlab package (https://github.com/rowg/hfrprogs). Since HF radar derived surface currents can also be used as an alternative of the models for backtracking drifting objects, with a demonstrated effectiveness of the HF radar short term predictions (Zelenke 2005; Barrick et al. 2012; Frolov et al. 2012; Orfila et al. 2015; Solabarrieta et al. 2016; Vilibić et al. 2016; Abascal et al. 2017) in coastal risk-prone regions, they have also been evaluated. However, although not included in this section, HF radar could also be used as a benchmark (i.e. reference source), complementing the drifter observations, allowing us to routinely and systematically evaluate the performance of model prediction over wider coastal areas.

The methodology used in IBISAR evaluates the reliability of each current forecast and HF radar observations available within the period and region of interest in three steps (see Figure 3.4.1): (1) for each available satellite-tracked drifter, simulated trajectories are initialised hourly from the observed drifter locations and the virtual particles are tracked for the next 6 h, a relatively short time scale (e.g. tidal to synoptic weather) for model assessment useful for maritime safety and environmental protection applications (Liu and Weisberg 2011) and also adapted to the usual operational time framework of safety agencies; (2) it evaluates the distance between pairs of observed-predicted trajectories and computes a metric named Skill Score at hourly intervals over the 6 h of simulation; (3) it averages the Skill Scores obtained for each simulated trajectory over the area and period of interest. The Skill Score is based on the Normalized Cumulative Lagrangian Separation (NCLS) distances (Liu and Weisberg 2011; see equations in Figure 3.4.1). It is a dimensionless index ranging from 0 to 1; the higher the skill score value, the better the model performance, with a value equal 1 implying a perfect match between observation and simulation. This approach is gaining popularity in evaluating trajectory models for oil spill and SAR operations (Ivichev et al. 2012; Mooers et al. 2012; Röhrs et al. 2012; Liu et al. 2014) after being used in the context of the Deepwater Horizon oil spill (Liu and Weisberg 2011; Mooers et al. 2012; Halliwell et al. 2014). As it is stated in Liu and Weisberg (2011), this methodology is particularly useful when the number of drifter trajectories is limited and neither a conventional Eulerian-based velocity nor a Lagrangian-based probability density function may be estimated. However, the current lack of drifter availability in coastal risk-prone areas restrict the robustness of the methodology and consequently it would reduce the

potential of the downstream data service based on it. Addressing this drawback, the IBISAR service provides both real-time and historical evaluations according to the data availability.

For this study, the simulated trajectories of virtual particles advected by different surface velocity fields were all computed using the COSMO Lagrangian model (described by Jiménez Madrid et al. 2016) from the Institute of Marine Sciences of Barcelona, which is a free software available in github repository (https://github.com/quimbp/cosmo, version from 5 Jun 2019, DOI:10.5281/zenodo.3522268). It consists of a fifth-order Runge–Kutta integration scheme, bicubic spatial interpolation of the gridded velocity field and third order Lagrange polynomials in time. Although the validation of the Lagrangian model COSMO is out of the scope of this section, it was verified that the trajectories simulated by COSMO using SOCIB-WMOP currents agreed with the ones simulated with CDrift (Sayol et al. 2014), as shown in Figure 3.4.2.

Furthermore, the use of a single Lagrangian model for all experiments allows a more accurate cross-area comparison of the results. Here we present and discuss the results of applying and testing this methodology in two of four of the considered pilot areas, where CMEMS, regional and coastal ocean models overlap and several observational networks are available (with HF radar systems included). These regions are the Balearic Sea (Figure 3.4.3), which is an area with complex dynamic due to the interaction between different water masses and associated permanent density-driven currents (Font et al. 1988; La Violette et al. 1990; Pinot et al. 2002; André et al. 2005), and the southeastern Bay of Biscay (Figure 3.4.4), which is marked by a strong seasonality of the Iberian Poleward Current (Rubio et al. 2019) and related mesoscale variability along the slope (Rubio et al. 2018). The full report gathering the results from the four pilot areas, comprising the evaluation with 144 drifters is available in www.ibisar.es.

Figure 3.4.3 shows the skill score obtained over the four drifters tracked in the Balearic Sea from July to September 2016, after 6 h of simulation using three CMEMS models, the regional model SOCIB-WMOP and the HF radar. During this experiment, all drifters got entrained into the Balearic Current, being transported northeastward through the Balearic Sea. Considering the entire region, the CMEMS global (product ref 3.4.1) and the regional model of the Iberian-Biscay-Irish seas (product ref. 3.4.2) show the best performance with similar averaged skill scores of 0.261 and 0.26, respectively. Higher score values (>0.7) in the northern part of Ibiza island and Mallorca channel indicate better model performances in this area. The SOCIB-WMOP model (product ref. 3.4.7) and its parent model, the CMEMS regional
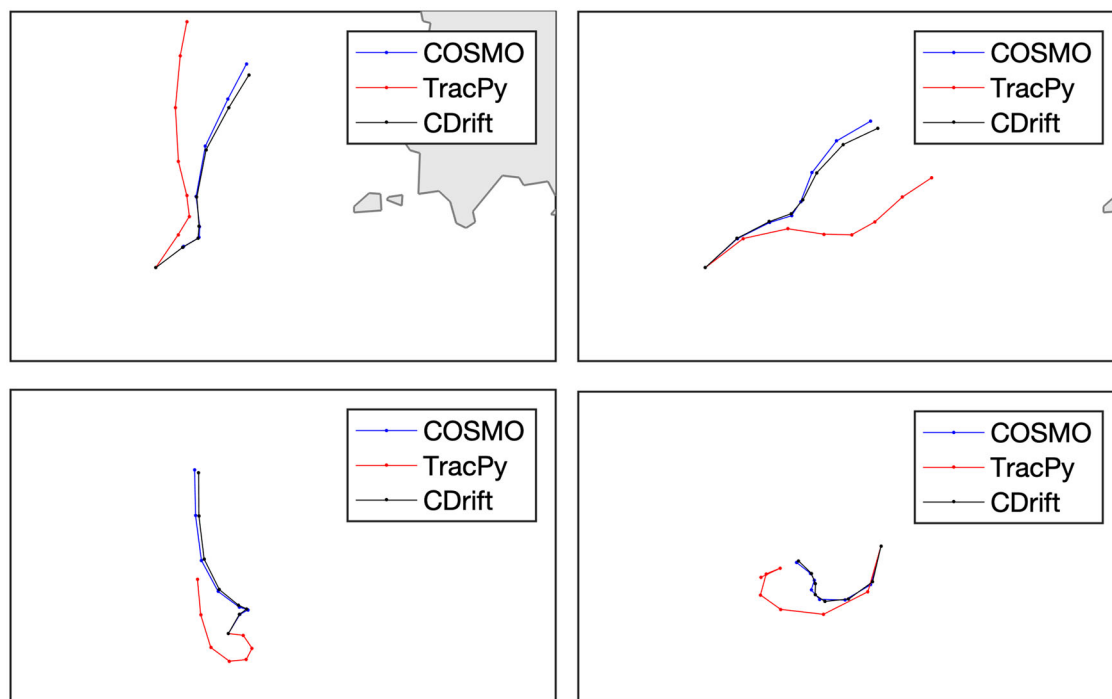
Figure 3.4.2. Virtual particle trajectories simulated by three different Lagrangian models: COSMO (blue line); TracPy-TRACMASS (red line) and CDrift (black line) with diverse advection schemes and different spatio-temporal interpolation, advected by the surface current field from SOCIB-WMOP (product ref. 3.4.7)

model of the Mediterranean Sea (product ref. 3.4.3), present also similar skill score values of 0.213 and 0.241, respectively. However, in the north-northwest part of Ibiza island, SOCIB-WMOP presents higher values (> 0.6). Focusing on the northern part of the Balearic Sea (north of latitude 40°N), none of the models show a good performance, probably due to their difficulties in representing the soutwestward quasi-permanent barotropic large-scale alongshore Northern Current – NC – jet (Font et al. 1988). However, the CMEMS regional model of the Iberian-Biscay-Irish seas performs better than the others along the Catalan shelf, reaching skill score values > 0.6. On the contrary, when focusing on the Ibiza Channel (black-line rectangle in Figure 3.4.3), most of the models and the HF radar present good skills (> 0.4). In this area, the CMEMS regional model for the Mediterranean Sea (product ref 3.4.3) shows the best performance (skill score of 0.619) for this specific period, which somewhat unexpectedly, improves the skills of the HF radar (skill score of 0.482, product ref 3.4.5) and the solution of its child model forecast, the regional model SOCIB-WMOP (skill score of 0.362, product ref. 3.4.7). This is because the CMEMS regional model was capable of predicting the observations of inertial oscillations depicted by drifters (not shown), while the HF radar gap-filled surface currents were not able to properly reproduce some of these circularly polarised currents in this specific event (dark blue points of Figure 3.4.3

(d)). It must also be considered the strong smoothing character of the OMA analysis, which can remove small features from the velocity field (Kaplan and Lekien 2007; Hernández-Carrasco, Solabarrieta, et al. 2018). In addition, the meridional velocities of the surface current are only moderately well reproduced by the HF radar as previously reported by Lana et al. (2016) and, in this particular case, the flow across the Ibiza Channel was predominantly meridional.

Figure 3.4.4 shows the skill score over the two drifters released in the southeastern Bay of Biscay after 6 h of simulation using four CMEMS models, the PUERTOS-SAMOA-Bilbao coastal model and the HF radar. Drifter 1 was tracked for two days during late summer (17–19 September 2018) while it became temporarily trapped in an eddy. Drifter 2 was tracked for two days during winter (12–14 February 2019) and got entrained into the shelf-slope Iberian Poleward Current, which is particularly persistent and intense during this season (Le Cann and Serpette 2009; Herbert et al. 2011; Charria et al. 2013; Rubio et al. 2019), being transported eastward along the Spanish coast. On average, the regional CMEMS model of the Iberian-Biscay-Irish regional seas (product ref. 3.4.2) shows the best performance (∼0.357) for both periods, reaching skill score values higher than 0.9 in some areas, and better than the higher-resolution downscaled coastal model PUERTOS-SAMOA-Bilbao (∼0.329). As expected, the
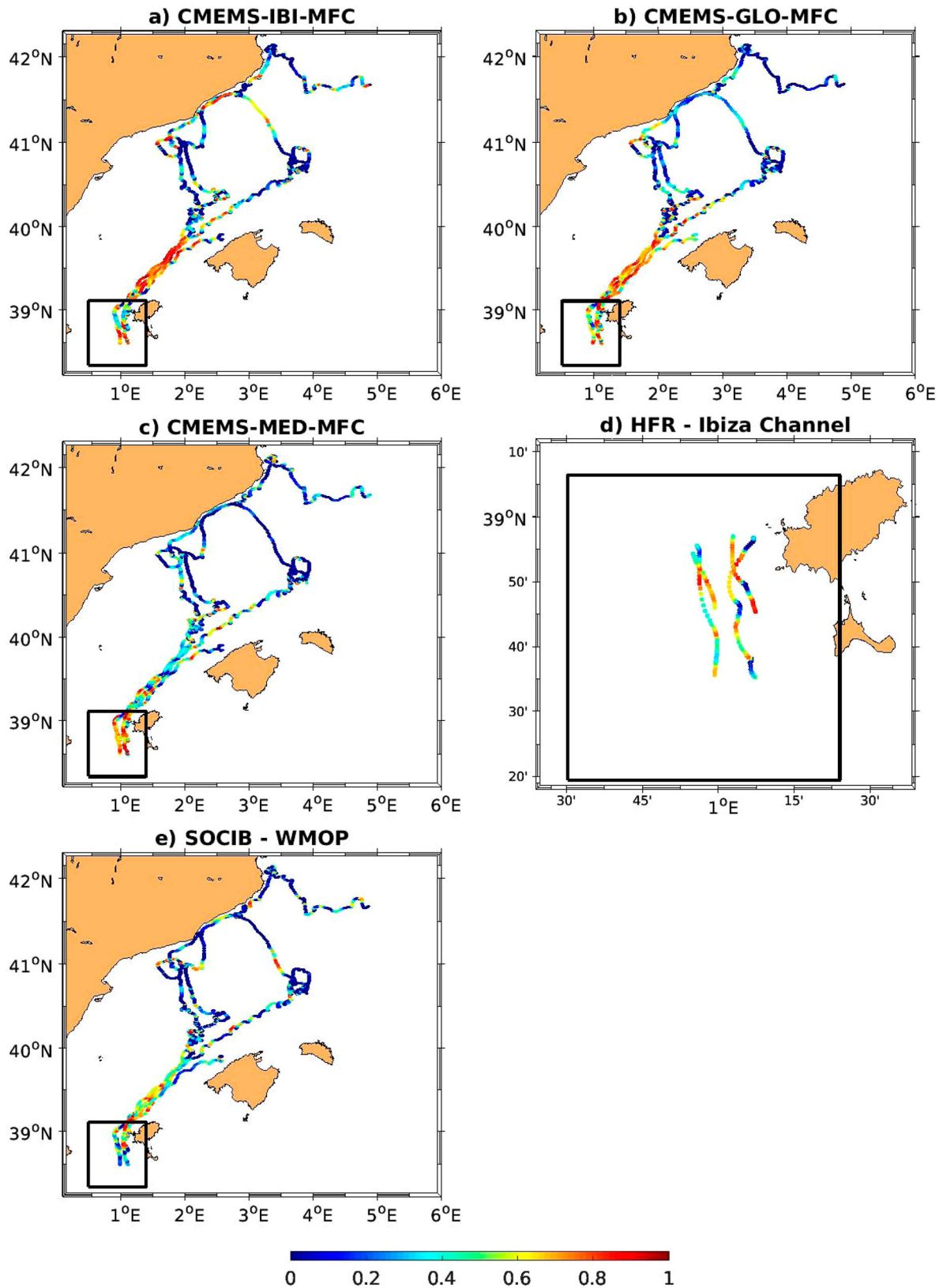
Figure 3.4.3. Map of the Balearic Sea showing the spatial distribution of skill scores for the following datasets: (a) CMEMS IBI-MFC (product ref. 3.4.2); (b) CMEMS GLO-MFC 1/12 (product ref. 3.4.1); (c) CMEMS MED-MFC (product ref. 3.4.3); (d) HF radar data from the Ibiza Channel system (product ref. 3.4.5) and (e) SOCIB-WMOP (product ref. 3.4.7); after 6 h of simulation comparing 4 real drifters available in the area from July to September 2016. Black-line rectangle shows the bounding box around the region of interest over the Ibiza Channel, covering the HF radar footprint area.
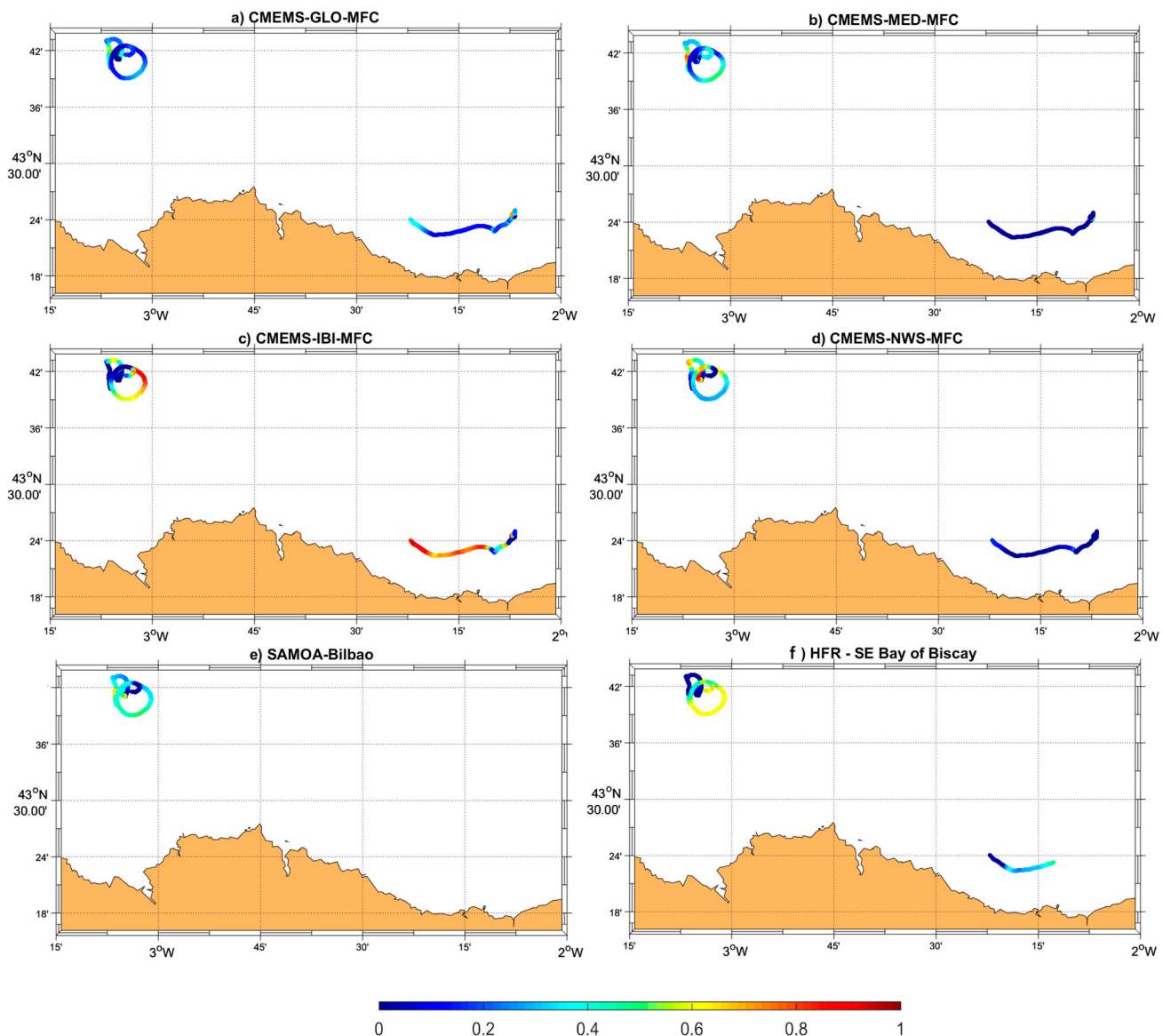
Figure 3.4.4. Map of the SE Bay of Biscay showing the spatial distribution of skill scores for the following datasets: (a) CMEMS GLO-MFC 1/12° (product ref. 3.4.1); (b) CMEMS MED-MFC (product ref. 3.4.3); (c) CMEMS IBI-MFC (product ref. 3.4.2); (d) CMEMS NWS-MFC (product ref. 3.4.4); (e) PUERTOS-SAMOA-Bilbao (product ref. 3.4.8); and (f) HF radar data from the Biscay system (product ref. 3.4.5). The simulation periods were from 17 to 19 September 2018 for drifter 1 – product ref. 3.4.9 – (temporarily trapped in an eddy) and from 12 to 14 February 2019 for drifter 2 – product ref. 3.4.9 – (transported eastward along the Spanish coast). PUERTOS-SAMOA-Bilbao dataset was only available for drifter 1 and the HF radar dataset was available for about 20 h for drifter 2.

regional CMEMS model of the Mediterranean shows the lowest skill score (∼0.158), since it does not include tidal forcing, which is particularly important in this area (Piraud et al. 2003). When considering only drifter 1, the former model and the HF radar present similar skill score values on average (∼ 0.3), while the highest scores are reached by the CMEMS-NWS-MFC (∼0.403). However, none of the models neither the HF radar are able to reproduce the entire eddy-like trajectory of the drifter. In this experiment, the HF radar surface currents (product ref. 3.4.5) do not perform better than the simulated ones, probably because the drifter trajectories were very close to the edge of the areas where HF radar total currents can be computed. In this area the resulting currents are known (Chapman et al. 1997; Cook et al. 2007) to have a higher observational error amplified through the geometric dilution of precision.

In conclusion, selecting the most accurate ocean current prediction for running an application might be a key concern for end users, particularly when multiple choices are available and each one provides a different outcome. Here we have presented the results of applying and testing the methodology envisioned by the IBISAR service

for assessing the performance of all available current forecasts in the Balearic Sea and the southeastern Bay of Biscay. The models have shown varying levels of skills in predicting the trajectory of the observed drifters, depending on the region and on the analysed period, mainly related to their different capacities to reproduce coastal processes (e.g. inertial oscillations, submesoscale eddy activity, intensification of the Iberian poleward current) and diverse flow regimes (including seasonal modulation).

One surprising result is the better performance of some models when compared to the HF radar derived surface currents for some of the scenarios considered. As the skill score is region-dependant and scenario-specific, this might not be a general rule, and more similar experiments are needed to be able to draw some conclusions. Furthermore, it should be considered that skill scores computed at the model domain boundaries and in areas with higher HF radar observational errors penalises the overall results.

Findings highlight the need of including this type of skill assessment services to evaluate and monitor the performance of operational systems and the accuracy of its products in order to unlock their potential for different applications.

Acknowledgements

Section 3.5: Surface picture of the Levantine Basin as derived by drifter and satellite data

Authors: Milena Menna, Giulio Notarstefano, Pierre-Marie Poulain, Elena Mauri, Pierpaolo Falco, Enrico Zambianchi

Statement of main outcome: Ocean circulation derived from drifter data covers not only oceanographic and climate research but also spread and retention of pollutants. The latter field has a strong societal impact because it is able to give the measure of political action efficiency in such a delicate sector. Moreover, it is able to actively improve the policy-making of the environmental governance. The scientific knowledge derived from such a topic is transferable easily to the public in an accessible form to benefit the relationship between science and society and to respond better to the human needs.

The surface circulation in the Levantine Basin derives from the complex interaction among multi-scale flow patterns, producing a high spatio-temporal variability of the current field. A considerable amount of in situ data has been collected in this region, giving us the opportunity to produce an updated version of the surface current paths (1993–2018). Drifter data are compared with satellite altimetry data in order to define a detailed and complete picture of the main quasi-permanent structures and of the along-slope currents. This updated description of the circulation pattern reinforces the work of the scientific-societal communities in defining the southeastern Levantine basin as the most critical area of marine litter accumulation.

Data use:

Ref. No.	Product name and type	Documentation
3.5.1	SEALEVEL_MED_PHY_L4_NRT_ OBSERVATIONS_008_050 SEALEVEL_MED_PHY_L4_REP_ OBSERVATIONS_008_051	PUM: http://marine.copernicus.eu/ documents/PUM/CMEMS-SL-PUM-008-032-051.pdf QUID: http://marine.copernicus.eu/ documents/QUID/CMEMS-SL-QUID-008-032-051.pdf
3.5.2	INSITU_MED_NRT_ OBSERVATIONS_013_035	PUM: http://marine.copernicus.eu/ documents/PUM/CMEMS-INS-PUM-013.pdf QUID: http://marine.copernicus.eu/ documents/QUID/CMEMS-INS-QUID-013-030-036.pdf

3.5.1. Introduction

The marine litter has really become a serious problem in the Mediterranean Sea. This issue is intensified by the limited exchanges of the Mediterranean with the open ocean, the high degree of urbanisation along the coasts and the high level of maritime traffic. The pollution caused by marine litter can deeply impact human and animal health and create an economic damage to the societal environment. The most abundant marine litter items worldwide are plastics (Gregory and Ryan 1997)

and they constitute more than 80% of the floating debris in the Mediterranean Sea (Galgani 2014; Suaria and Aliani 2014). Their persistence in the marine environment and their slow degree of degradation (Barnes et al. 2009) make the plastics a threat that has to be monitored and possibly reduced.

The geography of the Mediterranean basin and its general surface circulation scheme contribute to create a sort of re-circulation system of floating debris in which they are distributed into possibly retention and stranding areas within the basin.

Recently, Lagrangian models and in-situ data have been used to estimate the drift of floating debris (Mansui et al. 2015; Liubartseva et al. 2018) and the probability of debris particles to reach different areas of the Mediterranean basin (Zambianchi et al. 2017). The results of the mentioned studies have defined the Southern Levantine basin as a sort of 'garbage patch' of the Mediterranean, where the surface currents contribute to enhance the local increase of floating litter (Zambianchi et al. 2017). In particular, the southern coast of the Levantine seems to be a site of destination/accumulation of pollution that extent also towards Syria and the Cilician area (Mansui et al. 2015; Liubartseva et al. 2018). Currently, the statistics performed in Zambianchi et al. (2017) are based on Lagrangian drifter data updated to 2014. The aim of this work is to provide an updated version of the surface circulation patterns in the Levantine sub-basin, adding the copious drifter data collected after 2014.

3.5.2. Results and discussion

Drifter velocities (CMEMS product Ref. No. 3.5.2), collected in the Levantine basin during the period 1993–2018 (Figure 3.5.1), are compared with the concurrent satellite altimetry products (Absolute Dynamic Topography – ADT, CMEMS product Ref. No. 3.5.1) in order to add new and further insights to the mean and seasonal circulation patterns of this area. More details about the drifter data processing are available in Menna et al. (2017, 2018).

The two datasets fit rather well (Figure 3.5.1(b)) and define the well-known cyclonic coastal circuit in the Levantine sub-basin (Menna et al. 2012) with strength as large as 15 cm/s along the southern and eastern coasts (Libyo-Egyptian Current – LEC) and larger than 25 cm/s along the northern coast (Cilician Current – CC – and Asia Minor Current – AMC), in agreement with the results of Menna et al. (2012). The interior of the Levantine basin is longitudinally divided into two parts by the zonal meandering Mid-Mediterranean Jet (MMJ; speeds of 10–15 cm/s), with prevalent anticyclonic/cyclonic

structures located southern/northern of the MMJ pathway. For some years after the publication of Millot and Taupier-Letage (2005) and Millot and Gerin (2010) there was a debate about the existence of the MMJ. According to the above-mentioned authors, the MMJ may not be a proper eastward current but it can correspond to the northern limb of the anticyclonic eddies generated by the instability of the along-slope LEC. Nevertheless, the work published thereafter by Menna et al. (2012), Poulain et al. (2012), Schroeder et al. (2012) and more recently by Mauri et al. (2019) demonstrate unambiguously the existence of the MMJ.

The main anticyclonic structures that characterise the surface current field south of the MMJ signature are the mesoscale Egyptian eddies (EE; speeds of 10 cm/s) derived from the instability of the along-slope current (Hamad et al. 2005, 2006; Menna et al. 2012), the sub-basin scale Mersa-Matruh Gyre (MMG; maximum speeds of ∼ 25 cm/s) and Cyprus Gyre (CG, mean speeds of 10–20 cm/s) (Gertman et al. 2007; Mauri et al. 2019). The Shikmona Eddy (ShE) is defined in literature as a very complex system, composed of several cyclonic and anticyclonic eddies (Gertman et al. 2007; Mauri et al. 2019), and formed as pinched off meanders from the instability of the coastal current (Menna et al. 2012); its position, sizes and intensities vary markedly over time (Mauri et al. 2019). The mean pattern of the ShE is cyclonic (Figure 3.5.1(b)) in the period 1993–2018.

The main cyclonic structures located north of the MMJ signature (Figure 3.5.1(b)) are the sub-basin scale Western Cretan Gyre (WCG; speeds of 10–15 cm/s) and the Rhodes Gyre (RG; speeds of 15–25 cm/s). In addition to these large cyclones, there is a mesoscale cyclonic eddy generally squeezed between Syria and the eastern Cyprus coasts, known as Latakia Eddy (LTE; speeds of 10 cm/s). The LTE is generated by the interaction between the MMJ and the northward coastal current (Zodiatis et al. 2003; Menna et al. 2012). The cyclonic pattern along the northern coasts of the Levantine is interrupted only by the anticyclonic, wind-driven Ierapetra Gyre (IG; speeds of 15 cm/s), induced by the northeasterly Etesian winds (Amitai et al. 2010). Altimetry data point out another cyclonic mesoscale structure (centred at 33.7°N and 25.3°E) that has never been described before in literature as a stand-alone structure, but sometimes it is included in the WCG system (e.g. Poulain et al. 2012; Pinardi et al. 2015). The occurrence of a recurrent cyclonic structure in this region is confirmed by the DYNED-Atlas database (Le Vu et al. 2017; https://dyned.cls.fr/seewater/#!&page=isv-mainPage), that uses the Angular Momentum Eddy Detection Algorithm in the period 2000–2017, to locate and track the surface signature of mesoscale eddies in
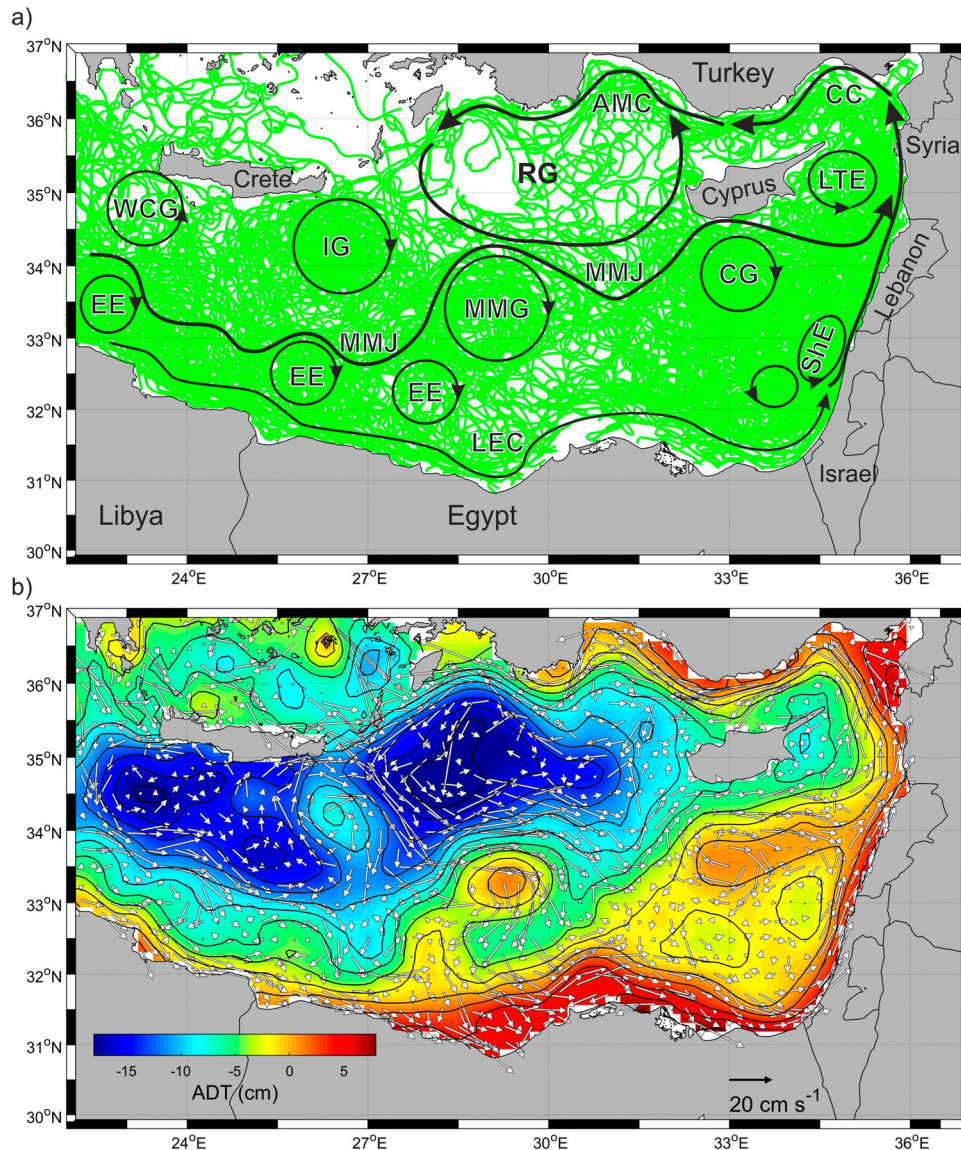
Figure 3.5.1. (a) Drifter trajectories and (b) mean drifter currents (arrows, CMEMS product Ref. No. 3.5.2) in bins of 0.25° x 0.25° super-imposed on the mean map of ADT (CMEMS product Ref. No. 3.5.1) between 1993 and 2018. Black arrows in (a) emphasise the location of the main currents, sub-basin and mesoscale eddies and gyres adapted from Menna et al. (2012); acronyms are defined in the text. Black contour lines in (b) are referred to the ADT field.

the Mediterranean Sea. The DYNED-Atlas database describes a cyclonic structure whose core is located between 33.4°N and 34.3°N and between 24.7°E and 25.7°E for over a third of the 17 years analysed. This mesoscale cyclone, located southwest of the IG, is defined hereafter as Southern Cretan Eddy (SCE; speeds of 5–10 cm/s). Drifter derived currents do not clearly identify the edge of the SCE (due to their non-homogenous spatial and temporal sampling) but detect the occurrence of a cyclonic meander in this region.

The seasonal variability of the surface currents field was estimated dividing the dataset in two extended seasons, selected following the suggestion of Menna et al. (2012): the extended winter corresponds to January–

June (Figure 3.5.2(a)), and the extended summer to July–December (Figure 3.5.2(b)). The dataset used in this work allows to add more details than the previous literature on the seasonal variability of circulation structures, especially in the easternmost part of the Levantine where, after 2010, a conspicuous amount of drifter data was collected in the framework of some international projects. The WCG, IG, MMG, and the southern limb of the RG are more dynamic in summer (Figure 3.5.2 (b); speeds up to 30 cm/s), as well as the CC, AMC and the LTE (speeds larger than 20 cm/s). The CG is more intense in winter (Figure 3.5.2(b); speeds of 10–15 cm/s), whereas it appears weaker and zonally elongated during summer (Figure 3.5.2(b); speeds of

10–15 cm/s). The ADT values are generally higher in summer. The SCE is a permanent structure observed in both the seasons with greater intensity during summer (speeds of 18 cm/s); its shape and location are influenced by the seasonal and interannual variability of IG.

The year 2018 is characterised by higher intensity of the anticyclonic structures (Figure 3.5.3(a)) compared to the mean field of the period 1993–2018 (Figure 3.5.1 (b)). Drifters entrapped in the MMG show a strengthening of this feature (speeds larger than 40 cm/s) and an increase of its longitudinal extension (diameter of about 400 km). The centre of the CG (Figure 3.5.3(a)) is shifted to the west with respect to its mean location (Figure 3.5.1(b)), and the main lobe of the ShE is anticyclonic and located south east of Cyprus (Figure 3.5.3 (a)). The cyclonic activity is weakened in the region of the RG and the SCE disappears (Figure 3.5.3(a)). The sea level rises almost everywhere with larger increments along the coasts, in the IG and MMG and south of Cyprus (Figure 3.5.3(b)).

Figure 3.5.2. Mean drifter currents (arrows, CMEMS product Ref. No. 3.5.2) in bins of 0.25°x 0.25° superimposed on mean map of ADT (CMEMS product ref. No. 3.5.1) in the extended winter (a) and extended summer (b). Contour lines refer to the ADT field.

Model results by Zambianchi et al. (2017) represent probabilities of finding particle retention areas based on the transition matrix of drifters deployed in the Mediterranean and floating until 2014, showing a marked asymptotic maximum in the southeastern Levantine basin. The above discussed more recent drifter data show, in particular, an intensification of anticyclonic eddies developing in that same area, namely south of the MMJ. As recently

discussed by Brach et al. (2018) in a comparative analysis between cyclonic and anticyclonic eddies in a similar context, the latter show a much stronger capacity to entrap litter particles. For this reason, we expect that the situation of 2018 may have led to an even enhanced accumulation off the coasts of Libya and Egypt, and a possible resulting northeastward migration as hypothesised by Liubartseva et al. (2018).
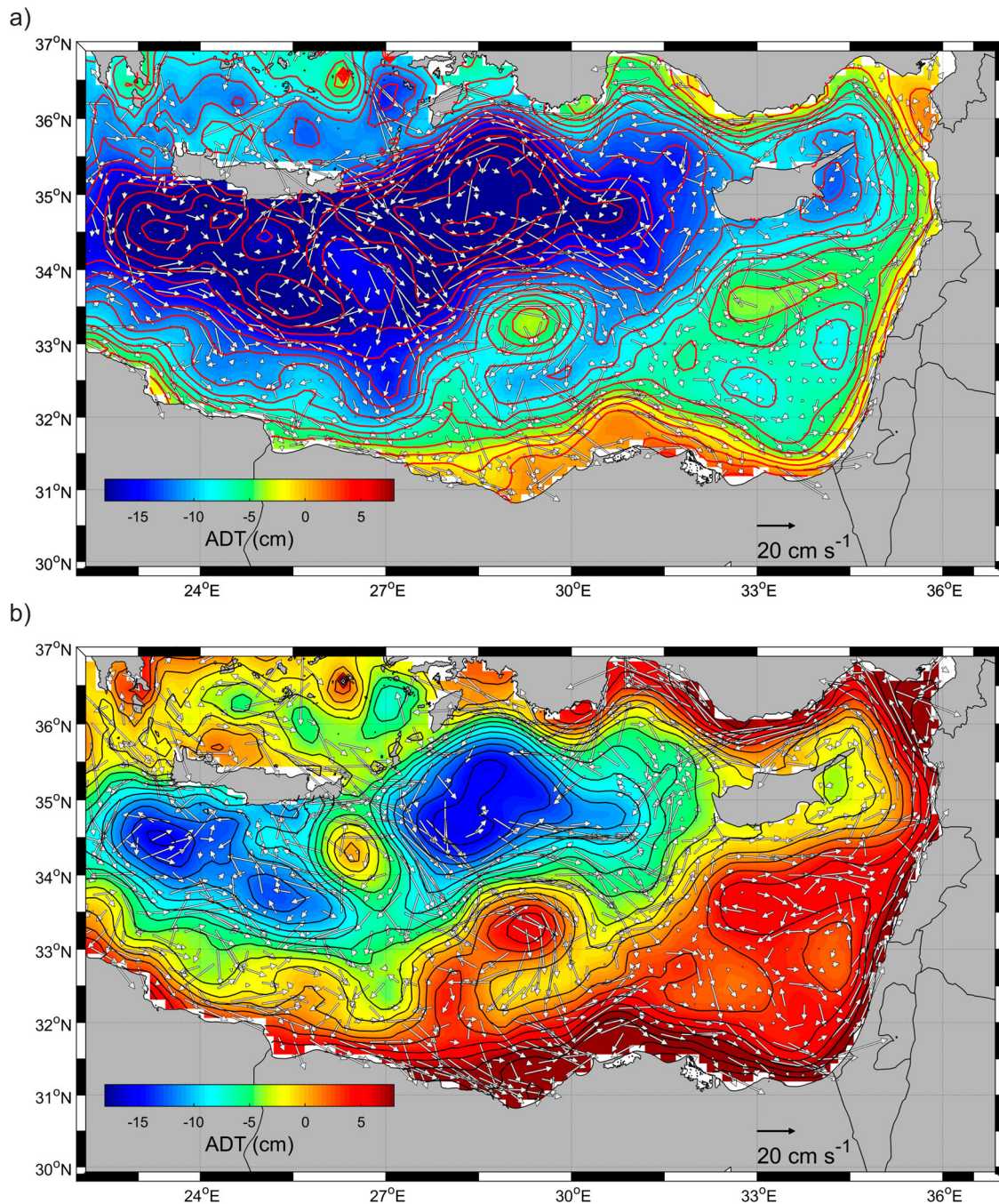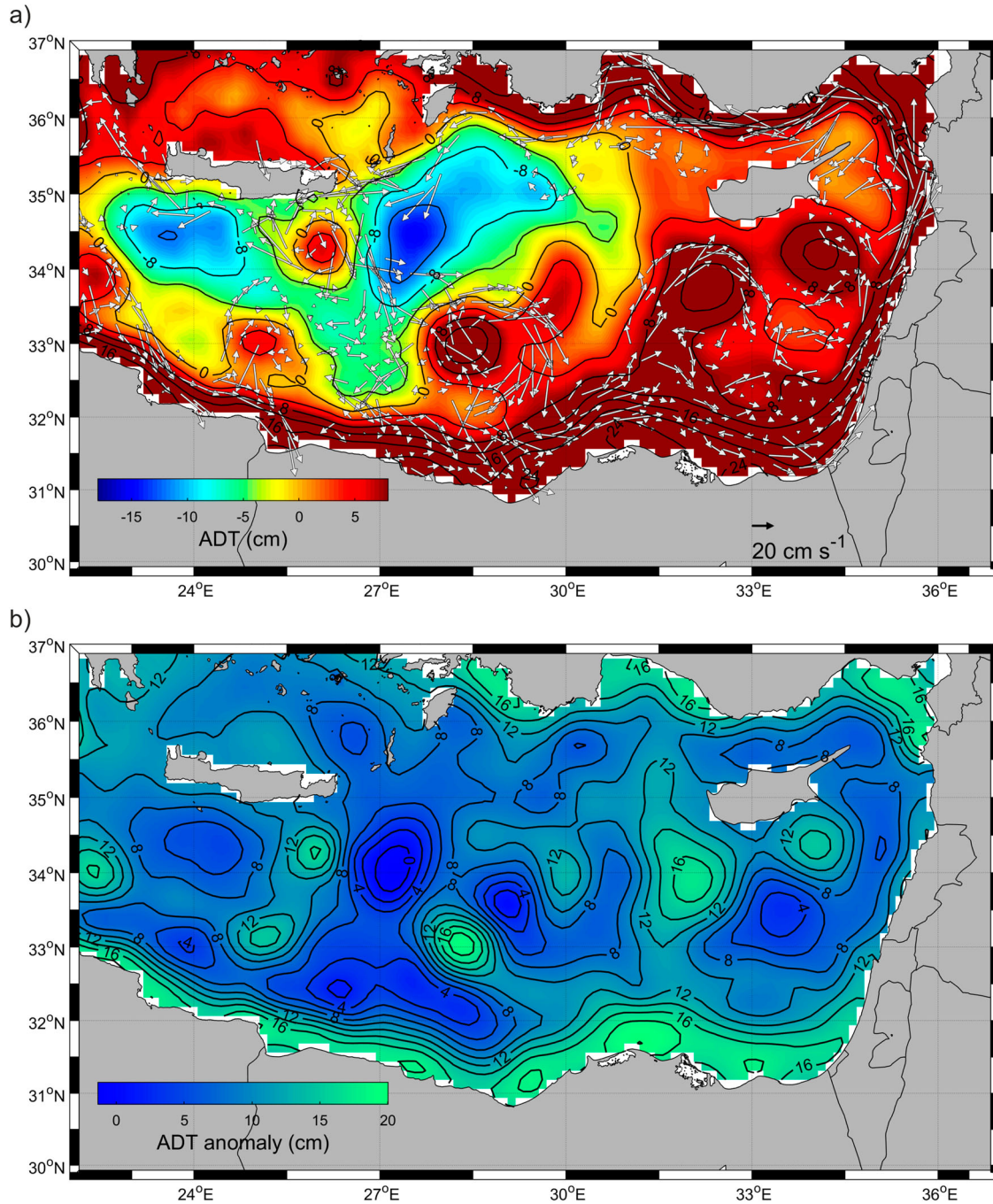

Figure 3.5.3. Mean drifter currents (arrows, CMEMS product Ref. No. 3.5.2) in bins of 0.25°x 0.25° superimposed on the mean map of ADT (colours, CMEMS product Ref. No. 3.5.1) in 2018 (a); anomaly of the ADT field in 2018 with respect to the period 1993–2018 (b).

3.5.3. Conclusions

The Mediterranean drifter dataset updated to 2018 not only provides more data but also guarantees a more complete spatial and temporal coverage in areas that were previously less sampled (like the northern part of the Levantine sub-basin).

The improvement of the drifter dataset is fundamental in strengthening and supporting present and future studies on the transport of marine litter. Indeed, a more detailed and robust description of the main currents and sub-basin/mesoscale structures (eddies and gyres) has been provided in this work: the SCE has been mentioned here for the first time and the CC and AMC are now much better tracked in winter seasons. It has been recently declared that the Mediterranean is most likely one of the areas of the global ocean most strongly impacted by the presence of microplastics (see, e.g. Suaria et al. 2016); within the Mare Nostrum, the Levantine sub-basin is a highly marine litter contaminated area and a deeper knowledge of the floating matter propagation is necessary to deeply understand the mechanisms of the waste dispersion. The drifter dataset will help in this context, providing a more robust description of the current field that will favour the learning mechanism of the distribution, retention and accumulation of the marine floating debris in the Mediterranean Sea and in particular in the Levantine sub-basin. This implies that enhancing the Lagrangian dataset is of great importance not only for the advancement of the knowledge of the mechanisms governing the dynamical functioning of the Mediterranean, but also for the strong societal impact that a deeper awareness of local dispersion processes may provide to the assessment of marine litter distribution and to the design of possible mitigation strategies of such a critical environmental issue.

Note

1. https://data.worldbank.org/indicator/ny.gdp.defl.zs.

References

Section 3.1: Evidence of the TOPEX – A Altimeter Instrumental Anomaly and Acceleration of the Global Mean Sea Level.

Ablain M, Meyssignac B, Zawadzki L, Jugier R, Ribes A, Cazenace A, Picot N. 2018. Error variance-covariance matrix of global mean sea level estimated from satellite altimetry (TOPEX, Jason 1, Jason 2, Jason 3). Seanoe. DOI:10. 17882/58344.

Ablain M, Jugier R, Zawadzki L, Taburet N, Cazenave A, Meyssignac B, Picot N. 2017. The TOPEX-A drift and impacts on GMSL time series. Poster presentation, OSTST 2017. [accessed 2019 April 11]. https://meetings.aviso. altimetry.fr/fileadmin/user_upload/tx_ausyclsseminar/files/ Poster_OSTST17_GMSL_Drift_TOPEX-A.pdf.

Ablain M, Legeais JF, Prandi P, Fenoglio-Marc L, Marcos M, Benveniste J, Cazenave A. 2017. Satellite altimetry-based sea level at global and regional scales. Surv Geophys 38:9– 33. DOI:10.1007/s10712-016-9389-8.

Ablain M, Meyssignac B, Zawadzki L, Jugier R, Ribes A, Cazenave A, Picot N. 2019. Uncertainty in satellite estimate of global mean sea level changes, trend and acceleration, Earth Syst Sci Data. 11:1189–1202. DOI:10.5194/essd-11-1189-2019.

Ablain M, Philipps S. 2005. AVISO 2005 annual report on TOPEX/Poseidon validation activities. CLS.DOS/NT/ 05.240. SALP-RP-MA-EA-21315-CLS. [accessed 2019 May 24]. https://www.aviso.altimetry.fr/fileadmin/documents/ calval/validation_report/TP/annual_report_tp_2005.pdf.

Beckley BD, Callahan PS, Hancock DW, Mitchum GT, Ray RD. 2017. On the 'Cal-mode' correction to TOPEX satellite altimetry and its effect on the global mean sea level time series. J Geophys Res C Oceans. 122(11):8371–8384. DOI:10.1002/2017jc013090.

Birkmann J, Licker R, Oppenheimer M, Campos M, Warren R, Luber G, O'Neill BC, Takahashi K. 2014. Cross-chapter box on a selection of the hazards, key vulnerabilities, key risks, and emergent risks identified in the WGII contribution to the fifth assessment report. In: Field CB, Barros VR, Dokken DJ, Mach KJ, Mastrandrea MD, Bilir TE, Chatterjee M, Ebi KL, Estrada YO, Genova RC, Girma B, Kissel ES, Levy AN, MacCracken S, Mastrandrea PR, White LL, editors. Climate change 2014: impacts, adaptation, and vulnerability. Part A: global and sectoral aspects. Contribution of working group ii to the fifth assessment report of the intergovernmental panel on climate change. Cambridge: Cambridge University Press; p. 113–121.

Cazenave A, Le Cozannet G. 2014. Sea level rise and coastal impacts. Earth's Fut. 2(2):15–34.

Cazenave A, Palanisamy H, Ablain M. 2018. Contemporary sea level changes from satellite altimetry: what have we learned? What are the new challenges? Adv Space Res. 62 (7):1639–1653. DOI:10.1016/j.asr.2018.07.017.

Chen X, Zhang X, Church JA, Watson CS, King MA, Monselesan D, Legresy B, Harig C. 2017. The increasing rate of the global mean sea level rise during 1993–2014. Nat Clim Change. DOI:10.1038/nclimate3325.

Cheng LK, Trenberth E, Fasullo J, Boyer T, Abraham J, Zhu J. 2017. Improved estimates of ocean heat content from 1960 to 2015. Sci Adv. 3:3. DOI:10.1126/sciadv.1601545.

Church J, White N, Arblaster J. 2005. Significant decadal-scale impact of volcanic eruptions on sea level and ocean heat content. Nature. 438:74–77. DOI:10.1038/nature04237.

Church JA, Clark PU, Cazenave A, Gregory JM, Jevrejeva S, Levermann A, Merrifield MA, Milne GA, Nerem RS, Nunn PD, et al. 2013. Sea level change. In: Stocker TF, Qin D, Plattner G-K, Tignor M, Allen SK, Boschung J, Nauels A, Xia Y, Bex V, Midgley PM, editors. Climate change 2013: the physical science basis. contribution of working group I to the fifth assessment report of the intergovernmental panel on climate change. Cambridge: Cambridge University Press.

Church JA, White NJ. 2011. Sea-level rise from the late 19th to the early 21st century. Surv Geophys. 32:585. DOI:10.1007/ s10712-011-9119-1.

Copernicus European State of the Climate: Sea Level. 2019. https://climate.copernicus.eu/sea-level. https://climate.copernicus.eu/sites/default/files/2019-04/Brochure_Final_Interactive_1.pdf, last access: 23/05/2019.

Couhert A, Cerri L, Legeais JF, Ablain M, Zelensky N, Haines B, Lemoine F, Bertiger W, Desai S, Otten M. 2014. Towards the 1 mm/y stability of the radial orbit error at regional scales. Adv Space Res. DOI:10.1016/j.asr.2014.06.041.

Dangendorf S, Marcos M, Wöppelmann G, Conrad CP, Frederikse T, Riva R. 2017. Reassessment of 20th century global mean sea level rise. Proc Natl Acad Sci. 114 (23):5946–5951. DOI:10.1073/pnas.1616007114.

Dasgupta S, Laplante B, Meisner C, Wheeler D, Yan J. 2009. The impact of sea level rise on developing countries: a comparative analysis. Clim Change. 93(3–4):379–388.

Decharme B, Delire C, Minvielle M, Colin J, Vergnes J-P, Alias A, Saint-Martin D, Séférian R, Sénési S, Voldoire A. 2019. Recent changes in the ISBA-CTRIP land surface system for Use in the CNRM-CM6 climate model and in global Off-line Hydrological applications. J Adv Model Earth Syst. 11(5):1207–1252. DOI:10.1029/2018MS001545.

Dieng HB, Cazenave A, Meyssignac B, Ablain M. 2017. New estimate of the current rate of sea level rise from a sea level budget approach. Geophys Res Lett. 44:3744–3751.

Escudier P, Couhert A, Mercier F, Mallet A, Thibaut P, Tran N, Amarouche L, Picard B, Carrère L, Dibarboure G, et al. 2017. Satellite radar altimetry: principle, geophysical correction and orbit, accuracy and precision. In: Stammer D, Cazenave A, editors. Satellite altimetry over oceans and land surfaces. Boca Raton (FL): CRC Press, Taylor & Francis; p. 1–70.

Fasullo J, Nerem R, Hamlington B. 2016. Is the detection of accelerated sea level rise imminent? Sci Rep. 6:31245. DOI:10.1038/srep31245.

Gleckler PJ, AchutaRao K, Gregory JM, Santer BD, Taylor KE, Wigley TML. 2006. Krakatoa lives: the effect of volcanic eruptions on ocean heat content and thermal expansion. Geophys Res Lett. 33:17. DOI:10.1029/2006GL026771.

Gouretski V, Reseghetti F. 2010. On depth and temperature biases in bathythermograph data: development of a new correction scheme based on analysis of a global ocean database. Deep Sea Research I. 57(6):812–833. DOI:10.1016/j.dsr.2010.03.011.

Gregory JM, Lowe JA, Tett SFB. 2006. Simulated global-mean sea level changes over the last half-millennium. J Clim. DOI:10.1175/JCLI3881.1.

Hay CC, Morrow E, Kopp RE, Mitrovica JX. 2015. Probabilistic reanalysis of twentieth-century sea-level rise. Nature. 517:481–484. DOI:10.1038/nature14093.

Hayne GS, Hancock DW. 1998. Observations from long-term performance monitoring of the TOPEX radar altimeter. TOPEX/Poseidon/Jason-1 Science Working Team Meeting, Keystone.

Hinkel J, Lincke D, Vafeidis AT, Perrette M, Nicholls RJ, Tol RSJ, Marzeion B, Fettweis X, Ionescu C, Levermann A. 2014. Future coastal flood damage and adaptation costs. Proc Natl Acad Sci USA. 111(9):3292–3297. DOI:10.1073/pnas.1222469111.

Jevrejeva S, Jackson LP, Grinsted A, Lincke D, Marzeion B. 2018. Flood damage costs under the sea level rise with warming of 1.5 °C and 2 °C. Environ Res Lett. 13 (7):074014. https://iopscience.iop.org/journal/1748-9326.

Jevrejeva S, Moore JC, Grinsted A, Matthews AP, Spada G. 2014. Trends and acceleration in global and regional sea levels since 1807. Global Planet Change. 113:11–22. DOI:10.1016/j.gloplacha.2013.12.004.

Jouzel J. 2015. Rapport « Le climat de la France au XXIe siècle », ministère de l'Écologie, du Développement durable et de l'Énergie. Volume 5 mars 2015 p.40. http://www.senat.fr/rap/r15-014/r15-0143.html.

Kebede AS, Nicholls RJ. 2012. Exposure and vulnerability to climate extremes: population and asset exposure to coastal flooding in Dar es Salaam, Tanzania. Reg Environ Change. 12:81–94.

Kleinherenbrink M, Riva R, Scharroo R. 2019. A revised acceleration rate from the altimetry-derived global mean sea level record. Sci Rep. 9:10908. DOI:10.1038/s41598-019-47340-z.

Legeais J-F, Ablain M, Thao S. 2014. Evaluation of wet troposphere path delays from atmospheric reanalyses and radiometers and their impact on the altimeter sea level. Ocean Sci. 10:893–905. DOI:10.5194/os-10-893-2014.

Legeais J-F, Ablain M, Zawadzki L, Zuo H, Johannessen JA, Scharffenberg MG, Fenoglio-Marc L, Fernandes MJ, Andersen O, Rudenko S, Cipollini P. 2018. An accurate and homogeneous altimeter sea level record from the ESA climate change initiative. Earth Syst Sci Data Discuss. 1–35. DOI:10.5194/essd-2017-116.

Legeais J-F, von Schuckmann K, Melet A, Storto A, Meyssignac B. 2018. Sea level, in Copernicus marine service ocean state report, issue 2. J Oper Oceanogr. 11(S1):s13–s16. DOI:10.1080/1755876X.2018.1489208.

Levitus S, Antonov JI, Boyer TP, Baranova OK, Garcia HE, Locarnini RA, Mishonov AV, Reagan JR, Seidov D, Yarosh ES, Zweng MM. 2012. World ocean heat content and thermosteric sea level change (0–2000 m), 1955–2010. Geophys Res Lett 39:L10603. DOI:10.1019/2012GL051106.

Llovel W, Guinehut S, Cazenave A. 2010. Regional and interannual variability in sea level over 2002–2009 based on satellite altimetry, Argo float data and GRACE ocean mass. Ocean Dyn. 60:1193–1204. DOI:10.1007/s10236-010-0324-0.

Llovel W, Willis JK, Landerer FW, Fukumori I. 2014. Deepocean contribution to sea level and energy budget not detectable over the past decade. Nat Clim Change. 4:1031–1035.

Marzeion B, Jarosch AH, Hofer M. 2012. Past and future sealevel change from the surface mass balance of glaciers. Cryosphere. 6:1295–1322. DOI: 10.5194/tc-6-1295-2012.

McGranahan G, Balk D, Anderson B. 2007. The rising tide: assessing the risks of climate change and human settlements in low elevation coastal zones. Environ Urban. 19(1):17–37. DOI:10.1177/0956247807076960.

Nerem RS, Beckley BD, Fasullo J, Hamlington BD, Masters D, Mitchum GT. 2018. Climate change driven accelerated sea level rise detected in the altimeter era. PNAS. 115 (9):2022–2025.

Nerem S, Ablain M, Cazenave A. 2017. A 25-year long satellite altimetry-based global mean sea level record; closure of the sea level budget & missing components. In: Stammer C, editor. Satellite altimetry over oceans and land Surfaces. Boca Raton (FL): CRC Press, Taylor & Francis; p. 187–210.

Neumann B, Vafeidis AT, Zimmermann J, Nicholls RJ. 2015. Future coastal population growth and exposure to Sea-level rise and coastal flooding – a global assessment. PLoS ONE. 10(3). DOI:10.1371/journal.pone.0118571.

Oppenheimer M, Glavovic BC, Hinkel J, van de Wal R, Magnan AK, Abd-Elgawad A, Cai R, CifuentesJara M, DeConto RM, Ghosh T, et al. 2019. Sea level rise and Implications for low-lying Islands, coasts and communities. In: Pörtner H-O, Roberts DC, Masson-Delmotte V, Zhai P, Tignor M, Poloczanska E, Mintenbeck K, Alegría A, Nicolai M, Okem A, Petzold J, Rama B, Weyer NM, editors. IPCC special report on the ocean and cryosphere in a changing climate. https://www.ipcc.ch/srocc/cite-report/.

Peltier R. 2004. Global glacial isostasy and the surface of the ice-age earth: the ICE-5G (VM2) model and GRACE. Annu Rev Earth Planet Sci. 32:111–149.

Purkey S, Johnson GC. 2010. Warming of the global abyssal and deep southern ocean waters between the 1990s and 2000s: contributions to global heat and sea level rise budgets. Jour Clim. DOI:10.1175/2010JCLI3682.1.

Quartly GD, Legeais JF, Ablain M, Zawadzki L, Fernandes MJ, Rudenko S, Carrère L, García PN, Cipollini P, Andersen OB, Poisson JC. 2017. A new phase in the production of quality-controlled sea level data. Earth Syst Sci Data. 9:557–572. DOI:10.5194/essd-9-557-2017.

Ray RD, Douglas C. 2011. Experiments in reconstructing twentieth-century sea levels. Prog Oceanogr. 91:495–515.

Shepherd A, Ivins ER, Barletta VR, Bentley MJ, Bettadpur S, Briggs KH, Bromwich DH, Forsberg R, Galin N, et al. 2012. A reconciled estimate of ice-sheet mass balance. Science. 338(6111):1183–1189. DOI: 10.1126/science.1228102.

Taburet G, Sanchez-Roman A, Ballarotta M, Pujol M-I, Legeais J-F, Fournier F, Faugere Y, Dibarboure G. 2019. DUACS DT2018: 25 years of reprocessed sea level altimetry products. Ocean Sci. 15:1207–1224. DOI:10.5194/os-15-1207-2019.

United Nations. 2017. The ocean conference, the Ocean fact sheet. https://www.un.org/sustainabledevelopment/wp-content/uploads/2017/05/Ocean-fact-sheet-package.pdf.

United Nations projections. 2015 Jul 29. The world population prospects: 2015 revision. https://www.un.org/en/development/desa/publications/world-population-prospects-2015-revision.html.

von Schuckmann K, Palmer MD, Trenberth KE, Cazenave A, Chambers D, Champollion N, Wild M. 2016. Earth's energy imbalance: an imperative for monitoring. Nat Clim Change. 26:138–144.

Vousdoukas MI, Mentaschi L, Voukouvalas E, Bianchi A, Dottori F, Feyen L. 2018. Climatic and socioeconomic controls of future coastal flood risk in Europe. Nat Clim Change. 776–780:8–9. DOI:10.1038/s41558-018-0260-4.

Watson CS, White NJ, Church JA, King MA, Burgette RJ, Legresy B. 2015. Unabated global mean sea level over the satellite altimeter era. Nat Clim Change. DOI:10.1038/NCLIMATE2635.

WCRP. 2018. Global sea level budget group: global sea-level budget 1993–present. Earth Syst Sci Data. 10:1551–1590. DOI:10.5194/essd-10-1551-2018.

WMO. 2018. Statement on the state of the global climate 2018, World Meteorological Organization, WMO-No 1233. https://library.wmo.int/doc_num.php?explnum_id=5789.

Wong PP, Losada IJ, Gattuso J-P, Hinkel J, Khattabi A, McInnes KL, Saito Y, Sallenger A. 2014. Coastal systems and low-lying areas. In: Field CB, Barros VR, Dokken DJ, Mach KJ, Mastrandrea MD, Bilir TE, Chatterjee M, Ebi KL, Estrada YO, Genova RC, Girma B, Kissel ES, Levy AN, MacCracken S, Mastrandrea PR, White LL, editors. Climate change 2014: impacts, adaptation, and vulnerability. Part A: global and sectoral aspects. Contribution of working group II to the fifth assessment report of the inter-governmental panel on climate change. Cambridge: Cambridge University Press; p. 361–409.

Wöppelmann G, Marcos M. 2016. Vertical land motion as a key to understanding sea level change and variability. Rev Geophys. 54:64–92.

Section 3.2: Using CMEMS satellite and model data to help assess eutrophication status in Northwest European Shelf Seas.

Báez JC, Real R, López-Rodas V, Costas E, Enrique Salvo A, García-Soto C, Flores-Moya A. 2014. The North Atlantic oscillation and the Arctic oscillation favour harmful algal blooms in SW Europe. Harmful Algae. 39:121–126. DOI:10.1016/j.hal.2014.07.008.

Best MA, Wither AW, Coates S. 2007. Dissolved oxygen as a physico-chemical supporting element in the water framework directive. Mar Pollut Bull. 55(1–6):53–64. DOI:10.1016/j.marpolbul.2006.08.037.

Butenschön M, Clark J, Aldridge JN, Allen JI, Artioli Y, Blackford J, Bruggeman J, Cazenave P, Ciavatta S, Kay S, et al. 2016. ERSEM 15.06: a generic model for marine biogeochemistry and the ecosystem dynamics of the lower trophic levels. Geosci Model Dev. 9:1293–1339. DOI:10.5194/gmd-9-1293-2016.

Ciavatta S, Kay S, Saux-Picart S, Butenschön M, Allen JI. 2016. Decadal reanalysis of biogeochemical indicators and fluxes in the North West European Shelf-Sea ecosystem. J Geophys Res Oceans. 121(3):1824–1845. DOI:10.1002/2015JC011496.

Ferreira JG, Andersen JH, Borja A, Bricker SB, Camp J, da Silva MC, Garcés E, Heiskanen AS, Humborg C, Ignatiades L, Lancelot C. 2011. Overview of eutrophication indicators to assess environmental status within the European marine strategy framework Directive. Estuarine Coastal Shelf Sci. 93(2):117–131. DOI:10.1016/j.ecss.2011.03.014.

Glibert PM, Icarus Allen J, Artioli Y, Beusen A, Bouwman L, Harle J, Holmes R, Holt J. 2014. Vulnerability of coastal ecosystems to changes in harmful algal bloom distribution in response to climate change: projections based on model analysis. Glb Chg Bio. 20(12):3845–3858. DOI:10.1111/gcb.12662.

Gohin F, Van der Zande D, Tilstone GH, Eleveld MA, Lefebvre A, Andrieux-Loyer F, Blauw AN, Bryère P, Devreker D, Garnesson P, Fariñas TH. 2019. Twenty years of satellite and in situ observations of surface chlorophyll-a from the northern Bay of Biscay to the eastern English Channel. Is the water quality improving? Remote Sens Environ. 233:111343.

Grizzetti B, Bouraoui F, Aloe A. 2012. Changes of nitrogen and phosphorus Loads to European seas. Glb Chg Bio. 1. DOI:10.1111/j.1365-2486.2011.02576.x.

Große F, Greenwood N, Kreus M, Lenhart H-J, Machoczek D, Pätsch J, Salt L, Thomas H. 2016. Looking beyond stratification: a model-based analysis of the biological drivers of oxygen deficiency in the North Sea. Biogeosciences. 13 (8):2511–2535. DOI:10.5194/bg-13-2511-2016.

Levin LA, Ekau W, Gooday AJ, Jorissen F, Middelburg JJ, Naqvi SWA, Neira C, Rabalais NN, Zhang J. 2009. Effects of natural and human-induced Hypoxia on coastal Benthos. Biogeosciences. 6(10):2063–2098. DOI:10.5194/bg-6-2063-2009.

McQuatters-Gollop A, Raitsos DE, Edwards M, Pradhan Y, Mee LD, Lavender SJ, Attrill MJ. 2007. A long-term chlorophyll data set reveals regime shift in North Sea phytoplankton biomass unconnected to nutrient trends. Limnol Oceanogr. 52:635–648.

Novoa S, Chust T, Sagarminaga Y, Revilla M, Borja A, Franco J. 2012. Water quality assessment using satellite-derived chlorophyll-a within the European directives, in the southeastern Bay of Biscay. Mar Pollut Bull. 64(4):739–750. DOI:10.1016/j.marpolbul.2012.01.020. ISSN 0025-326X.

O'Dea E, Furner R, Wakelin S, Siddorn J, While J, Sykes P, King R, Holt J, Hewitt H. 2017. The CO5 configuration of the 7 km Atlantic margin model: large-scale biases and sensitivity to forcing, physics options and vertical resolution. Geosci Model Dev. 10:2947–2969. DOI:10.5194/gmd-10-2947-2017.

OSPAR. 2008. Second OSPAR integrated report on the eutrophication status of the OSPAR maritime area. OSPAR publication 372.

OSPAR. 2017. Third integrated report on the eutrophication status of the OSPAR maritime area. OSPAR Publication 694.

Romero E, Garnier J, Lassaletta L, Billen G, Le Gendre R, Riou P, Cugier P. 2013. Large-scale patterns of river inputs in southwestern Europe: seasonal and interannual variations and potential eutrophication effects at the coastal zone. Biogeochemistry. 113 (1–3):481–505. DOI:10.1007/s10533-012-9778-0.

Sathyendranath S, Brewin R, Brockmann C, Doerffer R, Farman A, Krasemann H, Mélin F, et al. 2016. OC-CCI: products and their use. Ocean colour CCI products report V2.

Schaeffer BA, Hagy JD, Conmy RN, Lehrter JC, Stumpf RP. 2012. An approach to developing numeric water quality criteria for coastal waters using the SeaWiFS satellite data record. Environ Sci Technol. 46(2):916–922. DOI:10.1021/es2014105.

Skákala J, Ford D, Brewin RJW, McEwan R, Kay S, Taylor B, Mora L, Ciavatta S. 2018. The assimilation of phytoplankton functional types for operational forecasting in the Northwest European Shelf. J Geophys Res Oceans. 123 (8):5230–5247. DOI:10.1029/2018JC014153.

Tinker T, Renshaw R, Barciela R, Wood R. 2019. Regional mean time series for the Northwest European Shelf seas. In: Copernicus marine service ocean state report, issue 3. J Operat Oceanogr. 12(sup1):s26–s30. DOI: 10.1080/1755876X.2019.1633075.

Topcu HD, Brockmann UH. 2015. Seasonal oxygen depletion in the North Sea, a review. Mar Pollut Bull. 99(1–2):5–27. DOI:10.1016/j.marpolbul.2015.06.021.

van Beusekom JEE, Bot P, Carstensen J, Grage A, Kolbe K, Lenhart H-J, Pätsch J, Petenati T, Rick J. 2017. Eutrophication. In: Kloepper S, Baptist MJ, Bostelmann A, Busch J, Buschbaum C, Gutow L, Janssen G, Jensen K, Jørgensen H, de Jong F, Lüerßen G, Schwarzer K, Strempel R, Thieltges D, editor. Wadden Sea quality status report

2017. Wilhelmshaven: Common Wadden Sea Secretariat. https://qsr.waddensea-worldheritage.org/.

Vaquer-Sunyer R, Duarte CM. 2008. Thresholds of hypoxia for marine biodiversity. Proc Natl Acad Sci USA. 105 (40):15452–15457. DOI:10.1073/pnas.0803833105.

Section 3.3: The value of carbon sink sequestration ecosystem services in the Mediterranean Sea.

Beaumont NJ, Austen MC, Atkins JP, Burdon D, Degraer S, Dentinho TP, Derous S, Holm P, Horton T, van Ierland E, et al. 2007. Identification, definition and quantification of goods and services provided by marine biodiversity: implications for the ecosystem approach. Mar Pollut Bull. 54(3):253–265.

CICES V5.1. 2018. Common international classification of ecosystem services (CICES, v5.1). http://www.cices.eu.

EUA. 2019. Primary market auction report. [Accessed 2019 April 10]. https://www.eex.com/en/market-data/environmental-markets/auction-market/european-emission-allowances-auction/european-emission-allowances-auction-download.

Flanders Marine Institute. 2018. Maritime boundaries geodatabase: maritime boundaries and exclusive economic zones (200NM), version 10. http://www.marineregions.org/doi:10.14284/312.

Gattuso J-PJ, Magnan A, Billé R, Cheung WWL, Howes EL, Joos F, Allemand D, Bopp L, Cooley SR, Eakin CM, et al. 2015. Contrasting futures for ocean and society from different anthropogenic CO_2 emissions scenarios. Science. 349 (6243):aac4722. DOI:10.1126/science.aac4722.

IPCC. 2019. Summary for policymakers. In: Pörtner H-O, Roberts DC, Masson-Delmotte V, Zhai P, Tignor M, Poloczanska E, Mintenbeck K, Alegría A, Nicolai M, Okem A, Petzold J, Rama B, Weyer NM, editors. IPCC special report on the ocean and cryosphere in a changing climate. https://www.ipcc.ch/srocc/cite-report/.

Le Quéré C, Andrew R, Friedlingstein P, Sitch S, Hauck J, Pongratz J, Pickers P, Ivar Korsbakken J, Peters G, Canadel J, et al. 2018. Global carbon budget 2018. Earth Syst Sci Data. 10:2141–2194. DOI:10.5194/essd-10-2141-2018.

Liquete C, Piroddi C, Macías D, Druon J-N, Zulian G. 2016. Ecosystem services sustainability in the Mediterranean Sea: assessment of status and trends using multiple modelling approaches. Sci Rep. 6:34162. DOI:10.1038/srep34162.

MEA (Millennium Ecosystem Assessment). 2005. Ecosystems and human well-being. Ecosystems. DOI:10.1196/annals.1439.003.

Melaku CD, Ghermandi A, Nunes PLD, Lazzari P, Cossarini G, Solidoro C. 2015. Estimating the value of carbon sequestration ecosystem services in the Mediterranean Sea: an ecological economics approach. Glob Environ Change. 32 (1):87–95.

Nordhaus WD. 2017. Revisiting the social cost of carbon. PNAS. 114(7):1518–1523.

Pendleton L, Donato DC, Murray BC, Crooks S, Jenkins WA, Sifleet S, Craft C, Fourqurean JW, Kauffman JB, Marbà N, et al. 2012. Estimating global 'blue carbon' emissions from conversion and degradation of vegetated coastal ecosystems. Plos One. 7(9):e43542. DOI:10.1371/journal.pone.0043542.

Perruche C, Solidoro C, Cosssarini G. 2018. Air to sea carbon flux in Von Shuckmann et al., (2018). Copernicus marine service ocean state report, issue 2. J Operat Oceanogr. 11 (sup1):103–106.

Pörtner HO, Karl DM, Boyd PW, Cheung WWL, Lluch-Cota SE, Nojiri Y, Schmidt DN, Zavialov PO. 2014. Ocean systems. In: Field CB, Barros VR, Dokken DJ, Mach KJ, Mastrandrea MD, Bilir TE, Chatterjee M, Ebi KL, Estrada YO, Genova RC, Girma B, Kissel ES, Levy AN, MacCracken S, Mastrandrea R, White LL, editors. Climate change 2014: impacts, adaptation, and Vulnerability. Part A: global and sectoral aspects. Contribution of working group II to the fifth assessment report of the intergovernmental panel on climate change. Cambridge: Cambridge University Press; p. 411–484.

Ricke K, Drouet L, Caldeira K, Tavoni M. 2018. Country-level social cost of carbon. Nat Clim Change. 8:895–900.

Sabine CL, Feely RA, Gruber N, Key RM, Lee K, Bullister JL, Wanninkhof R, Wong CS, Wallace DWR, Tilbrook B, et al. 2004. The oceanic sink for anthropogenic CO_2. Science. 305(5682):367–371.

TEEB. 2010. The economics of ecosystems and biodiversity ecological and economic foundations. Pushpam Kumar, editor. London: Earthscan.

Tol RJS. 2018. The economic impact of climate change. Rev Environ Econ Policy. 12(1):4–25.

van den Bergh JCJM, Botzen WJW. 2014. A lower bound to the social cost of CO_2 emissions. Nat Clim Change. 4:253–258.

Watkiss P, Anthoff D, Downing T, Hepburn C, Hope C, Hunt A, Tol R. 2005. Social costs of carbon review – methodological approaches for using SCC estimates in policy assessment. AEA Technology Environment, UK.

Section 3.4: IBISAR service for real-time data ranking in the IBI area for emergency responders and SAR operators.

Abascal AJ, Sanchez J, Chiri H, Ferrer MI, Cárdenas M, Gallego A, Castanedo S, Medina R, Alonso-Martirena A, Berx B, et al. 2017. Operational oil spill trajectory modelling using HF radar currents: a northwest European continental shelf case study. Mar Pollut Bull. 119(1):336–350.

André G, Garreau P, Garnier V, Fraunié P. 2005. Modelled variability of the sea surface circulation in the North-Western Mediterranean Sea and in the Gulf of Lions. Ocean Dyn. 55:294–308.

Álvarez FE, García SM, Pérez GB, Grifoll CM, Espino IM, Mestres RM, Cerralbo PP, Sánchez-Arcilla CA. 2018. The SAMOA project: downscaling operational oceanography for improving harbour operations. A: EuroGOOS International Conference. "Operational Oceanography serving Sustainable Marine Development: Proceedings of the Eight EuroGOOS International Conference: 3–5 October 2017, Bergen". European Global Ocean Observing System (EuroGOOS). p. 379–386.

Barrick D, Fernandez V, Ferrer MI, Whelan C, Breivik Ø. 2012. A short term predictive system for surface currents from a rapidly deployed coastal HF radar network. Ocean Dyn. 62(5):725–740.

Chapman RD, Shay LK, Graber HC, Edson JB, Karachintsev A, Trump CL, Ross DB. 1997. On the accuracy of HF radar surface current measurements: Intercomparisons with ship-based sensors. J Geophys Res Oceans. 102:18737–18748.

Charria G, Lazure P, Le Cann B, Serpette A, Reverdin G, Louazel S, Batifoulier F, Dumas F, Pichon A, Morel Y. 2013. Surface layer circulation derived from Lagrangian drifters in the Bay of Biscay. J Mar Syst. 109–110:S60–S76.

Cook TM, DePaolo T, Terrill EJ. 2007. Estimates of radial current error from high frequency radar using MUSIC for bearing determination. OCEANS 2007, Vancouver, IEEE. p. 1–6.

Font J, Salat J, Tintore J. 1988. Permanent features of the circulation in the Catalan Sea. Pelagic Mediterranean oceanography. Oceanol Acta. 9:51–57.

Frolov S, Paduan J, Cook M, Bellingham J. 2012. Improved statistical prediction of surface currents based on historic HF- radar observations. Ocean Dyn. 62(7):1111–1122.

Halliwell GR, Srinivasan A, Kourafalou V, Yang H, Willey D, Hénaff M, Atlas R. 2014. Rigorous evaluation of a fraternal twin ocean OSSE system for the open Gulf of Mexico. J Atmos Ocean Technol. 31(1):105–130.

Herbert G, Ayoub N, Marsaleix P, Lyard F. 2011. Signature of the coastal circulation variability in altimetric data in the southern Bay of Biscay during winter and fall 2004. J Mar Syst. 88(2):139–158.

Hernández F, Blockley E, Brassington GB, Davidson F, Divakaran P, Drévillon M, Ishizaki S, Garcia-Sotillo M, Hogan PJ, Lagemaa P, et al. 2015. Recent progress in performance evaluations and near real-time assessment of operational ocean products. J Operat Oceanogr. 8(sup2): s221–s238.

Hernández F, Melet A. 2016. Product quality strategic plan in CMEMS (CMEMS-PORQUE-StrategicPlan). Mercator Océan International, editor. Toulouse: Mercator Océan International.

Hernández-Carrasco I, Orfila A, Rossi V, Garçon V. 2018. Effect of small-scale transport processes on phytoplankton distribution in coastal seas. Sci Rep. 8(1):8613.

Hernández-Carrasco I, Solabarrieta L, Rubio A, Esnaola G, Reyes E, Orfila A. 2018. Impact of HF radar current gap-filling methodologies on the Lagrangian assessment of coastal dynamics. Ocean Sci. 14:827–847.

Ivichev I, Hole LR, Karlin L, Wettre C, Röhrs J. 2012. Comparison of operational oil spill trajectory forecasts with surface drifter trajectories in the Barents Sea. J Geol Geosci. 1:105.

Jiménez Madrid JA, García-Ladona E, Blanco-Meruelo B. 2016. Oil spill beaching probability for the Mediterranean Sea. In: Carpenter A, Kostianoy A, editors. Oil pollution in the Mediterranean Sea: part I. The international context. Cham: Springer International Publishing; p. 305–324.

Juza M, Mourre B, Renault L, Gómara S, Sebastián K, Lora S, Beltran JP, Frontera B, Garau B, Troupin C, et al. 2016. SOCIB operational ocean forecasting system and multi-platform validation in the Western Mediterranean Sea. J Operat Oceanogr. 9(sup1):s155–s166.

Kaplan DM, Lekien F. 2007. Spatial interpolation and filtering of surface current data based on open-boundary modal analysis. J Geophys Res Oceans. 112(C12):C12007.

La Violette PE, Tintoré J, Font J. 1990. The surface circulation of the Balearic Sea. J Geophys Res Oceans. 95:1559–1568.

Lana A, Fernández V, Tintoré J. 2015. SOCIB continuous observations of Ibiza channel using HF radar. Sea Technol. 56(3):31–34.

Lana A, Marmain J, Fernández V, Tintoré J, Orfila A. 2016. Wind influence on surface current variability in the Ibiza channel from HF radar. Ocean Dyn. 66(4):483–497.

Le Cann B, Serpette A. 2009. Intense warm and saline upper ocean inflow in the southern Bay of Biscay in autumn-winter 2006–2007. Cont Shelf Res. 29(8):1014–1025.

Le Traon PY, Alfatih A, Alvarez Fanjul A, Aouf L, Axell L, Aznar R, Ballarotta M, Behrens A, Benkiran M, Bentamy A, et al. 2017. The Copernicus marine environmental monitoring service: main scientific achievements and future prospects, in: #56. Mercator.

Lekien F, Coulliette C, Bank R, Marsden J. 2004. Open-boundary modal analysis: interpolation, extrapolation, and filtering. J Geophys Res Oceans. 109:C12004.

Liu Y, Weisberg RH. 2011. Evaluation of trajectory modeling in different dynamic regions using Normalized Cumulative Lagrangian Separation. J Geophys Res Oceans. 116(C9):C09013.

Liu Y, Weisberg RH, Vignudelli S, Mitchum GT. 2014. Evaluation of altimetry-derived surface current products using Lagrangian drifter trajectories in the eastern Gulf of Mexico. J Geophys Res Oceans. 119(5):2827–2842.

Mooers CNK, Zaron ED, Howard MK. 2012. Final report for phase I of Gulf of Mexico 3-D operational ocean forecast system pilot prediction project (GOMEX-PPP). U.S. Department of Energy.

Mourre B, Aguiar E, Juza M, Hernández-Lasheras J, Reyes E, Heslop E, Escudier R, Cutolo E, Ruiz S, Mason E, et al. 2018. Assessment of high-resolution regional ocean prediction systems using multi-platform observations: illustrations in the Western Mediterranean Sea. In: Chassignet EP, Pascual A, Tintoré J, Verron J, editors. New frontiers in operational oceanography. GODAE Ocean View; p. 663–694. DOI:10.17125/gov2018.ch24.

Orfila A, Molcard A, Sayol JM, Marmain J, Bellomo L, Quentin C, Barbin Y. 2015. Empirical forecasting of HF-radar velocity using genetic algorithms. Trans Geosci Remote Sensing. 53(05):2875–2886.

Pinot JM, López-Jurado JL, Riera M. 2002. The CANALES experiment (1996-1998). Interannual, seasonal, and mesoscale variability of the circulation in the Balearic Channels. Prog Oceanogr. 55(3–4):335–370.

Piraud I, Marseleix P, Auclair F. 2003. Tidal and thermohaline circulation in the Bay of Biscay. Geophys Res. 5:07058.

Röhrs J, Christensen KH, Hole LR, Broström G, Drivdal M, Sundby S. 2012. Observation-based evaluation of surface wave effects on currents and trajectory forecasts. Ocean Dyn. 62(10):1519–1533.

Rubio A, Caballero A, Orfila A, Hernández-Carrasco I, Ferrer L, González M, Solabarrieta L, Mader J. 2018. Eddy-induced cross-shelf export of high Chl-A coastal waters in the SE Bay of Biscay. Remote Sens Environ. 205:290–304. DOI:10.1016/j.rse.2017.10.037.

Rubio A, Manso-Narvarte I, Caballero A, Corgnati L, Mantovani C, Reyes E, Griffa A, Mader A. 2019. The seasonal intensification of the slope Iberian Poleward current. In: Copernicus marine service ocean state report, issue 3. J Oper Oceanogr. 12:s26–s30.

Sayol JM, Orfila A, Simarro G, Conti D, Renault L, Molcard A. 2014. A Lagrangian model for tracking surface spills and SAR operations in the ocean. Environ Model Softw. 52:74–82.

Solabarrieta L, Frolov S, Cook M, Paduan J, Rubio A, González M, Mader J, Charria G. 2016. Skill assessment of HF radar-derived products for Lagrangian simulations in the Bay of Biscay. J Atmos Ocean Technol. 33(12):2585–2597.

Solabarrieta L, Rubio A, Castanedo S, Medina R, Charria G, Hernández C. 2014. Surface water circulation patterns in the southeastern Bay of Biscay: new evidences from HF radar data. Cont Shelf Res. 74:60–76.

Tintoré J, Vizoso G, Casas B, Heslop E, Pascual A, Orfila A, Ruiz S, Martínez-Ledesma M, Torner M, Cusí S, et al. 2013. SOCIB: the Balearic Islands observing and forecasting system responding to science, technology and society needs. Mar Technol Soc J. 47(1):101–117.

Vilibić I, Šepić J, Mihanović H, Kalinić H, Cosoli S, Janeković I, Žagar N, Jesenko B, Tudor M, Dadić V, Ivanković D. 2016. Self-organizing maps-based ocean currents forecasting system. Sci Rep. 6:22924.

Zelenke BC. 2005. An empirical statistical model relating winds and ocean surface currents: implications for short-term current forecasts [master's thesis]. Corvallis: Oregon State University.

Section 3.5: Surface picture of the Levantine Basin as derived by drifter and satellite data.

Amitai I, Lehahn Y, Lazar A, Heifetz E. 2010. Surface circulation of the eastern Mediterranean Levantine basin: insights from analyzing 14 years of satellite altimetry data. J Geophys Res. 115:C10058.

Barnes DK, Galgani F, Thompson RC, Barlaz M. 2009. Accumulation and fragmentation of plastic debris in global environments. Philos Trans R Soc B. 364:1985–1998. DOI:10.1098/rstb.2008.0205.

Brach L, Deixonne P, Bernard MF, Durand E, Desjean MC, Perez E, van Sebille E, Ter Halle A. 2018. Anticyclonic eddies increase accumulation of microplastic in the North Atlantic subtropical gyre. Mar Poll Bull. 126:191–196.

Galgani F. 2014. Distribution, composition and abundance of marine litter in the Mediterranean and black seas. In: F Briand, editor. CIESM workshop monograph 46: marine litter in the Mediterranean and black seas. Monaco: CIESM Publisher; p. 23–30.

Gertman I, Zodiatis G, Murashkovsky A, Hayes D, Brenner S. 2007. Determination of the locations of southeastern Levantine anticyclonic eddies from CTD data. Rapp Commun Int Mer Mediterr. 38:151.

Gregory MR, Ryan PG. 1997. Pelagic plastics and other sea-borne persistent synthetic debris: a review of Southern Hemisphere perspectives. In: Coe JM, Rogers DB, editors. Marine debris – sources, impacts and solutions. New York: Springer-Verlag; p. 49–66.

Hamad N, Millot C, Taupier-Letage I. 2005. A new hypothesis about the surface circulation in the eastern basin of the Mediterranean Sea. Prog Oceanogr. 66:287–298.

Hamad N, Millot C, Taupier-Letage I. 2006. The surface circulation in the eastern basin of Mediterranean Sea. Sci Mar. 70(3):457–503.

Le Vu B, Stegner A, Arsouze T. 2017. Angular momentum eddy detection and tracking algorithm (AMEDA) and its

application to coastal eddy formation. J Atmos Ocean Tecnol. 35:739–761. DOI: 10.1175/JTECH-D-17-0010.1.

Liubartseva S, Coppini G, Lecci R, Clementi E. 2018. Tracking plastics in the Mediterranean: 2D Lagrangian model. Mar Pollut Bull. 129:151–162.

Mansui J, Molcard A, Ourmieres Y. 2015. Modelling the transport and accumulation of floating marine debris in the Mediterranean basin. Mar Pollut Bull. 91:249–257.

Mauri E, Sitz L, Gerin R, Poulain P-M, Hayes D, Gildor H. 2019. On the variability of the circulation and water mass properties in the eastern Levantine Sea between September 2016–August 2017. Water. 11:1741. DOI:10.3390/w11091741.

Menna M, Gerin R, Bussani A, Poulain PM. 2017. The OGS Mediterranean drifter database: 1986–2016, Technical report 2017/92 Sez. OCE 28 MAOS, 2017.

Menna M, Poulain PM, Bussani A, Gerin R. 2018. Detecting the drogue presence of SVP drifters from wind slippage in the Mediterranean Sea. Measurement. 125:447–453. DOI:10.1016/j.measurement.2018.05.022.

Menna M, Poulain PM, Zodiatis G, Gertman I. 2012. On the surface circulation of the Levantine sub-basin derived from Lagrangian drifters and satellite altimetry data. Deep Sea Res I. 65:46–58.

Millot C, Gerin R. 2010. The mid-Mediterranean Jet Artefact. Geophys Res Lett. 37:L12602.

Millot C, Taupier-Letage I. 2005. Circulation in the Mediterranean Sea. Handb Environ Chem. 5:29–66.

Pinardi N, Zavatarelli M, Adani M, Coppini G, Fratianni C, Oddo P, Simoncelli S, Tonani M, Lyubartsev V, Dobricic S, Bonaduce A. 2015. Mediterranean Sea large-scale low-frequency ocean variability and water mass formation rates from 1987 to 2007: a retrospective analysis. Prog Ocean. 132:318–332. DOI:10.1016/j.pocean.2013.11.003. ISSN 0079-6611.

Poulain PM, Menna M, Mauri E. 2012. Surface geostrophic circulation of the Mediterranean Sea derived from drifter and satellite altimeter data. J Phys Ocean. 42(6):973–990. DOI:10.1175/JPO-D-11-0159.1.

Schroeder K, Garcia-Lafuente J, Josey SA, Artale V, Buongiorno Nardelli B, Carrillo A, Gacic M, Gasparini GP, Herrmann M, Lionello P, et al. 2012. Circulation of the Mediterranean Sea and its variability. In: Lionello P, editor. Climate of the Mediterranean region – from the past the future. Elsevier; p. 187–256. https://www.sciencedirect.com/book/9780124160422/the-climate-of-the-mediterranean-region#book-description.

Suaria G, Aliani S. 2014. Floating debris in the Mediterranean Sea. Mar Pollut Bull. 86:494–504. DOI:10.1016/j.Marpolbul.2014.06.025.

Suaria G, Avio CG, Mineo A, Lattin GL, Magaldi MG, Belmonte G, Moore CJ, Regoli F, Aliani S. 2016. The Mediterranean plastic soup: synthetic polymers in Mediterranean surface waters. Sci Rep. 6:37551.

Zambianchi E, Trani M, Falco P. 2017. Lagrangian transport of marine litter in the Mediterranean Sea. Front Mar Sci. 5:5.

Zodiatis G, Lardner R, Lascaratos A, Georgiou G, Korres G, Syrimis M. 2003. High resolution nested model for Cyprus, NE Levantine basin, eastern Mediterranean Sea: implementation and climatological runs. Ann Geophys. 21:221–236.

CMEMS OSR4, Chapter 4: Specific events 2018

Section 4.1. A most unusual winter sea-ice opening north of Greenland

Authors: Signe Aaboe, Vidar S. Lien, Gilles Garric, Laurent Bertino, Thomas Lavergne, Anton Korosov, Malte Müller

Statement of main outcome: An unusual opening in the sea-ice pack (also called polynya) occurred north of Greenland mid-winter 2018. Never before has a polynya of such dimensions been observed during winter in this region of the Arctic Ocean, which is known for its very compact and thick sea ice. Sea ice was pushed offshore by very warm and strong southeasterly winds, and a large area of open water was exposed directly to the atmosphere for a little less than a week. The polynya then closed, partly because older sea ice drifted back towards the coast but to a larger extent because of the formation of new sea ice in the open water. This region was therefore dominated by first-year ice until the end of the winter. Although the response in the ocean to the anomalous polynya event was most likely limited, we find indications of low resilience to changes induced by anomalous events in the Arctic.

Ref. No.	Product name & type	Documentation
4.1.1	SEAICE_GLO_SEAICE_L4_NRT_ OBSERVATIONS_011_001 Global ocean sea ice near-real-time products from EUMETSAT OSI SAF: concentration, edge, type, drift	PUM: https://marine.copernicus. eu/documents/PUM/CMEMS-SI-PUM-011-001.pdf QUID: https://marine. copernicus.eu/documents/ QUID/CMEMS-OSI-QUID-011-001to007-009to012.pdf
4.1.2	GLOBAL_ANALYSIS_FORECAST_ PHY_001_024	PUM: https://marine.copernicus. eu/documents/PUM/CMEMS-GLO-PUM-001-024.pdf QUID: https://marine. copernicus.eu/documents/ QUID/CMEMS-GLO-QUID-001-024.pdf
4.1.3	ARCTIC_REANALYSIS_PHYS_ 002_003	PUM: https://marine.copernicus. eu/documents/PUM/CMEMS-ARC-PUM-002-ALL.pdf QUID: https://marine. copernicus.eu/documents/ QUID/CMEMS-ARC-QUID-002-003.pdf
4.1.4	EUMETSAT OSI SAF AMSR-2 sea-ice concentration product, near-real-time (non CMEMS product)	Data and documentation from https://www.osi-saf.org
4.1.5	Products from GLO MFC but not available in the CMEMS portfolio: MLD AVT, Surface Net Heat Flux	Products on demand to Mercator Service Desk (communication@mercator-ocean.fr)
4.1.6	ARCTIC_ANALYSISFORECAST_ PHY_ICE_002_011	PUM: as 4.1.3. QuID: https://marine.copernicus. eu/documents/QUID/CMEMS-ARC-QUID-002-011.pdf

4.1.1. Introduction

Polynyas are openings within the sea-ice cover and are categorised as either a 'sensible-heat polynya' formed by melting of the sea ice in a region due to heating from the water below, or a 'latent-heat polynya' which is mechanically forced often by wind blowing the sea ice away from the coast (also called a 'coastal polynya') (Morales Maqueda et al. 2004). Winter polynyas play an important climatic role, through increased air-sea heat fluxes and sea-ice formation (Morales Maqueda et al. 2004). When polynyas form in winter, the ocean becomes exposed to the overlying, colder atmosphere, leading to rapid warming of the atmosphere affecting mesoscale atmospheric dynamics (e.g. Alam and Curry 1995; Fiedler et al. 2010; Tetzlaff et al. 2015). The subsequent cooling of the ocean may enhance sea-ice production and consecutive brine rejection into the underlying ocean. Such buoyancy loss may trigger cascading of dense water off the continental shelves and into the deep ocean (e.g. Ivanov et al. 2004), which is a mechanism that provides a substantial part of the Arctic cold halocline water (e.g. Cavalieri and Martin 1994; Winsor and Björk 2000) and ventilates the deep water of the Arctic Ocean (Martin and Cavalieri 1989; Swift et al. 1997; Schauer and Fahrbach 1999; Winsor and Björk 2000).

In February and early March 2018, the north coast of Greenland was dominated by unusual strong and persistent southwesterly winds (maximum wind speed exceeding 25 ms^{-1} on February 24th) and unusual warm air ($T > 0$°C) (Moore et al. 2018). These atmospheric conditions caused a latent-heat polynya to open in the Wandel Sea along the Greenland coast (Figure 4.1.1) and was the first time ever recorded in winter during the satellite era (since 1978) (Moore et al. 2018; Ludwig et al. 2019). The first sign of reduced ice concentration (<70%) in the Wandel Sea appeared on February 16th, and almost three weeks later, on March 8th, the Wandel Sea was again covered with ice concentration exceeding 70% (Figure 4.1.2a). The polynya reached its maximum extent on February 25th with approximately 13,000 km^2 of open water (sea-ice concentration below 30%) and a total area of 80,000 km^2 with sea-ice concentration below 70%. After February 25th, the temperature decreased rapidly to below −20°C as the wind direction shifted along with a decrease in the wind speed (Ludwig

OSI SAF AMSR2

NeXtSIM

CMEMS ARC MFC

CMEMS GLO MFC
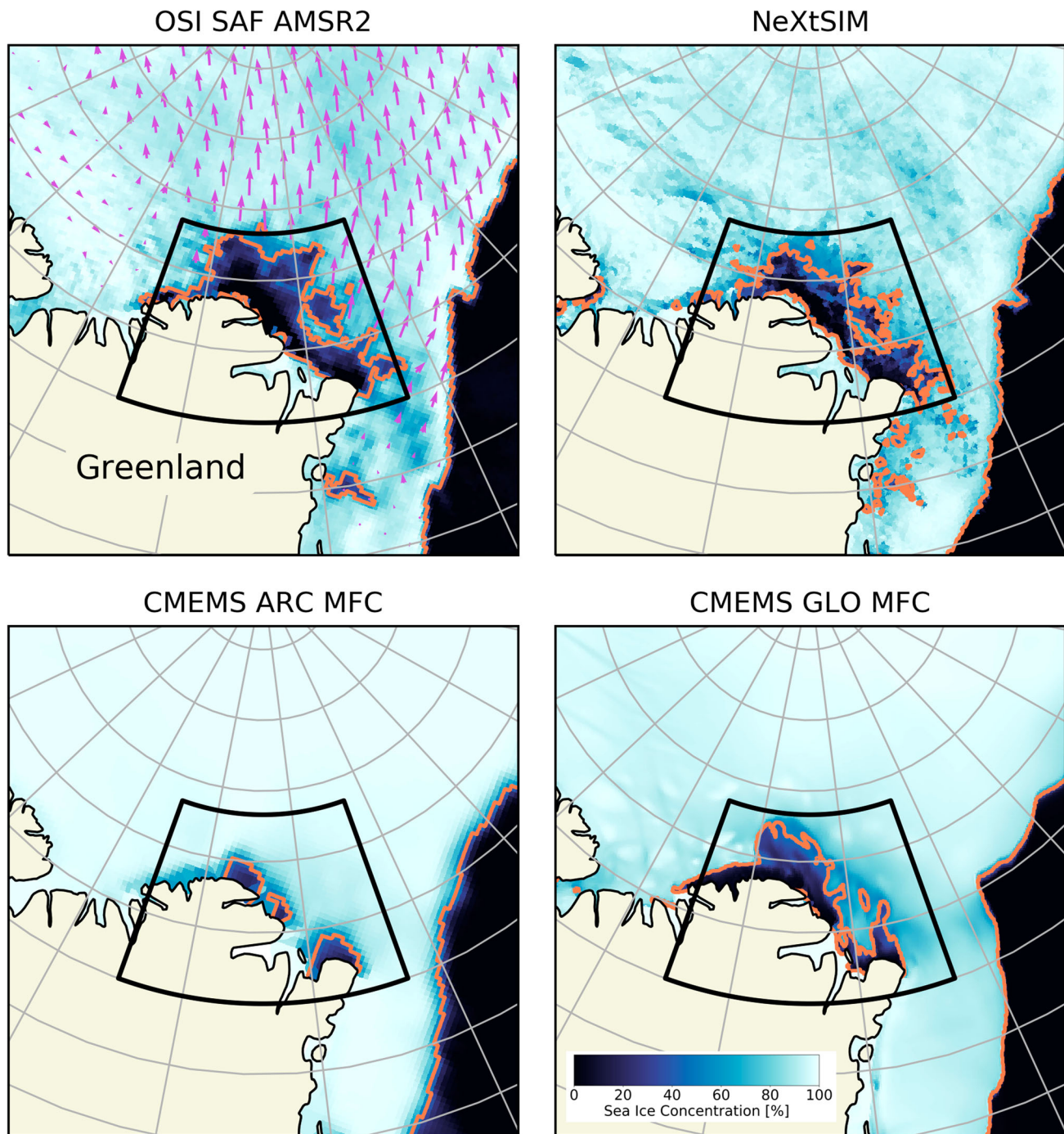
Figure 4.1.1. Sea-ice concentration (%) on the 25th of February 2018 showing the polynya north of Greenland, (a) from AMSR-2 passive microwave imagery (product 4.1.4) overlaid with sea-ice drift displacement vectors (23rd to 25th February) (product 4.1.1), and from the model analyses of (b) neXtSIM (product 4.1.6), (c) Arctic MFC (product 4.1.2), (d) Global MFC (product 4.1.3). The red contour is the 50% concentration isoline. The black box represents the polynya region and is used in Figure 4.1.2 to compute mean values of satellite sea ice data.

et al. 2019). These changes in atmospheric conditions caused new sea ice to rapidly form in the polynya (Figure 4.1.2). Eventually, the sea-ice drift became east – and southeastward (later southward) over the polynya region, pushing the older multiyear ice back toward the northern Greenland coast (sea-ice drift quick looks

from EUMETSAT OSI SAF https://www.osi-saf.org; Ludwig et al. 2019). However, the formation of new sea ice due to cooling at the surface limited to some extent the return of the multiyear ice, and the polynya area, usually dominated by thick multiyear ice, retained a substantial fraction of first-year ice for the remaining of the
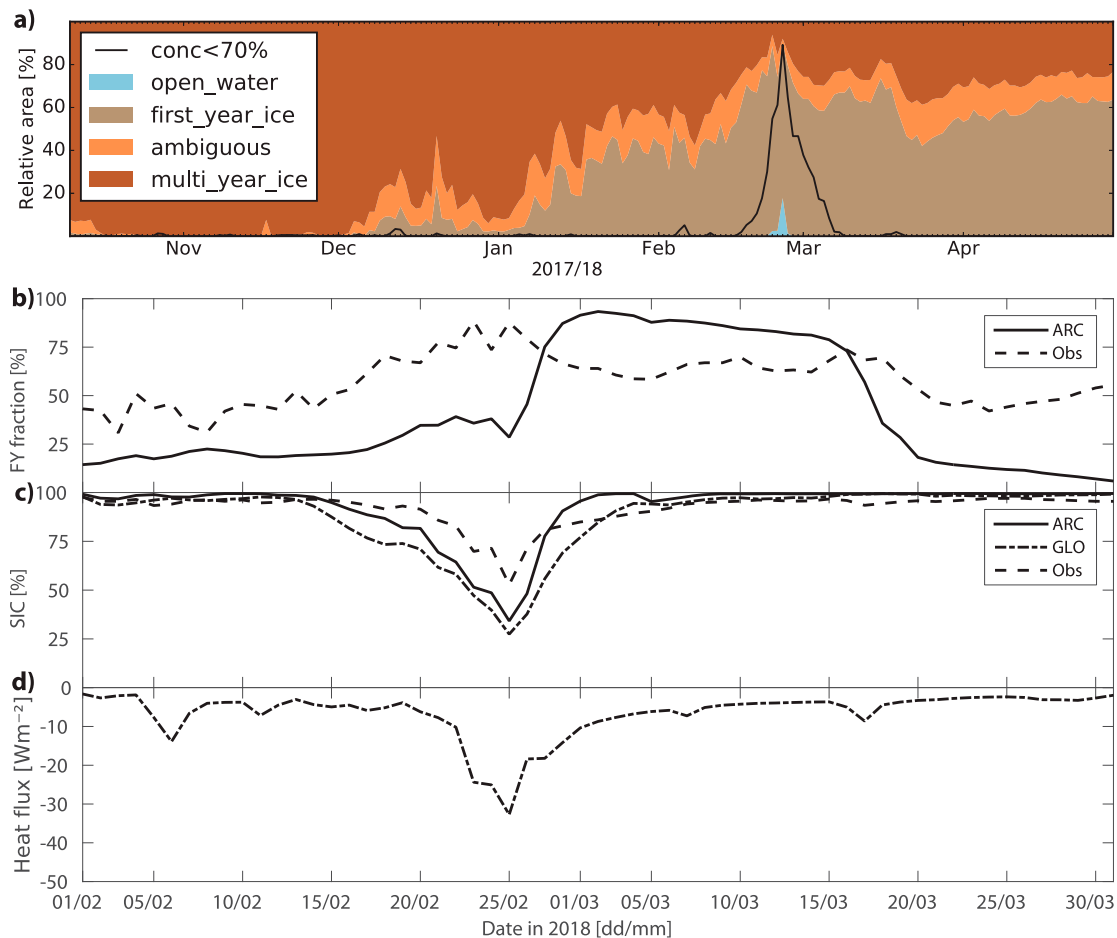
Figure 4.1.2. Evolution of sea-ice conditions during winter 2017/2018. (a) Relative areal distribution [%] of the sea-ice classes: multi-year-ice, first-year-ice, open-ice (concentration < 70%), open-water (concentration < 30%), and ambiguous = either multiyear-ice or first-year-ice (October 2017–April 2018) from product 4.1.1 of sea-ice type and sea-ice edge. (b) Fraction of first-year ice (FY) relative to the total ice cover (February-March) from product 4.1.1 and 4.1.3. (c) Sea-ice concentration (February-March) from product 4.1.2, 4.1.3 and product 4.1.4. (d) Net surface heat flux [Watts per m², positive downwards] from product 4.1.5. All values are daily averaged of the polynya region, defined by the black box in Figure 4.1.1 for products 4.1.1 and 4.1.4, and for products 4.1.2, 4.1.3 and 4.1.5 data is averaged over area where SIC < 50% on February 25th.

winter (Figure 4.1.2a,b). The fraction of first-year ice is high already from January (Figure 4.1.2a,b) and may have contributed to favourable preconditioning for the polynya. However, before the polynya, the fraction is highly variable in time and space, which is an effect of the unusually intense and frequent intrusions of warm air into the European Arctic with record high surface air temperatures for February (ESOTC 2018). These warm air intrusions over sea ice are known for causing short term misclassification of multiyear ice as first-year ice (Ye et al. 2016).

Coastal openings (here defined as ice concentration <30%) in the ice pack north of Greenland are not unusual during the summer months. Still, the replacement of thick older ice with first-year ice during the 2018 winter polynya in the Wandell sea, most probably played a key role in forming the extraordinary large coastal polynya in the following August and early September which

almost decoupled the sea-ice pack entirely off the coast of north Greenland (Bertino 2018).

4.1.2. Data and analysis

The polynya and the atmospheric conditions causing the polynya are analysed and presented elsewhere (Moore et al. 2018; Ludwig et al. 2019). Here, we investigate the impacts of the opening of the polynya on the underlying ocean. Due to the lack of direct, in-situ observations in the area (Dmitrenko et al. 2017), we rely our analysis on numerical model products: The Global and Arctic MFC operational systems (products 4.1.2, 4.1.3, 4.1.5) and a pre-operational run from a new stand-alone neXtSIM model (product 4.1.6). The first two models are driven at the surface by ECMWF operational data whereas neXtSIM was run with Climate Forecast System Reanalysis winds from the National Center for

Atmospheric Research. The Arctic MFC model (product 4.1.3) is the TOPAZ4 system based on a North Atlantic and Arctic configuration of the HYCOM ocean model coupled to a modified version of the CICE3 sea ice model at a horizontal resolution of 12 km, assimilating various observations once a week, including sea-ice concentrations from OSI SAF (redistributed by CMEMS, product 4.1.1) and thin-ice thickness (from SMOS) with an Ensemble Kalman Filter (Xie et al. 2016). The best estimate output is the average of the 100-members ensemble. The Global MFC model (product 4.1.2) is the coupled NEMO-LIM2 model at 1/12th deg horizontal resolution (about 3 km) using a fixed-basis SEEK filter to assimilate various observations, including sea-ice concentrations from OSI SAF as well (product 4.1.1). The neXtSIM stand-alone sea ice model (product 4.1.6) used here is a pre-operational configuration of a new CMEMS forecast product to be released in November 2019. neXtSIM is using the Maxwell-EB sea ice rheology (Dansereau et al. 2016) in a pure Lagrangian adaptive finite element mesh to preserve highly local features like cracks, leads and ridges (Rampal et al. 2019). The typical mesh edge is 3.5 km long. The ocean forcing (30 m) below the ice is taken from the TOPAZ4 operational runs. neXtSIM-F runs daily assimilation of both sea-ice concentrations from AMSR-2 provided by OSI SAF (Tonboe et al. 2017) and thin-ice thickness from

SMOS provided by UNI Hamburg (Tietsche et al. 2018) using a simple nudging (Williams et al. 2019).

4.1.3. Results

In our analysis, we define our study region as the area that experienced a sea-ice concentration of less than 50% at the peak of the polynya on February 25th (Figure 4.1.1b–d). While the models differ from the observations with regard to the area of the polynya and also somewhat the sea-ice concentration within the polynya, all three models show a polynya that qualitatively compares well with the observations with regard to position and temporal evolution of the polynya (Figures 4.1.1 and 4.1.2). Moreover, all models assimilate the observed sea-ice cover with respect to concentration.

As the polynya opened and the ocean became exposed to the colder atmosphere, there was a distinct increase in the ocean-to-air heat flux, from around 5 Wm^{-2} before and after the event to values exceeding 30 Wm^{-2} during the event (Figure 4.1.2d). Turbulent (latent and sensible) fluxes and radiative (longwave) cooling contributed equally to the increased heat fluxes (not shown). This increase in air-sea heat exchange was one order of magnitude less than typical heat fluxes observed during polynya events elsewhere in the Arctic during winter (e.g. Schneider and Budéus 1997; Morales Maqueda et al.
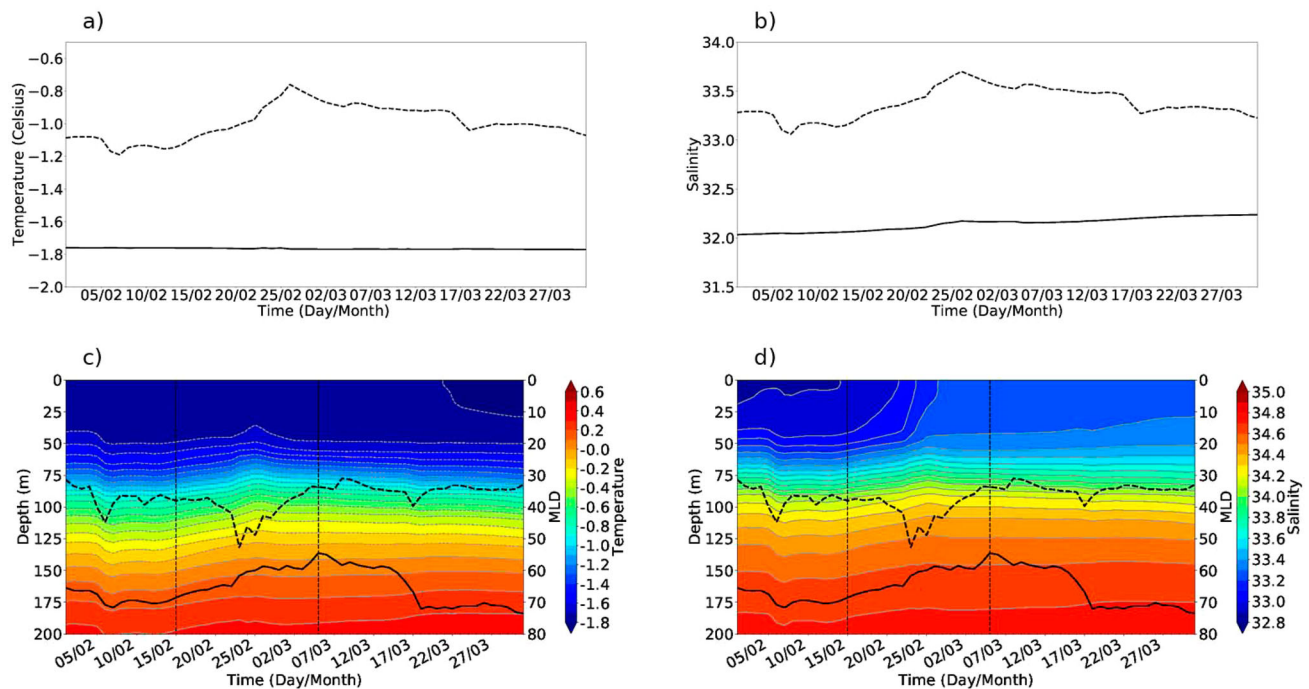
Figure 4.1.3. Time series of daily average of (a) Temperature at 30 m (solid) and 300 m (dotted) depth and (b) salinity at 30 m (solid) and 300 m (dotted) depth from product 4.1.3, (c) surface averaged temperature and (d) salinity profiles from product 4.1.2 with mixed-layer depth diagnosed from density from product 4.1.3 (solid) and mixed layer depth diagnosed from vertical eddy diffusivity from product 4.1.5 (dotted). The values are averaged on the area where sea-ice concentration is less than 50% on February 25th (see Figure 4.1.1). The dates (15th of February-5th of March) of occurrence of the open polynia is shown in vertical dotted lines.

2004; Ivanov and Shapiro 2005) due to the unusual warm air temperatures comparable to the sea surface temperatures. However, the difference between observing heat fluxes above open water and calculating heat fluxes in partially ice-covered grid cells in the models likely also contributes to the discrepancy.

The response in the ocean mixed-layer depth to the opening of the polynya depends on the definition of the mixed-layer depth. Using the turbocline depth, that is, the depth where the vertical eddy diffusivity falls below a given value, we find that the mixed-layer depth increased during the opening of the polynya (dashed line in Figure 4.1.3c,d), which indicates an increase in the transfer of momentum from the atmosphere to the ocean and subsequently increased ocean mixing during the polynya event. Using temperature or density to define the mixed-layer depth revealed however no significant changes during the polynya event (solid line in Figure 4.1.3c,d).

An upwelling event was triggered by the offshore winds that also caused the polynya to open (Figure 4.1.3). In the upper 50 m of the water column, the salinity increased by approximately 0.3 units (Figure 4.1.3b) indicating an upwelling of the deeper and more saline water masses. For temperature the change in the upper 50 m was less (Figure 4.1.3a). The upwelling caused both the salinity and temperature to increase down to at least 300 m depth (Figure 4.1.3a,b). The salinity in the upper layer remained elevated throughout the remainder of the winter and further increased somewhat, likely due to freezing of sea ice subsequent to the opening of the polynya (Figure 4.1.3b). These results indicate a weak resilience of the upper ocean to extreme, atmospherically-driven events in the polar region. Despite the salinity increase and the transient upwelling event associated with the offshore wind that caused the polynya, the impact of the polynya on the underlying ocean was limited. The increase in density of the surface water following the increase in salinity and modest cooling from increased heat loss to the atmosphere and subsequent formation of new sea ice, was not sufficient to induce convection through the pycnocline. For the water in the surface layer to attain the density of the water masses below the pycnocline, the salinity would have to increase by approximately 1.5 units (not shown). Assuming a salinity of newly formed sea ice of 0.31 times the initial salinity (Martin and Cavalieri 1989) and using a surface-layer thickness of 50 m, it would require approximately 3 m of sea-ice production to add enough salt for the surface waters to penetrate through the pycnocline.

While the polynya occurred during the Arctic night, it may potentially have had a subsequent impact on the marine biological production. First, the thinner ice cover due to the first-year ice replacing thicker multiyear ice changed the amount of light penetrating into the water column when the sunlight returned in spring, potentially leading to a stronger sea-ice algal bloom, and an increased food supply to zooplankton and benthic communities (e.g. Assmy et al. 2017). Furthermore, changes to the water column stability and the mixed-layer depth may alter the nutrient availability in the upper mixed layer, and, thus, the potential for primary production in the region. However, observations are needed to address questions regarding possible impact of such polynya openings on the biological production in the region and the ecosystem's resilience to potentially changing conditions, although bio-geochemical numerical modelling could also provide some useful insights. Based on the model results on the impact from the polynya on the physical conditions, however, we anticipate that the impact on biological production in 2018 was limited.

4.1.4. Conclusions

The unusual winter polynya north of Greenland in 2018 was captured in both regional and global numerical ocean models. The analyses suggest that the impact of the polynya on the underlying ocean was limited most likely due to the extraordinary small air-sea temperature difference. However, with the frequency of anomalous events, such as this polynya event, expected to increase in the Arctic in the coming decades (e.g. Mann et al. 2017), our results underscore the need for further investigations of the potential impacts of climate change in the Arctic.

Section 4.2. Geographical and seasonal coverage of sea ice in the Baltic Sea

Authors: Urmas Raudsepp, Rivo Uiboupin, Kaari Laanemäe, Ilja Maljutenko
Statement of main outcome: The Bothnian Bay, the Bothnian Sea, the Gulf of Finland and the Gulf of Riga are covered by sea ice during winter. Sea ice extent, ice probability, ice mobility and start, end and length of the ice period were evaluated based on the satellite remote sensing ice concentration data for the period 1982–2019. All four sub-basins of the Baltic Sea showed similar interannual variations in these ice cover conditions explained by the large atmospheric circulation. Correlation coefficients between the length and end date of the ice period, maximum ice extent and mean NAO index were between −0.4 and −0.5 for all sub-basins (except maximum ice extent and NAO for the

Bothnian Bay). A longer ice formation period than ice melting period is inherent for all four sub-basins of the Baltic Sea. In the Bothnian Bay, the northeastern Gulf of Finland, coastal and archipelago areas, the ice processes are dominated by ice thermodynamics, while in the Bothnian Sea, the southern and central Gulf of Finland and the Gulf of Riga, by the ice dynamics. The latter areas are characterised by high ice mobility, i.e. drift ice conditions. The ice period length has a statistically significant trend between −1 and −2 days/year in the almost entire Bothnian Bay.

Ref. No.	Product name & type	Documentation
4.2.1	SST_BAL_SST_L4_REP_OBSERVATIONS_010_016 Satellite observations	PUM: https://marine.copernicus.eu/documents/PUM/CMEMS-OSI-PUM-010-016.pdf QUID: https://marine.copernicus.eu/documents/QUID/CMEMS-OSI-QUID-010-016.pdf
4.2.2	SEAICE_BAL_SEAICE_L4_NRT_OBSERVATIONS_011_004 Satellite observations	PUM: https://marine.copernicus.eu/documents/PUM/CMEMS-SI-PUM-011-004-011.pdfQUID: https://marine.copernicus.eu/documents/QUID/CMEMS-SI-QUID-011-001to007-009to013.pdf
4.2.3	Monthly mean NAO index	Barnston and Livezey (1987), Chen and Van den Dool (2003), Van den Dool et al. (2000)

4.2.1. Introduction

Climatology of the seasonal ice cover in the Baltic Sea has been of interest for a long time. The century-long (1900–2000) time series of the freezing and breakup dates, the length of the ice season and maximum annual ice thickness of landfast ice in the Baltic Sea were analysed by Jevrejeva et al. (2004). In a climatological timescale, the ice breakup date has shown a statistically significant decreasing trend in the northern Baltic Sea. The longest time series of the maximum annual ice extent covering the period of 1720–2008 has been compiled by Vihma and Haapala (2009), based on original information collected by Jurva (1952) and published by Palosuo (1953), and extensions of the time series by Seinä (1994) and Seinä and Palosuo (1996). Vihma and Haapala (2009) concluded that there is a noticeable shift towards a warmer climate in the latter half of the nineteenth century and a decreasing trend of the length of the ice season in the twentieth century.

The Baltic Sea has a north-south elongated shape, with the Gulf of Finland extending to the east from the main basin. Geographically, the Gulf of Bothnia belongs to the subpolar climatic region, while the Gulf of Finland and the Gulf of Riga are part of the humid continental climate region (after Köppen, Peel et al. 2007). The ice extent of the Baltic Sea is a valuable indicator of the impact of global warming in the region. For the winter navigation and development, as well as operation of offshore constructions, knowledge of ice conditions of different sub-basins of the Baltic Sea is relevant.

Different sub-basins possess different hydrophysical conditions i.e geometry, depth, stratification and mixed layer depth, which all influence the heat content of the total water volume and therefore play an important role in the ice climate and ice conditions of the particular sub-basins. Previous studies have generalised the ice conditions over the whole Baltic Sea without focusing on different sub regions (Omstedt and Chen 2001; Karpechko et al. 2015; Höglund et al. 2017). The aim of the current study is to characterise ice climate in the different sub-basins of the Baltic Sea in terms of ice season statistics (Figure 4.2.1).

4.2.2. Methods

The satellite remote sensing data of ice coverage from the years of 1982–2019 is used. Copernicus product reference 4.2.1 provides daily sea ice concentration data derived from the Swedish Meteorological and Hydrological Institute's (and the operational product by Finnish Meteorological Institute) high resolution ice charts at a 5 km horizontal resolution for the period of 1982–2011. The near real-time observations (NRT) product reference 4.2.2 provides ice concentration data for the period of 2012–2019 on 1 km grid, therefore the data was resampled on the reanalysis grid. The missing data from the Copernicus NRT FTP service were requested directly from the respective Copernicus production unit. The sea ice concentration is an estimated fraction of an area which is covered by ice in the grid cell.

The maximum extent of the ice season is from the beginning of October until the end of May. A grid cell is considered ice covered when the sea ice concentration of the grid cell exceeds 0.15. Within the ice season we have calculated ice probability as the ratio between days when sea ice is present and the length of the ice season (243 days). The beginning of ice period in each grid cell is defined as the first day when sea ice concentration exceeded threshold value of 0.15. Likewise, the last day when the sea ice concentration exceeded 0.15 is assumed to be the end of the ice covered period. The length of the ice covered period is the number of days between the first and last ice day. The ratio between the total number of ice days and total length of the ice period shows the ice persistency, while one minus ice persistency could be interpreted as ice mobility, i.e. the ratio between the total number of ice free days and total length of the ice period.
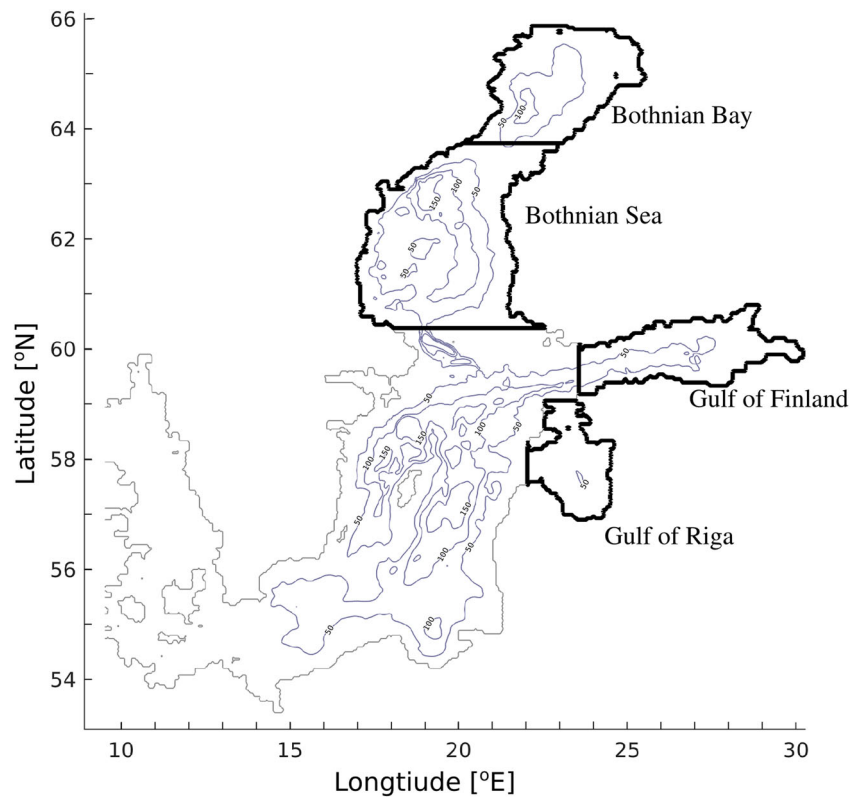
Figure 4.2.1. The map of the Baltic Sea showing locations of sub-basins. Isodepths 50-m, 100-m and 150-m are marked with a grey line.

Interannual variations of the ice extent in the Baltic Sea, which are calculated from the product reference 4.2.1 are consistent with the observations provided by Höglund et al. (2017), except for the absolute value of the ice extent, which could be overestimated in our study.

4.2.3. Results

The sea ice probability is very low, less than 0.05, in the Baltic Proper. In the open Baltic Proper, the extensive presence of the sea ice was registered in 5 years: 1984–86, 2009 and 2010, while only the Northern Baltic Proper, i.e. north of Gotland Island, was covered by ice in the years of 1993, 1994, 2002 and 2005. Due to the scarcity of years with extensive sea ice cover we did not analyse the ice statistics of the Baltic Proper. Ice probability is the highest in the northern Bothnian Bay and decreases gradually towards the Bothnian Sea (Figure 4.2.2a). In the Gulf of Finland, maximum ice probability is lower than in the Bothnian Bay. The spatial distribution of ice probability shows higher values in the northern than in the southern part of the Gulf of Finland. In the Gulf of Riga, maximum ice probability (0.44) is lower than in the Gulf of Finland (0.57). The ice probability is higher in the shallow archipelago area and has a gradual decrease in the northern part of the gulf.

In the Bothnian Sea, ice probability is highest along the coast and decreases circularly towards the central parts of the basin.

Ice starts to form in the Bothnian Bay in November, in the Gulf of Finland at the beginning of December and in the Gulf of Riga at the end of December (Figure 4.2.2b). The start of the ice period is gradually shifted to a later date from the coastal areas towards the centre of the basin in all sub-basins of the Baltic Sea. Excluding the Bothnian Bay, the end of the ice period is in April (Figure 4.2.2c). In the Bothnian Bay, ice melting is shifted to a later date, moving from southwest to northeast. In the Gulf of Finland, ice melting starts from the southern part and has a northeastward gradient. In the Bothnian Sea and in the Gulf of Riga, ice period ends in the central part of the basin. Mean ice period is the longest in the Bothnian Bay, reaching up to 183 days in the northeast, and the shortest in the Bothnian Sea and the Gulf of Riga, where it is around 70 days (Figure 4.2.2d). Spatial distribution of the mean ice period shows qualitatively similar conditions in the Bothnian Bay, the northeastern Gulf of Finland and the coastal and archipelago areas. In the latter, the ice conditions are most likely defined by ice thermodynamics, while in the Bothnian Sea, the western and central Gulf of Finland and the Gulf of Riga, ice dynamics have the biggest influence (Herman et al. 2011). This is illustrated by the ice mobility map (Figure
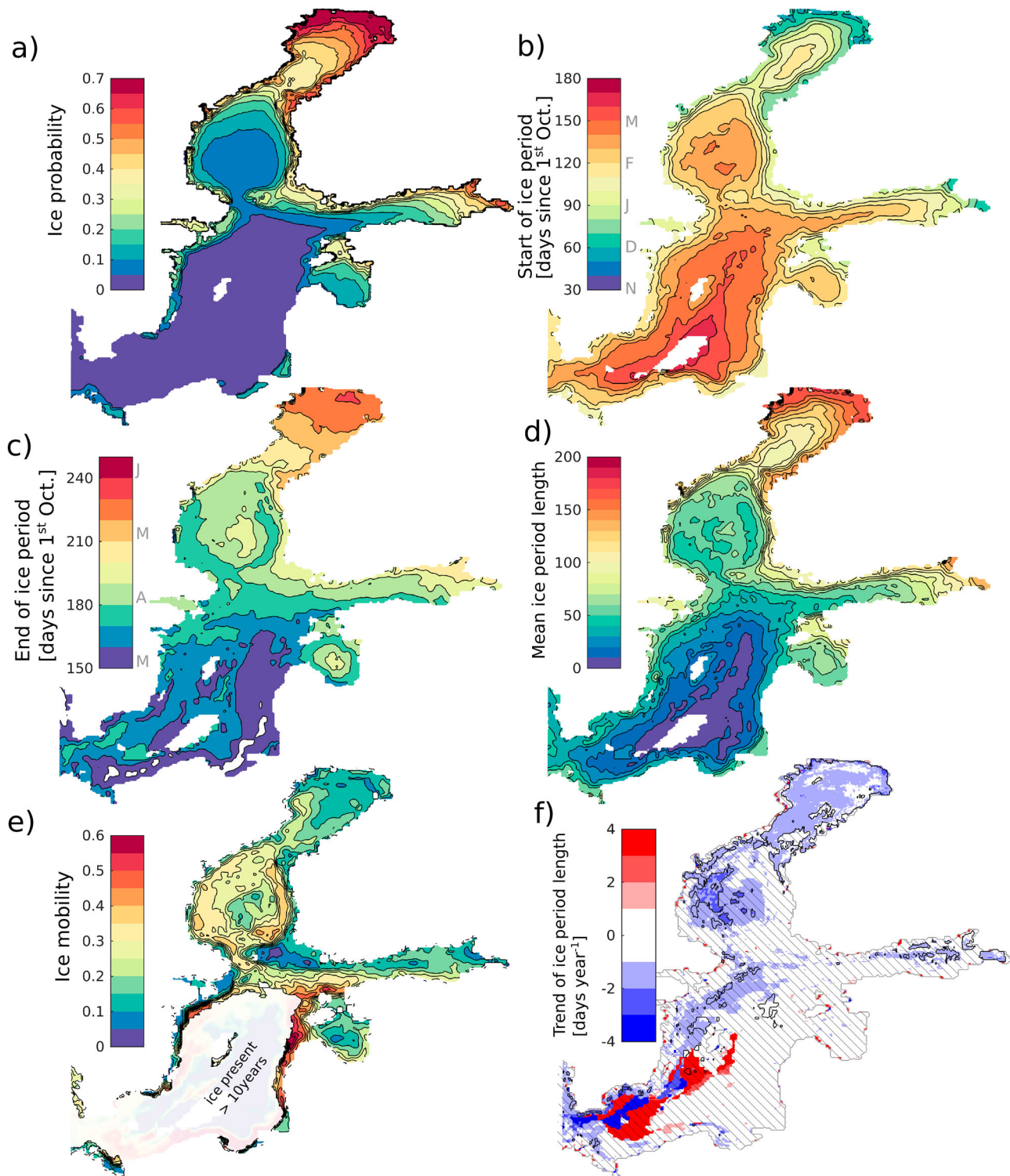
Figure 4.2.2. The maps of sea ice statistics calculated for the period of 1982–2019 (product reference 4.2.1). The sea ice probability for the ice season from the start of October until the end of May (a). The average first (b) and last (c) day of sea ice period. Mean length of the sea ice period (d). Sea ice mobility (e). The trend of sea ice period (f). Hatcheted area shows the area where the calculated trends had p-value > 0.05. The data is derived from the product references 4.2.1 and 4.2.2.

4.2.2e). Ice mobility is very low at the coasts and in the archipelago areas, which are usually covered with land-fast ice, and high in the open sea outside the landfast ice zone. Relatively low mobility in the centre of the sub-basins is related to the presence of the drift ice there as the leads form at the edge of land-fast ice zone.

The ice period length has a statistically significant (p-value < 0.05) trend between -1 and -2 days/year in
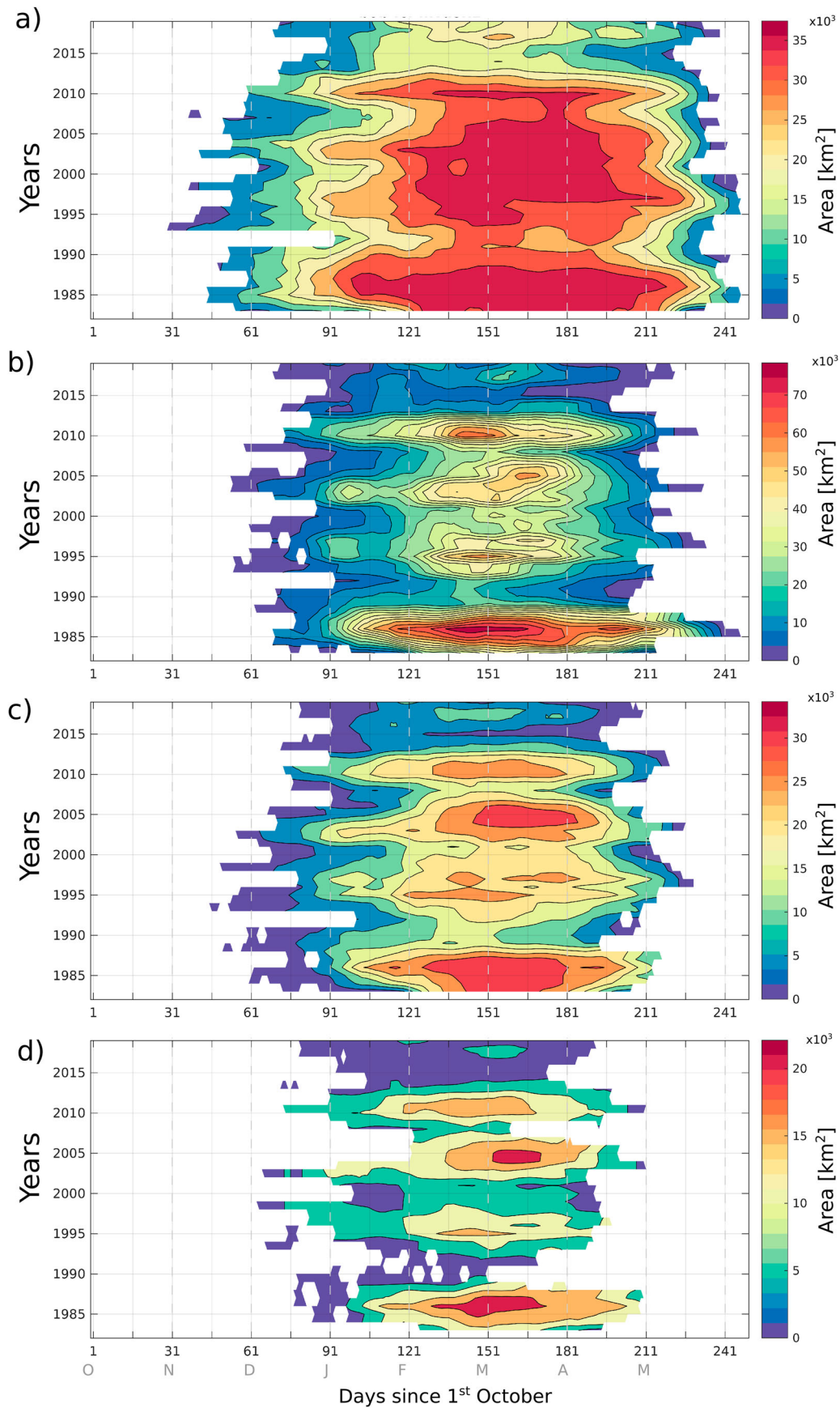
Figure 4.2.3. The area of sea ice extent calculated for the different regions of Baltic Sea: The Bothnian Bay (a), The Bothnian Sea (b), The Gulf of Finland (c) and the Gulf of Riga (d). The data is from the product references 4.2.1 and 4.2.2.

the almost entire Bothnian Bay (Figure 4.2.2f). There are also statistically significant negative trends in the western part of the Bothnian Sea, northeastern Gulf of Finland and northwestern Baltic Proper, but over a limited area and scattered in space. To some extent, the location of these patches corresponds to the area where spatial gradient of ice probability is high (Figure 4.2.2a) and the ice is mobile (Figure 4.2.2e). No such zones are seen in the southern and eastern parts of the sub-basins, nor in the Gulf of Riga.

Interannual variability of the ice extent in different sub-basins shows that colder and warmer winters are represented similarly in the Bothnian Sea, Gulf of Finland and the Gulf of Riga (Figure 4.2.3). The Bothnian Bay is almost every year until 2012 filled with ice. In general, ice starts to form successively in the Bothnian Bay, the Bothnian Sea and the Gulf of Finland, and eventually in the Gulf of Riga. A reverse pattern holds for the ice melting. There is an obvious asymmetry between the time period from the first ice occurrence to the maximum ice extent, and the last day of maximum ice extent and complete ice melting. The freezing-up takes about 30-days longer than the melting.

4.2.4. Discussion

In general, climatological mean southwesterly winds over the Baltic Sea (Soomere and Keevallik 2003) favour lower ice probability at the southwestern parts of the sub-basins. Interannual variations of maximum ice extent are coherent in the Bothnian Sea, the Gulf of Finland and the Gulf of Riga with a minimum correlation coefficient (R) of 0.83 between the sub-basins. Although the Bothnian Bay is fully covered with ice more frequently than the Bothnian Sea, the Gulf of Finland and the Gulf of Riga (Figure 4.2.3), the length of maximum ice extent period and the temporal dynamics of ice formation or melting is similar to a coherent pattern of the interannual variations between the sub-basins. This suggests that the large atmospheric circulation determines the severity of the ice season (Omstedt and Chen 2001; Karpechko et al. 2015). Jevrejeva et al. (2004) has shown correlation coefficients of −0.4 to −0.7 between the North Atlantic Oscillation (NAO) winter index (Jones et al. 1997) and ice break-up date for different coastal locations of the Baltic Sea. We have calculated correlation coefficients (R) between the length, start date and end date of the ice period, maximum ice extent and mean NAO index (product reference 4.2.3) for the ice season (October–May) in different sub-basins of the Baltic Sea. The correlation coefficient for the length of the ice period and NAO was −0.4 for the Gulf of Bothnia and about −0.5 for the Gulf of Finland

and Gulf of Riga. There was no correlation between the start date of the ice period and NAO, but a correlation of about −0.5 was found for the end date of the ice period and NAO in all the four sub-basins. Uotila et al. (2015) found correlation coefficient of −0.6 between maximum ice extent of the Baltic Sea and NAO index from 1979 to 2015. Our results show correlation coefficients for the maximum ice extent and NAO of −0.4 to −0.5 for the Bothnian Sea, Gulf of Finland and the Gulf of Riga. There is no correlation for the Bothnian Bay, as this basin is fully covered with ice more frequently than the other basins (Figure 4.2.3). A longer ice formation period than ice melting period is inherent for all four sub-basins of the Baltic Sea. Similar asymmetry has been observed for the Bohai Sea and explained by the different temperature change rate during the freezing and melting phases (Yan et al. 2017).

Regional differences of the ice statistics are most pronounced between the Bothnian Bay and the Gulf of Riga, which is not surprising as the Bothnian Bay is located between the latitudes of 64° N and 66° N, while the Gulf of Riga is located between 56° 30′ N and 59° N. In general, ice formation starts one month later and ice melts one month earlier in the Gulf of Riga (Siitam et al. 2017) than in the Bothnian Bay (Ronkainen et al. 2018). The most general difference between the Bothnian Bay and other sub-basins is that the ice stays longer there, which could be explained by thicker ice and colder weather (Pemberton et al. 2017) and a spatially large fast ice zone (Ronkainen et al. 2018).

Spatial distribution of the start and end of the ice period, mean ice period length and ice mobility in the sub-basins indicates that the Bothnian Sea, the southern and central Gulf of Finland and the Gulf of Riga have similar ice dynamics, which is determined by the large fraction of drift ice there (Haapala 2000). In the Bothnian Sea, fast ice is formed at the coast, while drift ice is present offshore (Leppäranta and Myrberg 2009). The Bothnian Sea is relatively large and deep (Figure 4.2.1), has weak vertical stratification (Leppäranta and Myrberg 2009) and large heat content, which all delays the ice formation. Drift ice can form due to break-off from the ice floes from the offshore edge of the landfast ice. Climatological mean cyclonic circulation (Myrberg and Andrejev 2006) contributes to the ice break-up outside landfast ice zone at the coast, as well as high mobility of the ice and converging of melting ice in the centre of the basin.

The southern and central Gulf of Finland have similar hydrographical conditions, i.e. water depth, vertical stratification (Liblik and Lips 2017) and the role of water circulation. Development of westward coastal current at the southern coast (Maljutenko and Raudsepp 2019)

supports earlier ice break-up and higher ice mobility at the southern coast. Ice mobility is lower in the Gulf of Finland than in the Bothnian Sea due to the elongated shape of the Gulf of Finland compared to the circular shape of the Bothnian Sea.

The Gulf of Riga is a small and shallow basin, which is vertically well mixed during winter (Raudsepp 2001) and it has the lowest heat content of the 4 basins. The southernmost location of the Gulf of Riga, compared the other sub-basins under study, and the correspondingly higher climatological air temperature and thinner ice (Pemberton et al. 2017) hamper formation of the stable ice there. The dominant anticyclonic circulation (Soosaar et al. 2014), momentum input and development of the Daugava River bulge and coastal current (Soosaar et al. 2016) in the southern part of the gulf in spring favours earlier ice breakup and relatively high ice mobility there (Figure 4.2.2).

Section 4.3. The resurgence of the North Pacific marine heatwave in 2018

Authors: F. Gasparin, A. Mignot, C. Perruche
State of main outcome: Unusual warm and fresh near-surface waters extending over thousands of square kilometres have been observed in late 2018 in the northeast Pacific, a signature similar to that of the North Pacific 'warm blob' during the winter of 2013/2014 and 2014/2015. These pronounced warm and fresh anomalies were forced by persistent atmospheric anticyclonic conditions during the 2018 spring and summer periods. By increasing the thermal stratification, the early year warming reduced the vertical entrainment of cold water in the surface mixed layer during the seasonal convective cooling in autumn 2018, enhancing the initial warming. These dynamical changes were associated with changes in surface chlorophyll concentrations in the subpolar and subtropical North Pacific, suggesting that these warm anomalies impacted phytoplankton biomass. This section demonstrates the critical need for better understanding the physical and biogeochemical mechanisms associated with prolonged, anomalously warm water events – also known as 'marine heatwaves' – which are expected to intensify with global warming.

Ref. no.	Product name & type	Documentation
Product 4.3.1	GLOBAL_REANALYSIS_PHY_ 001_025 Parameters: 3-dimensional ocean temperature, salinity and currents	PUM: https://marine. copernicus.eu/ documents/PUM/CMEMS- GLO-PUM-001-025.pdf QUID: https://marine. copernicus.eu/ documents/QUID/CMEMS- GLO-QUID-001-025.pdf

(Continued)

Continued.

Ref. no.	Product name & type	Documentation
Product 4.3.2	ECMWF Era-Interim reanalysis (atmosphere) Parameters: Heat and freshwater fluxes + Sea level pressure	Dee et al. (2011), Downloaded from the website https://data. ecmwf.int/data/
Product 4.3.3	OCEANCOLOUR_GLO_ CHL_L4_REP_OBSERVATIONS_ 009_082 Parameter: Surface chlorophyll-*a*	PUM: https://marine. copernicus.eu/ documents/PUM/CMEMS- OC-PUM-009-ALL.pdf QUID: https://marine. copernicus.eu/ documents/QUID/CMEMS- OC-QUID-009-030-032- 033-037-081-082-083-085- 086-098.pdf

In late 2018, the northeast Pacific experienced warm near-surface ocean conditions, reminiscent of the strong marine heatwave during the winter of 2013/2014 and 2014/2015, and coined as `the Blob' in the North Pacific (Bond et al. 2015; Walsh et al. 2018). The 2013–2015 event was the warmest event ever recorded in the region, and numerous studies have investigated its causes and consequences on regional climate (e.g. Hartmann 2015) and marine ecosystems (e.g. Peña et al. 2019). Based on a mixed layer temperature budget, Bond et al. (2015) have shown that this warm anomaly mainly resulted from a reduced e loss of heat of the ocean in addition to a relatively weaker cold horizontal advection in the surface layer. By increasing ocean thermal stratification, this large-scale anomaly has been identified as impacting both open ocean and coastal areas in changing marine ecosystems (Whitney 2015) and vertical dynamics (Zaba and Rudnick 2016). Recent papers have identified that large-scale modes of climate variability are key mechanisms driving marine heatwaves (e.g. Holbrook et al. 2019). As for the persistence of the northeast Pacific marine heatwave, several studies have documented its relation with the tropical variability through El Niño-Southern Ocean teleconnection (Di Lorenzo and Mantua 2016). Additionally, recent research has shown that the frequency, intensity and duration of marine heatwaves has increased over the past several decades and century (e.g. Hobday et al. 2018; Oliver et al. 2018), a trend expected to continue through the twenty-first century (Frolicher et al. 2018). The processes triggering 'marine heatwaves are still not well understood – although a number of isolated case studies provide valuable insights into their drivers (Holbrook et al. 2019). In particular, a temperature tendency budget provides a useful framework for diagnosing the important drivers (Holbrook et al. 2019). Here, we also consider the potential importance of the salinity budget for understanding marine heatwaves and discuss the potential impact on phytoplankton biomass.

Associated with persistent anticyclonic atmospheric conditions in mid-2018, sea surface waters in the Gulf of Alaska were characterised by unusual warm and fresh surface waters (2°C warmer and 0.2 psu fresher than the climatological cycle) over more than 4000 square kilometres in September–November 2018 (Figure 4.3.1a,b). These anomalously warm and fresh waters were associated with an intensification of the near-surface stratification, marked by a shallow winter mixed layer depth (around 30 m shallower than the climatology). The sea surface temperature pattern in September–November 2018 was analogous to the 2013/2014 winter conditions (Di Lorenzo and Mantua 2016), except that the 2018 warm anomaly was weaker and did not extend as deep (Figure 4.3.1c,d). This is potentially explained by the weaker duration and amplitude of the 2018 anticyclonic atmospheric conditions than was evident during the 2013–2015 period. For instance, the

anomalous atmospheric sea level pressure was up to +5 HPa in 2018 while it reached up to +9 HPa in 2014 (Bond et al. 2015). Both events ended up with anomalous negative sea level pressure in December 2016 and December 2018, increasing winds and causing higher turbulent mixing (not shown).

To detail the oceanic processes associated with the observed conditions in the northeast Pacific, the terms of the temperature and salinity mixed layer budgets are shown in Figure 4.3.2 using an ocean reanalysis. Seasonal variations of temperature in the mixed layer are typically characterised by a warming from March to August and a cooling from September to February, mainly driven by sea surface heat fluxes and vertical entrainment fluctuations due to the deepening and shallowing of the mixed layer (Figure 4.3.2a). Note that temperature changes are approximately explained by the contributions of sea surface heat fluxes, and vertical
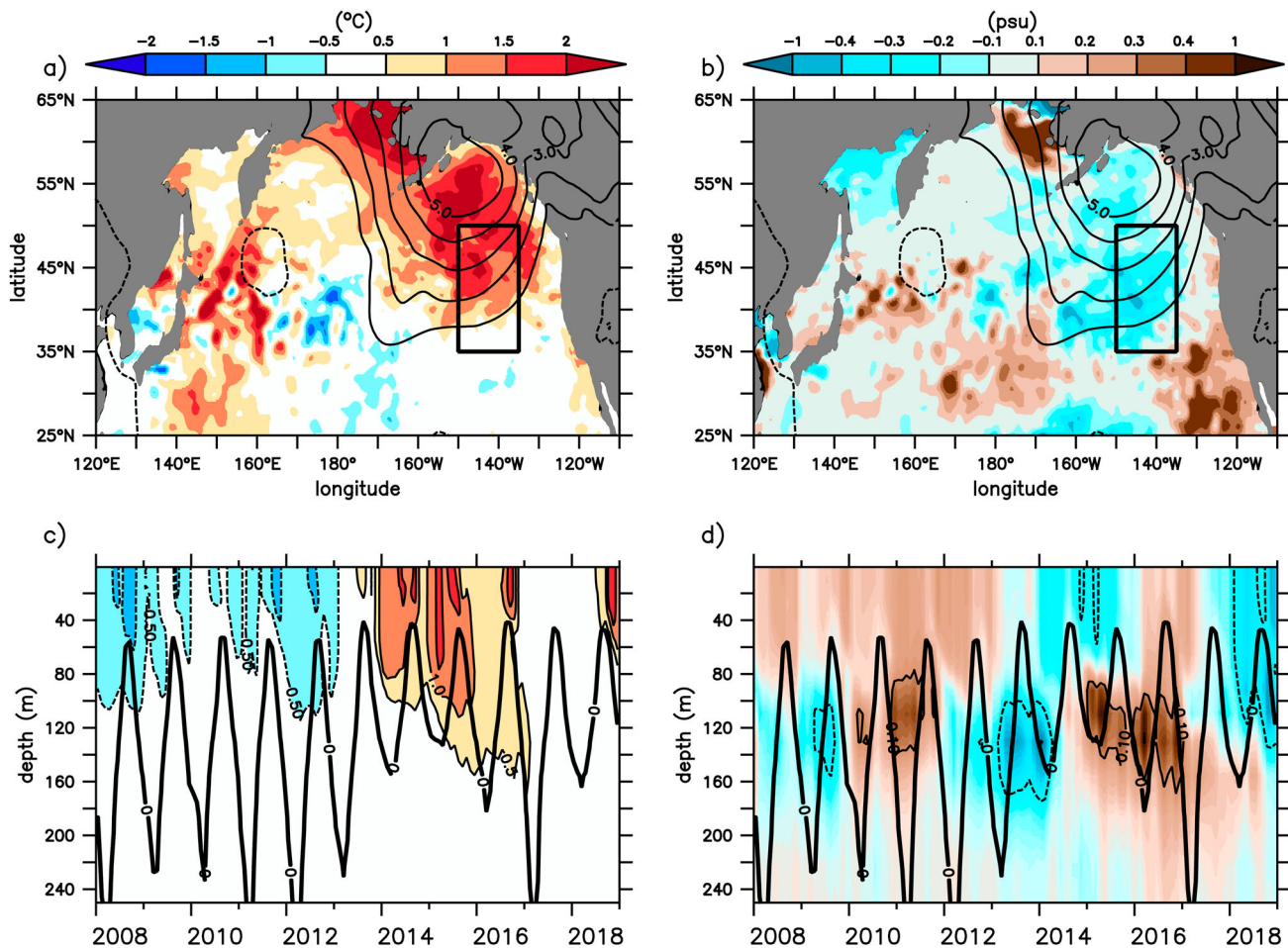
Figure 4.3.1. (a,b) Sea surface temperature (in °C) and salinity anomalies (psu) in the North Pacific for the period October–November 2018 (colour shading), and sea level pressure anomaly (in hPa) for the period July–September 2018. The black square indicates the marine heatwave region (135°–155°W; 35°–50°N). (c,d) Temperature and salinity anomalies area-averaged in the marine heatwave region for the period 2008–2018 (shading) and the corresponding mixed layer depth (black line, defined as the depth equivalent to the surface density plus 1 kg/m^3; as in Bond et al. 2015). Anomalies are obtained after removing the 2008–2018 climatological cycle, but no long-term warming trend (product reference 4.3.1, 4.3.2).

entrainment since the variations of the vertical entrainment estimate (often considered as residuals; e.g. Bond et al. 2015) are consistent with the 'temperature changes minus advection minus surface heat flux' residuals. Compared to seasonal variations, the surface layer heat budget in 2018 shows a maximum warming at the beginning of the seasonal cooling in September–October, mainly due to a reduced vertical entrainment cooling (Figure 4.3.2b). The dominant role of vertical physics was not pointed out during the onset of the 2013–2016 marine heatwave by Bond et al. (2015), but rather in maintaining the warm sea surface temperature over two years (Schmeisser et al. 2019). In Figure 4.3.2c, the freshwater budget also illustrates the dominant contribution of the entrainment term in seasonal variations in salinity, marked by a freshening from March to August and salinification from September to February. In early 2018, the observed freshening mostly resulted from an enhanced vertical entrainment during the seasonal freshening (Figure 4.3.2d). Through the barrier layer mechanism, this surface freshening might have contributed to enhance the vertical stratification and reinforce the near-surface warming by reducing the mixed layer (Sprintall and Tomczak 1992). In order to assess the salinity contribution to the thinning of the mixed layer, the mixed layer depth, estimated with salinity replaced by the mean value, was subtracted from the mixed layer depth with the observed salinity included. The freshening of near-surface waters appears to reduce the mixed layer by more than 15 m (not shown), illustrating the important role of salinity in the 2018 marine heatwave in the northeast Pacific. Further investigation is needed to properly determine the contribution of the salinity anomaly in the processes associated with marine heatwaves. The mixed layer temperature and salinity budgets have thus demonstrated the essential role of the entrainment term and the contribution of salinity in reducing the mixed layer depth during the 2018 marine heatwave in the northeast Pacific. The important role of the processes at the base of the mixed layer in the maintenance of the 2013–2016 northeast Pacific marine heatwave has been recently pointed out by Schmeisser et al. (2019).
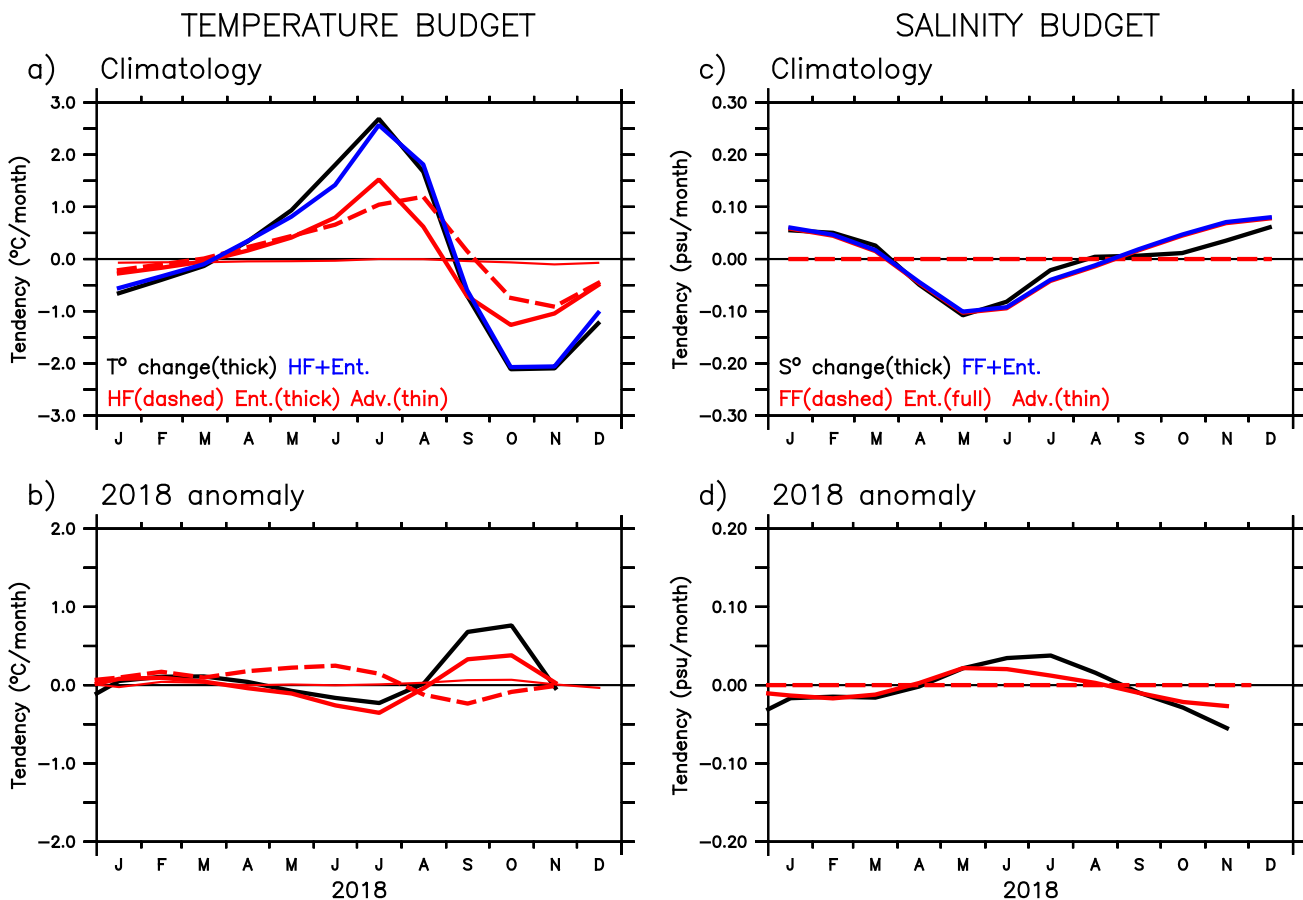
Figure 4.3.2. (a) 2008–2017 climatological mixed layer heat balance terms (in °C/month), area-averaged in the marine heatwave region, i.e. temperature change (full black line), horizontal advection (dashed red line, as in Lee et al. 2004), net surface heat flux (dashed red line) and entrainment (full red line, as a function of mixed layer depth variations and temperature differences between the mixed layer and at the base of the mixed layer). The sum of entrainment and atmospheric fluxes are indicated in blue. (b) Same as (a), except for the 2018 anomaly from the climatological cycle. (c,d) Same as (a,b), except for salinity (product reference 4.3.1).
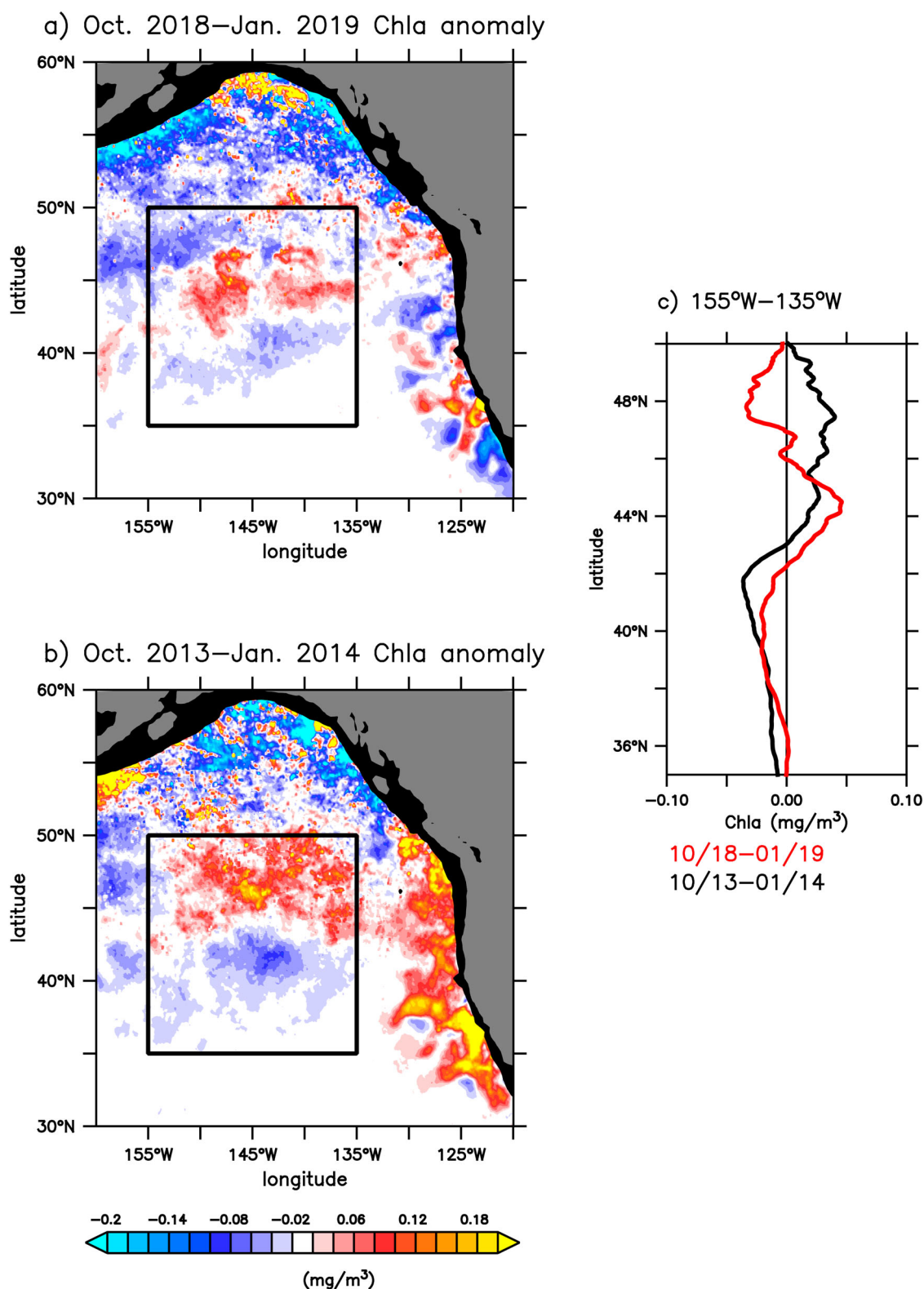
Figure 4.3.3. Chla anomaly (October–January) in the northeast Pacific during winter of 2018/2019 and 2013/2014 ((a,b) spatial maps, (c) zonal average in the marine heatwave region). The black square indicates the marine heatwave (135°–155°W; 35°–50°N). Anomalies are obtained after removing the 2008–2018 climatological cycle, but no long-term trend (product reference 4.3.3).

Numerous studies have identified the impact of marine heatwaves on marine ecosystems and marine productivity (e.g. Greene 2016; Yang et al. 2018), but also on atmospheric conditions including North America weather (e.g. Smale et al. 2019). As the heat and freshwater budgets have identified the role of vertical

entrainment in the near-surface temperature and salinity variations in 2018, the consequences regarding phytoplankton biomass are briefly investigated using surface chlorophyll-*a* concentrations from a satellite product as a proxy. The surface chlorophyll-*a* concentrations anomaly, shown for the winter of 2018/2019 and 2013/2014 in the northeastern Pacific in Figure 4.3.3, exhibits a north-south dipole in the marine heatwave region, with higher than usual chlorophyll concentrations in the northern part and lower in the southern part. In the subtropical gyre, phytoplankton growth is strongly limited by the availability of nitrate in the surface sunlight layer (Whitney 2015; Peña et al. 2019). We thus hypothesise that the reduction of vertical entrainment during the warm blob dampened the nitrate supply in the euphotic layer (the layer where there is enough light to sustain photosynthesis), which in turn decreased phytoplankton growth and primary production. In the subarctic region, phytoplankton growth is limited by iron availability and light in winter when phytoplankton are mixed from the surface to the base of the deep mixed layer (Whitney 2015; Westberry et al. 2016). In the subarctic North Pacific, we surmise that the shallow mixed layers during the warm blob have increased the light exposure of phytoplankton and thus phytoplankton growth and primary production (Whitney et al. 2005; Peña et al. 2019), but other mechanisms might cause an enhanced biological activity such as iron supply from sea ice melting (Paik et al. 2017) Thus, the different relationship of the sea surface temperature and primary production observed in the subtropical and subarctic gyres demonstrates that the enhanced stratification associated with marine heat waves might impact differently on phytoplankton biomass as mentioned by Yu et al. (2019).

In conclusion, the 2018 ocean conditions in the northeast Pacific were characterised by anomalous warm and fresh waters. A detailed description of the heat and freshwater balances have identified that the enhanced stratification reduced the vertical exchanges of temperature and salinity. The impact of the enhanced stratification on chlorophyll-*a* is of opposite sign in the subarctic and subtropical North Pacific, as already observed by Yu et al. (2019) for the 2013/2015 blob. A question arises about the long-term consequences of global warming for ecosystems (Webb and Werner 2018), given the projected increases in marine heatwaves in the future (Frolicher et al. 2018). Thus, a better understanding of the processes associated with marine heatwaves could be improved with the deployment of biogeochemical-Argo floats in this region (Jaine et al. 2017). In addition, improving the ability of biogeochemical models to represent such ocean mechanisms is essential to monitor and anticipate impacts on marine ecosystems (Figure 4.3.3b).

Section 4.4. Anomalous surface warming in the Baltic Sea in summer 2018 and mechanism analysis

Authors: Jun She, Jian Su, Ann-Sofie Zinck
Statement of main outcomes: The summer 2018 is one of the two warmest summers recorded over the past 37 years in the Baltic Sea. This warm summer also showed unique features in synoptic extreme events – marine heatwaves (MHWs). MHWs in the Baltic Sea during 2018 lasted for the entire summer period (May–September) and showed great intra-seasonal variability on the spatial pattern. MHW duration ranges between 80 and 110 days in most of the southern Baltic Sea and below 60 days north of 59°N in most of the Baltic Sea. No marine heatwave events are found in open waters in Bothnian Sea and Bothnian Bay in May and June. Results show that the large scale atmospheric circulation in summer 2018 was featured by the highest seasonal Arctic Oscillation index and North Atlantic Oscillation index since 1950. Strong blocking in atmospheric circulation in summer 2018 was accompanied by a deepening and eastward shifting Low over Greenland-Iceland and also a very strong jet stream further north than normal. The Baltic Sea MHW duration in summer 2018 was positively correlated with surface air temperature anomaly, which was caused by prevailing high pressure systems over northern Europe and Scandinavia. Atmospheric reanalysis shows that the shortwave solar radiation is the dominant factor contributing to the positive anomaly of the net surface heat flux.

Products used

Ref. no.	Product name & type	Documentation
4.4.1	SST_BAL_SST_L4_REP_ OBSERVATIONS_010_016 Baltic Sea sea surface temperature reprocessed data	PUM: https://marine.copernicus. eu/documents/PUM/CMEMS-OSI-PUM-010-021-022.pdf QUID: https://marine.copernicus. eu/documents/QUID/CMEMS-OSI-QUID-010-021-022.pdf
4.4.2	C3S ERA5 Model reanalysis	ECMWF (2019); CC3S ERA5: Fifth generation of ECMWF atmospheric reanalyses of the global climate. Copernicus Climate Change Service Climate Data Store (CDS). [accessed 16.02.2019]. https://cds.climate. copernicus.eu/cdsapp#!/home ECMWF: ERA5 data documentation [accessed 16.02.2019] https://confluence. ecmwf.int/display/CKB/ERA5 +data+documentation
4.4.3	Monthly values of the NAO and AO indexes during January 1950–November 2019	Climate Prediction Center, NOAA Center for Weather and Climate Prediction, USA: https://www. cpc.ncep.noaa.gov/products/ precip/CWlink/daily_ao_index/

(Continued)

Continued.

Ref. no.	Product name & type	Documentation
		monthly.ao.index.b50.current. ascii.table https://www.cpc.ncep.noaa.gov/ products/precip/CWlink/pna/ norm.nao.monthly.b5001. current.ascii.table

Extreme ocean warming, termed as marine heatwaves (MHWs, similar to heatwaves occurring on land), has been recorded more frequently, both on global (Hobday et al. 2015, 2018; Frölicher and Laufkötter 2018) and regional scale (Bensoussan et al. 2019). MHWs can be quantitatively defined as an event with a prolonged period (5 consecutive days or more) of anomalously warm water condition (e.g. warmer than the 90th percentile of local temperatures to the long-term climatological mean) (Hobday et al. 2015). Mean duration and frequency of annual MHWs have increased globally (Oliver et al. 2018). Compared to the open ocean, MHW

events are stronger in the coastal waters, with significant environmental impacts on the coastal marine ecosystems (Frölicher and Laufkötter 2018; Bensoussan et al. 2019).

The Baltic Sea is a semi-enclosed sea (Figure 4.4.1a) which has experienced significant climate warming over the past decades, especially in the upper ocean layer. Høyer and Karagali (2016) showed that the Baltic Sea underwent a surface warming trend at a rate of 0.041°C yr^{-1} during 1983–2012. This trend however varied regionally. Generally, north of 59°N the 30-year trends were larger compared to those further south. It was also noted that the warming trend in summer was the largest among the seasons. The summer mean Sea Surface Temperature (SST) time series in the past 37 years is given in Figure 4.4.1c. In addition to the warming trend, there is also significant inter-annual variability. Years 2002 and 2018 are both around 15.5°C and marked as the highest records in the past 37 years.

On seasonal scale, anomalous surface warming in the Baltic Sea is mainly affected by anomalies of atmospheric
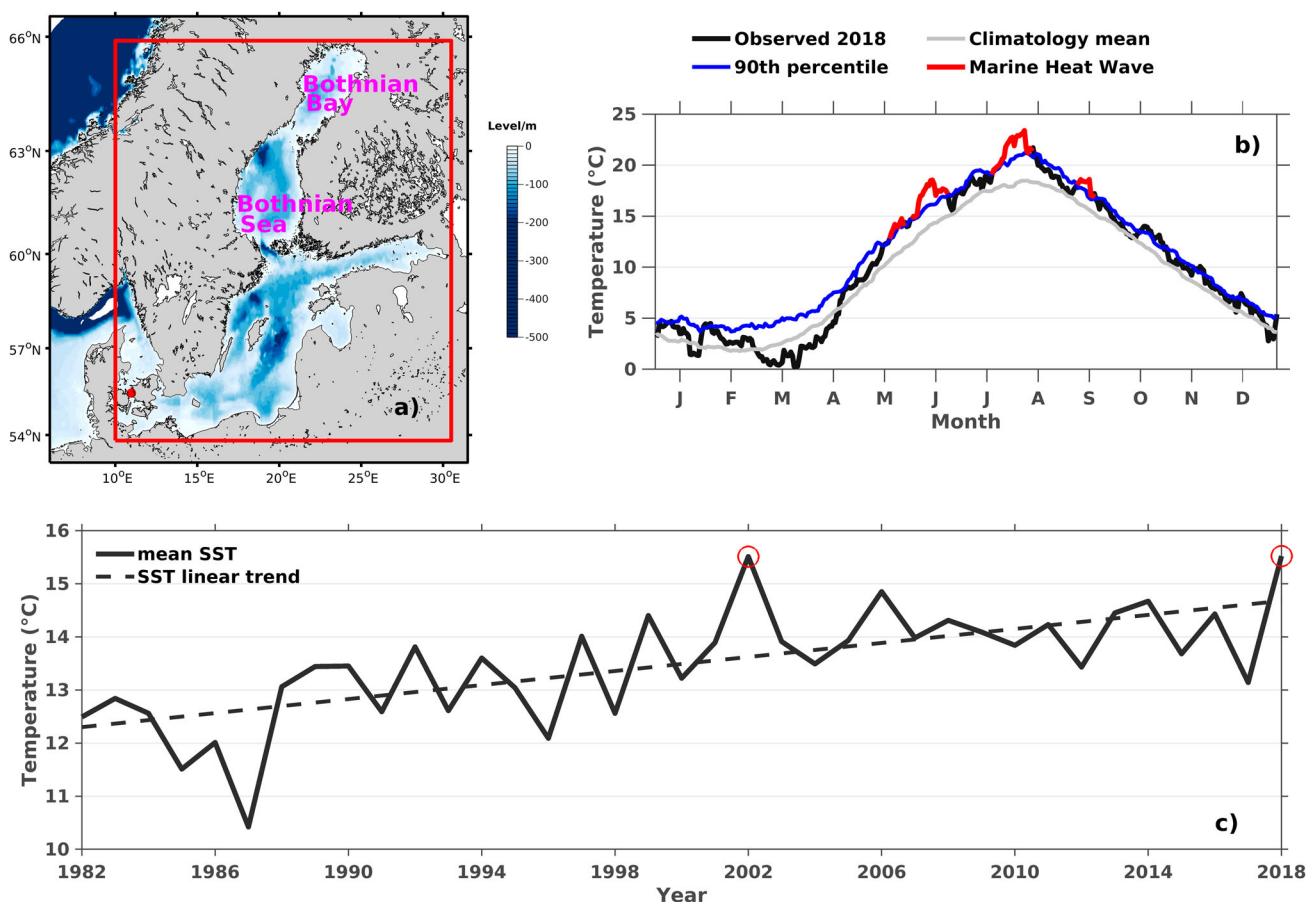
Figure 4.4.1. (a) Bathymetry (units: m) in the Baltic Sea. (b) Illustration of MHWs in 2018 at location (10.98°E, 55.48°N), as indicated by the red dot in a). The climatological mean (grey line) and the 90th percentiles (blue dashed line) of daily SST were calculated over the period 1983–2012. A MHW (red line) is defined when SST (black line) exceeds the climatological 90th percentile (blue line) for 5 days in a row. c) Time series of summer (May–September) Baltic Sea area mean SST over the period 1982 to 2018. The average area is indicated as a red box in a). Two warmest years 2002 and 2018 are highlighted with circles. The results in b) and c) are generated by using product ref. 4.4.1.

heat fluxes and vertical mixing. On synoptic scale, horizontal advection of heat flux, e.g. from North Sea inflow, can also be important for surface warming but mainly for the transition waters. A comprehensive introduction on the Baltic Sea hydrodynamics can be found in Leppäranta and Myrberg (2009).

In summer 2018, the Baltic Sea experienced extremely warm weather and upper ocean conditions. What were the major spatiotemporal features of this warming and reasons generating them? Are they related to significant anomaly in atmospheric circulation and on which spatial and temporal scales? The purpose of this study is to quantify the level of the surface ocean heat anomaly in the Baltic Sea and its potential driving factors.

In this context, we will use a CMEMS level 4 reprocessed SST dataset over the period 1982–2018 (product ref. 4.4.1) to quantify spatiotemporal patterns of MHWs in the Baltic Sea during summer 2018. In addition, we use the ERA5 reanalysis dataset (product ref. 4.4.2), a most recent version of European global atmospheric reanalysis produced by European Centre for Medium Range Weather Forecast (ECMWF), to analyse anomalous atmospheric conditions, e.g. geopotential height, air temperature at 2 m elevation and surface heat fluxes and their potential impacts on SST.

4.4.1. Identification of MHW events

The definition of a MHW and its continuation used in this study followed that described in Hobday et al. (2015). It is defined as a period in which the water temperature is above the 90th percentile for that area's historical conditions for five or more days, where the climatological threshold is a time-of-year dependent 11-day shifting window. The method allows comparison of MHW duration and intensity across time and space from sites with different thermal regimes. The 30-year climatological mean and 90th percentiles of SST were calculated over the 1983–2012 period, using an 11-day centred window and additional smoothing on the climatology with a 30-day running mean (Hobday et al. 2015). Figure 4.4.1b illustrates an example of MHW in 2018 at a site (10.98°E, 55.48°N), which gives three MHW periods, i.e. May – mid-June, July and the first half of September. Note that the identification of MHW events can be sensitive to the presence of significant climate trends and/or long-period variability, in particular the choice of 30-year climatological standard normal period. Therefore, the employment of the definition of the MHW in the future climate adaptation applications should be with caution, e.g. climate adaptation for the marine ecosystem.

4.4.2. Spatial and temporal variability of 2018 MHW events

For period May–September 2018, most of the Baltic Sea surface experienced at least one MHW event except for a minor part of Swedish coastal waters in the Bothnian Bay (Figure 4.4.2b). The accumulated summer MHW duration ranges between 80 and 110 days in most of the southern Baltic Sea and below 60 days north of 59°N (Figure 4.4.2b). However, the mean MHW intensity north of 59°N (2–4°C) is stronger than most of the southern Baltic Sea (1–2°C, Figure 4.4.2a).

Monthly spatial distribution of MHW duration shows notable intra-seasonal variability (Figure 4.4.2c–f). In May, major MHW events are found between 56° N and 60° N, featured by MHW days >15. Areas without MHWs are only found in the central Bothnian Sea and Bothnian Bay. In June, non-MHW areas remain similar to May while MHWs are intensified south of 59°N. MHWs covered the entire Baltic Sea in July and August but areas with longer MHW duration were moved to north of 59°N in July and back to south of 59°N in August. Only very limited area in Swedish nearshore waters in western Bothnian Bay were free from MHWs.

4.4.3. Atmospheric conditions in summer 2018

The summer of 2018 was exceptionally hot and dry in northern Europe, which led to droughts, heatwaves and wildfires (Copernicus Climate Change Service 2019). Most of the areas affected by the drought were across northern and central Europe, including Austria, Denmark, Finland, France, Germany, Ireland, Lithuania, Sweden, the northeast part of Switzerland and the UK (EUMETSAT 2018). Because of the drought, farmers experienced a significantly reduced harvest, leading to concerns about food shortages in the coming months. Wildfires were reported in Denmark, Finland, Germany, Greece, Latvia, Norway, Portugal, Sweden and the UK, severely damaging hundreds of acres of scrubland, forests and moorland. Maximum and mean temperature records were broken in many places (Copernicus Climate Change Service 2019).

In seasonal scale, Arctic Oscillation (AO) (Ambaum et al. 2001) and North Atlantic Oscillation (NAO) (Barnston and Livezey 1987) are major teleconnection patterns affecting weather in northern Europe and Scandinavia. The former is related to the degree of which Arctic air penetrates into the middle latitudes. Large positive AO index often helps the extra-tropical westerly jet stream to blow strongly and consistently, thus keeps the cold Arctic air locked in the polar region. Using published
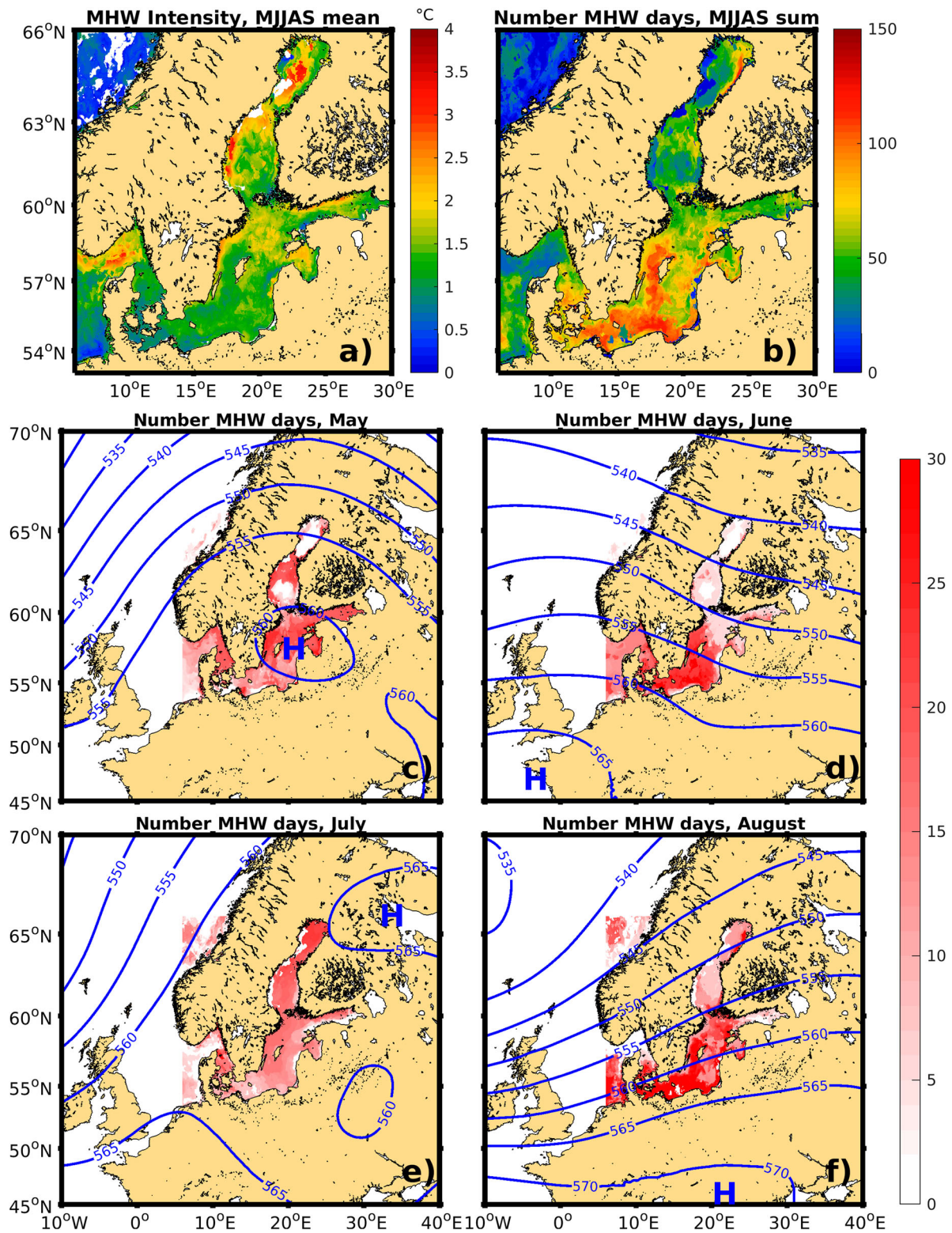
Figure 4.4.2. Spatial distribution of MHW intensity and duration in 2018: (a) summer (May–September) mean MHW intensity (in °C); (b) accumulated summer MHW duration (number of days); (c)–(f) MHW duration by month May to August 2018, overlapped by corresponding monthly mean geopotential height in 500 hPa. The results are generated from product ref. 4.4.1 and product ref. 4.4.2.

monthly values of the AO index from Climate Prediction Center, NOAA Center for Weather and Climate Prediction, USA (product ref. 4.4.3), it is found that May–September mean AO index in 2018 is 0.72 and reaches its 70-year maximum. This means that less Arctic cold air was transported to the south in summer 2018 and the Arctic condition was in favour of warm weather in northern Europe.

The NAO index reflects direction and strength of the westerlies into Europe and is correlated with location of the jet stream. By analysing data in 1881–2003, Folland et al. (2009) found that there existed statistically significant positive correlation between the positive phase of summer NAO (SNAO) and anticyclonic and sunny conditions over northwest European land from Ireland to the eastern Baltic. Variations of the SNAO are associated with changes in the North Atlantic storm track such that a positive SNAO index is associated with northward movement of the storm track over northwest Europe. This happened in summer 2018. Using monthly values of the NAO index from product 4.4.3, it is found that the SNAO index (May–September mean) in 2018 (1.65) is the highest in the past 70 years for the 5 month moving average values. This implies a high possibility of prevailed anticyclonic circulation and dry, sunny weather in northern Europe and the Baltic Sea.

At 500 hPa in summer 2018, an unusual geopotential high anomaly can be found over the Baltic-North Sea region (lower panel in Figure 4.4.3) which implies that the summer experienced more frequent occurrence of the high pressure systems. The jet stream (zone with the highest horizontal gradient of the geopotential height) was strengthened and moved to the Nordic Seas (upper right panel in Figure 4.4.3) from its normal position between 45 and 60° N over the North Atlantic (upper left panel in Figure 4.4.3), so that Baltic-North Sea region experienced stable sunny weather.

It should be noted that Figure 4.4.3 only represents summer mean condition instead of daily weather. There exists significant intra-seasonal variability on the
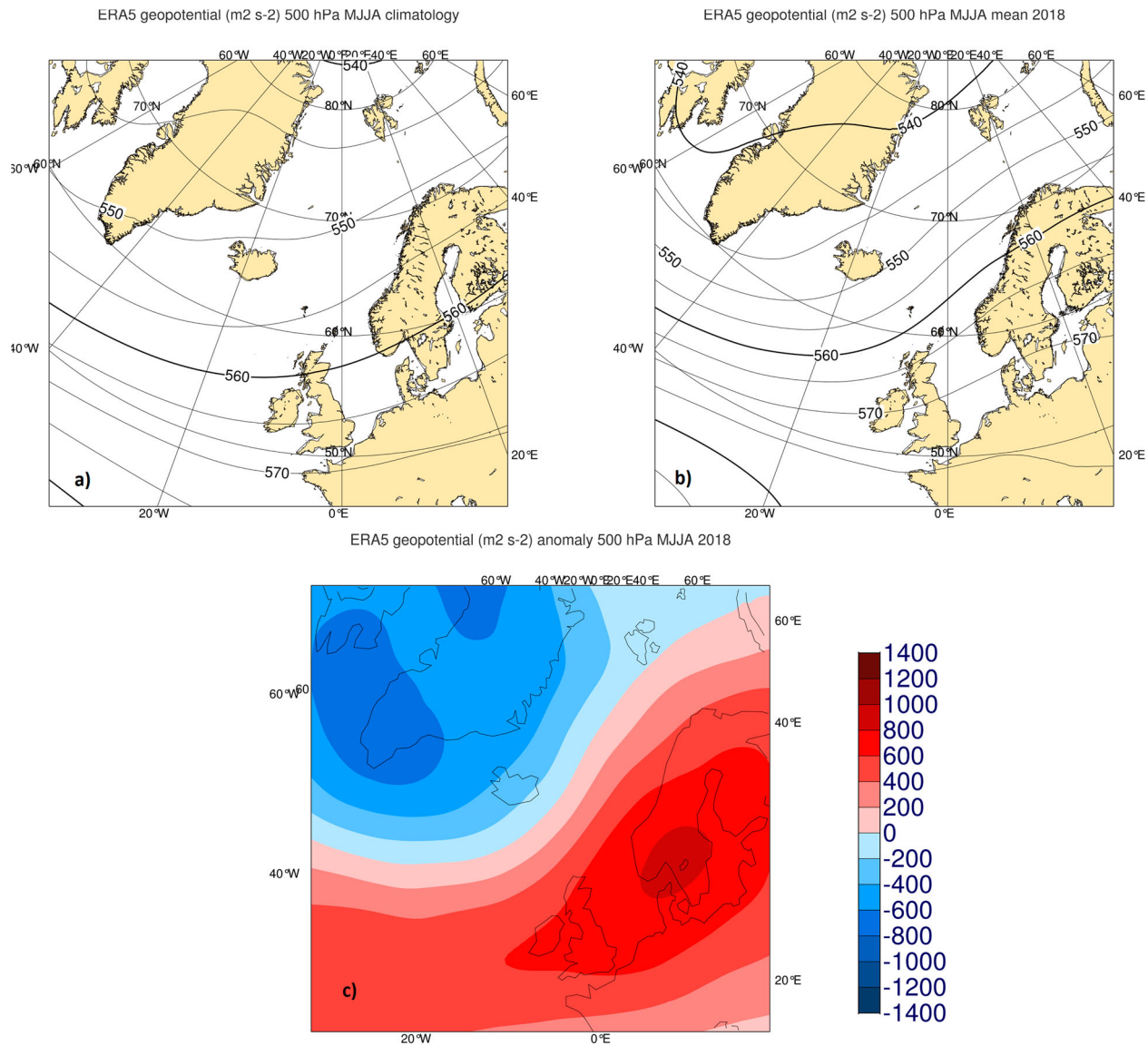

Figure 4.4.3. May-August mean circulation at 500 hPa in 2018: (a) geopotential height climatology; (b) geopotential height in 2018 and (c) geopotential anomaly (m² s⁻²) relative to 1981–2010 climatology. The results are generated from product ref. 4.4.2.

weather pattern, which can be found in the monthly mean geopotential height distribution from May to August, as shown in Figure 4.4.2(c–f). By looking at daily synoptic maps from ERA5 reanalysis, it was found that the summer period was dominated by several blocking events ranging 8–14 days which were separated by transient highs and lows with shorter synoptic scales (figures not shown). The first blocking event started from 6 May, lasting for 8 days, and followed by a 5 day period of transient weather systems. Afterwards there was a major blocking event with duration of about 14 days. In June, the transient synoptic systems dominated the northern Baltic while the stable high pressure system retreated to south. From 23 June, high pressure system re-gained control over the northern Baltic Sea, which prevailed for most of July. After 8 August, a transient low controlled Baltic Sea and brought cool and wet air to the Baltic Sea.

Further investigations show that the intra-seasonal variability in the atmosphere circulation causes similar variability in the 2 m air temperature, as shown in Figure 4.4.5. In May, positive 2 m air temperature anomaly above 4°C can be found in most of the northern European

continent and Scandinavia, with maximum anomaly above 6°C around 61°N in Norway and 55–60°N over the Baltic Sea. In June, the positive air temperature anomaly retreated to south of 61°N. Most areas north of 61°N were dominated by negative temperature anomalies with exceptions in the northern Baltic Sea. The positive air temperature anomaly was enhanced again in July, and expanded to the northeast in Scandinavia and to the west in the northern European continent. In August the positive air temperature anomaly was less significant than in July. The southern and mid-Baltic Sea was dominated by positive air temperature anomalies of 2–3°C while the Bothnian Sea and the Bothnian Bay were 1°C cooler.

4.4.4. Relationship between the MHWs and the anomalous atmospheric conditions

The areas with largest positive air temperature anomaly in the Baltic Sea (Figure 4.4.4) are well correspondent to areas with high MHW duration (Figure 4.4.2). The spatial correlation coefficients between the monthly air temperature anomaly and the number of MHW days are 0.47, 0.54, 0.60 and 0.59 for May, June, July and
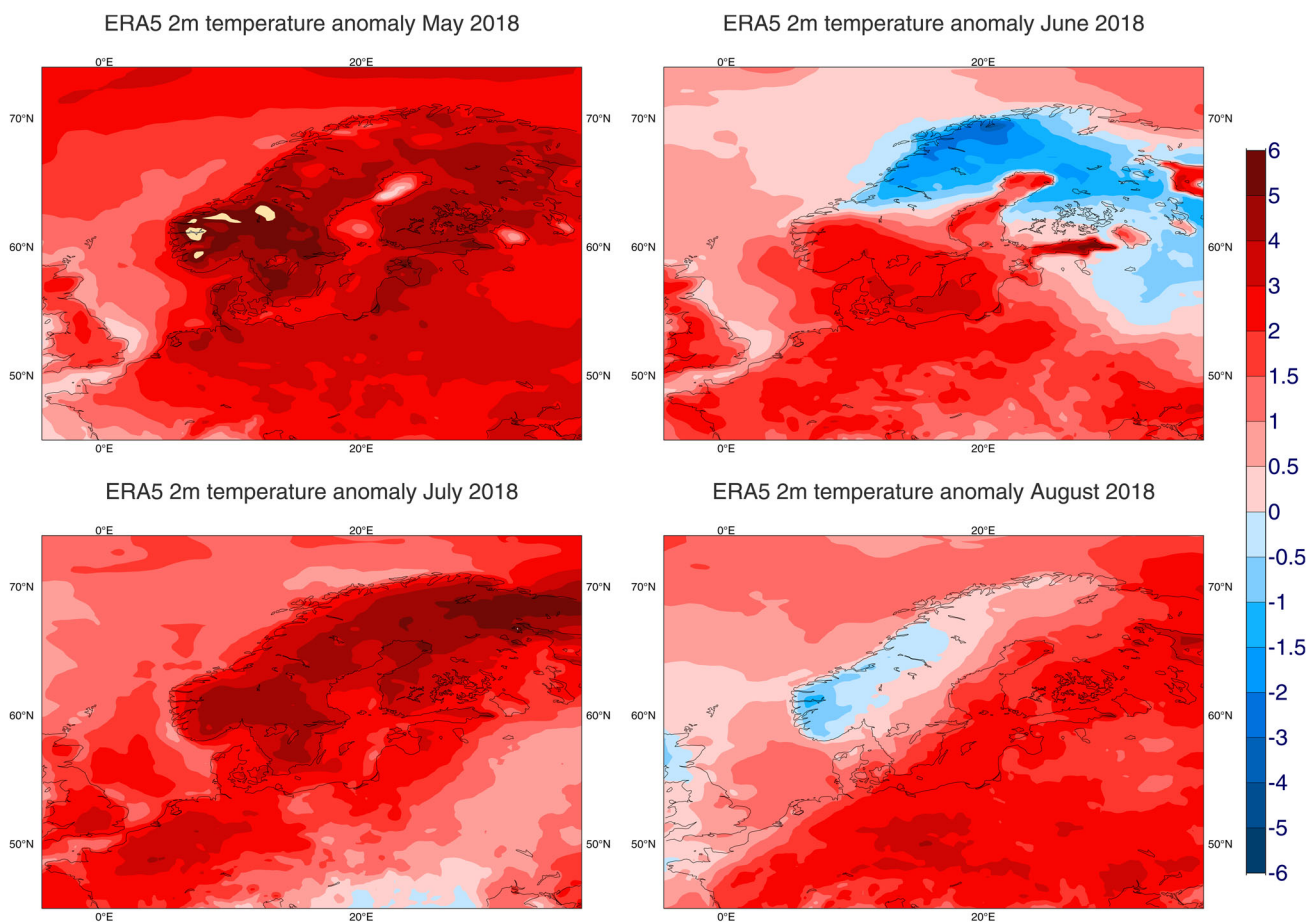

Figure 4.4.4. Monthly averages of 2 m air temperature (°C) anomaly from May to August 2018, relative to 1981–2010 climatology. The results are generated from product ref. 4.4.2.
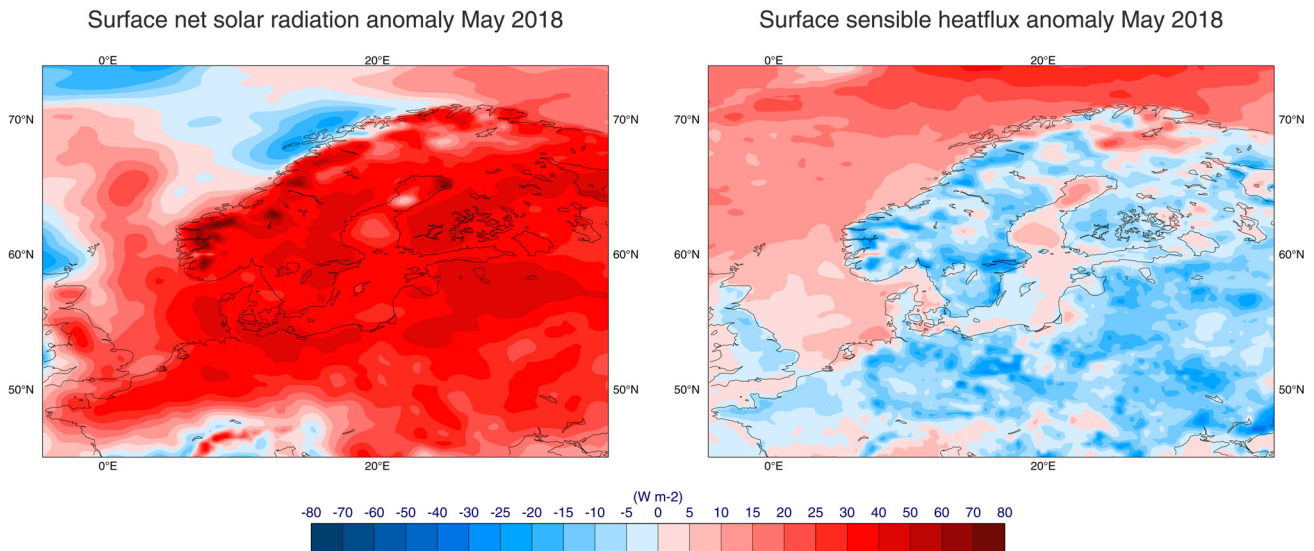
Surface net solar radiation anomaly May 2018   Surface sensible heatflux anomaly May 2018

Figure 4.4.5. Anomaly of mean net solar radiation (shortwave, left panel) and sensible heat flux (right panel) in May 2018, relative to 1981–2010 climatology. The unit is W m^{-2}. The results are generated from product ref. 4.4.2.

August, respectively, which are all above a p-level of 0.0001. This means that there exist common factors impacting both surface air and sea temperature and/or they affect each other.

Analysis on the atmospheric circulation anomalies from ERA5 suggests that the prevailed blocking events over northern Europe and Scandinavia are the common cause of positive air temperature anomaly and high MHW duration. The blocking high pressure system caused strong downward movement of air which led to strong warming in the mid- and the lowest levels of the atmosphere. This also prevented the formation of clouds and rain, leading to more than 80% of precipitation deficit associated with cloudless conditions in central and northern Europe (Copernicus Climate Change Service 2019). This led to excessive amount of shortwave radiation reaching the sea surface. On the other hand, due to high evaporation and low precipitation, the latent heat has a strong negative anomaly. In such conditions latent heat contributed negatively to the surface warming. Sensible heat anomaly and longwave radiation anomaly are the secondary contributors to the sea surface warming comparing to the shortwave radiation and latent heat as their impacts depend on negative air-sea feedback mechanisms among surface air temperature, SST, humidity and longwave radiation. Eventually the sensible heat flux and longwave radiation do not move too far from the climatology in the Baltic Sea in summer 2018 (± 20 Wm^{-2}, figures not shown), as shown by the ERA5 reanalysis. Another factor which may contribute to the warming is enhanced upper layer stratification in the sea, which could reduce the upper ocean mixing and retain the heat in the thinner upper layer. This also formed a positive feedback

mechanism of surface warming. However, a quantitative, detailed analysis of this factor should be attributed to a modelling study, since the resolution of the ERA5 is not enough to resolve all the air-sea coupling processes.

The above mechanism is partly illustrated in Figure 4.4.5, using May as an example. Most of the Baltic Sea has shortwave radiation flux anomalies from 20 to 50 Wm^{-2} (Figure 4.4.5 left) while sensitive heat flux anomaly ranges from −5 to 15 Wm^{-2}. The high shortwave radiation anomaly is found south of 59°N, which corresponds to the high MHW duration in the same region. The two areas with the minimum shortwave anomalies are found in the Bothnian Sea and Bothnian Bay, which are reported as areas with no MHW events in May (Figure 4.4.2c).

4.4.5. Conclusion

Extremes of surface marine heat anomaly in summer 2018 in the Baltic Sea are investigated. In most parts of the Baltic Sea, MHWs occurred 50-100 days, with their maximum duration in the southern Baltic Sea. The MHW spatial pattern showed significant intraseasonal variability, featured by meridional movement of the MHW areas. Similar fluctuations were also found in surface air temperature and atmospheric circulation patterns. The impact study of the associated changes in the subsurface structure of the water column is interesting and important but will be the subject of a separate paper.

Large scale atmospheric circulation in summer 2018 was characterised by the highest summer AO and NAO indexes in past 70 years. Anomalous blocking high pressure systems were dominant over Northern

Europe and Scandinavia during most periods of May–August 2018, accompanied with an eastward shifting Greenlandic low pressure system and a northward shifting jet stream. Such atmospheric circulation anomalies brought extremely warm and sunny weather over the Baltic Sea during summer 2018 and high surface solar radiation. It is found that MHW duration is significantly correlated with surface air temperature anomaly, which is caused by the anomalous atmospheric circulation patterns. The results also suggest that, among all atmospheric surface heat flux components, the very high positive anomaly of the surface solar radiation is the primary contributor to the extremely warm surface water in the Baltic Sea in summer 2018.

Acknowledgements

Section 4.5. Space-based observations of surface signatures in the wake of the 2018 Eastern Pacific tropical cyclones

Authors: Clément Combot, Yves Quilfen, Alexis Mouche, Jérôme Gourrion, Clément de Boyer Montégut, Bertrand Chapron, Jean Tournadre.

Statement of main outcome: In this section, a new focus is given on the ocean response induced by Tropical Cyclones. Tropical Cyclones are among the most devastating and destructive natural hazards. Unfortunately, predicting the intensity and evolution of such individual event is still extremely difficult, owing to various internal and environmental factors, including interactions with the ocean interior. In that context, multiple satellite remote sensing observations are essential, and today, combined with denser ARGO interior measurements, the upper ocean responses to moving tropical cyclones can be more efficiently captured and monitored.

Ref No.	Product name & type	Documentation
4.5.1	SST_GLO_SST_L4_NRT_ OBSERVATIONS_010_001	PUM: https://marine. copernicus.eu/documents/ PUM/CMEMS-SST-PUM-010- 001.pdf QUID: https://resources. marine.copernicus.eu/ documents/QUID/CMEMS- OSI-QUID-010-001.pdf
4.5.2	SEALEVEL_GLO_PHY_L3_NRT_ OBSERVATIONS_008_044	PUM: https://marine. copernicus.eu/documents/ PUM/CMEMS-SL-PUM-008-

Continued.

Ref No.	Product name & type	Documentation
		032-062.pdf QUID: https://marine. copernicus.eu/documents/ QUID/CMEMS-SL-QUID-008- 032-062.pdf
4.5.3	INSITU_GLO_TS_NRT_ OBSERVATIONS_013_001_B	PUM: https://marine. copernicus.eu/documents/ PUM/CMEMS-INS-PUM-013. pdf QUID: https://resources. marine.copernicus.eu/ documents/QUID/CMEMS- INS-QUID-013.pdf
4.5.4	Non-CMEMS product: ISAS13-clim Monthly climatology of temperature and salinity profile used as a background stratification information, in case of argo absence. Developed by F.Gaillard & al 2016 (LOPS/ IFREMER).	Downloaded from: https:// www.seanoe.org/data/ 00348/45945/ Reference paper: https:// journals.ametsoc.org/doi/pdf/ 10.1175/JCLI-D-15-0028.1
4.5.5	Non-CMEMS product: IBTrACS Best-tracks are post-storm analyses at every 6-hours of Tropical and subtropical cyclones, giving several characteristic parameters (position, intensity,size) . They are produced by several dedicated centres and gathered in a homogeneous database named IBTrACS: International Best Track Archive for Climate Stewardship.	Downloaded from: https:// www.ncdc.noaa.gov/ibtracs/ index.php?name=ibtracs- data-access User Manual: ftp://eclipse. ncdc.noaa.gov/pub/ibtracs/ v04r00/doc/IBTrACS_v04_ column_documentation.pdf Quality information: https:// journals.ametsoc.org/doi/ pdf/10.1175/ 2009BAMS2755.1
4.5.6	Non-CMEMS product: SAR-Sentinel-1A/B wind field: C-band radar with high resolution and dual polarisation (Co- & Cross- pol) signal. The wind product used was retrieved by the inversion scheme published by Mouche & al 2017 (LOPS/ IFREMER) from L1 sigma0 of ESA Copernicus. Data were collected in the context of ESA's SHOC campaign. (SHOC: Satellite Hurricane Observations Campaign).	- ESA Copernicus L1 sigma0: Copernicus open access hub (https://scihub.copernicus.eu/) and Sentinel-1 Mission Performance Center (MPC S-1) - SAR's Tropical Cyclone Wind Product: (Distribution site to come soon) Contact: alexis.mouche@ ifremer.fr

4.5.1. Introduction

Over the Eastern Pacific region, 2018 has been a very active Tropical Cyclone season. The accumulated cyclone energy reaches a record value of $316.10^4 \, kt^2$ (NOAA, Annual 2018 report; Kruk and Schreck 2019). As shown in the background of Figure 4.5.1a, a persistent positive Sea Surface Temperature Anomaly (SSTA) up to 1.5°C extended over the entire region, to explain this very active 2018 season in combination with an enhanced convection (Kruk and Schreck 2019).

Associated to the extreme wind forcing conditions, distinctive localised impacts have long been attracting considerable attention. Indeed, quite systematically, a tropical cyclone will leave persistent signatures in its

wake (Leipper 1967; Price 1981). The vigorous induced mixing and resulting intense upwelling generally cool the upper ocean mixed layer, stirring warm surface waters with colder waters below (Ginis 2002). Consequently, a tropical cyclone wake is generally characterised by a surface cold anomaly, possibly accompanied with nutrient blooms. Moreover, governed by intense isopycnal displacements (Geisler 1970), a tropical cyclone can also leave prominent sea-surface height anomalies in its wake. Resulting surface depressions can reach 0.3–0.5 m, depending upon the forcing intensity, size, translation speed, and ocean stratification conditions (Kudryavtsev et al. 2019a). Building on the actual satellite altimeter constellation (presently up to 6 satellites are available), satellite sea surface height estimates may more likely cross such trenches. Using both sea surface height and temperature observation, a more consistent view of the tropical cyclone characteristics can thus be obtained with additional support of a semi-empirical

2D model to interpret the oceanic answer. Here, the wakes of seven Eastern Pacific tropical systems are presented. To illustrate and further discuss the influence of the forcing parameters, the analysis mainly focuses on three particular major tropical cyclones: Hector (August), Lane (August) and Sergio (October). Hector experienced two intensification periods with maximum winds over 110 kt that lasted up to 7 days (NHC archive). Lane was the second wettest storm in USA territory with 1341 mm accumulated rainfall (NHC archive). Finally, Sergio left a particularly deep ocean signature (Figure 4.5.1). Above all, these three tropical cyclones are relevant cases as they benefit from longer time monitoring by satellites.

4.5.2. Data analysis

A database has been set up that merges satellite observations, from altimeters, radiometers, and high-
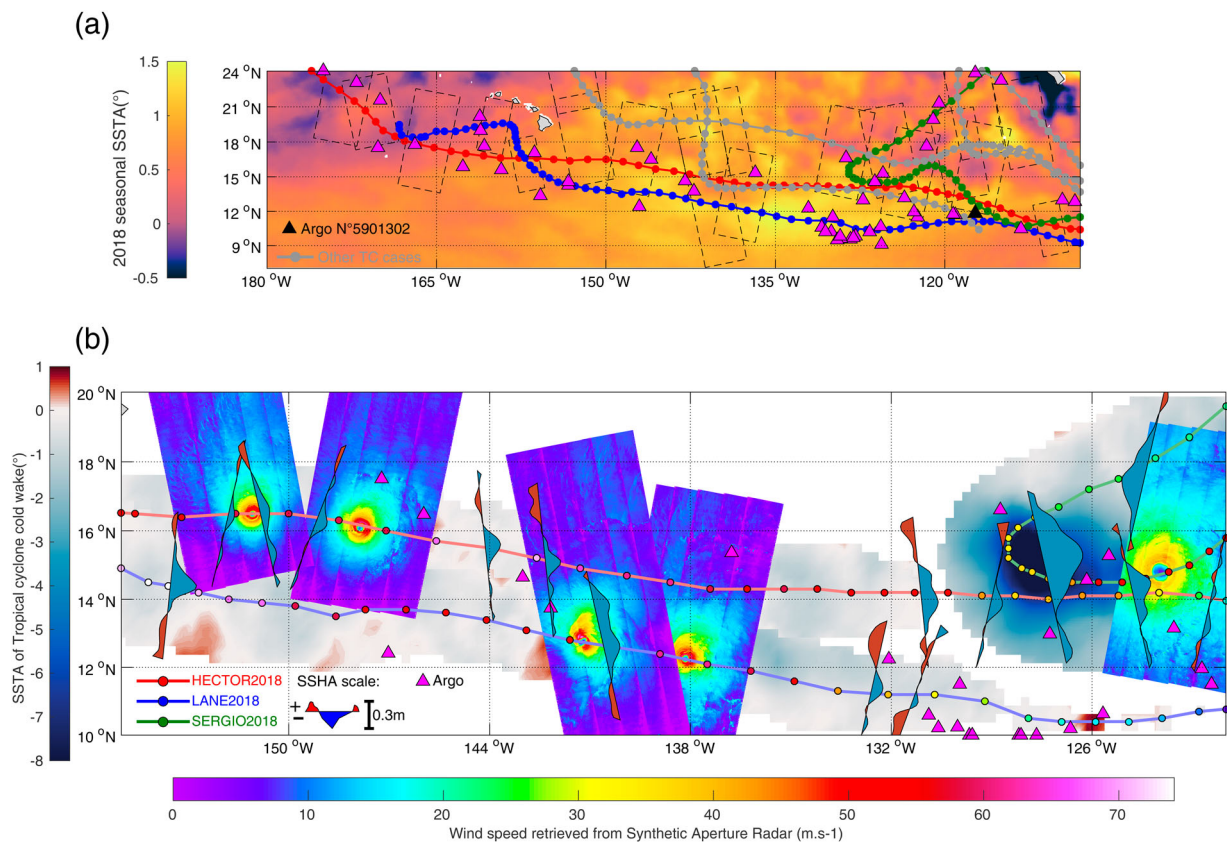
Figure 4.5.1. Constellation of satellite (product ref 4.5.1 & 4.5.2) and in-situ observations (product ref 4.5.3 & 4.5.4) for wake analysis over Eastern Pacific in 2018. (a) Overview of the database with all the tracks (coloured lines), SAR swaths (dashed contours) and Argo floats (magenta triangles) represented. The background field depicts the 2018 seasonal thermal anomalies (globally positive). (b) A zoom on Hector, Lane and Sergio. The 3 tropical cyclones wakes are represented by shaded areas for SSTA (see colorbar) as well as for SSHA anomalies (blue = negative, red = positive). Specific Sentinel 1A/B swaths were selected to map the tropical cyclone wind fields (product ref. 4.5.6). To clarify, not all the altimetry and SAR crossings available for the 3 tropical cyclones are displayed. Best-track information were added as the synoptic positions and intensities (coloured circles, product ref 4.5.5), with Hector and Lane heading westward and Sergio drawing a loop that ends northeast.

resolution Synthetic Aperture Radars (SAR), with Argo float data. The 6-hour Best-Track data set further provides several parameters over the tropical cyclone life such as position, intensity and specific wind radii (Product ref. 4.5.5). For each track, all available altimeter observations from the L3 CMEMS products were assembled for the different storm positions (Figure 4.5.1, product ref. 4.5.2), keeping only altimeter passes crossing the tropical cyclone wake afterwards. The well-defined trough left behind the tropical cyclones (blue shaded areas on the altimetry tracks in Figure 4.5.1) was used to directly estimate the sea surface height anomaly, i.e. the maximum difference between the bottom and the top of the altimeter sea surface height profile. As the tropical cyclone generates near-inertial oscillations (Geisler 1970), the altimeter may not sample the maximum trough value. For each Best-Track synoptic time, we thus kept the largest sea surface height anomalies among all the closest time/space colocated altimeter passes. When only one altimeter pass is available, the unique anomaly estimate was kept. This can thus introduce a slight underestimation of the altimeter trough.

The daily CMEMS L4 sea surface temperature product is used to estimate the thermal anomalies at each Best-Track synoptic position (product ref. 4.5.1). The cold wake intensity was estimated as the difference between a 2-week average of pre-storm sea surface temperature conditions and the daily post-storm sea surface temperature field. In case of pre-existing storms or loop trajectory, this pre-storm time window was reduced to withdraw the cooling of previous forcing. Shaded areas in Figure 4.5.1b trace the maximum cooling, from 1 to 3 days after the Best-Track synoptic time (Dare and McBride 2011; Vincent et al. 2012). Finally, using wind radii information from Best-Track, all Argo data inside the 34 kt wind radius were selected to infer the ocean stratification parameters (magenta triangles in Figure 4.5.1, product ref 4.5.3). From the nearest profile, we extracted the Brunt-Väisälä frequency N in the thermocline (Figure 4.5.2c), known to strongly influence the oceanic response to tropical cyclone forcing (Reul et al. 2014). In absence of Argo floats, the ISAS-13 climatology was used (product ref 4.5.4). As obtained in Figure 4.5.1b, rather moderate signatures are found for Hector and Lane, with maximum thermal and height anomalies amplitude of −1.7° and −0.17 m, respectively. A stronger cooling and a deeper trough are found for Sergio, with respective signatures larger than −7°C and −0.3 m. The first two cyclone cases were small intense storms with fast translation speed (V_{fm} = 7 m s^{-1}), while Sergio had a weaker wind intensity but is a large and slowly moving

cyclone (V_{fm} = 4 m s^{-1}). As anticipated, the overall tropical cyclone induced-stirring process depends on its intensity, but also on its size and translation speed (Reul et al. 2014; Kudryavtsev et al. 2019a). The tropical cyclone wind structure is therefore of paramount importance, and the Best-Track data may not be precise enough to depict it, especially the determination of the maximum wind radius (R_{max}) can be subject to large errors (Kossin et al. 2007; Knaff et al. 2015).

To overcome such a limitation, SAR measurements have therefore been used (product ref. 4.5.6), which can provide unique observations of high resolution wind patterns in tropical cyclones (Mouche et al. 2019). As collected, 1-km resolution data from Copernicus/ESA's Sentinel 1A/B operating in C-band and VH cross-polarisation provide reliable surface winds up to 70 m s^{-1} (Mouche et al. 2017; Mouche et al. 2019). A total of 23 SAR scenes were collected with maximum winds ranging from 25 to 70 m s^{-1} (Figure 4.5.2a), representing small to medium size systems (Figure 4.5.2b). For each SAR scene, an objective analysis was used to determine the centre of the storm and to extract the maximum wind speed (Vmax) and radius of maximum wind information (Combot et al. 2020). These estimates are compared to the Best-Track ones in Figures 4.5.2a, b. An excellent consistency is found for the maximum wind speed parameter, with a correlation coefficient of 0.95, a very weak normalised bias, and a root mean square difference of about 4 m s^{-1}, that is partly associated with the discretization of the Best-Track estimates. For the radius of maximum winds, the correlation is significantly lower but still high (0.80). Yet, compared to Best-Track values, SAR estimates are not discrete and therefore more likely to provide accurate values for small size TCs (Rmax < 30 km, Combot et al. 2020).

Pre-storm ocean stratification and heat content are key variables that determine ocean/atmosphere feedback mechanisms and the associated evolution of tropical cyclones. The lower panels in Figure 4.5.2 show the temperature, salinity and density profiles measured by an Argo float a few days before (∼7 days, in blue) and after (∼3 days, in magenta) Sergio's passage in category 4 at that time. The corresponding ISAS profiles are also displayed for the two climatological months close to the Argo profile time (black lines). As obtained from the pre-storm Argo profile, the ocean stratification was much stronger than the climatological values (values indicated in the lower right panel), mainly due to a 30-m thick surface layer much fresher than usual, which is confirmed by the surrounding floats. As a result, mixing and associated salinity and temperature anomalies are reduced, and the
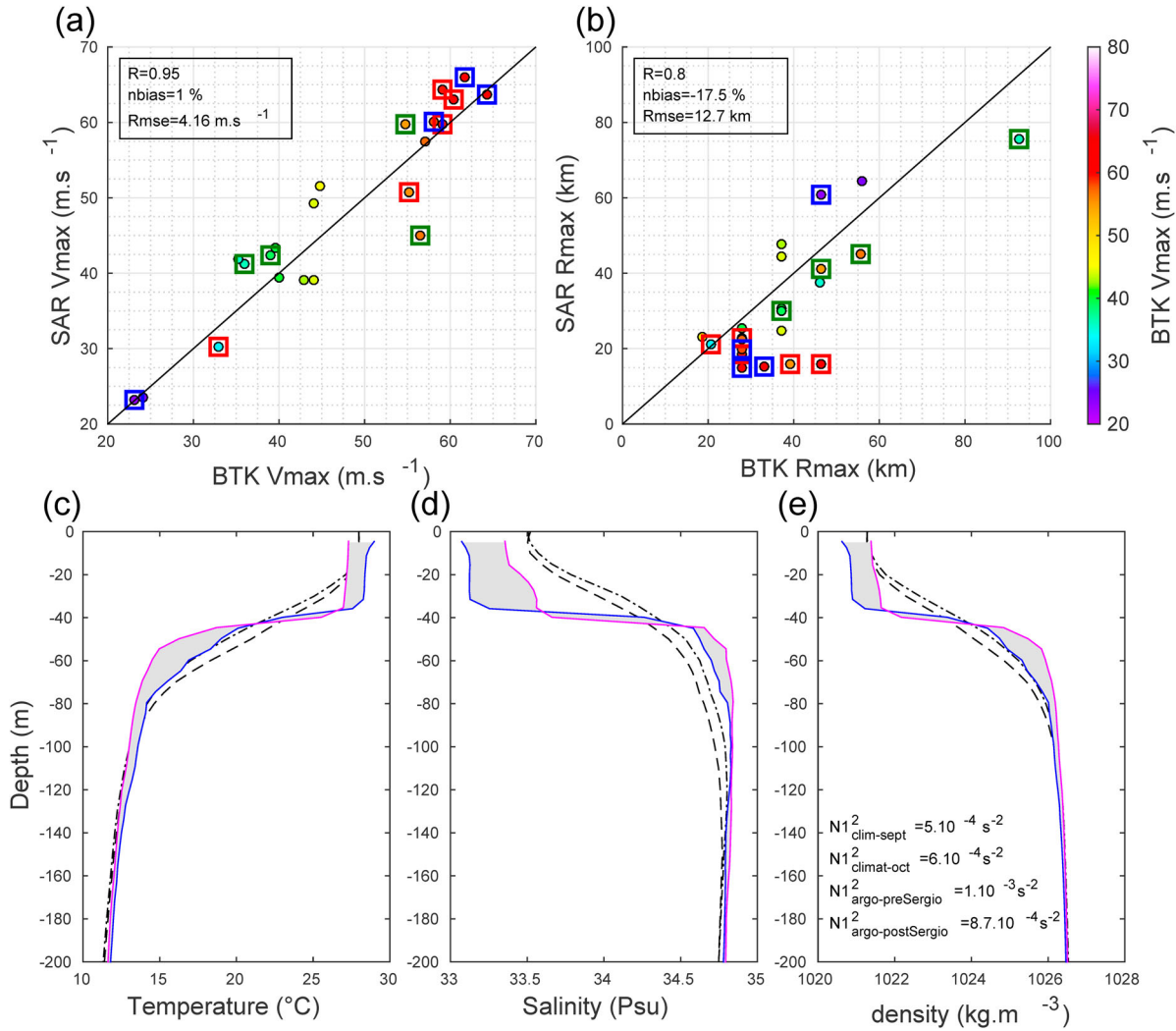
Figure 4.5.2. Upper panel: Comparison between Best-Track (product ref 4.5.5) and SAR (product ref 4.5.6). Maximum wind speed (a) and radius of maximum wind speed (b) with dots coloured as a function of Vmax. Following the Figure 4.5.1 convention, the three particular TCs dots are notified with coloured squares, red = Hector, blue = Lane, green = Sergio. Lower panel: Profiles of temperature (c), salinity (d) and density (e) of Argo and ISAS climatology (product ref 4.5.3 & 4.5.4) at the Sergio's location on 3rd October 2018 at 13h40, when it was particularly strong (∼60 m s⁻¹). The two surrounding months, September (dashed line) and October (dashed dotted line), from the ISAS climatology profiles are shown. Two Argo profiles were selected, one before (26th September 2018 in blue) and one after (6th October 2018 in magenta) the Sergio path. Shaded areas illustrate the anomalies left by Sergio, a slight deepening (∼10 m) and cooling (∼2°C) of the mixed layer are observed. These profiles were acquired near 117 °W and 12 °N (black triangle in Figure 4.5.1.a, profiler number: 5901302).

stratification remains very strong during and after Sergio's passage which is an important limiting factor for oceanic feedback on tropical cyclones evolution.

4.5.3. Analysis from a semi-empirical model

Following Geisler (1970) and Price (1981), Kudryavtsev et al. (2019a) proposed a semi-empirical framework to jointly analyse and interpret tropical cyclones sea surface temperature and height anomalies. It is assumed that the ocean response to a moving TC is largely dominated by baroclinic effects. Considering this assumption,

scaling laws issued from the semi-empirical modelling approach developed by Kudryavtsev et al. (2019) can be expressed as

$$\frac{SSTA}{V_{\max} \cdot N^{(3/2)}/(g \cdot \alpha \cdot f^{(1/2)})} \propto \left(\frac{V_{fm}}{f \cdot R_{\max}}\right)^{-1} \quad (1)$$

$$\frac{g \cdot SSHA}{V_{\max}^2} \propto \frac{R_{\max} \cdot N}{V_{fm}} \quad (2)$$

with f, the Coriolis parameter, V_{fm} the translation speed, α the thermal expansion coefficient, g the gravitational acceleration on Earth, and N the Brunt-Väisälä
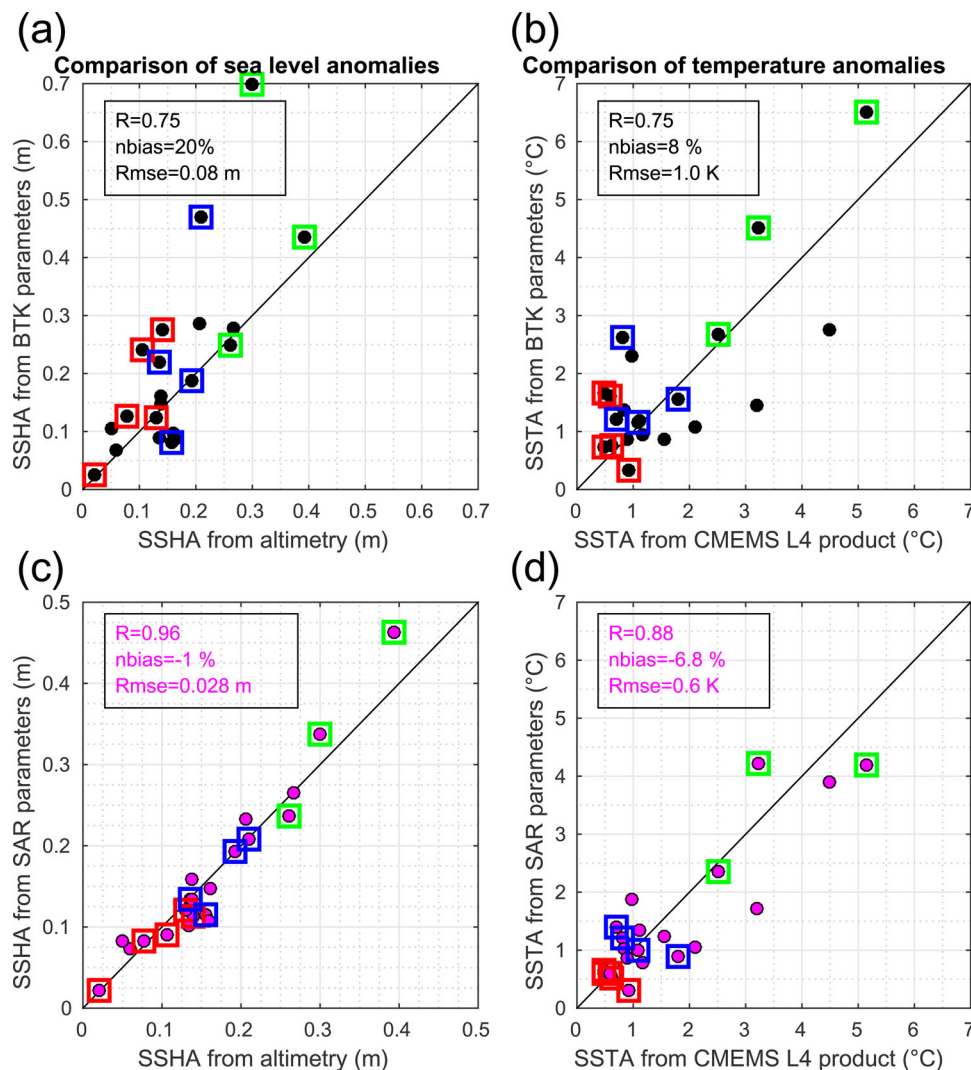
Figure 4.5.3. Comparison of Sea Surface Height (left column, product ref 4.5.2) and Sea Surface Temperature (right column, product ref 4.5.3) anomalies between satellite measurements (*x*-axis) and estimation from the semi-empirical model (*y*-axis): (a) and (b) represent the estimates inferred from Best-Track information (product ref 4.5.5); (c) and (d) from SAR-derived wind field (product ref 4.5.6). The 3 reference cases are reported according to the same convention than in Figure 4.5.2. The required spatial collocation between SAR and altimetry has slightly reduced the numbers of points (21) as used for Figure 4.5.2(a,b).

frequency. Best-Track and SAR offer two different sets of Vmax/Rmax estimates, giving different semi-empirical predictions that are compared in Figure 4.5.3. Overall, the results agree well with large correlation between observations and predictions ($R \geq 0.75$). These correlation coefficients are significant at the 95% confidence level but, due to the rather small sample size, this cannot be accurately assessed. However, ongoing research confirms these findings with a much larger sample size including $N > 100$ SAR scenes colocated with TCs for the recent years and over all the ocean basins. Bringing improved high-resolution description within the maximum wind region, SAR estimates give a significantly closer agreement with the proposed scaling laws ($R \geq 0.88$). The Hector case (red squares)

remarkably illustrates the improvement, as large maximum wind radius discrepancies were indeed observed between the two data sources (Figure 4.5.2b). As also shown in Figure 4.5.3, the Sergio case highlights a larger dynamical range for its wake signature, going from 2.5°C to 5.2°C cooling and from 0.26 to 0.39 m sea level drop. This overall stronger induced oceanic answer arises from its larger size and lower translation speed and is well accounted for by the semi-empirical model when fed by the SAR observations. This is particularly true with regard to the two points departing the most from the 1:1 line, Sergio and Lane (Figure 4.5.3a), for which overestimation of Best-Tracks for maximum wind speed and its radius (Figure 4.5.2) led to unrealistic predictions of sea surface anomalies.

The proposed interpretation framework can thus guide the combined use of sea surface temperature and height amplitude changes measured in the wake of tropical cyclones. It can help to inform about the resulting strength of hurricane-induced mixing and upwelling. This opens a bottom-up approach to guide future investigations to help document the resulting wind forcing and practical drag coefficient under extreme tropical cyclone conditions (Kudryavtsev et al. 2019a, 2019b).

4.5.4. Summary

This study highlights the use of multi-platform observations for the analysis of tropical cyclones and their induced oceanic answer. As a main outcome, it is shown that the combination of low and high resolution satellite sensors are of paramount importance to better depict and monitor the tropical cyclones wind patterns, and to interpret the air/sea coupling that imprints the cyclone wake. In particular the study shows that altimeter and SAR measurements can provide unique information to help analysis and monitoring of extreme events. The wide-swath altimetry SWOT mission foreseen in 2021 will be a unique opportunity for further research and applications, notably since it will provide a 2D mapping of sea level anomalies left by tropical cyclones.

Acknowledgements

Section 4.6. Record wave storm in the Gulf of Cadiz over the past 20 years and its impact on harbours

Authors: Marta de Alfonso, José María García-Valdecasas, Roland Aznar, Begoña Pérez-Gómez, Pablo Rodríguez, Francisco Javier de los Santos and Enrique Álvarez-Fanjul
Statement of main outcome: The Gulf of Cadiz region suffered the most severe wave storm over the past 20 years produced by the storm Emma in March 2018. The combined effect of high waves and sea level surge aggravated the storm risk potential. The CMEMS products, the local wave and sea level forecasting systems (PORTUS system) and their associated alerts and downstream services worked properly and warnings were sent in advance to the users. Several actions were carried out to mitigate the

impact of the event. For example, harbours stopped operations to prevent accidents and assure safety. The material damages were considerable but, probably due to the preventive actions, no personal damages were suffered.

CMEMS products used

Ref. No.	Product name & type	Documentation
4.6.1	INSITU_IBI_TS_REP_ OBSERVATIONS_013_040 Observations reprocessed	PUM: https://marine.copernicus. eu/documents/PUM/CMEMS-INS-PUM-013.pdf QUID: https://marine.copernicus. eu/documents/QUID/CMEMS-INS-QUID-013-040.pdf
4.6.2	INSITU_IBI_NRT_ OBSERVATIONS_013_033 Observations	PUM: https://marine.copernicus. eu/documents/PUM/CMEMS-INS-PUM-013.pdf QUID: https://marine.copernicus. eu/documents/QUID/CMEMS-INS-QUID-013-030-036.pdf
4.6.3	INSITU_GLO_WAVE_REP_ OBSERVATIONS_013_045 Observations reprocessed	PUM: https://marine.copernicus. eu/documents/PUM/CMEMS-INS-PUM-013.pdf QUID: https://marine.copernicus. eu/documents/QUID/CMEMS-INS-QUID-013-045.pdf
4.6.4	IBI_ANALYSIS_FORECAST_ WAV_005_005 Model analysis and forecast	PUM: https://marine.copernicus. eu/documents/PUM/CMEMS-IBI-PUM-005-005.pdf QUID: https://marine.copernicus. eu/documents/QUID/CMEMS-IBI-QUID-005-005.pdf
4.6.5	IBI_REANALYSIS_WAV_005_006 Model reanalysis	PUM: https://marine.copernicus. eu/documents/PUM/CMEMS-IBI-PUM-005-006.pdf QUID: https://marine.copernicus. eu/documents/QUID/CMEMS-IBI-QUID-005-006.pdf
4.6.6	PORTUS coastal and local wave forecast in the Gulf of Cadiz (non CMEMS product)	URL: https://www.puertos.es/en-us/oceanografia/Pages/portus. aspx OPeNDAP: https://opendap. puertos.es
4.6.7	PORTUS sea level/storm surge forecasting system (NIVMAR-ENSURF) (non CMEMS product)	URL: https://www.puertos.es/en-us/oceanografia/Pages/portus. aspx. OPeNDAP: https://opendap. puertos.es
4.6.8	Puertos del Estado downstream SAMOA/CMA services for Port Authorities (non CMEMS product)	URL: https://cma.puertos.es/ OPeNDAP: https://opendap. puertos.es

4.6.1. Introduction

During February-March 2018 several storms including Emma, affected the maritime area in the south of Europe. In particular, Emma was characterised by an area of deep low pressure located west of the Iberian Peninsula, channelling strong southwesterly winds over the Gulf of Cadiz, and generating the highest significant wave heights recorded in the region. The impact of these huge waves in the coastal infrastructures was strengthened by less extreme, but still important, sea level and surge. In this paper, this event is studied employing data from the PORTUS system (Product refs: 4.6.6 and

4.6.7), a series of forecasting models (sea level, waves and wind) and measuring instrumentation (buoys and tide gauges integrated into Copernicus Marine Service) operated by Puertos del Estado at the Spanish Coast.

During the event, waves were especially severe there, where the deep water buoy 'Golfo de Cadiz' (WMO: 6200085), part of the PORTUS system and moored since 1996, surpassed its significant wave height record of 6.6 m, reaching 7.2 m during the 1st of March. In this paper, the historical information from measurements and model reanalysis from 1992 to 2018 has been analysed, confirming this event as the most severe over the past 20 years.

This extreme wave value coincided with extreme high sea levels produced by the combination of spring tides (high tides reaching the 99.95 percentile of historical high tides) and a storm surge over the 99.5 percentile of historical surge data as measured by Puertos del Estado tide gauges network in the region. The combined effect of extreme waves and sea levels produced a huge impact at the coast causing serious damages in the harbours of the area. These storms were correctly forecasted by the CMEMS regional wave model for Iberia-Biscay-Ireland region (product ref. 4.6.4), by the local wave forecast (product ref. 4.6.6) (Gómez Lahoz et al. 2005) and by Puertos del Estado sea level forecast system (product ref. 4.6.7) (Alvarez Fanjul et al. 2001), and provided through the downstream services developed by Puertos del Estado and Algeciras Port Authority for the harbours (product ref: 4.6.8) (Alvarez Fanjul et at. 2018). The warning system was activated and alerts were sent to prevent accidents.

This paper studies the storm Emma and the values forecasted and measured during the event, then these values are compared with the historical information recorded in the area and finally it focuses on the impact on harbours, that nowadays are huge logistic centres with wide and complex infrastructures (https://www.puertos.es/en-us). For the Port Authorities, the met-ocean information is required during all the phases of their life: planning and design, construction and daily operation. The Gulf of Cádiz area is the basin that connects the North Atlantic and the Mediterranean Sea with an intense vessel traffic and a high maritime and commercial activity in the harbours of the area. The monitoring and forecasting of storms are essential to assure the security conditions for harbour operations.

The location of the measuring instruments and the harbours affected in the area of interest is shown in Figure 4.6.1.

4.6.2. Data and analysis

Description of the forecasting systems and instrumentation: Two wave forecasting systems have been used in this article, the CMEMS system (product refs 4.6.4 and 4.6.5) used to compare the historical time series and the PORTUS system (product ref 4.6.6) used in the forecast and downstream services. Both systems employ, at the regional scale, the same numerical model WAM (WAMDI Group 1988; Günther et al. 1992) but with different implementations, bathymetry and forcing. PORTUS system has, in addition, a set of models to downscale to the harbours. The local domains run SWAN model (Booij et al. 1999) and provide boundary conditions to the MSP model used in Algeciras Bay Port to obtain wave agitation inside the port and a Boussinesq + VOF models (Losada et al. 2008) used to obtain overtopping at Tarifa Port. Both MSP and Overtopping models use the results from Nivmar storm surge forecasting system to include water level time series.
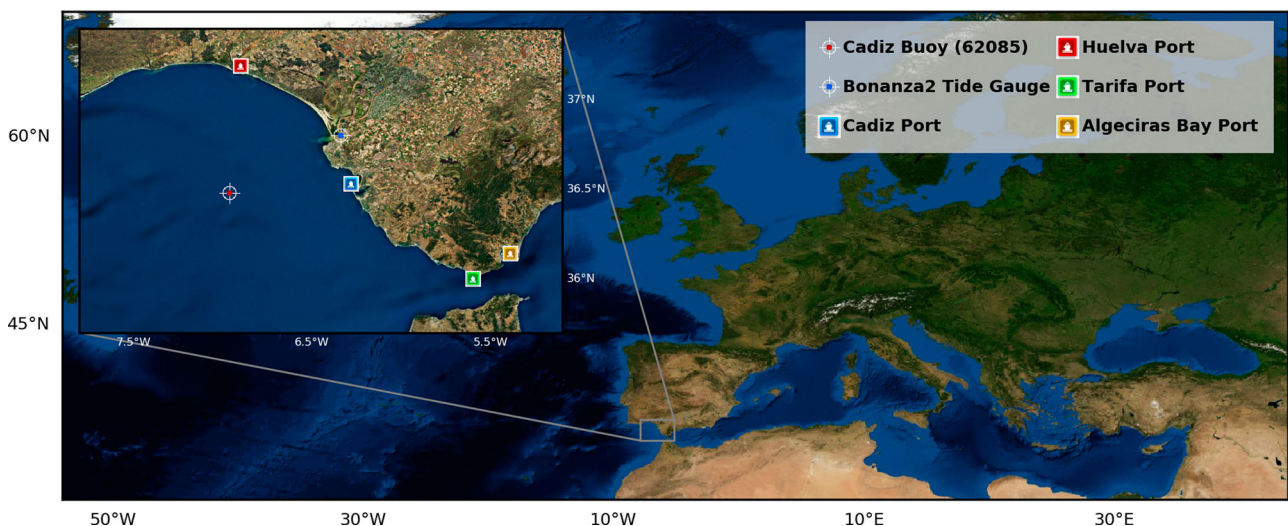

Figure 4.6.1. Location of the measuring instruments (buoy and tide gauge) and the harbours in the area of the Gulf of Cadiz.

Table 4.6.1. Statistical comparison between 6200085 buoy and both wave systems (CMEMS and Puertos del Estado) for the period 1996–2018.

	BIAS	RMSE	Scatter Index	Correlation Coef.
CMEMS system	−0.473	0.586	0.483	0.858
PORTUS system	−0.003	0.314	0.259	0.902

These systems are validated periodically with the statistical results at regional scale shown in Table 4.6.1 for the comparison period: 1996–2018. For the CMEMS system the bias is clearly negative with a general underestimation of the values probably due to the same underestimation in the forcing. The PORTUS system has better results, but we have observed that, for severe storms, it tends to overestimate the values. More details in CMEMS system validation can be found in the CMEMS Quality Information Document, periodically updated (Toledano et al. 2018).

The Nivmar storm surge forecasting system is in operation since 1998: based on a 2D barotropic implementation of the HAMSOM model, and forced by atmospheric pressure and winds provided today by the ECWMF, it provides hourly forecasts of sea level along the whole Spanish coast with a 72 h prediction horizon. It combines tide gauge data and surge forecasts, adding the tide at each harbour as the one obtained from the tide gauge data, and allowing correction of the forecasts by means of a nudging technique (by means of operational comparison with recent surge data recorded at the stations, Alvarez Fanjul et al. 2001). Based on previous validation studies of the Nivmar storm surge forecasting system, the RMSE error of the model forecasted surge is 4.7 cm in Huelva and 6.1 cm in Bonanza (Pérez-Gómez 2014). These figures must be considered a qualitative assessment of the model performance at these two stations. Bias of the system is not provided, because this is computed and corrected in near-real time, as already mentioned, by the nudging technique.

The instrumentation in the area is composed by a deep-water buoy and two tide gauges. The deep-water buoy named 'Golfo de Cadiz' (WMO: 6200085) is one of the fifteen measurement stations along the Spanish Coast of the network owned by Puertos del Estado (Alvarez Fanjul et al. 2003). It is a multiparametric buoy measuring since 1996 hourly met-ocean parameters including directional waves. The two tide gauges, named 'Bonanza2' and 'Huelva' are part of the REDMAR network, composed by 37 tide gauges operated by Puertos del Estado (Pérez-Gómez et al. 2008, 2013) and installed at the Ports facilities in 1992 and 1996 respectively (product ref. 4.6.1). Today these stations are based on radar type sensors providing 1-min, 5-min and hourly sea levels (standard sampling of
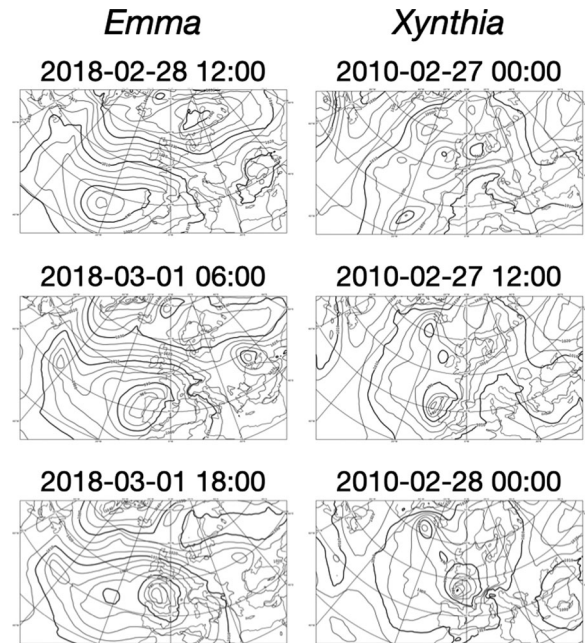
Figure 4.6.2. Snapshots of mean sea level pressure isobars (in hPa) taken as Emma (left panel) and Xynthia (right panel) storms moved in February-March 2018 and February 2010, respectively, over the Iberian Peninsula. Data obtained from ERA5 atmospheric reanalysis.

final products). The position of the instruments is showed in Figure 4.6.1.

Synoptic description of the event as derived from model results: The storm Emma was formed on the 26th of February 2018 as a low-pressure system over the Atlantic Ocean and followed a track towards the Iberian Peninsula. Although most of the storms affecting the northeastern Atlantic tend to seek septentrional trajectories, crossing areas of the British Isles, northern France, Netherlands or the Baltic Sea (i.e. Lothar and Martin in December 1999), others, as Emma, sometimes develop at more meridional latitudes and then pursue tracks towards Northeastern Europe, touching the Iberian Peninsula. This southwest-northeast storm path has also characterised in the past other damaging storms (such as the windstorm of 1941 or storm Xynthia in February 2010) in that area (Garnier et al. 2018; Ferreira et al. 2019).

The comparison of Emma with Xynthia storm is particularly interesting since both systems shared similar evolutions. Figure 4.6.2 highlights the similitude of the mean sea level pressure patterns featured by the Emma and Xynthia storms, as they moved towards northeastern Europe crossing the northwestern tip of the Iberian Peninsula. In both cases, the low-pressure system deepened suddenly in roughly the same area, and the specific track induced an increase of strong winds and waves impacting the western and northern Iberian coastline. Focusing on Emma, as the storm approached the

west of the Iberian Peninsula during the following hours and the associated pressure gradient intensified, it gave rise to strong geostrophic southwesterly winds over the Gulf of Cadiz. These winds generated high waves and a storm surge in the area. On the 1st of March 2018 Emma shifted northwards, moving across the western coastal areas of the Iberian Peninsula with associated gale force southwesterly winds. Once the trough moved away from the Iberian Peninsula and continued its trajectory towards northern Europe, the prevailing winds turned from southwesterly to westerly direction over the Gulf of Cadiz and their intensity decreased.

This evolution is clearly depicted by the two wave systems referenced in this article. Figure 4.6.3 shows the wind field, the significant wave height from PORTUS system and the sea level residuals during the 1st of March 2018, at 00h and 12h, presenting the evolution of the storm before and at the time of hitting the coasts of the Gulf of Cadiz. The forecasting models correctly predicted the storm moving north-eastwards from the Azores Islands towards the Gulf of Cadiz, with significant wave heights over 7 m and sea level residuals over 0.4 m.

Analysis of the measurements during the storm: The event was properly recorded by the instruments of Puertos
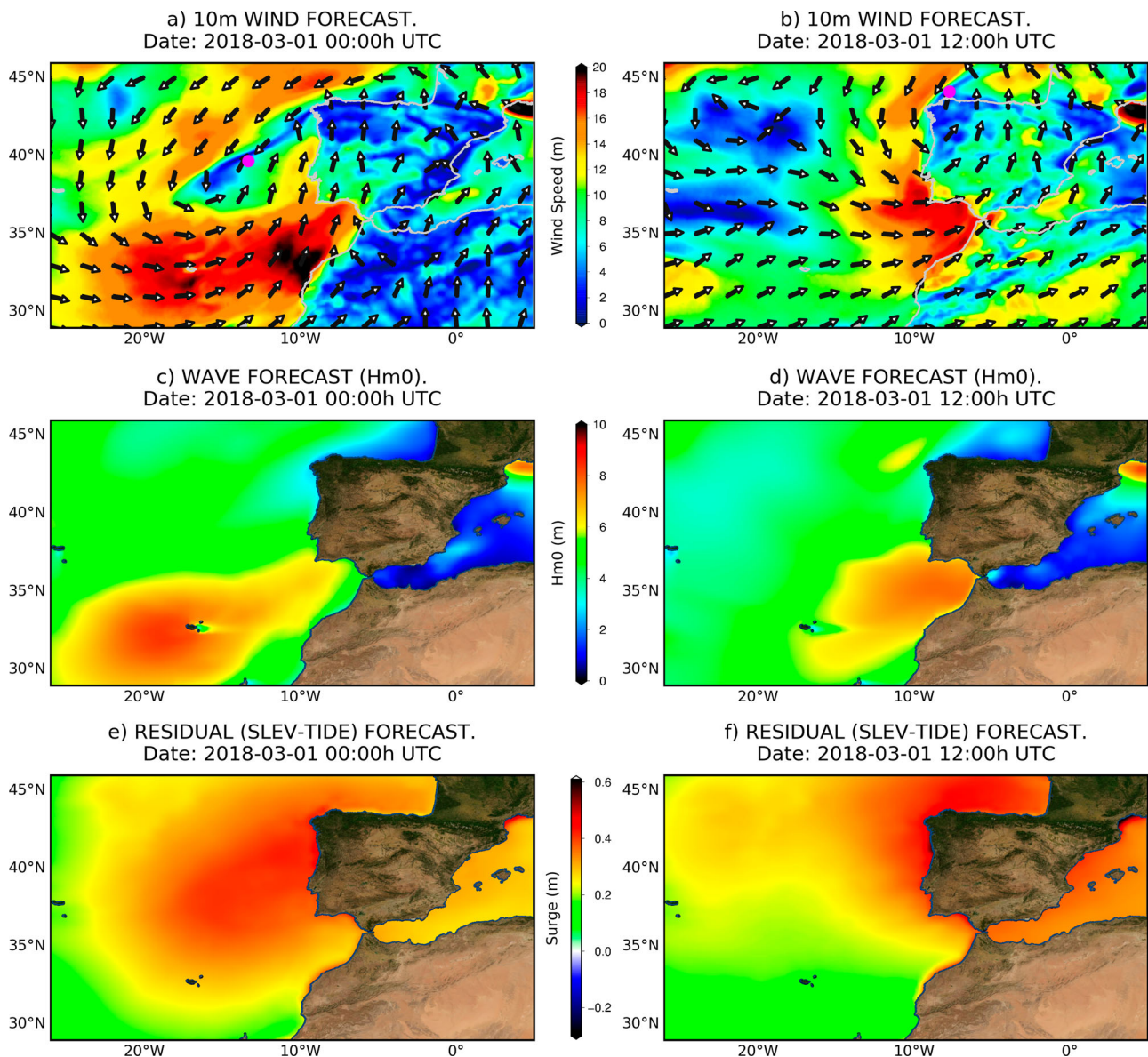
Figure 4.6.3. (a) and (b): Module (colour) and direction (vectors) of 2 m wind forecasted for March, 1st, 2018 at 00h and 12h. The magenta circles mark the low pressure minima at 00h and 12h. (c) and (d): Significant wave height (SWH) forecasted for March, 1st, 2018 at 00h and 12h. Wave heights over 7 m were forecasted in the area of the Gulf of Cadiz (product ref. 4.6.6). (e) and (f): Residual or surge (sea level – tide) forecasted for March, 1st, 2018 at 00h and 12h. Residuals over 0.4 m were forecasted along the coast the Gulf of Cadiz (product ref. 4.6.7).
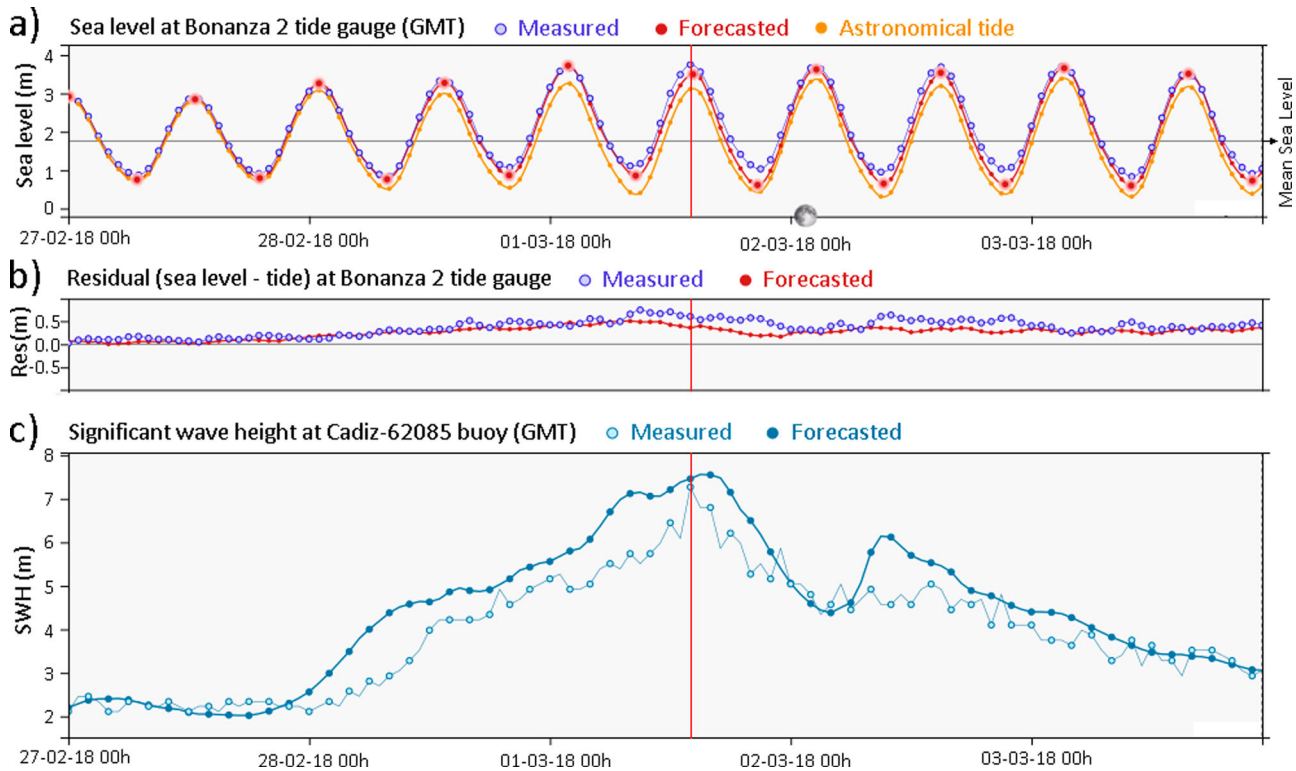
Figure 4.6.4. Values forecasted and measured by the models and instruments during the storm Emma, as displayed in the PORTUS system. (a) Sea level forecast and measurements at Bonanza2 tide gauge: observations in blue colour (product ref. 4.6.2), PORTUS sea level forecast in red colour (product ref. 4.6.7) and astronomical tide (orange colour). (b) Same for just the surge or residual component (subtracting the tide) at Bonanza2 tide gauge: measurements in blue colour (product ref. 4.6.2) and forecasted residuals in red colour (product ref. 4.6.7). c) Significant wave height (SWH) measured (light blue) at the 6200085 buoy (product ref. 4.6.3) and forecasted by PORTUS wave model (dark blue) (product ref. 4.6.6). The vertical red line shows the moment of the significant wave height peak (2018-03-01 14 GMT).

del Estado measure networks. Figure 4.6.1 shows the location of these instruments in the area and Figure 4.6.4 the values measured by the instruments together with the values provided by PORTUS sea level and wave forecasting systems. The vertical red line shows the moment of the significant wave height peak (2018-03-01 14 GMT) with a value of 7.2 m. We have compared this value with the extreme analysis performed for this buoy for the period 1996–2017 applying peaks over threshold method and Weibull distribution and it coincides with the central estimation estimated for a return period of 50 years (https://bancodatos.puertos.es/BD/informes/extremales/EXT_1_2_2342.pdf). The values from the WAM model used at PORTUS wave forecast system (product ref. 4.6.6) were very accurate following the shape of the measurements, but slightly overestimated remaining about 0.5–1 m over the values measured during the storm. The maximum in the wave value coincides exactly with the high tide maximum levels (14:00 GMT at 'Bonanza 2' and 14:10 GMT at 'Huelva', not shown).

Analysis of the historical wave information in the area: Since its first mooring, the data coverage of 6200085 buoy has been excellent with a mean annual percentage of 92.5% of valid recorded data. However, every year, some data are lost due to accidents, sensor malfunctions or ordinary planned maintenance operations, so we have compared the historical information (product ref. 4.6.3) with model values to be sure that no higher storm passed during the past 20 years. The comparison has been made with the wave reanalysis performed by CMEMS Iberia-Biscay-Ireland Monitoring and Forecasting Centre with ERA INTERIM homogeneous atmospheric forcing for the period: 1992–2018 (product ref. 4.6.5). We have compared the buoy wave measurements with the CMEMS system instead of PORTUS system because the forcing in the first one is homogeneous for the whole period. In the second one, the system has evolved over time and we cannot assure the consistency of the results in the comparison. The results of this reanalysis have been validated with in situ and satellite data showing a good performance of the model (see Table 4.6.1). In Figure 4.6.5, the historical time series are plotted showing clearly the maximum on 1st March 2018 for both data sets (product ref. 4.6.3, product ref. 4.6.5). In this figure are also shown the scatter plot corresponding to both time series and the Quantile-Quantile plot performed with both data sets.
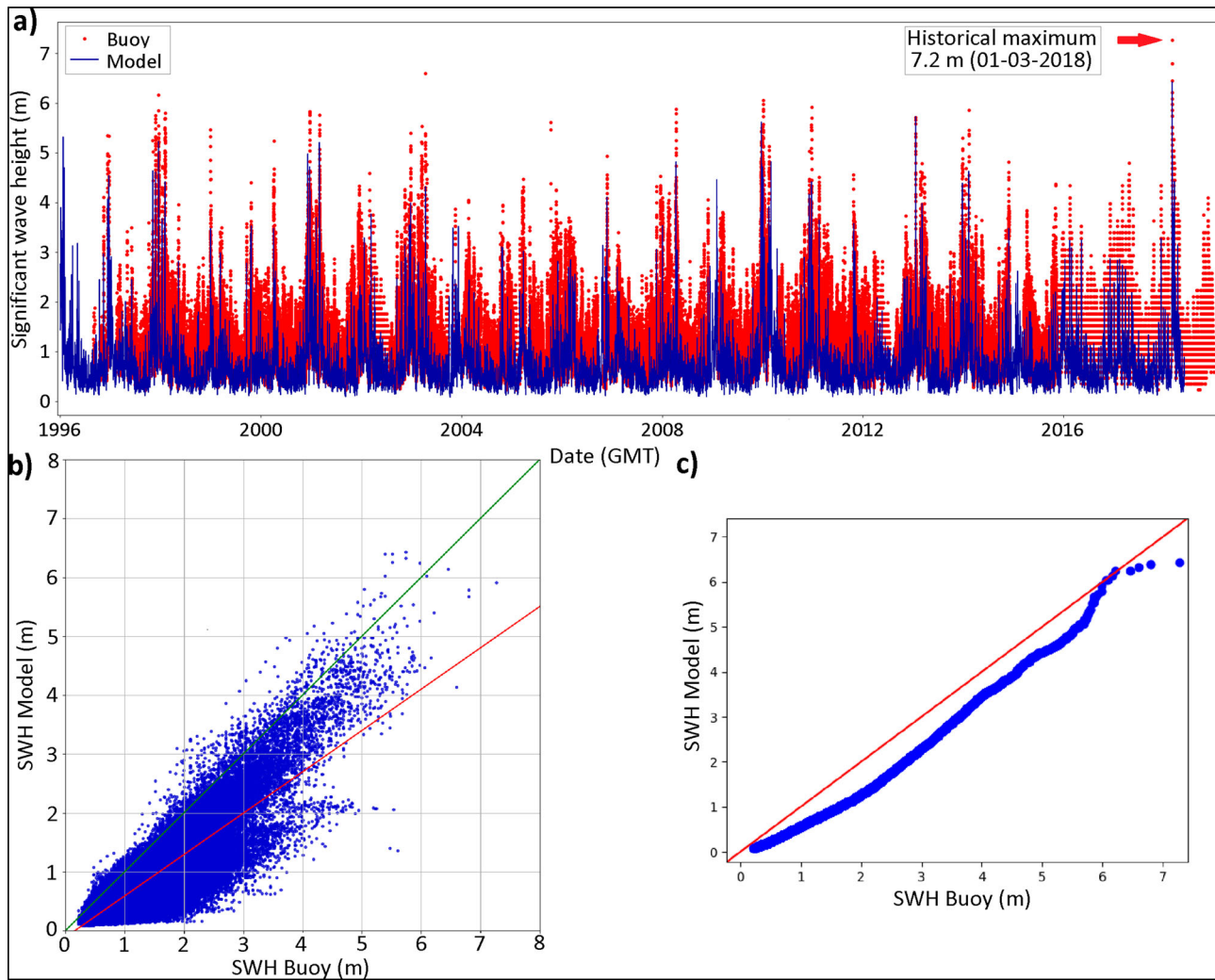
Figure 4.6.5. (a) Historical significant wave height (SWH) time series during the period 1996–2018. Red dots: values measured by the 6200085 buoy (product ref. 4.6.3); blue line: values from CMEMS Iberia-Biscay-Ireland Monitoring and Forecasting Centre wave model (product ref. 4.6.5). The historical maximum measured (7.2 m) is reached on March 1st, 2018. (b) Scatter plot with both time series (Buoy-Model). c) Quantile-Quantile plot for both datasets.

Analysis of the historical sea level information: From an analysis of hourly sea levels from tide gauges in the area, the recorded values near the high tide on March 1st 2018 at 14:00 GMT (time of the wave record) were over the 99.95th percentile of all observed high tides for 'Bonanza 2' station (second highest sea level for 1992–2018 period) and 'Huelva' station (third highest sea level for 1996–2018 period). From extreme variability assessment based on the evolution of the 99th percentile of hourly sea level and surge (Pérez-Gómez et al. 2018), the mean 99th percentile of the surge or residual (sea level-tide) is 0.34 m for 'Bonanza 2' (1992–2017) and 0.24 m for 'Huelva' (1996–2017 period). During Emma storm, the surge reached at these tide gauges 0.60 and 0.36 m, respectively, at 14:00 GMT (time of the record wave height), which is well over its mean 99th percentile. Interestingly, the maximum surge was in both cases recorded a few hours before

the high tide, reaching up to 0.72 m at 'Bonanza 2' and 0.65 m at 'Huelva'. In the latter, the surge was in fact over the 99.5th percentile for 15 h.

Nevertheless, these values were not a record on the sea level measurements in the region: the highest residual or surge in 'Bonanza 2' was recorded on the 6th of November, 1997 (reaching 0.80 m), being the maximum value measured during Emma storm (0.72 m) the second highest residual value recorded at this location since 1992. In agreement to this, extreme analysis of historical tide gauge surge data (based on the Peak Over Threshold method, and fit to a Weibull distribution) revealed, that recorded surge values during Emma were well below the 20 year return period (central estimate) at both stations (81.3 cm for Bonanza, data period: 1992–2019 and 84 cm for Huelva, data period: 1996–2019). Therefore the extreme total sea levels (surge+tide) during

that particular high tide on March 1st could have been higher and the impact of the storm and waves much more severe.

The main explanation for the differences observed between Bonanza and Huelva tide gauges is that Bonanza is very affected by Guadalquivir river discharge. Historically, this is reflected in larger residual values than in nearby tide gauges. The amount of residual or surge magnitude caused by river discharge or by the storm surge itself at Bonanza coast is not easy to determine exactly, however. Having a look to the model forecast, that does not include river discharge as a forcing mechanism, could be of help: some underestimation of the forecasted surge is observed in Figure 4.6.3b. However, this underestimation is less significant than others observed in the history of this tide gauge. This allows us to say that possibly a significant part of the difference in this case is due to spatial variations of the surge along the coast.

It is important to emphasise that hourly sea levels (and surge) are typical sea level products derived from tide gauges, obtained by means of an adequate filter on original <10 min sampling (in this case, the Pugh filter is applied, as described in Pugh and Woodworth 2014). They are usually sufficient to measure the storm surge magnitude (in fact, the output of the Nivmar forecasting system is also hourly), and all values provided here come from hourly sampling. However, other high frequency oscillations and local effects may be present that would conduct to temporary higher sea levels in higher sampling data. Original 1-min data from both tide gauges were examined, and no significant variability was observed, however, in higher frequencies, on March 1st, when this wave record value was measured.

Analysis of the activated alerts, actions taken and damages at the ports: During the 1st of March the Port of Huelva, as the rest of the Gulf of Cadiz coast, was affected by the storm Emma, starting the 27th of February. Previously, forecasts, along with its associated alerts, were forwarded to the Port Authorities located in the area of the Gulf of Cadiz. Thanks to these warnings received the days and hours before, the impact of the event was mitigated. Particularly, the reports service of Puertos del Estado and its downstream service for the ports CMA (*Cuadro de Mando Ambiental – Harbour Environmental Monitoring Dashboard*) (product ref. 4.6.8) and the special alert received from the Spanish Meteorological Office (AEMET; https://www.aemet.es/en/portada) for the storm, which was re-sent for the rest of the port community, allowed to take the appropriate measures. This downstream service, able to send user defined alerts at different points of interest, is fed by the PORTUS system and additional high-resolution local models (Alvarez Fanjul et al. 2018). Other early warning

systems have been implemented successfully before in ports, like the Zeebrugge harbour (Bolle et al. 2018). In this particular case, the system is focused in flooding warnings, with the model train ending in a 2D hydrodynamic model used to simulate the inundation in the port facilities. This system has been set up in a unique case study site and has an additional Bayesian decision support system trained with previous simulations. The CMA downstream service, implemented in most of the state-owned ports in Spain, has been designed to be directly managed by the Port Authorities, following a less specialised and more flexible approach. Therefore, it is the final user the one defining the thresholds and details of the alert system. One of the particularities of the design of the CMA alert system is the possibility to create complex alerts, considering at the same time more than one physical variable, or restricting vector ones to given directions. For example, it is quite common the implementation of an alert combining high waves with elevated sea level (typical situation for overtopping), or limiting the winds alerts to winds from a given direction (dangerous for navigation at the port mouth). Furthermore, the system contains two kinds of alerts: (1) the administration ones, implemented directly by the port manager, and accessible to all users and (2) the individual alerts, created and used only by the final user to fit its own needs. Thanks to this two level alert system, the different departments of the port (operations, piloting, infrastructures, water quality, etc.) can be coordinated thanks to the existence of common alerts and, at the same time, the software retains the flexibility to cope with the individual user needs. It is also worth to mention that many port managers are opening this system to companies working on their facilities, therefore creating a tool useful to coordinate all the Port Community.

During Emma storm, port access was restricted as the pilots boarding was extremely complicated even in sheltered waters (pilots are who decide to go ahead with the operation or not). In the docks, the appropriate instructions were given like cancelling operations with heavy equipment (cranes, machines …), ensuring safety. The port activity could be resumed once the storm started to decline. Despite these actions, the strength of the storm Emma caused important damages in the main breakwater of Huelva Port, from beginning to end, along six kilometres. Both the outer and inner part of the mantle were affected with blocks losses that caused a section reduction of more than one metre of the section in some points. No personal damages and very limited material damages at Algeciras and Tarifa Ports were suffered. Port access for certain types of vessels and time period during the storm were restricted and planned in advance thanks to the CMA service. Some

special vessels and floating construction facilities were assured with tugs to prevent any damage. Furthermore, marine terminals and works in anchorage areas were planned and stopped accordingly taking into account CMA met-ocean forecasts and operativity and safety thresholds. High-resolution met-ocean forecast system was crucial to be able to restrict or go ahead with certain operations, taking into account the different areas of Algeciras Bay and Tarifa and the effects on different types of vessels. This fact was highly valued by port operators in order to guarantee safety and reduce business discontinuity.

On the other hand, this event caused devastating effects throughout the Huelva and Gulf of Cadiz coastline. In certain areas the water literally guzzled seafront, promenades and houses close to the beaches, in a region where the tourism is a very important social-economic factor. The damages in the area have been estimated to more than 30M€: 7M€ in the port of Huelva, 5M€ in the Coast of Huelva, 250K€ in the Port of Cadiz, 20M€ in the Coast of Cadiz (direct communication from the harbour infraestructures responsibles). These numbers correspond only to direct costs due to harbour facilities and coastal damages and don't include the indirect losses due to pause of activity.

4.6.3. Outcomes and conclusions

The most severe wave storm measured in the area of the Gulf of Cadiz occurred in March 2018. The measurement recorded by a permanent station in the area, the deep-water buoy *Bahia de Cadiz* (6200085 station) the 1st of March (7.2 m of significant wave height) has been compared with the historical wave information and with the CMEMS wave reanalysis in the same location and the wave record has been confirmed. This extreme sea state, produced by the storm called Emma and aggravated by the combined effect of waves, high tide and sea level surge, caused devastating effects in the coastal area. The recorded sea levels were also extreme in both the tidal and surge component (e.g. the surge recorded by *Bonanza2* tide gauge, 0.74 m, is the second highest recorded since tide gauge installation in 1992), although historical records were not reached in this case, what would have aggravated the consequences of the storm.

Several ocean monitoring services were working operationally in the area during this event: CMEMS products and coastal and local wave and sea level forecast systems developed by Puertos del Estado. These services were accurate and the storm was properly forecasted. The downstream services, including alert systems, worked properly and users were warned in advance.

Thanks to the accuracy of the forecasts and the actions taken accordingly, even though the storm had a catastrophic potential and caused numerous material damages, safety could be assured in the ports facilities and no personal damages took place. These services provide essential information in the daily operations in the harbour community and their users (shipping companies, stevedores, pilots and tugboats, etc.), and for other stakeholders like tourism sector, maritime infrastructures and transport, fisheries, etc.

Section 4.7. Predictability of large wave heights in the western Black Sea during the 2018 winter storms

Authors: Joanna Staneva, Arno Behrens, Gerhard Gayer
Statement of main outcome: Over the past decade, European seas have been afflicted by severe storms, which caused serious damages in offshore and coastal zones. Severe storms hit the western Black Sea at the beginning of 2018. Wave conditions in the western Black Sea during the storms were high in winter 2018 and the maximum value of the significant wave height reached more than 7 m. Making use of the annual time scale provides enough samples to examine quantiles even higher than the 99th percentile supporting the understanding of the peak values in the western part of the Black Sea. The predictability of the expected largest wave heights during the winter marine storms in 2018 is demonstrated. Close match of the Black Sea CMEMS data with the satellite measurements for high waves is observed. We evaluated the extreme wave conditions in the Black Sea in 2018, based on satellite and model data, when several strong storms have been identified, considering maximum significant wave heights over a given threshold (e.g. 6 events with significant wave height >5 m in the western Black Sea).

Data use:

Ref. No.	Product name & type	Documentation
4.7.1	WAVE_GLO_WAV_L3_SWH_ NRT_OBSERVATIONS_014_ 001Observations	https://marine.copernicus.eu/ documents/PUM/CMEMS-WAV- PUM-014-001-002-003.pdf https://marine.copernicus.eu/ documents/QUID/CMEMS-WAV- QUID-014-001.pdf
4.7.2	AVISO Jason-1, Jason-2 from 2002 https://www.aviso.altimetry.fr Satellite observations	https://www.aviso.altimetry.fr/ fileadmin/documents/data/ tools/hdbk_j1_gdr.pdf https://www.aviso.altimetry.fr/ fileadmin/documents/data/ tools/hdbk_j2.pdf https://www.aviso.altimetry.fr/ fileadmin/documents/data/ tools/hdbk_j3.pdf

(Continued)

Continued.

Ref. No.	Product name & type	Documentation
4.7.3	BLKSEA_ANALYSIS_FORECAST_ WAV_007_003 Model analysis and forecast	PUM: https://marine.copernicus. eu/documents/PUM/CMEMS-BLKSEA-PUM-007-005.pdf QUID: https://marine.copernicus. eu/documents/QUID/CMEMS-BLKSEA-QUID-007-003.pdf
4.7.4	BLKSEA_REANALYSIS_WAV_ 007_006 Model reanalysis	PUM: https://marine.copernicus. eu/documents/PUM/CMEMS-BLKSEA-PUM-007-006.pdf QUID: https://marine.copernicus. eu/documents/QUID/CMEMS-BLKSEA-QUID-007-006.pdf

Reliable prediction of the largest waves during a storm event has always been foremost for offshore platform design, coastal activities, and navigation. Indeed, many severe accidents and casualties at sea have been most likely ascribed to abnormal and unexpected waves (Didenkulova et al. 2006). However, predicting extreme waves is a challenging task, because of their inherent randomness and because the mode of observation of ocean waves, which is of primary importance to verify wind-wave models. That is limited by the costs and risks of deployment during severe open-ocean sea-state conditions. As a consequence, in many cases, the theoretical and modelling frameworks used to estimate wave maxima have been ineffective in warning seafarers or avoiding structural damage to offshore facilities (Forristal 2007).

Significant efforts are being undertaken to better understand and predict the waves in the Black Sea (e.g. Rusu 2016). Polonsky et al. (2011) studied the wind waves variability estimated in the Black Sea in 1979–2008 and studied the occurrence of high waves. Onea and Rusu (2014) studied the variability of the sea states conditions using reanalysis dataset and satellite measurements. Local assessment of the wave conditions for the Black Sea is done in Erselcan and Kükner (2017) and Akpınar and Kömürcü (2012). Akpınar et al. (2016) and Van Vledder and Akpinar (2016) analysed the

distribution of the maximum wave heights in the Black Sea in the period from 1979 to 2009 and identified the areas in which the magnitudes of significant wave heights reach maximum values (southwest, east and in the region of the Crimean peninsula). The spatiotemporal variability of the Black Sea waves was also investigated by Divinsky and Kosyan (2017) over an extended time interval, using the results of a spectral wave model. Recently, Divinski et al. (2019) studied the extreme wind waves in the Black Sea using the MIKE21 spectral wave model with the atmospheric forcing based on the ERA-Interim data until 2017.

The capability of predicting the expected largest wave heights during marine storms for the Black Sea has been evaluated with the wave model WAM (product ref. 4.7.3 and 4.7.4). WAM is a third-generation spectral wave model; the source function integration scheme of Hersbach and Janssen (1999) and the reformulated wave model dissipation source function (Bidlot et al. 2005), later reviewed by Bidlot et al. (2007) and Janssen (2008) are incorporated. A description of the WAM set-up for the Black Sea and validation against observational data can be found in Staneva et al. (2019).

4.7.1. Anomalies in 2018

We first calculated the average annual 99th percentiles in the distribution of the significant wave height (Álvarez Fanjul et al. 2019) within the period from 2002 to 2017 (Figure 4.7.1). The right panel in Figure 4.7.1 shows the difference between the year 2018 and the average map shown in the left panel of Figure 4.7.1. It is a known pattern (e.g. Rusu and Butunoiu 2014) demonstrating that the highest values of the average of annual 99th percentiles are in the areas where high winds and long fetch are simultaneously present (Staneva et al. 2019). Figure 4.7.1(a) shows that wave extremes vary with latitude (Pontes 1998), being larger in the southwestern part of the Black Sea (99th percentile of the
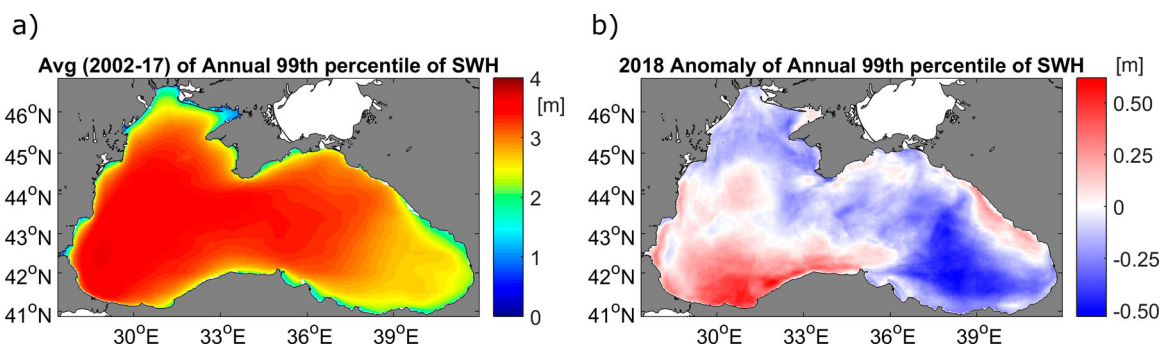

Figure 4.7.1. Map of (a) mean 99th percentile (2002–2017), (b) map of the anomaly of 99th percentile in 2018 of the significant wave height [m] computed from reanalysis model data for the Black Sea. (Product ref 4.7.3 and 4.7.4)

significant wave height larger than 3 m. The mean extreme values are largest in the western Black Sea, with values as high as 3.5 m, while 99th percentile values in the eastern part of the basin are around 2.5 m. This pattern is consistent with the previous studies, e.g. of (Akpınar et al. 2016; Van Vledder and Akpinar 2016).

The year 2018 shows positive anomalies of the significant wave height in the south-western part of the Black sea (Figure 4.7.1b), with values up to 75 cm. In the eastern Black Sea, the anomalies are negative. It is consistent with the yearly west-east displacement of the tracks of the largest storms. These latitudinal displacements alter the wind patterns over the region and, therefore, the extreme waves (Staneva et al. 2019). In general, the results from wave fields for 2018 are in good agreement with satellite data (Jason-3 and Sentinel-3a) as well as with the Varna wave-buoy, showing values of mean SWH up to 1.8 m in the centre of the Black Sea (Quality information document (QUID) of product 4.7.3 and 4.7.4).

4.7.2. Time series

The Black Sea is a data sparse European Sea regarding the availability of traditional in situ wave measurements recorded by usual wave-rider buoys. We used satellite measurements as the only available long-term observational data over the region (ref. 4.7.1 and 4.7.2) to assess the model predictability for higher waves and to demonstrate the variability of the significant wave height in the western Black Sea. It is noteworthy to note here, that the wave model multi-year products (ref 4.7.4) don't assimilate the satellite data and therefore we are analysing two truly independent datasets. The spatial resolution of the observations is also extremely poor for extracting conclusions for the entire basin (Divinski et al. 2019). In addition, recent research of Onea and Rusu (2017) has shown that in the western and eastern parts of the sea the existing trends in wave power fluctuations have different signs. The annual analyses in this section are made over the western part of the Black Sea only (up to 34° E). We also demonstrate the skill of the CMEMS products used here against the satellite observations. The data from the wave model have been collocated with along-track satellite observations be using always the closest grid point to the satellite observation in space and time. Description of the following statistical parameters is given in Appendix A. As shown in Figure 4.7.2b, the annual mean significant wave heights increase from around 0.7–1.1 m from 2002 to 2018 in WAM, and from about 0.9–1.1 m in the satellite measurements. The WAM model shows a small underestimation of

the mean significant wave height which is reflected in a negative bias of about 4 cm and a relative error of 4.1% (Figure 4.7.2b) . However, the mean significant wave heights of WAM and from satellite measurements are highly correlated. At a correlation of 0.916, the variability of the model and of satellite measurements agrees. The maximum significant wave heights over the western Black Sea derived from satellite measurements and from WAM show a correlation of 0.937, which demonstrates that WAM can simulate well the temporal variability of maximum significant wave heights over the tracks and sampling period of the JASON satellite data. On the other side, WAM overestimates the maximum significant wave height (Figure 4.7.2c) resulting in a positive bias of 23.9 cm (translating to a relative error of 5.11%). The maximum value of the significant wave high in the year 2018 over the western Black Sea tracks is 7.5 m. It occurred during the winter storm event in the western Black Sea. However, the temporal frequency of the satellite data is definitely inadequate, especially over the regional basins as the Black Sea one. Thus, it may happen that entire storms and definitely storm peaks may be totally missed by the satellites. With the lack of consistent in-situ wave observations over the Black Sea area, the satellite data are the only data source that can be used for assessing the predictability of the CMEMS wave products including also one of the higher waves.

The quality of the satellite measurements depends on the frequency band of the radar altimeter, for instance with Saral (Ka band), Aouf and Lefevre (2015) were able to detect SWH of 0.3 m accurately. Observations of small waves from the satellite (Hs $\lesssim$ 0.3 m) are difficult to be identified. It is worth to notice that the agreement between the satellite measurements and WAM median and mean wave height has been improved significantly in recent years.

The annual quantiles of significant wave heights from the 25th to the 75th percentiles (Figure 4.7.2d–f) representing almost three-quarters of the distribution show a temporal behaviour similar to that of the annual mean significant wave height (Figure 4.7.2b). With higher percentiles considered, the annual variability increases.

Making use of the annual time scale provides enough samples to examine quantiles even higher than the 99th percentile supporting the understanding of the peak values in the western part of the Black Sea in 2018 with respect to transitioning from the lower parts of the distribution to the uppermost part. Figure 4.7.2 (bottom panels) shows the time series of the annual 99th, 99.9th, and 99.99th percentiles of significant wave heights. While the annual 99th percentiles show variability evenly distributed over the whole period with a very
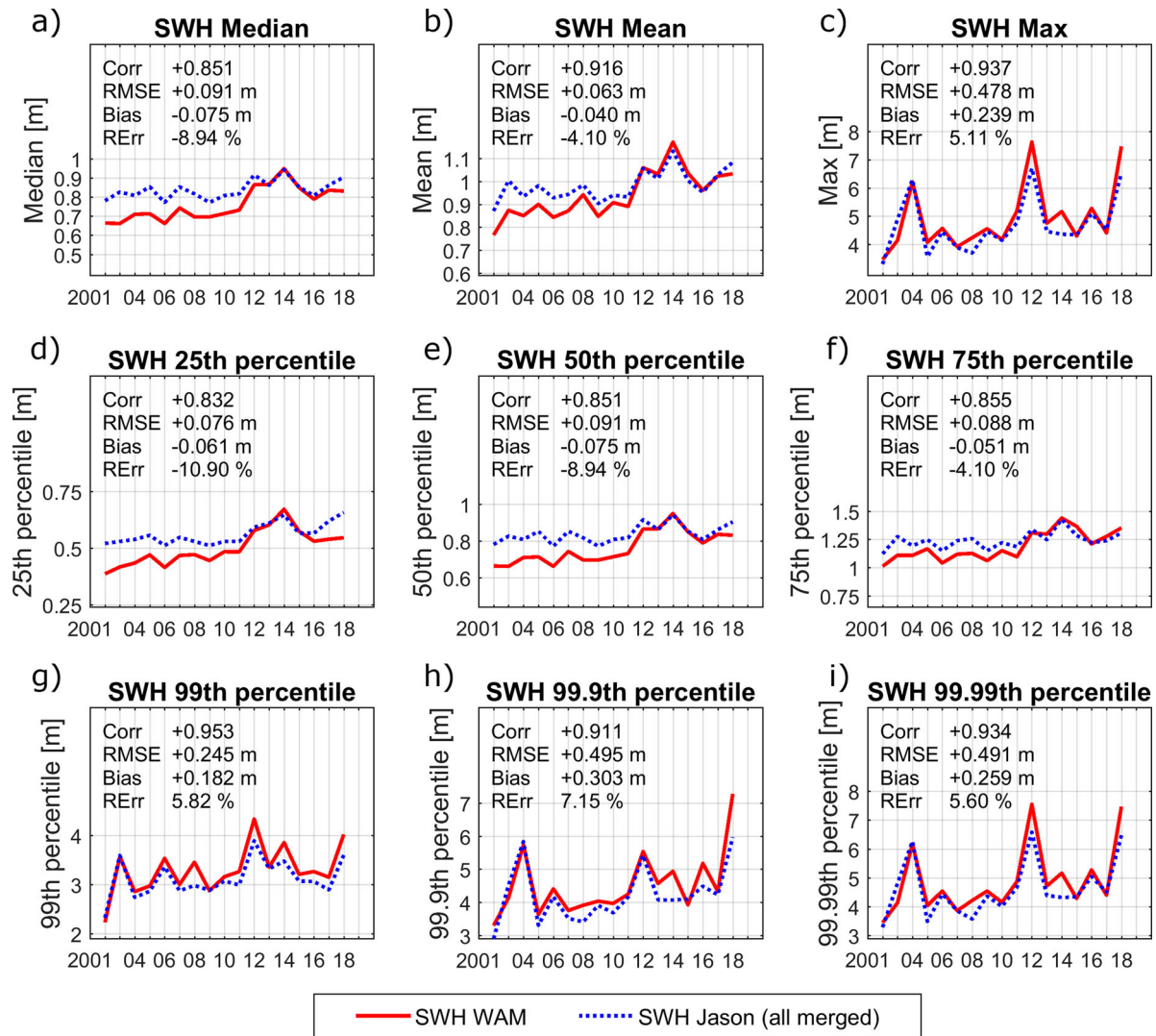
Figure 4.7.2. Time series during 2002–2018 of the annual Black Sea (western basin) (a) median, (b) mean, and (c) maximum significant wave height [m], as well (d–i) specific annual quantiles of significant wave height [m] derived from Jason satellite measurements (blue dots) and from WAM (red line). The satellite data used are ref 4.7.1 and 4.7.2 the model data used are ref 4.7.3 and 4.7.4.

good agreement in the time series behaviour, the 99.9th and 99.99th percentiles in WAM become dominated by the peaks in 2018 and 2012. The correlations increase from 0.85 for 99th to 0.91 for the 99.99th percentile). The correlations range between 0.83 and 0.86 for the percentiles up to 99th and 0.911–0.953 for percentiles of 99th and higher demonstrate very good skill in characterising the variability of wave heights in the western Black Sea. Even though the absolute bias increases for increasing quantiles (Figure 4.7.2g–i), the bias for the annual 99th percentile is 0.18 m. The skill of WAM thus increases with higher percentiles, which possibly relates to parametrizations within WAM that slightly degrade the skill for smaller wave heights in favour of larger waves. It is interesting to note that the peaks that are seen in the year 2018 and 2012 in the 99.99th percentiles

(Figure 4.7.2i) resemble those of the maximum significant wave height (Figure 4.7.2c). On the other hand, for the 99.99th percentile, the maximum peak is in 2018.

These very high percentiles represent only a very small number of observations attributable to single events that do not affect markedly lower quantiles of the distribution. Several factors might hamper the assessment of extreme significant wave heights. First, the wind-wave model WAM, for which simulated wave heights depend on the wind forcing to a large extent, requires wind fields that include high wind speeds at the right time and place to model wave heights in general good agreement with satellite observations. Here, the used wind fields are taken from the ERA-Interim reanalysis, which provides 6-hourly data and runs on a reduced Gaussian grid with

approximately 79 km spatial resolution. Jason along track measurements have a resolution of 7 km and the model simulation of 3 km. In addition, the satellites, and in particular the class exemplified by Jason have their own issues estimating extreme waves this they cannot be considered as the 'truth'. It is however likely that elevated wind speeds that cause very high significant wave heights, as seen from the satellite observations, are not well present in the forcing wind fields – possibly explaining the deviations for the uppermost percentiles and maximum wave heights. The 'true' scale of the model is affected by the wind resolution which is quite coarse, thus a higher

resolution forcing is of crustal importance for regional and coastal CMEMS products.

4.7.3. Winter storms in 2018

Figure 4.7.3 shows two winter ocean storms, one of them detected by the higher percentiles statistics in 2018. This is the event on the 18th of January, 2018 (Figure 4.7.3a). During the storm at the 18th of January, the driving Era-Interim wind fields show very high speeds up to 20 m/s (at 18:00 UTC), generating high significant wave heights up to 9 m in the western part of the Black Sea. Three satellites crossed the storm area, namely Jason 3

Figure 4.7.3. 18 January 2018: Distribution of (a) wind speed and wind direction, and of significant wave height and mean wave direction and Jason-3 track (b), wave field and Saral Altika track 2 h earlier (c), and wave field and Cryosat 2 track 1 h later (d)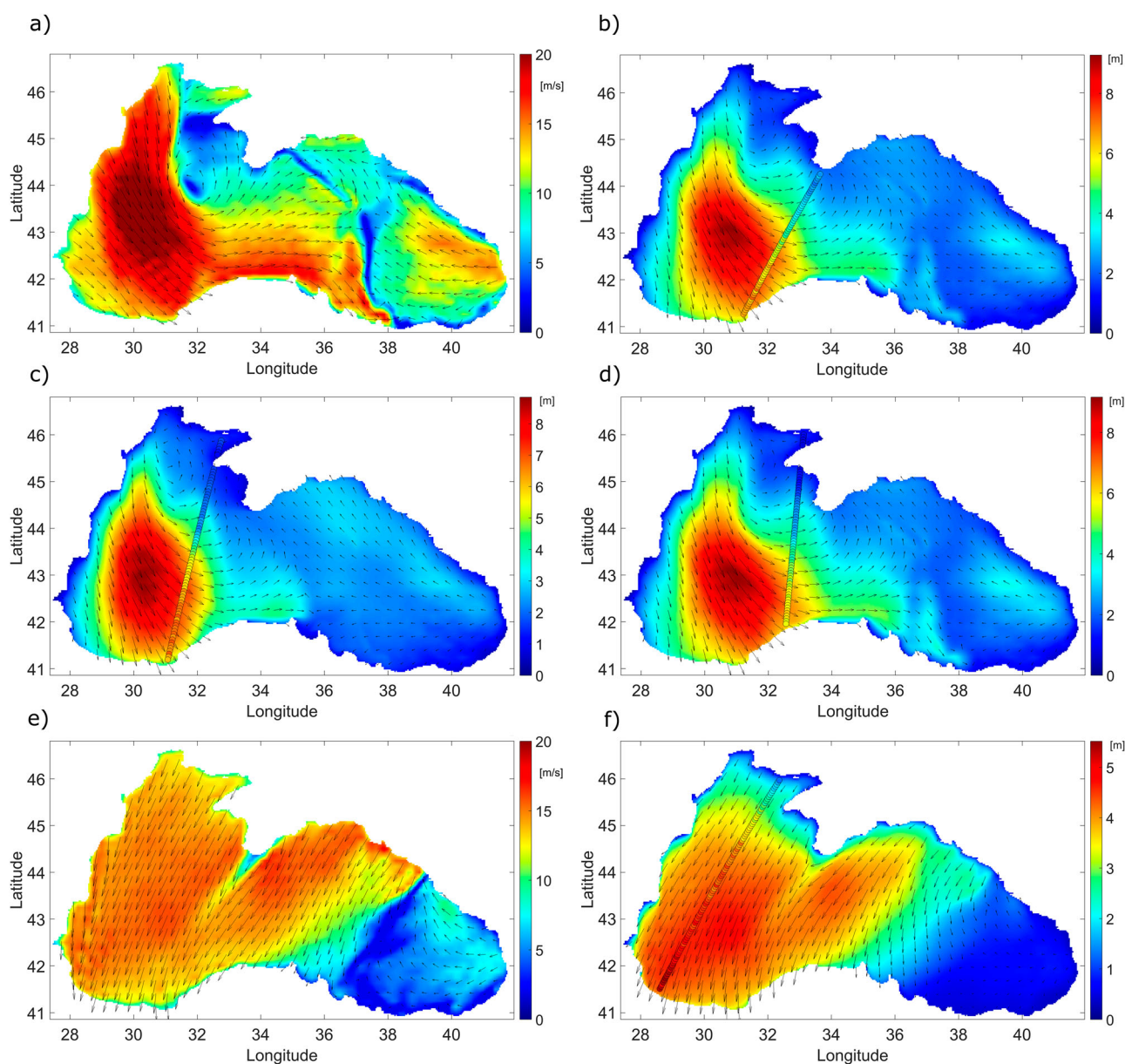. Distribution of (e) wind speed and wind direction, (f) of significant wave height and mean wave direction and Jason-3 track on 28 November 2018. The data used are ref 4.7.1 and 4.7.4.

Table 4.7.1. The Black Sea specific annual quantiles and anomaly in 2018 relative to the mean of significant wave height [m] derived from Jason satellite measurements (sat) and from WAM (wam). The data used are ref 4.7.1, 4.7.2, 4.7.3 and 4.7.4.

	Wam Perc99	Sat Perc99	Wam Perc99.9	Sat Perc99.9	Wam Perc99.99	Sat Perc99.99	Wam H_Max	Sat HMax
Mean 2002–2017 [m]	3.141	2.96	4.54	4.26	5.028	4.753	5.096	4.928
Anomaly in 2018 [m]	0.209	0.215	1.969	1.808	2.442	2.231	2.395	2.220

(Figure 4.7.3b), two hours earlier Saral Altika (Figure 4.7.3c), and one hour later Cryosat 2 (Figure 4.7.3d). The agreement between measurements and wave model data near the peak of the storm is fairly well. The wind field shows a sharp front in north-easterly direction, which is not reproduced in the modelled wave fields which show broader transition zones instead. After these transition areas, the model values and measurements compare well again. The distribution of significant wave height shows good agreement with the Jason 3 observations for the November storm (Figure 4.7.3f) and less good agreement for the storm in January (Figure 4.7.3b).

The January 2018 winter storm caused very high waves, especially over the south-western Black Sea. It contributes to the anomaly of the higher percentiles. The mean 99.9th percentile for the period of 2002–2017 from the satellite measurements is 4.26 m and is slightly overestimated for WAM (4.53 m). The anomaly of 99.9th percentile in 2018 relative to the multi-year mean is 1.9 and 1.8 m respectively. In our analysis, we match satellite measurements with their closest match in WAM introducing a sampling error that affects all parts of the wave distribution (Table 4.7.1).

4.7.4. Outcomes and conclusions

Severe storms have been identified and analysed during the fall-winter of 2018. The purpose of this study was to assess the wave model multi-year simulations for high waves using satellite measurements The measurements recorded by the satellite observations has been compared with the Black Sea CMEMS wave reanalysis in the same locations and the wave records in 2018 have been confirmed. The annual time scale of the investigation provides enough samples to examine quantiles even higher than the 99th percentile. That supports the understanding of the peak values. Different human activities, e.g. the offshore wind power and oil industries and coastal recreation necessitates information about the sea state with high resolution in space and time. There is a consensus that high-quality predictions of extreme events caused by storms could substantially contribute to avoiding or minimising human and material damages and losses. Therefore, reliable wave forecasts, together with long-term statistics (of extreme conditions) are of utmost importance for the marine areas. That can be achieved by demonstrating and predicting the characteristics of the largest waves.

Appendix A:

mean of measurements and model values	$\bar{x} = \frac{1}{n}\sum x_i, \quad \bar{y} = \frac{1}{n}\sum y_i$
Bias	$bias = \bar{y} - \bar{x}$
root mean square error (rmse)	$rmse = \left[\frac{1}{n}\sum (y_i - x_i)^2\right]^{0.5}$
relative error	$RErr = bias/mean\ of\ measurements$
standard deviation	$std = \left[\frac{1}{n-1}((x_i - \bar{x}) - (y_i - \bar{y}))^2\right]^{0.5}$
scatter index	$sci = \frac{std}{\bar{x}} *100$

Section 4.8. Small scale ocean weather during an extreme wind event in the Ligurian Sea

Authors: Maristella Berta, Lorenzo Corgnati, Marcello G. Magaldi, Annalisa Griffa, Carlo Mantovani, Anna Rubio, Emma Reyes and Julien Mader

Statement of main outcome: We investigate the response of the coastal ocean circulation during an extreme event at the end of October 2018, that caused extensive damage along the coast of the Ligurian Sea in the western Mediterranean Sea. In particular, we consider the response of ageostrophic small scale eddies and jets (submesoscales), that are present in the area. During the extreme event, sea surface velocity as measured by High Frequency Radars increases approximately four times while vorticity and divergence associated with the small features are almost doubled. High (positive/negative) divergence values indicate upward/downward motion that may inject/eliminate pollutants, nutrients and biological quantities into/from the surface of the ocean. The understanding of the 'ocean weather' and related processes that can modify horizontal and vertical transport is necessary to comprehend bio-physical interactions that may have a significant impact on the coastal marine ecosystems (e.g. fisheries, primary production, carbon budget, etc.).

Products used

Ref. no.	Product name & type	Documentation
4.8.1	WIND_GLO_WIND_L3_NRT_OBSERVATIONS_012_002 Gridded sea surface wind observations from scatterometer.	PUM: https://marine.copernicus.eu/documents/PUM/CMEMS-WIND-PUM-012-002-005.pdf QUID: https://marine.copernicus.eu/documents/QUID/CMEMS-WIND-QUID-012-002-003-005.pdf

Continued.

Ref. no.	Product name & type	Documentation
4.8.2	INSITU_GLO_UV_NRT_OBSERVATIONS_013_048 Gridded sea surface current velocity observations from High Frequency Radar.	PUM: https://resources.marine.copernicus.eu/documents/PUM/CMEMS-INS-PUM-013-048.pdf QUID: https://resources.marine.copernicus.eu/documents/QUID/CMEMS-INS-QUID-013-048.pdf
4.8.3	OCEANCOLOUR_MED_CHL_L3_NRT_OBSERVATIONS_009_040 Gridded mass concentration of chlorophyll-*a* in seawater retrieved by ocean colour observations from satellite.	PUM: https://marine.copernicus.eu/documents/PUM/CMEMS-OC-PUM-009-ALL.pdf QUID: https://marine.copernicus.eu/documents/QUID/CMEMS-OC-QUID-009-038to045-071-073-078-079-095-096.pdf
4.8.4	INSITU_MED_NRT_OBSERVATIONS_013_035 Temperature and salinity profiles along glider track.	PUM: https://marine.copernicus.eu/documents/PUM/CMEMS-INS-PUM-013.pdf QUID: https://marine.copernicus.eu/documents/QUID/CMEMS-INS-QUID-013-030-036.pdf

4.8.1. Introduction

We are used to the concept of 'atmospheric weather' because it affects our everyday life with meteorological features, like storms or low-pressure systems. The typical horizontal scale of these features is of the order of 100–1000 km, i.e. the so-called atmospheric 'mesoscale'. We have also experience with smaller atmospheric 'submesoscale' features, like tornadoes or thunderstorms, that have typical horizontal scales of the order of 100 m to 100 km.

We are less familiar with the equivalent concept in the ocean: 'ocean weather', and its impact on the ecosystem, is often ignored even by most scientists (Bates et al. 2018). Like the atmosphere, the ocean is characterised by the presence of eddies and jets at various scales. These structures, though, are significantly smaller than their atmospheric counterparts, because of the different fluid properties and stratification. Mesoscale eddies in the ocean are of the order of tens to hundreds km, while submesoscale features are characterised by smaller scales (typically in the range of 1-10 km) and by vorticity values comparable or higher than the Coriolis parameter *f*, indicating ageostrophic dynamics.

The impact of ocean submesoscale structures is still only partially known, mostly because of the difficulties in collecting extensive measurements at the necessary high spatial and temporal resolution (Alkire et al. 2012). Submesoscale features are expected to be even more relevant than mesoscale ones for the lowest trophic levels of the ecosystem, mostly because they are characterised by higher vertical velocities and convergence areas that impact the distribution of nutrients, biological quantities as well as potential pollutants (Mahadevan and Campbell 2002; Gildor et al. 2009). It has been suggested, mostly on the basis of numerical model results

(Lévy et al. 2012) that submesoscale dynamics 'can change not only primary and export production, but also the structure and functioning of the planktonic ecosystem'. Direct measurements of submesoscale dynamics and ecosystem response, though, are still lacking, and several mechanisms are still unknown.

One still open question is the interaction between wind forcing and ocean submesoscale. Various mechanisms have been proposed, through which the wind could actually weaken or strengthen submesoscale eddies and jets (Mahadevan and Tandon 2006; Thomas et al. 2013; Berta et al. 2018; Zatsepin et al. 2019), but experimental evidences are still rare. Classic linear theory suggests that the wind generates a surface Ekman layer that tends to erase submesoscale features and induce coastal upwelling or downwelling, depending on wind direction (Berta et al. 2018), being the former most common along the west coast of continents. Theories on nonlinear Ekman pumping, on the contrary, suggest that submesoscale features and winds interact, possibly leading to local increases of divergence and vertical velocities (Mahadevan et al. 2008).

Here we investigate the response of submesoscale structures to an extreme wind event in October 2018 in an area located in the Ligurian Sea. The wind reached a speed of 20 m/s during October 29, which classifies as an 'extreme event' in the Ligurian area according to the climatology of Chronis et al. (2011), causing extended damages along the coast. The area is of particular interest because it is situated in front of a highly touristic coast, with an important Marine Protected Area (Cinque Terre), also well known to be a favourable habitat for anchovies. The work is mostly based on hourly sea surface current maps measured by a High Frequency Radar (HFR) network (product ref. 4.8.2: spatial grid resolution 1.5 km, ranging approximately 40 km from the coast), together with meteorological and oceanographic data from satellite (product refs. 4.8.1 and 4.8.3, respectively) and in situ platforms (product ref. 4.8.4).

The investigation describes the evolution of ocean currents and wind during a 2-month period (October–November 2018), focusing on the extreme event during the period 25 October–1 November. The aim is to characterise the evolution of the ocean weather at scales of a few kilometres, especially in terms of divergence/convergence, causing upwelling/downwelling, that can be diagnosed from the surface velocity and that have a direct impact on the ecosystem and on fishery.

4.8.2. Data and analysis

The HFR-TirLig High Frequency Radar (HFR) network is composed of 3 Codar SeaSonde systems (VIAR, TINO, PCOR) with antennas locations and coverage as shown

(a)

(b)
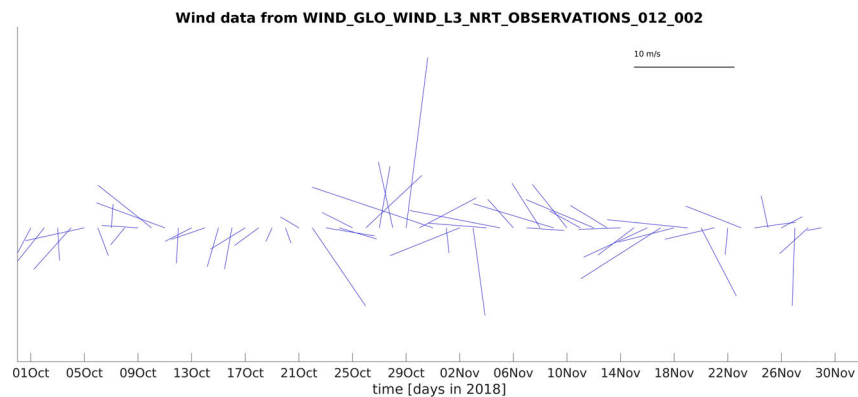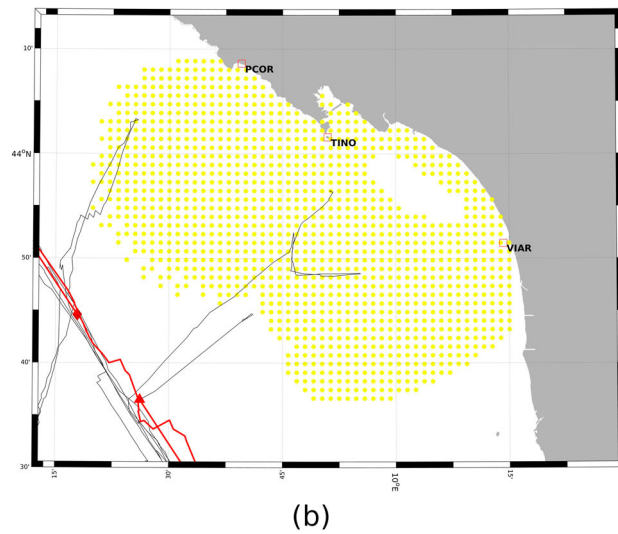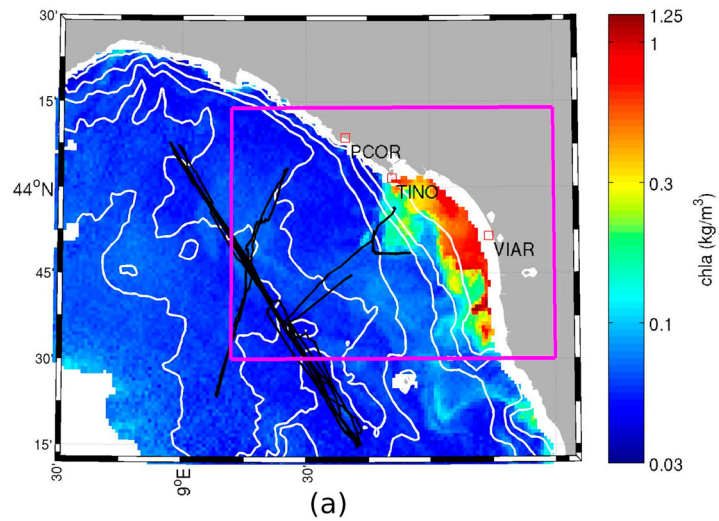
(c)

Figure 4.8.1. Overview of the explored datasets. (a) Chl-a map from a satellite data product (product ref 4.8.3) on 20 October 2018 in the Ligurian Sea with superimposed glider tracks (black lines, product ref. 4.8.4) and outlines of the area of interest (purple square). Bathymetric levels (white contours) are at 25, 50, 100, 250, 500, 1000 and 2000 m. (b) Details of the study area, the average coverage of the HFR TirLig network (yellow dots, product ref 4.8.2) and the (black) glider track with the red part indicating the position of the glider during the event of interest, 25 October (red diamond)–1 November (red triangle). (c) Stickplot of averaged winds measured by satellite scatterometers (product ref 4.8.1).

in Figure 4.8.1(a,b). The systems generate hourly maps of the radial components of the surface velocity on a polar grid over a range of ~40 km from the coast, with typical range resolution of 1 km, angular resolution of 5° and integration time of 1 h. The radial velocities are then combined into total velocities over a cartesian grid with spatial resolution equal to 1.5 km. The sea surface velocity field from HFR is characterised here considering 2D hourly maps of surface currents and computing kinematic properties, such as vorticity and divergence, normalised with respect to *f*. Values of order 1 indicate that the flow is highly non-linear and characterised by convergence/divergence areas and significant vertical velocities (Mc Williams 2016; D'Asaro et al. 2018). As a second step, the average magnitude of velocities and kinematic properties are evaluated as Root Mean Square (RMS) values over the area of HFR coverage, and time series of these RMS quantities are considered.

The used wind dataset consists of daily L3 gridded sea surface wind observations at 10 m from ASCAT scatterometers onboard METOP-A and METOP-B satellites with resolution 0.125 degrees based on 12.5 km swath observations. Vector velocities from both ascending and descending paths of the two satellites are temporally and spatially averaged over the HFR domain. Time series of this average are shown in Figures 4.8.1(c) and 4.8.3 (top panel), with stick plots and magnitudes, respectively.

Satellite ocean colour observations are used to retrieve the mass concentration of chlorophyll a (Chl-a) for the Mediterranean Sea according to the algorithms developed by Berthon et al. (2002), D'Alimonte et al. (2003),

D'Alimonte and Zibordi (2003), Volpe et al. (2007). The L3 dataset consists of daily mean gridded (1 km × 1 km) maps of the average Chl-a content at the sea surface. In Figure 4.8.1(a) we show Chl-a concentration on 20 October to provide some general information in the area of interest. A complete time series of L3 Chl-a product is not available because of extensively cloudy conditions, especially during the extreme event.

One glider track is covering the Eastern Ligurian Sea in the period 19 September to 3 November 2018, with initial and final mission points within the HFR domain (Figure 4.8.1a). During the event, the glider trajectory covers a segment just to the South-West of the HFR coverage (red lines in Figure 4.8.1b). The glider dives from the surface to about 874 m providing profiles of temperature and salinity that are used for background information on water stratification and estimate of the mesoscale Rossby radius. Unfortunately, biogeochemical data are not available, so that a direct evaluation of the ecosystem response cannot be performed.

4.8.3. Results

We first provide background information on the environmental characteristics of the area of interest, to then consider the evolution of winds, current velocities and kinematic properties before and after the extreme wind event.

Figure 4.8.1(a) shows high Chl-a concentration in the area of interest compared to the surrounding waters, probably due to the presence of the Magra
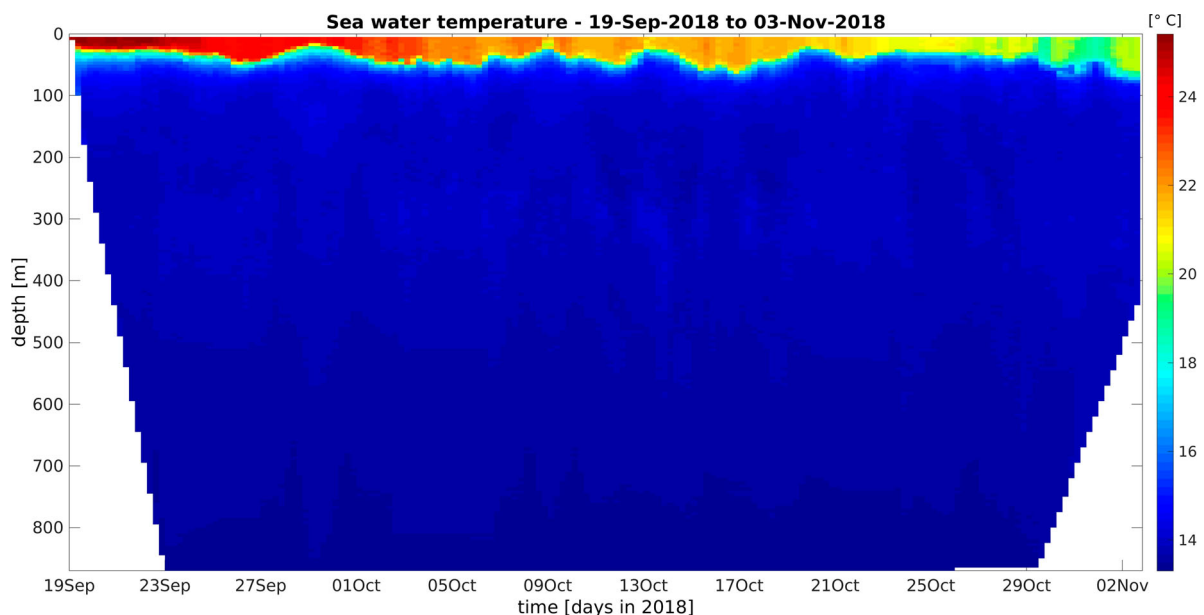

Figure 4.8.2. Water column temperature evolution observed along the glider track (product ref. 4.8.4) from 19 September to 3 November 2018.
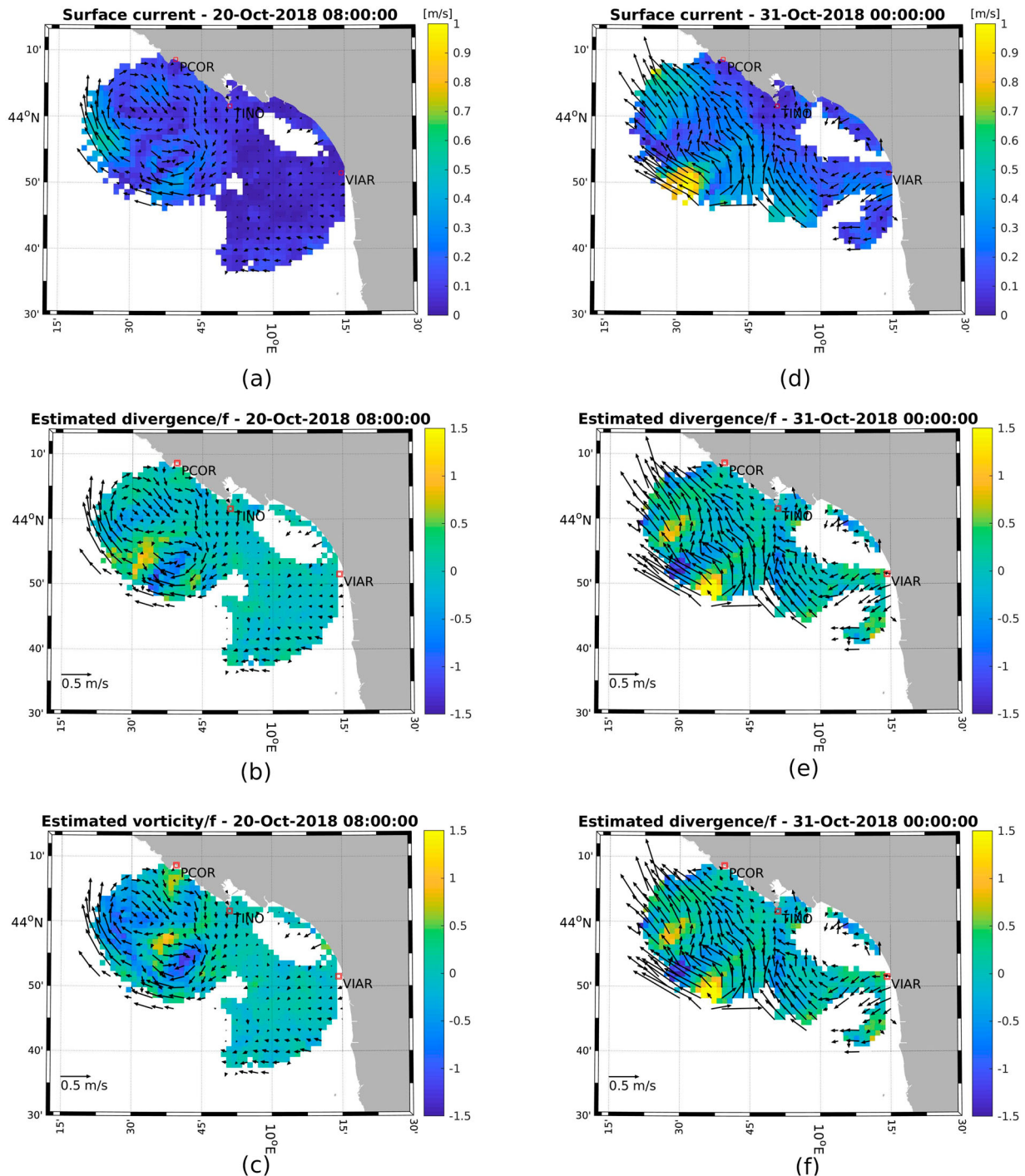
Figure 4.8.3. Examples of maps of hourly surface currents (top panels) measured by HFR (product ref. 4.8.2), surface horizontal divergence –normalised by f- (middle panels) and surface relative vorticity -normalised by f- derived from HFR current measurements (product ref. 4.8.2) (bottom panels) fields before (20 October 2018, left panels) and after (31 October 2018, right panels) the extreme wind event. The arrows indicate velocity vectors, the colours indicate the magnitude of the panel-specific scalar quantities.

river (Cattaneo Vietti et al. 2010). The spatial variability suggests the influence of small velocity structures.

Scatterometer winds (Figure 4.8.1c) before the event are weak (<10 m/s) and predominantly north-easterly. The wind event starts around 25 October and winds

reach 20 m/s on 29 October, with winds that are initially southwesterly to become then southeasterly. After the event, winds are again ~10 m/s and northerly, even with alternate directions. Temperature and salinity profiles from glider measurements in the area of interest indicate that during late October the water column

undergoes an abrupt cooling of the upper layers and an intense mixing process, with a deepening of the mixed layer and a decrease of its temperature approximately from 26°C to 19°C (Figure 4.8.2).

An example of surface currents from HFR before the event is shown in Figure 4.8.3 (left panels). The northern area of the domain is more energetic than the southern part, and is characterised by jets and eddies with typical radius of approximately 5–6 km, smaller than the mesoscale Rossby radius of 10–15 km in the area, as reported in the literature (Grilli and Pinardi 1998), and directly estimated by the stratification shown in the glider data (Figure 4.8.2). The structures have relatively low velocity (∼10–30 cm/s), but their vorticity and divergence reach order f, indicating ageostrophic dynamics and confirming that they can be classified as 'submesoscale' structures. During and immediately after the storm, the sea surface velocity goes through significant changes (Figure 4.8.3, right panels). Areas characterised by high velocities and kinematic properties are wider and stronger than before the event, exceeding f and suggesting enhanced horizontal and vertical velocities (e.g. D'Asaro et al. 2018). The increase in horizontal and vertical transport in the water column might impact biological quantities, nutrients and pollutants with potential consequences on the ecosystem. It is important to note that the areas of divergence/convergence appear mostly related to the structure shapes, rather than coastally induced upwelling/downwelling, which hints to nonlinear interactions between submesoscale and wind forcing.

Figure 4.8.4 shows the time series of daily wind and surface current speed and the RMS of kinematic properties, averaged over the HFR domain. Before the storm, kinematic property values are approximately 0.3–0.4f. As the wind speeds up (25 October), kinematic properties increase and reach average values exceeding 0.6f, while currents increase from 0.1 to 0.4 m/s. Notice that the higher uncertainty (indicated by the highest standard deviation values) occurs during the peak of the storm, on 29 October, when the HF radar coverage is partial (∼50%) due to the extreme weather conditions that increase the noise in the received echoes and thus reduce the coverage (Barrick 1971; Gurgel et al. 1999). After the storm values of velocity and kinematic properties tend to decrease to pre-storm conditions.

4.8.4. Conclusions

In this paper, the effects of an extreme wind event on the local circulation in the Ligurian Sea are investigated. The
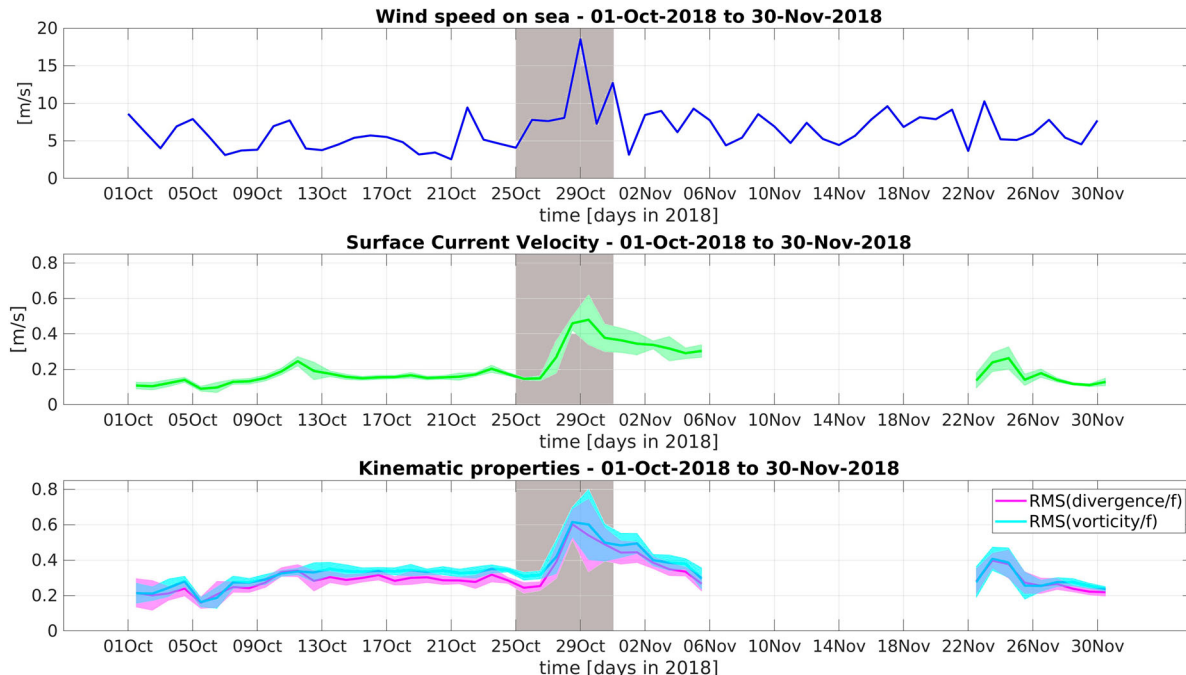
Figure 4.8.4. Time series of (from top to bottom panel): daily averaged wind magnitudes (scatterometry, product ref 4.8.1) spatially averaged over the HFR domain, daily averaged surface current speed (product ref. 4.8.2) spatially averaged over the HFR domain, daily averaged RMS of divergence and vorticity normalised by the local Coriolis parameter f and spatially averaged on the HFR domain. Hourly divergence and vorticity are evaluated from the hourly surface current velocity fields measured by HFR (product ref. 4.8.2). The gray area highlights the event period (25th October to 1st November 2018). The event peak is on 29th October. The shaded coloured areas in the bottom panels indicate the standard deviation of the surface currents and of the kinematic properties. The HFR dataset has a gap in the period November 6–22 because the TINO antenna suffered from a power outage.

evolution of the structures suggest nonlinear interactions with the wind forcing, with local values of divergence exceeding the Coriolis parameter f, indicating significant submesoscale vertical velocity in the water column. The results show that the simplified paradigm of Ekman transport and induced coastal upwelling/downwelling can be significantly altered by the presence of submesoscale. The specific mechanisms of interaction, as well as the role of high resolution inhomogeneity in the wind magnitude and direction (Zatsepin et al. 2019) need further investigation.

Results also show that small scale ocean weather strongly modifies horizontal and vertical transport, suggesting a potential impact on the biological response. Unfortunately, though, no glider biogeochemical data are available during the event, so that the ecosystem response cannot be directly evaluated. The study indicates the importance of further investigating data from multi-platform observations such as water column information from gliders or fixed buoys within the HFR coverage. Further investigations are also planned to assess the generality of the results as a function of ocean state, wind conditions and seasonality.

Acknowledgements

Section 4.9. Drifter observations and Lagrangian tracking of the 2018 easterly wind event in the North Sea

Authors: M. Ricker, E. V. Stanev, T. H. Badewien, H. Freund, J. Meyerjürgens, J.-O. Wolff, O. Zielinski
Statement of main outcome: Persistent easterly winds in spring 2018 reversed the circulation in the North Sea for more than a month. This reversal has been documented by GPS-drifter observations, as well as by the stranding positions of wooden drifters released along the German North Sea coast. The latter information came from members of the public, the majority of which are likely to be non-scientists. It provided a valuable contribution to the GPS-drifter experiment and demonstrates an excellent example of the usefulness of citizen science. Lagrangian numerical experiments were also performed and helped explain and quantify the anomalous transport and the reversal of the circulation at the sea surface and in deeper layers. It has been shown that the CMEMS surface current products agree well with drifter observations, even under extreme wind conditions, which adds to their credibility.

Products used

Ref. No.	Product name & type	Documentation
4.9.1	NORTHWESTSHELF_ANALYSIS_FORECAST_PHYS_004_001_b Model analysis and forecast	PUM: https://marine.copernicus.eu/documents/PUM/CMEMS-NWS-PUM-004-001.pdf QUID: https://marine.copernicus.eu/documents/QUID/CMEMS-NWS-QUID-004-001-b.pdf
4.9.2	NORTHWESTSHELF_ANALYSIS_FORECAST_WAV_004_012 Model analysis and forecast	PUM: https://marine.copernicus.eu/documents/PUM/CMEMS-NWS-PUM-004-012.pdf QUID: https://marine.copernicus.eu/documents/QUID/CMEMS-NWS-QUID-004-012.pdf
4.9.3	Wooden drifters Observations	http://portal.macroplastics.de/index.php?page=drifter-meldung
4.9.4	GPS drifters Observations	Data: Stanev et al. (2019) (Drifter 1) Technical description: Meyerjürgens et al. (2019)

4.9.1. Introduction

The present research was motivated by observations made during the project 'Macroplastics Pollution in the Southern North Sea' (http://www.macroplastics.de/), one aim of which was to study the propagation pathways of marine litter in the North Sea (e.g. Stanev et al. 2019). It describes the response of the circulation in the North Sea to non-typical atmospheric situations in 2018 and the validation of available CMEMS surface and Stokes drift velocities against observations from drifters during extreme weather conditions. Data of two drifter types have been used: 1. GPS drifters providing temporally highly resolved trajectories (Meyerjürgens et al. 2019) and 2. Wooden drifters providing a large amount of beaching positions and emphasising the benefits of citizen science (Garcia-Soto et al. 2017).

The sense of circulation in the North Sea is overall anti-clockwise (Mathis et al. 2015), which is illustrated in Figure 4.9.1 by the annual mean surface currents during 2018 computed using the Copernicus product for the European North West shelf (product ref. 4.9.1). Earlier research on the wind effects focused mostly on the annual mean circulation, on the circulation patterns resulting from wind blowing from different directions and with varying magnitudes, or on the coupled wind-tidal variability (Maier-Reimer 1977; Backhaus 1989; Otto et al. 1990; Sündermann and Pohlmann 2011; Jacob and Stanev 2017). However, not much is known about the role of extreme, or specific, wind conditions (e.g. untypical change of wind-direction, very strong magnitudes, persistence of anomalous conditions for a
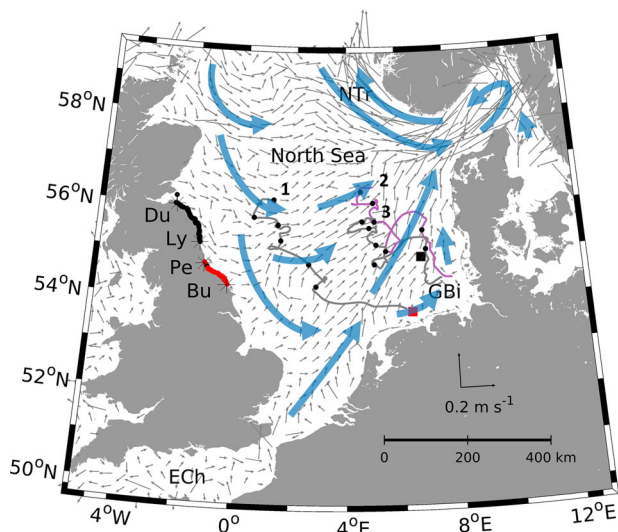
Figure 4.9.1. Mean surface currents (grey vectors) in 2018 in the area of the North Sea plotted on a grid with a resolution of ~30 km (product ref.: 4.9.1). Superimposed are schematic current patterns (blue arrows). The squares indicate the locations (red: Borkum Riffgrund, black: Sylter Außenriff) where wooden drifters have been released. The respective beaching locations between the towns (stars) Dunbar (Du), Lynemouth (Ly), Peterlee (Pe) and Burniston (Bu) are shown with smaller black and red symbols where the colour of the beaching locations relates to the colour of the release points. Grey/purple lines: the trajectories of three GPS drifters in 10-day intervals (black dots) from 24.02.2018 to 25.04.2018. The trajectories start in the German Bight and end at their respective numbers. ECh: English Channel, GBi: German Bight and NTr: Norwegian Trench.

long time), neither about the associated changes of the general circulation in the North Sea. To enable reliable future studies of the influence of extreme wind events on the North Sea circulation, the validation of the numerical models during such events is inevitable.

The North Sea is a shallow shelf sea with an average depth of ~90 m. Large areas of it are shallower than 30 m, and the whole water column there can be directly impacted by wind forcing as the upper Ekman layer can reach the bottom. The response to variable winds can thus change the circulation down to the bottom in a very short time (about one inertial period, i.e. about 15 h in this region). Short-periodic reversals are not untypical in this sea, because the circulation is essentially dominated by daily and semi-daily tidal periodicity. Whether pronounced reversals of the circulation could persist for very long times, is not well known. If they do, this would suggest a long-range displacement and mixing of large bodies of water. An improved knowledge on the non-typical transformations of the North Sea circulation is needed also for trajectory forecasts and many related activities, e.g. search and rescue operations (Röhrs et al. 2012), propagation of fish eggs, larvae and marine litter (Christensen et al. 2007; van der Molen et al. 2007; Gutow et al. 2018), or for optimising the use of the marine environment and preserving its environmental status (Emeis et al. 2015).

In the present study, we analyse the propagation pathways of surface water using surface drifters, which are advected by the Lagrangian current that includes the wave-induced Stokes drift, as well as the direct wind drag. Lagrangian tracking using data from an operational model is also performed.

4.9.2. Methods

The research methods are based on observations of three GPS and wooden drifters, as well as Lagrangian tracking. A total of 1600 wooden drifters (Schöneich-Argent et al. 2019; Stanev et al. 2019) were released during the research cruise HE503 of the RV Heincke (Figure 4.9.2). The first 800 wooden drifters were released on 24.02.2018 in the southern North Sea at approximately 53.11° N, 6.42° E

(a)

(b)

Figure 4.9.2. 1600 wooden drifters were released on 24.02.2018 and 27.02.2018 during the research cruise HE503 of the RV Heincke (Figure 4.9.1). (a) The wooden drifter (message in English is on the back side: 'Help us understand the distribution of marine litter! Please report the number and position of this drifter to the University of Oldenburg'). (b) Floating drifters after the deployment at Borkum Riffgrund.

(Borkum Riffgrund, red square in Figure 4.9.1) which is situated northwest of the Dollart, i.e. in the Ems estuary. The second release of 800 wooden drifters was conducted on 27.02.2018 at approximately 54.97° N, 6.79° E (Sylter Außenriff, black square in Figure 4.9.1).

The wooden drifters are cut from solid, FSC-certified spruce wood, and measure 10 × 12 cm and 2 to 4 cm in height, respectively. Finders are asked to report the drifters via the project website (Aden and Stephan 2017). Hence, a message in German and English as well as a unique identification number are branded on either side (Figure 4.9.2a). Each report contains information on the drifter ID, the location and time of finding, as well as any additional comments that the finder may want to leave. More technical details and further information about stranding are given in Stanev et al. (2019).

GPS drifters (Meyerjürgens et al. 2019) have a cylindrical shaped housing (500 mm in length) made of polyvinyl chloride (PVC), which is divided into two parts (Figure 4.9.3). The upper part (140 mm in diameter) holds the positioning and transmission unit. The lower part (90 mm in diameter) contains a battery pack which powers the GPS transmitter, yielding an average battery life span of 4 months by transmitting the positions at an interval of 10 min. Four drag-producing cruciform wings are mounted directly to the lower part of the housing to reduce the direct windslip-induced motion to the drifter. Positions of the drifter were sampled with an accuracy of ∼2.5 m.

Start and end positions and times are the only information known for the wooden drifters (Figure 4.9.1). The GPS drifter also provides the trajectory, but does not fully describe the circulation over the entire North Sea. Therefore, for the period of drifter observations, data from the CMEMS numerical model for the European Northwest Shelf (product ref. 4.9.1), which is

based on version 3.9 of NEMO (Madec 2008) have been additionally used (see also O'Dea et al. 2012). The second set of data from operational modelling included Stokes drift velocities (product ref. 4.9.2). These are produced from the North-West European Shelf Wave Analysis and Forecast system using the WAVEWATCH III model (version 4.18; The WAVEWATCH III Development Group 2016).

Particle tracking was used to analyse the transport in the studied area and to support the observations from the GPS and wooden drifters. The model, which is known as OpenDrift (Dagestad et al. 2018), uses a 2nd-order Runge-Kutta scheme. Experiments were carried out 'offline' using data from the circulation and wave model, as well as 10 m winds. The horizontal diffusion is accounted for as described in Stanev et al. (2019). The calibration of the tracking model (weights of currents, Stokes drift and wind drag) using drifter observations is also described in their work.

4.9.3. Wooden drifters

Wooden drifters (product ref. 4.9.3) released within a distance of 40–120 km to the German coastline stranded at the east coast of England and Scotland (Figure 4.9.1). In total, 782 validated drifter reports (out of 1600 released drifters) were recorded between the time of deployment and 05.06.2018. All these reports were made along the British northeast coast (Figure 4.9.1). This is contrary to the 'canonic' circulation scheme described above. A simple explanation for this finding could be that easterlies persisted for a relatively long time after the release of the drifters. These events are known as the 'Beast from the East', a phrase used to describe cold conditions in the UK caused by easterly winds from the continent. The general wind direction

Figure 4.9.3. One of the GPS drifters (a) and their deployment (b) during the RV Heincke cruise HE503 at Borkum Riffgrund (Meyerjürgens et al. 2019).

was mostly towards the west with peak values of up to 22.6 m s^{-1}. The time period 19.02.2018 to 15.04.2018 exhibited the strongest easterlies. Ocean surface velocities responded to the wind speeds which resulted in

a general westward ocean surface circulation accompanied by westward Stokes drift velocities.

The calibration of wind drag for the wooden drifters was conducted by comparing the simulated stranding
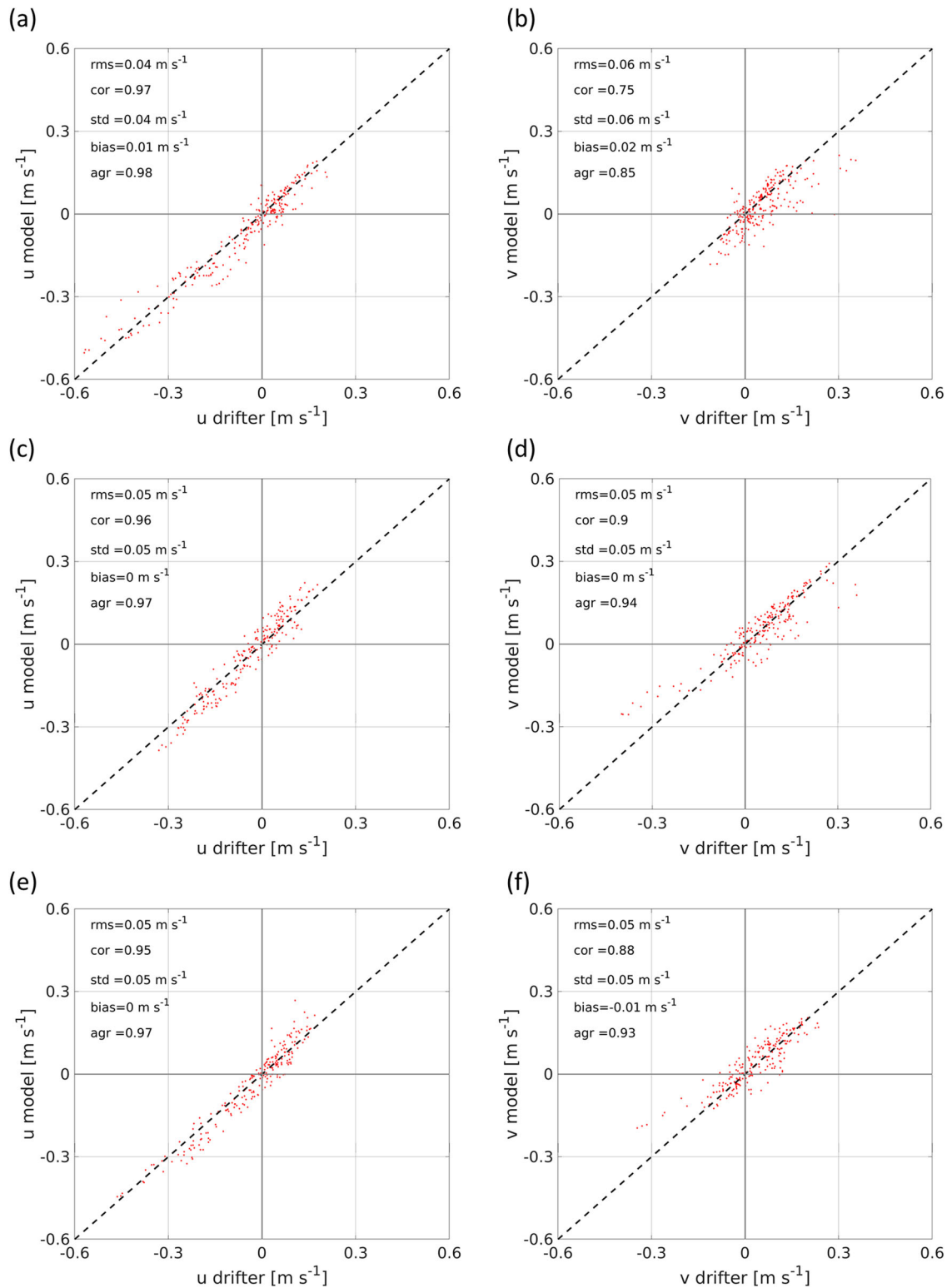

Figure 4.9.4. Validation of model surface currents against observations from GPS drifters. Top, middle and bottom panels correspond to drifters 1, 2, and 3, respectively. Left panels: zonal velocity component (u), right panels: meridional velocity component (v). The dashed line is the diagonal and the optimal location of the dots.

positions with the real ones and finding the appropriate coefficient for which the difference between stranding positions of real and simulated drifters was minimal. The additional contribution of the wind to the current and Stokes drift is estimated at ∼2.5%. The pathways of simulated wooden drifters (see their stranding positions in Figure 4.9.1) demonstrated that their movement is dominated by several strong eastward wind events followed by several stagnation periods. The stranding positions of model drifters with characteristics of the wooden drifters from the two releases coincided almost perfectly with the observations (Stanev et al. 2019).

4.9.4. GPS drifters

The trajectories of the three grey/purple (grey solid lines in Figure 4.9.1) complement the propagation patterns of floating objects (product ref. 4.9.4). The strong easterly wind conditions resulted in a substantial westward displacement, opposite to the canonic pattern. During the two months considered here, the drifters travelled 790, 722, and 668 km, respectively.

The experiments with Lagrangian tracking showed that the GPS drifter can be considered to be primarily driven by the Eulerian currents and Stokes drift. The influence of wind on the simulated drifters was found to be ∼0.3% of the 10 m winds. This result is in very good accordance with Meyerjürgens et al. (2019) who determined a direct wind drag of 0.27% from the drifter surfaces above and below water.

A validation experiment is presented in the following by comparing the observed and modelled data. Surface velocity was computed using observed positions and times of GPS drifters. For each observed location and time, model data was extracted and compared with observations by linear interpolation. Besides the root mean square error (*rms*), linear correlation (*cor*), standard deviation (*std*) and *bias*, the skill of the calibrated Lagrangian model was also estimated by the index of agreement (*agr*)

$$agr = 1 - \frac{\sum_{i=1}^{n} (P_i - O_i)^2}{\sum_{i=1}^{n} (|P_i - \bar{O}| + |O_i - \bar{O}|)^2},$$

where *n* is the number of observations (index *i*) of the observed (*O*) or model (*P*) data and the overbar is the temporal mean (Willmott 1981). The *agr* was 0.98/0.85, 0.97/0.94, and 0.97/0.93 for the zonal/meridional velocity component, respectively, of which the latter is slightly worse. Seeding experiments over the entire model area with particles having the characteristics of the GPS drifters showed that many of the particles covered distances of more than 400 km, which is ∼2/3 of the

zonal extension of the North Sea. The results of validation of surface currents from the operational model against observations (Figure 4.9.4) are shown separately for the zonal (left panels) and meridional velocity (right panels) components. Statistics of agreement between observed and modelled data (Eulerian currents, Stokes drift and wind) are shown in each panel for the respective dataset. The conclusion is, that the model gives accurate estimates of surface currents even for these extreme wind conditions. For comparison, during regular westerly winds, Ricker and Stanev (2020) found similar statistics for the German Bight and Johnson et al. (2007) for the world ocean. However, even in deeper water Stokes drift cannot be neglected during extreme wind events. Further analyses reveal, that the model performance in terms of velocity direction is almost the same for westerly and reversed wind conditions emphasising the good model performance. This validation experiment is of great value, because so far not many direct observations exist over large areas in the North Sea.

4.9.5. Conclusions

Drifter releases were conducted in early 2018 in German waters using three drifters equipped with Global Positioning System devices, as well as 1600 wooden drifters. Some of the wooden drifters stranded in different coastal areas, a large number of them on the UK coast. These unique observations appeared successful, because individuals finding the stranded objects gave their valuable feedback about the position and time of drifter findings. This public participation in scientific research further demonstrated the usefulness of citizen science.

An anomalous propagation of the drifters was observed. Some of them reached the British coast in just a few weeks. Using observed and numerically simulated drifters allowed us to calibrate the Lagrangian model in a way to adequately resolve the wind drag. This further enabled us to reconstruct the propagation pathways during the period of strong easterlies in early 2018.

The agreement between direct observations of surface currents and the CMEMS products demonstrates that the modelled data are of good quality. Furthermore, it can be concluded that the model replicates ocean dynamics well even under extreme weather conditions.

Acknowledgements

Section 4.10. Coastal ocean variability related to the most extreme Ebro River discharge over the last 15 years

Authors: Inmaculada Ruiz-Parrado, Ana Genua-Olmedo, Emma Reyes, Baptiste Mourre, Paz Rotllán, Pablo Lorente, Marcos García-Sotillo, Joaquín Tintoré

Statement of main outcomes: Extreme rivers discharges contribute to enhance the shelf/open ocean fronts and the associated currents, being also one of the crucial factors controlling sediment supply and dispersal, impacting in turn water quality in highly sensitive environments. The most extreme Ebro river freshwater discharge event recorded over the past 15 years was observed in April 2018 at the Tortosa gauge in the Western Mediterranean. This freshwater-pulse discharge had a high impact on the surface current patterns which was captured by many different observational sources provided by the Copernicus Marine Environment Monitoring Services (CMEMS hereinafter): three-site High Frequency Radars (HF Radar, hereinafter) around the Ebro delta (CMEMS In Situ TAC) and satellite-derived surface Chlorophyll-*a* (CMEMS Ocean Color TAC) as well as satellite-derived suspended matter (Sentinel 2-ESA). Furthermore, the intercomparison of various simulations from CMEMS Monitoring Forecasting Centres (CMEMS MFCs) and other regional ocean models with increased resolutions highlighted the advantages of downscaling and the importance of implementing realistic runoff forcing to properly represent the river plume and its impacts on the coastal circulation.

Products used

Ref No.	Product name & type	Documentation
4.10.1	OCEANCOLOUR_MED_ CHL_L4_NRT_ OBSERVATIONS_009_041	PUM: https://resources.marine. copernicus.eu/documents/PUM/ CMEMS-OC-PUM-009-ALL.pdf QUID: https://resources.marine. copernicus.eu/documents/QUID/ CMEMS-OC-QUID-009-038to045-071-073-078-079-095-096.pdf
4.10.2	INSITU_MED_NRT_ OBSERVATIONS_013_035	PUM: https://resources.marine. copernicus.eu/documents/PUM/ CMEMS-INS-PUM-013.pdf QUID: https://resources.marine. copernicus.eu/documents/QUID/ CMEMS-INS-QUID-013-030-036. pdf
4.10.3		

(Continued)

Continued.

Ref No.	Product name & type	Documentation
	GLOBAL_ANALYSIS_ FORECAST_PHY_001_024	PUM: https://resources.marine. copernicus.eu/documents/PUM/ CMEMS-GLO-PUM-001-024.pdf QUID: https://resources.marine. copernicus.eu/documents/QUID/ CMEMS-GLO-QUID-001-024.pdf
4.10.4	IBI_ANALYSIS_FORECAST_ PHYS_005_001	PUM: https://resources.marine. copernicus.eu/documents/PUM/ CMEMS-IBI-PUM-005-001.pdf QUID: https://resources.marine. copernicus.eu/documents/QUID/ CMEMS-IBI-QUID-005-001.pdf
4.10.5	MEDSEA_ANALYSIS_ FORECAST_PHY_006_013	PUM: https://resources.marine. copernicus.eu/documents/PUM/ CMEMS-MED-PUM-006-013.pdf QUID: https://resources.marine. copernicus.eu/documents/QUID/ CMEMS-MED-QUID-006-013.pdf
4.10.6	ESA-Copernicus Sentinel 2A	WEB: https://sentinels.copernicus. eu/web/sentinel/missions/ sentinel-2/data-products
4.10.7	INSITU_GLO_UV_NRT_ OBSERVATIONS_013_048	PUM: https://resources.marine. copernicus.eu/documents/PUM/ CMEMS-INS-PUM-013-048.pdf QUID: https://resources.marine. copernicus.eu/documents/QUID/ CMEMS-INS-QUID-013-048.pdf Data source: HF Radar Ebro: http:// opendap.puertos.es/thredds/ catalog/radar_local_deltaebro/ catalog.html
4.10.8	A027 Tortosa River gauge	WEB: http://www.saihebro.com/ saihebro/index.php?url=/datos/ ficha/estacion:A027
4.10.9	Western Mediterranean Operational Model (WMOP)	WEB: http://www.socib.es/? seccion=modelling&facility= forecast_system_description REFERENCES: http://socib.es/? seccion=modelling&facility= research
4.10.10	Ebro River basin and tributaries (Ebro Hydrographic Confederation)	WEB: http://iber.chebro.es/geopor tal/
4.10.11	2010 CORINE (the Coordination of Information on the Environment programme initiated by the EU) Habitats distribution maps in the Ebro Delta (Department of Planning and Sustainability of the Generalitat de Catalunya)	WEB: https://territori.gencat.cat/ca/ 01_departament/12_cartografia_ i_toponimia/bases_cartografique s/medi_ambient_i_sostenibilita t/bases_miramon/territori/29_ha bitats_1_5000_perfulls/ REFERENCES: https://land. copernicus.eu/user-corner/ technical-library/tech40add.pdf
4.10.12	Sistema de Apoyo Meteorológico y Oceanográfico de la Autoridad Portuaria (SAMOA)	REFERENCES: https://upcommons. upc.edu/bitstream/handle/2117/ 116102/21977687.pdf;jsessionid =F3CEFB5D06F92BA3CD4F4 F890295A95F?sequence=3

The coastal ocean, here defined as the region extending from the coast to the continental shelf break, is a highly variable environment that provides direct benefits to society, being subject to continental, atmospheric and ocean forcings. In this context, CMEMS models and in-situ data products, as well as other complementary datasets, have been used to characterise the impact of an extreme river discharge on the local shelf circulation. The area of interest is the Western Mediterranean Sea

off the northeastern coast of the Iberian Peninsula, where the Ebro River (910 km long) provides the main source of continental freshwater inputs draining through a deltaic formation, the Ebro Delta (Figure 4.10.1a). Most of the deltaic surface (65 %) is devoted to intensive rice cultivation (Figure 4.10.1a), and is the main economic activity in the area. In contrast to these non-natural areas, the Ebro Delta contains a diversity of natural habitats, including coastal lagoons and marshes (Figure 4.10.1a), which comprise the Ebro Delta Natural Park and are part of the Natura 2000 network (https://natura2000.eea.europa.eu/Natura2000/SDF.aspx?site=ES0000020). These varied mosaic of environments allow the thriving of economic activities such as tourism, agriculture, aquaculture and industry. The Ebro Delta is a wave-dominated coast, which suffers from retreat and intense reshaping by wave erosion (Sánchez-Arcilla et al. 1996) and is also a relevant Marine Protected Area (MPA) which deserves protection and more stringent and knowledge based management. The shelf south of the Ebro Delta widens considerably. In this area, the circulation and the variability of physical and
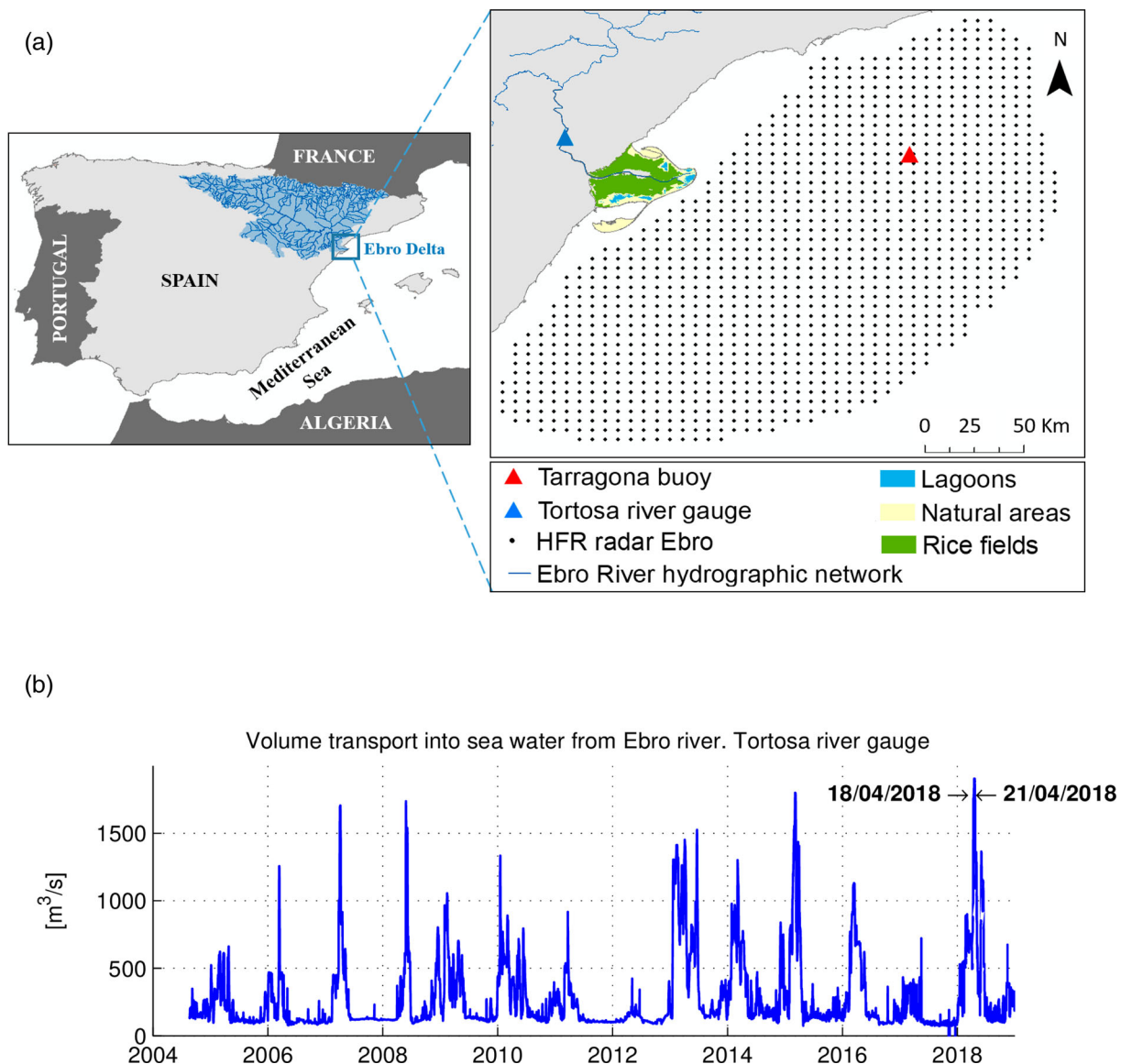
Figure 4.10.1. (a) Map of the Iberian Peninsula, showing the study area (the Ebro River, the Ebro Delta and its coast). The inset map at the right represents the Ebro Delta, showing the positions of the Tarragona Buoy -red triangle- and the Tortosa river gauge -blue triangle- (product references 4.10.2 and 4.10.8, respectively). Blue line is the Ebro River hydrographic network (product reference 4.10.10). Black dots denote the coverage of HF Radar Ebro System (product reference 4.10.7). Green section represents the rice fields. Yellow colour shaded areas are the natural areas. Light blue shaded sections are the lagoons (product reference 4.10.11). (b) Historical time series of the Ebro River daily freshwater discharge (blue line) from 2004 to 2019 (product reference 4.10.8). The most extreme event registered over the last 15 years is marked by the arrows showing the analysed dates.

biogeochemical properties are highly influenced by the Ebro River runoff (Fernández-Nóvoa et al. 2015; Teruzzi et al. 2018), as well as wave (Sánchez-Arcilla et al. 2019) and wind conditions (Grifoll Colls et al. 2016; Ràfols et al. 2017; Ràfols Bundó et al. 2019). Previous qualitative (Sánchez-Arcilla and Simpson 2002) and quantitative (Sánchez-Arcilla et al. 2019) studies have demonstrated that the Region Of Freshwater Influence (ROFI) was depending not only on river discharges but also on the prevailing meteo-oceanographic conditions.

The Ebro River is highly regulated by the construction of several dams, irrigation channels and reservoirs along its watercourse (Palanques et al. 1990) and therefore the discharge at the mouth is fully controlled (Figure 4.10.1b). The most extreme event registered over the past 15 years was observed in April 2018 (Figure 4.10.1b), as measured by the Tortosa river gauge (product reference 4.10.8). The main peak was observed from the 18th to the 21st of April 2018, with a maximum river flow of 1.904 $m^3 s^{-1}$, which corresponds to more than six times the mean runoff near the mouth. Notice that discharges larger than 1.500 $m^3 s^{-1}$ were also observed in 2007, 2008, 2013 and 2015, but without reaching the intensity of the 2018 event.

Sentinel 2A satellite images of suspended matter concentration were provided by the European Space Agency (product reference 4.10.6, Figure 4.10.2) and processed by the Cartographic and Geological Institute of Catalonia (ICGC) using a radiometric treatment based on a Red-Green-Blue bands analysis. This methodology isolates land and water areas by applying normalisation functions to enhance desired image features.

To highlight the extreme event under study, a low river flow (~100 $m^3 s^{-1}$) observed on the 1st of January 2018 has been used as reference conditions (Figure 4.10.2a -left panel-), where no suspended matter is observed. This is the typical condition of the Ebro River which is sediment-starved, mostly due to its retention in the approximately 200 dams built in the river catchment. On the contrary, a large amount of suspended matter is observed, which ejects up to 20 km into the Mediterranean Sea, as a consequence of the extreme event observed from the 18th to the 21st April 2018 (Figure 4.10.2a -middle and right panel, respectively-).

HF Radar deployed at the Ebro Delta (product reference 4.10.7) is operated by Puertos del Estado (Spain) and is composed of three-sites (Salou, Alfaca, Vinaroz). A central frequency of 13.5 MHz and a 90 kHz bandwidth is emitted and hourly surface current maps with a spatial resolution of 3 km are provided. The impact of the impulsive-type freshwater discharge in the sea surface circulation in the Ebro deltaic region (derived from reliable HF Radar surface current measurements) has been analysed in Lorente et al. 2015.

Following this approach, results show that surface current patterns (Figure 4.10.2b -middle and right panel, respectively-) are influenced by the river discharge and have a clear correspondence with the high concentrations of satellite-derived Chlorophyll-a (product reference 4.10.1). During low-flow (~100 $m^3 s^{-1}$) reference conditions (1st of January 2018, Figure 4.10.2b -left panel-), the sea surface circulation was uniform and the Chlorophyll-a concentration was lower compared to the values registered during and after the extreme event.

The Tarragona Buoy salinity measurements (product reference 4.10.2, Figure 4.10.1a) were studied to see if the Ebro River freshwater discharge had an impact in the decay of the salinity values. At the reference conditions (1st of January 2018) the salinity range is from 37.69 to 37.78 PSU, and during the extreme event (18th to the 21st April 2018) is from 37.85 to 38.14 PSU. This shows that the extension of the freshwater input discharge and thus the plume area do not reach this buoy (Figure 4.10.1a).

Hovmöller diagrams of HF Radar-derived meridional and zonal currents (Figure 4.10.2c, product reference 4.10.7) show an increase of the southward current around the longitude 1.5°E during the second half of April and an increase of the eastward velocity, close to the latitude 40.6°N, during the days 17, 18, 22 and 23 of April (period of the extreme river discharge).

An analysis of forecasting models was carried out using models of different extensions and resolutions (Figure 4.10.3a). The models represented here (products ref. 4.10.3, 4.10.4, 4.10.5, 4.10.9, and 4.10.12) included the Ebro River freshwater discharge from hydrological models data or climatological values, which resulted in some underrepresentation of the discharge and then overestimation of the coastal the salinity values. The river runoff forcing for each one of the ocean models is specified as follows:

(1) The Global forecast system (CMEMS GLOBAL-MFC) (product reference 4.10.3), which provided 10 days of 3D global ocean forecasts daily updated and used coastal runoffs from 100 major rivers from the Dai et al. 2009 database.

(2) The Iberian-Biscay-Ireland Monitoring and Forecast Center (CMEMS IBI-MFC) (product reference 4.10.4), which produced near-real-time with river discharge inputs daily updated, including discharge for 33 rivers. Combination of daily observations from PREVIMER (Ebro River runoff not included),
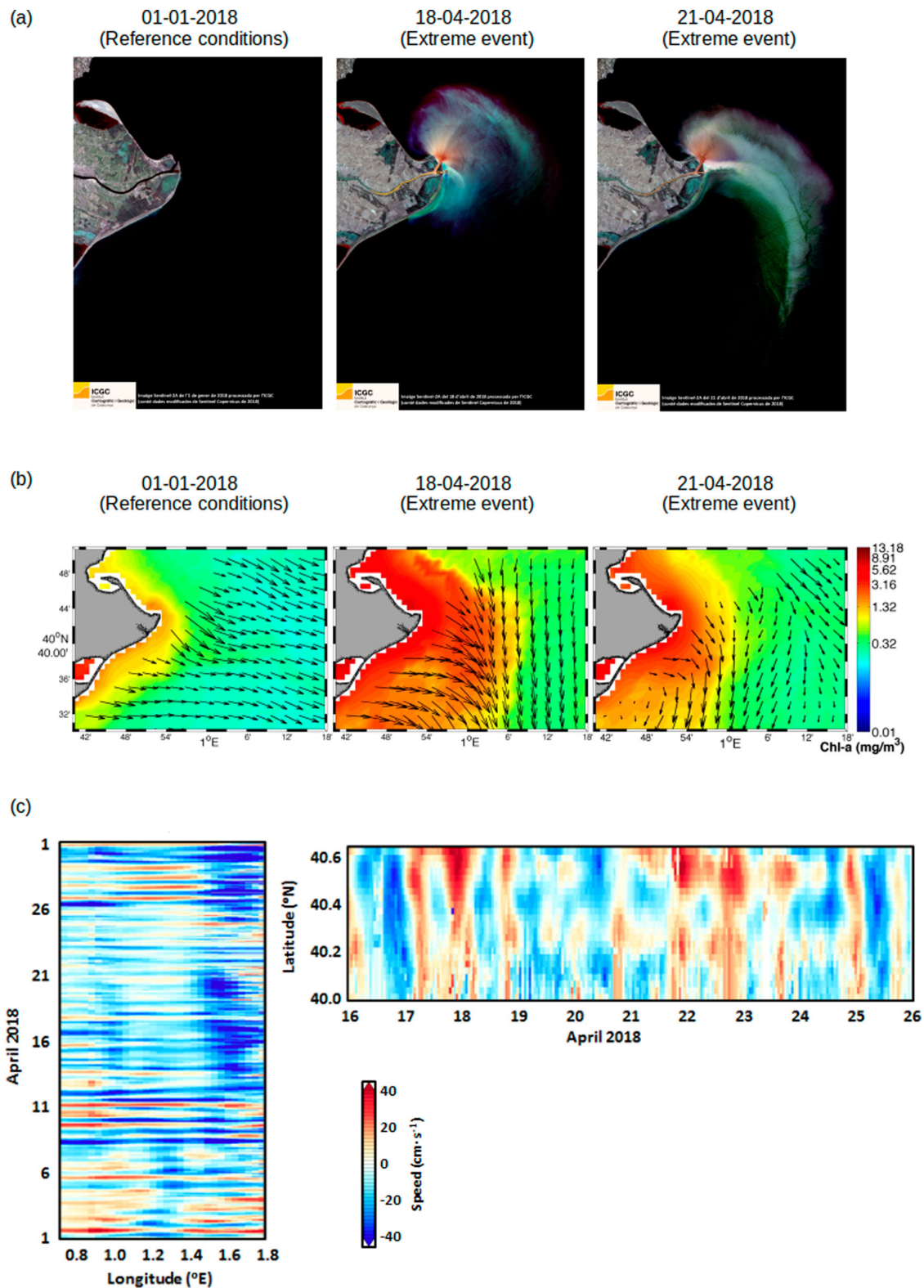
Figure 4.10.2. (a) Satellite images of suspended matter in the Ebro River plume (Sentinel 2A, Copernicus Academy Network, product ref 4.10.6) processed by the Cartographic and Geological Institute of Catalonia (ICGC) during reference conditions (01-01-2018) and the extreme discharge (18 and 21-04-2018). (b) Map showing the snapshots of HF Radar surface currents (black vectors, product ref. 4.10.7) and surface Chlorophyll-*a* concentration (product ref. 4.10.1), for Reference conditions (1st of January 2018, Ebro River low-flow conditions) and Extreme discharge event during 18th and 21st of April, 2018, are represented in the middle and right panels, respectively. (c) Hovmöller diagrams of HF Radar-derived meridional (northward) and zonal (eastward) currents (positive values, red colours indicating northward and eastward currents; negative values, blue colours indicating southward and westward currents, for meridional and zonal components, respectively; product ref. 4.10.7).

simulated data from SMHI E-HYPE hydrological model, monthly climatology from GRDC and French Banque Hydro dataset plus (since April 2017) extra coastal runoff rate (derived from monthly climatology) for consistency with the parent CMEMS GLOBAL system.
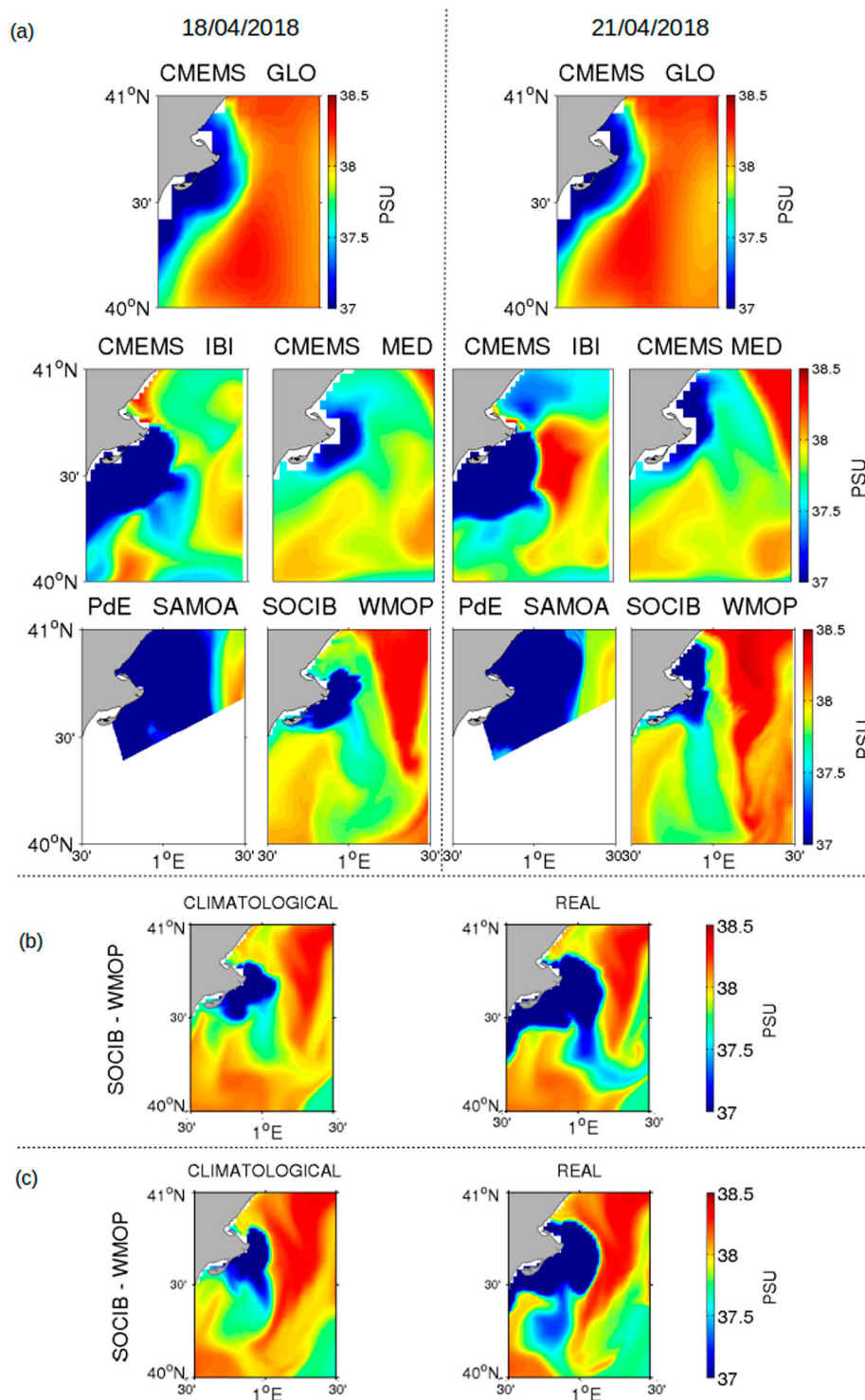
Figure 4.10.3. (a) Maps of surface salinity distribution in the Ebro River Delta from 5 different ocean models: (i) CMEMS GLO-MFC (Product ref. 4.10.3); (ii) CMEMS IBI-MFC (Product ref. 4.10.4); (iii) CMEMS MED-MFC (Product ref. 4.10.5); (iv) PdE-SAMOA (Product ref. 4.10.12); (v) SOCIB-WMOP (Product ref. 4.10.9). Panel (a) is divided in 18 and 21 April 2018, respectively. (b) 18-April-2018 WMOP (Product ref. 4.10.9) daily average surface salinity distribution and currents (hindcast simulation climatological and real runoff) and (c) 21-April-2018 WMOP (Product ref. 4.10.9) daily average surface salinity distribution and currents (hindcast simulation climatological and real runoff).

(3) The Mediterranean Sea Forecast (CMEMS MED-MFC) (product reference 4.10.5), which included river runoff for 39 rivers from monthly mean datasets (Global Runoff Data Centre, Raicich 1996, UNEP-MAP, PERSEUS).

(4) The SAMOA Puertos del Estado forecast system (product reference 4.10.12; García Sotillo et al. 2019; Fanjul et al. 2018) were CMEMS downstream services, being the coastal models nested into the regional CMEMS IBI-MFC forecast solution. At the surface, models were forced by water fluxes from the Spanish Meteorological Agency (AEMET) forecast services. This system offers an increasingly higher resolution with a nested approach going down to grid sizes of 350 m near the Ebro coast.

(5) The Western Mediterranean sea OPerational model, (WMOP, product ref. 4.10.9) is a SOCIB (Balearic Islands Coastal Observing and Forecasting System) added value product (Juza et al. 2016; Mourre et al. 2018) that uses the CMEMS Mediterranean Sea Analysis and Forecast products (product ref. 4.10.5) as parent model (initial and boundary conditions). The operational version includes daily climatological values over 2009–2016 for 6 rivers from the French HYDRO database and the Spanish hydrographic confederations of Ebro and Júcar river. Particularly, for this study, river forcing using the daily observed runoff of the Ebro River has been considered.

The model intercomparison (Figure 4.10.3a) shows that the salinity horizontal variations in the Ebro River plume identified after the extreme event in the suspended matter distribution of the satellite images (product ref. 4.10.6, Figure 4.10.2a) is well represented in the regional scale models (CMEMS-MED-MFC and WMOP) and in the coastal scale one (SAMOA). On the contrary, it is not well represented in the global scale (CMEMS-GLO-MFC) and the other regional (CMEMS-IBI-MFC) model.

In order to demonstrate the importance of including real river discharge data to properly represent the flow and salinity structure near the river mouth, two scenarios have been simulated with WMOP (product ref. 4.10.9); the first one using climatological runoff (Figure 4.10.3b,c -left panel-) and the second one, using daily river discharge inputs (Figure 4.10.3b,c -right panel-) for the 18th and the 21st April 2018 (Figure 4.10.3b,c, respectively). Maps of daily averaged surface salinity allow to characterise coastal circulation patterns associated with the impulsive-type freshwater discharge. The Ebro River plume signature simulated by the WMOP model (product ref. 4.10.9), in real discharge case (Figure 4.10.3b,c -right panel-) is very similar to the one observed either in the

satellite observations (Figure 4.10.2a, product ref. 4.10.6), in the HF Radar surface currents (Figure 4.10.2b, product ref. 4.10.7) and the surface circulation pattern induced by the spatial distribution of the Chl-*a* concentration (Figure 4.10.2b, product ref. 4.10.1).

In conclusion, the evaluation of the ability of the different models to reproduce the extreme Ebro River discharge event, highlights the need to include daily observational runoff data in both regional and coastal forecast systems to accurately reproduce the plume and the importance of using a high-resolution model to study its impact at coastal scales.

The proper representation of the flow, the salinity gradient and the concentration of suspended matter near the river mouth due to discharge extreme events is crucial to identify their impacts (i.e. decrease of water quality, deltaic morphodynamics, etc.) on high-sensitive coastal water ecosystems.

In this context, the extreme event presented here, as seen in the Sentinel-2 images (product ref 4.10.6) showed a high capacity for sediment transport to the river mouth and Delta, which is of great interest taking into account that the sediment transport continuity was disrupted due to construction of dams, where a 99 % of the sediment is retained (Rovira and Ibáñez 2007). The capacity for sediment transport encourages the feasibility of implementing sediment management plans for restoring the sediment flux artificially redistributed as existing studies showed (*i.e.* Martín-Vide et al. 2004; Rovira and Ibáñez 2007).

Acknowledgements

References

Section 4.1: A most unusual winter sea-ice opening north of Greenland

Alam A, Curry J. 1995. Lead-induced atmospheric circulations. J Geophys Res. 100:4643–4651.

Assmy P, Fernández-Méndez M, Duarte P, Meyer A, Randelhoff A, Mundy CJ, Olsen LM, Kauko HM, Bailey A, Chierici M, et al. 2017. Leads in Arctic pack ice enable early phytoplankton blooms below snow-covered sea ice. Sci Rep. 7:40850. doi:10.1038/srep40850.

Bertino L. 2018. "Last sea ice area" in the Arctic breaks up. CMEMS News October 2018. https://marine.copernicus.eu/last-sea-ice-area-arctic-breaks-up.

Cavalieri DJ, Martin S. 1994. The contribution of Alaskan, Siberian, and Canadian coastal polynyas to the cold

halocline layer of the Arctic Ocean. J Geophys Res. 99:18,343–18,362.

Dansereau V, Weiss J, Saramito P, Lattes PA. 2016. Maxwell elasto-brittle rheology for sea ice modelling. The Cryosphere. 10:1339–1359. doi:10.5194/tc-10-1339-2016.

Dmitrenko IA, Kirillov SA, Rudels B, Babb DG, Pedersen LT, Rysgaard S, Kristoffersen Y, Barber DG. 2017. Arctic Ocean outflow and glacier–ocean interactions modify water over the Wandel Sea shelf (northeastern Greenland). Ocean Sci. 13:1045–1060. doi:10.5194/os-13-1045-2017.

[ESOTC 2018] European State of the Climate. 2018. General, European Arctic. https://climate.copernicus.eu/european-arctic.

Fiedler EK, Lachlan-Cope TA, Renfrew IA, King JC. 2010. Convective heat transfer over thin ice-covered coastal polynyas. J Geophys Res-Oceans. 115:C10051.

Ivanov VV, Shapiro GI. 2005. Formation of a dense water cascade in the marginal ice zone in the Barents Sea. Deep-Sea Res I. 52:1699–1717.

Ivanov VV, Shapiro GI, Huthnance JM, Aleynik DL, Golovin PN. 2004. Cascades of dense water around the world ocean. Progr Oceanogr. 60:47–98.

Ludwig V, Spreen G, Haas C, Istomina L, Kauker F, Murashkin D. 2019. The 2018 North Greenland polynya observed by a newly introduced merged optical and passive microwave sea-ice concentration dataset. The Cryosphere. 13 (7):2051–2073. doi:10.5194/tc-13-2051-2019.

Mann ME, Rahmstorf S, Kornhuber K, Steinmann BA, Miller SK, Moumou D. 2017. Influence of anthropogenic climate change on planetary wave resonance and extreme weather events. Sci Reports. 7:45242.

Martin S, Cavalieri DJ. 1989. Contributions of the Siberian shelf polynyas to the Arctic Ocean intermediate and deep water. J Geophys Res. 94:12,725–12,738.

Moore GWK, Schweiger A, Zhang J, Steele M. 2018. What caused the remarkable February 2018 North Greenland Polynya? Geophys Res Lett. 45:13,342–13,350. doi:10.1029/2018GL080902.

Morales Maqueda MA, Willmott AJ, Biggs NRT. 2004. Polynya dynamics: a review of observations and modeling. Rev Geophys. 42:RG1004. 37p.

Rampal P, Dansereau V, Olason E, Bouillon S, Williams T, Korosov A, Samaké A. 2019. On the multi-fractal scaling properties of sea ice deformation. The Cryosphere. 13:2457–2474. doi:10.5194/tc-13-2457-2019.

Schauer U, Fahrbach E. 1999. A dense bottom-water plume in the western Barents Sea: downstream modification and interannual variability. Deep-Sea Res I. 46:2095–2108.

Schneider W, Budéus G. 1997. Summary of the Northeast Water Polynya formation and development (Greenland Sea). J Mar Sys. 10:107–122.

Swift JH, Jones EP, Aagaard K, Carmack EC, Hingston M, MacDonald RW, McLaughlin FA, Perkin RG. 1997. Waters of the Makarov and Canada Basins. Deep-Sea Res Part II. 44:1503–1529.

Tetzlaff A, Lupkes C, Hartmann J. 2015. Aircraft-based observations of atmospheric boundary-layer modification over Arctic leads. Q J Roy Meteor Soc. 141(692):2839–2856.

Tietsche S, Alonso-Balmaseda M, Rosnay P, Zuo H, Tian-Kunze X, Kaleschke L. 2018. Thin Arctic Sea ice in L-band observations and an ocean reanalysis. The Cryosphere. 12:2051–2072. doi:10.5194/tc-12-2051-2018.

Tonboe R, Lavelle J, Pfeiffer RH, Howe E. 2017. Product user manual for OSI SAF global sea ice concentration, OSI-401-b. EUMETSAT.

Williams T, Korosov A, Rampal P, Ólason E. 2019. Presentation and evaluation of the Arctic Sea ice forecasting system neXtSIM-F. The Cryosphere Discuss. doi:10.5194/tc-2019-154.

Winsor P, Björk G. 2000. Polynya activity in the Arctic Ocean from 1958 to 1997. J Geophys Res. 105:8789–8803.

Xie J, Counillon F, Bertino L, Tian-Kunze X, Kaleschke L. 2016. Benefits of assimilating thin sea ice thickness from SMOS into the TOPAZ system. Cryosphere. 10:2745–2761. DOI:10.5194/tc-10-2745-2016.

Ye Y, Heygster G, Shokr M. 2016. Improving multiyear ice concentration estimates with reanalysis airtemperatures. IEEE Trans Geosci Remote Sens. 54:2602–2614.

Section 4.2: Geographical and seasonal coverage of sea ice in the Baltic Sea

Barnston AG, Livezey RE. 1987. Classification, seasonality and persistence of low-frequency atmospheric circulation patterns. Mon Weather Rev. 115(6):1083–1126.

Chen WY, Van den Dool H. 2003. Sensitivity of teleconnection patterns to the sign of their primary action center. Mon Weather Rev. 131(11):2885–2899.

Haapala J. 2000. On the modelling of ice-thickness redistribution. J Glaciol. 46(154):427–437.

Herman A, Jedrasik J, Kowalewski M. 2011. Numerical modelling of thermodynamics and dynamics of sea ice in the Baltic Sea. Ocean Sci. 7:257–276. doi:10.5194/os-7-257-2011.

Höglund A, Pemberton P, Hordoir R, Schimanke S. 2017. Ice conditions for maritime traffic in the Baltic Sea in future climate. Boreal Environ Res. 22:245–265.

Jevrejeva S, Drabkin VV, Kostjukov J, Lebedev AA, Leppäranta M, Mironov YU, Schmelzer N, Sztobryn M. 2004. Baltic Sea ice seasons in the twentieth century. Clim Res. 25 (3):217–227.

Jones PD, Jonsson T, Wheeler D. 1997. Extension using early instrumental pressure observations from Gibraltar and SW Iceland to the North Atlantic oscillation. Int J Climatol. 17:1433–1450.

Jurva R. 1952. On the variations and changes of freezing in the Baltic during the last 120 years. Fennia. 75(52):17–24.

Karpechko AY, Peterson KA, Scaife AA, Vainio J, Gregow H. 2015. Skilful seasonal predictions of Baltic Sea ice cover. Environ Res Lett. 10(4):044007.

Leppäranta M, Myrberg K. 2009. Physical oceanography of the Baltic Sea. Berlin: Springer Science & Business Media.

Liblik T, Lips U. 2017. Variability of pycnoclines in a three-layer, large estuary : the Gulf of Finland. Boreal Environ Res. 22:27–47.

Maljutenko I, Raudsepp U. 2019. Long-term mean, interannual and seasonal circulation in the Gulf of Finland — the wide salt wedge estuary or gulf type ROFI. J Mar Syst. 195:1–19. doi:10.1016/J.JMARSYS.2019.03.004.

Myrberg K, Andrejev O. 2006. Modelling of the circulation, water exchange and water age properties of the Gulf of Bothnia. Oceanologia. 48:55–74.

Omstedt A, Chen D. 2001. Influence of atmospheric circulation on the maximum ice extent in the Baltic Sea. J Geophys Res Oceans. 106(C3):4493–4500.

Palosuo E. 1953. A treatise on severe ice conditions in the Baltic Sea. Helsinki: Publications of the Finnish Institute of Marine Research. 156p.

Peel MC, Finlayson BL, McMahon TA. 2007. Updated world map of the Köppen-Geiger climate classification. Hydrol Earth Syst Sci Discuss. 4(2):439–473.

Pemberton P, Löptien U, Hordoir R, Höglund A, Schimanke S, Axell L, Haapala J. 2017. Sea-ice evaluation of NEMO-Nordic 1.0: a NEMO–LIM3.6-based ocean–sea-ice model setup for the North Sea and Baltic Sea. Geosci Model Dev. 10:3105–3123. doi:10.5194/gmd-10-3105-2017.

Raudsepp U. 2001. Interannual and seasonal temperature and salinity variations in the Gulf of Riga and corresponding saline water inflow from the Baltic proper. Hydrol Res. 32(2):135–160.

Ronkainen I, Lehtiranta J, Lensu M, Rinne E, Haapala J, Haas C. 2018. Interannual sea ice thickness variability in the Bay of Bothnia. The Cryosphere. 12:3459–3476.

Seinä A. 1994. Extent of ice cover 1961–1990 and restrictions to navigation 1981–1990 along the Finnish Coast. Finn Mar Res. 262:3–34.

Seinä A, Palosuo E. 1996. The classification of the maximum annual extent of icecover in the Baltic Sea 1720–1995. Meri Rep Ser Finn Inst Mar Res. 20:79–910.

Siitam L, Sipelgas L, Pärn O, Uiboupin R. 2017. Statistical characterization of the sea ice extent during different winter scenarios in the Gulf of Riga (Baltic Sea) using optical remote-sensing imagery. Int J Remote Sens. 38(3):617–638.

Soomere T, Keevallik S. 2003. Directional and extreme wind properties in the Gulf of Finland. Proc Est Acad Sci Eng. 9:73–90.

Soosaar E, Maljutenko I, Raudsepp U, Elken J. 2014. An investigation of anticyclonic circulation in the southern Gulf of Riga during the spring period. Cont Shelf Res. 78:75–84.

Soosaar E, Maljutenko I, Uiboupin R, Skudra M, Raudsepp U. 2016. River bulge evolution and dynamics in a non-tidal sea–Daugava River plume in the Gulf of Riga. Baltic Sea Ocean Sci. 12(2):417–432.

Uotila P, Vihma T, Haapala J. 2015. Atmospheric and oceanic conditions and the extremely low Bothnian Bay sea ice extent in 2014/2015. Geophys Res Lett. 42(18):7740–7749.

Van den Dool HM, Saha S, Johansson Å. 2000. Empirical orthogonal teleconnections. J Clim. 13(8):1421–1435.

Vihma T, Haapala J. 2009. Geophysics of sea ice in the Baltic Sea: a review. Prog Oceanogr. 80(3–4):129–148.

Yan Y, Shao D, Gu W, Liu C, Li Q, Chao J, Tao J, Xu Y. 2017. Multidecadal anomalies of Bohai Sea ice cover and potential climate driving factors during 1988–2015. Environ Res Lett. 12(9):094014.

Section 4.3: The resurgence of the North Pacific marine heatwave in 2018

Bond NA, Cronin MF, Freeland H, Mantua N. 2015. Causes and impacts of the 2014 warm anomaly in the NE Pacific. Geophys Res Lett. 42(9):3414–3420.

Dee DP, Uppala SM, Simmons AJ, Berrisford P, Poli P, Kobayashi S, Andrae U, Balmaseda MA, Balsamo G, Bauer P. 2011. The ERA-Interim reanalysis: configuration and performance of the data assimilation system. Q J R Meteorolog Soc. 137(656):553–597.

Di Lorenzo E, Mantua N. 2016. Multi-year persistence of the 2014/15 North Pacific marine heatwave. Nat Clim Change. 6(11):1042.

Frolicher TL, Fischer EM, Gruber N. 2018. Marine heatwaves under global warming. Nature. 560:360–364. doi:10.1038/s41586-018-0383-9.

Greene CH. 2016. North America's iconic marine species at risk due to unprecedented ocean warming. Oceanography. 29(3):14–17.

Hartmann DL. 2015. Pacific sea surface temperature and the winter of 2014. Geophys Res Lett. 42(6):1894–1902.

Hobday AJ, Oliver EC, Gupta AS, Benthuysen JA, Burrows MT, Donat MG, Holbrook NJ, Moore PJ, Thomsen MS, Wernberg T, Smale DA. 2018. Categorizing and naming marine heatwaves. Oceanography. 31(2):162–173.

Holbrook NJ, Scannell HA, Gupta AS, Benthuysen JA, Feng M, Oliver EC, Alexander LV, Burrows MT, Donat MG, Hobday AJ, Moore PJ. 2019. A global assessment of marine heatwaves and their drivers. Nat Commun. 10(1):2624.

Jayne SR, Roemmich D, Zilberman N, Riser SC, Johnson KS, Johnson GC, Piotrowicz SR. 2017. The argo program: present and future. Oceanography. 30(2):18–28. DOI:10.5670/oceanog.2017.213.

Lee T, Fukumori I, Tang B. 2004. Temperature advection: internal versus external processes. J Phys Oceanogr. 34(8):1936–1944.

Oliver EC, Donat MG, Burrows MT, Moore PJ, Smale DA, Alexander LV, Benthuysen JA, Feng M, Gupta AS, Hobday AJ, Holbrook NJ. 2018. Longer and more frequent marine heatwaves over the past century. Nat Commun. 9(1):1324.

Paik S, Min SK, Kim YH, Kim BM, Shiogama H, Heo J. 2017. Attributing causes of 2015 record minimum sea-ice extent in the Sea of Okhotsk. J Clim. 30(12):4693–4703.

Peña MA, Nemcek N, Robert M. 2019. Phytoplankton responses to the 2014–2016 warming anomaly in the northeast subarctic Pacific Ocean. Limnol Oceanogr. 64(2):515–525.

Schmeisser L, Bond NA, Siedlecki SA, Ackerman TP. 2019. The role of clouds and surface heat fluxes in the maintenance of the 2013–2016 Northeast Pacific marine heatwave. J Geophys Res Atmos. 124(20):10772–10783.

Smale DA, Wernberg T, Oliver EC, Thomsen M, Harvey BP, Straub SC, Burrows MT, Alexander LV, Benthuysen JA, Donat MG, Feng M. 2019. Marine heatwaves threaten global biodiversity and the provision of ecosystem services. Nat Clim Change. 1.

Sprintall J, Tomczak M. 1992. Evidence of the barrier layer in the surface layer of the tropics. J Geophys Res Oceans. 97(C5):7305–7316.

Walsh JE, Thoman RL, Bhatt US, Bieniek PA, Brettschneider B, Brubaker M, Danielson S, Lader R, Fetterer F, Holderied K, Iken K. 2018. The high latitude marine heat wave of 2016 and its impacts on Alaska. Bull Am Meteorol Soc. 99(1):S39–S43.

Webb RS, Werner FE. 2018. Explaining extreme ocean conditions impacting living marine resources. Bull Am Meteorol Soc. 99(1):S7–S10.

Westberry TK, Schultz P, Behrenfeld MJ, Dunne JP, Hiscock MR, Maritorena S, Sarmiento JL, Siegel DA. 2016. Annual

cycles of phytoplankton biomass in the subarctic Atlantic and Pacific Ocean. Global Biogeochem Cycles. 30(2):175–190.

Whitney FA. 2015. Anomalous winter winds decrease 2014 transition zone productivity in the NE Pacific. Geophys Res Lett. 42:428–431. doi:10.1002/2014GL062634.

Whitney FA, Crawford DW, Yoshimura T. 2005. The uptake and export of silicon and nitrogen in HNLC waters of the NE Pacific Ocean. Deep Sea Res Pt II. 52(7–8):1055–1067.

Yang B, Emerson SR, Peña MA. 2018. The effect of the 2013–2016 high temperature anomaly in the subarctic Northeast Pacific (the "Blob") on net community production. Biogeosciences. 15(21):6747–6759.

Yu J, Wang X, Fan H, Zhang RH. 2019. Impacts of physical and biological processes on spatial and temporal variability of particulate organic carbon in the North Pacific Ocean during 2003–2017. Sci Rep. 9(1):1–15.

Zaba KD, Rudnick DL. 2016. The 2014–2015 warming anomaly in the Southern California current system observed by underwater gliders. Geophys Res Lett. 43(3):1241–1248.

Section 4.4: Anomalous surface warming in the Baltic Sea in summer 2018 and mechanism analysis

Ambaum MHP, Hoskins BJ, Stephenson DB. 2001. Arctic oscillation or North Atlantic oscillation? J Clim. 14:3495–3507. doi:10.1175/1520-0442(2001)014<3495:AOONAO>2.0.CO;2.

Barnston AG, Livezey RE. 1987. Classification, seasonality, and persistence of low-frequency atmospheric circulation patterns. Mon Weather Rev. 115:1083–1126.

Bensoussan N, Jacopo C, Bruno BN, Andrea P, Joaquim G. 2019. Insights on 2017 marine heat waves in the Mediterranean Sea. In CMEMS ocean state report 2017, accepted.

Copernicus Climate Change Service. 2019. Climate in 2018 (events): dry and warm spring and summer. https://climate.copernicus.eu/dry-and-warm-spring-and-summer.

EUMETSAT. 2018. A summer of heatwaves and drought for many. https://www.eumetsat.int/website/home/Images/ImageLibrary/DAT_4040662.html.

Folland CK, Knight J, Linderholm HW, Fereday D, Ineson S, Hurrell JW. 2009. The summer North Atlantic oscillation: past, present and future. J Clim. 22:1082–1103.

Frölicher TL, Laufkötter C. 2018. Emerging risks from marine heat waves. Nat Commun. doi:10.1038/s41467-018-03163-6.

Hobday AJ, Alexander LV, Perkins SE, Smale DA, Straub SC, Oliver ECJ, Benthuysen J, Burrows MT, Donat MG, Feng M, et al. 2015. A hierarchical approach to defining marine heatwaves. Prog Oceanogr. doi:10.1016/j.pocean.2015.1012.1014.

Hobday AJ, Oliver ECJ, Sen Gupta A, Benthhuysen JA, Burrow MT, Donat MG, Holbrook NJ, Moore PJ, Thomsen MS, Wernberg T, Smale DA. 2018. Categorizing and naming marine heatwaves. Oceanography. 31:2. doi:10.5670/oceanog.2018.205.

Høyer JL, Karagali I. 2016. Sea surface temperature climate data record for the North Sea and Baltic Sea. J Clim. 29:2529–2541. doi:10.1175/JCLI-D-15-0663.1.

Janssen P, Bidlot J-R. 2009. On the extension of the freak wave warning system and its verification. Technical Memorandum. ECMWF.

Leppäranta M, Myrberg K. 2009. Physical oceanography of the Baltic Sea. Heidelberg (Germany): Springer-Praxis. 378p.

Oliver ECJ, Donat MG, Burrows MT, Moore PJ, Smale DA, Alexander LV, Benthuysen JA, Feng M, Sen Gupta A, Hobday AJ, et al. 2018. Longer and more frequent marine heatwaves over the past century. Nat Commun. 9(1324). doi:1310.1038/s41467-41018-03732-41469.

Section 4.5: Space-based observations of surface signatures in the wakes of the 2018 Eastern Pacific Tropical Cyclones

Combot C, Mouche A, Knaff JA, Zhao Y, Zhao Y, Vinour L, Quilfen Y, Chapron B. 2020. Extensive high-resolution Synthetic Aperture Radar (SAR) data analysis of tropical cyclones: comparison of SFMR flights and best-track. Submitted to Monthly Weather Review.

Dare RA, McBride JL. 2011. Sea surface temperature response to tropical cyclones. Mon Wea Rev. 139:3798–3808.

Geisler JE. 1970. Linear theory of the response of a two-layer ocean to a moving hurricane. Geophys Astrophys Fluid Dynam. 1(1–2):249–272.

Ginis I. 2002. Tropical cyclone-ocean interactions. Adv Fluid Mech. 33:83–114.

Knaff JA, Longmore SP, DeMaria RT, Molenar DA. 2015. Improved tropical-cyclone flight-level wind estimates using routine infrared satellite reconnaissance. J Appl Meteorol Climatol. 54(2):463–478.

Kossin JP, Knaff JA, Berger HI, Herndon DC, Cram TA, Velden CS, Murnane RJ, Hawkins JD. 2007. Estimating hurricane wind structure in the absence of aircraft reconnaissance. Weather Forecast. 22(1):89–101.

Kruk MC, Schreck CJ. 2019. Tropical cyclones, Eastern North Pacific and Central North Pacific basins [in "state of the climate in 2018"]. Bull Amer Meteor Soc. 100(9): S181–S185.

Kudryavtsev V, Monzikova A, Combot C, Chapron B, Reul N. 2019a. A simplified model for the baroclinic and barotropic ocean response to moving tropical cyclones: 2. Model and simulations. J Geophys Res Oceans. 124:3462–3485.

Kudryavtsev V, Monzikova A, Combot C, Chapron B, Reul N, Quilfen Y. 2019b. A simplified model for the baroclinic and barotropic ocean response to moving tropical cyclones: 1. Satellite observations. J Geophys Res Oceans. 124:3446–3461.

Leipper DF. 1967. Observed ocean conditions and Hurricane Hilda, 1964. J Atmos Sci. 24:182–186.

Mouche A, Chapron B, Knaff J, Zhao Y, Zhang B, Combot C. 2019. Co- and cross-polarized SAR measurements for high resolution description of major hurricane wind structures: application to Irma category-5 hurricane. J Geophys Res Oceans. 124(6):3905–3922.

Mouche A, Chapron B, Zhang B, Husson R. 2017. Combined co- and cross-polarized SAR measurements under extreme wind conditions. IEEE Trans Geosci Remote Sens. 55 (12):6746–6755.

National Hurricane Center Archive. https://www.nhc.noaa.gov/archive.

NOAA national centers for environmental information, state of the climate: hurricanes and tropical storms for annual 2018, published online January 2019 [accessed 2019 May 16]. https://www.ncdc.noaa.gov/sotc/tropical-cyclones/201813.

Price JF. 1981. Upper ocean response to a hurricane. J Phys Oceanogr. 11(2):153–175.

Reul N, Quilfen Y, Chapron B, Fournier S, Kudryavtsev V, Sabia R. 2014. Multisensor observations of the A mazon - O rinoco river plume interactions with hurricanes. J Geophys Res Oceans. 119:8271– 8295. DOI:10.1002/2014JC010107.

Vincent EM, Lengaigne M, Madec G, Vialard J, Samson G, Jourdain NC, Menkes CE, Jullien S. 2012. Processes setting the characteristics of sea surface cooling induced by tropical cyclones. J Geophys Res Oceans. 117(C2):C02020. DOI:10.1029/2011JC007396.

Section 4.6: Record wave storm in the Gulf of Cadiz over the past 20 years and its impact on harbors

Alvarez Fanjul E, Alfonso M, Ruiz MI, Lopez JD, Rodriguez I. 2003. Real time monitoring of Spanish coastal waters: the deep water network. Proc 3rd EuroGOOS Conf Elsevier Oceanogr Ser. 69:398–402. doi:10.1016/S0422-9894(03)80066-1.

Alvarez Fanjul E, García Sotillo M, Pérez Gómez B, García Valdecasas JM, Pérez Rubio S, Rodríguez Dapena A, Martínez Marco I, Luna Y, Padorno E, Santos Atienza I, et al. 2018. Operational oceanography at the service of the ports. In: Chassignet E, Pascual A, Tintoré J, Verron J, editors. New frontiers in operational oceanography. GODAE OceanView; p. 729–736. DOI:10.17125/gov2018.ch27.

Alvarez Fanjul E, Pérez Gómez B, Rodríguez I. 2001. Nivmar: a storm surge forecasting system for Spanish waters. Sci Mar. 65(1):145–141.

Bolle A, das Neves L, Smets S, Mollaert J, Buitrago S. 2018. An impact-oriented early warning and Bayesian-based decision support system for flood risks in Zeebrugge harbour. Coast Eng. 134:191–202. https://hdl.handle.net/10.1016/j.coastaleng.2017.10.006.

Booij N, Ris RC, Holthuijsen LH. 1999. A third-generation wave model for coastal regions, part I, model description and validation. J Geophys Res C4. 104:7649–7666.

Ferreira O, Plomaritis TA, Costas S. 2019. Effectiveness assessment of risk reduction measures at coastal areas using a decision support system: findings from Emma storm. Sci Total Environ V. 657:124–135.

Garnier E, Ciavola P, Spencer T, Ferreira O, Armaroli C, McIvor A. 2018. Historical analysis of storms events: case studies in France, England, Portugal and Italy. Coast Eng. 134:10–23.

Gómez Lahoz M, Carretero Albiach JC. 2005. Wave forecasting at the Spanish coasts. J Atmos Ocean Sci. 10(4):389–405. doi:10.1080/17417530601127522.

Günther H, Hasselmann S, Janssen PA. 1992. The WAM model cycle 4 (No. DKRZ-TR–4 (REV. ED.)). Deutsches Klimarechenzentrum (DKRZ).

Losada IJ, Lara JL, Guanche R, Gonzalez-Ondina JM. 2008. Numerical analysis of wave overtopping of rubble mound breakwaters. Coast Eng Elsevier. 55(1):47–62.

Pérez-Gómez B, Alvarez Fanjul E, Pérez Rubio S, de Alfonso M, Vela J. 2013. Use of tide gauge data in operational oceanography and sea level hazard warning systems. J Oper Oceanogr. 6(2):1–18.

Pérez-Gómez B, De Alfonso M, Zacharioudaki A, Perez-González I, Álvarez-Fanjul E, Müller M, Marcos M, Manzano F, Korres G, Ravdas M, Tamm S. 2018. Sea level, SST and waves: extremes variability. In: Copernicus marine service ocean state report, issue 2. J Oper Oceanogr. 11(Sup. 1):s13–s16. doi:10.1080/1755876X.2018.1489208.

Pérez-Gómez B, Vela J, Alvarez-Fanjul E. 2008. A new concept of multi-purpose sea level station: example of implementation in the REDMAR network. In: Proceedings of the Fifth International Conference on EuroGOOS, May 2008: Coastal to global operational oceanography: achievements and challenges.

Pérez-Gómez B. 2014. Design and implementation of an operational sea level monitoring and forecasting system for the Spanish coast. PhD Thesis, University of Cantabria (Spain). https://repositorio.unican.es/xmlui/handle/10902/5876.

Pugh DT, Woodworth PL. 2014. Sea-level science: understanding tides, surges, tsunamis and mean sea-level changes. Cambridge: Cambridge University Press. ISBN 9781107028197. 408pp.

Toledano C, Dalphinet A, Lorente P, Renaud R, Alfonso M, Aouf L, Sotillo MG. 2018. Quality information document for Atlantic -Iberian Biscay Ireland- wave reanalysis product, CMEMS web site. https://marine.copernicus.eu/documents/QUID/CMEMS-IBI-QUID-005-006.pdf.

WAMDI Group. 1988. The WAM model—a third generation ocean wave prediction model. J Phys Oceanogr. 18(12): 1775–1810. https://journals.ametsoc.org/doi/abs/10.1175/1520-0485(1988)018%3C1775:TWMTGO%3E2.0.CO;2.

Section 4.7: Predictability of large wave heights in the western Black Sea during the 2018 winter storms

Akpınar A, Bingölbali B, Van Vledder G. 2016. Wind and wave characteristics in the Black Sea based on the SWAN wave model forced with the CFSR winds. Ocean Eng. 126:276–298. doi:10.1016/j.oceaneng.2016.09.026.

Akpınar A, Kömürcü MI. 2012. Wave energy potential along the south-east coasts of the Black Sea. Energy. 42:289–302.

Álvarez Fanjul E, de Pascual Collar Á, Pérez Gómez B, De Alfonso M, García Sotillo M, Staneva J, Clementi E, Grandi A, Zacharioudaki A, Korres G, et al. 2019. Sea level, sea surface temperature and SWH extreme percentiles: combined analysis from model results and in situ observations. In: Schuckmann K, et al., editors, Copernicus marine service ocean state report, issue 3, chapter 2.7. J Oper Oceanogr. doi:10.1080/1755876X.2019.1633075

Aouf L, Lefevre J-M. On the impact of the assimilation of SARAL/AltiKa wave data in the operational wave model MFWAM. 2015.

Bidlot J, Janssen P, Abdalla S. 2005. A revised formulation for ocean wave dissipation in CY29R1. MEMORANDUM RESEARCH DEPARTMENT of ECMWF, April 7, 2005 File: R60.9/JB/0516.

Bidlot J-R, Janssen P, Abdalla S. 2007. A revised formulation of ocean wave dissipation and its model impact. ECMWF Tech. Memo. 509. ECMWF, Reading, United Kingdom. 27pp.

Didenkulova II, Slunyaev AV, Pelinovsky EN, Kharif C. 2006. Freak waves in 2005. Nat Hazards Earth Syst Sci. 6(6):1007–1015.

Divinski BV, Fomin VR, Kosyan RD, Ratner YD. 2019. Extreme wind waves in the Black Sea. Oceanologia. doi:10.1016/j.oceano.2019.06.003.

Divinsky BV, Kosyan RD. 2017. Spatiotemporal variability of the Black Sea wave climate in the last 37 years. Cont Shelf Res. 136:1–19.

Erselcan IÖ, Kükner A. 2017. A numerical analysis of several wave energy converter arrays deployed in the Black Sea. Ocean Eng. 2017(131):68–79.

Forristal GZ. 2007. Wave crest heights and deck damage in hurricanes Ivan, Katrina, and Rita. OTCPaper 18620. Houston: May.

Hersbach H, Janssen P. 1999. Improvements of the short fetch behaviour in the WAM model. J Atmos Oceanic Techn. 16:884–892.

Janssen PAEM. 2008. Progress in ocean wave forecasting. J Comput Phys. 227(7):3572–3594. doi:10.1016/j.jcp.2007.04.029.

Onea F, Rusu E. 2014. An evaluation of the wind energy in the north-west of the Black Sea. Int J Green Energy. 11:465–487.

Onea F, Rusu L. 2017. A long-term assessment of the Black Sea wave climate. Sustainability. 9:1875.

Polonsky AB, Fomin VV, Garmashov AV. 2011. Characteristics of wind waves of the Black Sea. Rep Nat Acad Sci Ukraine. 8:108–112.

Pontes MT. 1998. Assessing the European wave energy resource. J Offshore Mech Arctic Eng ASME. 120:226–231.

Rusu L, Butunoiu D. 2014. Evaluation of the wind influence in modeling the Black Sea wave conditions. Environ Eng Manag J. 13:305–314.

Rusu, E. 2016. Reliability and applications of the numerical wave predictions in the Black Sea. Front Mar Sci. 3. Article no. 95. doi:10.3389/fmars.2016.00095.

Staneva J, Behrens A, Gayer G, Aouf L. 2019. Synergy between CMEMS products and newly available data from SENTINEL. In: Schuckmann K, et al., editors, Copernicus marine service ocean state report, issue 3, chapter 3.3. J Oper Oceanogr. doi:10.1080/1755876X.2019.1633075.

Van Vledder G, Akpinar A. 2016. Spectral partitioning and swells in the Black Sea. Coastal Eng Proc. 35. https://dx.doi.org/10.9753/icce.v35.waves.21, 14. p. 422–424, 441–442: CMEMS QUID: https://marine.copernicus.eu/documents/QUID/CMEMS-BLKSEA-QUID-007-003.pdf; CMEMS QUID: https://marine.copernicus.eu/documents/QUID/CMEMS-BLKSEA-QUID-007-006.pdf

Section 4.8: Small scale ocean weather during an extreme wind event in the Ligurian Sea

Alkire MB, D'Asaro E, Lee C, Perry MJ, Gray A, Cetinić I, Briggs N, Rehm E, Kallin E, Kaiser J, González-Posada A. 2012. Estimates of net community production and export using high-resolution, Lagrangian measurements of O_2, NO_3, and POC through the evolution of a spring diatom bloom in the North Atlantic. Deep Sea Res Pt I. 64:157–174.

Barrick DE. 1971. Theory of HF and VHF propagation across the rough Sea, 2, application to HF and VHF propagation above the sea. Radio Sci. 6(5):527–533.

Bates AE, Helmuth B, Burrows MT, Duncan MI, Garrabou J, Guy-Haim T, Lima F, Queiros AM, Seabra R, Marsh R, et al. 2018. Biologists ignore ocean weather at their peril. Nature. 560(7718):299–301.

Berta M, Bellomo L, Griffa A, Magaldi MG, Molcard A, Mantovani C, Gasparini GP, Marmain J, Vetrano A, Béguery L, et al. 2018. Wind-induced variability in the northern current (northwestern Mediterranean Sea) as depicted by a multi-platform observing system. Ocean Sci. 14:689–710.

Berthon J-F, Zibordi G, Doyle J-P, Grossi S, van der Linde D, Targa C. 2002. Coastal Atmosphere and Sea Time Series (CoASTS), part 2: data analysis NASA Tech. Memo. 20. In: Hooker SB, Firestone ER, editors. Greenbelt, Maryland: NASA Goddard Space Flight Center.

Cattaneo Vietti R, Albertelli G, Aliani S, Bava S, Bavestrello G, Benedetti Cecchi L, Bianchi CN, Bozzo E, Capello M, Castellano M, et al. 2010. The Ligurian Sea: present status, problems and perspectives. Chem Ecol. 26:319–340.

Chronis T, Papadopoulos V, Nikolopoulos EI. 2011. QuickSCAT observations of extreme wind events over the Mediterranean and Black Seas during 2000–2008. Int J Climatol. 31:2068–2077.

D'Alimonte D, Mlin F, Zibordi G, Berthon JF. 2003. Use of the novelty detection technique to identify the range of applicability of empirical ocean color algorithms. IEEE Trans Geosci Remote Sens. 41(12):2833–2843.

D'Alimonte D, Zibordi G. 2003. Phytoplankton determination in an optically complex coastal region using a multilayer perceptron neural network. IEEE Trans Geosci Remote Sens. 41(12):2861–2868.

D'Asaro EA, Shcherbina AY, Klymak JM, Molemaker J, Novelli G, Guigand CM, Haza AC, Haus BK, Ryan EH, Jacobs GA, et al. 2018. Ocean convergence and the dispersion of flotsam. Proc Nat Acad Sci. 115 (6):1162–1167.

Gildor H, Fredj E, Steinbuck J, Monismith S. 2009. Evidence for submesoscale barriers to horizontal mixing in the ocean from current measurements and aerial photographs. J Phys Oceanogr. 39:1975–1983.

Grilli F, Pinardi N. 1998. The computation of Rossby radii of deformation for the Mediterranean Sea. MTP News. 6(4):4–5.

Gurgel KW, Essen HH, Kingsley SP. 1999. High-frequency radars: physical limitations and recent developments. Coast Eng. 37(3–4):201–218.

Lévy M, Ferrari R, Franks PJS, Martin AP, Rivière P. 2012. Bringing physics to life at the submesoscale. Geophys Res Lett. 39:L14602.

Mahadevan A, Campbell JW. 2002. Biogeochemical patchiness at the sea surface. Geophys Res Lett. 29(19):1926.

Mahadevan A, Tandon A. 2006. An analysis of mechanisms for submesoscale vertical motion at ocean fronts. Ocean Model. 14(3–4):241–256.

Mahadevan A, Thomas LN, Tandon A. 2008. Comment on "Eddy/wind interactions stimulate extraordinary mid-ocean plankton blooms". Science. 320(5875):448.

Mc Williams JK. 2016. Submesoscale currents in the ocean. Proc R Soc A. 472:20160117.

Thomas LN, Tandon A, Mahadevan A. 2013. Submesoscale processes and dynamics. In: Hecht MW, Hasumi H, editors. Ocean modeling in an Eddying regime.

Volpe G, Santoleri R, Vellucci V, Ribera d'Alcala R, Marullo S, D'Ortenzio F. 2007. The colour of the Mediterranean Sea: global versus regional bio-optical algorithms evaluation and implication for satellite chlorophyll estimates. Remote Sens Environ. 107:625–638.

Zatsepin A, Kubryakov A, Aleskerova A, Elkin D, Kukleva O. 2019. Physical mechanisms of submesoscale eddies generation: evidences from laboratory modeling and satellite data in the Black sea. Oc. Dynam.

Section 4.9: Drifter observations and Lagrangian tracking of the 2018 easterly wind event in the North Sea

Aden C, Stephan K. 2017. Web-based citizen involvement in research into pathways and hotspots of marine litter in the Southern North Sea. GI_Forum. 2017(2):60–77. doi:10.1553/giscience2017_02_s60.

Backhaus J. 1989. The North Sea and the climate. Dana A J Fish Mar Res. 8:69–82.

Christensen A, Daewel U, Jensen H, Mosegaard H, St. John M, Schrum C. 2007. Hydrodynamic backtracking of fish larvae by individual-based modelling. Mar Ecol Prog Ser. 347:221–232. doi:10.3354/meps06980.

Dagestad K-F, Röhrs J, Breivik Ø, Adlandsvik B. 2018. Opendrift v1.0: a generic framework for trajectory modeling. Geosci Model Dev. 11:1405–1420. doi:10.5194/gmd-11-1405-2018.

Emeis K, van Beusekom J, Callies U, Ebinghaus R, Kannen A, Kraus G, et al. 2015. The North sea — a shelf sea in the anthropocene. J Mar Syst. 141:18–33. doi:10.1016/j.jmarsys.2014.03.012.

Garcia-Soto C, van der Meeren GI, Busch JA, Delany J, Domegan C, et al. 2017. Advancing Citizen Science for Coastal and Ocean Research. In: French V, Kellett P, Delany J, McDonough N, editors. Position Paper 23 of the European Marine Board, Ostend, Belgium. 112 pp. ISBN: 978-94-92043-30-36.

Gutow L, Ricker M, Holstein JM, Dannheim J, Stanev EV, Wolff J-O. 2018. Distribution and trajectories of floating and benthic marine macrolitter in the southeastern North Sea. Mar Poll Bull. 131–A:763–772. doi:10.1016/j.marpolbul.2018.05.003.

Jacob B, Stanev EV. 2017. Interactions between wind and tidally induced currents in coastal and shelf basins. Ocean Dynam. 67:1263–1281. doi:10.1007/s10236-017-1093-9.

Johnson ES, Bonjean F, Lagerloef GSE, Gunn JT, Mitchum GT. 2007. Validation and error analysis of OSCAR sea surface currents. J Atmos Ocean Tech. 24(4):688–701. doi:10.1175/JTECH1971.1.

Madec G. 2008. NEMO ocean engine (Note du Pole de Modélisation, 27) France. Institut Pierre-Simon Laplace (IPSL). 300 p.

Maier-Reimer E. 1977. Residual circulation in the North Sea due to the M2-tide and mean annual wind stress. Deutsche Hydrografische Zeitschrift. 30(3):69–80. doi:10.1007/BF02227045.

Mathis M, Elizalde A, Mikolajewicz U, Pohlmann T. 2015. Variability patterns of the general circulation and sea water temperature in the North Sea. Prog Oceanogr. 135:91–112. doi:10.1016/j.pocean.2015.04.009.

Meyerjürgens J, Badewien TH, Garaba SP, Wolff J-O, Zielinski O. 2019. A state-of- the-art compact surface drifter reveals pathways of floating marine litter in the German bight. Front Mar Sci. 6:58. doi:10.3389/fmars.2019.00058.

van der Molen J, Rogers SI, Ellis JR, Fox CJ, McCloghrie P. 2007. Dispersal patterns of the eggs and larvae of spring-spawning fish in the Irish Sea, UK. J Sea Res. 58(4):313–330. doi:10.1016/j.seares.2007.07.003.

O'Dea EJ, Arnold AK, Edwards KP, Furner R, Hyder P, Martin MJ, et al. 2012. An operational ocean forecast system incorporating NEMO and SST data assimilation for the tidally driven European north-west shelf. J Oper Oceanogr. 5(1):3–17. doi:10.1080/1755876X.2012.11020128.

Otto L, Zimmerman J, Furnes G, Mork M, Saetre R, Becker G. 1990. Review of the physical oceanography of the North Sea. Neth J Sea Res. 26(2):161–238. doi:10.1016/0077-7579(90)90091-T.

Ricker M, Stanev EV. 2020 Circulation of the European north-west shelf: a Lagrangian perspective. Ocean Sci. 16(3):637–655. doi:10.5194/os-16-637-2020.

Röhrs J, Christensen KH, Hole LR, Brostrom G, Drivdal M, Sundby S. 2012. Observation-based evaluation of surface wave effects on currents and trajectory forecasts. Ocean Dynam. 62:1519–1533. doi:10.1007/s10236-012-0576-y.

Schöneich-Argent RI, Hillmann F, Cordes D, Wansing RAD, Merder J, Freund JA, Freund H. 2019. Wind, waves, tides, and human error? – influences on litter abundances and composition on German North Sea coastlines: an exploratory analysis. Mar Poll Bull. 146:155–172. doi:10.1016/j.marpolbul.2019.05.062.

Stanev EV, Badewien TH, Freund H, Grayek S, Hahner F, Meyerjürgens J, Ricker M, Schöneich-Argent RI, Wolff J-O, Zielinski O. 2019. Extreme westward surface drift in the North Sea: public reports of stranded drifters and Lagrangian tracking. Cont Shelf Res. 177:24–32. doi:10.1016/j.csr.2019.03.003.

Sündermann J, Pohlmann T. 2011. A brief analysis of North Sea physics. Oceanologia. 53(3). doi:10.5697/oc.53-3.663.

The WAVEWATCH III Development Group. 2016. User manual and system documentation of WAVEWATCH III version 5.16, vol. 329. NOAA/NWS/NCEP/MMAB Technical Note, pp. 326 (+ Appendices).

Willmott CJ. 1981. On the validation of models. Phys Geogr. 2(2):184–194. doi:10.1080/02723646.1981.10642213.

Section 4.10: Coastal ocean variability related to the most extreme Ebro River discharge over the last 15 years

Dai A, Qian TT, Trenberth KE, Milliman JD. 2009. Changes in continental freshwater discharge from 1948 to 2004. J Climate. 22:2773–2792. doi:10.1175/2008JCLI2592.1.

Fanjul EÁ, Sotillo MG, Gomez BP, Valdecasas JG, Rubio SH, Atienza IS, Mestres M. 2018. The Samoa initiative: operational oceanography at the service of the ports. https://www.doi.org/10.17125/gov2018.ch27.

Fernández-Nóvoa D, Mendes R, deCastro M, Dias JM, Sánchez-Arcilla A, Gómez-Gesteira M. 2015. Analysis of the influence of river discharge and wind on the Ebro turbid plume using MODIS-Aqua and MODIS-Terra data. J Mar Syst. 142:40–46, ISSN 0924-7963. doi:10.1016/j.jmarsys.2014.09.009.

García Sotillo M, Cerralbo P, Lorente P, Grifoll M, Espino M, Sánchez-Arcilla A, Álvarez-Fanjul E. 2019. Coastal ocean forecasting in Spanish ports: the SAMOA operational service. J Oper Oceanogr. doi:10.1080/1755876X.2019.1606765.

Grifoll Colls M, Navarro J, Pallarès López E, Ràfols Bundó L, Espino Infantes M, Palomares A. 2016. Ocean–atmosphere–wave characterisation of a wind jet (Ebro shelf. NW Mediterranean Sea). Nonlinear Proc Geophys. 23 (3):143–158. doi:10.5194/npg-23-143-2016.

Juza M, Mourre B, Renault L, Gómara S, Sebastián K, Lora S, Beltran JP, Frontera B, Garau B, Troupin C, et al. 2016. SOCIB operational ocean forecasting system and multi-platform validation in the Western Mediterranean Sea. J Oper Oceanogr. 9(Supp. 1):s155–s166. https://www.doi.org/10.1080/1755876X.2015.1117764.

Lorente P, Piedracoba S, Soto-Navarro J, Alvarez-Fanjul E. 2015. Evaluating the surface circulation in the Ebro delta (northeastern Spain) with quality-controlled high-frequency radar measurements. Ocean Sci. 11:921–935. doi:10.5194/os-11-921-2015.

Martín-Vide JP, Mazza de Almeida GA, Helmbrecht J, Ferrer C, Rojas Lara DL. 2004. Estudio técnico-económico de alternativas del programa para corregir la subsidencia y regresión del delta del Ebro. Technical Report (unpublished).

Mourre B, Aguiar E, Juza M, Hernandez-Lasheras J, Reyes E, Heslop E, Escudier R, Cutolo E, Ruiz S, Mason E, Pascual A, Tintoré J. 2018. Assessment of high-resolution regional ocean prediction systems using muli-platform observations: illustrations in the Western Mediterranean Sea. In: Chassignet E, Pascual A, Tintoré J, Verron J, editors. "New Frontiers in Operational Oceanography". GODAE Ocean View, 663-694. https://www.doi.org/10.17125/gov2018.ch24

Palanques A, Plana A, Maldonado A. 1990. Recent influence of man on the Ebro margin sedimentation system, northwestern Mediterranean Sea. Mar Geol. 95(3):247–263. doi:10.1016/0025-3227(90)90119-5.

Ràfols Bundó L, Grifoll Colls M, Espino Infantes M. 2019. Wave–current interactions in a wind-jet region. Ocean Sci (Online). 15(1):1–20. doi:10.5194/os-15-1-2019.

Ràfols L, Pallares E, Espino M, Grifoll M, Sánchez-Arcilla A, Bravo M, Sairouní A. 2017. Wind-wave characterization in a wind-jet region: the Ebro Delta case. J Mar Sci Eng. 5 (1):12. https://www.doi.org/10.3390/jmse5010012.

Raicich F. 1996. On the fresh balance of the Adriatic Sea. J Mar Syst. 9(3–4):305–319. doi:10.1016/S0924-7963(96)00042-5.

Rovira A, Ibáñez C. 2007. Sediment management options for the lower Ebro River and its delta. J Soils Sediments. 7 (5):285–295. doi:10.1065/jss2007.08.244.

Sánchez-Arcilla A, Jiménez JA, Stive MJF, Ibanez C, Pratt N, Day Jr JW, Capobianco M. 1996. Impacts of sea-level rise on the Ebro Delta: a first approach. Ocean Coast Manage. 30(2–3):197–216. doi:10.1016/0964-5691(95)00063-1.

Sánchez-Arcilla A, Lin-Ye J, García-León M, Gràcia V, Pallarès E. 2019. The land–sea coastal border: a quantitative definition by considering the wind and wave conditions in a wave-dominated, micro-tidal environment. Ocean Sci. 15:113–126. doi:10.5194/os-15-113-2019.

Sánchez-Arcilla A, Simpson JH. 2002. The narrow shelf concept: couplings and fluxes, Cont Shelf Res. 22(2):153–172, ISSN 0278-4343. doi:10.1016/S0278-4343(01)00052-8.

Teruzzi A, Bolzon G, Salon S, Lazzari P, Solidoro C, Cossarini G. 2018. Assimilation of coastal and open sea biogeochemical data to improve phytoplankton simulation in the Mediterranean Sea. Ocean Modell. 132:46–60. ISSN 1463-5003. doi:10.1016/j.ocemod.2018.09.007.